Stability of $nTiO_2$ Particles and Their Attachment to Sand: Effects of Humic Acid at Different pH

by

© Yang Wu

A Thesis submitted to the

School of Graduate Studies

in partial fulfillment of the requirements for the degree of

Master of Science

Department of Earth Sciences

Memorial University of Newfoundland

June 2015

St. John's Newfoundland

ABSTRACT

Influence of humic acid (HA) on stability and attachment of $nTiO_2$ particles to sand was investigated. Results showed that HA can either promote or hinder $nTiO_2$ stability, depending on pH and HA concentration. HA can either enhance or reduce $nTiO_2$ attachment to Fe oxyhydroxide coating at pH 5, depending on HA concentration. Results further showed that at pH 5, Fe oxyhydroxide coating reduced $nTiO_2$ attachment to sand in the absence of HA but increased $nTiO_2$ attachment in the presence of low concentration of HA. Derjaguin-Landau-Verwey-Overbeek (DLVO) theory was invoked to analyze particle-to-particle and particle-to-sand interactions in order to elucidate the roles of pH, HA, quartz, and Fe coating in controlling $nTiO_2$ stability and attachment. Overall, this study showed that changes in zeta potential of $nTiO_2$ and Fe coating due to pH changes and/or HA adsorption are the key factors that influence stability and attachment of $nTiO_2$.

ACKNOWLEDGEMENTS

I would like to express my gratitude to my supervisor, Dr. Tao Cheng, for offering mentorship all the time during my research. He loves his research work and helps me a lot whenever I need help. Dr. Cheng is the most amazing supervisor I ever met.

My appreciation also goes to Dr. Baiyu Zhang for serving on my Master committee and for providing lab equipment (such as spectrophotometer and centrifuge machine) and valuable advices on my research.

Special thanks are given to Dr. Valerie Booth and Ms. Donna Jackman for the use of zetasizer, Lakmali Hewa for the digestion and ICP-MS measurements, and Wanda Aylward for her help with XRD and SEM measurements.

Besides, I gratefully acknowledge financial support from the Natural Sciences and Engineering Research Council of Canada (NSERC) Discovery Grant and School of Graduate Studies Fellowship provided by Memorial University of Newfoundland.

The last but not least, I need to thank all of my friends for being with me when I felt depressed, and I would like to thank my family for their help and support in my research and life.

Table of contents

List of Tables

List of Figures

List of abbreviations and symbols

cm – centimeter

cm/min – centimeter per minute

cm^3 – cubic centimeter

EDL– electrical double layer

EDX– energy dispersive X-ray

Fe – iron

g – gram

g/cm^3 – grams per cubic centimeter

HA – humic acid

ICP-MS – inductively coupled plasma mass spectrometry

IEP – isoelectric point

kg – kilogram

L – liter

M – mole

MAC – maximum acceptable concentration

mg – milligram

ml – milliliter

mg/kg – milligrams per kilogram

mg/L –milligrams per liter

mm – millimeter

mol/L – moles per liter

nm – nanometer

NOM – natural organic matter

pH – power of hydrogen; a measure of hydrogen ion activity

PZC – point of zero charge

SEM – scanning electron microscope

vdW – van der Waals

XRD – X-ray diffraction

℃ – Degree Celsius

µg – microgram

µg/L – micrograms per liter

µm – micrometer

List of Appendices

Chapter 1: Introduction

1.1 Natural occurrence of nanoparticle

Nanoparticles are traditionally defined as particles in the range of 1-100 nm in size. Nanoparticles form suspensions rather than solutions, as they are particles instead of dissolved molecules. Due to their different transport behavior when comparing micron to sub-micron sized particles, the term "nanoparticles" is now often ascribed to any particle or colloid less than 1 μm.

The production of synthetic nanomaterials is increasing in the last decades due to the wide use of nanoparticles in commercial products, industries, and mining operations. No environmental regulation has been set up to directly control the release of nanoparticles into the environment yet. Large quantities of manufactured nanoparticles were observed to enter the natural environment either through effluent water from waste water treatment plants (Kiser et al., 2009, Miller et al. 2012) or through biosolids and mining operations (Jaynes and Zartman, 2005).

Exposure of organisms to the nanoparticles in surface and marine water is a potential concern as nanoparticles' biological impacts are not fully understood (Miller et al. 2012). Nanoparticles are toxic to mice, rats, aquatic organisms and human cells (Hund-Rinke and Simon, 2006; Wiesner et al., 2006; Warheit et al., 2007; Battin et al., 2009; Brunet et al., 2009; Liu et al., 2009; Madl and Pinkerton, 2009), and their toxicity are much stronger than bulk materials due to their high surface areas. Besides, another major concern about nanoparticles is their ability to associate with other dissolved contaminants in groundwater, which might facilitate the transport of contaminants in sub-surface environment (Grolimund and Borkovec, 2005; Karathanasis et al., 2005; Sun et al., 2007;

Zhang et al., 2007; Plathe et al., 2010; Wang et al., 2014; Wang et al., 2015). Therefore, our limited knowledge on their potential environmental and health effects has caused many public concerns.

1.2 Stability, dispersion and transport of nanoparticle in subsurface environment

Dispersed nanoparticles in the environment implies a higher mobility and a greater potential for risk of exposure since well dispersed nanoparticles will be transported to longer distances, exhibit longer effective persistence, and be potentially involved in particle-facilitated contaminant movement (Ryan and Elimelech, 1996; Sen and Khilar, 2006; Zhuang et al., 2003).

Stable nanoparticles mean the particles should not settle down while it is in dispersed state. If aggregation occurred, the hydrodynamic diameter will increase which leads the sedimentation of nanoparticles. A common method to determine the stability of the nanoparticle is to measure whether its light absorbance is stable during a certain time span. In addition to the measurement of light absorbance by spectrophotometer, zeta potential and hydrodynamic diameter should also be monitored. Zeta potential can reflect the surface potential on the particle surface which has a direct impact on particle-particle interaction forces. Generally, if the absolute value of zeta potential is below 10 mV, nanoparticles will tend to aggregate which results in the increase of hydrodynamic diameter. Although many nanomaterials are produced with a small targeted size, nanoparticles can frequently aggregate to larger particles (Wiesner et al., 2006). Anatase particles, one of the three mineral forms (anatase, rutile, ilmenite) of titanium dioxide, have a tendency to form aggregates with a narrow size distribution of ~200 nm, which are stable in pure water (Wiesner et al., 2006). The stability of nanoparticles in water solution is controlled by the

electrical double layer forces, which is influenced by solution pH and surface charge. (Kallay and Zalac, 2002; Dunphy Guzman et al., 2006). In the case of metal oxide particles, pH will change the surface charge. Two nanoparticles have similar surface potentials, resulting in repulsive double layer interactions except when the surface potential is zero (Dunphy Guzman et al., 2006). Because the degree of repulsion is determined by the difference between the pH of the solution and the pH_{zpc} (point of zero charge), the repulsion decreases when one approaches the pH_{zpc} (Dunphy Guzman et al., 2006). Dunphy Guzman et al. (2006) reported that over 80% of suspended $nTiO_2$ were mobile in micro-channels over the pH range of 1-12, except where the pH was close to the zero point change for $nTiO_2$ (pH_{zpc}=6.2). Inorganic salts also have a direct effect on nanoparticle aggregation (Snoswell et al., 2005), and additives such as surfactants and organic solvents can significantly improve the dispersion of $nTiO_2$ in aqueous solutions (Hsu and Chang, 2000; Tkachenko et al., 2006). For example, He et al. (2008) found particle aggregate size can increase with increasing concentration of background electrolyte. Joo et al. (2009) concluded that the addition of carboxymethyl cellulose to the anatase $nTiO_2$ resulted in the formation of a water-stable suspension.

Natural organic matter (NOM) has important influences on most physicochemical reactions, and it is expected to play an important role in the fate and transport of nanoparticles. Humic acid is frequently reported for effectively stabilizing nanoparticle suspensions by steric repulsion effect (Chen and Elimelech, 2007; Hyung et al., 2007). In soil systems, fulvic acids and humic acids are the major source of dissolved organic matter, and they favor the stabilization of nanoparticles because organic matters is well dispersed in soil solutions so that it can be adsorbed by nanoparticles. For example, humic acid-

coated magnetite nanoparticles can form stable suspension (Illés and Tombácz 2006), which prevent particle aggregation or sedimentation over a wide range of solution pH. Many mechanisms, such as electrostatic attractive forces, ligand exchange, and cation bridging, can be responsible for natural organic matter (NOM) adsorption on nanoparticles.

Knowledge of the transport of nanoparticles in water saturated porous media is important for developing an understanding of the potential mobility of nanoparticles in the soil environment and their potential risks to groundwater. The transport of nanoparticles in porous media is impeded by two processes, 1) straining or physical filtration where the particle is larger than the pore and is trapped and 2) physicochemical removal where the particle is removed from solution by interception, diffusion and sedimentation (Yao et al., 1971, Nowack and Bucheli, 2007). Dunphy Guzman et al. (2006) designed a two-dimensional model of porous media column, and found the passage of anatase slowly increased with time, suggesting that the mobility increased with time as deposition sites became saturated. Groundwater flow velocities could also influence transport and deposition of nanoparticles and an increase in the flow velocity increase nanoparticle concentration in column effluent (Lecoanet et al., 2004). In summary, nanoparticle transport can be influenced by water chemistry (pH, natural organic matter); groundwater flow velocity; nanoparticle surface properties; and porous media type.

However, most of the studies on nanoparticle transport were conducted in well-defined porous media, therefore they do not accurately represent the variety of mineral surface types and surface charge heterogeneities encountered in real soil systems. Soil properties such surface area, surface charge, types of minerals and organic matters will affect the aggregation and transport of nanoparticles (Kretzschmar et al., 1997). Therefore,

the environmental implications of these studies using well-defined porous media are limited. Joo et al. (2009) studied the influence of carboxymethyl cellulose on the transport of titanium dioxide nanoparticles in metal (hydro)oxide-coated sands, and found the mobility of carboxymethyl cellulose-anatase nanoparticles was retarded by the presence of amorphous Fe and Al hydroxide coating.

1.3 Stability of $nTiO_2$ and their attachment to sand collector

Most of the previous studies about nanoparticle transport used relatively inert nanoparticles such as latex in their research. However, titanium dioxide nanoparticles ($nTiO_2$) were reported as being one of the most widely used nanoparticle by a recent study (Robichaud et al., 2009). $nTiO_2$ are commonly used in commercial products, such as cosmetics, sunscreens, paints, coatings. $nTiO_2$ has also been used for the photocatalytic degradation of various pollutants in water, air and soil (Higarashi and Jardim, 2002; Nagaveni et al., 2004; Quan et al., 2005; Aarthi and Madras, 2007) and for immobilization of anions in soil (Mattigod et al., 2005). $nTiO_2$ is an effective disinfectant used to purify sewage wastewater (Miller et al. 2012). Unknown quantities of $nTiO_2$ are entering the environment, primarily through industrial and sewage wastewater discharges (Miller et al. 2012). $nTiO_2$ may pose potential risks to human health and ecosystems when applied in commercial quantities (Wiesner et al., 2006). It is essential to understand the fate and transport of $nTiO_2$ in the environment in order to assess possible routes of exposure to humans and the ecosystem.

Aggregation of $nTiO_2$ particles affects the stability and mobility of $nTiO_2$ in groundwater (Chowdhury et al. 2012). $nTiO_2$ normally exist as aggregates in water instead of individual nanoscale particles (Chen et al., 2012; French et al., 2009; Lin et al., 2010;

Lee et al., 2015). Aggregation of $nTiO_2$ are influenced by factors such as pH, ionic strength, surfactants and natural organic matters (NOM) such as humic acid (HA) (Hsu and Chang, 2000; Tkachenko et al., 2006, Dunphy Guzman et al., 2006; Fang et al., 2009; French et al., 2009, Godinez and Darnault, 2011). $nTiO_2$ water suspensions are stable when pH deviates from the point of zero charge (PZC) of $nTiO_2$, and NOM was found to enhance $nTiO_2$ stability via repulsive electrostatic and steric forces afforded by NOM adsorption to $nTiO_2$ (Chen et al., 2012; Chen and Elimelech, 2007; Espinasse et al., 2007; Navarro et al., 2008).

Physiochemical attachment to collector (transport medium grain) is a main mechanism that immobilizes nano- and micro-scale particulate matters in water-saturated porous media and has been shown to be influenced by physical properties of the particulate matter and transport medium (size, morphology, surface potential, and mineral composition), as well as water chemistry (pH, ionic strength, and NOM) (Wang et al, 2012b; Pensini et al., 2013; Lanphere et al., 2014; Jung et al., 2014). Most previous studies on particle transport focused on natural colloids (i.e. clays, quartz, bacteria, viruses, and particulate humic substances), which are negatively charged in the pH range of natural water due to their low PZC. It was found that attachment of these negatively charged colloids to quartz sand decreases with increasing pH, and that NOM decreases colloid attachment due to the increased repulsive electrostatic and steric forces attributable to NOM adsorption to colloids and transport medium. $nTiO_2$, in contrast, have a near neutral PZC (Boncagni et al., 2009; Han et al., 2014), suggesting that surface charge of $nTiO_2$ in natural water may change from positive to negative due to pH changes or due to adsorption of charged species such as NOM. Therefore, pH and NOM may influence $nTiO_2$

attachment and transport in a different manner. Attachment and transport of positively charged colloids have received only limited attention. Han et al. (2014) reported that $nTiO_2$ transport in water-saturated Fe oxide coated sand columns increased in the presence of HA, and that 10 mg/L HA caused a greater degree of increase than 1 mg/L HA. At high NOM concentrations, NOM adsorbed to $nTiO_2$ could neutralize and reverse the positive charges of $nTiO_2$ and therefore decrease $nTiO_2$ attachment and increase its transport. Concentration of NOM in groundwater, however, is generally low (0.25 to 5 mg/L) (Crittenden et al., 2012, Chowdhury et al., 2012). It can be hypothesized that at certain low NOM concentration ranges, surface charges of $nTiO_2$ are only partially neutralized by adsorbed NOM so that increase in aggregation and attachment, and therefore decrease in $nTiO_2$ transport are expected. However, there have been no studies on the influence of NOM on $nTiO_2$ at low concentrations representing groundwater conditions. Similar to $nTiO_2$, Fe oxyhydroxides have PZC values that are within the pH range of natural water, and the ubiquitous presence of patchy Fe oxyhydroxide coating on natural sediment grains could provide positively charged sites that have been shown to strongly attract negatively charged natural colloids and decrease their transport (Joo et al., 2009; Wang et al., 2012b, 2013; Foppen et al., 2006; Lin et al., 2011). It was also found that surface charge of Fe oxyhydroxides can change from positive to negative due to increase in pH and/or NOM adsorption (Abudalo et al., 2010; Hu et al., 2014). In natural water, $nTiO_2$ and Fe oxyhydroxides can be either like-charged or oppositely-charged depending on water chemistry conditions. As a result, Fe oxyhydroxides coatings are not always expected to promote $nTiO_2$ attachment. Experimental studies are necessary to determine how water

chemistry conditions affect the attachment and transport of $nTiO_2$ in the presence of Fe oxyhydroxides coating.

1.4 DLVO theory and filtration theory

Derjaguin-Landau-Verwey-Overbeek (DLVO) theory developed by Derjaguin and Landau (1941) and Verwey and Overbeek (1948) and filtration theory developed by Yao (1971) are commonly used to describe transport and attachment of colloids to porous media.

DLVO theory describes the van der Waals (vdW) and electrostatic and electrical double layer (EDL) forces occurring between two approaching surfaces. vdW forces are caused by momentary multipoles occurring between the particles at the molecular level, and are almost exclusively attractive. EDL forces are caused by the ions associating with the surface in solution, balancing out the charge of the surface; under most conditions, these forces cause repulsion when the double layers overlap. DLVO theory is the prevailing theory used in colloid transport to predict the possible forces occurring between colloids and a porous medium surface to determine the potential for attachment.

Filtration theory is used to predict colloid removal by filters for water and wastewater treatment, describing the physical forces acting on a particle during transport in a porous medium (diffusion, interception, sedimentation) and chemical interaction forces that result in the attachment of colloid to the grain surface (Yao et al., 1971). Generally, the porous media is taken as the “filter” or “collector” in filtration theory. The classical colloid filtration theory is used to determine the theoretical particle deposition distribution.

Under favorable attachment conditions, while the particle and the porous media are oppositely charged, both filtration theory and DLVO theory work well to depict colloid retention and transport because vdW interactions are always dominant while repulsive forces are negligible. Under unfavorable conditions, a typical colloid DLVO energy profile in mid-range ionic strength solution chemistries consists of a large attractive primary minimum immediately adjacent to the surface due to vdW interactions, a repulsive energy barrier somewhere between 10-500 nm from the surface due to EDL interactions, and potentially a small secondary attractive minimum further away from the surface than the repulsive barrier due to combination of vdW and EDL forces. While nanoparticles are less likely to be affected by straining than larger colloids due to their small size, attachment (sorption to the grain surface) is considered as the dominant mechanism in this work.

1.5 Thesis objectives

The objectives of this study are to better understand (1) the stability of $nTiO_2$ under various low HA concentration typically observed in groundwater systems ; (2) the influence of HA on the attachment of $nTiO_2$ to clean quartz sand and Fe-oxyhydroxide coated sand; and (3) the influence of HA on the transport of $nTiO_2$ in clean quartz sand column and Fe oxyhydroxide coated sand column. Systematic batch experiments including stability test, adsorption isotherms, and characterizations of nanoparticle and sand were described in Chapter 2 and 4. Interaction energies between $nTiO_2$ (particle to particle) based on classical Derjaguin-Landau-Verwey-Overbeek (DLVO) theory were described in Chapter 3 and 4. Interaction energies between $nTiO_2$ and sands (particle to plate) by extended classical DLVO theory which took physical heterogeneity and chemical

heterogeneity into consideration were described in Chapter 3, 4 and Appendix 3. $nTiO_2$ transport in porous media was described in Appendix 9.

Chapter 2: Materials and methods

2.1. $nTiO_2$ suspension and HA stock solution

Aeroxide^{TM} TiO_2 P25 powder with > 99.5% purity (Fisher Scientific) was used for preparation of $nTiO_2$ water suspensions. According to the manufacturer, the specific surface area (BET) of the powder and the average particle size of $nTiO_2$ were 50 $\pm$15 m^2/g and 21 nm respectively. Crystalline size and structure of the P25 powder were determined using powder X-ray diffraction (XRD). XRD analyses were performed using Rigaku Ultima IV diffractometer with Cu Kα radiation and operating at 40 kV and 44 mA. The samples were scanned from 2θ = 5° to 90° at a scan rate of 1°/min. The raw data were processed using the MDI Jade computer program and databases from International Centre for Diffraction Database (ICDD) and the Inorganic Crystal Structure Database (ICSD).

Deionized water (DI water) and ACS grade chemicals were used to prepare $nTiO_2$ water suspensions and HA stock solution. Aeroxide^{TM} TiO_2 P25 powder was weighed using an analytical balance and suspended in 1 mM background NaCl solution to achieve desired concentration of $nTiO_2$ (20−50 mg/L). pH of the suspension was adjusted to 5, 7 or 9 by adding small volumes of 0.1 M HCl or NaOH solution. The added amounts of HCl and NaOH solutions were small so that their influence on the volume and ionic strength of the solution was negligible. The $nTiO_2$-water mixture was then shaken and sonicated by a Branson Digital Sonifier (Crystal Electronics) for 30 min with 200 W power to disperse $nTiO_2$ particles.

To prepare HA stock solution, 0.050 g humic acid (HA) powder (Alfa Aesar) was weighed using an analytical balance, dissolved in 500 mL 1 mM background NaCl solution, and filtered through a 0.1 μm polyethersulfone membrane filter (Pall Life Sciences). The

filtration process was repeated three times, each time using a clean filter membrane. Our tests showed that HA solution thus prepared can pass through the 0.1 μm polyethersulfone membrane filter. HA concentration of the HA stock solution was determined to be 33 mg DOC (dissolved organic carbon)/L by a Shimadzu TOC-V analyzer. The HA stock solution was stored in darkness at 4 ℃ for subsequent use.

2.2. Preparation and characterization of clean quartz sand, Fe oxyhydroxide-coated quartz sand, and Fe oxyhydroxide powder

Quartz silica sand (U.S. Silica, Ottawa, Illinois, USA) was sieved using stainless steel sieves and the fraction with the size range of 0.425−0.600 mm was used in our experiments. Upon receiving from the manufacturer, the quartz grains were coated with trace quantities of metal oxides and organics, which influence surface charge and may promote nanoparticle deposition (Lenhart et al., 2002). The following procedure was used to clean the sand. The sand was boiled in 50% HNO_3 for 2 hours and then soaked in the acid for another 12 hours to dissolve metal oxides and organics. After decanting the acid, 0.1 M NaOH was used to wash the sand until solution pH reached near-neutral. The sand was then rinsed by deionized water for 10 times before soaked in 0.01 M NaOH solution for 12 hours to remove any remaining small particles, after which the sand was rinsed with deionized water until solution pH approached 7, and oven dried at 120 ℃. Finally, the sand was rinsed 10 times by deionized water to remove small particles until the supernatant had an absorbance < 0.004 measured by a GENESYS™ 10S UV-visible spectrophotometer (Thermo Scientific) at a wavelength of 368 nm.

Fe oxyhydroxide coated quartz sand (referred as “Fe coated sand” thereafter) was prepared following the procedure described by Mills et al. (1994). 200 g of quartz sand was

added to each 1 L HDPE bottle containing 20 g $FeCl_3$ dissolved in 400 ml deionized water. The initial pH of the solution was approximately 1.4. This mixture was placed on a shaker table, and 20 ml 1 M NaOH solution was added gradually until the pH reached 4.0. Small portions (1−2 ml) of 1 M NaOH was then added and pH was monitored a few minutes after each portion of NaOH addition. Approximately 250-300 ml 1 M NaOH was required for each bottle to buffer the pH around 4.5−5.0. After the pH was buffered, the mixture was shaken vigorously for 24−35 hours on a shaker table to coat the sand with Fe oxyhydroxide. The coated sand was then rinsed with deionized water multiple times. After that, the sand was soaked in 0.01 M NaOH solution for 12 hour to remove small particles. Finally, the sand was rinsed with deionized water and oven dried at 120 ℃. The Fe coated sand from each bottle was combined and well mixed before used in subsequent experiments.

Fe oxyhydroxide powder was prepared using a procedure similar to that for Fe coated sand. 2 g $FeCl_3$ were dissolved in 40 ml DI water and small portions (around 5-10 ml) of 1 M NaOH were added gradually until solution pH reached 5. The mixture was then shaken vigorously for 24-35 hours and centrifuged at 5000 rpm for 1 h. The supernatant was decanted and the residual solids were suspended in DI water for rinsing and next round of centrifugation. The rinsing process was repeated three times before the residual solids were oven dried at 120 ℃.

Fe concentration of Fe coated sand and Fe oxyhydroxide powder was determined by DCB (dithionite-citrate-bicarbonate) extraction method (Jackson et al., 1986) as 146 ±2.5 mg Fe/kg sand and 58.5 ±1.5 mg Fe/mg powder respectively. Surface morphology of the clean quartz sand and Fe coated sand was visualized by secondary electron scanning electron microscopy (SEM). Backscatter SEM coupled with energy dispersive X-ray (EDX)

were used to quantify the fraction of Fe coated sand surface that was covered by Fe oxyhydroxides (Abudalo et al., 2005; Wang et al., 2012b).

2.3. Zeta potential (ZP) and hydrodynamic diameter (HDD) measurement

Zeta potential (ZP) and/or hydrodynamic diameter (HDD) of $nTiO_2$ suspension, quartz sand, and Fe oxyhydroxides were measured using a Zetasizer Nano ZS (Malvern). Before each measurement, a well characterized standard sample (100 nm latex nanoparticle) was used to calibrate the instrument. 20 mg/L $nTiO_2$ suspensions in 1mM NaCl solution were prepared at pH, 5, 7, and 9 (described in Section 2.1) for ZP and HDD measurement.

To measure ZP of quartz sand, the quartz sand was crushed and suspended in 1 mM NaCl solution at pH 5 and 9. The suspensions were sonicated by a Branson Digital Sonifier for 60 min with 80 W power before ZP measurement.

To measure ZP of Fe oxyhydroxide, 125 mg/L Fe oxyhyrdroxide suspensions were prepared by suspending Fe oxyhyrdroxide powder in 1 mM NaCl solution at pH 5 and 9. The Fe oxyhydroxide suspensions were sonicated by a Branson Digital Sonifier for 60 min with 80 W power before ZP measurement.

2.4. Adsorption isotherms

2.4.1. HA adsorption to $nTiO_2$ suspension

Batch experiments were performed to determine isotherms of HA adsorption to $nTiO_2$ suspensions at pH 5 and 9. The experiments were performed in duplicates by mixing 20 mg/L $nTiO_2$ suspension with various concentrations of HA (0.33-6.6 mg DOC/L) in 50 mL HDPE Falcon centrifuge tubes at room temperature (22 ℃). pH of the solution was

adjusted to 5 or 9 by adding 0.1 M HCl or NaOH, and the ionic strength of the suspensions was adjusted to 1 mM by adding NaCl. The tubes were capped and gently shaken at a speed of 20 rpm on a VWR orbital shaker (Model 5000). After 3 hours of mixing, the tubes were removed from the shaker and uncapped, and the suspensions were withdrawn from the tubes and filtered through 0.1 μm polyethersulfone membrane filter. Our preliminary tests showed that while all $nTiO_2$ were retained by the filtration process, HA not adsorbed to $nTiO_2$ could pass through the filter. Light absorbance of the filtrate was measured by a spectrophotometer at a wavelength of 368 nm. Concentration of HA remaining in the water was determined based on the measured light absorbance and calibration curves for HA, which were made with a series of samples with known concentration of HA (Fig. A1, Appendix 1). The amount of HA adsorbed to $nTiO_2$ was calculated as the difference between initial HA concentration and concentration of HA remaining in water after mixing.

2.4.2. HA adsorption to sand

Batch adsorption experiments were performed to determine isotherms of HA adsorption to quartz sand and Fe coated sand at pH 5 and 9. The experiments were performed in duplicates by mixing 26 g sand with 36 mL 1 mM NaCl solution containing various concentrations of HA (0.33-6.6 mg DOC/L) in 50 mL HDPE Falcon centrifuge tubes at room temperature (22 ℃). pH of the solution was adjusted to 5 or 9 with HCl or NaOH. The tubes were capped and gently shaken at a speed of 20 rpm on a VWR orbital shaker (Model 5000) for 3 hours. Control experiments with sand but no HA (i.e., HA−free controls) were performed. After 3 hours mixing, the tubes were removed from the shaker, let settle for 60 seconds by gravity, and uncapped. Supernatant was withdrawn from the tubes and light absorbance of the supernatant was measured by a spectrophotometer at 368

nm. Light absorbance of the HA−free controls was negligibly small (< 0.004), indicating that the sand did not contribute to light absorbance, and that light absorbance of the supernatant was all due to HA. Measured light absorbance of the supernatant was used to determine HA concentration remaining in water based on HA calibration curves (Fig. A1, Appendix 1). The detection limit were about 0.04 mg/L humic acid. The amount of HA adsorbed to sand was calculated as the difference between initial HA concentration and HA concentration remaining in water after mixing.

2.4.3. $nTiO_2$ attachment to sand

Batch experiments were performed to determine isotherms of $nTiO_2$ attachment to quartz sand and Fe coated sand at pH 5 and 9. The experiments were performed in duplicates by mixing 26 g sand with 36 ml 1 mM NaCl solution containing various concentrations of $nTiO_2$ (0−50 mg/L) in 50 ml HDPE Falcon centrifuge tubes at room temperature (22 ℃). pH of the solution was adjusted to 5 or 9 before the tubes were shaken at a speed of 20 rpm on a VWR orbital shaker (Model 5000) for 3 hours. Control experiments with $nTiO_2$ but no sand (i.e., sand−free controls) were prepared to check the stability of $nTiO_2$ over 3 hours. Control experiments with sand but no $nTiO_2$ ($nTiO_2$−free controls) were also performed. After 3 hours mixing, the tubes were removed from the shaker, let settle for 60 seconds by gravity, and uncapped. Supernatant was withdrawn from the tubes and light absorbance was measured by a spectrophotometer at a wavelength of 368 nm. Light absorbance of sand−free controls did not change after mixing, indicating $nTiO_2$ was stable during the experiments. Light absorbance of $nTiO_2$−free controls was negligible (< 0.004), indicating that sand by itself did not contribute to light absorbance, and light absorbance of the supernatant was all due to $nTiO_2$. Measured light absorbance

of the supernatant was used to calculate concentration of $nTiO_2$ remaining suspended after mixing based on nTiO2 calibration curves, which were made with a series of samples containing known concentration of $nTiO_2$ (Fig. A2, Appendix 1). The detection limit were about 0.04 mg/L for $nTiO_2$. The amount of $nTiO_2$ attached to sand was calculated as the difference between initial $nTiO_2$ concentration and concentration of $nTiO_2$ remaining suspended after 3 hours mixing.

2.5. ZP and HDD of $nTiO_2$, and ZP of Fe oxyhydroxides at various HA concentrations

To investigate the influence of HA on ZP and HDD of $nTiO_2$, $nTiO_2$ suspension was prepared (described in Section 2.1) and gently mixed with various concentrations of HA in 1 mM NaCl solution at pH 5 or 9 in 50 mL HDPE Falcon centrifuge tubes at room temperature (22 ℃). The concentration of $nTiO_2$ after mixing was 20 mg/L, and the concentration of HA was from 0.07 to 6.6 mg DOC/L. ZP and HDD of $nTiO_2$ at each HA concentration were determined by a Zetasizer.

To investigate the influence of HA on ZP of Fe oxyhydroxide, Fe oxyhyrdroxide suspension were prepared (described in Section 2.3) and gently mixed with various concentrations of HA in 1 mM NaCl solution at pH 5 or 9 in 50 mL HDPE Falcon centrifuge tubes at room temperature (22 ℃). The concentration of Fe oxyhydroxide after mixing was 125 mg/L, and the concentration of HA was from 0.07 to 6.6 mg DOC/L. ZP of Fe oxyhydroxide at each HA concentration was measured by a Zetasizer.

2.6. Stability of $nTiO_2$ suspensions at various HA concentrations

To evaluate the influence of HA on stability of $nTiO_2$ suspension, $nTiO_2$ suspension was prepared (described in Section 2.1) and gently mixed with various concentrations of HA in 1 mM NaCl solution at pH 5 or 9 in 50 mL HDPE Falcon centrifuge tubes at room temperature (22 ℃). The concentration of $nTiO_2$ after mixing was 20 mg/L, and the concentration of HA was 0.07, 0.13, 0.33, and 0.66 mg DOC/L respectively. Light absorbance of the mixed suspensions at a wavelength of 368 nm was monitored using a spectrophotometer during a 3 hour timespan.

2.7. $nTiO_2$ attachment to sand at various HA concentrations

To evaluate the influence of HA on $nTiO_2$ attachment to sand, 36 ml 20 mg/L $nTiO_2$ suspension with various concentrations of HA (0, 0.33, 0.66, 1.65, 3.3 mg DOC/L) in 1 mM NaCl solution were mixed with 26 g quartz sand or Fe coated sand at pH 5 or 9 in 50 mL HEPE Falcon centrifuge tubes at room temperature (22 ℃). The tubes were shaken at a speed of 20 rpm on a VWR orbital shaker (Model 5000) for 3 hours. Control experiments with $nTiO_2$ but no sand (sand−free controls) were prepared to check the stability of $nTiO_2$ suspension over 3 hours. Control experiments with sand but no $nTiO_2$ ($nTiO_2$−free controls) were also performed. After 3 hours mixing, the tubes were removed from the shaker, let settle for 60 seconds by gravity, and uncapped. Supernatant was withdrawn from the tubes and light absorbance of the supernatant was measured by a spectrophotometer at a wavelength of 368 nm. Light absorbance of supernatant of the sand−free controls did not change after mixing, indicating $nTiO_2$ was stable during the experiments. Light absorbance of the supernatant of the $nTiO_2$−free controls was negligibly small (<0.004), indicating light absorbance of the supernatant was all due to $nTiO_2$ and HA. Light absorbance of the

filtered supernatant (through 0.1 μm polyethersulfone membrane filter) was measured by a spectrophotometer at a wavelength of 368 nm for determining aqueous-phase HA concentration. The difference in light absorbance of unfiltered and filtered supernatant was used to determine suspended concentration of $nTiO_2$ after mixing. Our preliminary tests showed that coexistence of $nTiO_2$ and HA in the suspension did not interfere with each other's light absorbance under the conditions used in this study, similar to Chen et al.'s observation (2012). $nTiO_2$ attached to sands was calculated as the difference between initial $nTiO_2$ concentration and concentration of $nTiO_2$ remaining suspended in water after 3 hours mixing with sand.

Chapter 3: DLVO interaction energy

DLVO (Derjaguin and Landau, 1941) theory was used in this study to explain stability of $nTiO_2$ and $nTiO_2$ attachment to sand under various water chemistry conditions. Total interaction energy was calculated by summing up London-van der Waals (LW) force and electric double layer force (Equation 1).

$$\Phi_{\text{Total}} = \Phi_{\text{LW}} + \Phi_{\text{EDL}} \tag{1}$$

Φ_{LW} and Φ_{EDL} between $nTiO_2$ particles was calculated using Equation (2) and (3) assuming sphere–sphere geometry, and Φ_{LW} and Φ_{EDL} between $nTiO_2$ particle and collector (sand grain) was calculated using Equation (4) and (5) assuming sphere–plate geometry.

$$\Phi_{\text{LW}} = -\frac{\text{AR}}{12\text{s}}\left[1 - \frac{5.32\text{s}}{\lambda}\ln\left(1 + \frac{\lambda}{5.32\text{s}}\right)\right] \tag{2}$$

$$\Phi_{\text{EDL}} = 2\pi\varepsilon_0\varepsilon_r \text{R}\psi_c^{\,2}\ln\left[1 + \exp(-\kappa\text{s})\right] \tag{3}$$

$$\Phi_{\text{LW}} = -\left(\frac{\text{AR}}{6\text{s}}\right)\left[1 + \left(\frac{14\text{s}}{\lambda}\right)\right]^{-1} \tag{4}$$

$$\Phi_{\text{EDL}} = \pi\varepsilon_0\varepsilon_r \text{R}\left\{2\psi_c\psi_s\ln\left[\frac{1 + \exp(-\kappa\text{s})}{1 - \exp(-\kappa\text{s})}\right] + (\psi_c^2 + \psi_s^2)\ln\left[1 - \exp(-2\kappa\text{s})\right]\right\} \tag{5}$$

where A (J) is Hamaker constant (Hamaker, 1937), R (m) is radius of particle, s (m) is separation distance, λ (m) is characteristic wavelength of interaction, usually taken as 10^{-7} m, ε_0 (8.85×10^{-12} $C^2J^{-1}m^{-1}$) is the permittivity of vacuum, ε_r (80) is the relative dielectric constant of the medium, κ (m^{-1}) is the inverse of Debye length, and $\kappa=2.32\times10^9$ $(\Sigma C_i Z_i^2)^{1/2}$, where C_i is the concentration of ion i and Z_i is its valency value. ψ_c (V) is surface potential

of particle, ψ_s (V) is surface potential of collector. In our calculations, zeta potential was used to approximate surface potential (Elimelech et al., 2013).

A value of $A_{TiO2\text{-}H2O\text{-}TiO2}$ = 3.5×10^{-20} J was chosen for the Hamaker constant of $nTiO_2$-water-$nTiO_2$ system (Gómez-Merino et al., 2007). A value of $A_{TiO2\text{-}H2O\text{-}silica}$ = 1.4×10^{-20} J was chosen for the Hamaker constant of the $nTiO_2$-water-silica system (Butt et al., 2005, Petosa et al., 2010). Hamaker constant for $nTiO_2$-water-Fe oxyhydroxides system was determined using the method described by Hiemenz et al. (1997), i.e., for the interactions of two dissimilar materials (1 and 2) via a third media (3), the Hamaker constant can be estimated in terms of Hamaker constant of each material (Appendix 2):

$$A_{132} = (\sqrt{A_{11}} - \sqrt{A_{33}})(\sqrt{A_{22}} - \sqrt{A_{33}}) \tag{6}$$

In our case, 1 is $nTiO_2$, 2 is Fe oxyhydroxide, and 3 is water. Based on published Hamaker constants, $A_{TiO2\text{-}TiO2}$=15.3×10^{-20} J (Bergström, 1997), $A_{H2O\text{-}H2O}$= 3.7×10^{-20} J (Israelachvili, 2011), and $A_{FeOx\text{-}FeOx}$= 68×10^{-20} J (Faure, 2011). Hamaker constant of $nTiO_2$-water-Fe oxyhydroxides was determined to be $A_{TiO2\text{-}H2O\text{-}FeOx}$= 1.257×10^{-19} J using Equation (6).

The surface of Fe coated sand could be chemically heterogeneous attributable to incomplete coverage by Fe coating. To account for this effect, modified DLVO calculations was applied to calculate interaction energy between $nTiO_2$ and Fe coated sand. Bendersky and Davis (2011) and Bradford and Torkzaban (2013) found that a linear combination of the interaction energies due to type 1 (Φ_1) and type 2 (Φ_2) surface can be used to calculate the mean interaction energy between particle and chemically heterogeneous surface:

$$\Phi_{Total} = \frac{N_1}{Nt}\Phi_1 + \frac{N_2}{Nt}\Phi_2 \tag{7}$$

where Φ_1 and Φ_2 are total interaction energy between particle and type 1 and type 2 surface respectively. In our case, 1 is quartz, 2 is Fe oxyhydroxide, N_1 and N_2 are surface area covered by quartz and Fe oxyhydroxide respectively, and $N_t = N_1 + N_2$, is total surface area of the Fe coated sand (Appendix 3).

Chapter 4: Results and Discussions

4.1. Mineral composition, particle size, ZP and HDD of $nTiO_2$, and ZP of quartz sand and Fe oxyhydroxide

XRD analysis showed that Aeroxi de™ TiO_2 P25 was a mixture of anatase (90%) and rutile (10%) (Fig. A1, Appendix 4), with average particle size of 23 and 40 nm respectively, consistent with previously reports (Godinez and Darnault, 2011). In the absence of HA, HDD of the $nTiO_2$ particles changed with pH, ranging from 244 to 907 nm (Fig. 1), much larger than the size determined by XRD, indicating $nTiO_2$ existed as aggregates in water solution.

HDD of $nTiO_2$ was inversely correlated to the absolute value of its ZP (Fig. 1), e.g., maximum HDD of 908 nm occurred at pH 7 where ZP = 8 mV, and the minimum HDD of 244 nm occurred at pH 9 where ZP = -32 mV. The differences in HDD at different pH was attributable to the influence of ZP on $nTiO_2$ aggregation, i.e., higher degree of aggregation and therefore larger HDD occurred when the repulsive electrostatic forces between $nTiO_2$ particles was low, as indicated by the low absolute value of ZP.

For both $nTiO_2$ and Fe oxyhydroxide, ZP changed from positive at pH 5 to negative at pH 9 (Fig. 1), consistent with reported point of zero charge (PZC) for $nTiO_2$ (pH_{PZC} (TiO_2) = 6.7; Boncagni et al., 2009) and Fe oxyhydroxides (pH_{PZC} (iron(III) oxide) = 8.4, Kosmulski, 2001, Wang et al., 2012a). For quartz sand, ZP was negative at both pH 5 and 9 and not sensitive to pH changes (Fig. 1), consistent with previous reports (Chen et al., 2012).

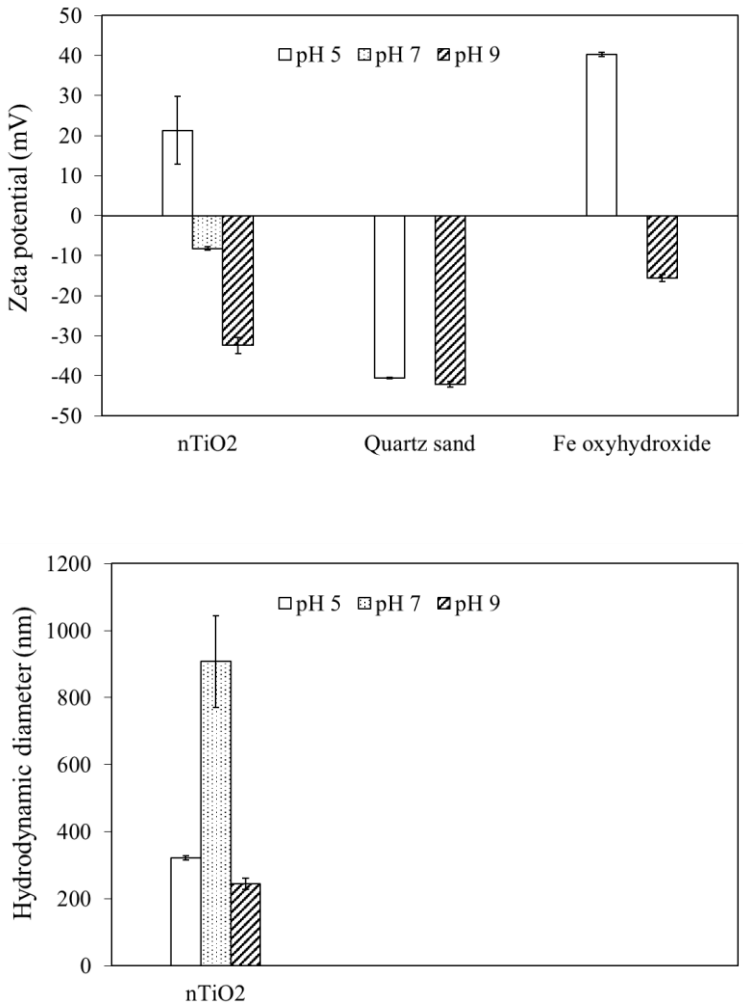

Fig.1 A: Zeta potential (ZP) of "bare" (i.e., with no adsorbed HA) $nTiO_2$, quartz sand, and Fe oxyhydroxide, and B :hydrodanamic diameter (HDD) of "bare" $nTiO_2$ at pH 5, 7, and 9 in 1 mM NaCl solution. Data is expressed as mean ± standard deviation of triplicate measurements.

4.2. HA adsorption to $nTiO_2$ and its influence on ZP and HDD of $nTiO_2$

Adsorption of HA to $nTiO_2$ suspension was pH-dependent, i.e., higher adsorption occurred at pH 5 than pH 9 (Fig. 2), consistent with the typical pattern of pH-dependent adsorption of anions. HA exist as negatively charged polyelectrolytes at ambient pH due to deprotonation of carboxylic and phenolic groups (Hu et al., 2010). At pH 5, $nTiO_2$ hold positive charges, strongly attracting negatively charged HA. While at pH 9, $nTiO_2$ hold

negative charges, resulting in lower HA adsorption. Adsorbed HA concentration (q) was found to increase with increasing aqueous-phase HA concentration (C_{eq}) in the low HA concentration range, but levelled off in the high HA concentration range (Fig. 2), indicating saturation of adsorptive sites. Langmuir adsorption isotherm (Equation A1, Appendix 5) was used to model the experimental data and showed that adsorption capacity of $nTiO_2$ for HA was q_{max} = 169.5 mg organic carbon/kg Ti at pH 5, and q_{max} = 35.3 mg organic carbon/kg Ti at pH 9 (Table 1).

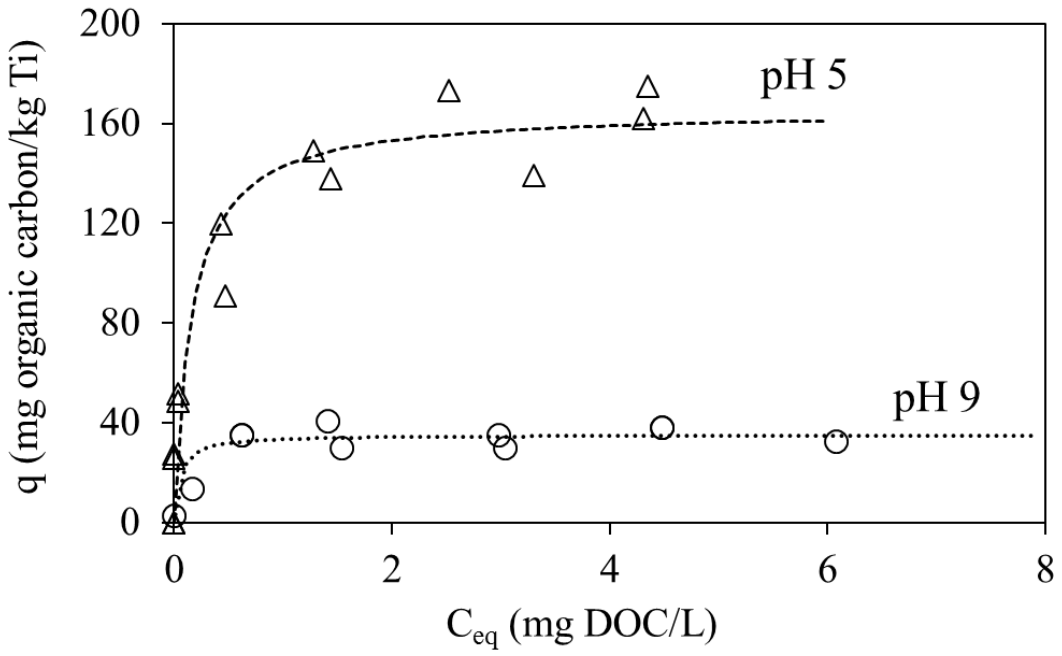

Fig. 2. Adsorption of humic acid (HA) to 20 mg/L $nTiO_2$ in 1 mM NaCl solution at pH 5 and 9. Symbols: experimental measurements; lines: simulated Langmuir adsorption isotherms. q: adsorbed HA concentration; C_{eq}: aqueous-phase HA concentration at equilibrium.

At pH 5, ZP of $nTiO_2$ sharply decreased from +21 mV to -41 mV when total HA concentration increased from 0 to 0.66 mg DOC/L, however, further increase in HA concentration (from 0.66 to 6.6 mg DOC/L) did not change ZP (Fig. 3a). Changes in ZP in

the presence of HA was attributable to HA adsorption to $nTiO_2$ surface, which neutralized or reversed the positive surface charges on $nTiO_2$. Shown in Fig. 3c is the ZP of $nTiO_2$ as a function of adsorbed HA concentration on $nTiO_2$ (q_{Ti}), which was calculated based on total HA concentration (C_{total}) by coupling adsorption isotherm (Equation A1, Appendix 5) with mass balance of HA (Equation A3, Appendix 5). At pH 5, for q_{Ti} < 50 mg organic carbon/kg, ZP of $nTiO_2$ decreased with increasing q_{Ti}. At q_{Ti} between 50 and 150 mg organic carbon/kg, ZP of $nTiO_2$ was not sensitive to increases in q_{Ti}. For total HA concentrations > 3 mg DOC/L, $nTiO_2$ was saturated by adsorbed HA, therefore q_{Ti} and ZP became stable and were not influenced by increase in total HA concentration (Fig. 3a and 3c). It is noticeable that ZP of $nTiO_2$ changed from positive to negative at a total HA concentration around 0.07 to 0.13 mg DOC/L, corresponding to an adsorbed HA concentration of ~9 mg organic carbon/kg.

At pH 5, HDD of $nTiO_2$ increased from 300 nm to 600 nm when total HA concentration increased from 0 to 0.13 mg DOC/L, and HDD decreased to 250 nm when total HA concentration further increased from 0.13 to 0.66 mg DOC/L (Fig. 4a). At total HA concentration > 0.5 mg DOC/L, HDD hovered around 250 nm and did not change with increasing HA concentration. HDD of $nTiO_2$ was found to be inversely related to the absolute value of ZP, e.g., the maximum HDD of 600 nm occurred when absolute value of ZP was the lowest (10 mV), and the minimum HDD (250 nm) occurred when absolute value of ZP was the highest (40 mV). The differences in HDD were attributable to changes in repulsive electrostatic forces between $nTiO_2$ particles at varying HA concentrations, which influenced ZP and therefore aggregation and HDD of $nTiO_2$.

At pH 9, ZP and HDD of $nTiO_2$ were stable at -34 mV and 210 nm respectively throughout the HA concentration range (Fig. 3b, 3d and Fig. 4b, 4d). The insensitivity of ZP and HDD to changes in HA concentration was presumably due to the negative ZP of "bare" $nTiO_2$ (i.e., $nTiO_2$ with no adsorbed HA, ZP = -34 mV) and low HA adsorption to $nTiO_2$（Chen et al., 2012）.

Table 1. Langmuir adsorption isotherm ($q = \frac{q_{max} k C_{eq}}{1 + k C_{eq}}$) parameters for HA adsorption to $nTiO_2$, quartz sand, and Fe coated sand, and for $nTiO_2$ attachment to quartz sand and Fe coated sand in 1 mM NaCl solution at pH 5 and 9.

	pH	q_{max} (mg/kg)	k (L/mg)	R^2
HA to $nTiO_2$	5	169.5	4.9	0.99
	9	35.3	15.7	0.98
HA to quartz sand	5	0	NA*	NA
	9	0	NA	NA
HA to Fe coated sand	5	4.4×10^{-3}	59.1	0.99
	9	6.7×10^{-4}	1.7	0.51
$nTiO_2$ to quartz sand	5	294.1	3.1	0.99
	9	0	NA	NA
$nTiO_2$ to Fe coated sand	5	181.8	2.9	0.98
	9	NA	NA	NA

* Not applicable. k and q_{max} were determined from the slope and intercept of a linear plot of 1/q against C_{eq}, and R^2 is the coefficient of linear regression.

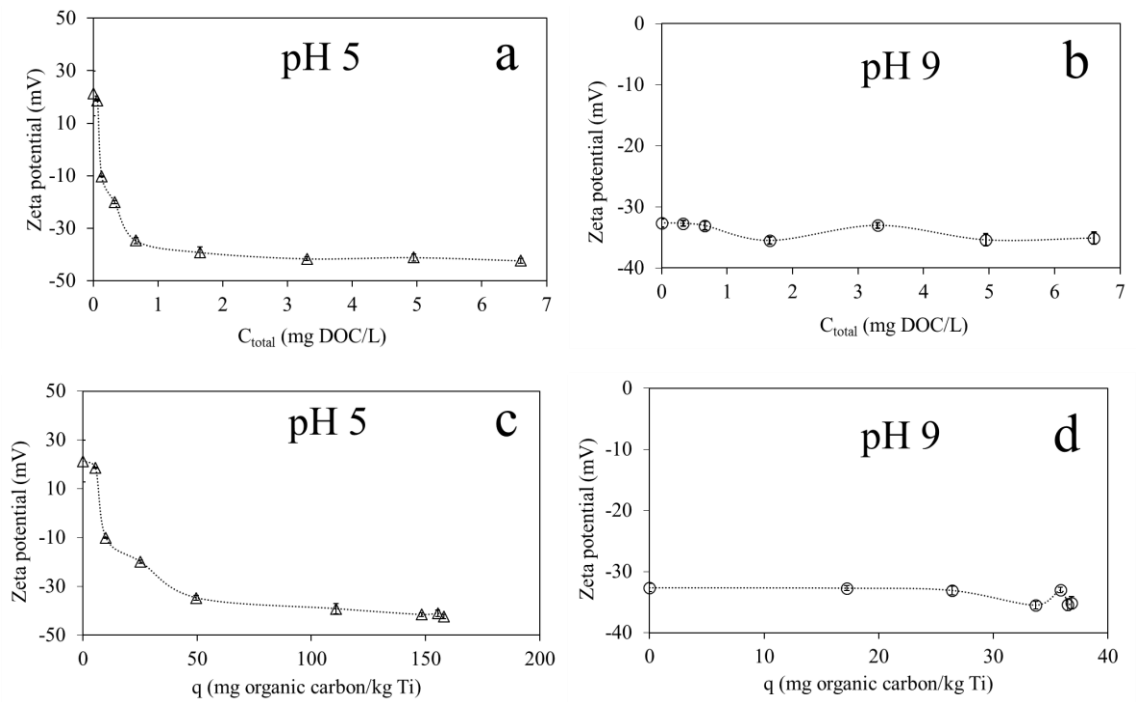

Fig.3. Zeta potential of $nTiO_2$ (20 mg/L) mixed with various concentrations of humic acid (HA) in 1 mM NaCl solution at pH 5 and 9. Measured zeta potential (symbols) is expressed as mean ± standard deviation of triplicate measurements. Trend lines (dotted lines) are added to guide visual inspection. (a) and (b): zeta potential of $nTiO_2$ as a function of total HA concentration (C_{total}); (c) and (d): zeta potential of $nTiO_2$ as a function of adsorbed HA concentration on $nTiO_2$ (q). q was calculated by Langmuir adsorption isotherm and mass balance.

4.3. HA adsorption to quartz sand and Fe coated sand and its influence on ZP of quartz and Fe oxyhydroxide

No HA (below the detection limit) was adsorbed to quartz sand at either pH 5 or 9 (Fig. 5), consistent with reported low adsorption capacity of quartz for HA (Chen et al., 2012). This result implies that ZP of quartz sand is not influenced by HA under our experimental conditions.

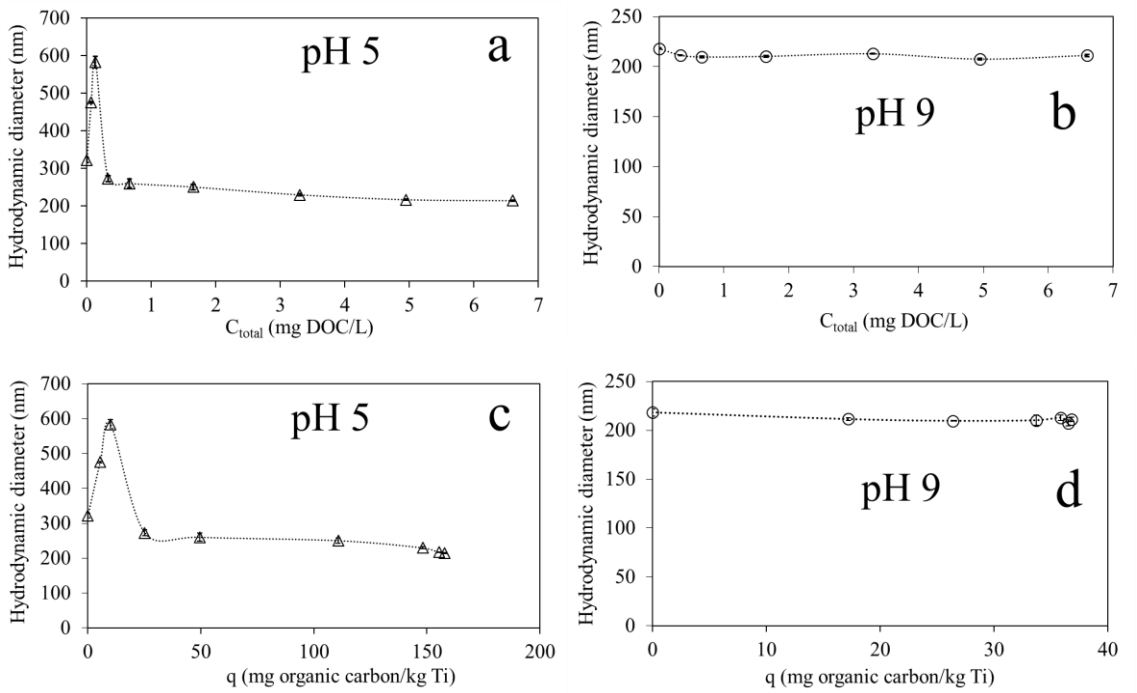

Fig. 4. Hydrodynamic diameter of $nTiO_2$ (20 mg/L) mixed with various concentrations of humic acid (HA) in 1 mM NaCl solution at pH 5 and 9. Measured hydrodynamic diameter (symbols) is expressed as mean ± standard deviation of triplicate measurements. Trend lines (dotted lines) are added to guide visual inspection. (a) and (b): hydrodynamic diameter of $nTiO_2$ as a function of total HA concentration (C_{total}); (c) and (d): hydrodynamic diameter of $nTiO_2$ as a function of adsorbed HA concentration on $nTiO_2$ (q). q was calculated by Langmuir adsorption isotherm and mass balance.

In contrast, HA was found to adsorb to Fe coated sand at both pH 5 and 9, with higher adsorption occurred at pH 5 (Fig. 5). HA adsorbs to Fe oxydroxides via ligand exchange or H-bonding with carboxyl/hydroxyl groups, association with aliphatic or aromatic carbon, and electrostatic interactions (Borggaard et al., 2005; Fein et al., 1999; Gu et al., 1994; Tipping, 1981; Yang et al., 2013). Adsorbed HA concentration (q) was found to increase with increasing dissolved HA concentration (C_{eq}) at low HA concentration range but levelled off at high HA concentration range (Fig. 5), indicating saturation of adsorptive sites. Langmuir adsorption isotherm model was used to simulate HA adsorption to Fe coated sand, assuming that HA adsorbed to Fe oxyhydroxides but not quartz. Modeling results showed that adsorption capacity of the Fe coated sand was q_{max} =

4.4×10^{-3} mg organic carbon/kg sand (or 33 mg organic carbon/kg Fe) at pH 5, and q_{max} = 6.7×10^{-4} mg organic carbon/kg sand (or 6 mg organic carbon/kg Fe) at pH 9 (Table 1).

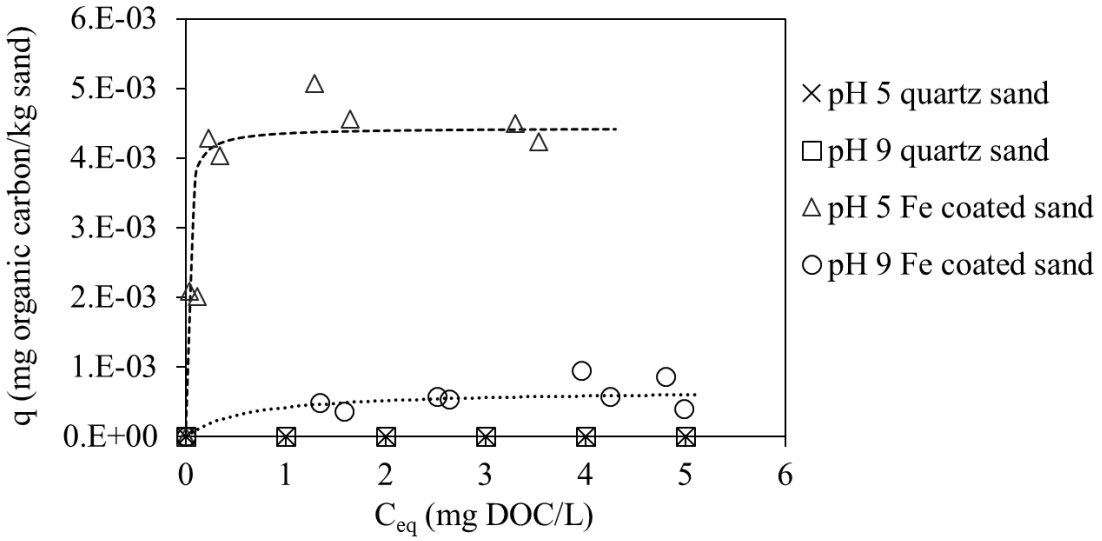

Fig. 5. Adsorption of humic acid (HA) to 26 g quartz sand or Fe coated sand in 36 mL 1 mM NaCl solution at pH 5 and 9. Symbols: experimental measurements; lines: simulated Langmuir adsorption isotherms. q: adsorbed HA concentration; C_{eq}: aqueous-phase HA concentration at equilibrium. HA was not adsorbed to quartz sand at either pH 5 (×) or pH 9 (□) as shown by these symbols on the x axis.

At pH 5, ZP of the Fe oxyhydroxide suspension decreased from +40 mV to -35 mV when total HA concentration increased from 0 to 2 mg DOC/L (Fig. 6a). As total HA concentration further increased from 2 to 6.6 mg DOC/L, ZP was not influenced by HA concentration and hovered near -40 mV (Fig. 6a). The ZP of the Fe oxyhydroxide as a function of adsorbed HA concentration (q_{Fe}), which was calculated based on C_{total} by coupling adsorption isotherm (Equation A2, Appendix 5) with mass balance of HA (Equation A4, Appendix 5), showed a similar trend, i.e., ZP decreased with increase in adsorbed HA concentration (q_{Fe}) for q_{Fe} < 20 mg organic carbon/kg Fe, but was not sensitive to increases in adsorbed HA concentration for q_{Fe} > 20 mg organic carbon/kg Fe (Fig. 6c). For total HA concentration > 3 mg DOC/L, Fe oxyhydroxide was saturated with

HA, and both q_{Fe} and ZP became stable and not influenced by increases in total HA concentration (Fig. 6a and 6c). It is noted that at a total HA concentration of 0.66 mg DOC/L (corresponding to q_{Fe} = 8 mg organic carbon/kg Fe), ZP of the Fe oxyhydroxides changed from positive to negative.

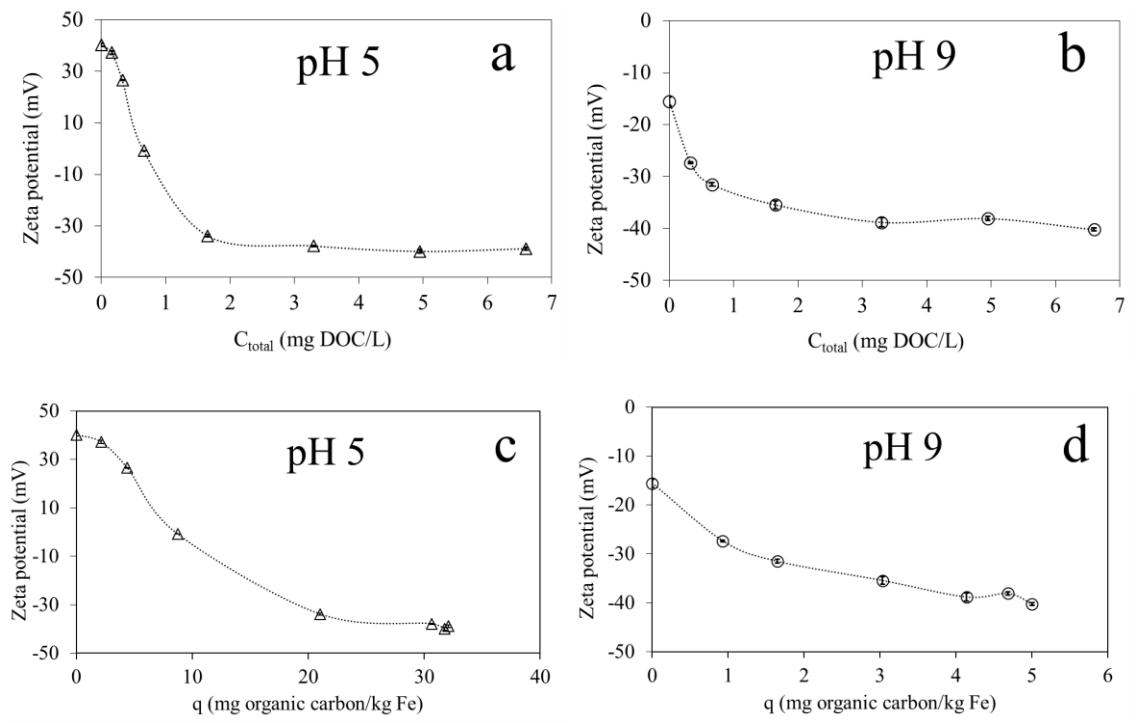

Fig. 6. Zeta potential of Fe oxyhydroxide suspension (125 mg Fe oxyhydroxide/L, or 73 mg Fe/L) mixed with various concentrations of humic acid (HA) in 1 mM NaCl solution at pH 5 and 9. Measured zeta potential (symbols) is expressed as mean ± standard deviation of triplicate measurements. Trend lines (dotted lines) are added to guide visual inspection. (a) and (b): zeta potential of Fe oxyhydroxide as a function of total HA concentration (C_{total}); (c) and (d): zeta potential of Fe oxyhydroxide as a function of adsorbed HA concentration on Fe oxyhydroxide (q). q was calculated by Langmuir adsorption isotherm and mass balance.

At pH 9, ZP of the Fe oxyhydroxide was negative (-15 to -40 mV) throughout the HA concentration range (Fig. 6b and 6d). In low HA concentration range (i.e., total HA concentration = 0 to 2 mg DOC/L, or q_{Fe} = 0 to 3 mg organic carbon/kg Fe), ZP of the Fe oxyhydroxides decreased from -15 to -35mV with increasing HA concentration. For higher

HA concentrations (i.e., total HA concentration > 2 mg DOC/L, or q_{Fe} > 3 mg organic carbon/kg Fe), ZP hovered around -40 mV and it was not sensitive to increase in HA concentration.

4.4. Influence of HA on $nTiO_2$ stability in water

At pH 5, light absorbance of the $nTiO_2$ suspensions was unchanged in the absence of HA, and in the presence of 0.33 mg DOC/L HA, but decreased with mixing time for intermediate HA concentrations of 0.07 and 0.13 mg DOC/L (Fig. 7). At pH 9, light absorbance of the $nTiO_2$ suspensions was stable either in the absence HA or for any of the HA concentrations used (0.07, 0.13, and 0.33 mg DOC/L) (Fig. 7). The above results showed that $nTiO_2$ suspension was stable under all the tested conditions except for HA concentrations of 0.07 and 0.13 mg DOC/L at pH 5, under which aggregation occurred, in good agreement with previous works which demonstrated HA can stabilize the $nTiO_2$ by electrostatic and steric forces (Chen et al., 2012; Chen and Elimelech, 2007; Espinasse et al., 2007; Navarro et al., 2008).

Stability of $nTiO_2$ in water is controlled by DLVO forces between $nTiO_2$ particles. The particle-to-particle DLVO interaction energy, based on classic DLVO theory by considering van der waals and electrostatic forces (described in Section 3), was calculated for each HA concentration at pH 5 and 9(Fig. 8). The secondary minimum (Φ_{min2}) term was negligibly low for all the calculated energy profiles (Table A1, Appendix 6), indicating $nTiO_2$ was not attracted by secondary minimum. At pH 5, in the absence of HA, a relatively high energy barrier (Φ_{max} = 5.8 kT) existed (Fig. 8a), which was attributable to the repulsive electrostatic forces between positively charged $nTiO_2$ particles (ZP = +21 mV) (Table A1, Appendix 6). At HA concentration of 0.07 mg DOC/L, the positive charges of $nTiO_2$ were

partially neutralized by the absorbed HA (ZP reduced from +21 to +18 mV) (Table A1, Appendix 6), resulting in lower energy barrier (Φ_{max} = 2.2 kT) that are comparable to the mean kinetic energy of small particles due to Brownian motion (~1.5 kT) (Treumann et al., 2014). At HA concentration of 0.13 mg DOC/L, absorbed HA not only neutralized the positive charges of $nTiO_2$, but also reversed the charge to negative (ZP = -10 mV) (Table A1, Appendix 6). However, due to the relatively low charge density, the repulsive electrostatic force was overshadowed by the van der waals force, leading to negative interaction energy (i.e., attractive forces) between $nTiO_2$ particles. At a HA concentration of 0.33 mg DOC/L, $nTiO_2$ became strongly negatively charged (ZP = -20 mV) due to high adsorbed HA concentration (Table A1, Appendix 6), and the energy barrier was relatively high (Φ_{max} = 3.6 kT) due to repulsive electrostatic forces between negatively charged $nTiO_2$ particles. Overall, the calculated energy profiles showed that for HA concentrations of 0 or 0.33 mg DOC/L, the energy barrier was relatively high, but for intermediate HA concentrations of 0.07 and 0.13 mg DOC/L, the energy barrier was very low or non-existent, consistent with the results of our stability test.

Although HA concentration > 0.33 mg DOC/L was not used in the stability test, ZP and HDD of 20 mg/L $nTiO_2$ in the presence of 0.66, 1.65, 3.30, 4.95, 6.60 mg DOC/L HA were measured (Section 2.5). Theoretical calculations showed that at these relatively high HA concentrations, the energy barrier further increased to 9.5, 36.6, 45.4, 45.9, and 46.5 kT respectively due to the more negative ZP afforded by higher adsorbed HA concentration (Table A1, Appendix 6).

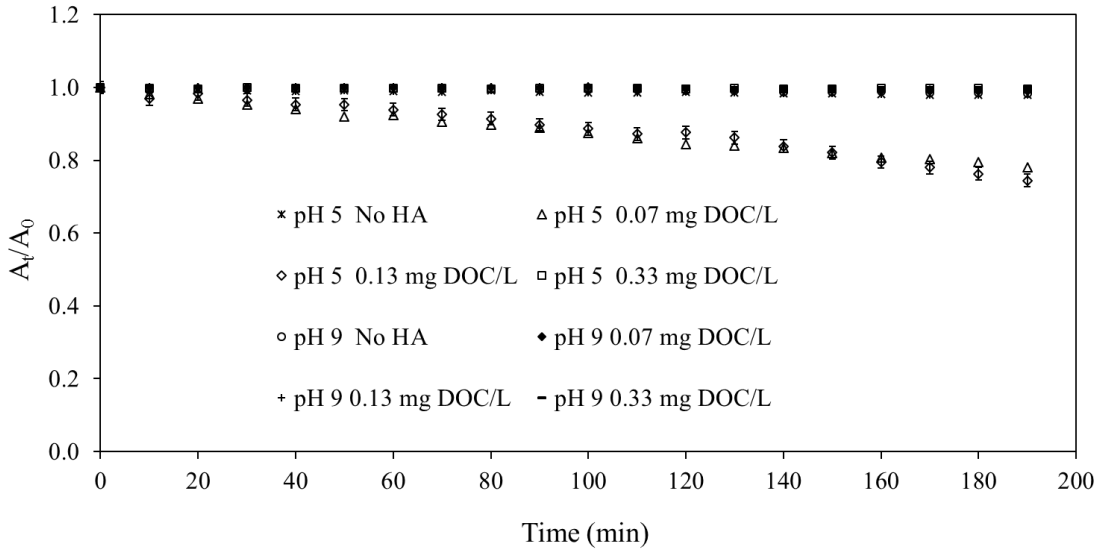

Fig. 7. Stability of 20 mg/L $nTiO_2$ suspension mixed with various concentrations of humic acid (HA) in 1 mM NaCl solution at pH 5 and 9. A_0: light absorbance at time t = 0; A_t: light absorbance at time t. Light absorbance was measured at a wavelength of 368 nm. Measured light absorbance (symbols) is expressed as mean ± standard deviation of duplicate measurements.

At pH 9, the calculated DLVO profiles showed high energy barrier (≥ 23 kT) for all the HA concentrations (0 to 0.33 mg DOC/L) (Fig. 8b), indicating stable suspension, consistent with the results of our stability test. As discussed before, ZP and HDD of $nTiO_2$ were not sensitive to changes in HA concentration at pH 9. Therefore, the interaction energy profiles for different HA concentrations were all similar. At higher HA concentrations (0.66 to 6.6 mg DOC/L), energy barrier lightly increased due to decrease in the ZP of $nTiO_2$ (Table A1, Appendix 6), indicating stable suspension.

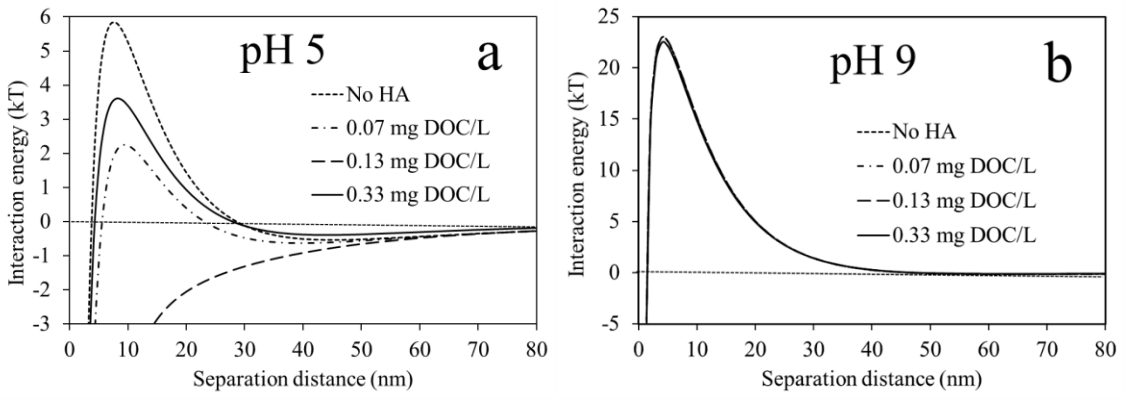

Fig. 8. $nTiO_2$-to-$nTiO_2$ DLVO interaction energy profiles for $nTiO_2$ suspensions (20 mg/L) mixed with various concentrations of humic acid (HA) in 1 mM NaCl solution at pH 5 (a) and pH 9 (b).

4.5. $nTiO_2$ attachment to quartz sand and Fe coated sand in the absence of HA

At pH 5, both quartz sand and Fe coated sand showed substantial capacity of retaining $nTiO_2$, but quartz sand had a higher capacity (Fig. 9). Concentration of $nTiO_2$ attached to sand (q) increased with increasing suspended $nTiO_2$ concentration (C_{eq}) at low concentration range but levelled off at high concentration range, indicating surface site saturation. Langmuir adsorption isotherm model fitting of the experimental data indicated that $nTiO_2$ holding capacity was q_{max} = 294.1 mg/kg for quartz sand, and q_{max} = 181.8 mg/kg for Fe coated sand (Table 1). At pH 9, $nTiO_2$ was not attached to the quartz sand, however, attachment of $nTiO_2$ to Fe coated sand was observed in some experiments but concentration of attached $nTiO_2$ (q) was very low (Fig. 9).

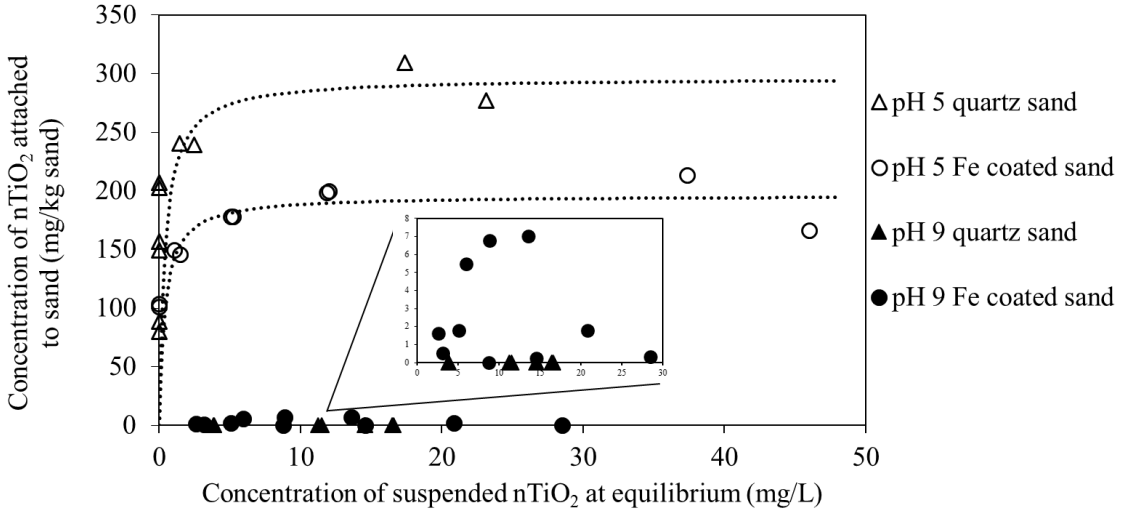

Fig. 9. Attachment of $nTiO_2$ to 26 g quartz sand or Fe coated sand in 36 mL 1 mM NaCl solution at pH 5 and 9. Symbols: experimental measurements; lines: simulated Langmuir adsorption isotherms. The insert shows close-up of $nTiO_2$ attachment at pH 9.

The high affinity of quartz sand for $nTiO_2$ at pH 5 was attributable to attractive electrostatic forces between positively-charged $nTiO_2$ and negatively-charged quartz sand (Chen et al., 2012; Hu et al., 2010). Calculated DLVO interaction energy profile confirmed that $nTiO_2$ attachment to quartz sand was under favorable conditions (Fig. 10a). At pH 9, $nTiO_2$ and quartz were both negatively charged, resulting in high energy barrier (Φ_{max} = 164.5 kT) (Fig. 10b). Therefore quartz sand was not expected to retain $nTiO_2$ at pH 9, consistent with our experimental observations.

At pH 5, calculated DLVO interaction energy profile based on the assumption of complete coverage of sand surface by Fe coating showed large energy barrier (53.9 kT) and negligible secondary minimum (-0.9 kT) (Fig. 10a), suggesting that attachment of $nTiO_2$ to Fe coated sand is not expected if sand surface was completed covered by Fe coating. Backscatter SEM images of the Fe coated sand showed that the Fe coating was patchy and heterogeneous (Fig. A4, Appendix 7). Backscatter SEM coupled with energy dispersive X-ray (EDX) showed that 38 ± 5 % of the Fe coated sand was covered by Fe

oxyhydroxide (Fig. A4, Appendix 7), indicating that 62% of the sand surface was quartz and its influence on $nTiO_2$ attachment needs to be considered. Calculated DLVO interaction energy between $nTiO_2$ and Fe coated sand by including both uncovered quartz surface and Fe coating showed that the overall interaction energy was negative (Fig. 10a), suggesting that $nTiO_2$ attachment was under favorable conditions, consistent with the experimental observations. Compared with the energy profile for $nTiO_2$-to-quartz sand, however, the energy profile for $nTiO_2$-to-Fe coated sand was less negative (Fig. 10), attributable to partial coverage of the sand surface by positively charged Fe coating, which reduced attachment of like-charged $nTiO_2$.

At pH 9, $nTiO_2$, quartz, and Fe coating were all negatively charged (Fig. 1), and the overall DLVO interaction energy between $nTiO_2$ and Fe coated sand by considering both uncovered quartz surface and Fe coating showed large energy barrier (Φ_{max} = 82.2 kT) and negligible secondary minimum (Φ_{min2} = -0.2 kT) (Fig. 10b), suggesting $nTiO_2$ should not attach to Fe coated sand. This result contradicts the experimental observation that a small fraction of $nTiO_2$ were attached (Fig. 9 insert). In DLVO calculations, it was assumed that $nTiO_2$ and sand surface were geometrically smooth. However, SEM images showed substantial depressions, protrusions, and roughness on sand surface, especially for Fe coated sand due to the presence of Fe coating (Fig. 11). Nano-scale and micro-scale surface roughness may provide favorable locations for particle retention due to lever arm considerations, and interactions between surface asperities and particle can reduce energy barrier between collector surface and particle (Bendersky & Davis, 2011; Shen et al., 2011; Treumann et al., 2014). Attachment of $nTiO_2$ to Fe coated sand at pH 9 observed in our experiments thus is presumably attributable to surface roughness of caused by Fe coating.

Nonetheless, the effects of surface roughness seems very small, as indicated by the very low concentration of $nTiO_2$ attached (< 8 mg $nTiO_2$/kg sand) (Fig. 9).

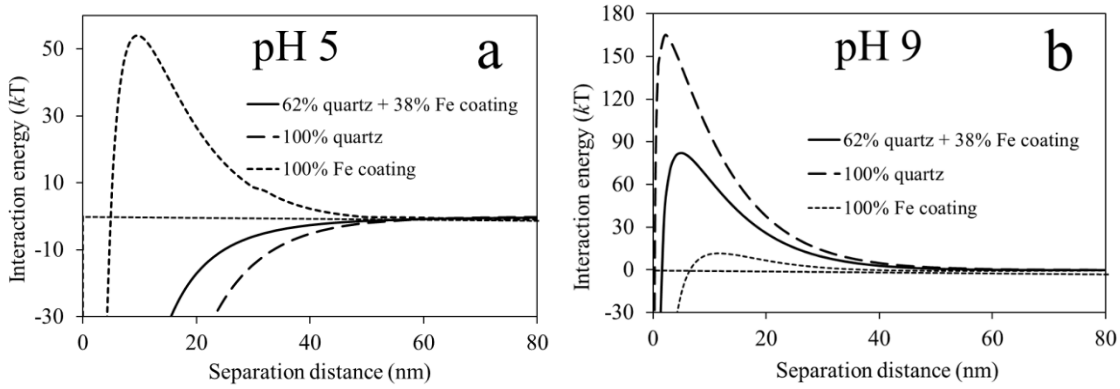

Fig. 10. DLVO interaction energy profiles for $nTiO_2$-to-quartz sand and $nTiO_2$-to-Fe coated sand in 1 mM NaCl solution in the absence of humic acid (HA) at pH 5 (a) and pH 9 (b).

4.6. Influence of HA on $nTiO_2$ attachment to quartz sand

At pH 5, nearly 100% of $nTiO_2$ were attached to quartz sand in the absence of HA (Fig. 12a). In contrast, the amount of $nTiO_2$ attached was much lower and close to detection limit in the presence of HA, even at a low HA concentration of 0.33 mg DOC/L. At pH 9, $nTiO_2$ with a concentration below detection limit was attached to quartz sand either in the absence or presence of HA.

In the absence of HA, $nTiO_2$ and quartz sand were oppositely-charged at pH 5 (Fig. 1), hence $nTiO_2$ attachment was under favorable conditions, resulting in complete $nTiO_2$ attachment. In the presence of HA, HA was adsorbed to $nTiO_2$ but not quartz sand. Therefore, ZP of quartz sand stayed constant (-41 mV) under varying HA concentrations, but ZP and HDD of $nTiO_2$ changed with HA concentration (Table A2, Appendix 6). For the HA concentrations used in the experiment (0.33 to 3.3 mg DOC/L), ZP of $nTiO_2$ were all negative at pH 5, ranging from -20 to -42 mV (Table A2, Appendix 6), and the energy

barrier was large (+21.9 to +224.9 mV) (Fig. 13a), indicating strong repulsions between $nTiO_2$ and quartz sand, in agreement with our experimental observation of low $nTiO_2$ attachment.

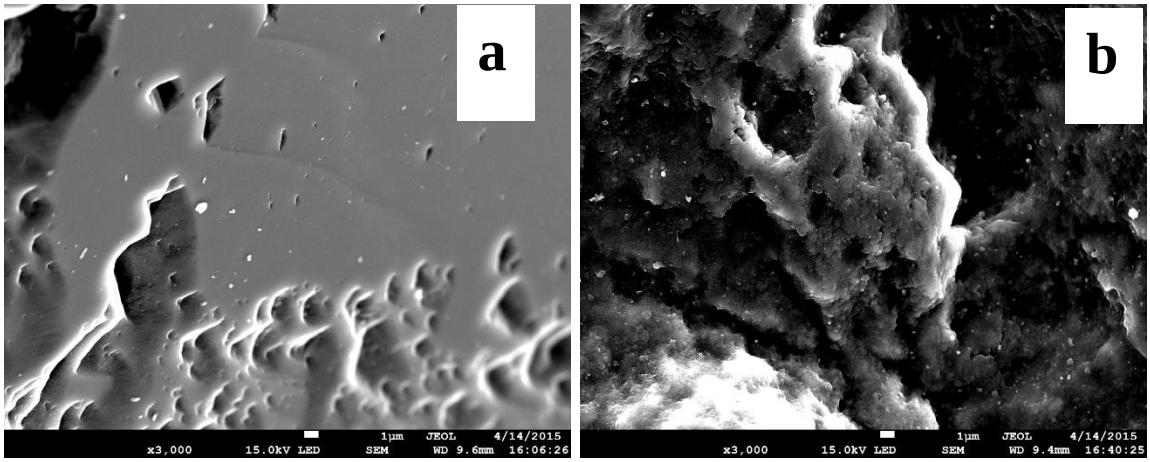

Fig. 11. Representative SEM images of quartz sand surface (a), and Fe coating on Fe coated sand (b).

At pH 9, both $nTiO_2$ and quartz sand were negatively charged either in the absence of HA or in the presence of HA (Table A2, Appendix 6). Large energy barrier (+163.4 to +177.9 mV) existed between $nTiO_2$ and quartz sand for all these HA concentrations (Fig. 13b), suggesting low $nTiO_2$ attachment, consistent with our experimental observation of low $nTiO_2$ attachment (Fig. 12a).

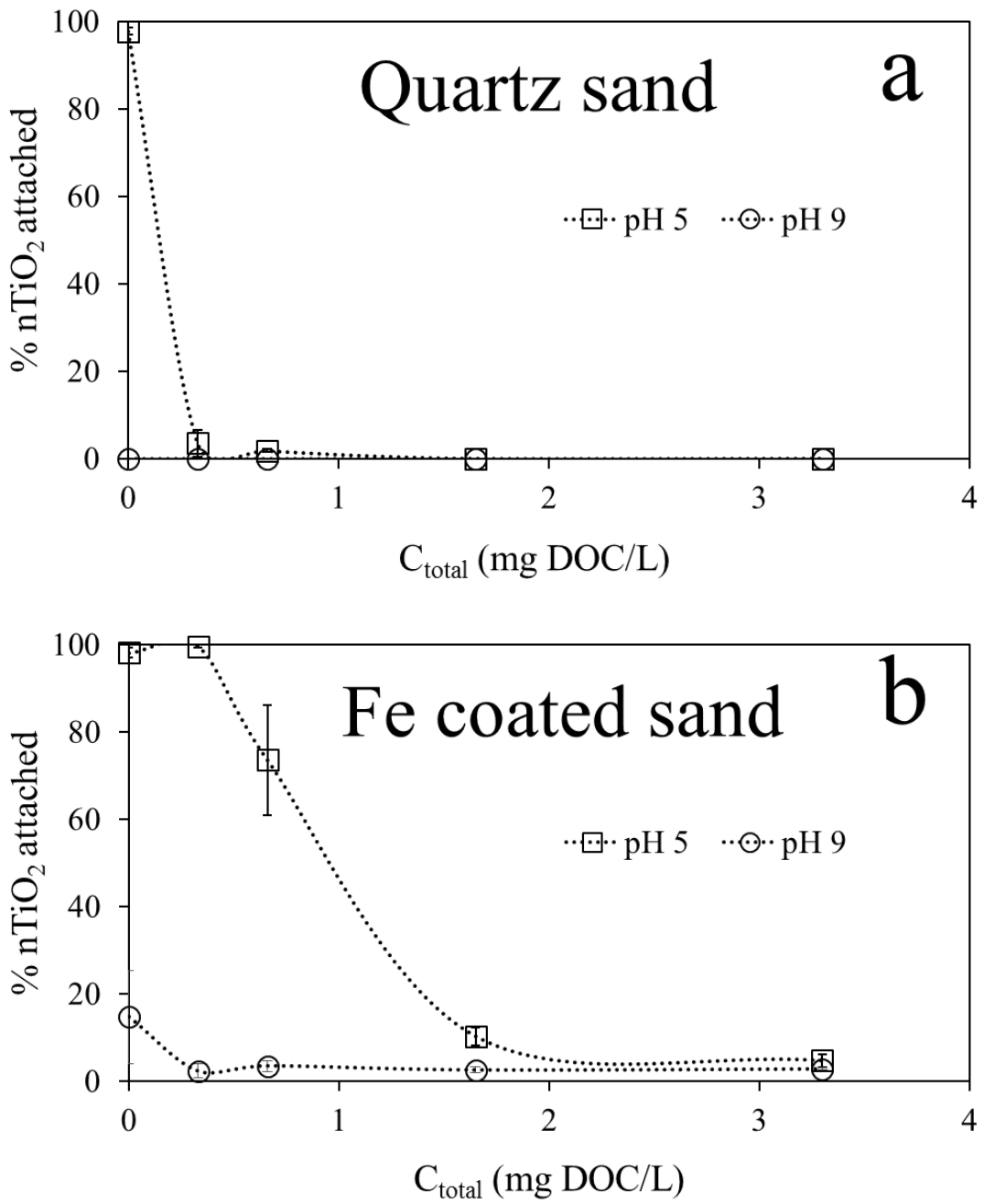

Fig. 12. Percentage of $nTiO_2$ (20 mg/L) attached to 26 g quartz sand (a) and 26 g Fe coated sand (b) in 36 mL 1 mM NaCl solution at various HA concentrations at pH 5 and 9. Symbols: experimentally measured % $nTiO_2$ attached to sand, expressed as mean ± standard deviation of duplicate experiments; dotted lines: trend lines added to guide visual inspection.

4.7. Influence of HA on $nTiO_2$ attachment to Fe coated sand

At pH 5, almost 100% of $nTiO_2$ was attached to Fe coated sand in the absence of HA and at a HA concentration of 0.33 mg DOC/L (Fig. 12b). At HA concentrations > 0.66 mg DOC/L, $nTiO_2$ attachment decreased with increasing HA concentration, and < 10 % $nTiO_2$ was attached at HA concentrations > 2 mg DOC/L. At pH 9, $nTiO_2$ attachment to Fe coated sand was considerably lower compared to that at pH 5 (Fig. 12b), e.g., in the absence of HA, 15% of $nTiO_2$ was attached, and in the presence of HA, < 3% $nTiO_2$ was attached. At pH 9, $nTiO_2$ attachment to Fe coated sand was slightly higher than its attachment to quartz sand throughout the HA concentration range (Fig. 12b vs. 12a).

It is noted that for low HA concentrations (< 1 mg DOC/L), at pH 5, percentage of $nTiO_2$ attached to the Fe coated sand was much higher than the percentage of $nTiO_2$ attached to quartz sand at the same HA concentration (Fig. 12b vs. 12a), e.g., % of $nTiO_2$ attached to Fe coated sand and quartz sand was 100% and less than detection limit respectively at HA concentration of 0.33 mg DOC/L, and was 74% and 0 at HA concentration of 0.66 mg DOC/L. These results indicate that Fe coating increased $nTiO_2$ attachment to sand at these low HA concentrations. Previously, however, we observed lower $nTiO_2$ attachment to Fe coated sand than quartz sand in the absence of HA at pH 5 (Fig. 9). Taken together, these results showed that Fe coating can either enhance or reduce $nTiO_2$ attachment at pH 5 depending on HA concentration.

In $nTiO_2$−Fe coated sand systems, HA adsorbed to both $nTiO_2$ and Fe coating, therefore, ZP of both $nTiO_2$ and Fe coating was influenced by HA concentration. To calculate the DLVO interaction energy between $nTiO_2$ and Fe coated sand, concentration of adsorbed HA on $nTiO_2$ (q_{Ti}) and Fe coating (q_{Fe}) needs to be quantified. For each total HA concentration, q_{Ti} and q_{Fe} were calculated using adsorption isotherms (Equation A1

and A2, Appendix 5) based on measured aqueous HA concentration at adsorption equilibrium (C_{eq}). For cases where C_{eq} was below detection limit, C_{eq}, q_{Ti}, and q_{Fe} were calculated by coupling HA adsorption isotherm equations for $nTiO_2$ and Fe coated sand (Equation A1 and A2, Appendix 5) with mass balance of HA (Equation A5, Appendix 5). ZP and HDD of $nTiO_2$ were determined based on the relationship between ZP/HDD of $nTiO_2$ and adsorbed HA concentration (Fig. 3, 4), and ZP of Fe coating were determined based on the relationship between ZP of Fe coating and adsorbed HA concentration (Fig. 6).

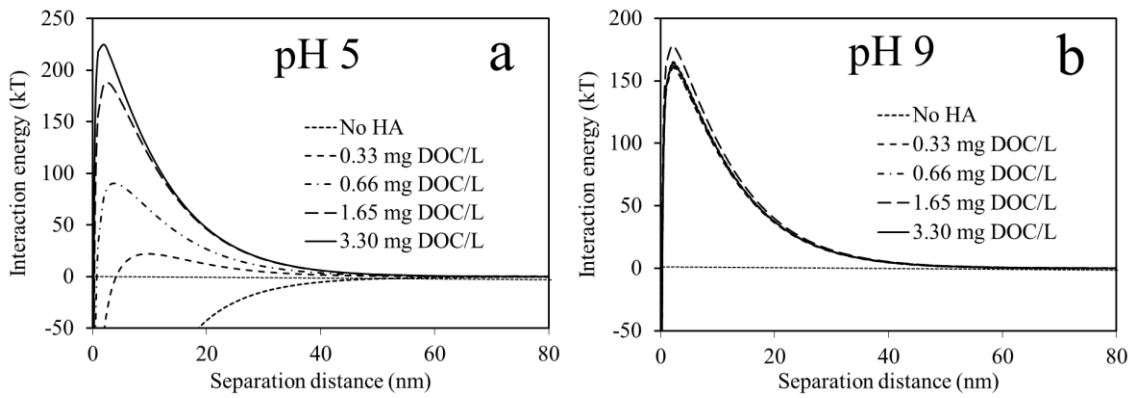

Fig. 13. Calculated DLVO interaction energy profiles for $nTiO_2$-to-quartz sand in 1 mM NaCl solution in the presence of various concentrations of humic acid (HA) at pH 5 (a) and pH 9 (b).

At pH 5, ZP of both $nTiO_2$ and Fe coating changed from positive to negative as the HA concentration increased (Table A3, Appendix 6). It is also noted that for each total HA concentration (C_{total}), ZP of $nTiO_2$ in $nTiO_2$−Fe coated sand system was generally less negative than that in $nTiO_2$−quartz sand systems (Table A2 and A3, Appendix 6). This was attributed to competition against $nTiO_2$ for HA by Fe coating, which decreased adsorbed HA concentration on $nTiO_2$. Calculated DLVO interaction energy profile for $nTiO_2$-to-Fe coated sand showed that at total HA concentrations of 0.33 and 0.66 mg DOC/L, the interaction energy was negative (Fig. 14a), indicating attraction between $nTiO_2$ and sand,

consistent with our experimental observation of high $nTiO_2$ attachment (Fig. 12b). These energy profiles were noticeably different from the energy profiles for $nTiO_2$-to-quartz sand at the same HA concentrations (0.33 and 0.66 mg DOC/L) (Fig. 13a), which showed large energy barrier caused by electrostatic repulsion between like-charged $nTiO_2$ and quartz sand. The higher $nTiO_2$ attachment at these HA concentrations in the $nTiO_2$−Fe coated sand systems was attributable to asynchronous changes in ZP of $nTiO_2$ and Fe coating due to HA adsorption (Table A3, Appendix 6). In $nTiO_2$−Fe coated sand systems, at HA concentration of 0.33 mg DOC/L, ZP of the $nTiO_2$ was positive (+16 mV), and ZP of quartz was negative (ZP = -41 mV), resulting in attraction of $nTiO_2$ to the uncovered quartz on sand surface. At HA concentration of 0.66 mg DOC/L, ZP of $nTiO_2$ became negative (-11 mV), but ZP of Fe coating was positive (+24 mV), resulting in attraction of $nTiO_2$ to the Fe coating. For HA concentrations > 0.66 mg DOC/L, both $nTiO_2$ and Fe coating became negatively charged, together with negatively charged quartz surface, leading to large energy barrier (32.5 and 124.8 kT respectively for HA concentration of 1.66 and 3.3 mg DOC/L) and low $nTiO_2$ attachment.

At pH 9, the calculated energy barrier was high (> 82.2 kT) for all the HA concentrations and increased with increasing HA concentration (Fig. 14b), indicating repulsion between $nTiO_2$ and sand, and therefore low attachment. However, a small fraction of $nTiO_2$ (15% in the absence of HA, and < 5% in the presence of HA) was found to attach to the sand (Fig. 12b). The attachment of $nTiO_2$ under these unfavorable conditions was presumably attributable to surface roughness of Fe coating as discussed in Section 4.5.

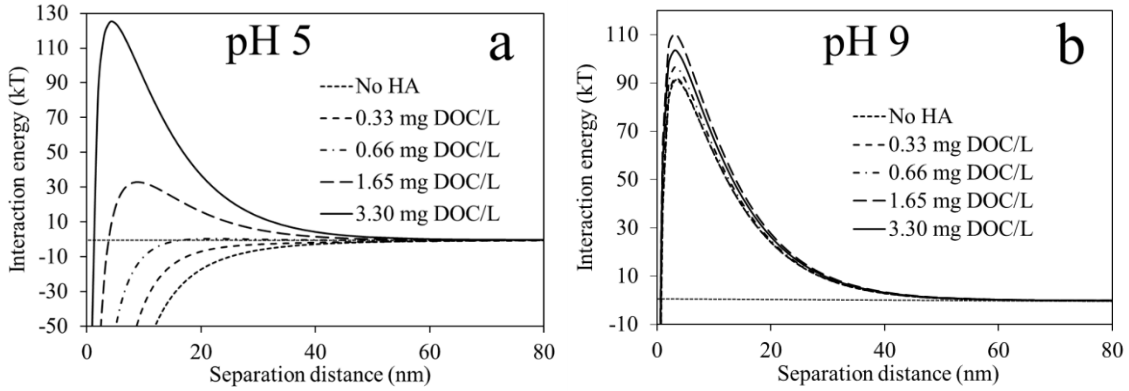

Fig. 14. Calculated DLVO interaction energy profiles for $nTiO_2$-to-Fe coated sand in 1 mM NaCl solution in the presence of various concentrations of humic acid (HA) at pH 5 (a) and pH 9 (b).

Chapter 5: Summary and conclusions

5.1 Result summary in this study

Nanoscale titanium dioxide particles ($nTiO_2$) are manufactured and used as pigment, sunscreen, photocatalyst, and semiconductor in many domestic products and industrial applications (Higarashi and Jardim, 2002; Nagaveni et al., 2004; Quan et al., 2005; Aarthi and Madras, 2007). $nTiO_2$ can be found in papers, plastics, paints, inks, toothpastes, skin care products, rubber, and some electronic devices. Large quantities of $nTiO_2$ are entering the subsurface environments as a result of production of $nTiO_2$ and $nTiO_2$ containing products, and consumption and disposal of these products (Miller et al. 2012). Mounting evidence has shown that $nTiO_2$ are toxic to microbes, plants, and animals, and may cause damages to ecosystems (Wiesner et al., 2006). To evaluate the potential risks of $nTiO_2$ to ecosystems, it is necessary to predict how far $nTiO_2$ may migrate once they are released to the environment, and therefore knowledge of $nTiO_2$ stability in water and how $nTiO_2$ transport in vadose zone and groundwater is important.

A systematic study has been performed to investigate the influence of pH and HA on the stability and attachment of $nTiO_2$ particles to quartz sand and Fe oxyhydroxide coated sand, with special attention to low HA concentration ranges that are relevant to typical groundwater conditions. Stability of $nTiO_2$ was examined under a range of low HA concentrations at pH 5 and 9, and batch experiments were performed to quantify HA adsorption to $nTiO_2$, quartz sand, and Fe oxyhydroxide coated quartz sand. $nTiO_2$ attachment to quartz and Fe oxyhydroxide coated sand at pH 5 and 9 was measured either in the absence of HA, or in the presence of low concentrations of HA. Derjaguin-Landau-Verwey-Overbeek (DLVO) theory was invoked to analyze the interaction energies

between $nTiO_2$ particles and between $nTiO_2$ particle and sand grain so that the role of pH, HA, quartz surface, and Fe oxyhydroxides coating can be elucidated. To our knowledge, this study is the first to report the effects of low concentrations of HA on the stability and attachment of $nTiO_2$ to heterogeneously charged sand.

This study showed that HA can either promote or hinder $nTiO_2$ stability in water depending on pH and HA concentration. Unlike many natural particulate matters such as clays, quartz, bacteria, viruses, and humic substances, which are negatively charged at ambient pH, $nTiO_2$ have a point of zero charge that is comparable to ambient pH and therefore $nTiO_2$ can carry either positive or negative surface charges in natural water. At pH 5, $nTiO_2$ was positively charged and formed stable suspension in the absence of HA. $nTiO_2$ had high capacity for HA adsorption at pH 5. At low HA concentrations, due to HA adsorption to $nTiO_2$, positive charges on $nTiO_2$ was partially neutralized, or $nTiO_2$ became negatively charged but with low charge density. Either case led to low energy barrier and attraction between particles and therefore instability and aggregation of $nTiO_2$ in water. At high HA concentrations, $nTiO_2$ surface became strongly negatively charged, resulting in large energy barrier and stable suspensions. At pH 9, ZP and HDD of $nTiO_2$ were not influenced by changes in HA concentration, and $nTiO_2$ were strongly negatively charged and formed stable suspension throughout the HA concentration range tested due to the repulsive electrostatic forces between $nTiO_2$ particles.

This study also showed that Fe oxyhydroxide coating on quartz sand, which had been reported to attract and immobilize many different types of colloidal particles, influenced $nTiO_2$ attachment in different manners. At pH 5, in the absence of HA, both quartz sand and Fe coated sand strongly attracted $nTiO_2$, but $nTiO_2$ holding capacity of Fe

coated sand was lower than that of quartz sand. The high capacity of quartz sand was due to attractive electrostatic forces between negatively charged quartz and positively charged $nTiO_2$, and the lower capacity of Fe coated sand was attributable to partial coverage of sand surface by positively charged Fe oxyhydroxides, which repulsed like-charged $nTiO_2$. At pH 9, $nTiO_2$ became negatively charged and did not attach to like-charged quartz sand. However, a small fraction of $nTiO_2$ was found to attach to like-charged Fe coated sand at pH 9, presumably due to extra attractive forces caused by surface roughness of the Fe oxyhydroxide coating.

This study further showed that HA influenced $nTiO_2$ attachment to sand by changing the ZP of $nTiO_2$ and Fe coating. In $nTiO_2$−quartz sand systems, at pH 5, even at a low HA concentration of 0.33 mg DOC/L, HA adsorption to $nTiO_2$ reversed of the ZP of $nTiO_2$ and therefore changed the electrostatic forces between $nTiO_2$ and quartz from attractive to repulsive. As a result, $nTiO_2$ attachment to quartz sand substantially decreased. At pH 9, both $nTiO_2$ and quartz were negatively charged, and the low adsorption of HA to $nTiO_2$ hardly changed the ZP of $nTiO_2$, consequently $nTiO_2$ attachment to quartz sand was low and not influenced by HA. In $nTiO_2$−Fe coated sand systems, HA adsorbed to both $nTiO_2$ and Fe coating. At pH 5, at low HA concentrations, changes in ZP of $nTiO_2$ and Fe coating was asynchronous, resulting in attraction between $nTiO_2$ and sand surface, and therefore high $nTiO_2$ attachment. At high HA concentrations, $nTiO_2$, Fe coating, as well as uncovered quartz surface were all negatively charged, leading to high energy barrier and low $nTiO_2$ attachment. At pH 9, $nTiO_2$, Fe coating, and quartz were all negatively charged either in the absence of presence of various concentrations of HA, resulting in strong repulsive forces between $nTiO_2$ and sand surface, and therefore low $nTiO_2$ attachment.

5.2 Conclusions and environmental implications

A series of adsorption experiments and zeta potential measurements were used to investigate the stability of $nTiO_2$ and the particle-surface interaction processes in the presence of humic acid at pH 5 and pH 9. Our results clearly indicate that the stability of $nTiO_2$ and the attachment of $nTiO_2$ to sand surface are depending on solution pH and the loading of HA. Zeta potential measurements show the presence of HA leads to notable surface modification on $nTiO_2$ and Fe oxyhydroxide. Electrostatic attractive interaction and van der Walls interaction dominate the adsorption of HA to $nTiO_2$ and Fe oxyhydroxide at pH 5, while hydrophobic interaction and ligand exchange might take effect at pH 9. Calculated DLVO energy provides consistent support to the experimental results, except for the attachment of $nTiO_2$ to Fe coated sand at pH 9. To the best of our knowledge, this study should be considered as an important step on the impact of humic acid concentration on nanoparticle stability and particle-surface affinity. Future work about the attachment of $nTiO_2$ to sand surface can focus on the $nTiO_2$ attachment from an unstable suspension which relies on the interplay between aggregation and sorption.

This research has provided sorely needed knowledge on nanoparticle dispersion and transport in subsurface environments. Besides, this study have important implications on the risk assessment and environmental remediation by engineered TiO_2 nanoparticle in natural subsurface environments with low HA concentration. The knowledge gained from this study will offer guidance for the Canadian government to develop proper policies and regulations that are aimed at minimizing negative environmental impacts of nanotechnology.

References

Aarthi, T., Madras, G. (2007). Photocatalytic degradation of Rhodamine dyes with nano-TiO_2. Industrial and Engineering Chemistry Research 46, 7-14.

Abudalo, R. A., Bogatsu, Y. G., Ryan, J. N., Harvey, R. W., Metge, D. W., Elimelech, M. (2005). Effect of ferric oxyhydroxide grain coatings on the transport of bacteriophage PRD1 and Cryptosporidium parvum oocysts in saturated porous media. Environmental Science & Technology 39(17), 6412-6419.

Abudalo, R. A., Ryan, J. N., Harvey, R. W., Metge, D. W., Landkamer, L. (2010). Influence of organic matter on the transport of Cryptosporidium parvum oocysts in a ferric oxyhydroxide-coated quartz sand saturated porous medium. Water Research 44(4), 1104-1113.

Battin, T. J., Kammer, F. V., Weilhartner, A., Ottofuelling, S., & Hofmann, T. (2009). Nanostructured TiO2: transport behavior and effects on aquatic microbial communities under environmental conditions. Environmental Science and Technology 43(21), 8098-8104.

Bendersky, M., Davis, J. M. (2011). DLVO interaction of colloidal particles with topographically and chemically heterogeneous surfaces. Journal of Colloid and Interface Science 353(1), 87-97.

Bergström, L. (1997). Hamaker constants of inorganic materials. Advances in Colloid and Interface Science 70, 125-169.

Borggaard, O. K., Raben-Lange, B., Gimsing, A. L., Strobel, B.W. (2005). Influence of humic substances on phosphate adsorption by aluminium and iron oxides. Geoderma 127, 270–279.

Buzea, C., Pacheco, I. I., & Robbie, K. (2007). Nanomaterials and nanoparticles: sources and toxicity. Biointerphases, 2(4), MR17-MR71.

Bradford, S.A., Torkzaban, S., (2013).Colloid interaction energies for physicallyand chemically heterogeneous porous media. Langmuir 29 (11), 3668–3676.

Boncagni, N. T., Otaegui, J. M., Warner, E., Curran, T., Ren, J., Fidalgo de Cortalezzi, M. M. (2009). Exchange of TiO_2 nanoparticles between streams and streambeds. Environmental Science & Technology 43(20), 7699-7705.

Brunet, L., Lyon, D. Y., Hotze, E. M., Alvarez, P. J., & Wiesner, M. R. (2009). Comparative photoactivity and antibacterial properties of C60 fullerenes and titanium dioxide nanoparticles. Environmental Science and Technology 43(12), 4355-4360.

Butt, H. J., Cappella, B., Kappl, M. (2005). Force measurements with the atomic force microscope: Technique, interpretation and applications. Surface Science Reports 59(1), 1-152.

Chen, G., Liu, X., Su, C. (2012). Distinct effects of humic acid on transport and retention of TiO_2 rutile nanoparticles in saturated sand columns. Environmental Science & Technology 46(13), 7142-7150.

Chen, K.L., Elimelech, M. (2007). Influence of humic acid on the aggregation kinetics of fullerenes (C60) nanoparticles in monovalent and divalent electrolyte solutions. Journal of Colloid and Interface Science 309 (1), 126-134.

Chowdhury, I., Cwiertny, D. M., Walker, S. L. (2012). Combined factors influencing the aggregation and deposition of nano-TiO_2 in the presence of humic acid and bacteria. Environmental Science & Technology 46(13), 6968-6976.

Crittenden, J. C., Trussell, R. R., Hand, D. W., Howe, K. J., Tchobanoglous, G. (2012). MWH's Water Treatment: Principles and Design. John Wiley & Sons.

Derjaguin, B. V. (1941). Theory of the stability of strongly charged lyophobic sols and the adhesion of strongly charged particles in solutions of electrolytes. Acta Physicochim. USSR 14, 633-662.

Dunphy Guzman, K. A., Finnegan, M. P., Banfield, J. F. (2006). Influence of surface potential on aggregation and transport of titania nanoparticles. Environmental Science & Technology 40(24), 7688-7693.

Elimelech, M., Gregory, J., Jia, X., Williams, R.A. (2013). Particle Deposition and Aggregation: Measurement, Modelling and Simulation. Butterworth-Heinemann, London.

Espinasse, B., Hotze, E.M., Wiesner, M.R. (2007). Transport and retention of colloidal aggregates of C-60 in porous media: effects of organic macromolecules, ionic composition, and preparation method. Environmental Science & Technology 41(21), 7396-7402.

Fang, J., Shan, X.Q., Wen, B., Lin, J.M., Owens, G. (2009). Stability of titania nanoparticles in soil suspensions and transport in saturated homogeneous soil columns. Environmental Pollution 157 (4), 1101-1109.

Faure, B., Salazar-Alvarez, G., Bergström, L. (2011). Hamaker constants of iron oxide nanoparticles. Langmuir 27(14), 8659-8664.

Fein, J. B., Boily, J.-F., Güçlü, K., Kaulbach, E. (1999). Experimental study of humic acid adsorption onto bacteria and Al-oxide mineral surfaces. Chemical Geology 162, 33-45.

Foppen, J. W. A., Okletey, S., Schijven, J. F. (2006). Effect of goethite coating and humic acid on the transport of bacteriophage PRD1 in columns of saturated sand. Journal of Contaminant Hydrology 85(3), 287-301.

French, R.A., Jacobson, A.R., Kim, B., Isley, S.L., Penn, R.L., Baveye, P.C. (2009). Influence of ionic strength, pH, and cation valence on aggregation kinetics of titanium dioxide nanoparticles. Environmental Science & Technology 43, 1354-1359.

Gómez-Merino, A. I., Rubio-Hernández, F. J., Velázquez-Navarro, J. F., Galindo-Rosales, F. J., Fortes-Quesada, P. (2007). The Hamaker constant of anatase aqueous suspensions. Journal of Colloid and Interface Science 316(2), 451-456.

Godinez, I. G., Darnault, C. J. G. (2011). Aggregation and transport of nano-TiO_2 in saturated porous media: effects of pH, surfactants and flow velocity. Water Research 45(2), 839-851.

Grolimund, D., and Borkovec, M. (2005). Colloid-facilitated transport of strongly sorbing contaminants in natural porous media: mathematical modeling and laboratory column experiments, Environmental Science and Technology 39(17): 6378-6386

Gu, B. H., Schmitt, J., Chen, Z. H., Liang, L. Y., McCarthy, J. F. (1994). Adsorption and desorption of natural organic matter on iron-oxide: mechanisms and models. Environmental Science & Technology 28, 38-46.

Guzman, K.A.D., Finnegan, M.P., Banfield, J.F. (2006). Influence of surface potential on aggregation and transport of titania nanoparticles. Environmental Science & Technology 40, 7688-7693.

Hamaker, H.C. (1937). The London–van der Waals attraction between spherical particles. Physica 4 (10), 1058-1072.

Han, P., Wang, X., Cai, L., Tong, M., Kim, H. (2014). Transport and retention behaviors of titanium dioxide nanoparticles in iron oxide-coated quartz sand: Effects of pH, ionic strength, and humic acid. Colloids and Surfaces A: Physicochemical and Engineering Aspects 454, 119-127.

Hiemenz, P. C.; Rajagopalan, R. (1997). Principles of Colloid and Surface Chemistry, 3rd Ed., Marcel Dekker, Inc..

Higarashi, M.M., Jardim, W.F. (2002). Remediation of pesticide contaminated soil using TiO_2 mediated by solar light. Catalysis Today 76, 201-207.

Hsu, J., Chang, Y. (2000). An experimental study of the stability of TiO_2 particles in organic–water mixtures. Colloids and Surfaces A: Physicochemical and Engineering Aspects 161, 423-437.

Hu, J. D., Zevi, Y., Kou, X. M., Xiao, J., Wang, X. J., Jin, Y. (2010). Effect of dissolved organic matter on the stability of magnetite nanoparticles under different pH and ionic strength conditions. Science of the Total Environment 408(16), 3477-3489.

Hund-Rinke, K., Simon M. (2006). Ecotoxic effect of photocatalytic active nanoparticles (TiO_2) on algae and daphnids, Environmental Science and Pollution Research 13(4): 225-232.

Hyung, H., Fortner, J.D., Hughes, J.B., Kim, J. (2007). Natural organic matter stabilizes carbon nanotubes in the aqueous phase. Environmental Science and Technology 41, 179–184.

Illés E, Tombácz E. (2006). The effect of humic acid adsorption on pH-dependent surface charging and aggregation of magnetite nanoparticles. Jounal of Colloid Interface Science 295:115–23.

Israelachvili, J. N. (2011). Intermolecular and Surface Forces: revised third edition. Academic Press.

Klute, A. (1986). Methods of Soil Analysis. Part 1. Physical and Mineralogical Methods (No. Ed. 2). American Society of Agronomy, Inc..

Jaynes, W. F. and Zartman, R. E. (2005). Talc, iron phosphates and other minerals in biosolids. Soil Science Society of America Journal 69(4):1047-1057.

Joo, S. H., Al-Abed, S. R., Luxton, T. (2009). Influence of carboxymethyl cellulose for the transport of titanium dioxide nanoparticles in clean silica and mineral-coated sands. Environmental Science & Technology 43(13), 4954-4959.

Jung, B., O'Carroll, D., Sleep, B. (2014). The influence of humic acid and clay content on the transport of polymer-coated iron nanoparticles through sand. Science of the Total Environment 496, 155-164.

Kallay, N., Zalac, S. (2002). Stability of nanodispersions: a model for kinetics of aggregation of nanoparticles. Journal of Colloid and Interface Science 253, 70–76

Karathanasis, A. D., Johnson, D. M. C., & Matocha, C. J. (2005). Biosolid colloid-mediated transport of copper, zinc, and lead in waste-amended soils. Journal of Environmental Quality, 34(4), 1153-1164.

Kiser, M. A., Westerhoff, P., Benn, T., Wang, Y., Perez-Rivera, J., & Hristovski, K. (2009). Titanium nanomaterial removal and release from wastewater treatment plants. Environmental Science and Technology 43(17), 6757-6763.

Kosmulski, M. (2001). Chemical Properties of Material Surfaces (Vol. 102). CRC Press.

Kretzschmar, R., Barmettler, K., Grolimund, D., Yan, Y., Borkovec, M., Sticher, H. (1997). Experimental determination of colloid deposition rates and collision efficiencies in natural porous media. Water Resources Research 33, 1129–1137.

Kretzschmar, R., Borkovec, M., Grolimund, D., Elimelech, M. (1999). Mobile subsurface colloids and their role in contaminant transport. Advances in agronomy 66, 121-193.

Lanphere, J. D., Rogers, B., Luth, C., Bolster, C. H., Walker, S. L. (2014). Stability and transport of graphene oxide nanoparticles in groundwater and surface water. Environmental Engineering Science 31(7), 350-359.

Lee, J., Bartelt-Hunt, S. L., Li, Y., Morton, M. (2015). Effect of 17β-estradiol on stability and mobility of TiO_2 rutile nanoparticles. Science of the Total Environment 511, 195-202.

Lecoanet, H. F., & Wiesner, M. R. (2004). Velocity effects on fullerene and oxide nanoparticle deposition in porous media. Environmental Science and Technology 38(16), 4377-4382.

Lenhart, J. J., Saiers, J. E. (2002). Transport of silica colloids through unsaturated porous media: Experimental results and model comparisons. Environmental Science & Technology 36(4), 769-777.

Lin, D., Tian, X., Wu, F., Xing, B. (2010). Fate and transport of engineered nanomaterials in the environment. Journal of Environmental Quality 39, 1896-1908.

Lin, S., Cheng, Y., Bobcombe, Y., L. Jones, K., Liu, J., Wiesner, M. R. (2011). Deposition of silver nanoparticles in geochemically heterogeneous porous media: predicting affinity from surface composition analysis. Environmental Science & Technology 45(12), 5209-5215.

Liu, H., Ma, L., Zhao, J., Liu, J., Yan, J., Ruan, J., & Hong, F. (2009). Biochemical toxicity of nano-anatase TiO2 particles in mice. Biological Trace Element Research, 129(1-3), 170-180.

Lenhart, J. J., Saiers, J. E. (2002). Transport of silica colloids through unsaturated porous media: Experimental results and model comparisons. Environmental Science & Technology 36(4), 769-777.

Madl, A. K., & Pinkerton, K. E. (2009). Health effects of inhaled engineered and incidental nanoparticles. Critical Reviews in Toxicology, 39(8), 629-658.

Mattigod, S.V., Fryxell, G.E., Alford, K., Gilmore, T., Parker, K., Serne, J., Engelhard, M. (2005). Functionalized TiO2nanoparticles for use for in situ anion immobilization. Environmental Science and Technology 39, 7306–7310.

Miller, R. J., Bennett, S., Keller, A. A., Pease, S., Lenihan, H. S. (2012). TiO_2 nanoparticles are phototoxic to marine phytoplankton. PloS One 7(1), e30321.

Mills, A. L., Herman, J. S., Hornberger, G. M., DeJesús, T. H. (1994). Effect of solution ionic strength and iron coatings on mineral grains on the sorption of bacterial cells to quartz sand. Applied and Environmental Microbiology 60(9), 3300-3306.

Nagaveni, K., Sivalingam, G., Hegde, M. S., Madras, G. (2004). Photocatalytic degradation of organic compounds over combustion-synthesized nano-TiO2. Environmental Science & Technology 38(5), 1600-1604.

Navarro, E., Baun, A., Behra, R., Hartmann, N.B., Filser, J., Miao, A. J., Quigg, A., Santschi, P.H., Sigg, L. (2008). Environmental behavior and ecotoxicity of engineered nanoparticles to algae, plants and fungi. Ecotoxicology 17 (5), 372-386.

Nowack, B., Bucheli, T.D. (2007). Occurrence, behavior and effects of nanoparticles in the environment. Environmental Pollution 150, 5–22.

Petosa, A. R., Jaisi, D. P., Quevedo, I. R., Elimelech, M., Tufenkji, N. (2010). Aggregation and deposition of engineered nanomaterials in aquatic environments: role of physicochemical interactions. Environmental Science & Technology 44(17), 6532-6549.

Pensini, E., Sleep, B. E., Yip, C. M., O'Carroll, D. (2013). Forces of interactions between iron and aluminum silicates: Effect of water chemistry and polymer coatings. Journal of Colloid and Interface Science 411, 8-15.

Plathe, K. L., Von der Kammer, F., Hassellöv, M., Moore, J., Murayama, M., Hofmann, T., Hochella, M. F. (2010). Using FlFFF and aTEM to determine trace metal–nanoparticle associations in riverbed sediment. Environmental Chemistry, 7(1), 82-93.

Quan, X., Zhao, X., Chen, S., Zhao, H., Chen, J., Zhao, Y. (2005). Enhancement of photodegradation on soil surfaces using TiO2 induced by UV-light. Chemosphere 60, 266-273.

Ryan, J.N., Elimelech, M. (1996). Colloid mobilization and transport in groundwater. Colloids and Surfaces A 107, 1–56.

Robichaud, C.O., Uyar, A.E., Darby, M.R., Zucker, L.G., Wiesner, M.R., (2009). Estimates of upper bounds and trends in nano-TiO2 production as a basis for exposure assessment, Environmental Science and Technology43 (12): 4227-4233

Sen, T.K., Khilar, K.C. (2006). Review on subsurface colloids and colloid-associated contaminant transport in saturated porous media. Advances in Colloid and Interface Science 119, 71–96.

Shen, C., Li, B., Wang, C., Huang, Y., Jin, Y. (2011). Surface roughness effect on deposition of nano-and micro-sized colloids in saturated columns at different solution ionic strengths. Vadose Zone Journal 10(3), 1071-1081.

Snoswell, D.R.E., Duan, J., Fornasiero, D., Ralston, J. (2005). Colloid stability of synthetic titania and the influence of surface roughness. Journal of Colloid and Interface Science 286, 526–535.

Sun, H., Zhang, X., Niu, Q., Chen, Y., & Crittenden, J. C. (2007). Enhanced accumulation of arsenate in carp in the presence of titanium dioxide nanoparticles. Water, Air, and Soil Pollution, 178(1-4), 245-254.

Tipping, E. (1981). The adsorption of aquatic humic substances by iron oxides. Geochimica et Cosmochimica Acta 45,191-199.

Tkachenko, N.H., Yaremko, Z.M., Bellmann, C., Soltys, M.M. (2006). The influence of ionic and nonionic surfactants on aggregative stability and electrical surface properties of aqueous suspensions of titanium dioxide. Journal of Colloid and Interface Science 299, 686-695.

Treumann, S., Torkzaban, S., Bradford, S. A., Visalakshan, R. M., Page, D. (2014). An explanation for differences in the process of colloid adsorption in batch and column studies. Journal of Contaminant Hydrology 164, 219-229.

Wang, D., Zhang, W., Zhou, D. (2013). Antagonistic effects of humic acid and iron oxyhydroxide grain-coating on biochar nanoparticle transport in saturated sand. Environmental Science & Technology 47(10), 5154-5161.

Wang, D., Bradford, S. A., Harvey, R. W., Gao, B., Cang, L., Zhou, D. (2012a). Humic acid facilitates the transport of ARS-labeled hydroxyapatite nanoparticles in iron oxyhydroxide-coated sand. Environmental Science & Technology 46(5), 2738-2745.

Wang, Q., Cheng, T., Wu, Y. (2014). Influence of mineral colloids and humic substances on uranium (VI) transport in water-saturated geologic porous media. Journal of Contaminant Hydrology 170, 76-85.

Wang, Q., Cheng, T., Wu, Y. (2015). Distinct Roles of Illite Colloid and Humic Acid in Mediating Arsenate Transport in Water-Saturated Sand Columns. Water, Air, and Soil Pollution 226(5), 1-15.

Wang, Y., Gao, B., Morales, V. L., Tian, Y., Wu, L., Gao, J., Bai, W., Yang, L. (2012b). Transport of titanium dioxide nanoparticles in saturated porous media under various solution chemistry conditions. Journal of Nanoparticle Research 14(9), 1-9.

Warheit, D. B., Webb, T. R., Reed, K. L., Frerichs, S., & Sayes, C. M. (2007). Pulmonary toxicity study in rats with three forms of ultrafine-TiO 2 particles: differential responses related to surface properties. Toxicology, 230(1), 90-104.

Wiesner, M. R., Lowry, G. V., Alvarez, P., Dionysiou, D., Biswas, P. (2006). Assessing the risks of manufactured nanomaterials. Environmental Science & Technology 40(14), 4336-4345.

Yang, Y., Saiers, J. E., Barnett, M. O. (2013). Impact of Interactions between natural organic matter and metal oxides on the desorption kinetics of uranium from heterogeneous colloidal suspensions. Environmental Science & Technology 47, 2661-2669.

Zhang, X., Sun, H., Zhang, Z., Niu, Q., Chen, Y., & Crittenden, J. C. (2007). Enhanced bioaccumulation of cadmium in carp in the presence of titanium dioxide nanoparticles. Chemosphere, 67(1), 160-166.

Zhuang, J., Flury, M., Jin, Y. (2003). Colloid-facilitated Cs transport through water saturated Hanford sediment and Ottawa sand. Environmental Science and Technology 37, 4905–4911.

Appendix 1: Calibration curves of humic acid (HA) and $nTiO_2$ at pH 5 and pH 9

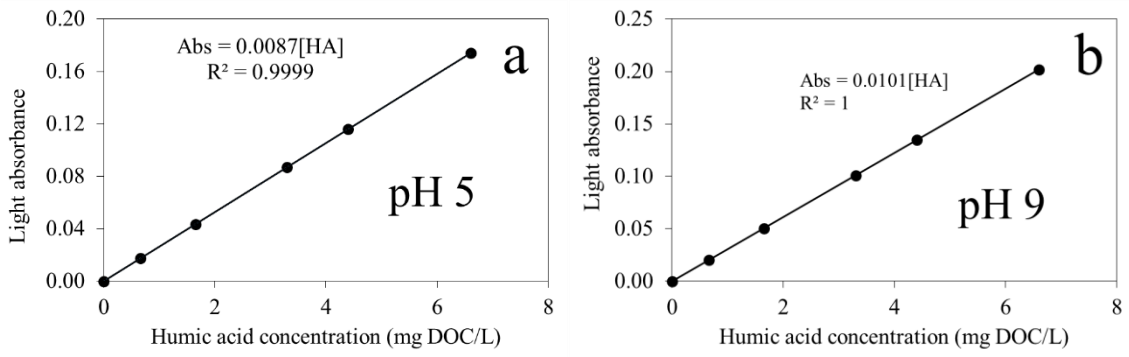

Fig. A1. Calibration curves of humic acid (HA) at pH 5 (a) and pH 9 (b) in 1 mM NaCl solution. Light absorbance was measured at a wavelength of 368 nm by a spectrophotometer.

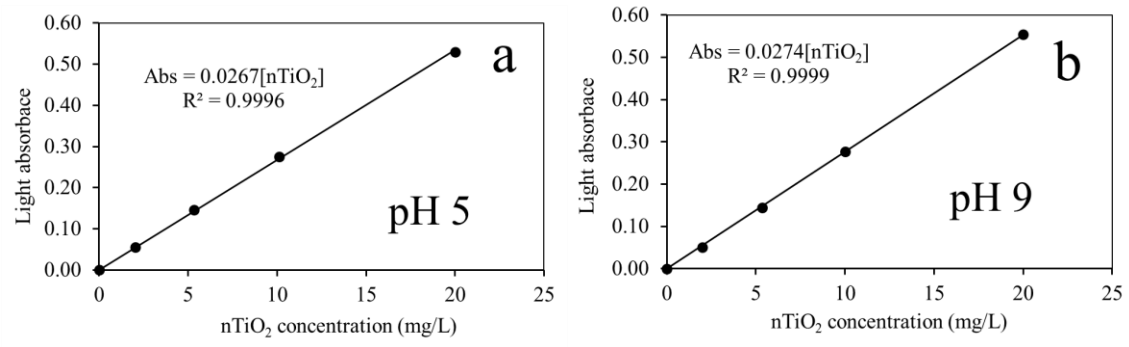

Fig. A2. Calibration curves of $nTiO_2$ suspensions at pH 5 (a) and pH 9 (b) in 1 mM NaCl solution. Light absorbance was measured at a wavelength of 368 nm by a spectrophotometer.

Appendix 2: Hamaker constant determination

Unknown Hamaker constant ($nTiO_2$ to Fe coated sand collector) can be determined by the following method (Hiemenz et al., 1997). For two dissimilar materials, the Hamaker constant can be estimated in term of Hamaker constant of each material. That is

$$A_{12} = \frac{2A_{11}A_{22}}{A_{11} + A_{22}} \approx \sqrt{A_{11}A_{22}} \tag{A6}$$

For contact of two dissimilar materials in the presence of a third media,

$$A_{132} = A_{12} + A_{33} - A_{13} - A_{23} \tag{A7}$$

$$A_{131} = A_{11} + A_{33} - 2A_{13} = \frac{(A_{11} - A_{22})^2}{A_{11} + A_{33}} \simeq (\sqrt{A_{11}} - \sqrt{A_{33}})^2 \tag{A8}$$

$$A_{132} \simeq (\sqrt{A_{11}} - \sqrt{A_{33}})(\sqrt{A_{22}} - \sqrt{A_{33}}) \tag{A9}$$

$$A_{TWF} \simeq (\sqrt{A_{TT}} - \sqrt{A_{WW}})(\sqrt{A_{FF}} - \sqrt{A_{WW}}) \tag{A10}$$

Appendix 3: Extended DLVO calculation with chemical heterogeneity and physical heterogeneity

Classic DLVO calculations do not take into account surface nano-heterogeneity on the sand surface. For example, when the quartz sand is coated with metal oxides, the surface potential of quartz sand under certain pH condition would be chemically heterogeneous because quartz and iron oxides have different point of zero charge. Besides, these Fe coating would generate different scales of physical surface roughness. Therefore, these patch-wise surface heterogeneities can generate localized regions where the interaction is less unfavorable or even favorable, even though the medium's average interaction is unfavorable.

Modified DLVO calculations considering both physical and chemical heterogeneities between $nTiO_2$ and Fe coated sands can be determined by the following method.

Bendersky and Davis (2011) found that a linear combination of the dimensionless interaction energies associated with type 1 (Φ1) and type 2 (Φ2) cells provided good agreement with grid surface integration technique results. The mean value of Φ within A_z is therefore determined as

$$\Phi_{Total} = \left(1 - \frac{A_{Fe}}{A_z}\right)\Phi_{C-Qz} + \frac{A_{Fe}}{A_z}\Phi_{C-Fe} \tag{A11}$$

Particle-asperity interactions can be treated as sphere-sphere interactions. Sphere-asperity interaction energies can be calculated by equations for two interacting spheres, where spherical particle radius and average hemispherical asperity radius need to be used.

Hence, the interaction energy between a spherical particle and Fe coated rough surface can be given as

$$\Phi_{C-Fe} = \eta\Phi_{C-A} + (1-\eta)\Phi_{C-FeP} \tag{A12}$$

Where η refers to the fraction of particle-rough surface interactions involving an asperity, $\Phi_{C\text{-}P}$ is the sphere–plate interaction energy, and $\Phi_{C\text{-}A}$ is the sphere–asperity (sphere–sphere) interaction energy.

DLVO interaction energy between Fe coated sand and $nTiO_2$ can be determined by the following equation:

$$\Phi_{Total} = \left(1 - \frac{A_{Fe}}{A_z}\right)\Phi_{C-Qz} + \frac{A_{Fe}}{A_z}\left(\eta\Phi_{C-A} + (1-\eta)\Phi_{C-FeP}\right) \tag{A13}$$

A_{Fe}/A_z can be determined by SEM with spectrum image to get the Fe coating coverage on sand surface. Combination of different η and A_{Fe}/A_z corresponds to different scenarios describing colloid approaching to sand surface.

Appendix 4: XRD characterization of AeroxideTM TiO_2 P25 powder

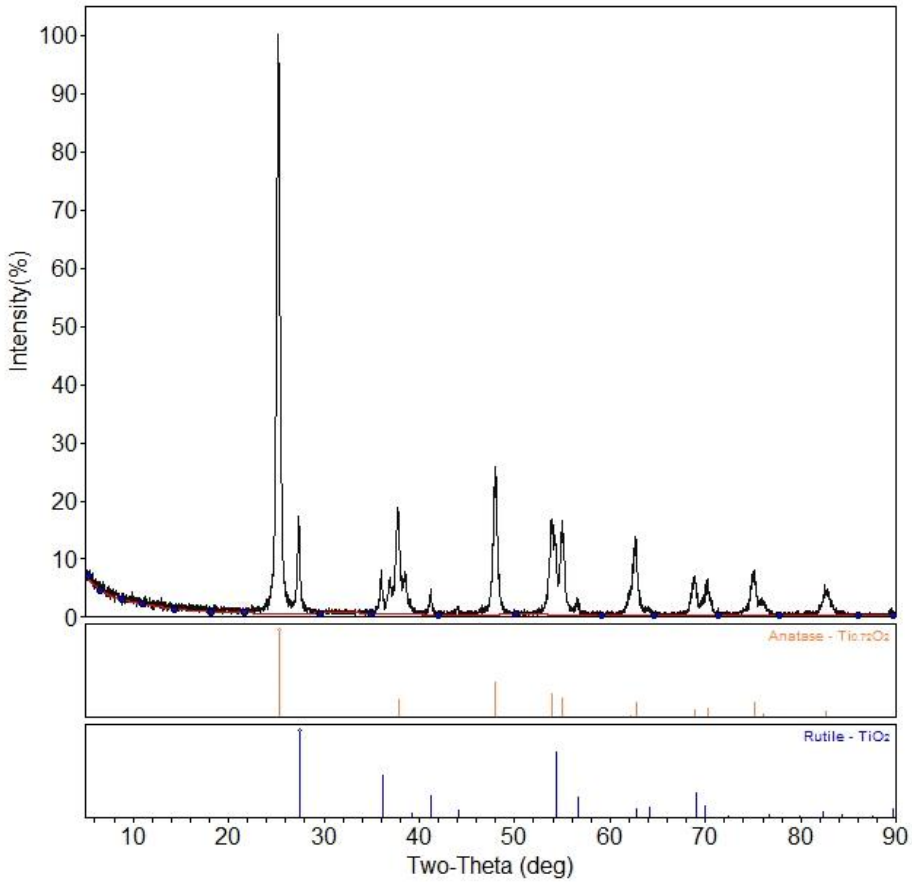

Fig. A1. XRD profile of Aeroxide^{TM} TiO_2 P25 powder.

Appendix 5: Langmuir adsorption isotherm and mass balance equations

Langmuir adsorption isotherm equation for humic acid (HA) adsorption to $nTiO_2$:

$$q_{Ti} = \frac{q_{max(Ti)} k_{Ti} C_{eq}}{1 + k_{Ti} C_{eq}} \qquad \text{(Eq A1)}$$

Langmuir adsorption isotherm equation for HA adsorption to Fe oxyhydroxide:

$$q_{Fe} = \frac{q_{max(Fe)} k_{Fe} C_{eq}}{1 + k_{Fe} C_{eq}} \qquad \text{(Eq A2)}$$

Mass balance equation for HA in (HA + $nTiO_2$) system:

$$C_{total} V = C_{eq} V + q_{Ti} m_{Ti} \qquad \text{(Eq A3)}$$

Mass balance equation for HA in (HA + Fe oxyhydroxide) system:

$$C_{total} V = C_{eq} V + q_{Fe} m_{Fe} \qquad \text{(Eq A4)}$$

Mass balance equation for HA in (HA + $nTiO_2$ + Fe oxyhydroxide) system:

$$C_{total} V = C_{eq} V + q_{Ti} m_{Ti} + q_{Fe} m_{Fe} \qquad \text{(Eq A5)}$$

Variables and parameters in the equations:

k_{Ti}: adsorption constant of $nTiO_2$ (L/mg)

k_{Fe}: adsorption constant of Fe oxyhydroxide (L/mg)

$q_{max(Ti)}$: adsorption capacity of $nTiO_2$ (mg/kg Ti)

$q_{max(Fe)}$: adsorption capacity of Fe oxyhydroxide (mg/kg Fe)

q_{Ti}: adsorbed HA concentration on $nTiO_2$ (mg/kg Ti)

q_{Fe}: adsorbed HA concentration on Fe oxyhydroxide (mg/kg Fe)

m_{Ti}: mass of Ti (kg)

m_{Fe}: mass of Fe (kg)

C_{total}: total HA concentration (mg/L)

C_{eq}: aqueous-phase HA concentration at adsorption equilibrium (mg/L)

V: volume of solution (L)

Appendix 6: Tables of DLVO calculating parameters and results

Table A1. Experimentally measured zeta potential (ZP) and hydrodynamic diameter (HDD) of $nTiO_2$ as well as calculated $nTiO_2$-to-$nTiO_2$ DLVO interaction energy parameters (Φ_{max}: energy barrier; Φ_{min2}: secondary minimum) in 1 mM NaCl solution at various humic acid (HA) concentrations (C_{total}) at pH 5 and 9. Aqueous-phase HA concentration at equilibrium (C_{eq}) and adsorbed HA concentration on $nTiO_2$ (q_{Ti}) were calculated based on Langmuir adsorption isotherm equation (Equation S1) and mass balance of HA (Equation S3).

pH	C_{total} (HA)	C_{eq} (HA)	q_{Ti} (HA)	ZP of $nTiO_2$	HDD of $nTiO_2$	Φ_{max}	Φ_{max} separation	Φ_{min2}	Φ_{min2} separation
	(mg DOC/L)	(mg DOC/L)	(mg OC/kg Ti)	(mV)	(nm)	(kT)	(nm)	(kT)	(nm)
5.0	0	0	0	21.3	322.6	5.83	8	-0.53	44
5.0	0.07	0.0052	5.41	18.6	475.6	2.24	7	-1.10	44
5.0	0.13	0.0099	10.02	-10.2	583.3	NE*	NE	NE	NE
5.0	0.33	0.0277	25.22	-20.0	273.1	3.61	8	-0.39	42
5.0	0.66	0.0662	49.54	-41.0	246.8	9.49	6	-0.30	50
5.0	1.65	0.3217	110.81	-39.1	219.0	36.60	4	-0.15	70
5.0	3.30	1.5229	148.25	-41.6	219.0	45.40	3	-0.11	70
5.0	4.95	3.0875	155.38	-41.1	214.5	45.90	3	-0.10	70
5.0	6.60	4.7041	157.92	-42.3	214.5	46.50	3	-0.10	70
9.0	0	0	0	-32.6	218.2	22.97	4	-0.13	60
9.0	0.07	0.0188	4.27	-32.6	216.9	22.72	4	-0.12	60
9.0	0.13	0.0377	7.70	-32.6	215.5	22.71	4	-0.12	60
9.0	0.33	0.1236	17.22	-32.7	211.5	22.47	4	-0.11	60
9.0	0.66	0.3436	26.40	-33.1	209.7	23.08	4	-0.11	60
9.0	1.65	1.2458	33.72	-35.5	210.3	28.46	4	-0.11	70
9.0	3.30	2.8701	35.86	-33.0	213.0	23.33	4	-0.12	60
9.0	4.95	4.512	36.51	-35.4	207.5	27.89	4	-0.10	70
9.0	6.60	6.159	36.82	-35.1	211.3	27.69	4	-0.10	70

* Not exist.

Table A2. Experimentally measured zeta potential (ZP) of quartz sand, and zeta potential (ZP) and hydrodynamic diameter (HDD) of $nTiO_2$ as well as calculated $nTiO_2$-to-quartz DLVO interaction energy parameters (Φ_{max}: energy barrier; Φ_{min2}: secondary minimum) in 1 mM NaCl solution at various humic acid (HA) concentrations (C_{total}) at pH 5 and 9. Aqueous-phase HA concentration at equilibrium (C_{eq}) and adsorbed HA concentration on $nTiO_2$ (q_{Ti}) were calculated based on Langmuir adsorption isotherm equation (Equation S1) and mass balance of HA (Equation S3).

pH	C_{total} (HA)	C_{eq} (HA)	q_{Ti} (HA)	ZP of quartz	ZP of $nTiO_2$	HDD of $nTiO_2$	Φ_{max}	Φ_{max} separation	Φ_{min2}	Φ_{min2} separation
	(mg DOC /L)	(mg DOC/L)	(mg OC/kg Ti)	(mV)	(mV)	(nm)	(kT)	(nm)	(kT)	(nm)
5.0	0	0	0	-40.6	21.3	322.6	NE*	NE	NE	NE
5.0	0.33	0.0277	25.22	-40.6	-20.0	273.1	21.9	10	-0.05	90
5.0	0.66	0.0662	49.54	-40.6	-41.0	267.7	90.1	4	-0.04	100
5.0	1.65	0.3217	110.81	-40.6	-39.1	246.8	187.1	2	-0.03	100
5.0	3.30	1.5229	148.25	-40.6	-41.6	219.0	224.9	2	-0.03	100
9.0	0	0	0	-42.1	-32.6	218.2	164.5	2	-0.03	100
9.0	0.33	0.1236	17.22	-42.1	-32.7	211.5	159.9	2	-0.03	100
9.0	0.66	0.3436	26.40	-42.1	-33.1	209.7	161.1	2	-0.03	100
9.0	1.65	1.2458	33.72	-42.1	-35.5	210.3	177.9	2	-0.03	100
9.0	3.30	2.8701	35.86	-42.1	-33.0	213.0	163.4	2	-0.03	100

* Not exist.

Table A3. Zeta potential (ZP) of quartz, Fe coating, and zeta potential (ZP) and hydrodynamic diameter (HDD) of $nTiO_2$ as well as calculated $nTiO_2$-to-Fe coated sand DLVO interaction energy parameters (Φ_{max}: energy barrier; Φ_{min2}: secondary minimum) in 1 mM NaCl solution at various humic acid (HA) concentrations (C_{total}) at pH 5 and 9. ZP of quartz, and ZP of Fe coating and ZP/HDD of $nTiO_2$ in the absence of HA were experimentally measured. ZP of Fe coating and ZP/HDD of $nTiO_2$ in the presence of HA were determined based on adsorbed HA concentration on Fe coating (q_{Fe}) and $nTiO_2$ (q_{Ti}), which were calculated based on Langmuir adsorption isotherm equations (Equation S1&S2) and mass balance of HA (Equation S5).

pH	C_{total} (HA)	C_{eq} (HA)	q_{Fe} (HA)	q_{Ti} (HA)	ZP of quartz	ZP of Fe coating	ZP of $nTiO_2$	HDD of $nTiO_2$	Φ_{max}	Φ_{max} separation	Φ_{min2}	Φ_{min2} separation
	(mg DOC/L)	(mg DOC/L)	$\left(\frac{\text{mg OC}}{\text{kg Fe}}\right)$	$\left(\frac{\text{mg OC}}{\text{kg Ti}}\right)$	(mV)	(mV)	(mV)	(nm)	(kT)	(nm)	(kT)	(nm)
5.0	0	0	0	0	-40.6	40.3	21.3	322.6	NE*	NE	NE	NE
5.0	0.33	0.0055	2.41	5.73	-40.6	36.0	16.0	461.3	NE	NE	NE	NE
5.0	0.66	0.0119	4.78	11.84	-40.6	24.0	-11.3	409.9	0.3	22	-0.49	46
5.0	1.65	0.0378	11.55	32.57	-40.6	-8.0	-25.0	269.3	32.5	10	-0.27	70
5.0	3.30	0.1313	21.37	75.68	-40.6	-34.9	-35.9	256.4	124.8	4	-0.20	80
9.0	0	0	0	0	-42.1	-15.6	-32.6	218.2	82.2	4	-0.20	80
9.0	0.33	0.1038	0.40	15.60	-42.1	-21.1	-32.7	211.5	88.7	5	-0.19	70
9.0	0.66	0.2714	0.95	24.45	-42.1	-27.9	-33.0	209.7	99.9	4	-0.18	80
9.0	1.65	1.0000	2.49	32.87	-42.1	-34.1	-35.2	210.3	121.1	4	-0.17	80
9.0	3.30	2.4723	3.87	35.58	-42.1	-38.2	-33.4	213.0	117.2	4	-0.17	80

* Not exist.

Appendix 7: Backscatter SEM image and spectrum image of Fe coated sand

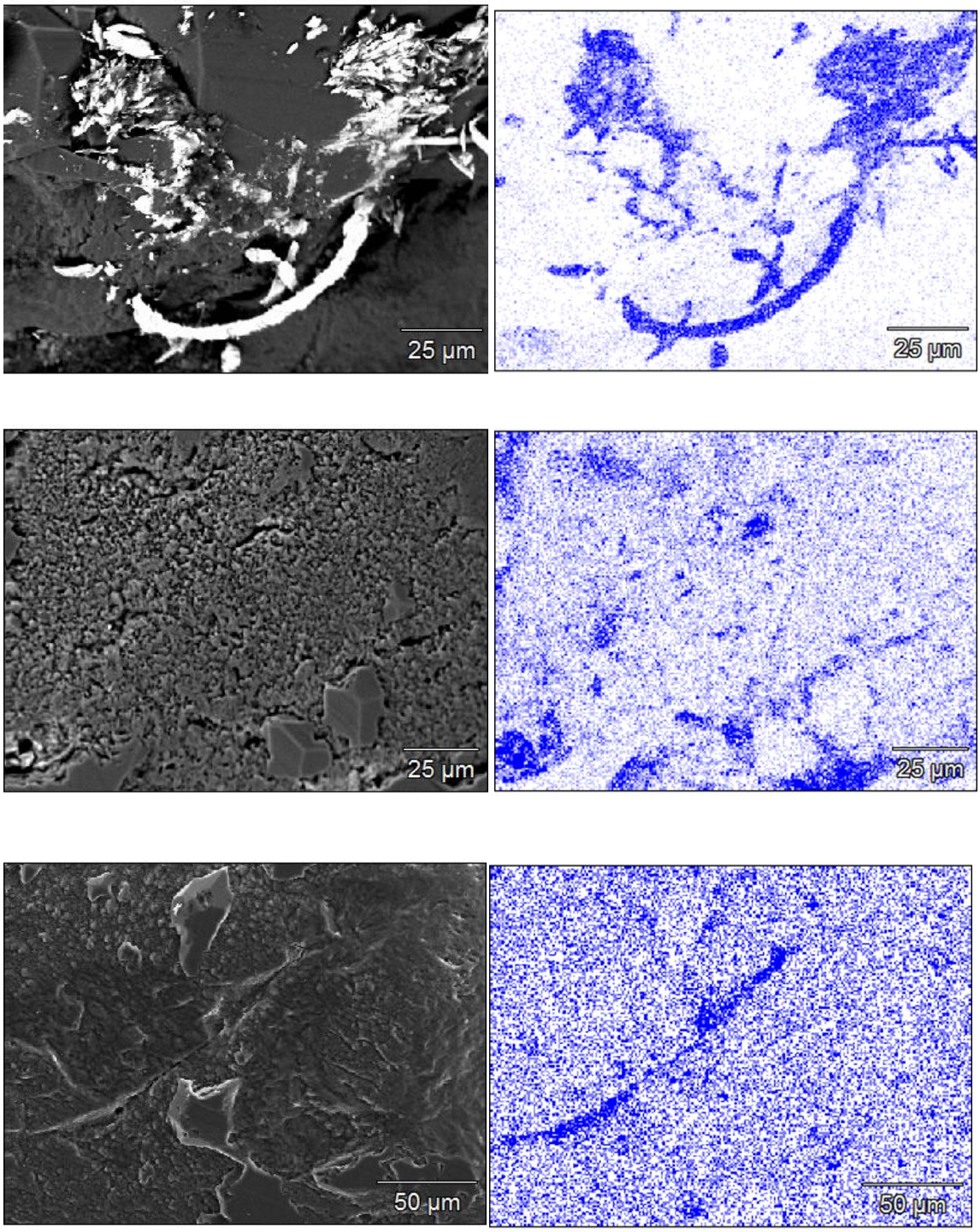

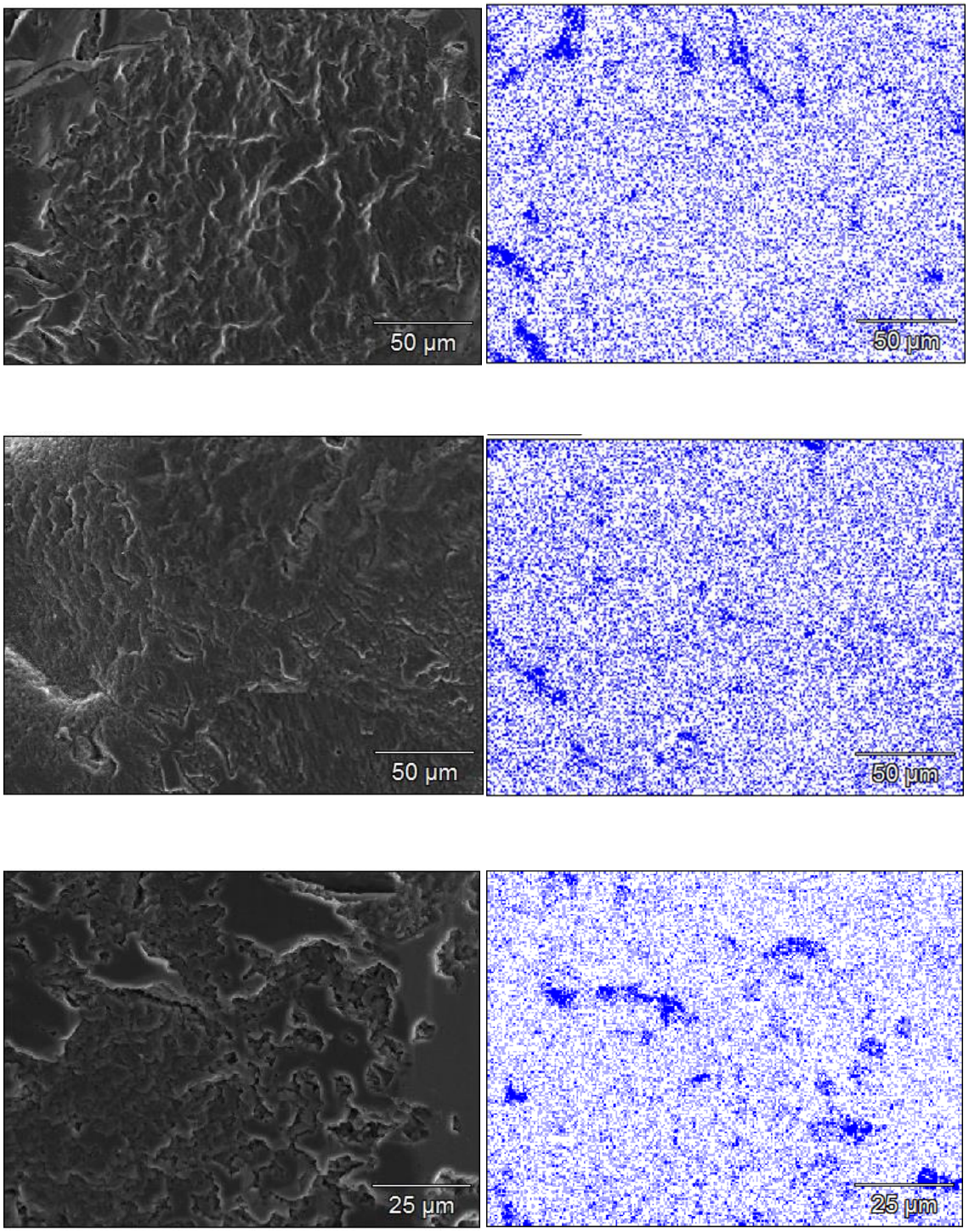

Fig. A1. Backscatter SEM image (left) and energy dispersive X-ray (EDX) spectrum of element distribution (right) of representative Fe coated sand surface. Blue color indicates Fe.

Appendix 8: Matlab code for getting Fe coating coverage on Fe coated sand

Open Matlab and retrieve Image Processing Toolbox

```
clear all;

clc;

I=imread('6.png'); //open image//

I1=im2bw(I,0.8); //binary, selecting appropriate threshold to get all area which are white

imshow(I1); //

p=sum(sum(I1(:,:)));// calculate all pixels which are white//

r=(1-p)/(size(I1,1)*size(I2,2)) // size(I1,1)*size(I2,2) is the pixel of the image, r is the
        ratio//
```

Appendix 9: $nTiO_2$ transport in porous media: effects of humic acid at different pH

1. Materials and methods:

Column experiments were conducted at room temperature (22 ℃). Kontes ChromaFlex™ Glass chromatography columns with 2.5 cm inner diameter and 15 cm length were full-filled with dry pure quartz sands or mixture of pure quartz sand and Fe coated sands, saturated with de-aired, distilled water or different water solutions. The column were tapped to maintain uniformity and to remove air bubbles with each increment of sands. Total dry mass of the porous media and volume of background solution used to pack each column (i.e., pore volume of the column) were around 128 g and 28 cm^3 (Table A1). Porosity and bulk density of packed column were 61.4% and 2.12 g/cm^3 respectively.

Each column experiment consisted of three major phases: (1) pre-condition phase with background solution injected into the column for ~12 h until the pH and IS of effluent was stable, followed by (2) suspension injection phase with 3 hours (~ 7 pore volumes of influent suspension), and (3) elution phase with 1 hour of background solution injected. A peristaltic pump (Masterflex, Cole-Parmer Instruments) was used to inject solutions/suspensions into the bottom of the vertically-positioned column to obtain specific discharge of 0.204 cm/min. Some of the $nTiO_2$ transport experiments were conducted in duplicate. Effluent samples were collected with an automatic fraction collector (CF-2, Spectrum Chromatography) and analyzed for $nTiO_2$ concentration by UV-Vis Spectrophotometer at wavelength of 368 nm. The experimental conditions for experiments are listed in Table A1. Briefly, two types of suspensions: $nTiO_2$ only and $nTiO_2$+ HA were

prepared by suspending 10 mg $nTiO_2$ suspension into 1 mM background NaCl solutions with various concentrations of HA (0, 0.13, 0.33, 0.66 mg/L) at pH 5 and 9 respectively in 500 mL glass beakers. (Table A1). The suspension was then sonicated by a Branson Digital Sonifier (Crystal Electronics) for 30 min with 200 W power to disperse the $nTiO_2$ particles before subsequent experiments.

Table A1. Conditions of column experiments

pH	Ionic strength (mM)	Influent	Porous media (Quartz : Fe)	Dry Mass of solid materials (g)	Volume of Pore Water (mL)
5	1	"$nTiO_2$ only"	No Fe	129.1711	27.5924
	1	"$nTiO_2$ + 0.13 mg DOC/L HA"	No Fe	128.7816	28.188
	1	"$nTiO_2$ + 0.33 mg DOC/L HA"	No Fe	128.8426	27.7934
	1	"$nTiO_2$ only"	9:1	128.7512	28.032
	1	"$nTiO_2$ + 0.33 mg DOC/L HA"	9:1	128.5657	28.125
	1	"$nTiO_2$ + 0.33 mg DOC/L HA	2:1	128.5338	27.8151
	1	"$nTiO_2$ + 0.66 mg DOC/L HA	2:1	129.1025	28.1215
9	1	"$nTiO_2$ only"	No Fe	129.135	27.9578
	1	"$nTiO_2$ only"	9:1	128.8696	28.2044
	1	"$nTiO_2$ only"	9:1	128.7538	27.6985
	1	"$nTiO_2$ only"	2:1	128.5241	27.6632
	1	"$nTiO_2$ + 0.33 mg/L HA	2:1	128.9195	27.5891

2. Results and discussion:

2.1 $nTiO_2$ transport in clean quartz sand column

Fig. A1 illustrated $nTiO_2$ breakthrough curves at pH 5 and pH 9 in clean quartz sand column and the influence of HA on $nTiO_2$ transport at each pH. Here normalized effluent concentrations (C/C_0) were plotted against the number of pore volumes (V/V_p). Both pH and HA had strong effects on $nTiO_2$ transport (Fig. A1): at pH 5, no $nTiO_2$ was detectable in the effluent, indicating all $nTiO_2$ in the influent were retained in the column. In contrast, high $nTiO_2$ breakthrough was observed in the experiment at pH 9 without HA, and complete breakthrough occurred at 1 pore volume (PV). Enhanced $nTiO_2$ transport was observed in the experiment with 0.33 mg DOC/L HA at pH 5: maximum effluent $nTiO_2$ concentration (C/C_0) increased from 0 to 0.97. However, no $nTiO_2$ was detected in the effluent in the experiment with 0.13 mg DOC /L HA at pH 5, indicating all $nTiO_2$ in the influent were also retained in the column in lower HA concentration.

The overall interactive forces (i.e., van der Waals forces, electric double layer forces, hydration forces, and steric repulsion) between nanoparticles and media grains domain the nanoparticle deposition (Kretzschmar et al., 1999), and thus influencing nanoparticle transport in porous media. pH influenced $nTiO_2$ deposition and transport by affecting surface charge of $nTiO_2$ and media grains. Clean quartz sand was always negatively charged at pH 5 and pH 9 because PZC of quartz sands is approximately 2.8. However, $nTiO_2$ was positively charged at pH 5 but negatively charged at pH 9. Therefore, our quartz sand column were expected to provide favorable deposition sites at pH 5 and unfavorable deposition sites at pH 9. As such, $nTiO_2$ deposition was under favorable conditions at pH 5 and high $nTiO_2$ transport was expected at pH 9. $nTiO_2$ transport was also enhanced in the

presence of HA at pH 5. This drastic increase was attributed to HA adsorption to $nTiO_2$ which reversed the surface charge of $nTiO_2$ as we discussed in batch experiment session. HA adsorption to $nTiO_2$ could increase both electrostatic and steric repulsions between $nTiO_2$ and quartz sands, which enhanced the $nTiO_2$ transport.

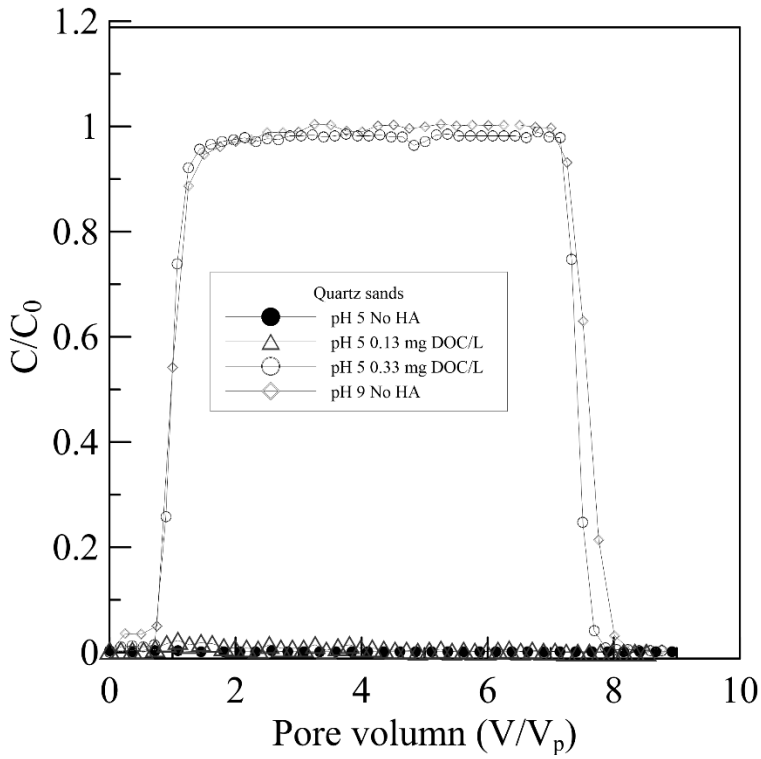

Fig A1. Breakthrough curves of 20 mg/L $nTiO_2$ through columns filled with quartz sand in the absence and presence of HA. (C: concentration in the effluent samples; C_0: concentration in the influent; C/C_0: normalized effluent concentration; V: total volume of effluent; Vp: pore volume of the packed column; V/Vp: normalized volume of effluent)

2.2 $nTiO_2$ transport in Fe coated sand column

The transport of $nTiO_2$ in Fe coated sand columns were examined under different proportions of Fe coated sand to quartz sand at pH 5 and pH 9 and the influence of HA on $nTiO_2$ transport was studied. In general, $nTiO_2$ breakthrough increased as the HA increased but decreased as the proportion of Fe coated sand increased (Fig. A2).

At pH 5 without HA, all $nTiO_2$ were retained in 1(Fe):9 sand column which was

similar to that observed in quartz sand column. However, the increase in HA concentration from 0 to 0.33 mg DOC/L resulted in 98% increase in the relative breakthrough of $nTiO_2$. At pH 5 in the 1(Fe coated sand):2(quartz sand) sand column, the increase in HA concentration from 0.33 to 0.66 mg DOC/L also enhanced the breakthrough of $nTiO_2$: maximum effluent $nTiO_2$ concentration (C/C_0) increased from 35% to 99%.

As expected, large amount of positively charged $nTiO_2$ could be attached to negatively charged quartz sand site in 1(Fe):9 sand column at pH 5 without HA. Surface charge of Fe coating was positive at pH 5 because PZC of Fe oxides was around 8.5. However, the surface charge of Fe coating in the column was expected to be reversed by the overnight flush of HA background solution. At pH 5, both Fe coating and the rest bare quartz sand in our columns carried negative charges and were expected to provide unfavorable deposition sites for negatively charged $nTiO_2$ in the presence HA. Interestingly, only 69 % $nTiO_2$ broke through the column at 1 pore volume and complete breakthrough (C/C_0 = 0.96) occurred at 2 pore volumes. Classical DLVO force was not enough to explain the deposition of $nTiO_2$ onto Fe coated sand at unfavorable conditions. Therefore, it was expected the surface roughness of Fe coating played a distinct role in $nTiO_2$ deposition which provided favorable deposition sites. In that case, $nTiO_2$ deposition was controlled by favorable deposition sites of these patch wise physically and chemically heterogeneous surfaces. This surface roughness effect was further proved when we increased the proportion of Fe coated sands in our column(proportion of Fe coated sands to quartz sands ratio increased from 1: 9 to 1:2) even in the presence of 0.33 mg DOC/L HA. As we noted from Fig. A2, the effluent concentration of $nTiO_2$ steadily increased and did not reach to a plateau within 3 hours injection.

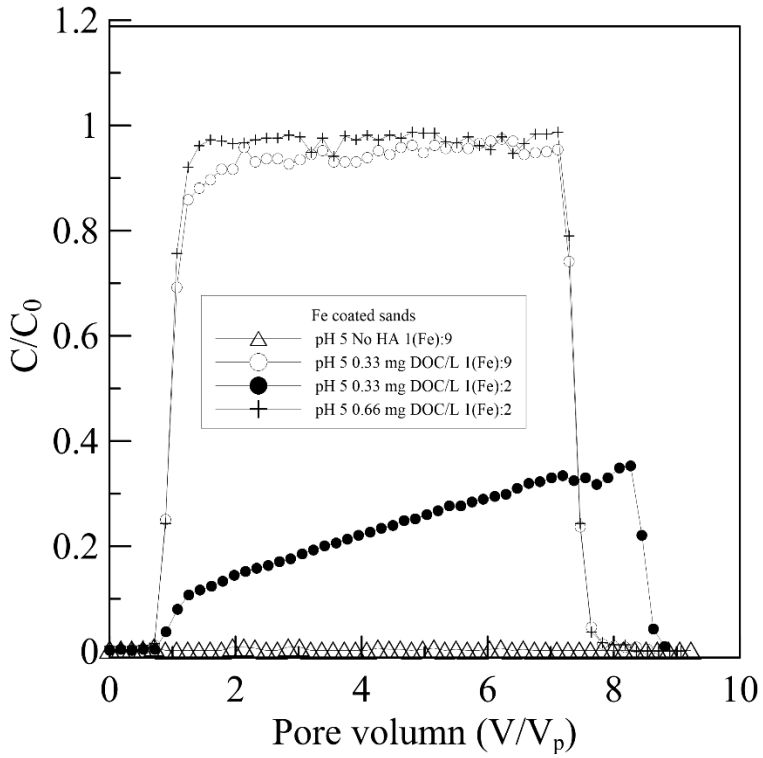

Fig A2. Breakthrough curves of 20 mg/L $nTiO_2$ through columns filled with mixture of quartz sand and Fe coated sands in the absence and presence of HA at pH 5. (C: concentration in the effluent samples; C_0: concentration in the influent; C/C_0: normalized effluent concentration; V: total volume of effluent; Vp: pore volume of the packed column; V/Vp: normalized volume of effluent)

Under conditions without HA at pH 9, as the proportions of Fe coated sand increased from 1(Fe):9 to 1(Fe):2, the arriving of C/C_0 plateau was delayed from 3 PV to 4.5 PVs (Fig. A3). The increase in HA concentration from 0 to 0.33 mg DOC/L significantly enhanced the breakthrough of $nTiO_2$ at either proportion of Fe coated sand: maximum effluent $nTiO_2$ concentration (C/C_0) reached 99% at approximately 1 PV (Fig. A3). Fe coating carried negative charges in all conditions and $nTiO_2$ became more negatively charged at pH 9. Electrostatic repulsion between Fe coating and $nTiO_2$ resulted in high $nTiO_2$ breakthrough although a slight retardation of complete breakthrough was noticed at pH 9 without HA. As we discussed above, Fe coated sands can always provide favorable deposition sites for $nTiO_2$ under both pH conditions (5 and 9) due to its surface roughness,

however, the mobile HA in aqueous solutions increased by increasing the total input HA. Therefore, the portion of HA present in aqueous solutions that did not adsorb on $nTiO_2$ surfaces was more likely to compete with $nTiO_2$ for the deposition sites on Fe coated sand. With the greater collision chance between relatively higher concentration of HA and Fe coated sand, the free HA would preferentially adsorb onto the Fe coated sand surfaces at both pH conditions (5 and 9), and thus decreasing available deposition sites, consequently increasing $nTiO_2$ transport in the column. Moreover, the addition of HA could also lead the surface charges of nanoparticle and sand grain surfaces to be more negative, which increased the DLVO force between nanoparticle and sand surface.

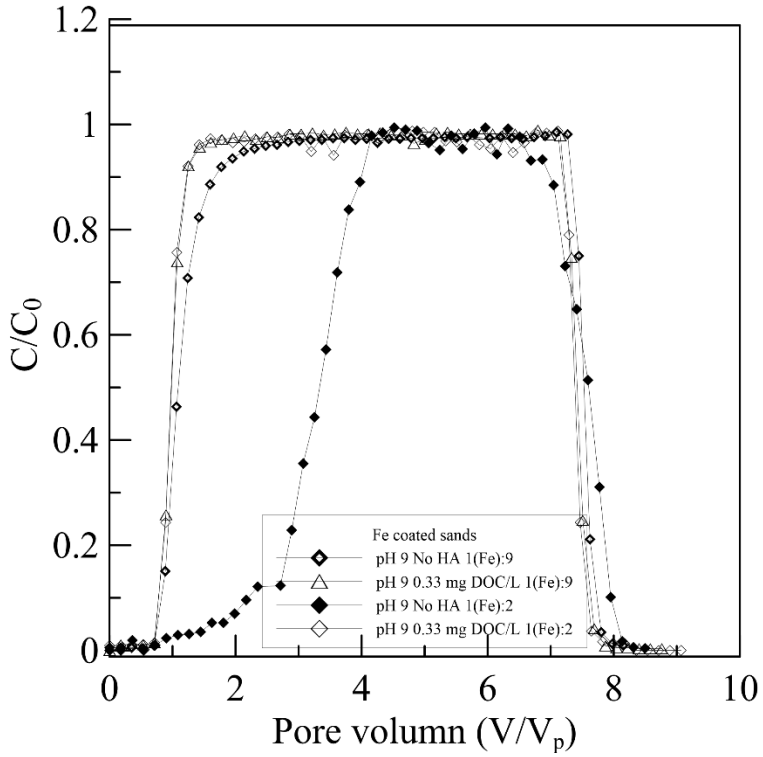

Fig A3. Breakthrough curves of 20 mg/L $nTiO_2$ through columns filled with mixture of quartz sand and Fe coated sands in the absence and presence of HA at pH 9. (C: concentration in the effluent samples; C_0: concentration in the influent; C/C_0: normalized effluent concentration; V: total volume of effluent; Vp: pore volume of the packed column; V/Vp: normalized volume of effluent)

Appendix 10: Hydrodynamic diameter and zeta potential measurement

1. Discussion about peak size and z-average size

Whether to pick peak size or z-average size in DLS (dynamic light scattering) is critically important. In DLS, there are two main fitting algorithms.

(1) Cumulant (or z-average) size and polydispersity (or polydispersity index PDI) with one overall average size and one overall average polydispersity (Retrieved from http://www.materials-talks.com/blog/2014/07/10/faq-peak-size-or-z-average-size-which-one-to-pick-in-dls/).

(2) Peak size (or distribution size) with a mean size and a width for each separate size peak of the distribution (Retrieved from http://www.materials-talks.com/blog/2014/07/10/faq-peak-size-or-z-average-size-which-one-to-pick-in-dls/).

ISO method is used to determine the z-average. From that method (ISO13321:1996 or its newer pendant ISO22412:2008), only the initial part of the correlation function (up to 10% of the intercept) is force fit to a single exponential decay. The decay rate is related to the overall mean size (Retrieved from http://www.materials-talks.com/blog/2014/07/10/faq-peak-size-or-z-average-size-which-one-to-pick-in-dls/).

Longer times (i.e. more of the data are fit, typically to 1% of the intercept) are applied for the distribution analysis. A distribution of different contributions can be obtained from the size classes or bins. Peaks can be defined with a statistical mean and standard deviation of that specific peak (Retrieved from http://www.materials-talks.com/blog/2014/07/10/faq-peak-size-or-z-average-size-which-one-to-pick-in-dls/).

For the size measurement of $nTiO_2$, the z-average generally tend to be the same as peak size, along with the low PDI value, indicating our samples are probably monodisperse.

2. Discussion about intensity and volume-based size distributions

According to the manufacturer, the intensity result is always correct. More detail about the sample can be obtained from the volume distribution, provided that the data quality is acceptable (Retrieved from http://www.materials-talks.com/blog/2014/01/23/intensity-volume-number-which-size-is-correct/).

As revealed by the figure A1, intensity based distribution tend to report relatively large size particle, while the volume or number distribution tend to report those small particles.

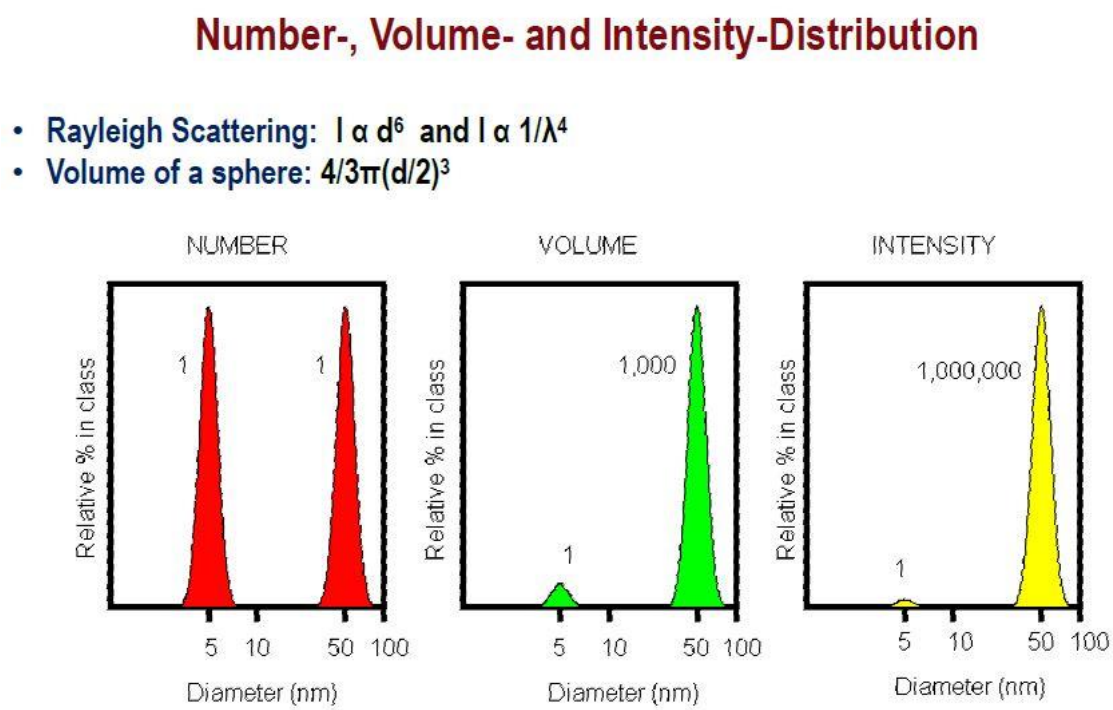

Fig A1: Comparison of the number, volume and intensity distribution (Figure adapted from a handout written by Nano Research Facility, School of Engineering & Applied Science, Washington University in St. Louis)

For the size measurement of humic acid, our aim of interest is particularly towards the smaller size end. Therefore, we prefer the volume distribution as this will generally report the smallest size measured. According to the volume distribution result, we conclude that the size of our humic acid filtrate is in the range of 1 nm to 10 nm which can be treated as dissolved molecular.

3. Discussion about zeta potential

In aqueous systems, almost all surfaces will acquire some kind of charge. The electrophoretic mobility or Zeta potential is highly dependent on both the sample surface and the medium in which it is immersed. Briefly, zeta potential is measured by laser Doppler velocimetry and phase analysis light scattering (PALS) (Retrieved from http://www.malvern.com/en/products/product-range/zetasizer-range/zetasizer-nano-range/zetasizer-nano-z/).

For the ZP measurement of $nTiO_2$, results were generally good and acceptable with small standard deviation. For the ZP measurement of humic acid with different concentrations, results were disorganized with large deviations for each sample. We assume the electrolyte (i.e. Na^+) in the solution might associate with the carboxylic group on the surface with HA, leading the ZP of HA to be concentration-dependant. At higher concentration with a fixed ionic strength, the ZP of HA tend be very negative and stable.

4. Discussion about the importance of refractive index

Generally, the optical properties of the scattering material have a significant influence on the scattering behavior. Mie theory is the best choice to fully describe these phenomena However, in many situations, the optical properties of the material itself are not known.

Firstly, for dynamic light scattering (DLS), the material properties requested in the setup of an experiment may be irrelevant. Indeed, the properties of the material directly affect the amount of scattering. However, it does not matter which material produced the intensity if only an average size by intensity and an average polydispersity (PDI) by intensity are required. When the intensity size distribution is transformed into a volume or number distribution, we have to know exactly how much light is scattered by each nanoparticle (Retrieved from http://www.materials-talks.com/blog/2014/08/05/faq-how-important-are-refractive-index-absorption-for-nanoparticles/).

Besides, the material properties will not matter for the volume distribution obtained from if the nanoparticles are less than 100nm.

In summary: useful information from nanoparticles can be obtained from DLS even without the parameters.

Hydrodynamic diameter and zeta potential of 20 ppm $nTiO_2$ with various humic acid concentration in 1 mM NaCl solution at pH 5 and pH 9

$nTiO_2$ + no HA at pH 5

			Size (d.nm):	% Intensity:	St Dev (d.nm):
Z-Average (d.nm):	433.7	Peak 1:	317.7	100.0	51.50
PdI:	0.394	Peak 2:	0.000	0.0	0.000
Intercept:	0.968	Peak 3:	0.000	0.0	0.000

Result quality : Refer to quality report

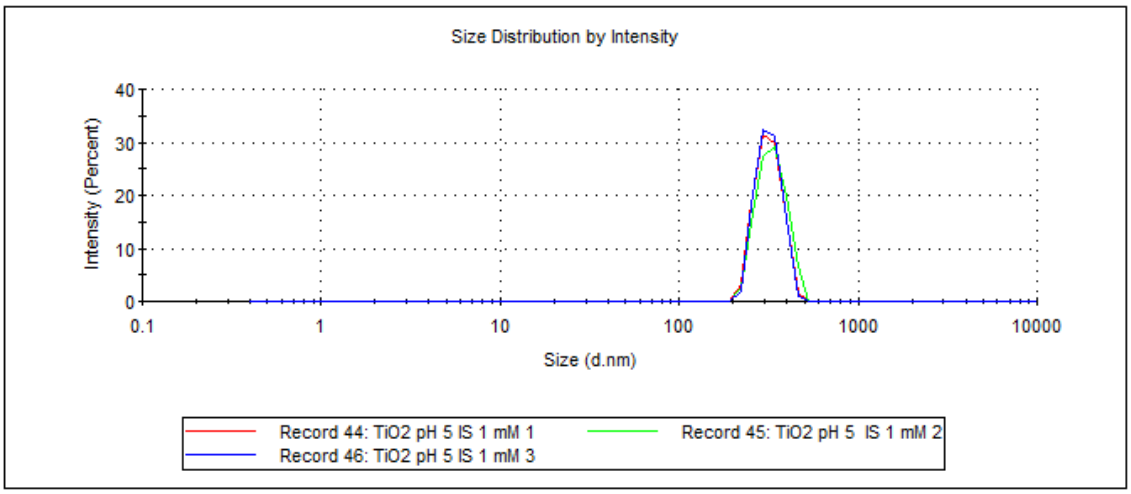

			Size (d.nm):	% Volume:	St Dev (d.nm):
Z-Average (d.nm):	433.7	Peak 1:	327.2	100.0	63.72
PdI:	0.394	Peak 2:	0.000	0.0	0.000
Intercept:	0.968	Peak 3:	0.000	0.0	0.000

Result quality : Refer to quality report

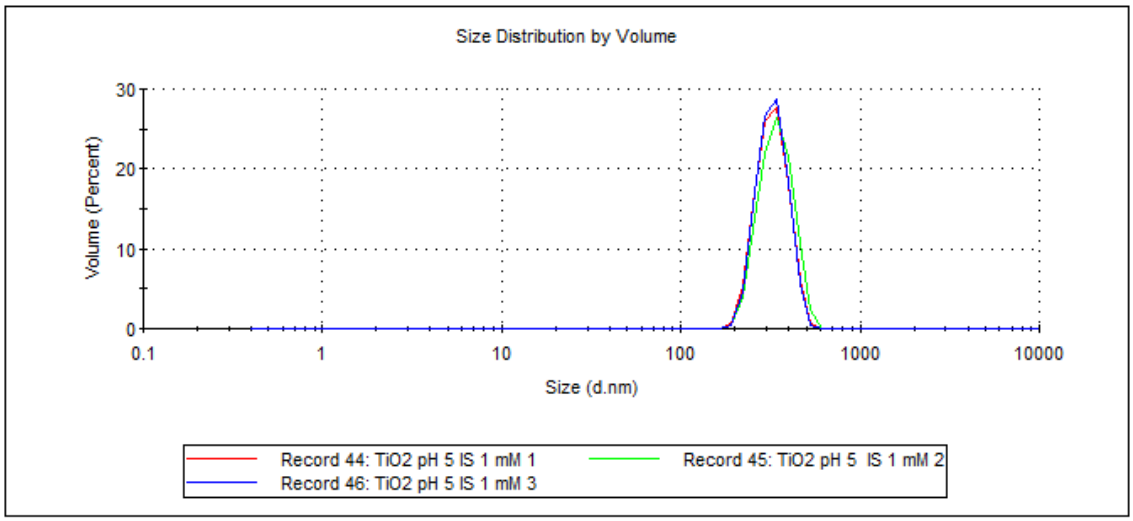

$nTiO_2$ + 0.07 mg/L DOC at pH 5

			Size (d.nm):	% Intensity:	St Dev (d.nm):
Z-Average (d.nm):	732.1	Peak 1:	478.2	100.0	64.52
PdI:	0.438	Peak 2:	0.000	0.0	0.000
Intercept:	0.958	Peak 3:	0.000	0.0	0.000

Result quality : Refer to quality report

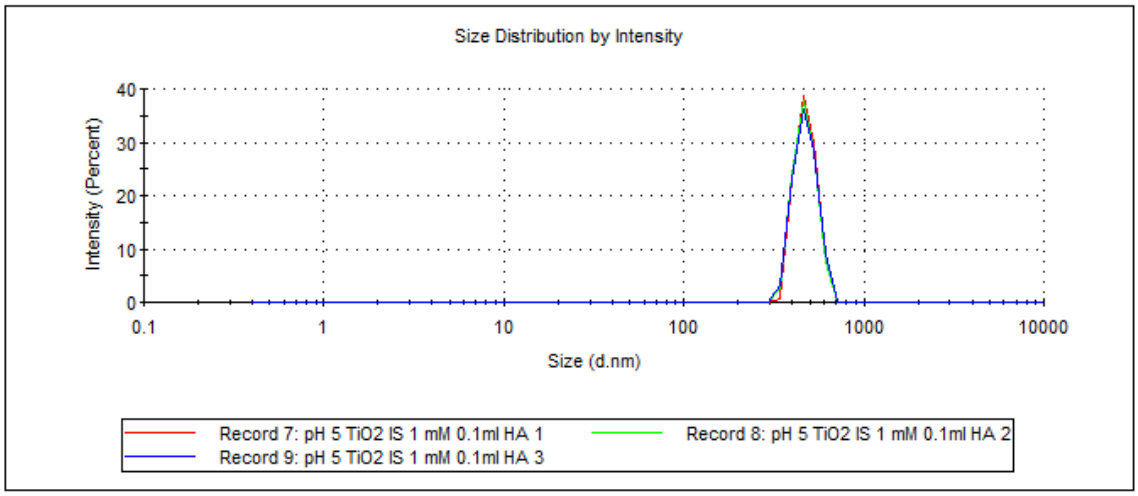

			Size (d.nm):	% Volume:	St Dev (d.nm):
Z-Average (d.nm):	732.1	Peak 1:	494.0	100.0	84.52
PdI:	0.438	Peak 2:	0.000	0.0	0.000
Intercept:	0.958	Peak 3:	0.000	0.0	0.000

Result quality : Refer to quality report

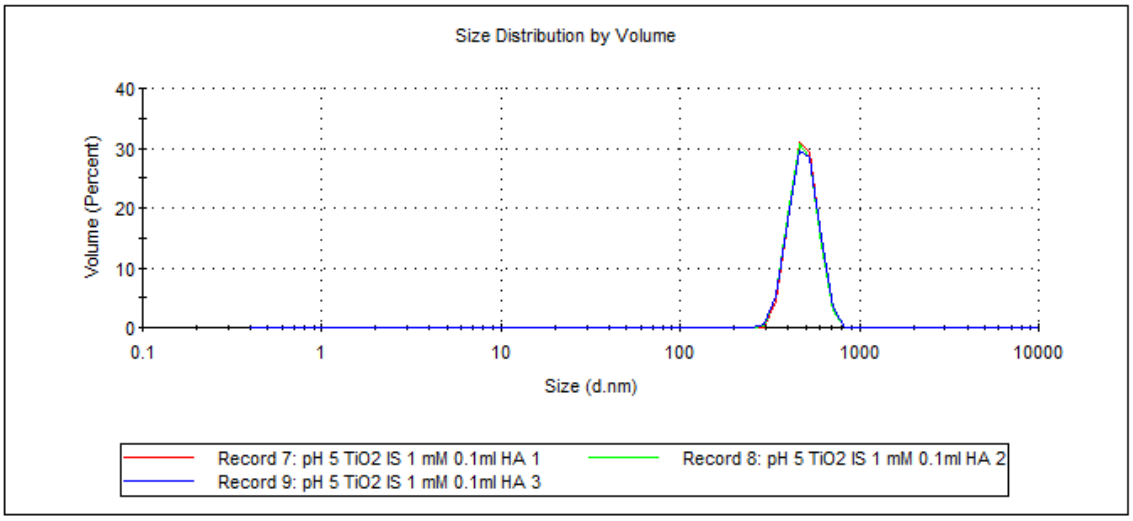

$nTiO_2$ + 0.13 mg/L DOC at pH 5

			Size (d.nm):	% Intensity:	St Dev (d.nm):
Z-Average (d.nm):	1032	Peak 1:	562.3	100.0	65.02
PdI:	0.488	Peak 2:	0.000	0.0	0.000
Intercept:	0.996	Peak 3:	0.000	0.0	0.000

Result quality : Refer to quality report

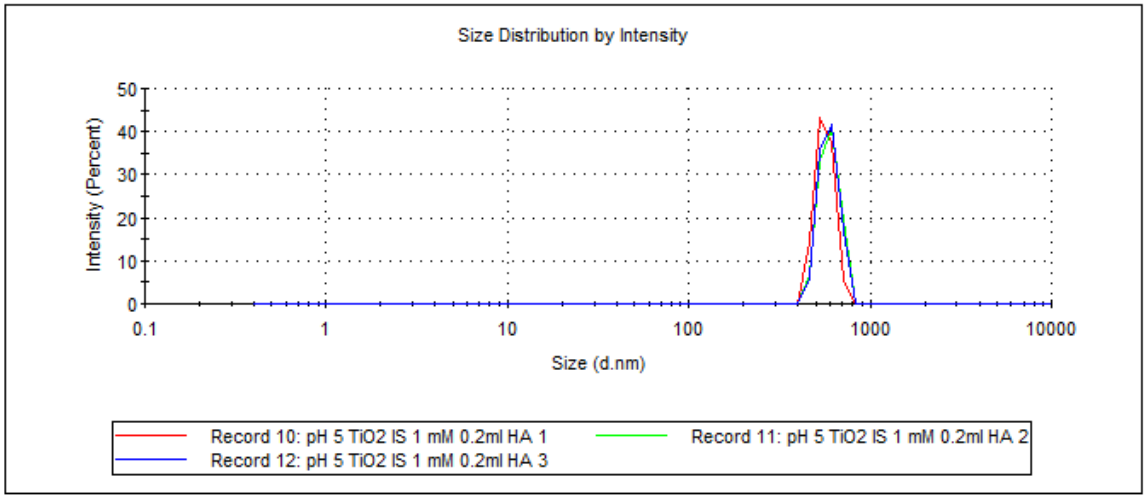

			Size (d.nm):	% Volume:	St Dev (d.nm):
Z-Average (d.nm):	1032	Peak 1:	575.9	100.0	88.57
PdI:	0.488	Peak 2:	0.000	0.0	0.000
Intercept:	0.996	Peak 3:	0.000	0.0	0.000

Result quality : Refer to quality report

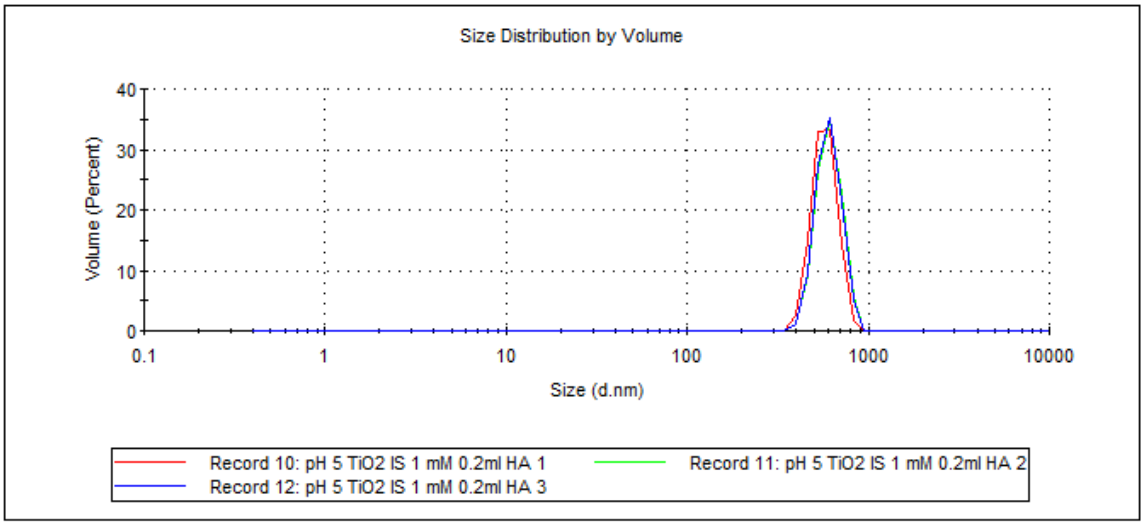

$nTiO_2$ + 0.33 mg/L DOC at pH 5

			Size (d.nm):	% Intensity:	St Dev (d.nm):
Z-Average (d.nm):	298.5	Peak 1:	265.1	100.0	64.95
PdI:	0.296	Peak 2:	0.000	0.0	0.000
Intercept:	0.951	Peak 3:	0.000	0.0	0.000

Result quality : Good

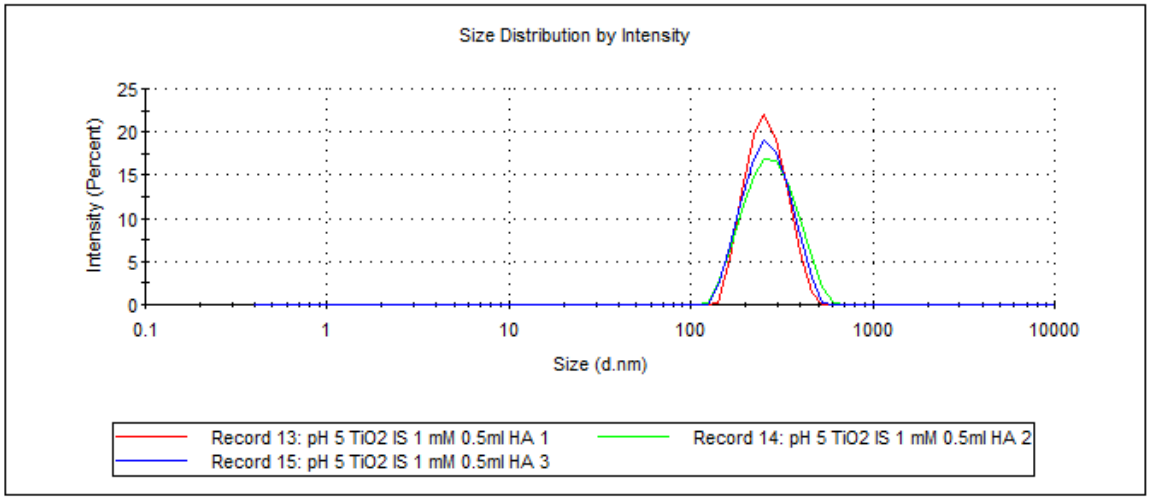

			Size (d.nm):	% Volume:	St Dev (d.nm):
Z-Average (d.nm):	298.5	Peak 1:	263.4	100.0	79.15
PdI:	0.296	Peak 2:	0.000	0.0	0.000
Intercept:	0.951	Peak 3:	0.000	0.0	0.000

Result quality : Good

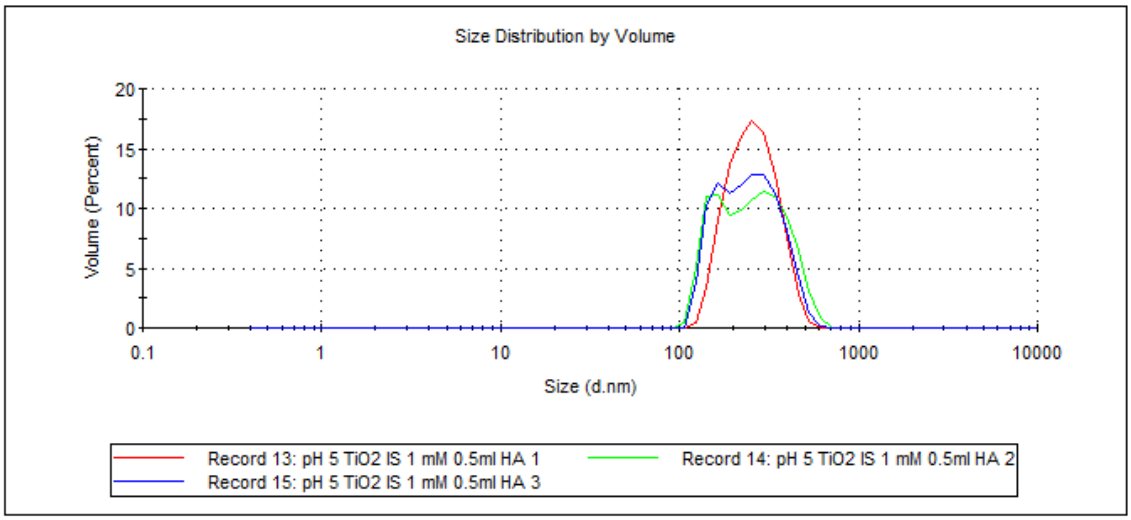

$nTiO_2$ + 0.66 mg/L DOC at pH 5

			Size (d.nm):	% Intensity:	St Dev (d.nm):
Z-Average (d.nm):	214.2	Peak 1:	263.1	100.0	126.8
PdI:	0.194	Peak 2:	0.000	0.0	0.000
Intercept:	0.949	Peak 3:	0.000	0.0	0.000

Result quality : Good

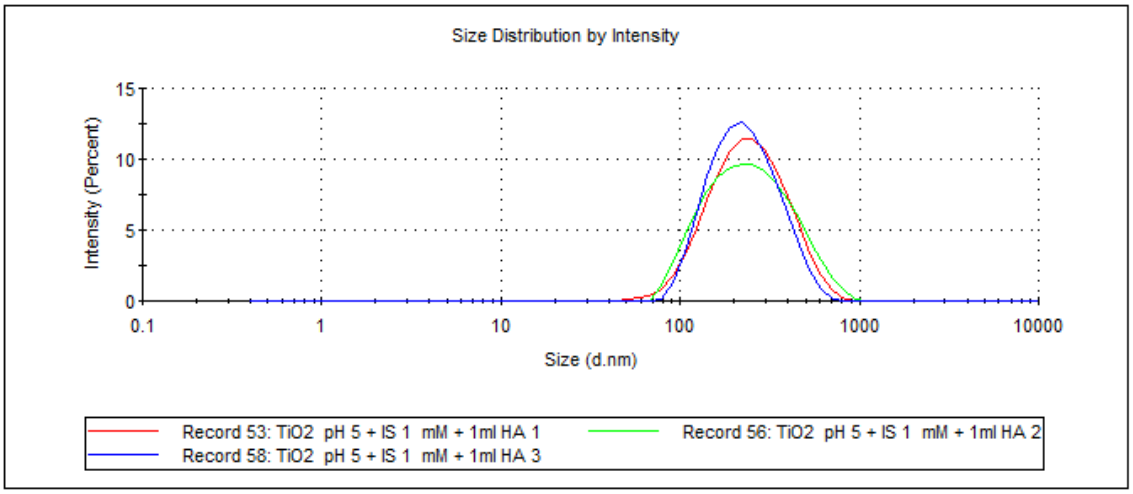

			Size (d.nm):	% Volume:	St Dev (d.nm):
Z-Average (d.nm):	214.2	Peak 1:	120.0	83.8	47.41
PdI:	0.194	Peak 2:	402.9	16.2	131.0
Intercept:	0.949	Peak 3:	0.000	0.0	0.000

Result quality : Good

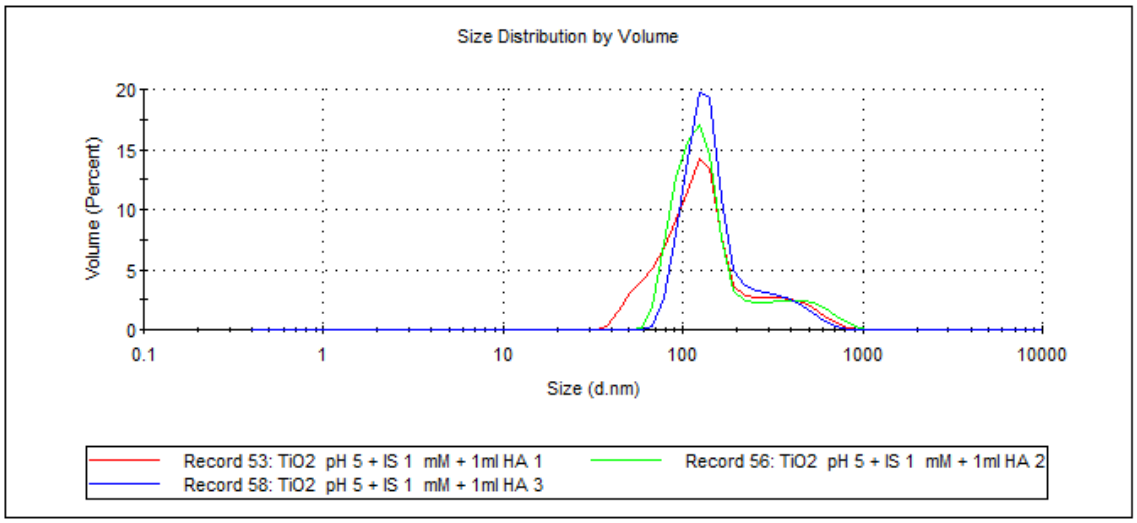

$nTiO_2$ + 1.65 mg/L DOC at pH 5

			Size (d.nm):	% Intensity:	St Dev (d.nm):
Z-Average (d.nm):	255.6	Peak 1:	267.6	85.8	134.4
PdI:	0.369	Peak 2:	3716	14.2	1154
Intercept:	0.941	Peak 3:	0.000	0.0	0.000
Result quality :	Good				

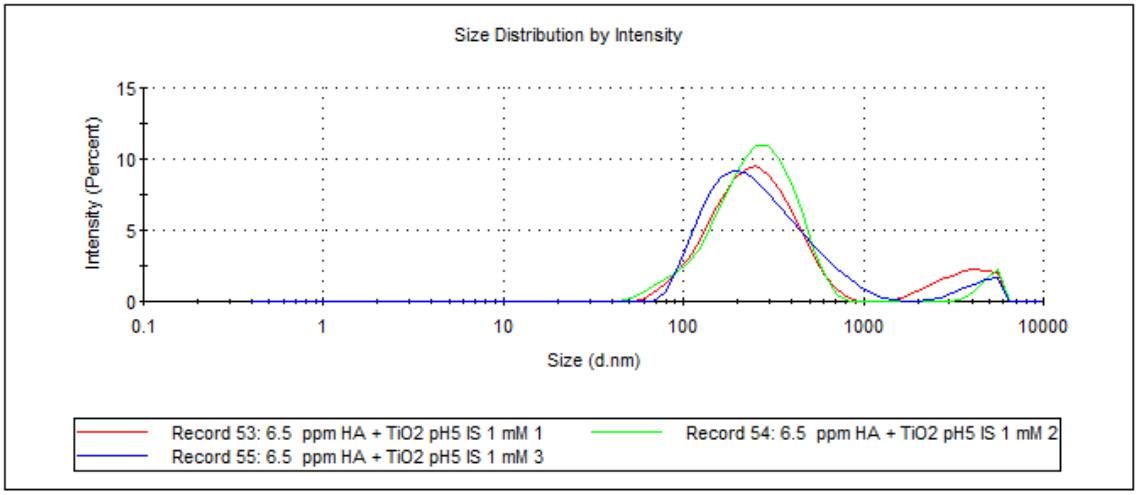

			Size (d.nm):	% Volume:	St Dev (d.nm):
Z-Average (d.nm):	255.6	Peak 1:	119.3	43.0	44.69
PdI:	0.369	Peak 2:	415.6	8.5	140.1
Intercept:	0.941	Peak 3:	4284	48.5	1144
Result quality :	Good				

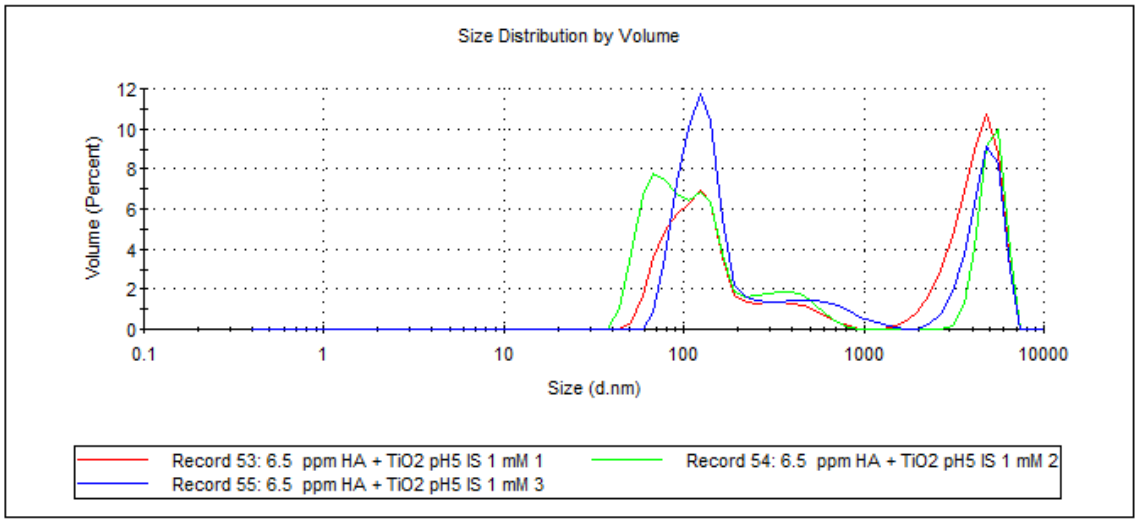

$nTiO_2$ + 3.3 mg/L DOC at pH 5

			Size (d.nm):	% Intensity:	St Dev (d.nm):
Z-Average (d.nm):	221.3	Peak 1:	206.8	100.0	54.95
PdI:	0.276	Peak 2:	0.000	0.0	0.000
Intercept:	0.949	Peak 3:	0.000	0.0	0.000

Result quality : Good

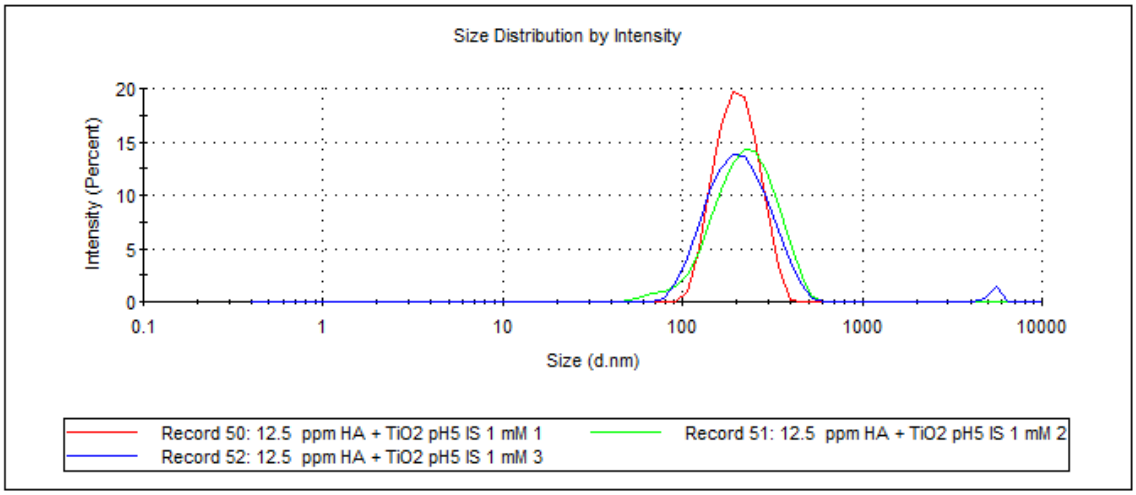

			Size (d.nm):	% Volume:	St Dev (d.nm):
Z-Average (d.nm):	221.3	Peak 1:	163.1	100.0	52.55
PdI:	0.276	Peak 2:	0.000	0.0	0.000
Intercept:	0.949	Peak 3:	0.000	0.0	0.000

Result quality : Good

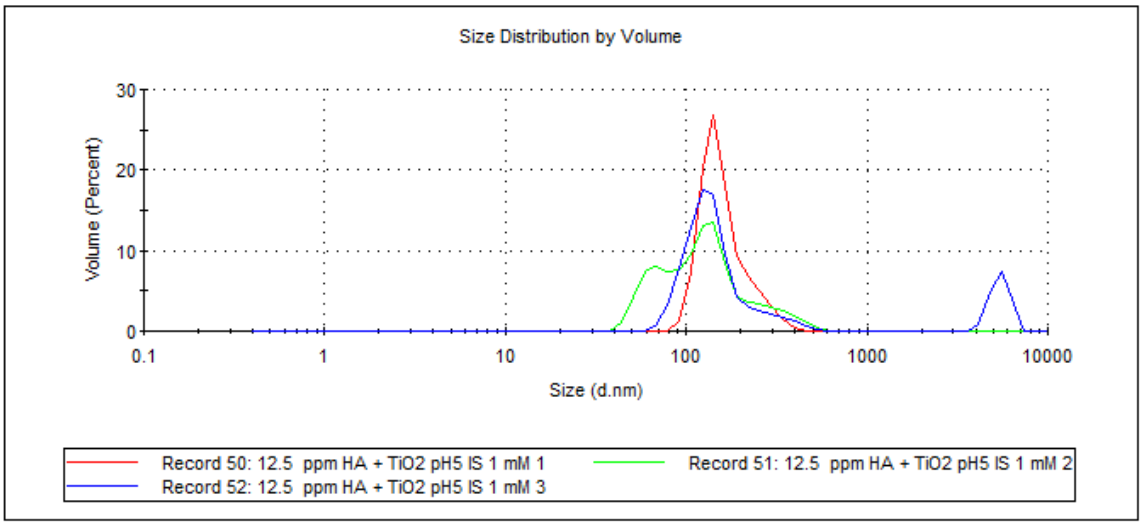

$nTiO_2$ + 4.95 mg/L DOC at pH 5

			Size (d.nm):	% Intensity:	St Dev (d.nm):
Z-Average (d.nm):	215.8	Peak 1:	200.9	100.0	58.00
PdI:	0.280	Peak 2:	0.000	0.0	0.000
Intercept:	0.957	Peak 3:	0.000	0.0	0.000

Result quality : Good

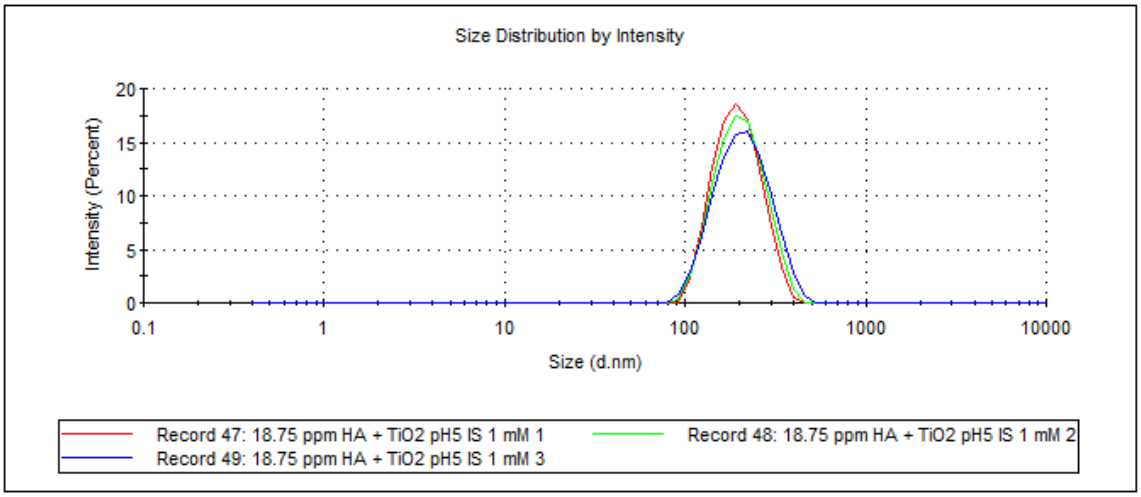

			Size (d.nm):	% Volume:	St Dev (d.nm):
Z-Average (d.nm):	215.8	Peak 1:	154.8	100.0	50.30
PdI:	0.280	Peak 2:	0.000	0.0	0.000
Intercept:	0.957	Peak 3:	0.000	0.0	0.000

Result quality : Good

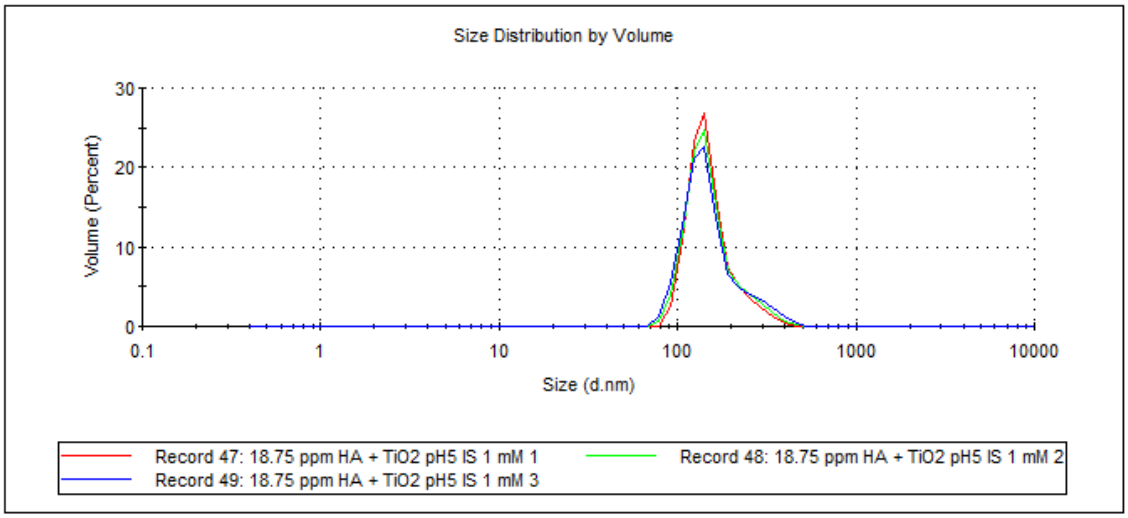

$nTiO_2$ + 6.60 mg/L DOC at pH 5

			Size (d.nm):	% Intensity:	St Dev (d.nm):
Z-Average (d.nm):	216.5	Peak 1:	218.4	100.0	78.71
PdI:	0.258	Peak 2:	0.000	0.0	0.000
Intercept:	0.952	Peak 3:	0.000	0.0	0.000

Result quality : Good

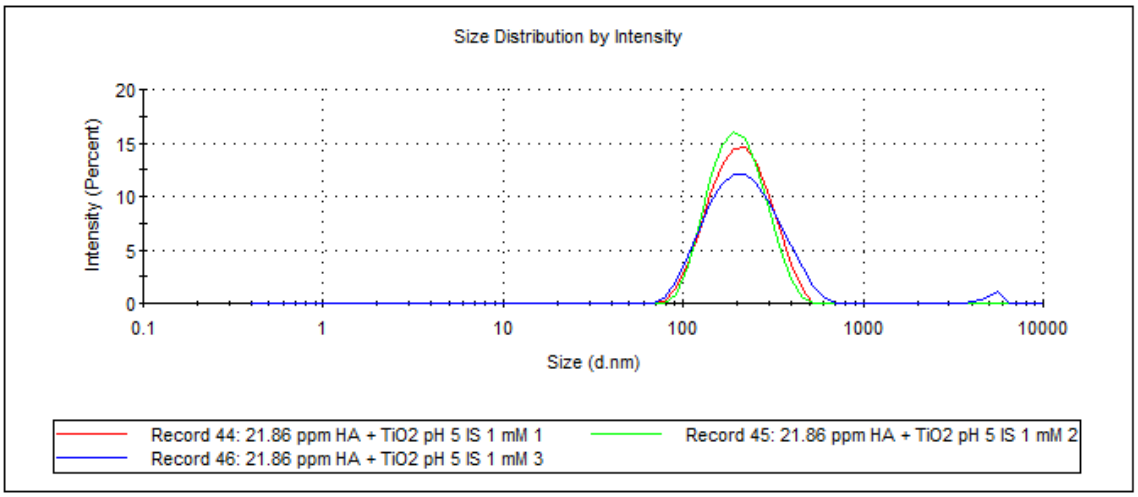

			Size (d.nm):	% Volume:	St Dev (d.nm):
Z-Average (d.nm):	216.5	Peak 1:	154.6	100.0	69.06
PdI:	0.258	Peak 2:	0.000	0.0	0.000
Intercept:	0.952	Peak 3:	0.000	0.0	0.000

Result quality : Good

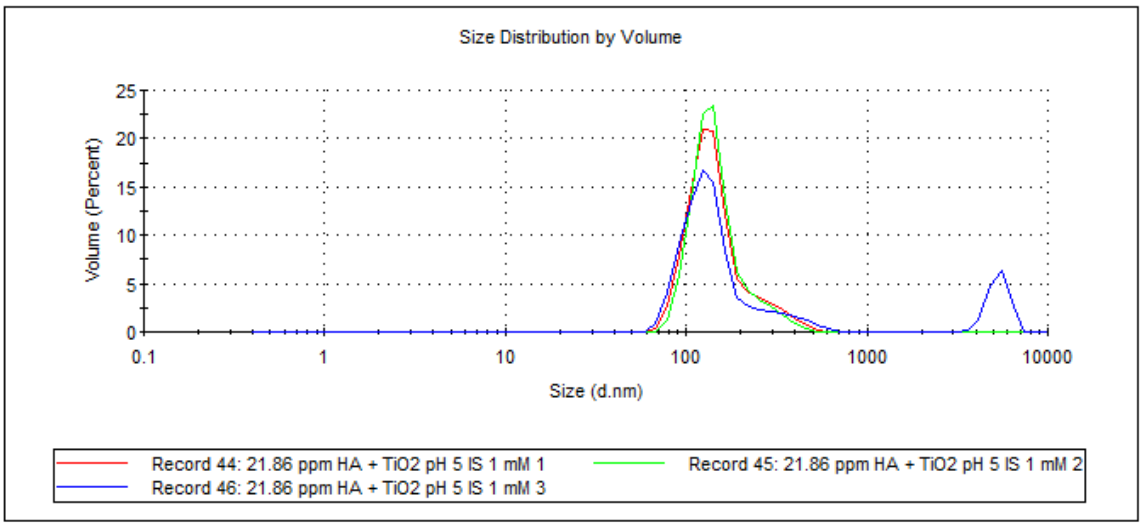

$nTiO_2$ + no HA at pH 9

			Size (d.nm):	% Intensity:	St Dev (d.nm):
Z-Average (d.nm):	193.5	Peak 1:	214.6	95.3	92.73
PdI:	0.198	Peak 2:	3588	4.7	1182
Intercept:	0.952	Peak 3:	0.000	0.0	0.000
Result quality :	Good				

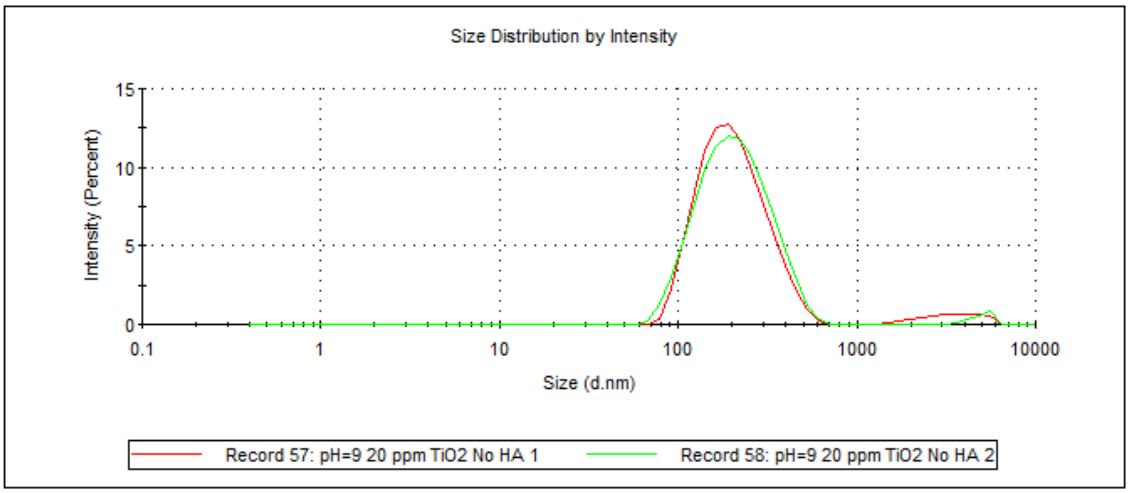

			Size (d.nm):	% Volume:	St Dev (d.nm):
Z-Average (d.nm):	193.5	Peak 1:	232.2	52.5	118.2
PdI:	0.198	Peak 2:	4237	47.5	1198
Intercept:	0.952	Peak 3:	0.000	0.0	0.000
Result quality :	Good				

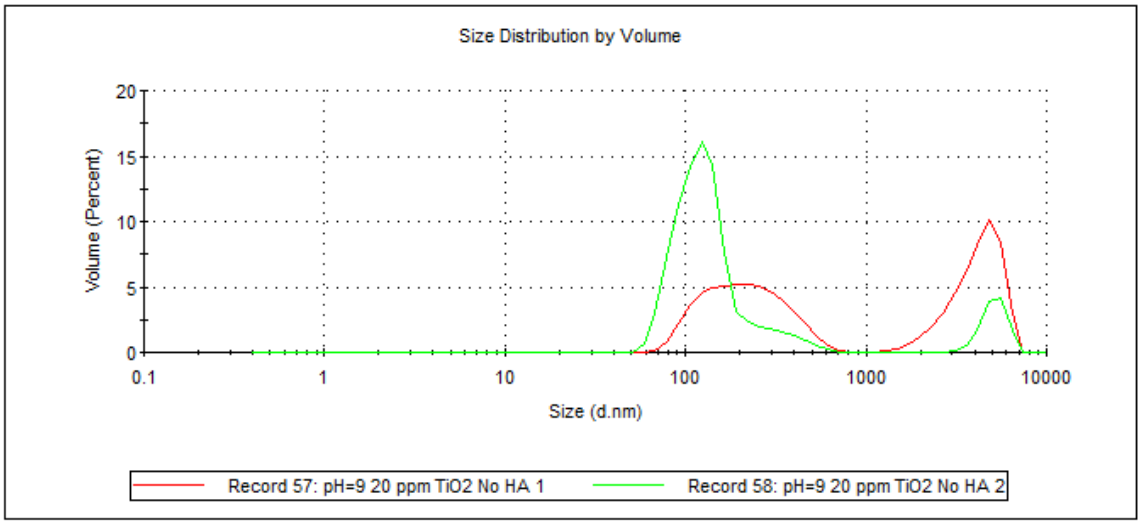

$nTiO_2$ + 0.33 mg/L DOC at pH 9

			Size (d.nm):	% Intensity:	St Dev (d.nm):
Z-Average (d.nm):	212.7	Peak 1:	225.9	98.7	85.41
PdI:	0.230	Peak 2:	5383	1.3	320.7
Intercept:	0.960	Peak 3:	0.000	0.0	0.000
Result quality :	Good				

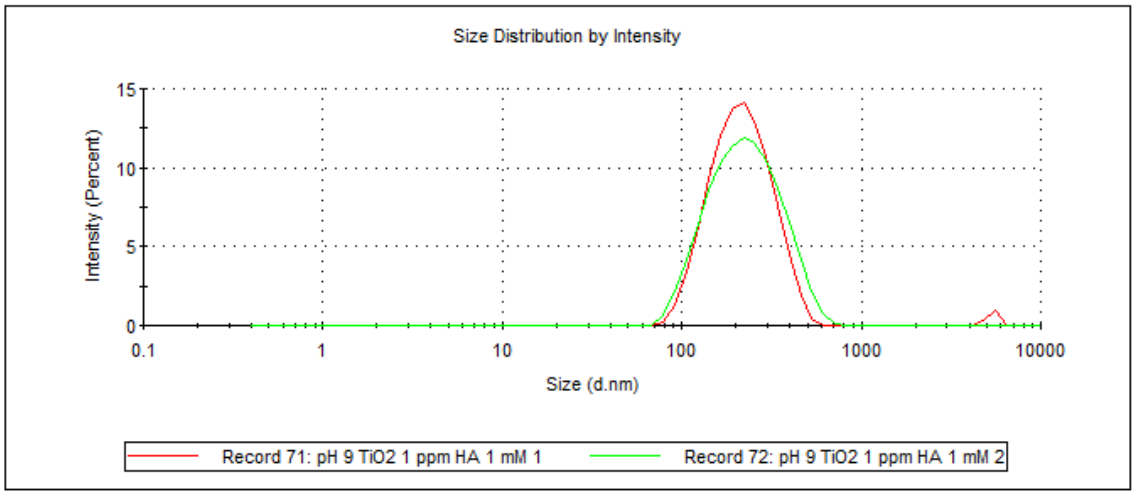

			Size (d.nm):	% Volume:	St Dev (d.nm):
Z-Average (d.nm):	212.7	Peak 1:	156.3	93.0	61.00
PdI:	0.230	Peak 2:	5439	7.0	641.5
Intercept:	0.960	Peak 3:	0.000	0.0	0.000
Result quality :	Good				

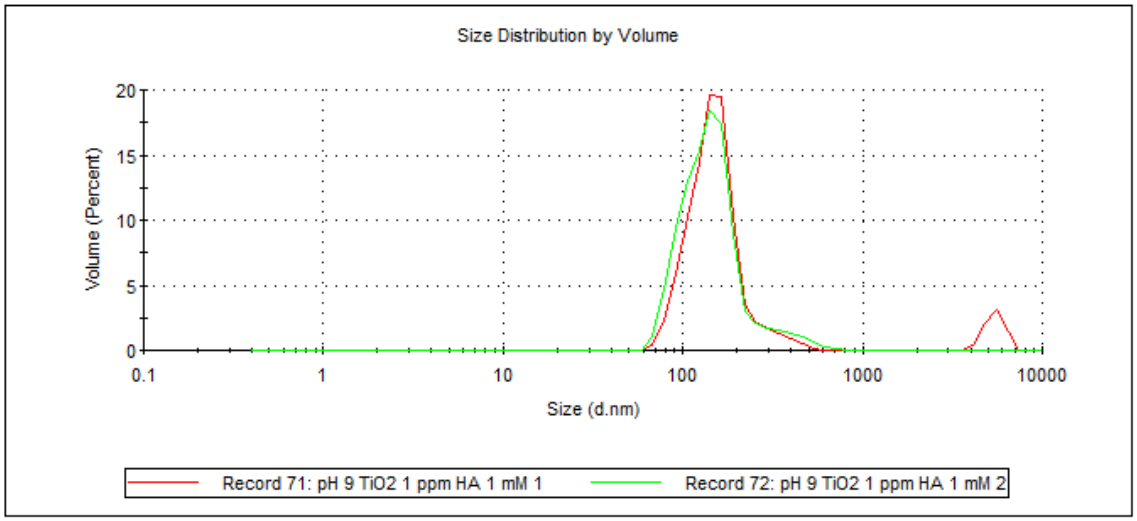

$nTiO_2$ + 0.66 mg/L DOC at pH 9

			Size (d.nm):	% Intensity:	St Dev (d.nm):
Z-Average (d.nm):	204.7	Peak 1:	214.1	98.8	77.05
PdI:	0.227	Peak 2:	5397	1.2	311.2
Intercept:	0.928	Peak 3:	0.000	0.0	0.000

Result quality : Good

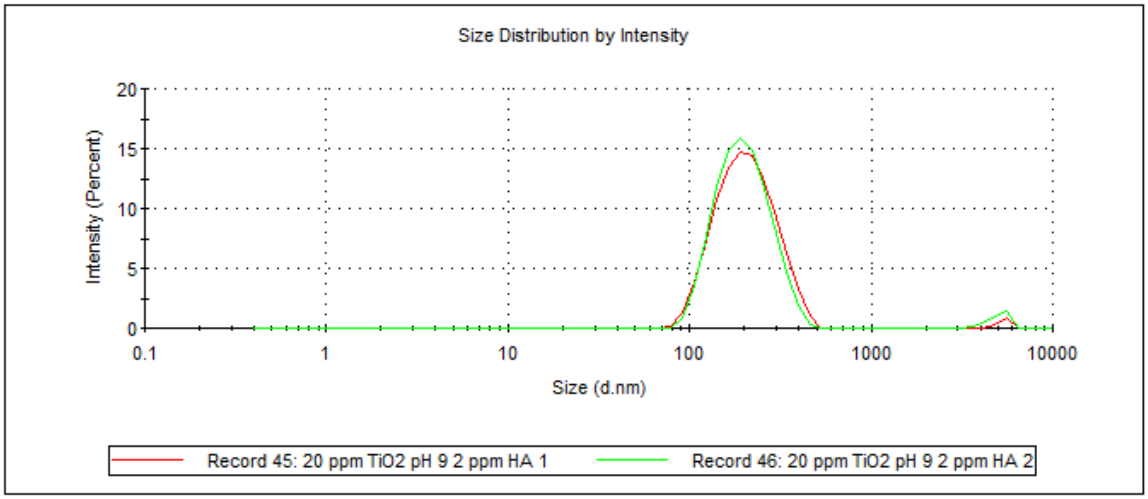

			Size (d.nm):	% Volume:	St Dev (d.nm):
Z-Average (d.nm):	204.7	Peak 1:	153.3	94.0	52.86
PdI:	0.227	Peak 2:	5452	6.0	637.9
Intercept:	0.928	Peak 3:	0.000	0.0	0.000

Result quality : Good

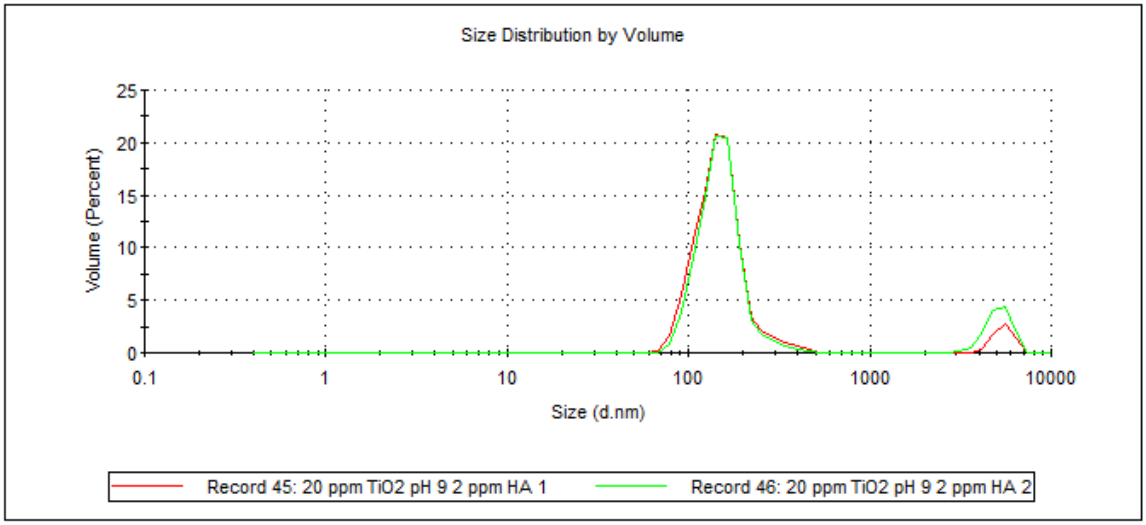

$nTiO_2$ + 1.65 mg/L DOC at pH 9

			Size (d.nm):	% Intensity:	St Dev (d.nm):
Z-Average (d.nm):	199.3	Peak 1:	216.6	99.0	81.96
PdI:	0.180	Peak 2:	5278	1.0	420.6
Intercept:	0.946	Peak 3:	0.000	0.0	0.000

Result quality : Good

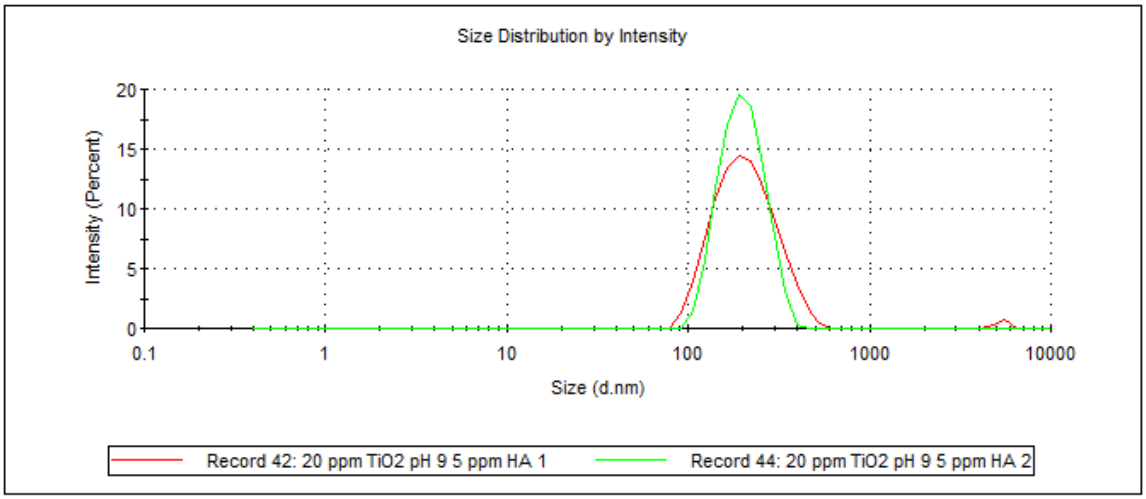

			Size (d.nm):	% Volume:	St Dev (d.nm):
Z-Average (d.nm):	199.3	Peak 1:	154.1	94.8	55.19
PdI:	0.180	Peak 2:	5353	5.2	682.4
Intercept:	0.946	Peak 3:	0.000	0.0	0.000

Result quality : Good

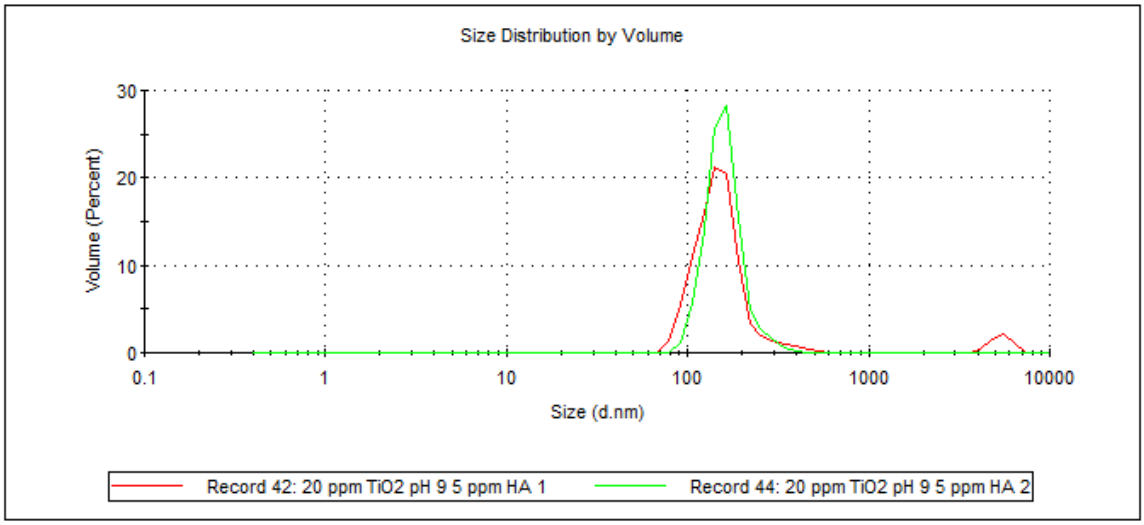

$nTiO_2$ + 3.30 mg/L DOC at pH 9

			Size (d.nm):	% Intensity:	St Dev (d.nm):
Z-Average (d.nm):	193.7	Peak 1:	206.6	97.5	72.49
PdI:	0.170	Peak 2:	4804	2.5	722.5
Intercept:	0.947	Peak 3:	0.000	0.0	0.000
Result quality :	Good				

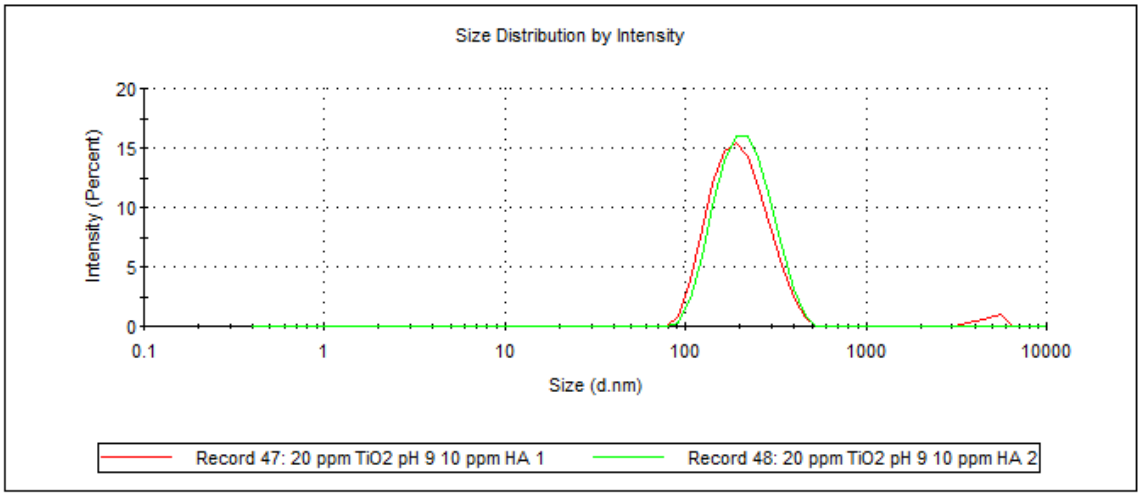

			Size (d.nm):	% Volume:	St Dev (d.nm):
Z-Average (d.nm):	193.7	Peak 1:	152.7	90.0	48.08
PdI:	0.170	Peak 2:	4967	10.0	858.9
Intercept:	0.947	Peak 3:	0.000	0.0	0.000
Result quality :	Good				

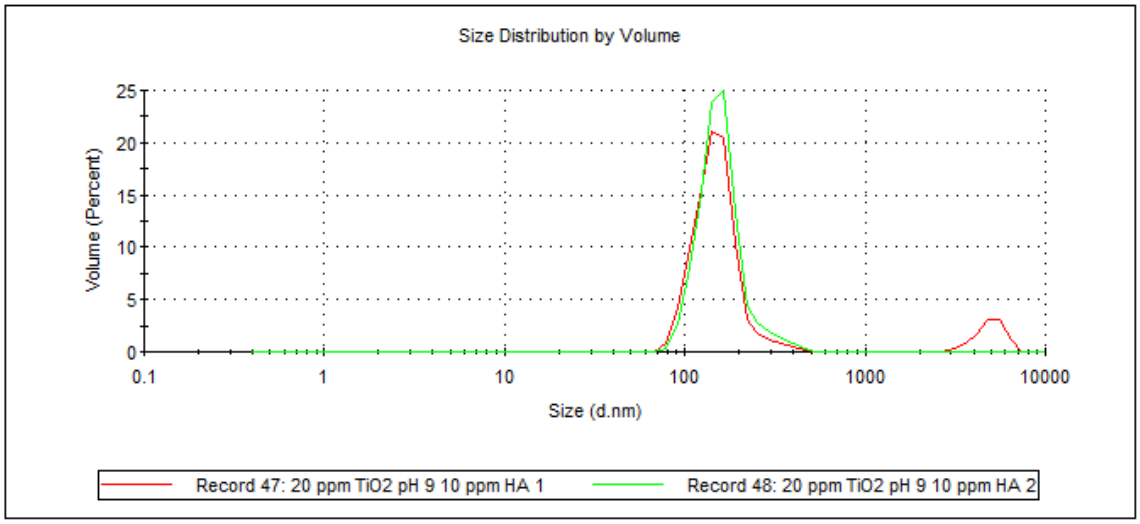

$nTiO_2$ + 4.95 mg/L DOC at pH 9

			Size (d.nm):	% Intensity:	St Dev (d.nm):
Z-Average (d.nm):	223.3	Peak 1:	218.0	99.0	73.25
PdI:	0.272	Peak 2:	5519	1.0	170.5
Intercept:	0.956	Peak 3:	0.000	0.0	0.000
Result quality :	Good				

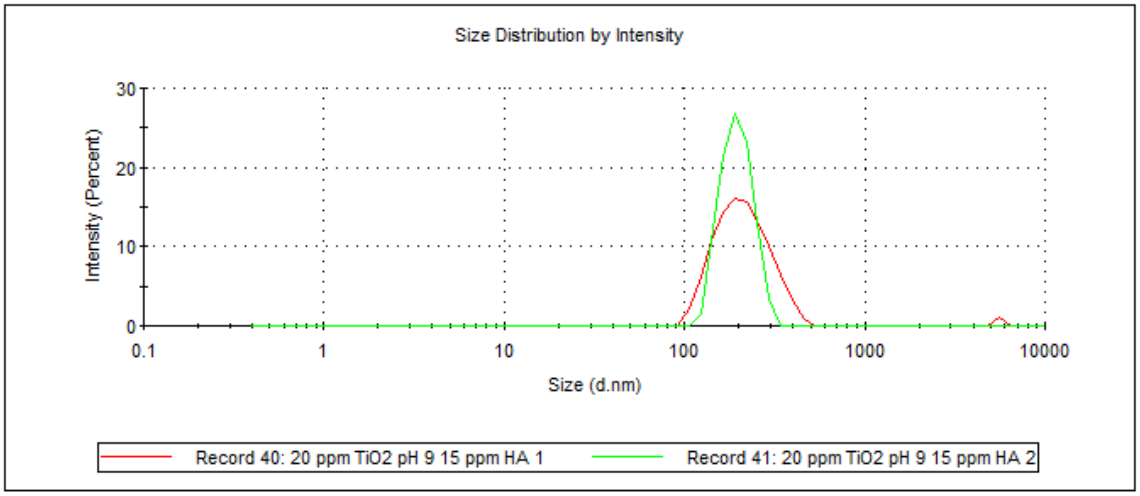

			Size (d.nm):	% Volume:	St Dev (d.nm):
Z-Average (d.nm):	223.3	Peak 1:	164.0	87.6	66.34
PdI:	0.272	Peak 2:	5556	12.4	597.6
Intercept:	0.956	Peak 3:	0.000	0.0	0.000
Result quality :	Good				

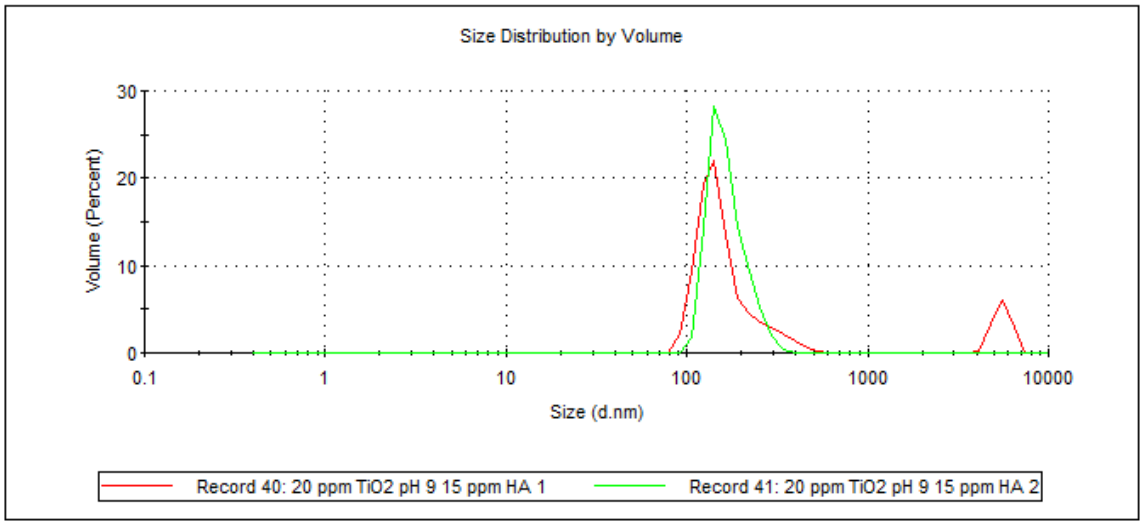

$nTiO_2$ + 6.6 mg/L DOC at pH 9

			Size (d.nm):	% Intensity:	St Dev (d.nm):
Z-Average (d.nm):	199.3	Peak 1:	216.6	99.0	81.96
PdI:	0.180	Peak 2:	5278	1.0	420.6
Intercept:	0.946	Peak 3:	0.000	0.0	0.000

Result quality : Good

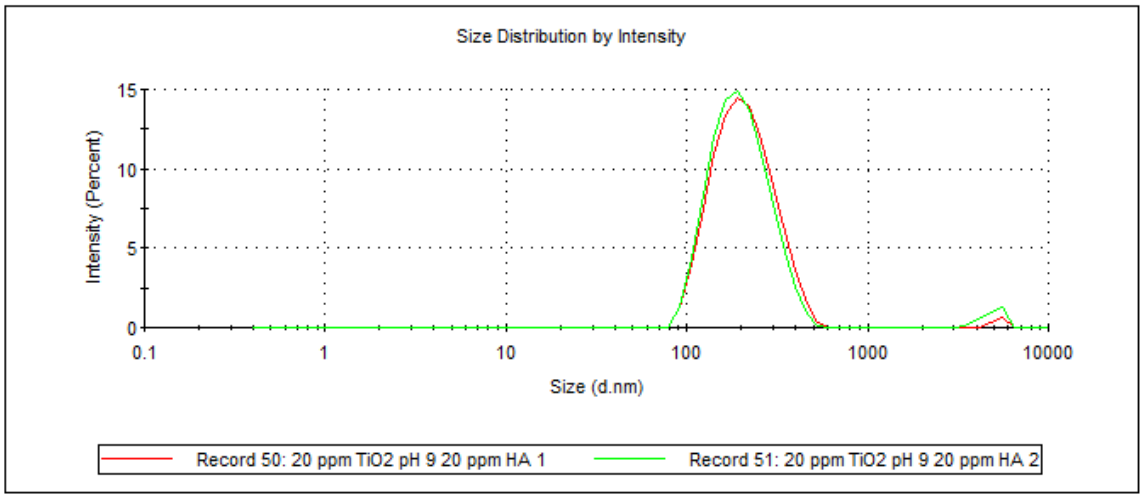

			Size (d.nm):	% Volume:	St Dev (d.nm):
Z-Average (d.nm):	199.3	Peak 1:	154.1	94.8	55.19
PdI:	0.180	Peak 2:	5353	5.2	682.4
Intercept:	0.946	Peak 3:	0.000	0.0	0.000

Result quality : Good

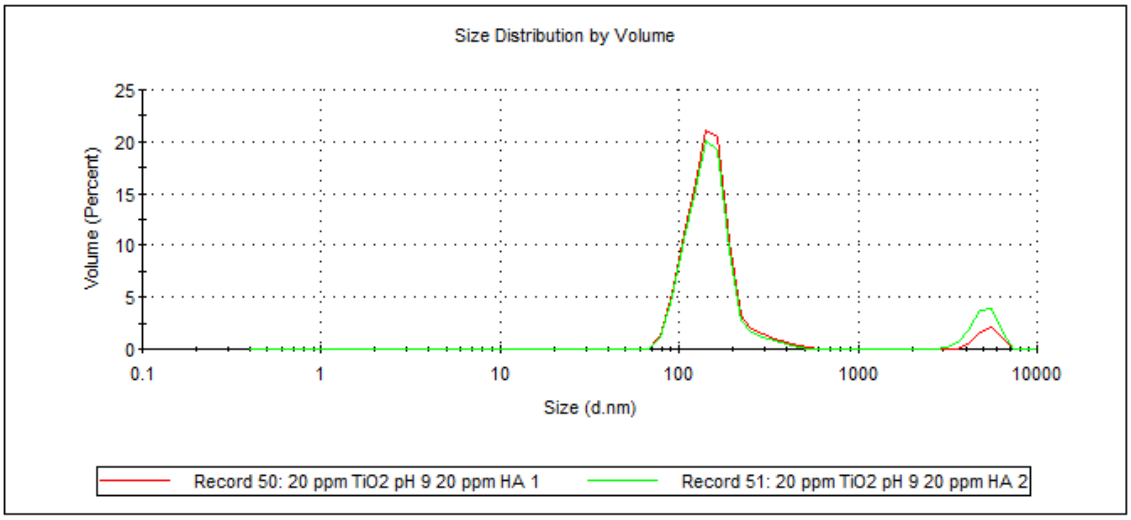

$nTiO_2$ + no HA at pH 5

			Mean (mV)	Area (%)	St Dev (mV)
Zeta Potential (mV):	29.8	Peak 1:	29.8	100.0	5.90
Zeta Deviation (mV):	5.90	Peak 2:	0.00	0.0	0.00
Conductivity (mS/cm):	1.36	Peak 3:	0.00	0.0	0.00

Result quality : Good

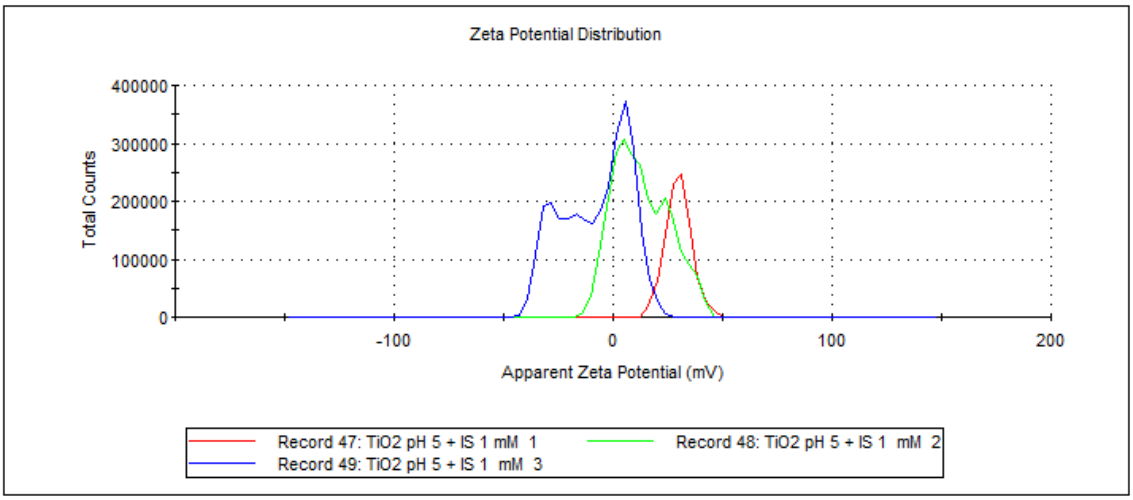

$nTiO_2$ + 0.07 mg/L DOC at pH 5

			Mean (mV)	Area (%)	St Dev (mV)
Zeta Potential (mV):	18.4	Peak 1:	18.4	100.0	5.42
Zeta Deviation (mV):	5.42	Peak 2:	0.00	0.0	0.00
Conductivity (mS/cm):	0.162	Peak 3:	0.00	0.0	0.00

Result quality : Good

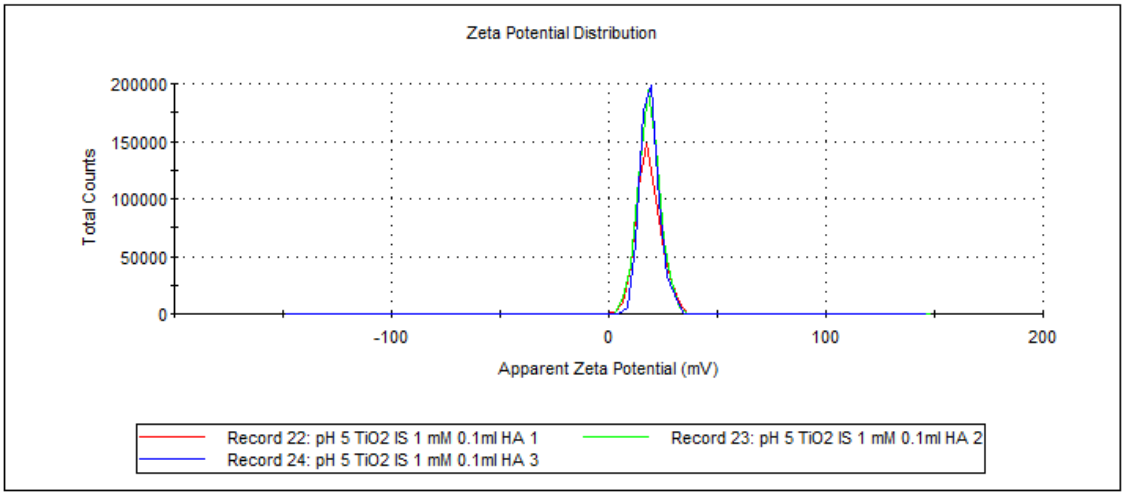

$nTiO_2$ + 0.13 mg/L DOC at pH 5

			Mean (mV)	Area (%)	St Dev (mV)
Zeta Potential (mV):	-9.99	Peak 1:	-9.99	100.0	5.42
Zeta Deviation (mV):	5.42	Peak 2:	0.00	0.0	0.00
Conductivity (mS/cm):	0.161	Peak 3:	0.00	0.0	0.00

Result quality : Good

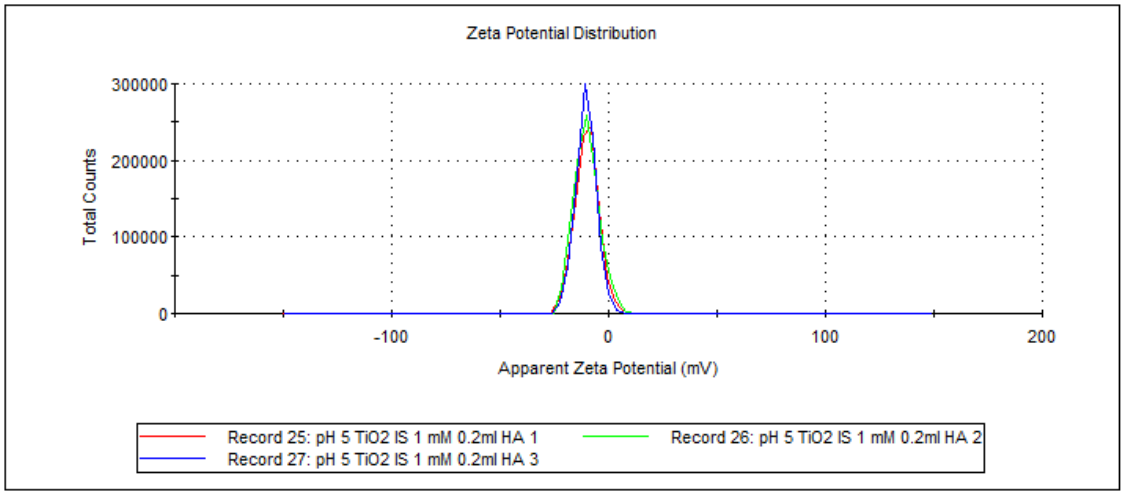

$nTiO_2$ + 0.33 mg/L DOC at pH 5

			Mean (mV)	Area (%)	St Dev (mV)
Zeta Potential (mV):	-19.1	Peak 1:	-19.1	100.0	7.37
Zeta Deviation (mV):	7.37	Peak 2:	0.00	0.0	0.00
Conductivity (mS/cm):	0.154	Peak 3:	0.00	0.0	0.00

Result quality : Good

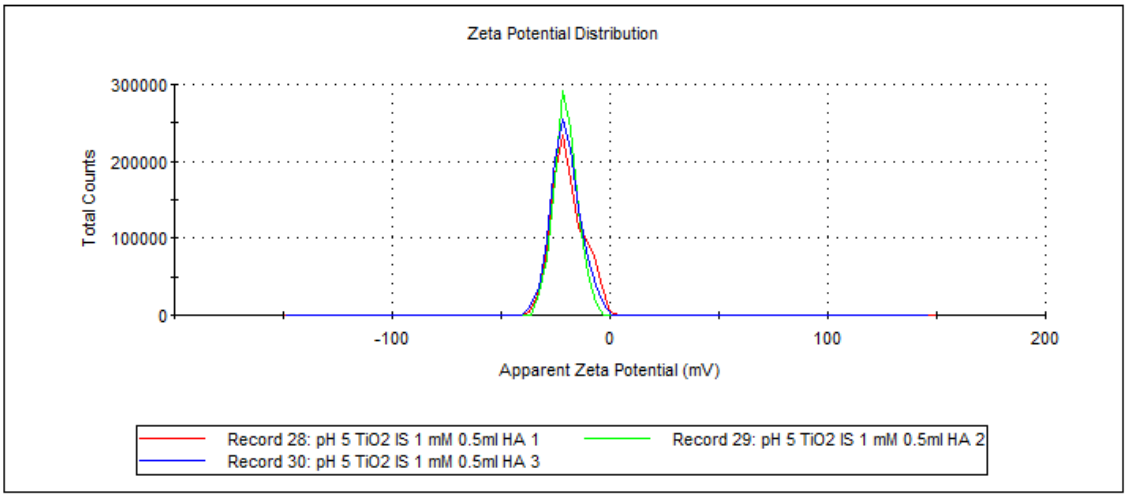

$nTiO_2$ + 0.66 mg/L DOC at pH 5

			Mean (mV)	Area (%)	St Dev (mV)
Zeta Potential (mV):	-33.2	Peak 1:	-33.2	100.0	4.57
Zeta Deviation (mV):	4.57	Peak 2:	0.00	0.0	0.00
Conductivity (mS/cm):	1.35	Peak 3:	0.00	0.0	0.00

Result quality : Good

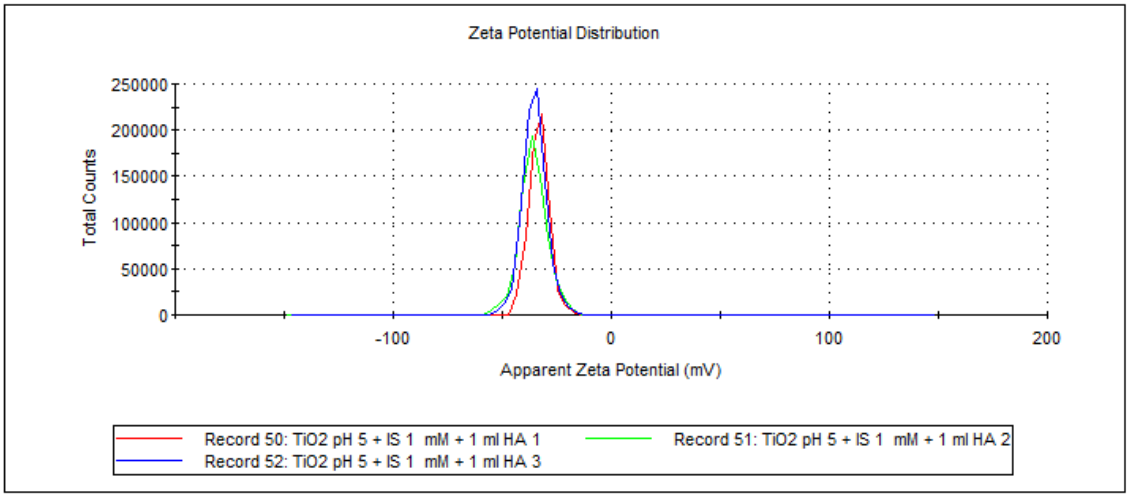

$nTiO_2$ + 1.65 mg/L DOC at pH 5

			Mean (mV)	Area (%)	St Dev (mV)
Zeta Potential (mV):	-43.0	Peak 1:	-43.0	100.0	9.39
Zeta Deviation (mV):	9.39	Peak 2:	0.00	0.0	0.00
Conductivity (mS/cm):	1.43	Peak 3:	0.00	0.0	0.00

Result quality : Good

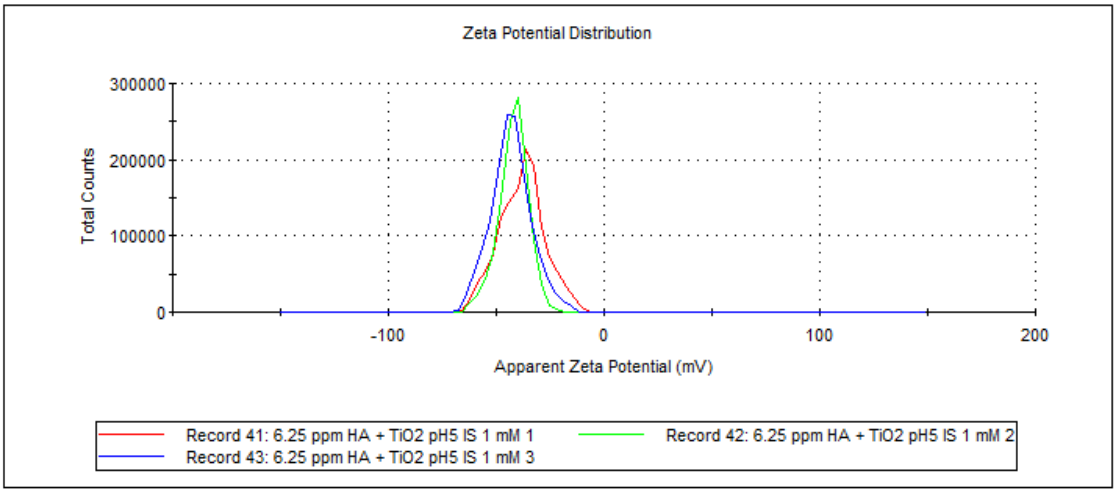

$nTiO_2$ + 3.3 mg/L DOC at pH 5

			Mean (mV)	Area (%)	St Dev (mV)
Zeta Potential (mV):	-40.7	Peak 1:	-41.8	94.8	9.80
Zeta Deviation (mV):	11.0	Peak 2:	-16.1	5.2	3.51
Conductivity (mS/cm):	1.40	Peak 3:	0.00	0.0	0.00

Result quality : See result quality report

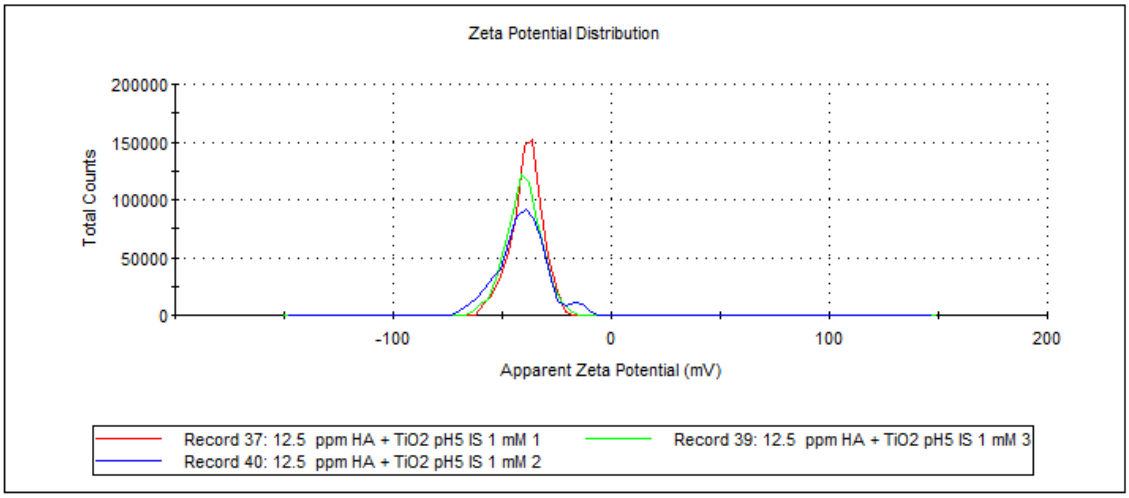

$nTiO_2$ + 4.95 mg/L DOC at pH 5

			Mean (mV)	Area (%)	St Dev (mV)
Zeta Potential (mV):	-44.7	Peak 1:	-44.7	100.0	6.95
Zeta Deviation (mV):	6.95	Peak 2:	0.00	0.0	0.00
Conductivity (mS/cm):	1.48	Peak 3:	0.00	0.0	0.00

Result quality : Good

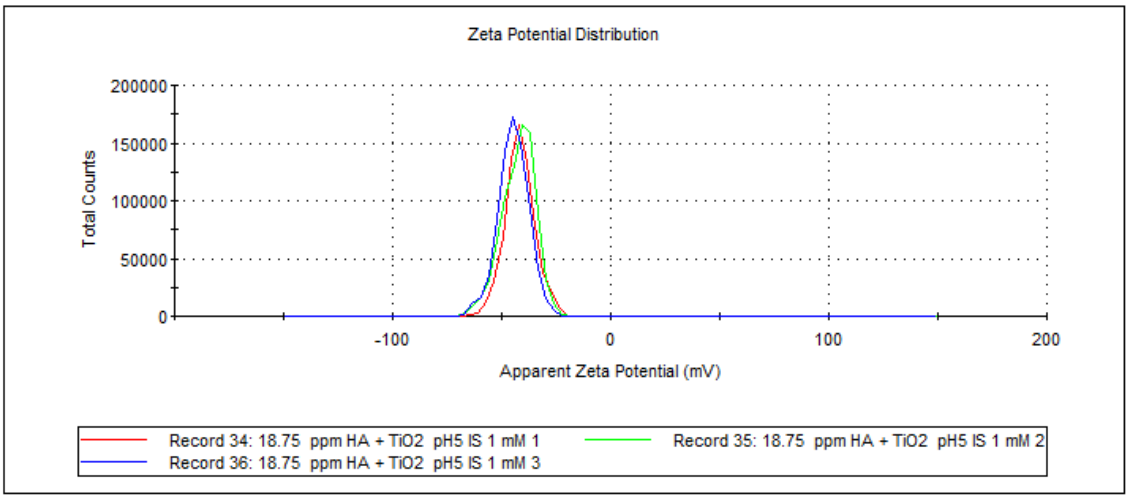

$nTiO_2$ + 6.60 mg/L DOC at pH 5

			Mean (mV)	Area (%)	St Dev (mV)
Zeta Potential (mV):	-41.0	Peak 1:	-41.0	100.0	7.82
Zeta Deviation (mV):	7.82	Peak 2:	0.00	0.0	0.00
Conductivity (mS/cm):	1.33	Peak 3:	0.00	0.0	0.00

Result quality : Good

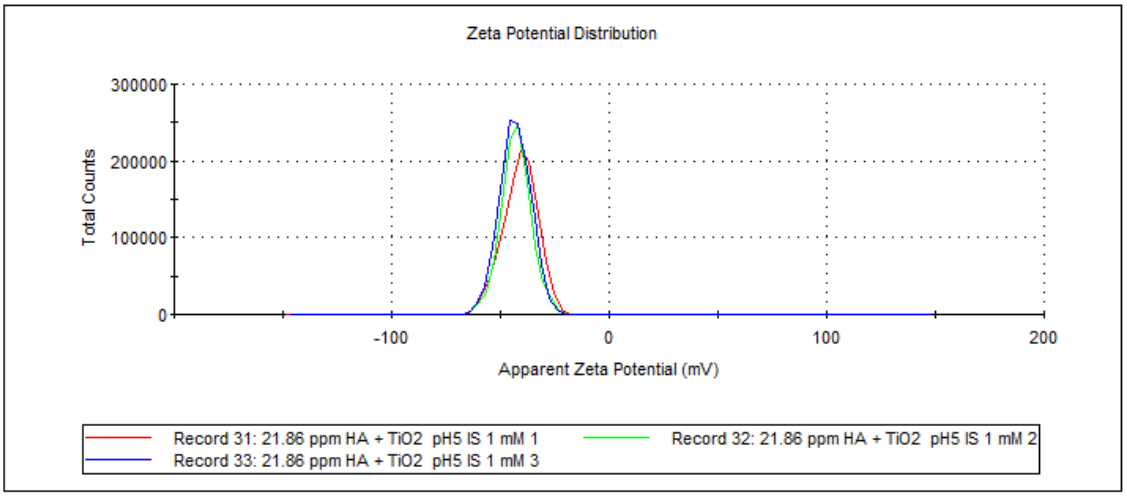

$nTiO_2$ + no HA at pH 9

			Mean (mV)	Area (%)	St Dev (mV)
Zeta Potential (mV):	-31.7	Peak 1:	-31.7	100.0	9.23
Zeta Deviation (mV):	9.23	Peak 2:	0.00	0.0	0.00
Conductivity (mS/cm):	0.214	Peak 3:	0.00	0.0	0.00

Result quality : Good

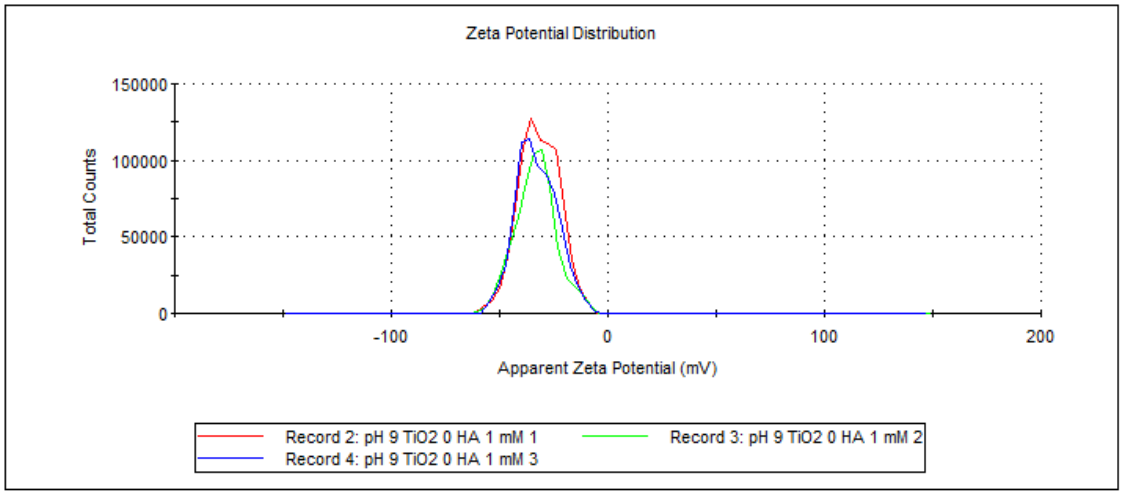

$nTiO_2$ + 0.33 mg/L DOC at pH 9

			Mean (mV)	Area (%)	St Dev (mV)
Zeta Potential (mV):	-32.3	Peak 1:	-32.3	100.0	7.47
Zeta Deviation (mV):	7.47	Peak 2:	0.00	0.0	0.00
Conductivity (mS/cm):	0.210	Peak 3:	0.00	0.0	0.00

Result quality : Good

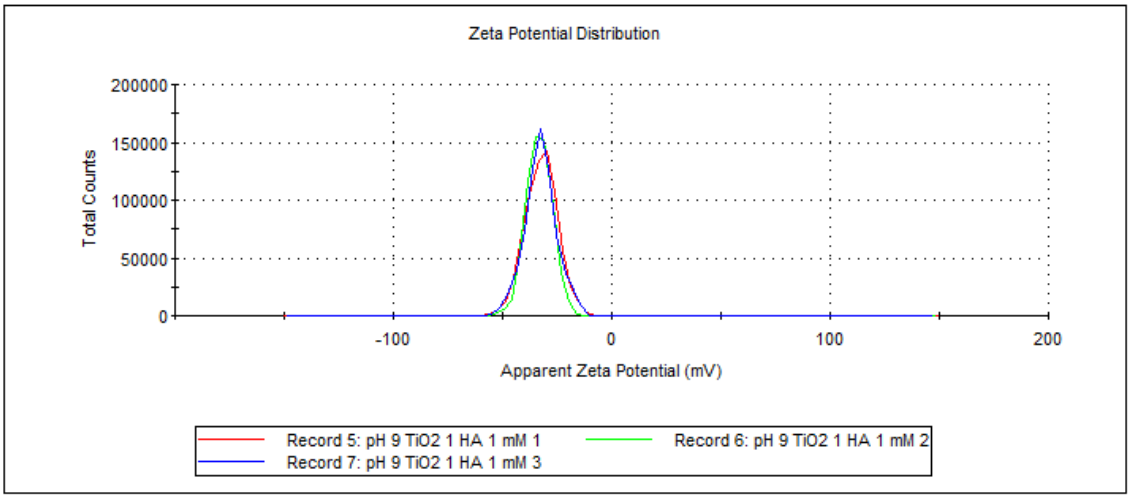

$nTiO_2$ + 0.66 mg/L DOC at pH 9

			Mean (mV)	Area (%)	St Dev (mV)
Zeta Potential (mV):	-33.8	Peak 1:	-33.8	100.0	8.96
Zeta Deviation (mV):	8.96	Peak 2:	0.00	0.0	0.00
Conductivity (mS/cm):	0.212	Peak 3:	0.00	0.0	0.00

Result quality : Good

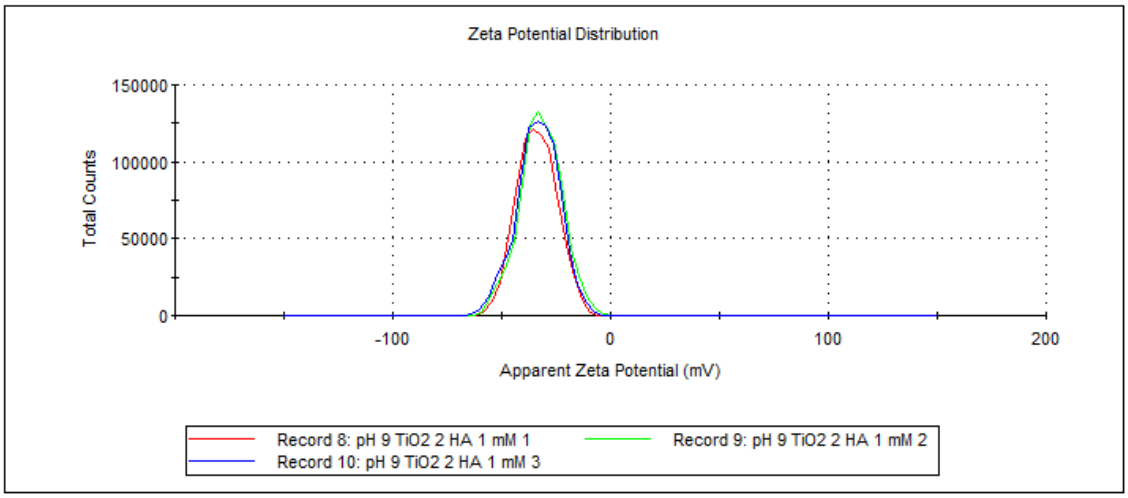

$nTiO_2$ + 1.65 mg/L DOC at pH 9

			Mean (mV)	Area (%)	St Dev (mV)
Zeta Potential (mV):	-34.7	Peak 1:	-34.7	100.0	10.2
Zeta Deviation (mV):	10.2	Peak 2:	0.00	0.0	0.00
Conductivity (mS/cm):	0.215	Peak 3:	0.00	0.0	0.00

Result quality : Good

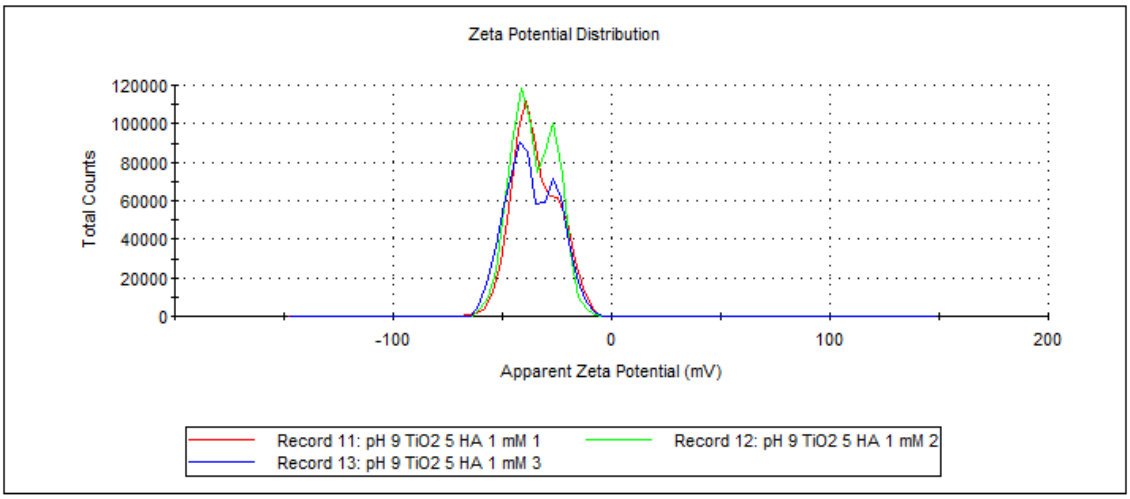

$nTiO_2$ + 3.30 mg/L DOC at pH 9

			Mean (mV)	Area (%)	St Dev (mV)
Zeta Potential (mV):	-33.6	Peak 1:	-33.6	100.0	9.50
Zeta Deviation (mV):	9.50	Peak 2:	0.00	0.0	0.00
Conductivity (mS/cm):	0.216	Peak 3:	0.00	0.0	0.00

Result quality : Good

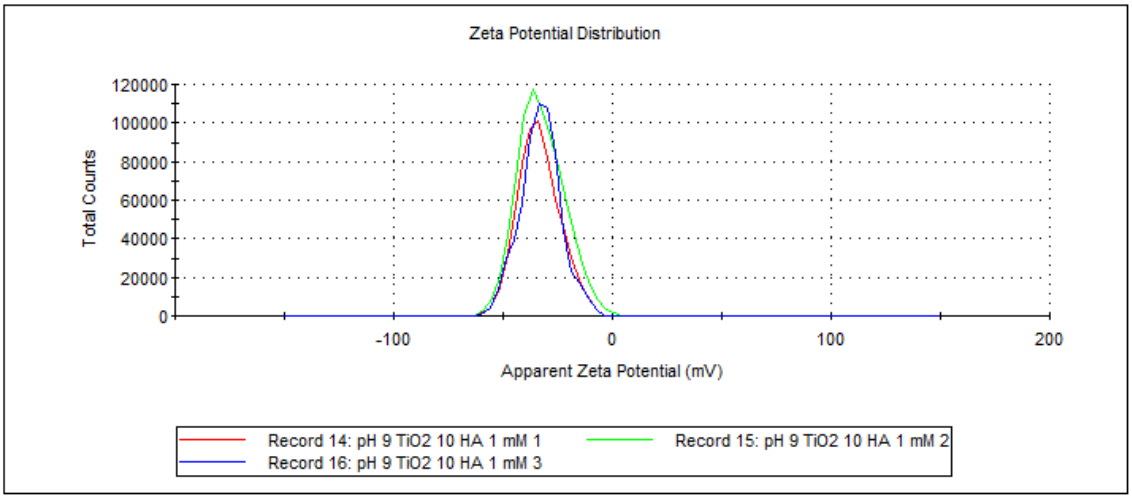

$nTiO_2$ + 4.95 mg/L DOC at pH 9

			Mean (mV)	Area (%)	St Dev (mV)
Zeta Potential (mV):	-44.6	Peak 1:	-44.6	100.0	12.3
Zeta Deviation (mV):	12.3	Peak 2:	0.00	0.0	0.00
Conductivity (mS/cm):	0.281	Peak 3:	0.00	0.0	0.00

Result quality : Good

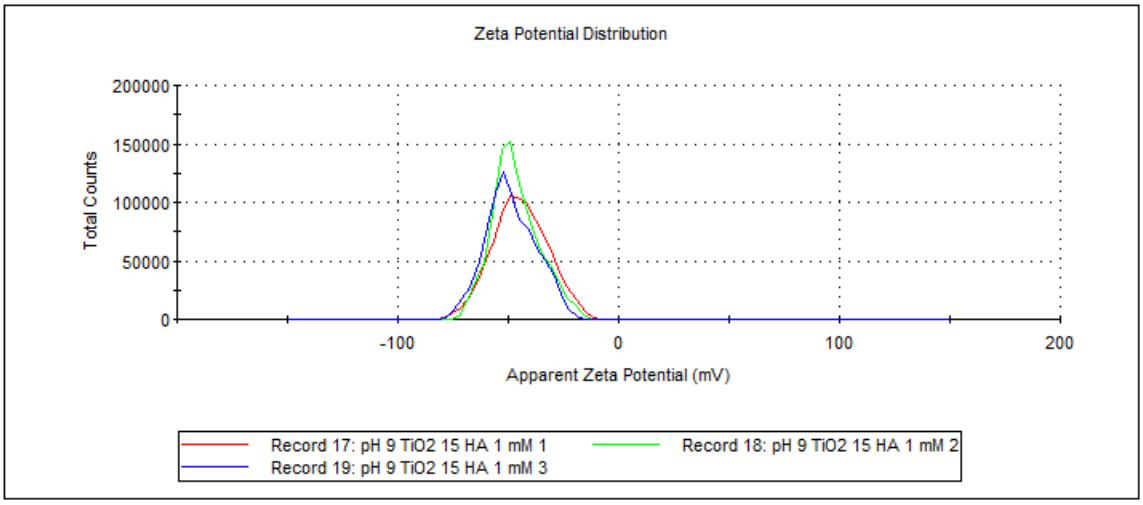

$nTiO_2$ + 6.6 mg/L DOC at pH 9

			Mean (mV)	Area (%)	St Dev (mV)
Zeta Potential (mV):	-33.7	Peak 1:	-25.6	55.9	7.17
Zeta Deviation (mV):	12.3	Peak 2:	-44.3	44.1	7.38
Conductivity (mS/cm):	0.223	Peak 3:	0.00	0.0	0.00

Result quality : See result quality report

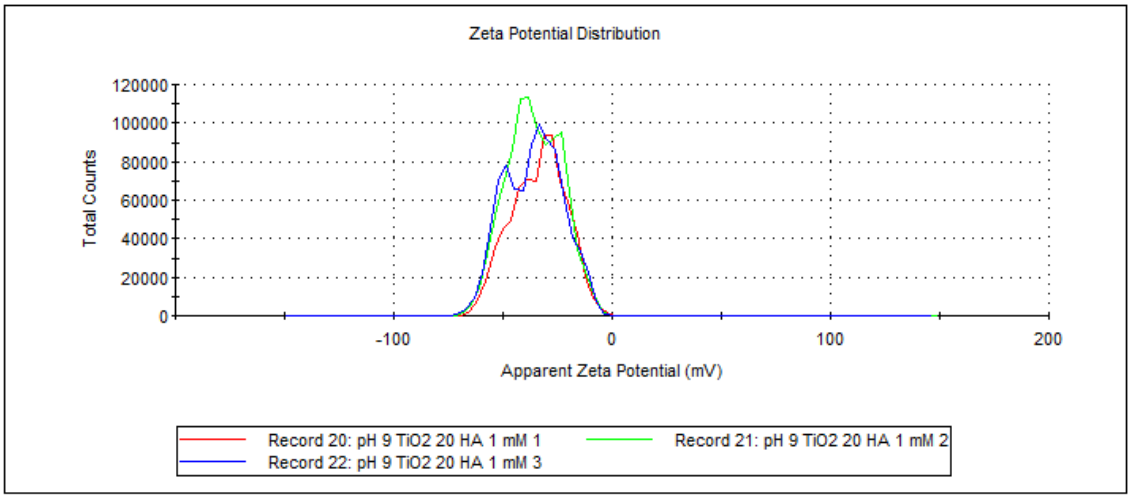

Zeta potential of 125 mg/L Fe oxyhydroxide as a function of humic acid concentration in 1 mM NaCl solution

Fe oxyhydroxide + no HA at pH 5

			Mean (mV)	Area (%)	St Dev (mV)
Zeta Potential (mV):	41.0	Peak 1:	41.0	100.0	6.39
Zeta Deviation (mV):	6.39	Peak 2:	0.00	0.0	0.00
Conductivity (mS/cm):	0.0184	Peak 3:	0.00	0.0	0.00

Result quality : Good

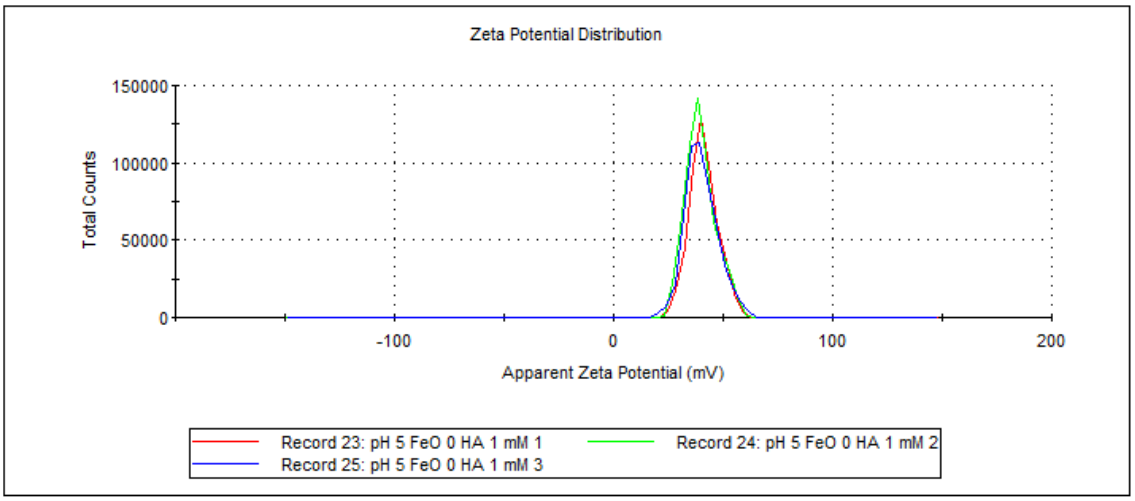

Fe oxyhydroxide + 0.17 mg/L DOC at pH 5

			Mean (mV)	Area (%)	St Dev (mV)
Zeta Potential (mV):	37.2	Peak 1:	37.2	100.0	7.10
Zeta Deviation (mV):	7.10	Peak 2:	0.00	0.0	0.00
Conductivity (mS/cm):	0.0457	Peak 3:	0.00	0.0	0.00

Result quality : Good

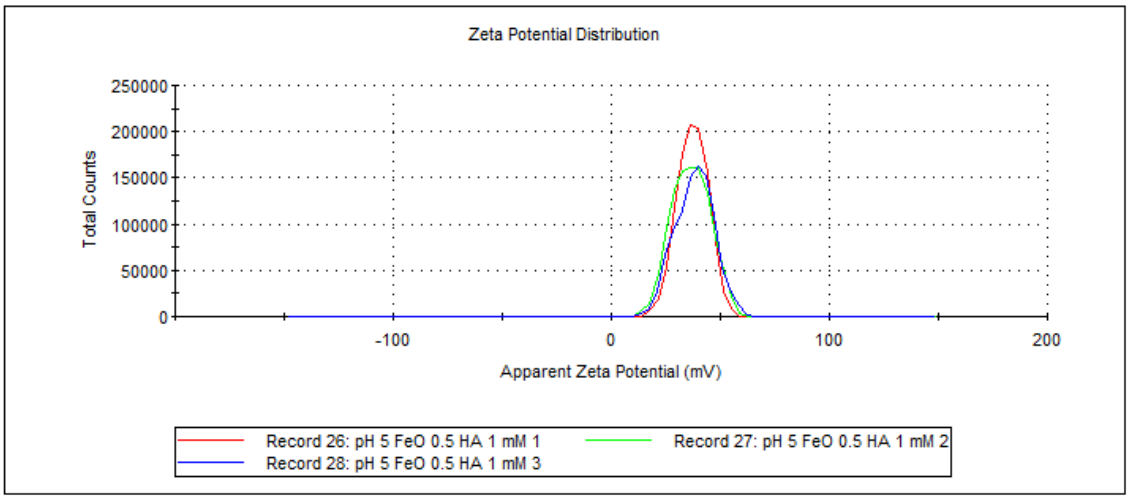

Fe oxyhydroxide + 0.33 mg/L DOC at pH 5

			Mean (mV)	Area (%)	St Dev (mV)
Zeta Potential (mV):	26.4	Peak 1:	26.4	100.0	6.55
Zeta Deviation (mV):	6.55	Peak 2:	0.00	0.0	0.00
Conductivity (mS/cm):	0.0163	Peak 3:	0.00	0.0	0.00

Result quality : Good

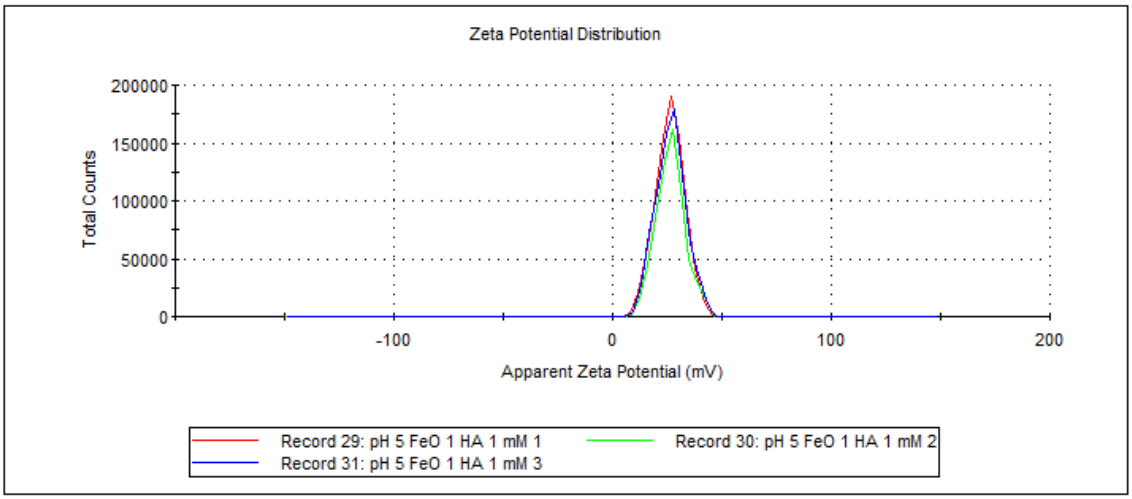

Fe oxyhydroxide + 0.66 mg/L DOC at pH 5

			Mean (mV)	Area (%)	St Dev (mV)
Zeta Potential (mV):	-0.859	Peak 1:	-0.859	100.0	5.20
Zeta Deviation (mV):	5.20	Peak 2:	0.00	0.0	0.00
Conductivity (mS/cm):	0.0151	Peak 3:	0.00	0.0	0.00

Result quality : Good

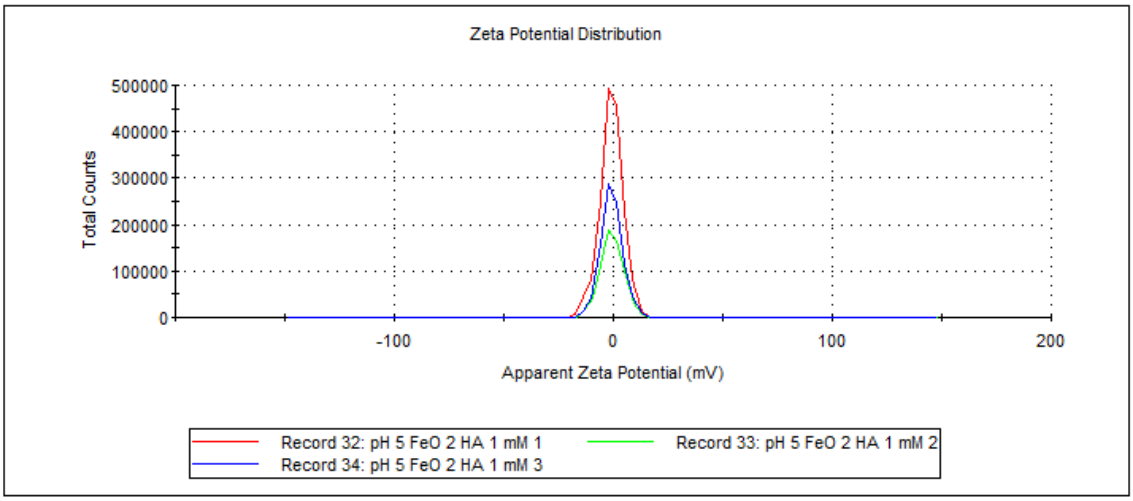

Fe oxyhydroxide + 1.65 mg/L DOC at pH 5

			Mean (mV)	Area (%)	St Dev (mV)
Zeta Potential (mV):	-33.9	Peak 1:	-33.9	100.0	6.77
Zeta Deviation (mV):	6.77	Peak 2:	0.00	0.0	0.00
Conductivity (mS/cm):	0.0159	Peak 3:	0.00	0.0	0.00

Result quality : Good

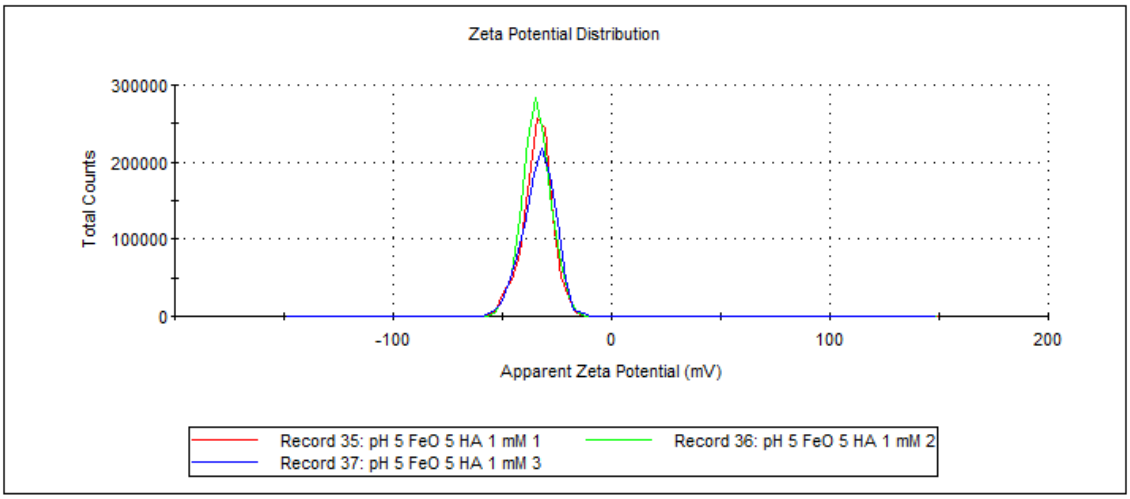

Fe oxyhydroxide + 3.3 mg/L DOC at pH 5

			Mean (mV)	Area (%)	St Dev (mV)
Zeta Potential (mV):	-37.5	Peak 1:	-37.5	100.0	10.1
Zeta Deviation (mV):	10.1	Peak 2:	0.00	0.0	0.00
Conductivity (mS/cm):	0.0190	Peak 3:	0.00	0.0	0.00

Result quality : Good

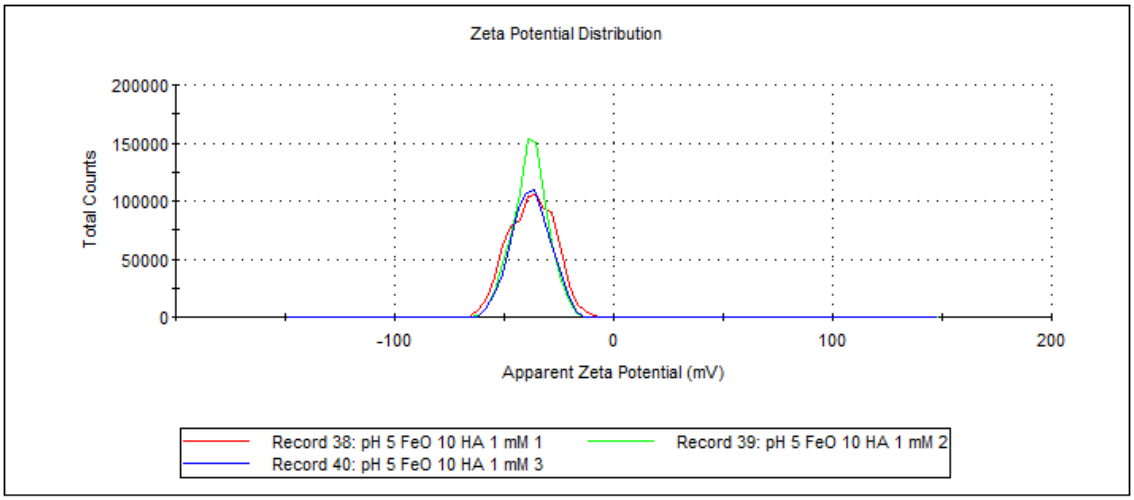

Fe oxyhydroxide + 4.95 mg/L DOC at pH 5

			Mean (mV)	Area (%)	St Dev (mV)
Zeta Potential (mV):	-40.7	Peak 1:	-40.7	100.0	9.49
Zeta Deviation (mV):	9.49	Peak 2:	0.00	0.0	0.00
Conductivity (mS/cm):	0.0140	Peak 3:	0.00	0.0	0.00

Result quality : Good

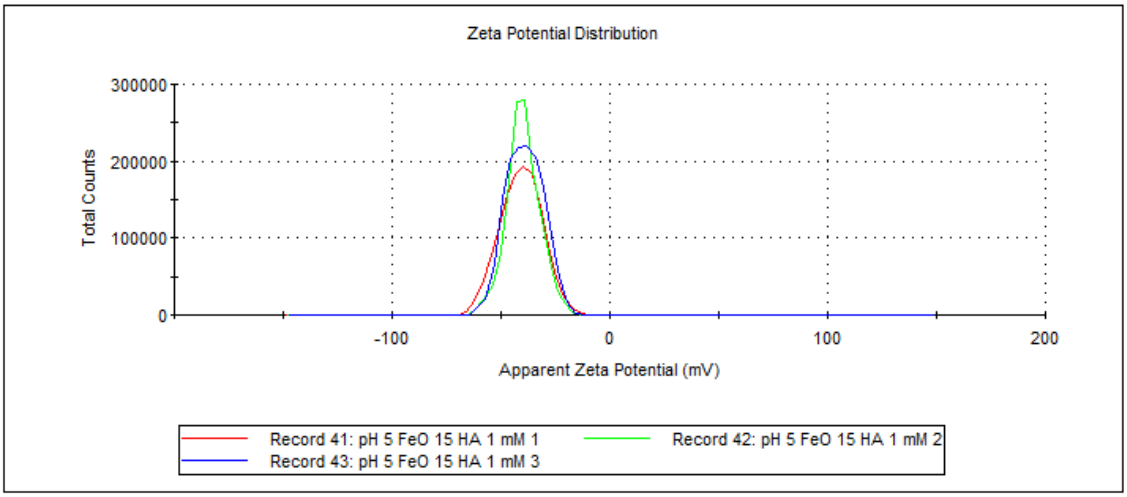

Fe oxyhydroxide + 6.6 mg/L DOC at pH 5

			Mean (mV)	Area (%)	St Dev (mV)
Zeta Potential (mV):	-39.4	Peak 1:	-39.4	100.0	8.80
Zeta Deviation (mV):	8.80	Peak 2:	0.00	0.0	0.00
Conductivity (mS/cm):	0.0162	Peak 3:	0.00	0.0	0.00

Result quality : Good

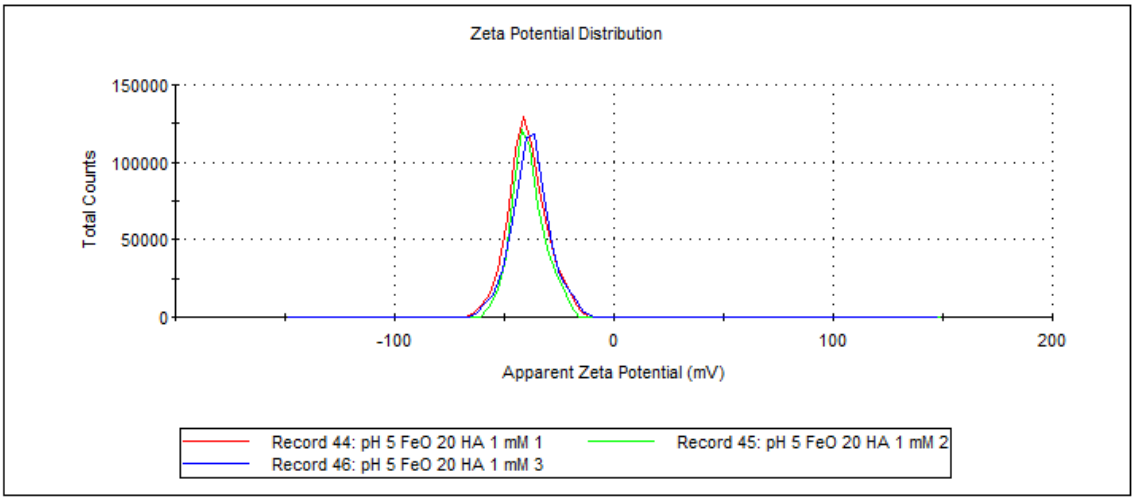

Fe oxyhydroxide + no HA at pH 9

			Mean (mV)	Area (%)	St Dev (mV)
Zeta Potential (mV):	-15.9	Peak 1:	-23.7	62.1	8.81
Zeta Deviation (mV):	13.9	Peak 2:	-2.20	37.9	7.68
Conductivity (mS/cm):	0.0110	Peak 3:	0.00	0.0	0.00

Result quality : See result quality report

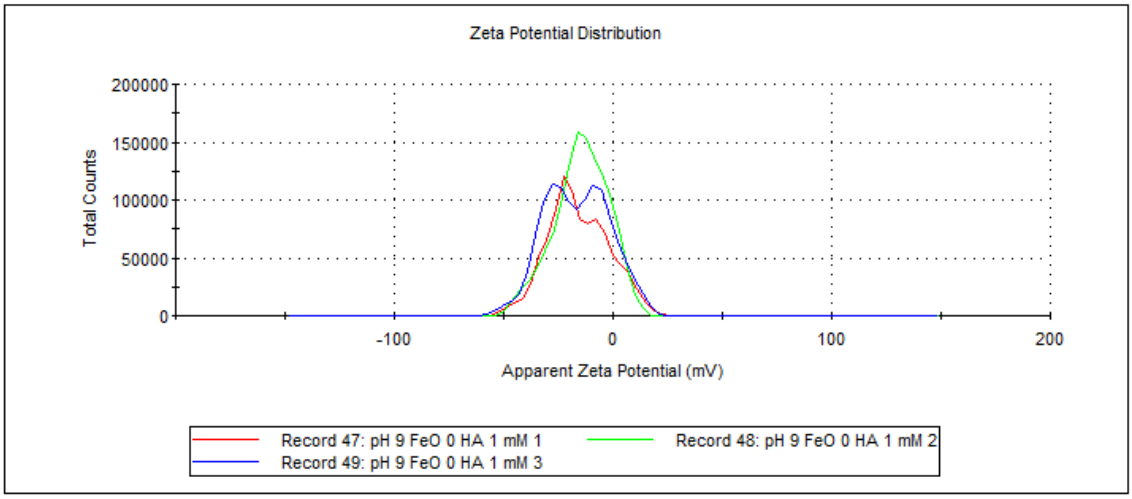

Fe oxyhydroxide + 0.33 mg/L DOC at pH 9

			Mean (mV)	Area (%)	St Dev (mV)
Zeta Potential (mV):	-27.6	Peak 1:	-18.4	60.3	9.90
Zeta Deviation (mV):	15.8	Peak 2:	-42.5	39.7	9.20
Conductivity (mS/cm):	0.0109	Peak 3:	0.00	0.0	0.00

Result quality : See result quality report

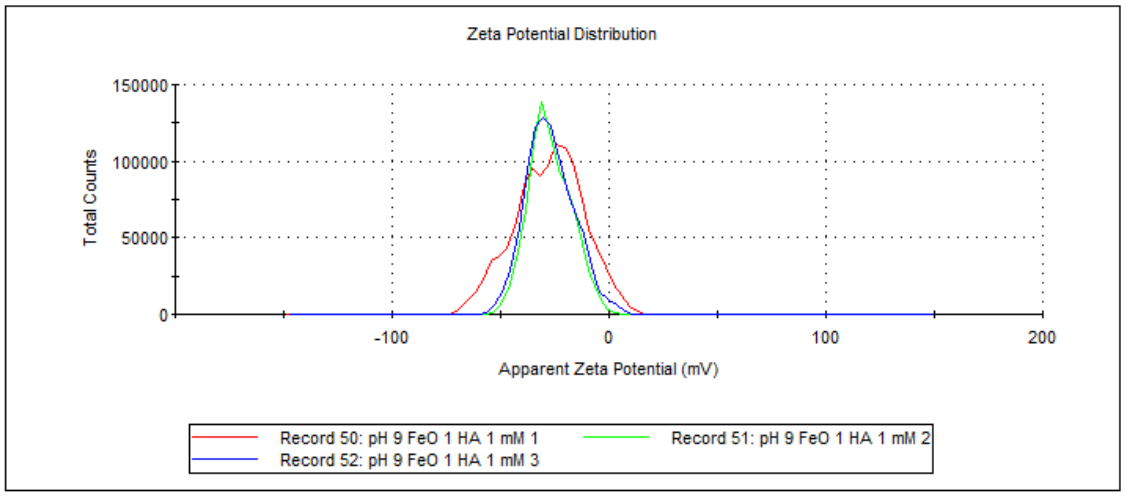

Fe oxyhydroxide + 0.66 mg/L DOC at pH 9

			Mean (mV)	Area (%)	St Dev (mV)
Zeta Potential (mV):	-31.9	Peak 1:	-31.9	100.0	10.9
Zeta Deviation (mV):	10.9	Peak 2:	0.00	0.0	0.00
Conductivity (mS/cm):	0.0123	Peak 3:	0.00	0.0	0.00

Result quality : Good

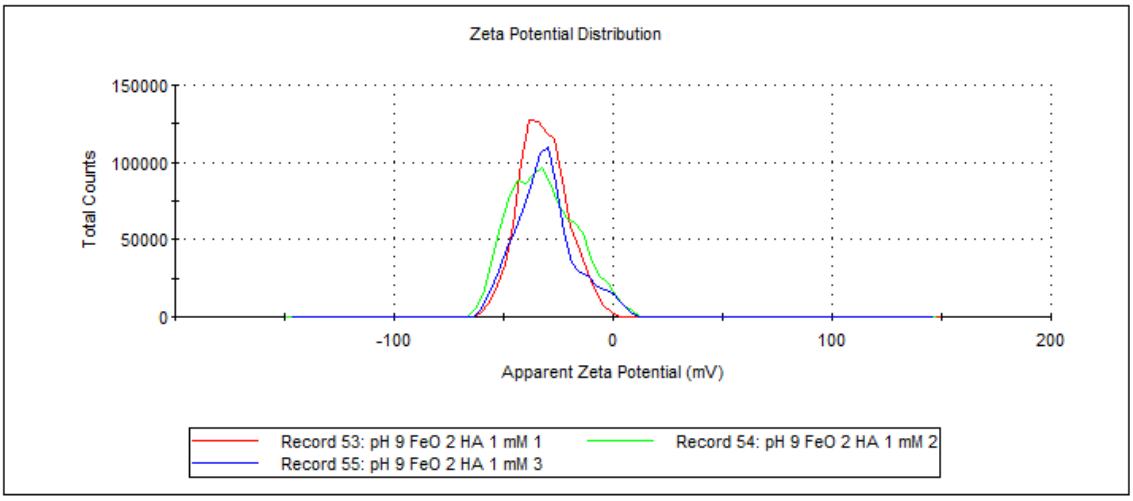

Fe oxyhydroxide + 1.65 mg/L DOC at pH 9

			Mean (mV)	Area (%)	St Dev (mV)
Zeta Potential (mV):	-35.4	Peak 1:	-35.4	100.0	10.3
Zeta Deviation (mV):	10.3	Peak 2:	0.00	0.0	0.00
Conductivity (mS/cm):	0.0131	Peak 3:	0.00	0.0	0.00

Result quality : Good

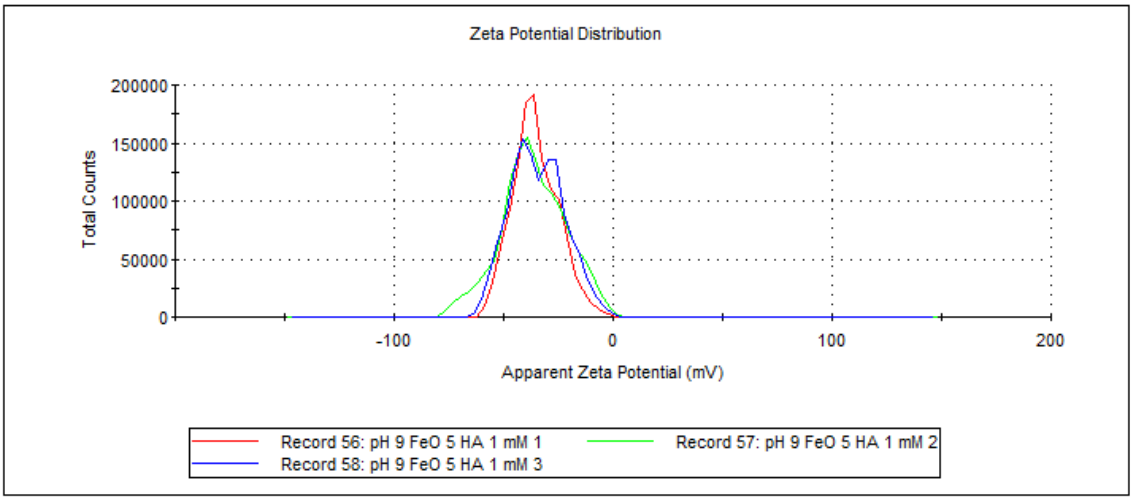

Fe oxyhydroxide + 3.3 mg/L DOC at pH 9

			Mean (mV)	Area (%)	St Dev (mV)
Zeta Potential (mV):	-37.8	Peak 1:	-42.9	68.5	8.28
Zeta Deviation (mV):	11.6	Peak 2:	-24.8	31.5	5.27
Conductivity (mS/cm):	0.0274	Peak 3:	0.00	0.0	0.00

Result quality : Good

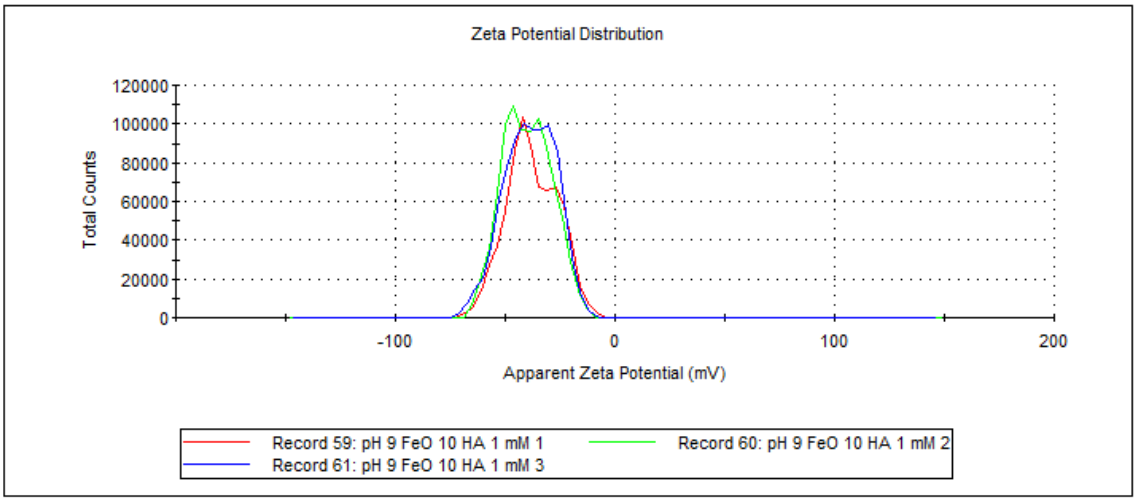

Fe oxyhydroxide + 4.95 mg/L DOC at pH 9

			Mean (mV)	Area (%)	St Dev (mV)
Zeta Potential (mV):	-37.6	Peak 1:	-43.3	57.8	6.28
Zeta Deviation (mV):	9.50	Peak 2:	-29.3	42.2	4.98
Conductivity (mS/cm):	0.0210	Peak 3:	0.00	0.0	0.00

Result quality : Good

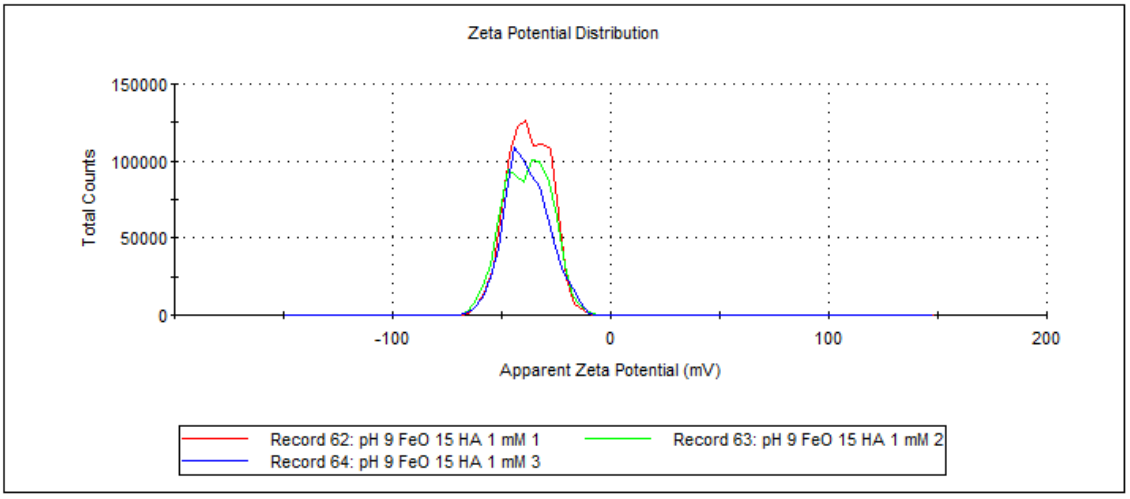

Fe oxyhydroxide + 6.6 mg/L DOC at pH 9

			Mean (mV)	Area (%)	St Dev (mV)
Zeta Potential (mV):	-40.3	Peak 1:	-40.3	100.0	12.3
Zeta Deviation (mV):	12.3	Peak 2:	0.00	0.0	0.00
Conductivity (mS/cm):	0.0224	Peak 3:	0.00	0.0	0.00

Result quality : Good

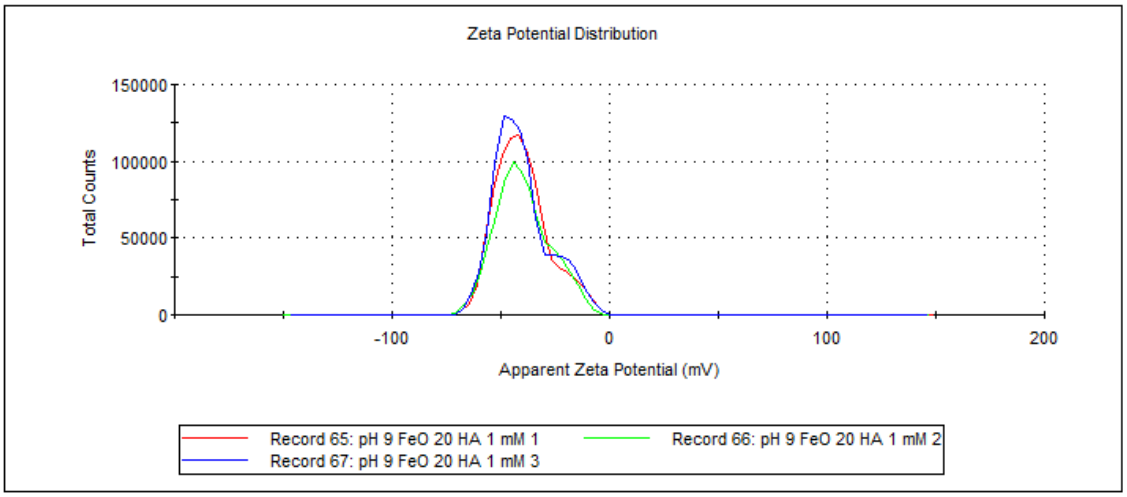

Zeta potential of quartz sand at pH 5 and pH 9

			Mean (mV)	Area (%)	St Dev (mV)
Zeta Potential (mV):	-40.6	Peak 1:	-40.6	100.0	6.25
Zeta Deviation (mV):	6.25	Peak 2:	0.00	0.0	0.00
Conductivity (mS/cm):	0.0191	Peak 3:	0.00	0.0	0.00

Result quality : Good

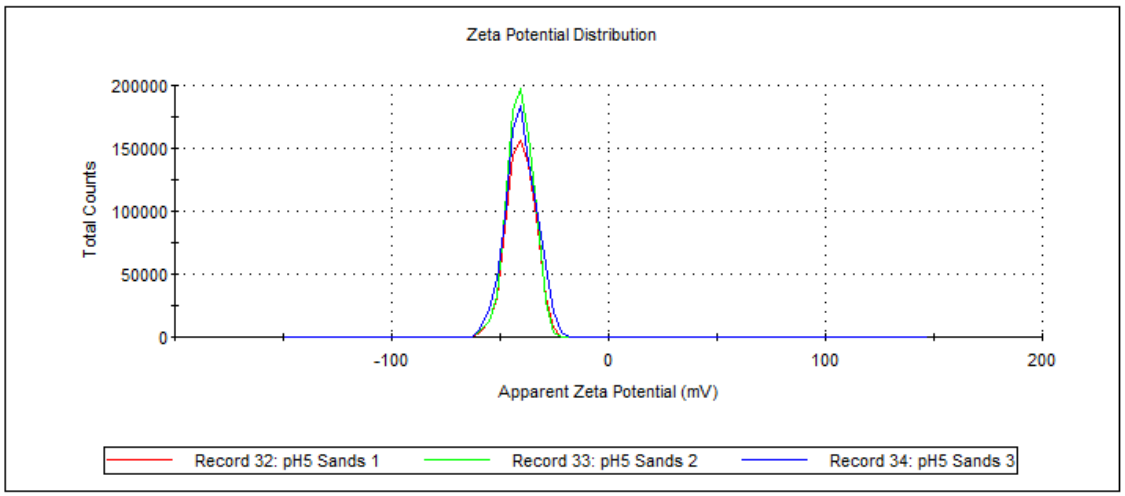

			Mean (mV)	Area (%)	St Dev (mV)
Zeta Potential (mV):	-42.5	Peak 1:	-42.5	100.0	8.74
Zeta Deviation (mV):	8.74	Peak 2:	0.00	0.0	0.00
Conductivity (mS/cm):	0.0218	Peak 3:	0.00	0.0	0.00

Result quality : Good

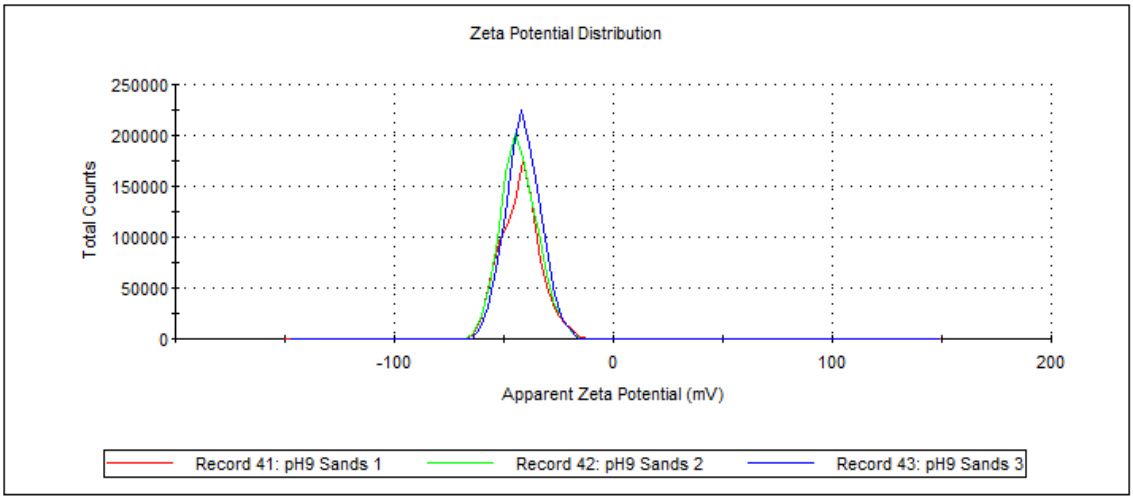

Hydrodynamic diameter and zeta potential of Humic acid as a function of humic acid concentration in 1 mM NaCl solution at pH 5 and pH 9

0.07 mg/L DOC at pH 5

			Size (d.nm):	% Intensity:	St Dev (d.nm):
Z-Average (d.nm):	1741	Peak 1:	168.7	100.0	27.63
PdI:	1.000	Peak 2:	0.000	0.0	0.000
Intercept:	0.268	Peak 3:	0.000	0.0	0.000

Result quality : Refer to quality report

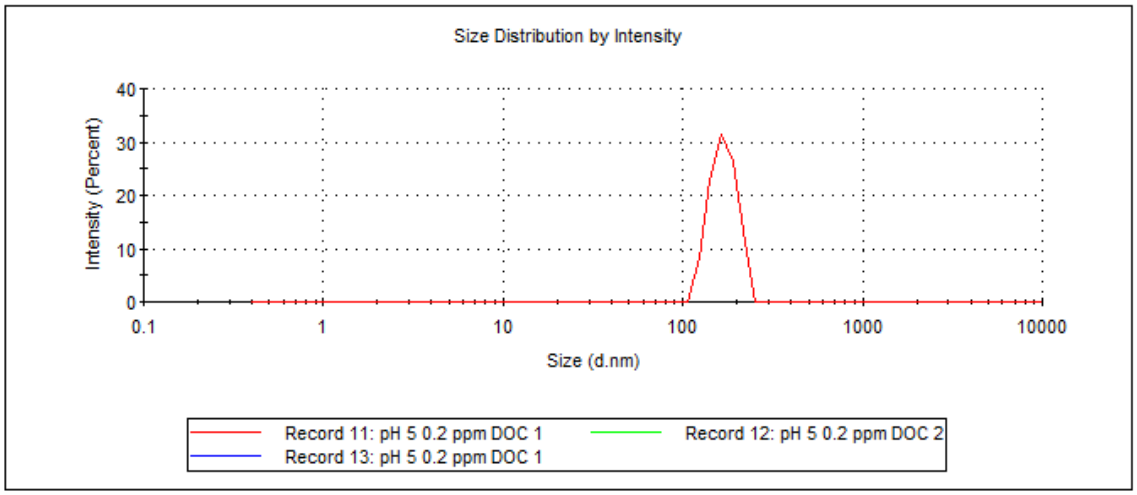

			Size (d.nm):	% Volume:	St Dev (d.nm):
Z-Average (d.nm):	1741	Peak 1:	168.1	100.0	33.40
PdI:	1.000	Peak 2:	0.000	0.0	0.000
Intercept:	0.268	Peak 3:	0.000	0.0	0.000

Result quality : Refer to quality report

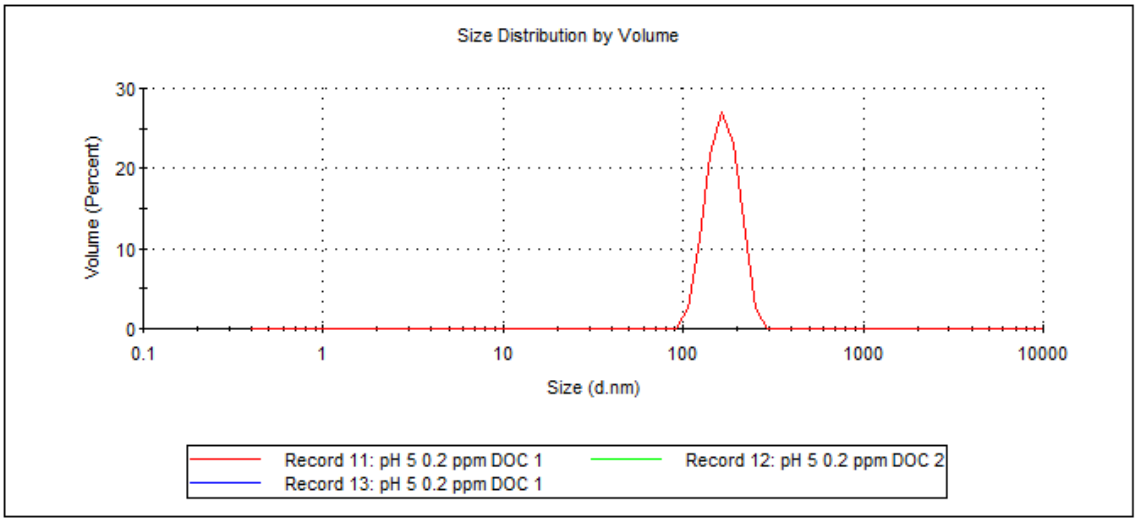

			Size (d.nm):	% Intensity:	St Dev (d.nm):
Z-Average (d.nm):	6134	Peak 1:	47.92	100.0	3.404
PdI:	1.000	Peak 2:	0.000	0.0	0.000
Intercept:	0.464	Peak 3:	0.000	0.0	0.000

Result quality : Refer to quality report

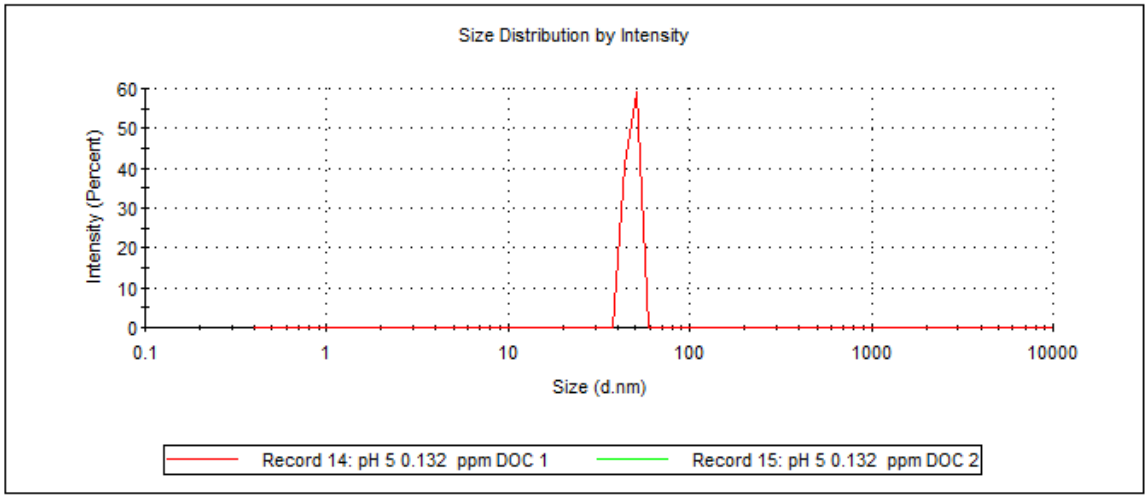

			Size (d.nm):	% Volume:	St Dev (d.nm):
Z-Average (d.nm):	6134	Peak 1:	47.46	100.0	6.040
PdI:	1.000	Peak 2:	0.000	0.0	0.000
Intercept:	0.464	Peak 3:	0.000	0.0	0.000

Result quality : Refer to quality report

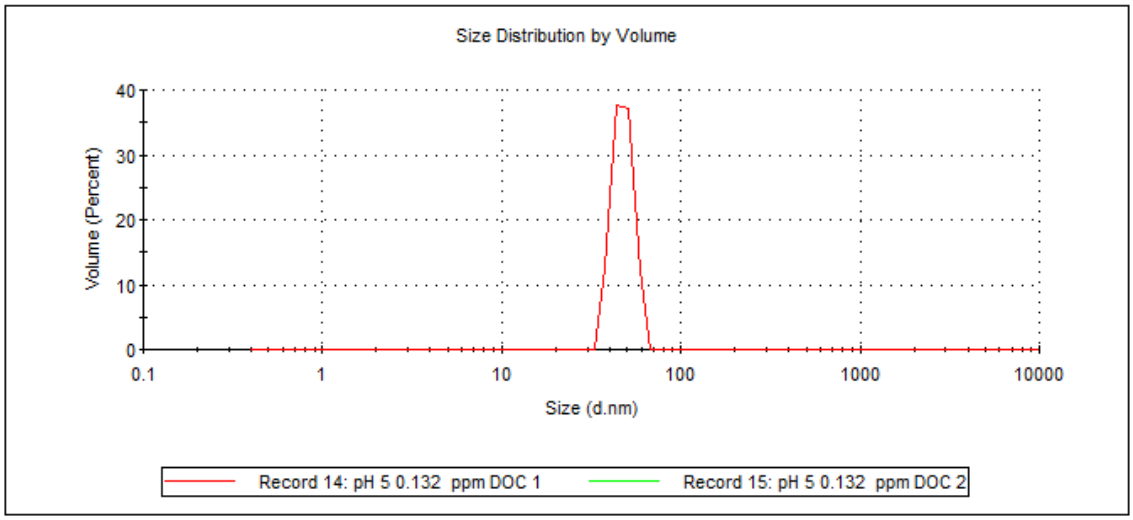

			Size (d.nm):	% Intensity:	St Dev (d.nm):
Z-Average (d.nm):	1184	Peak 1:	269.1	88.8	40.35
PdI:	0.824	Peak 2:	1.184	11.2	0.1228
Intercept:	0.276	Peak 3:	0.000	0.0	0.000

Result quality : Refer to quality report

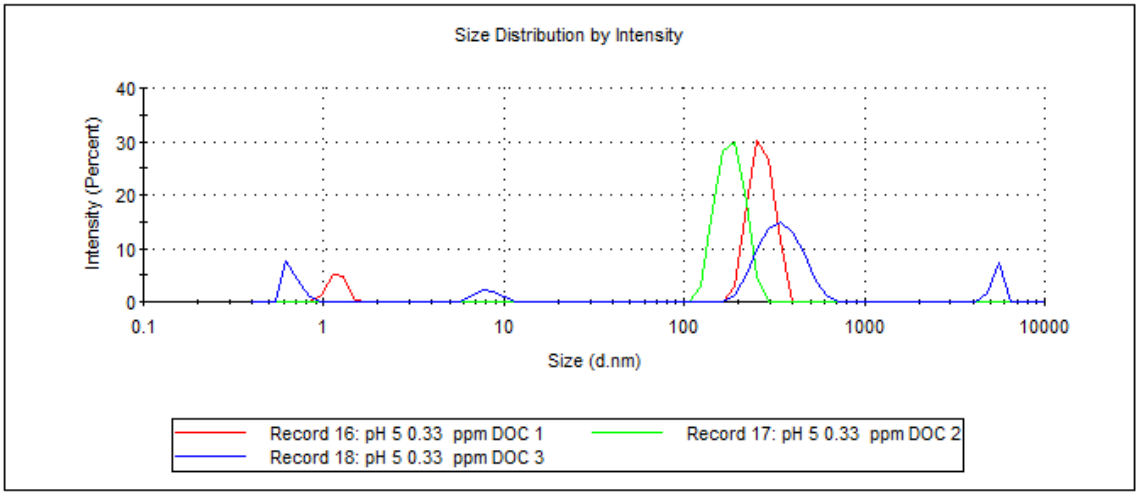

			Size (d.nm):	% Volume:	St Dev (d.nm):
Z-Average (d.nm):	1184	Peak 1:	1.151	100.0	0.1713
PdI:	0.824	Peak 2:	0.000	0.0	0.000
Intercept:	0.276	Peak 3:	0.000	0.0	0.000

Result quality : Refer to quality report

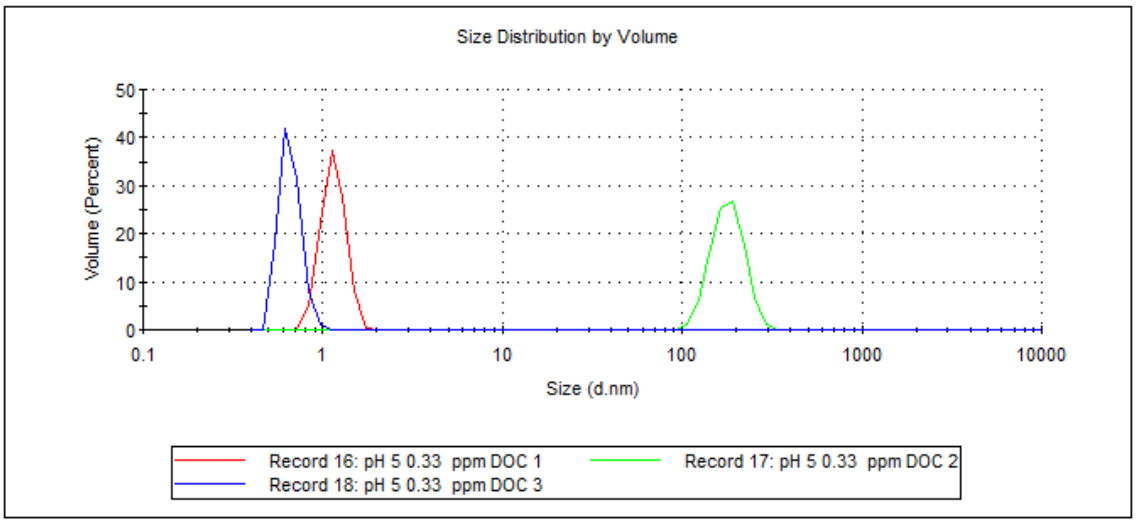

			Size (d.nm):	% Intensity:	St Dev (d.nm):
Z-Average (d.nm):	1042	Peak 1:	333.4	47.0	80.18
PdI:	0.803	Peak 2:	2.826	44.9	0.5355
Intercept:	0.289	Peak 3:	5560	8.1	6.104e-5

Result quality : Refer to quality report

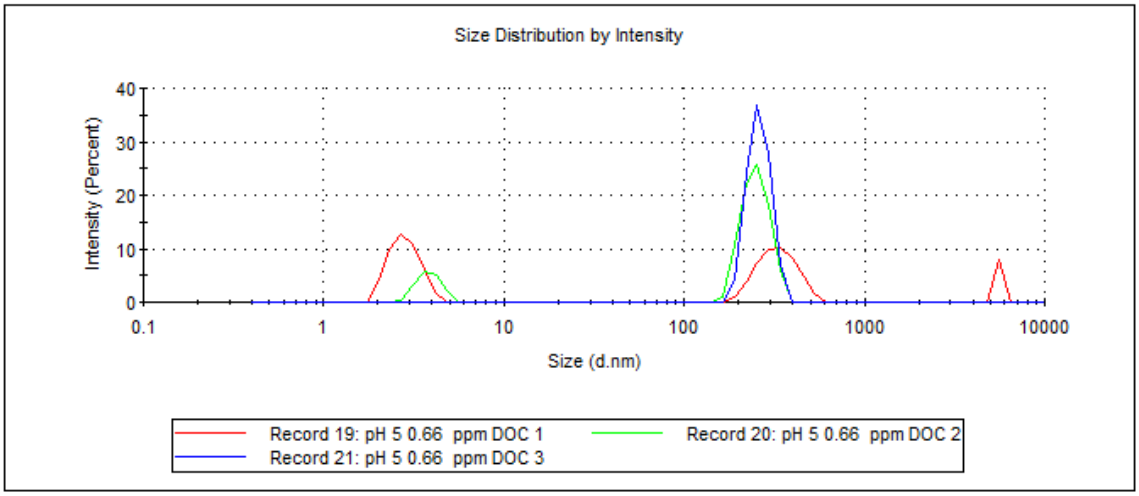

			Size (d.nm):	% Volume:	St Dev (d.nm):
Z-Average (d.nm):	1042	Peak 1:	2.569	100.0	0.5363
PdI:	0.803	Peak 2:	0.000	0.0	0.000
Intercept:	0.289	Peak 3:	0.000	0.0	0.000

Result quality : Refer to quality report

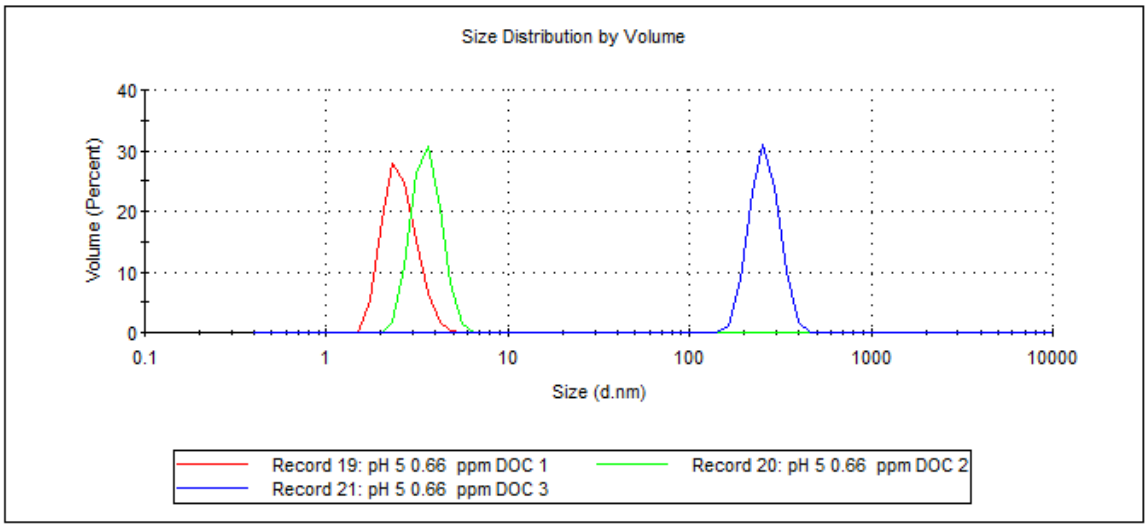

			Size (d.nm):	% Intensity:	St Dev (d.nm):
Z-Average (d.nm):	2589	Peak 1:	66.28	80.9	7.744
PdI:	1.000	Peak 2:	4.591	19.1	0.3989
Intercept:	0.417	Peak 3:	0.000	0.0	0.000

Result quality : Refer to quality report

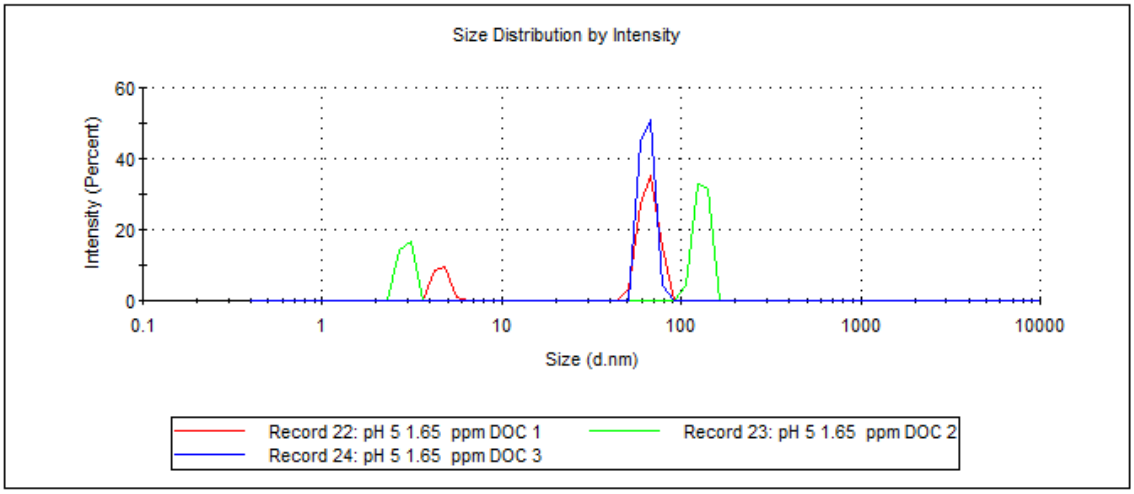

			Size (d.nm):	% Volume:	St Dev (d.nm):
Z-Average (d.nm):	2589	Peak 1:	64.20	0.2	10.10
PdI:	1.000	Peak 2:	4.519	99.8	0.6004
Intercept:	0.417	Peak 3:	0.000	0.0	0.000

Result quality : Refer to quality report

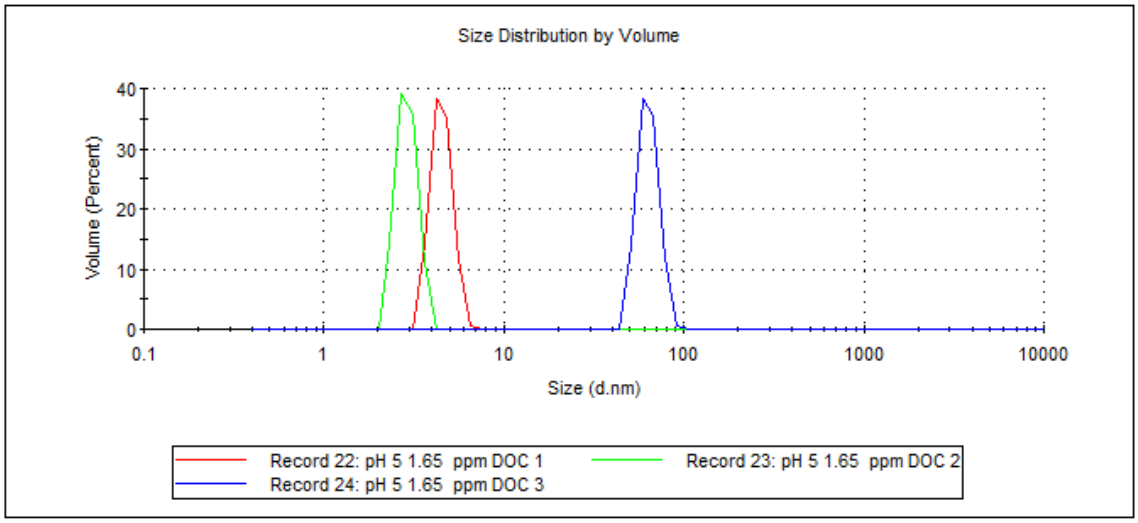

			Size (d.nm):	% Intensity:	St Dev (d.nm):
Z-Average (d.nm):	1903	Peak 1:	128.4	88.7	12.47
PdI:	1.000	Peak 2:	11.84	11.3	1.108
Intercept:	0.584	Peak 3:	0.000	0.0	0.000

Result quality : Refer to quality report

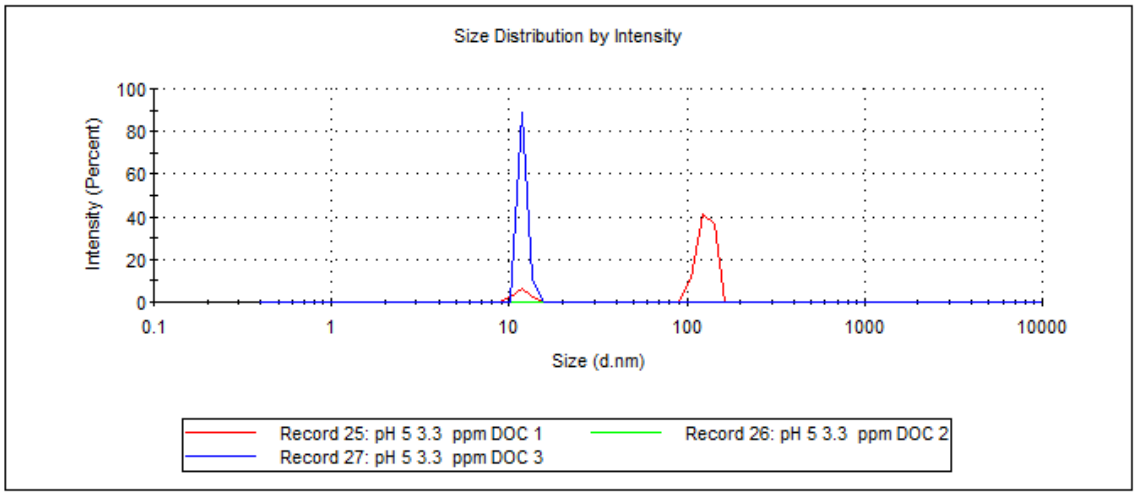

			Size (d.nm):	% Volume:	St Dev (d.nm):
Z-Average (d.nm):	1903	Peak 1:	126.9	1.1	18.46
PdI:	1.000	Peak 2:	11.59	98.9	1.625
Intercept:	0.584	Peak 3:	0.000	0.0	0.000

Result quality : Refer to quality report

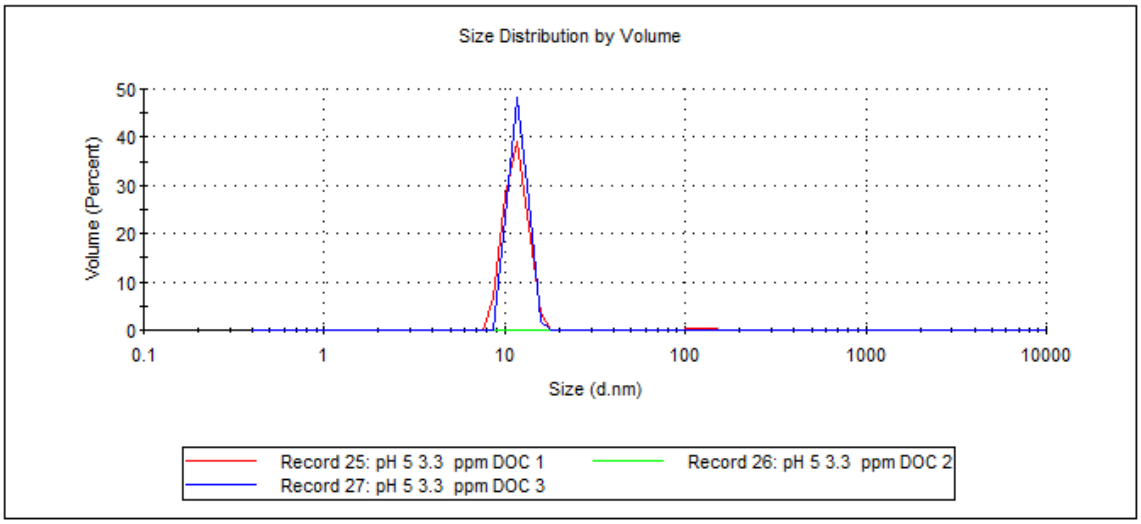

			Size (d.nm):	% Intensity:	St Dev (d.nm):
Z-Average (d.nm):	1490	Peak 1:	57.63	100.0	9.249
PdI:	1.000	Peak 2:	0.000	0.0	0.000
Intercept:	0.454	Peak 3:	0.000	0.0	0.000

Result quality : Refer to quality report

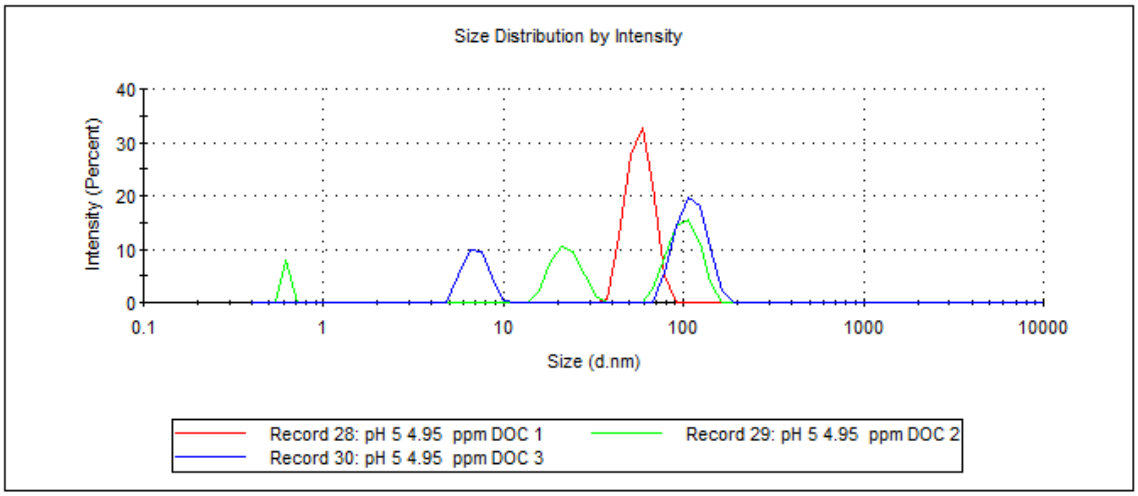

			Size (d.nm):	% Volume:	St Dev (d.nm):
Z-Average (d.nm):	1490	Peak 1:	53.97	100.0	10.31
PdI:	1.000	Peak 2:	0.000	0.0	0.000
Intercept:	0.454	Peak 3:	0.000	0.0	0.000

Result quality : Refer to quality report

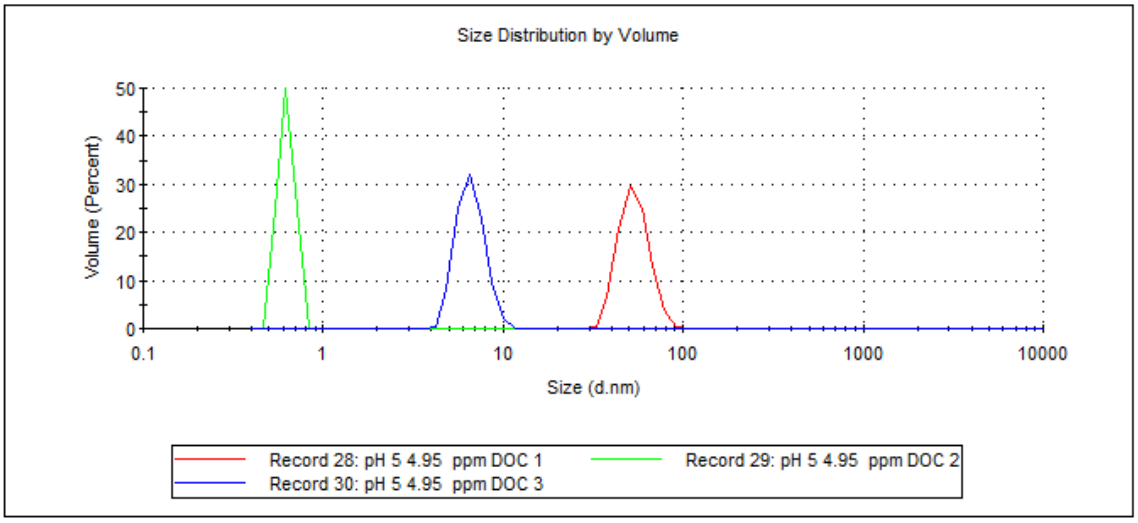

			Size (d.nm):	% Intensity:	St Dev (d.nm):
Z-Average (d.nm):	1093	Peak 1:	116.1	83.0	14.95
PdI:	1.000	Peak 2:	11.83	17.0	1.258
Intercept:	0.554	Peak 3:	0.000	0.0	0.000

Result quality : Refer to quality report

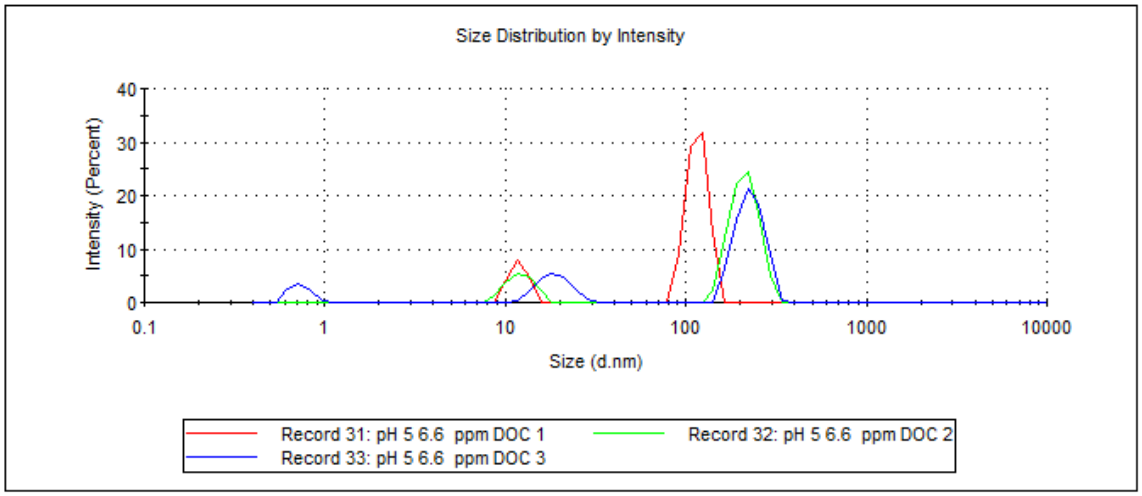

			Size (d.nm):	% Volume:	St Dev (d.nm):
Z-Average (d.nm):	1093	Peak 1:	113.0	0.8	19.01
PdI:	1.000	Peak 2:	11.49	99.2	1.712
Intercept:	0.554	Peak 3:	0.000	0.0	0.000

Result quality : Refer to quality report

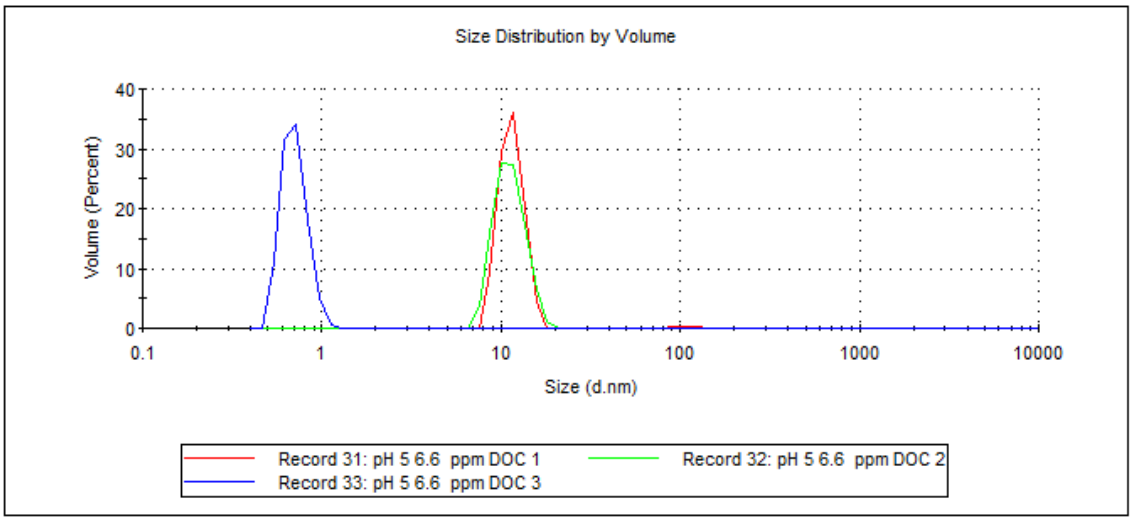

			Size (d.nm):	% Intensity:	St Dev (d.nm):
Z-Average (d.nm):	2109	Peak 1:	90.41	86.5	8.451
PdI:	1.000	Peak 2:	7.326	13.5	0.6218
Intercept:	0.871	Peak 3:	0.000	0.0	0.000

Result quality : Refer to quality report

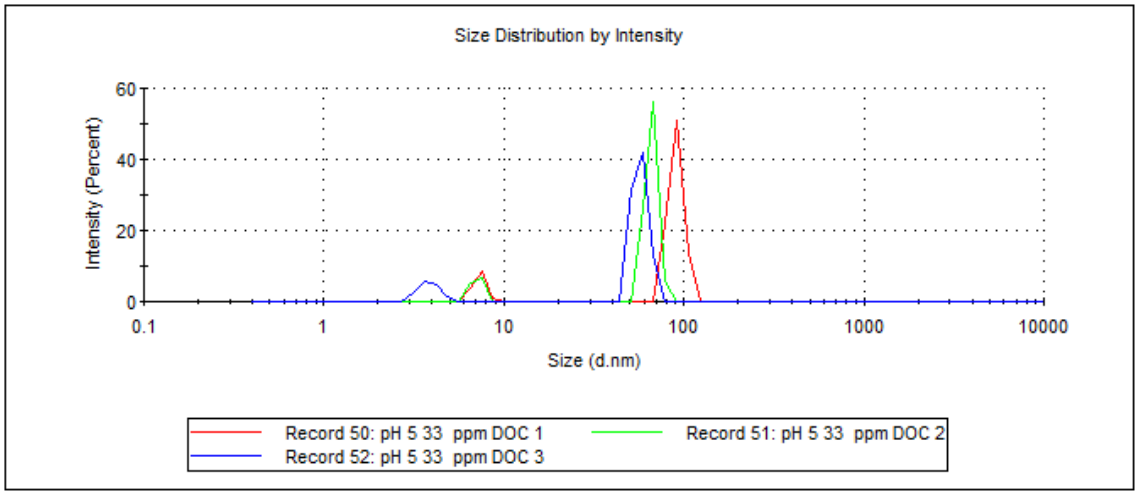

			Size (d.nm):	% Volume:	St Dev (d.nm):
Z-Average (d.nm):	2109	Peak 1:	89.03	0.4	12.43
PdI:	1.000	Peak 2:	7.210	99.6	0.9651
Intercept:	0.871	Peak 3:	0.000	0.0	0.000

Result quality : Refer to quality report

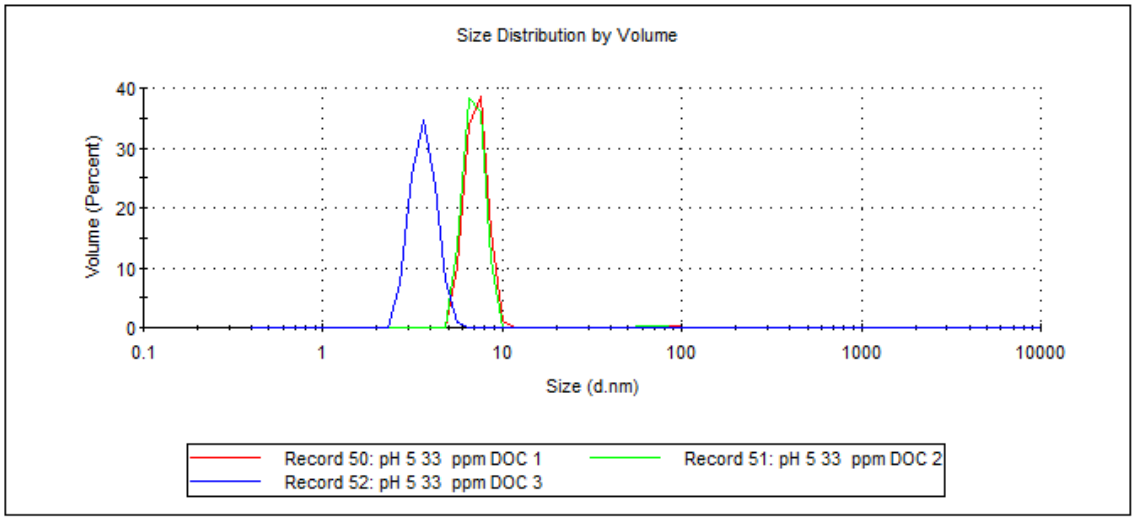

			Size (d.nm):	% Intensity:	St Dev (d.nm):
Z-Average (d.nm):	0.000	Peak 1:	0.000	0.0	0.000
PdI:	0.000	Peak 2:	0.000	0.0	0.000
Intercept:	0.00	Peak 3:	0.000	0.0	0.000

Result quality : Refer to quality report

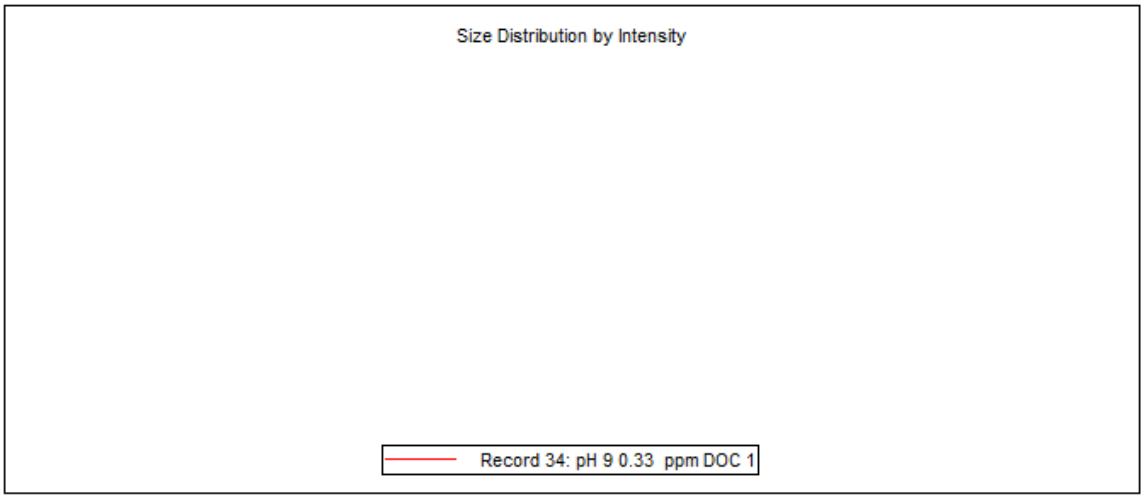

			Size (d.nm):	% Volume:	St Dev (d.nm):
Z-Average (d.nm):	0.000	Peak 1:	0.000	0.0	0.000
PdI:	0.000	Peak 2:	0.000	0.0	0.000
Intercept:	0.00	Peak 3:	0.000	0.0	0.000

Result quality : Refer to quality report

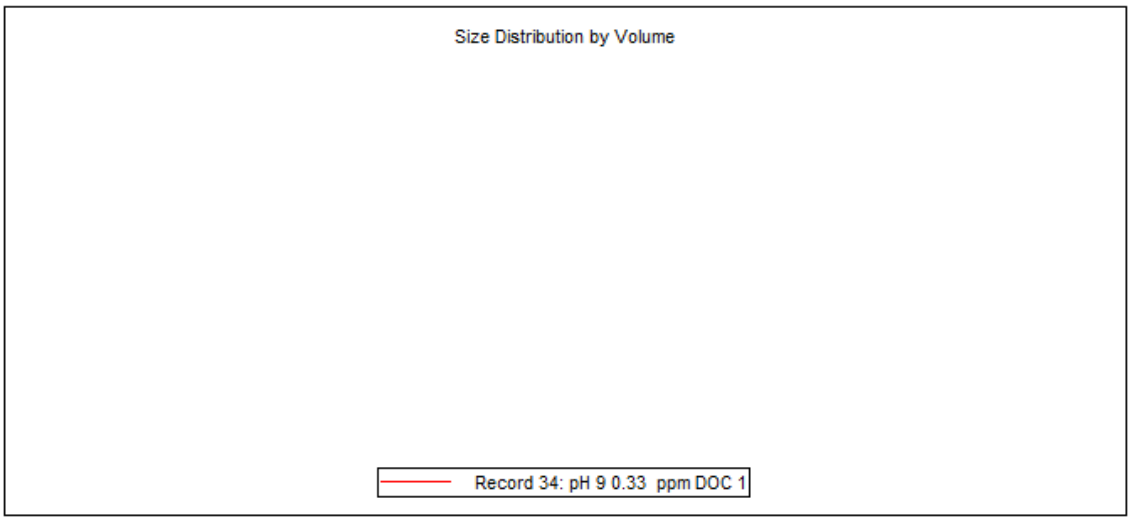

			Size (d.nm):	% Intensity:	St Dev (d.nm):
Z-Average (d.nm):	3697	Peak 1:	85.97	75.5	6.162
PdI:	1.000	Peak 2:	1.230	24.5	0.08489
Intercept:	1.05	Peak 3:	0.000	0.0	0.000

Result quality : Refer to quality report

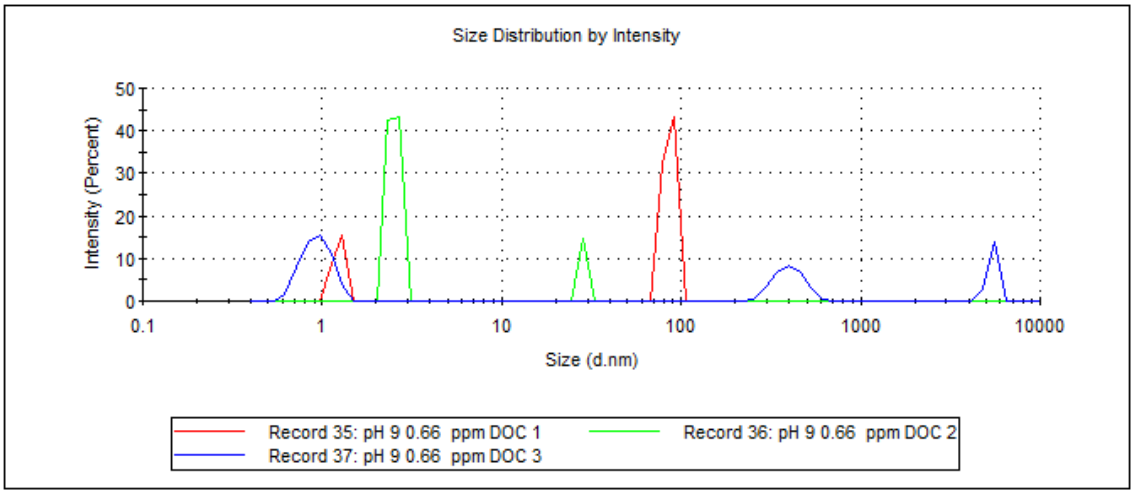

			Size (d.nm):	% Volume:	St Dev (d.nm):
Z-Average (d.nm):	3697	Peak 1:	1.218	100.0	0.1546
PdI:	1.000	Peak 2:	0.000	0.0	0.000
Intercept:	1.05	Peak 3:	0.000	0.0	0.000

Result quality : Refer to quality report

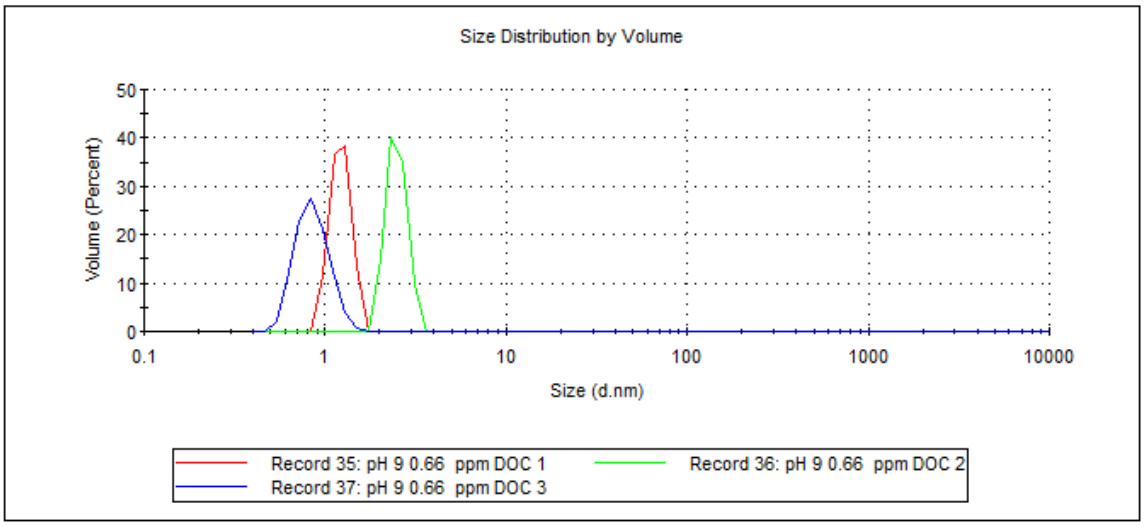

			Size (d.nm):	% Intensity:	St Dev (d.nm):
Z-Average (d.nm):	4881	Peak 1:	18.39	100.0	2.039
PdI:	1.000	Peak 2:	0.000	0.0	0.000
Intercept:	0.478	Peak 3:	0.000	0.0	0.000

Result quality : Refer to quality report

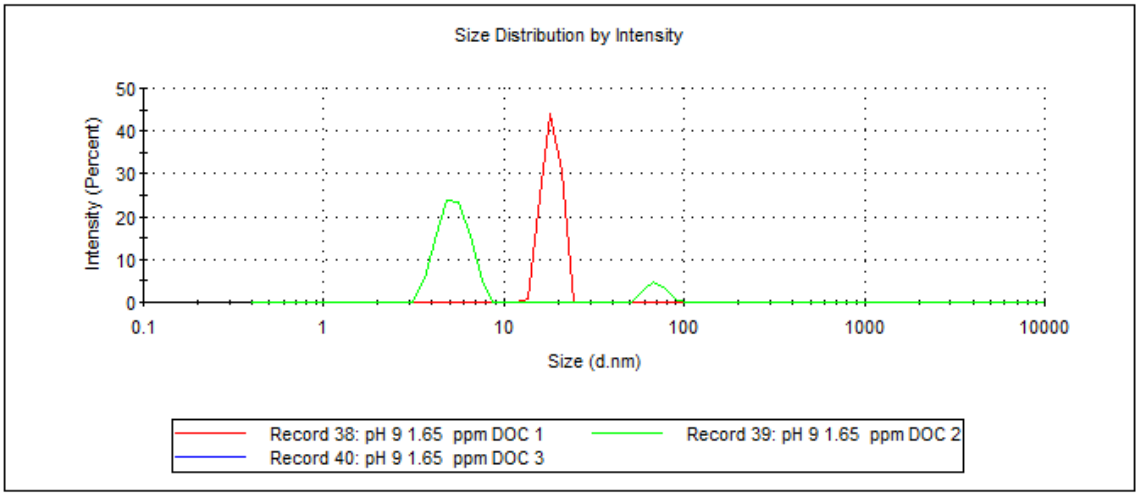

			Size (d.nm):	% Volume:	St Dev (d.nm):
Z-Average (d.nm):	4881	Peak 1:	17.81	100.0	2.743
PdI:	1.000	Peak 2:	0.000	0.0	0.000
Intercept:	0.478	Peak 3:	0.000	0.0	0.000

Result quality : Refer to quality report

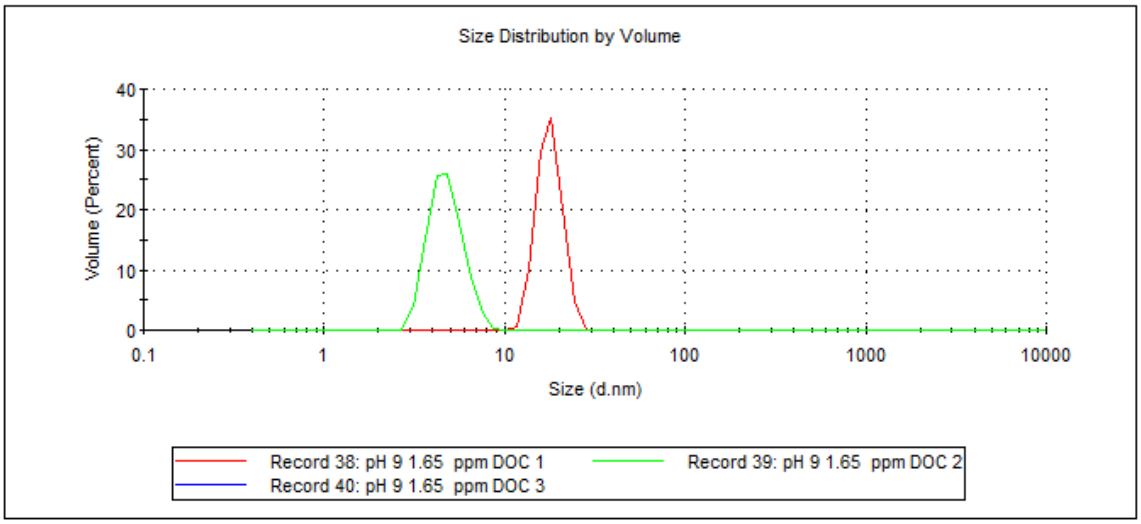

			Size (d.nm):	% Intensity:	St Dev (d.nm):
Z-Average (d.nm):	1436	Peak 1:	1.095	52.8	0.2012
PdI:	1.000	Peak 2:	289.1	33.2	80.02
Intercept:	0.289	Peak 3:	126.0	12.4	25.73

Result quality : Refer to quality report

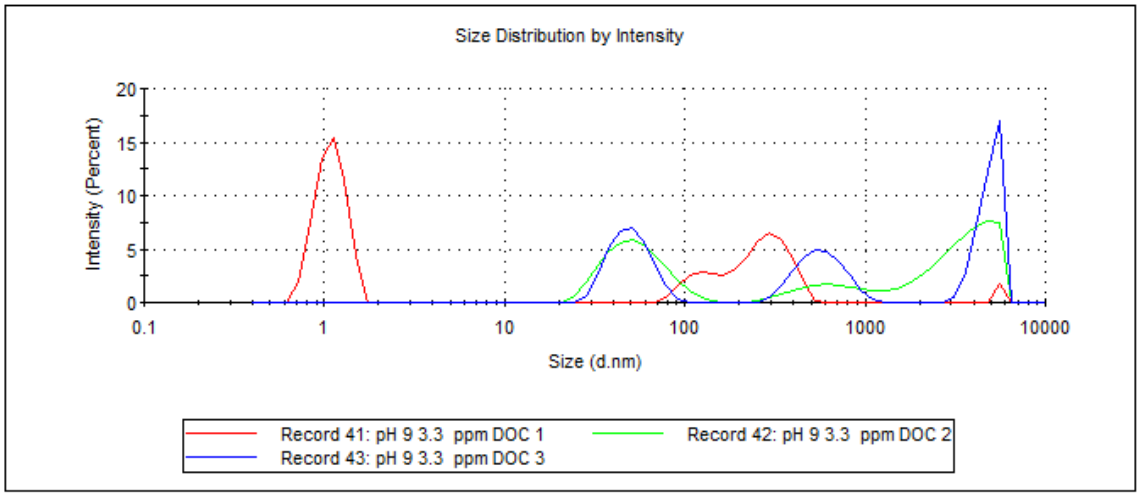

			Size (d.nm):	% Volume:	St Dev (d.nm):
Z-Average (d.nm):	1436	Peak 1:	0.9942	100.0	0.2122
PdI:	1.000	Peak 2:	0.000	0.0	0.000
Intercept:	0.289	Peak 3:	0.000	0.0	0.000

Result quality : Refer to quality report

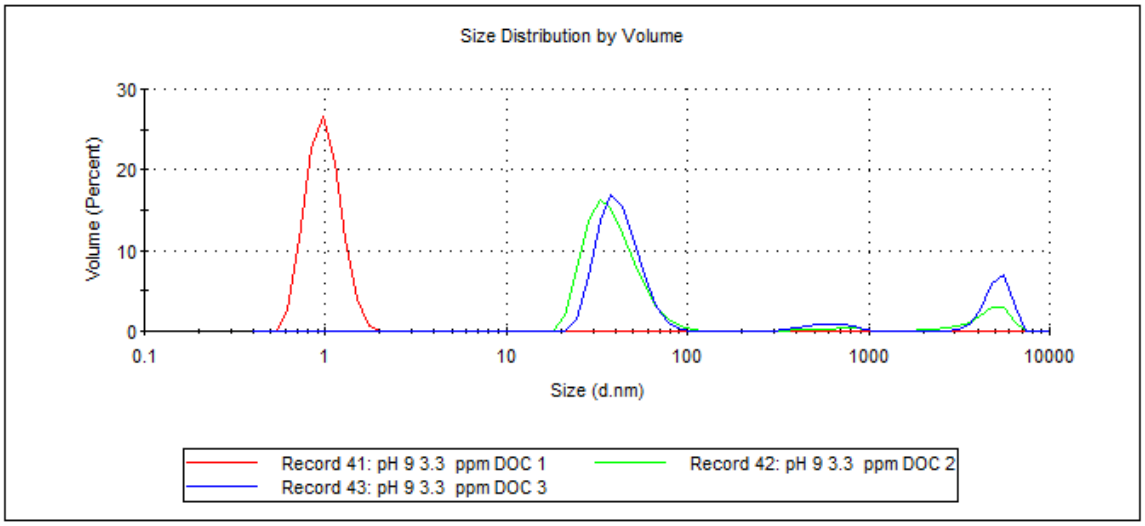

			Size (d.nm):	% Intensity:	St Dev (d.nm):
Z-Average (d.nm):	2505	Peak 1:	92.99	72.9	9.983
PdI:	1.000	Peak 2:	10.24	27.1	1.110
Intercept:	0.460	Peak 3:	0.000	0.0	0.000

Result quality : Refer to quality report

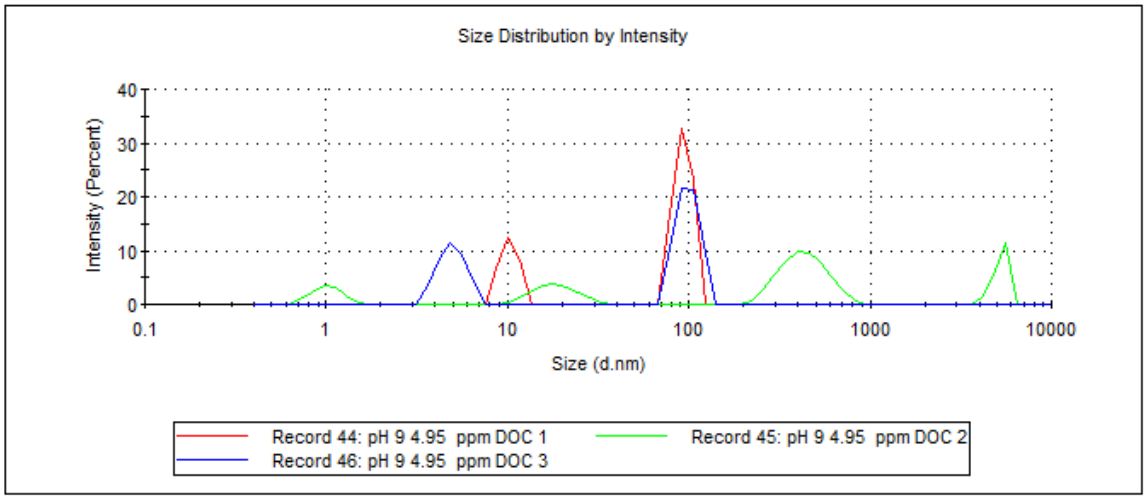

			Size (d.nm):	% Volume:	St Dev (d.nm):
Z-Average (d.nm):	2505	Peak 1:	90.89	0.5	13.74
PdI:	1.000	Peak 2:	9.943	99.5	1.496
Intercept:	0.460	Peak 3:	0.000	0.0	0.000

Result quality : Refer to quality report

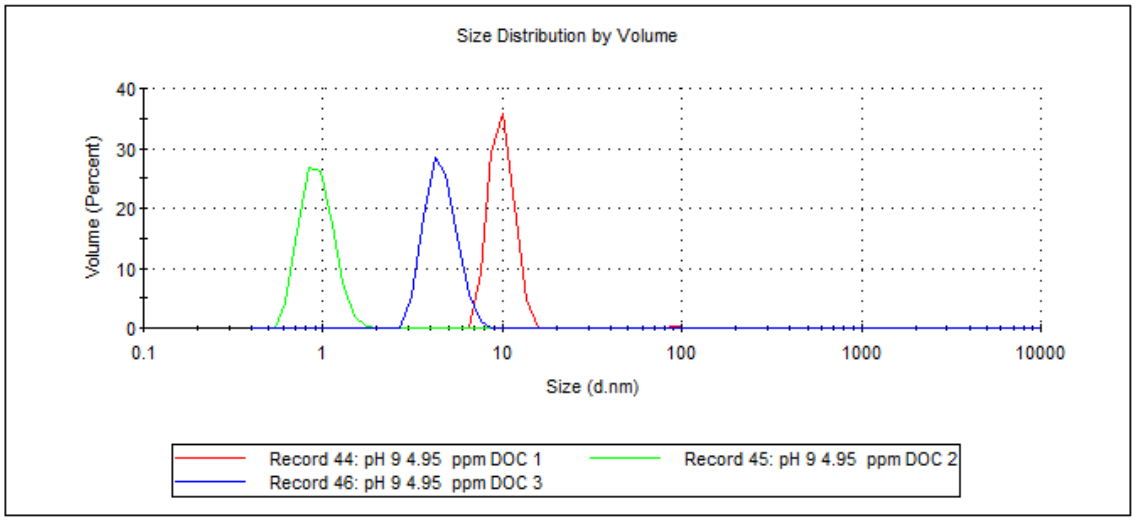

			Size (d.nm):	% Intensity:	St Dev (d.nm):
Z-Average (d.nm):	3948	Peak 1:	0.7722	51.7	0.1048
PdI:	1.000	Peak 2:	54.84	46.9	6.502
Intercept:	0.521	Peak 3:	11.14	1.4	0.7598

Result quality : Refer to quality report

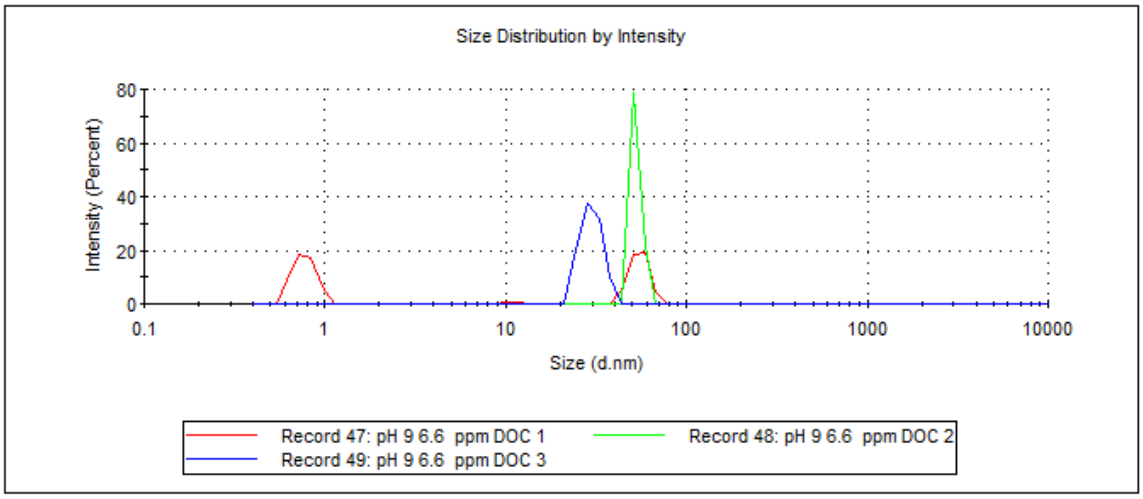

			Size (d.nm):	% Volume:	St Dev (d.nm):
Z-Average (d.nm):	3948	Peak 1:	0.7358	100.0	0.1243
PdI:	1.000	Peak 2:	0.000	0.0	0.000
Intercept:	0.521	Peak 3:	0.000	0.0	0.000

Result quality : Refer to quality report

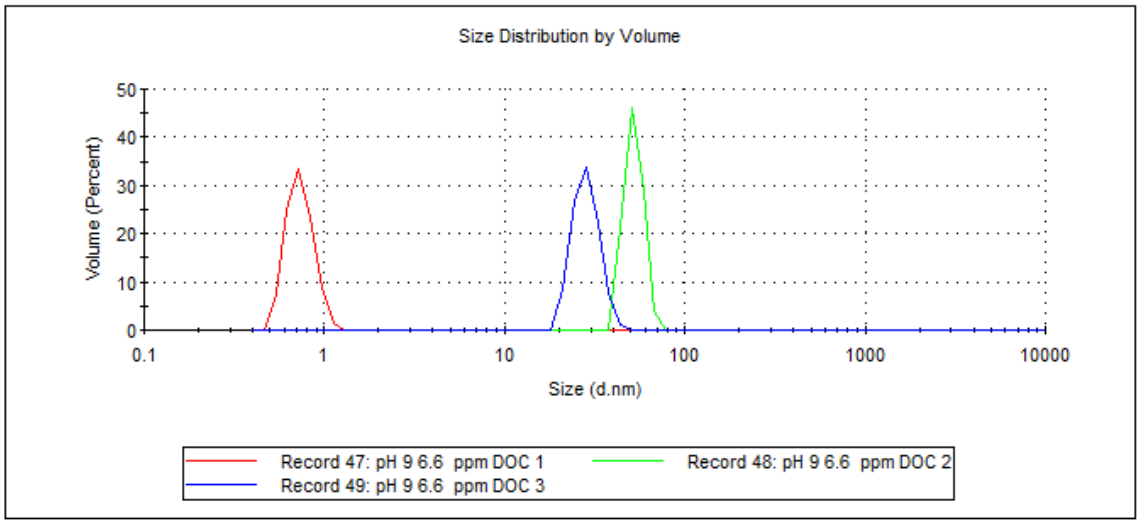

			Size (d.nm):	% Intensity:	St Dev (d.nm):
Z-Average (d.nm):	3127	Peak 1:	77.01	83.4	7.448
PdI:	1.000	Peak 2:	1.953	16.6	0.2263
Intercept:	0.632	Peak 3:	0.000	0.0	0.000

Result quality : Refer to quality report

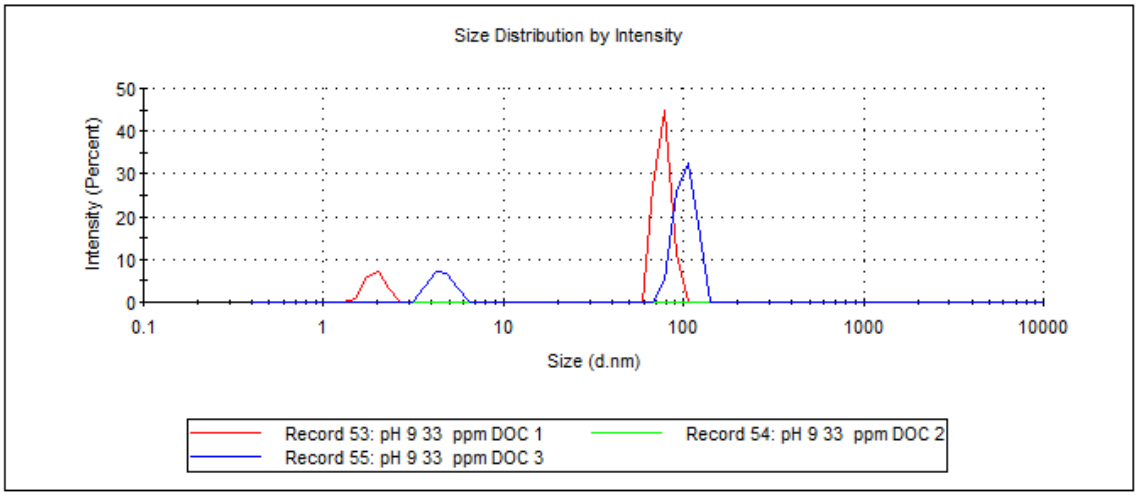

			Size (d.nm):	% Volume:	St Dev (d.nm):
Z-Average (d.nm):	3127	Peak 1:	1.887	100.0	0.2936
PdI:	1.000	Peak 2:	0.000	0.0	0.000
Intercept:	0.632	Peak 3:	0.000	0.0	0.000

Result quality : Refer to quality report

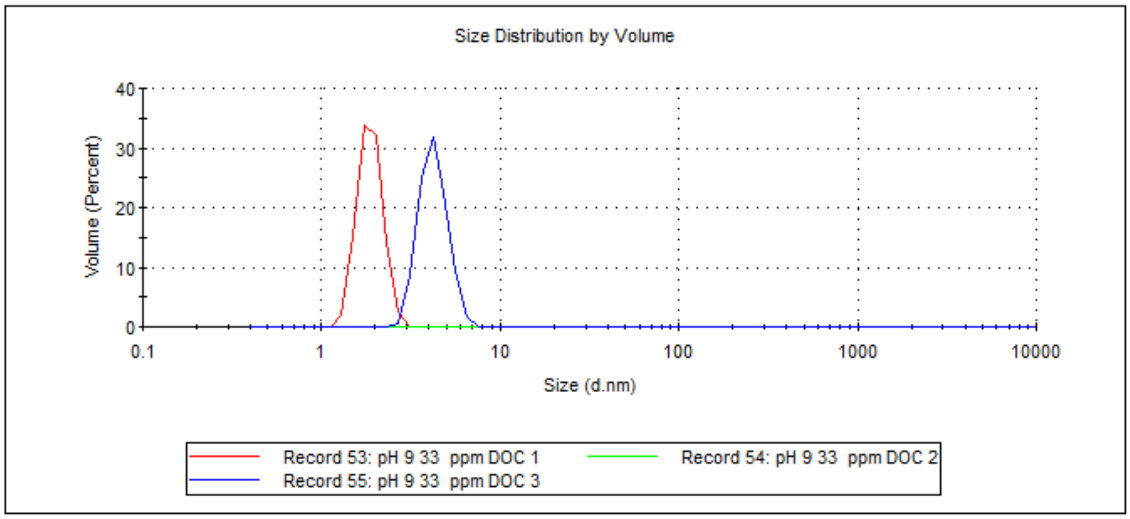

			Mean (mV)	Area (%)	St Dev (mV)
Zeta Potential (mV):	-3.54	Peak 1:	101	22.8	4.36
Zeta Deviation (mV):	149	Peak 2:	-17.0	8.8	7.43
Conductivity (mS/cm):	0.143	Peak 3:	-83.0	7.4	8.08

Result quality : See result quality report

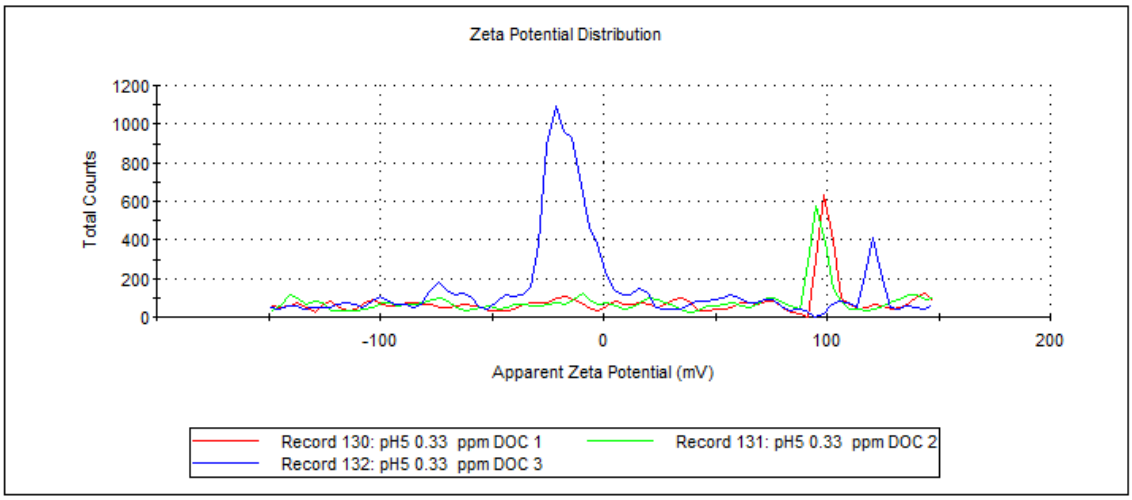

			Mean (mV)	Area (%)	St Dev (mV)
Zeta Potential (mV):	-6.47	Peak 1:	95.3	11.1	8.34
Zeta Deviation (mV):	146	Peak 2:	-98.5	9.7	7.10
Conductivity (mS/cm):	0.142	Peak 3:	28.5	7.5	7.82

Result quality : See result quality report

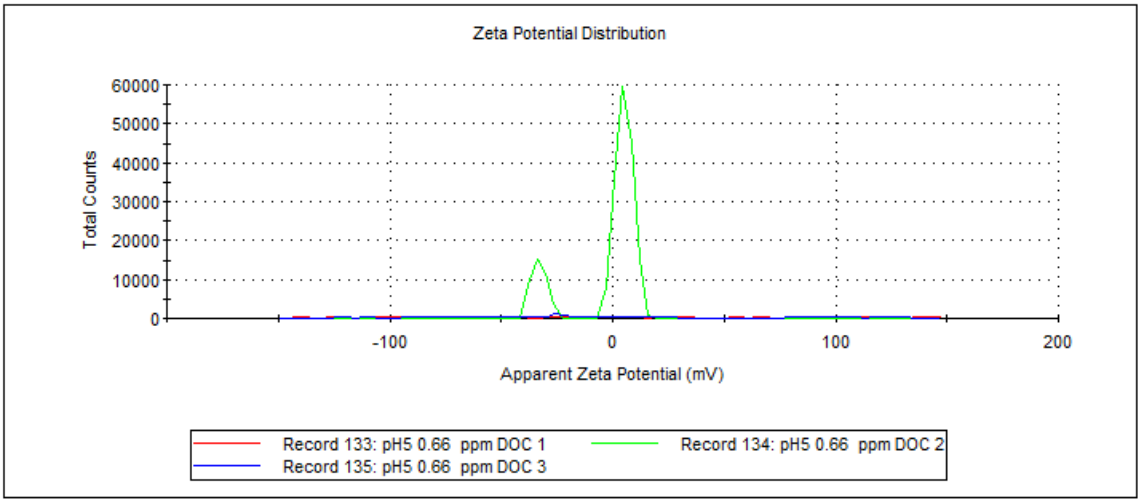

			Mean (mV)	Area (%)	St Dev (mV)
Zeta Potential (mV):	-0.919	Peak 1:	0.489	95.9	7.46
Zeta Deviation (mV):	13.0	Peak 2:	-45.8	3.8	3.47
Conductivity (mS/cm):	0.139	Peak 3:	116	0.2	1.35e-6

Result quality : See result quality report

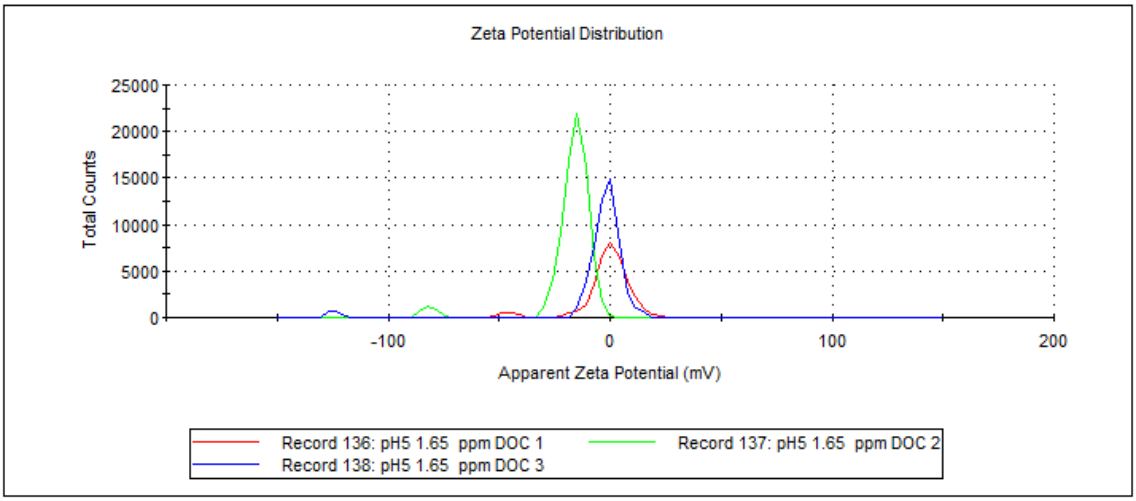

			Mean (mV)	Area (%)	St Dev (mV)
Zeta Potential (mV):	-22.8	Peak 1:	-22.0	94.2	6.30
Zeta Deviation (mV):	7.41	Peak 2:	-41.4	5.8	3.09
Conductivity (mS/cm):	0.134	Peak 3:	0.00	0.0	0.00

Result quality : Good

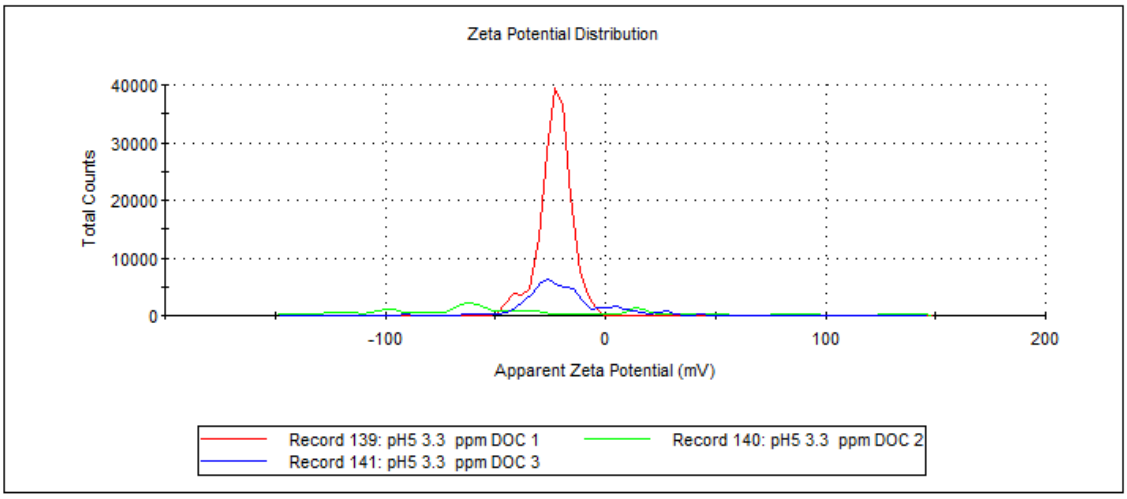

			Mean (mV)	Area (%)	St Dev (mV)
Zeta Potential (mV):	-19.8	Peak 1:	-15.9	58.8	8.88
Zeta Deviation (mV):	32.8	Peak 2:	-44.8	32.0	6.92
Conductivity (mS/cm):	0.125	Peak 3:	76.3	6.7	4.97

Result quality : See result quality report

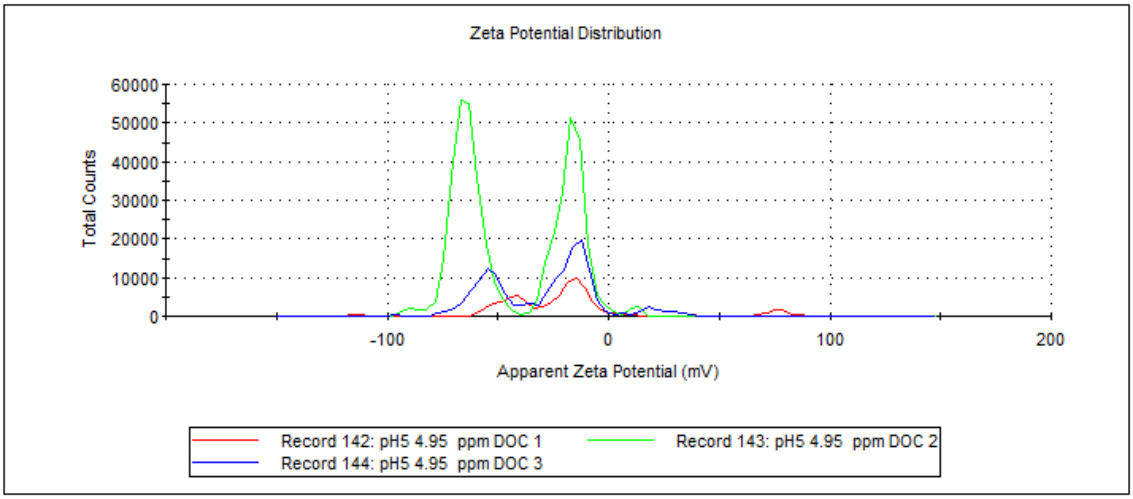

			Mean (mV)	Area (%)	St Dev (mV)
Zeta Potential (mV):	-29.7	Peak 1:	-29.9	99.6	7.03
Zeta Deviation (mV):	7.44	Peak 2:	7.45	0.4	8.43e-8
Conductivity (mS/cm):	0.125	Peak 3:	0.00	0.0	0.00

Result quality : Good

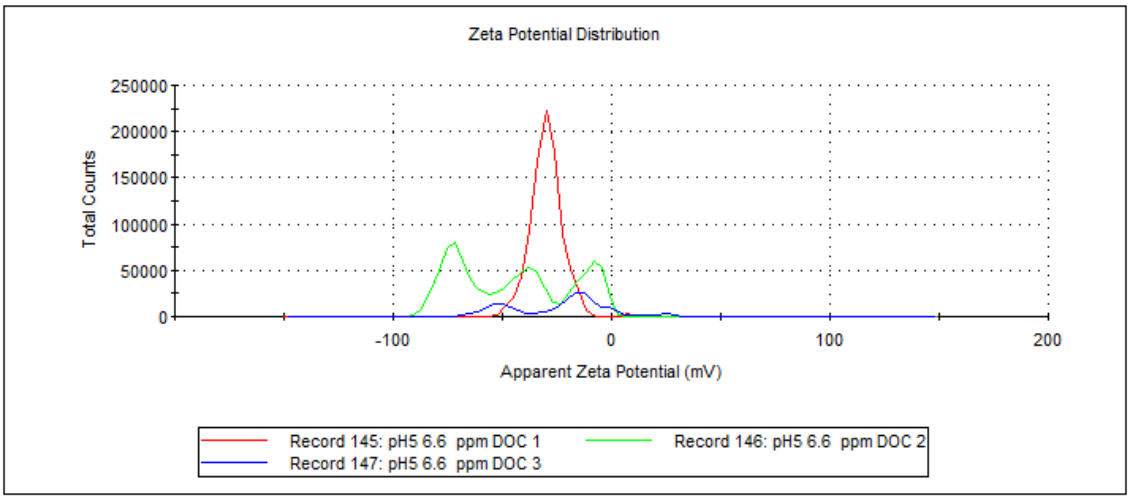

			Mean (mV)	Area (%)	St Dev (mV)
Zeta Potential (mV):	-53.8	Peak 1:	-54.7	92.6	6.52
Zeta Deviation (mV):	9.57	Peak 2:	-27.0	5.7	4.84
Conductivity (mS/cm):	0.0527	Peak 3:	-80.3	1.8	2.29

Result quality : See result quality report

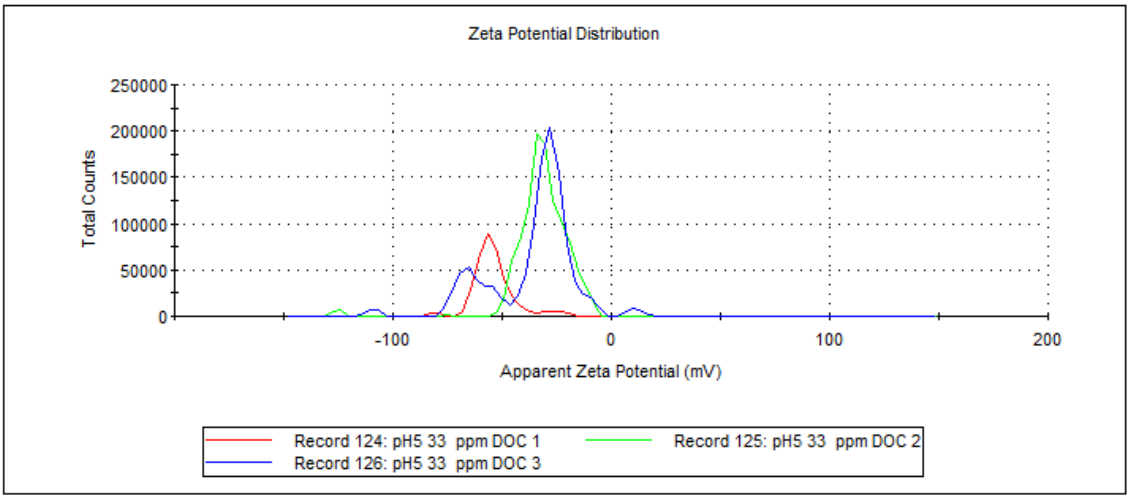

			Mean (mV)	Area (%)	St Dev (mV)
Zeta Potential (mV):	-4.48	Peak 1:	-13.2	82.2	6.48
Zeta Deviation (mV):	19.7	Peak 2:	35.7	17.8	4.67
Conductivity (mS/cm):	0.130	Peak 3:	0.00	0.0	0.00

Result quality : See result quality report

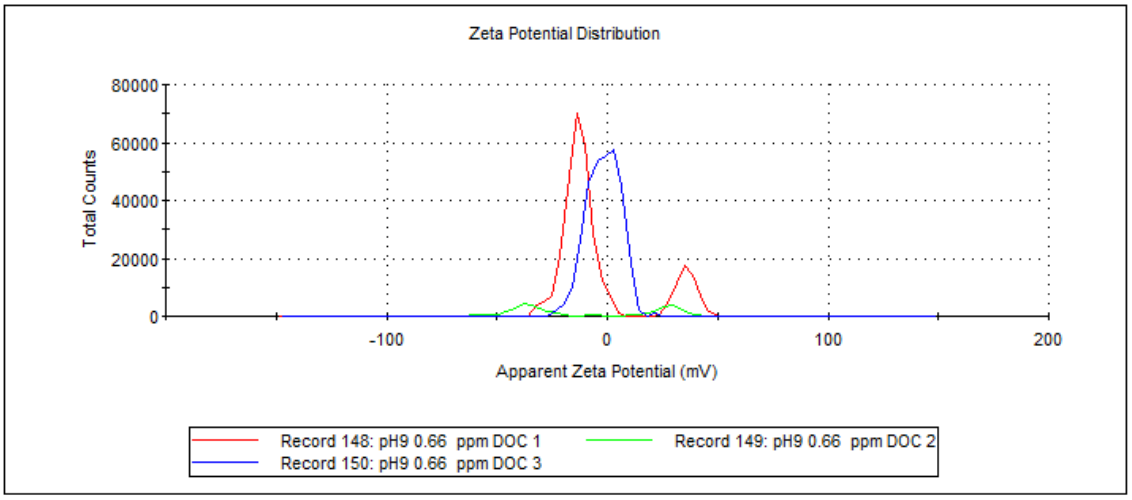

			Mean (mV)	Area (%)	St Dev (mV)
Zeta Potential (mV):	-8.52	Peak 1:	6.36	54.1	8.33
Zeta Deviation (mV):	21.4	Peak 2:	-32.1	33.0	6.93
Conductivity (mS/cm):	0.148	Peak 3:	-14.7	12.8	3.99

Result quality : See result quality report

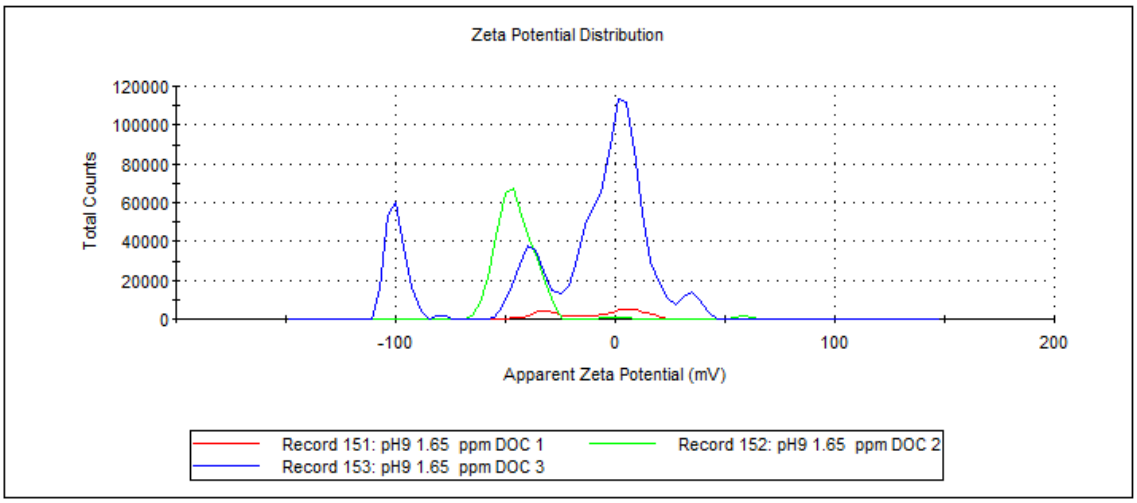

			Mean (mV)	Area (%)	St Dev (mV)
Zeta Potential (mV):	-20.3	Peak 1:	-20.5	99.7	5.69
Zeta Deviation (mV):	7.39	Peak 2:	64.1	0.3	0.283
Conductivity (mS/cm):	0.149	Peak 3:	0.00	0.0	0.00

Result quality : See result quality report

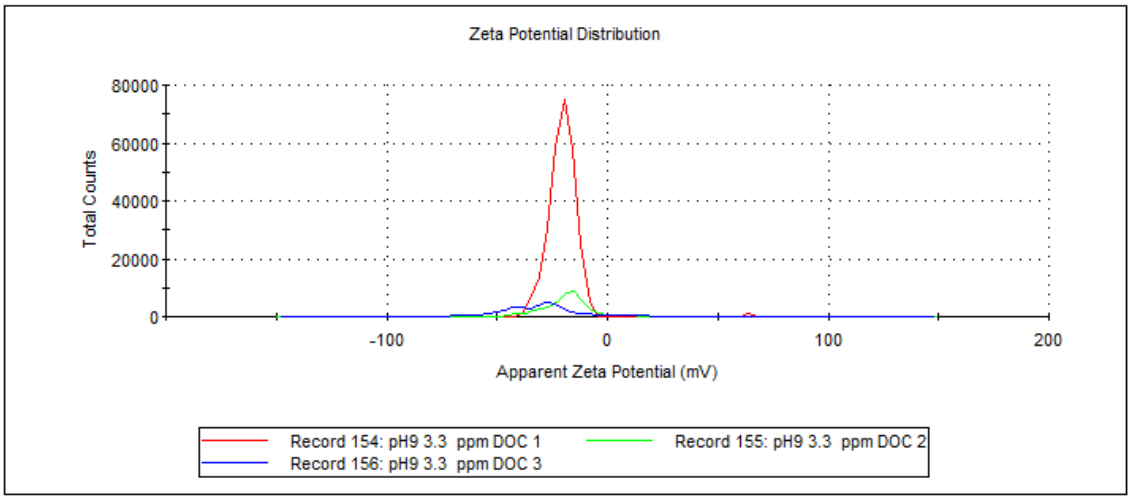

			Mean (mV)	Area (%)	St Dev (mV)
Zeta Potential (mV):	-26.1	Peak 1:	-26.6	98.9	10.4
Zeta Deviation (mV):	11.5	Peak 2:	21.6	1.1	2.50
Conductivity (mS/cm):	0.145	Peak 3:	0.00	0.0	0.00

Result quality : Good

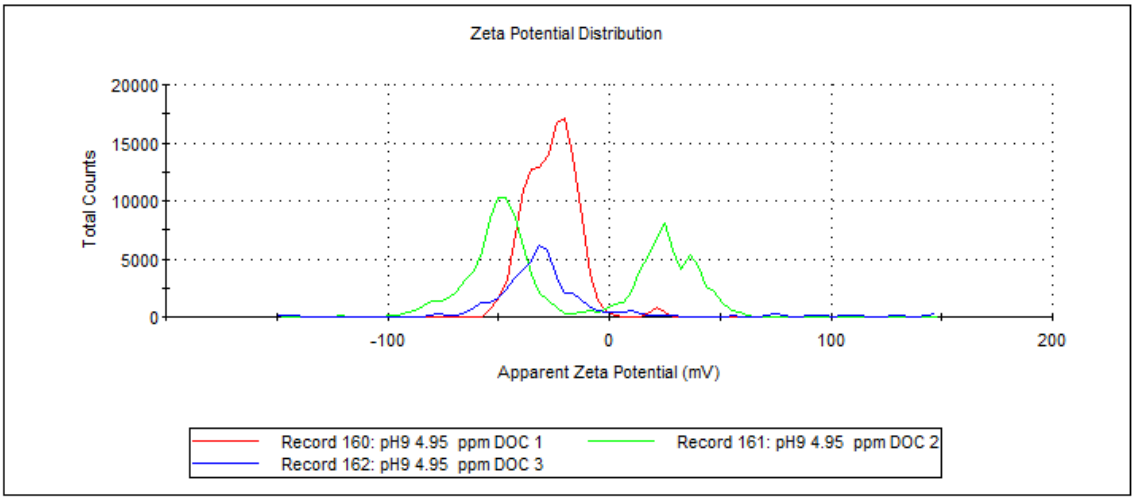

			Mean (mV)	Area (%)	St Dev (mV)
Zeta Potential (mV):	-13.3	Peak 1:	-1.08	62.6	9.63
Zeta Deviation (mV):	21.5	Peak 2:	-43.1	24.5	8.09
Conductivity (mS/cm):	0.148	Peak 3:	-26.3	12.2	4.03

Result quality : See result quality report

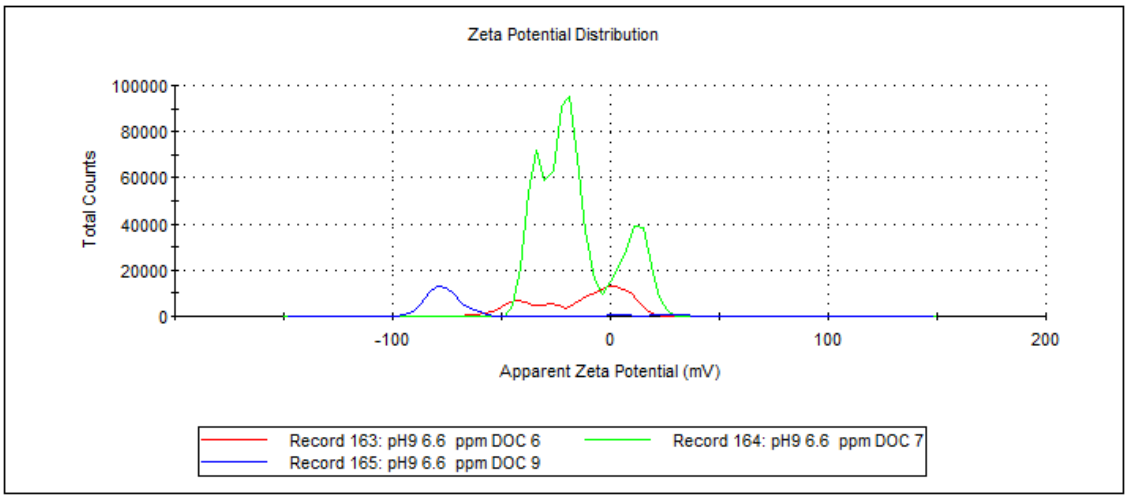

			Mean (mV)	Area (%)	St Dev (mV)
Zeta Potential (mV):	-41.0	Peak 1:	-51.2	49.7	7.04
Zeta Deviation (mV):	14.3	Peak 2:	-34.9	38.2	5.58
Conductivity (mS/cm):	0.0940	Peak 3:	-17.2	10.8	5.36

Result quality : See result quality report

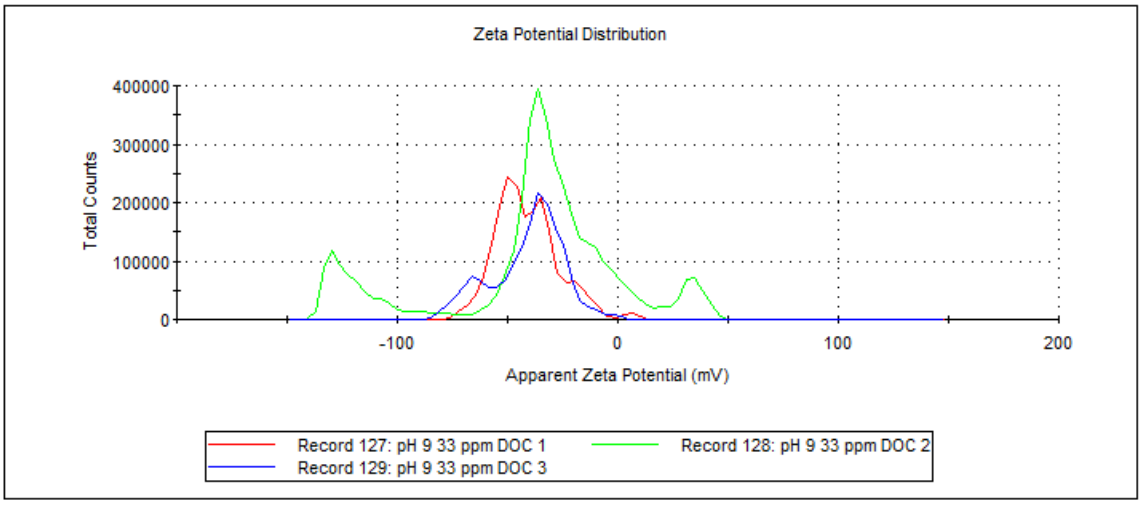

Appendix 11：SEM-EDX analyses

SEM-EDX analyses were performed using scanning electronic microscope equipped with a Bruker EDX system. The acceleration voltage used was 15 kV, and the beam current was adjusted at 50 nA. According to the manufacturer, spot size is assumed to be 10 to 1000 nm.

1. Energy-dispersive X-ray spectroscopy (EDX)

The scanning electron microscope (SEM) for chemical characterization is performed non-destructively with energy dispersive X-ray analysis (EDX). The electron beam stimulate the atoms in the sample with uniform energy and they instantaneously send out X-rays of specific energies for each element. This radiation gives information about the elemental composition of the sample. Chemical elements starting with the atomic number 6 (carbon) can be determined with this analysis method (Retrieved from http://www.sensore-electronic.com/en/SEMEDX_ChemicalElementalAnalysis.html).

Because the size of X-ray is larger than the particle size of $nTiO_2$ or Fe oxyhydroxide, Si was always detected in the spectral image while we were looking for $nTiO_2$ only or Fe oxyhydroxide only.

2. EDX Mapping (Element distribution images)

In addition to the conventional SEM image, EDX mapping provides a meaningful picture of the element distribution of a surface. The acquisition times for a satisfactory resolution and noise performance can take from 30 minutes to 12 hours, because a complete EDX spectrum is made from each image point (Retrieved from http://www.sensore-electronic.com/en/SEMEDX_ChemicalElementalAnalysis.html).

SEM image of quartz sand without $nTiO_2$

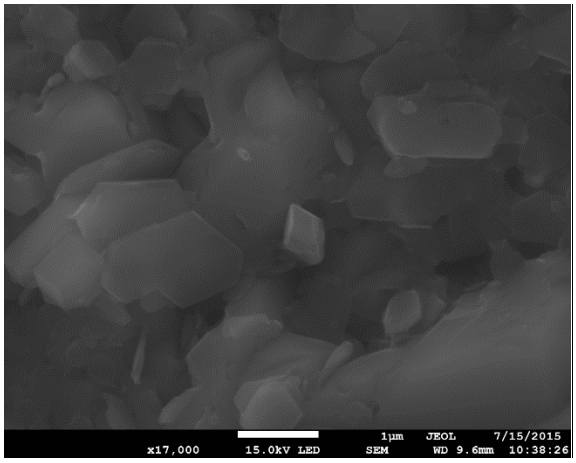

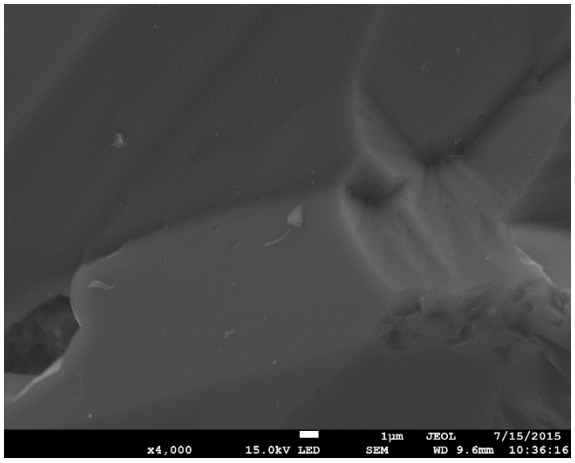

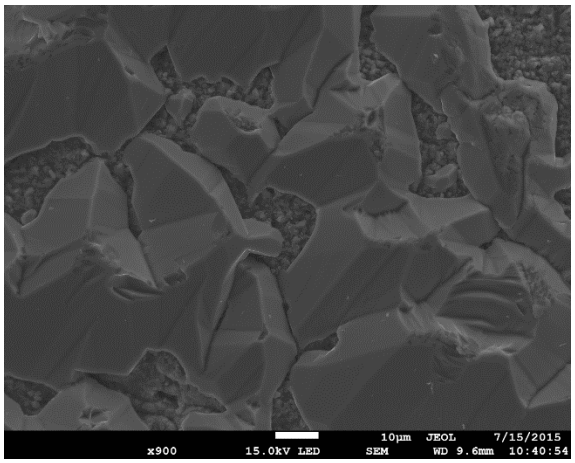

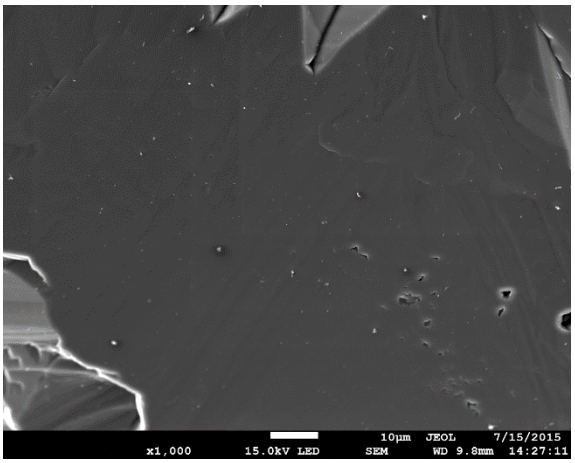

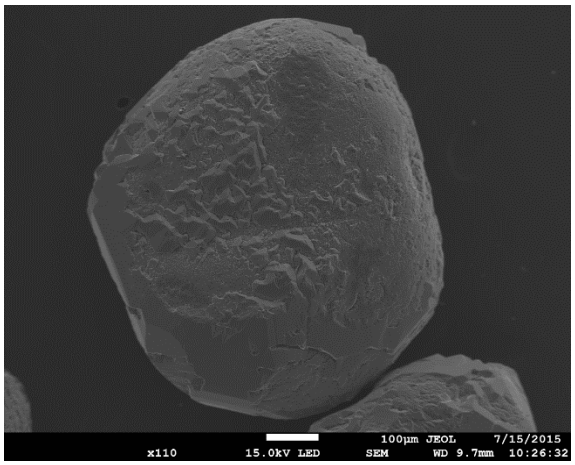

SEM image of Fe coated sand without $nTiO_2$

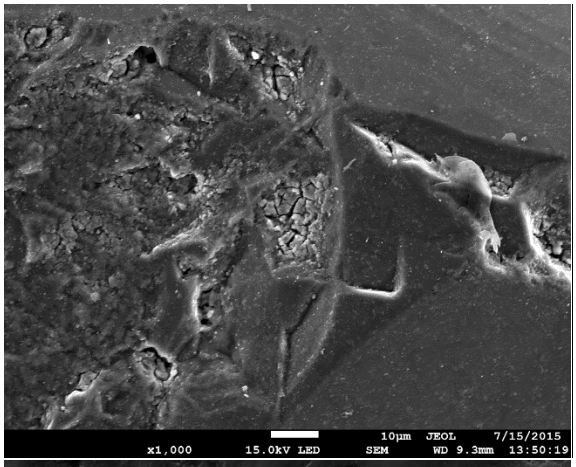

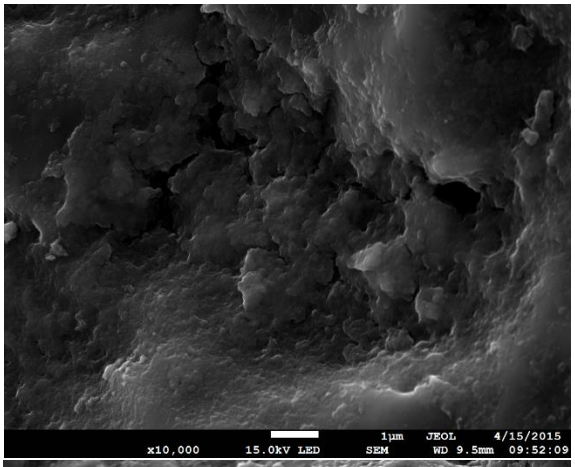

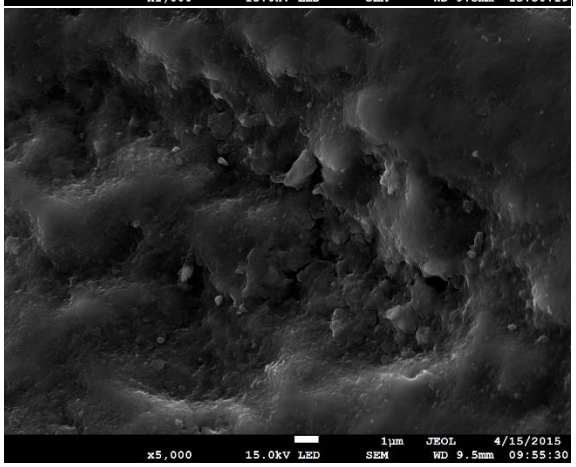

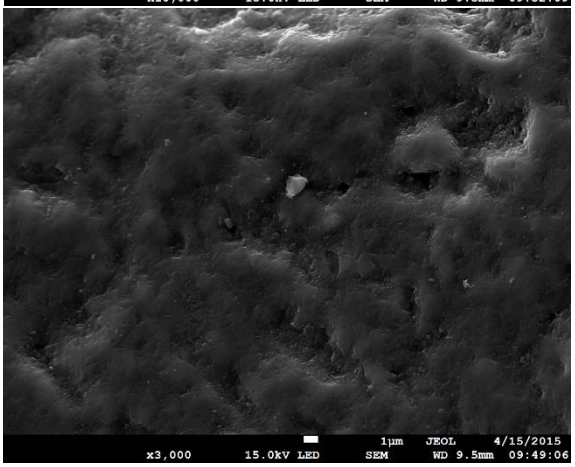

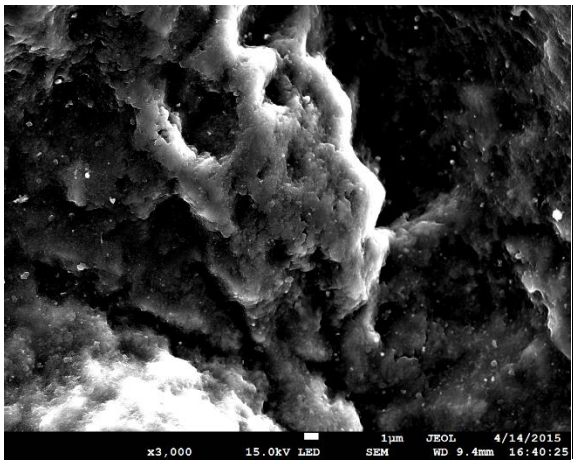

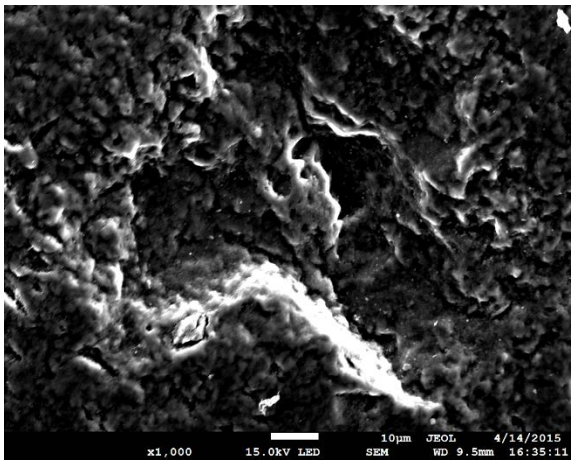

SEM image of quartz sand with 50 mg/L $nTiO_2$ at pH 5

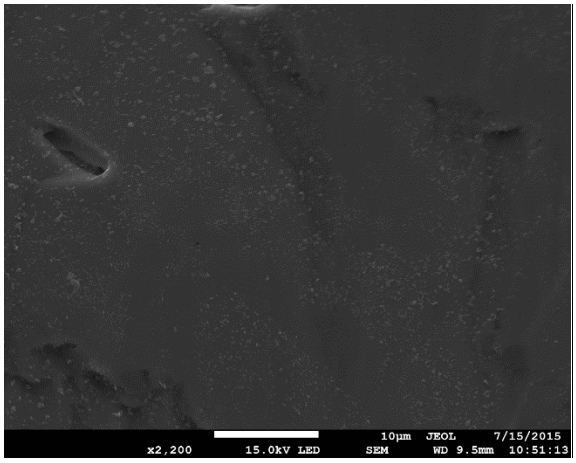

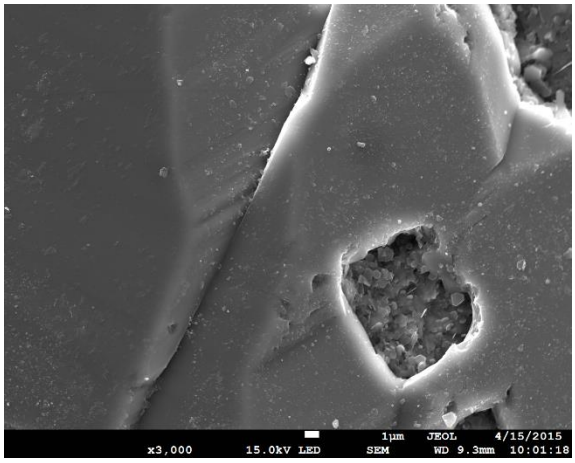

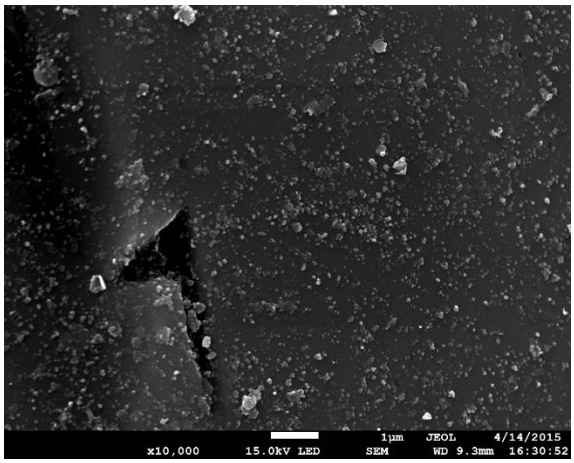

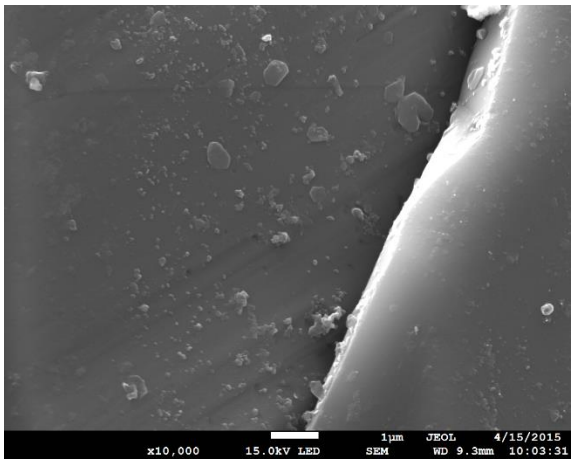

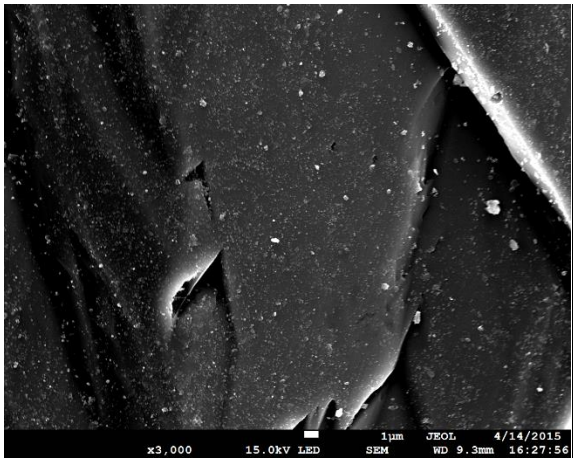

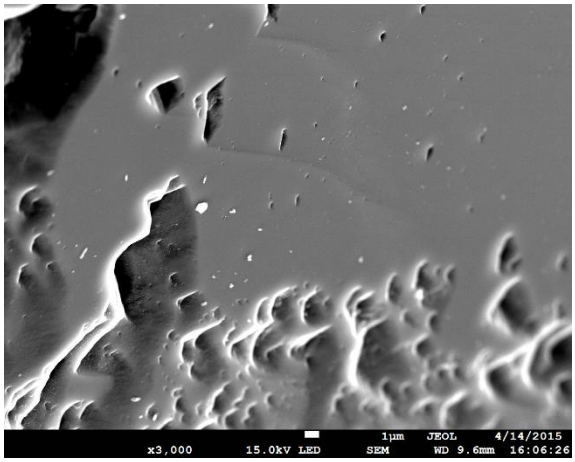

SEM image of Fe coated sand with 50 mg/L $nTiO_2$ at pH 5

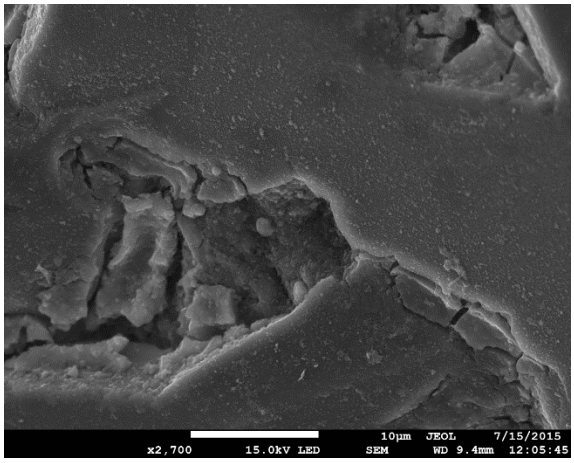

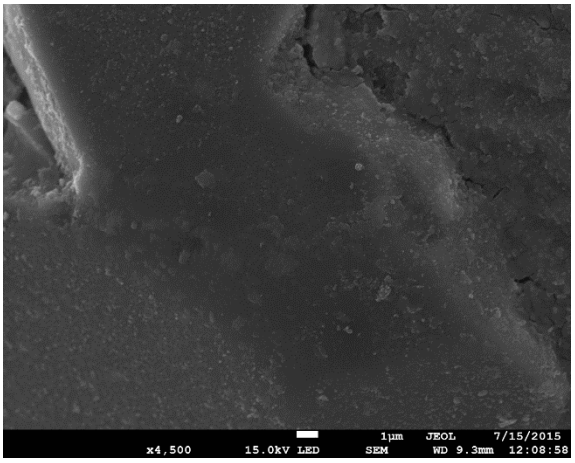

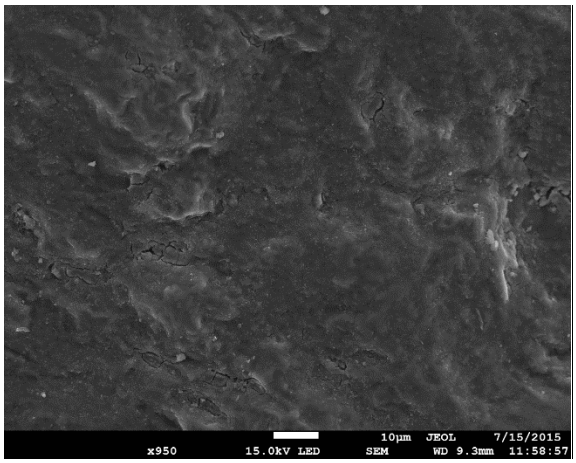

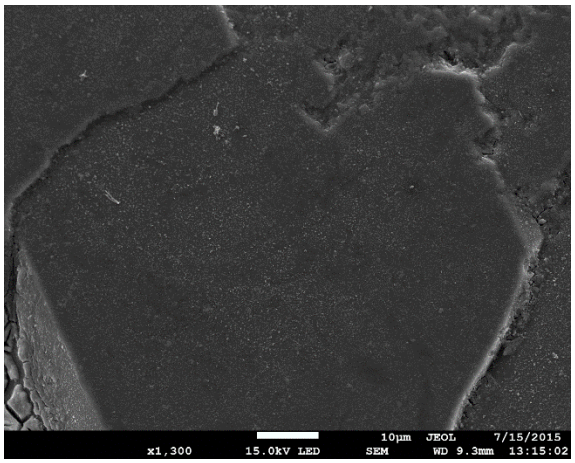

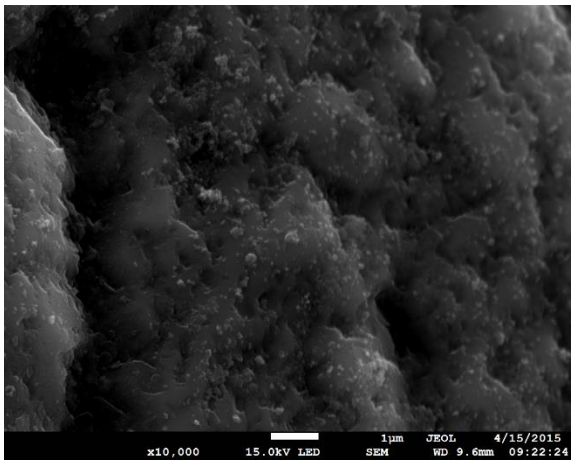

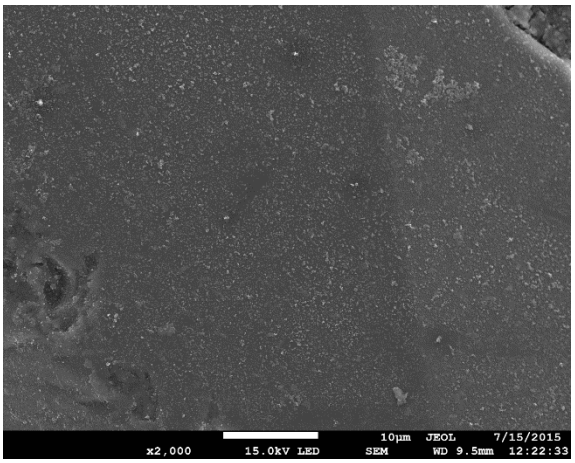

SEM image of quartz sand with 50 mg/L $nTiO_2$ at pH 9

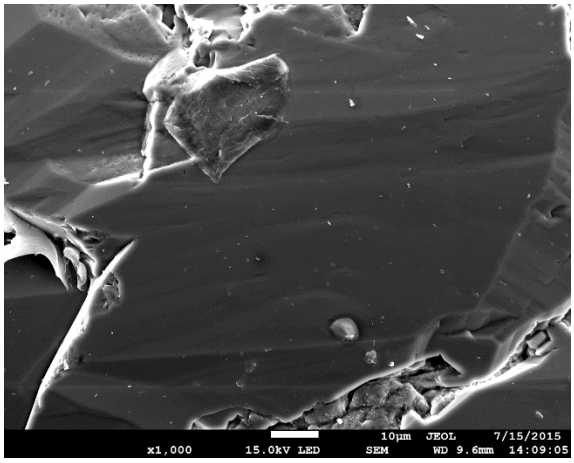

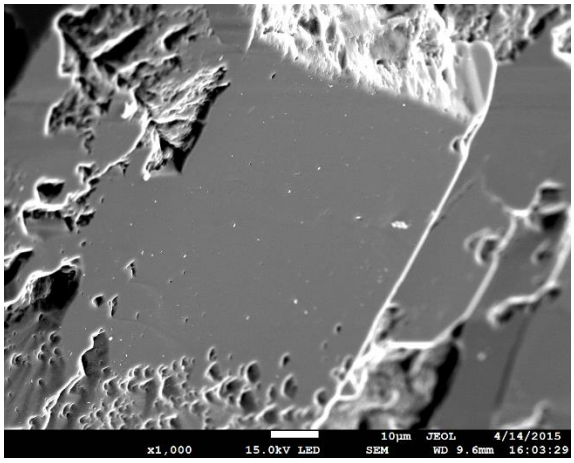

SEM image of Fe coated sand with 50 mg/L $nTiO_2$ at pH 9

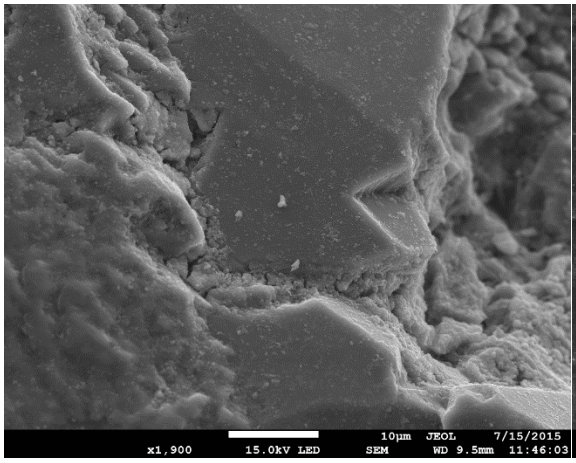

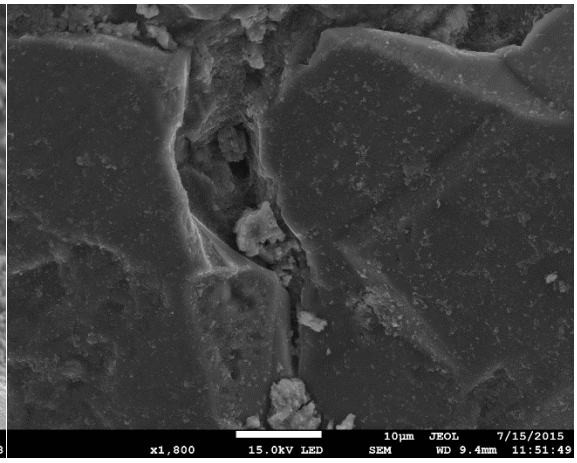

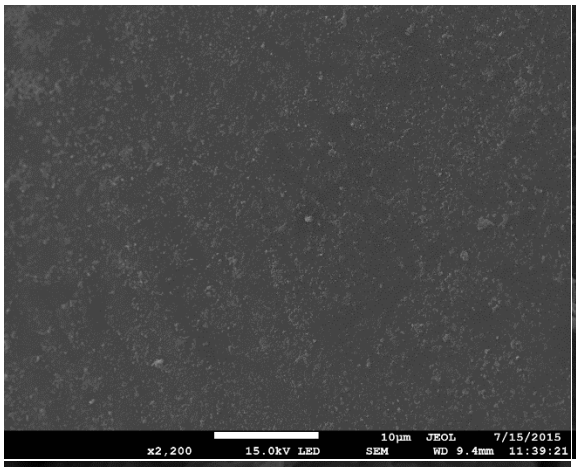

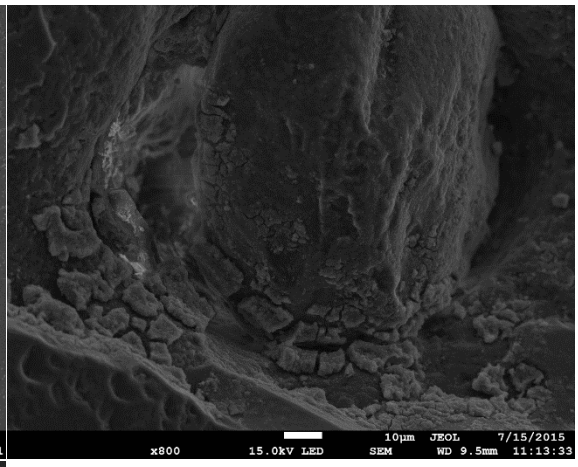

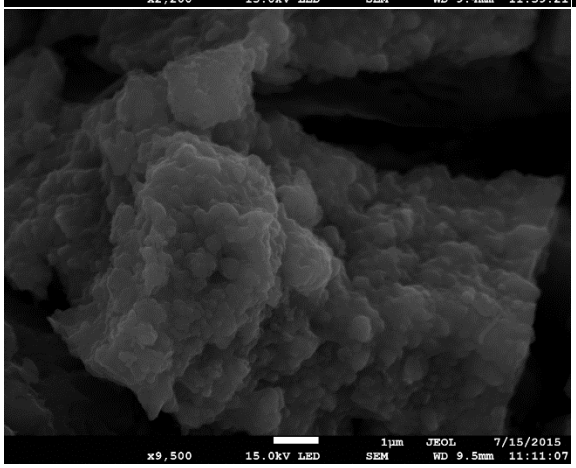

EDX of quartz sand

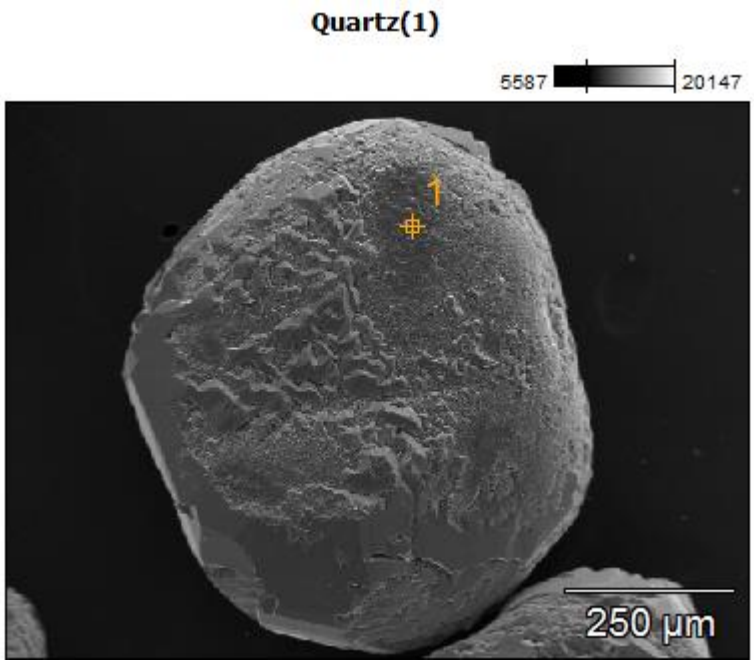

Image Name:	Quartz(1)
Image Resolution:	512 by 384
Image Pixel Size:	2.15 µm
Acc. Voltage:	15.0 kV
Magnification:	110

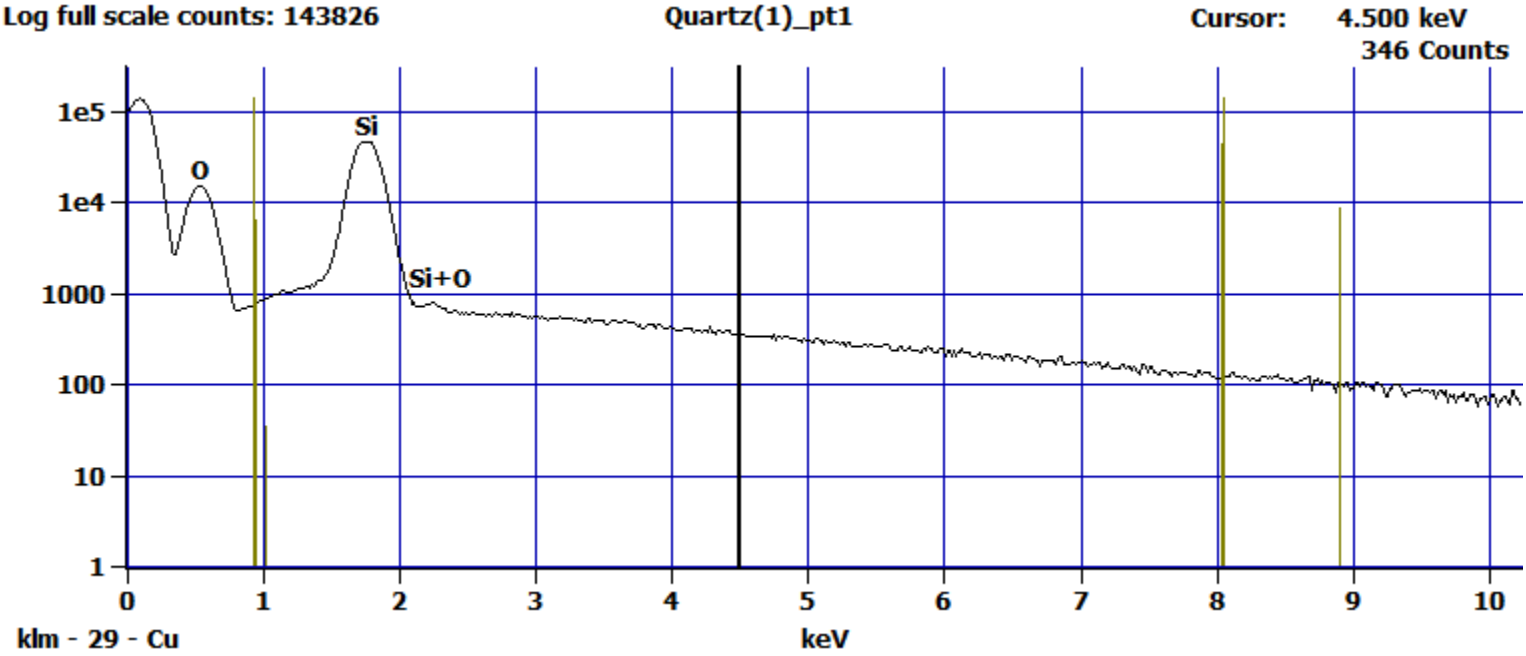

Project: Yang

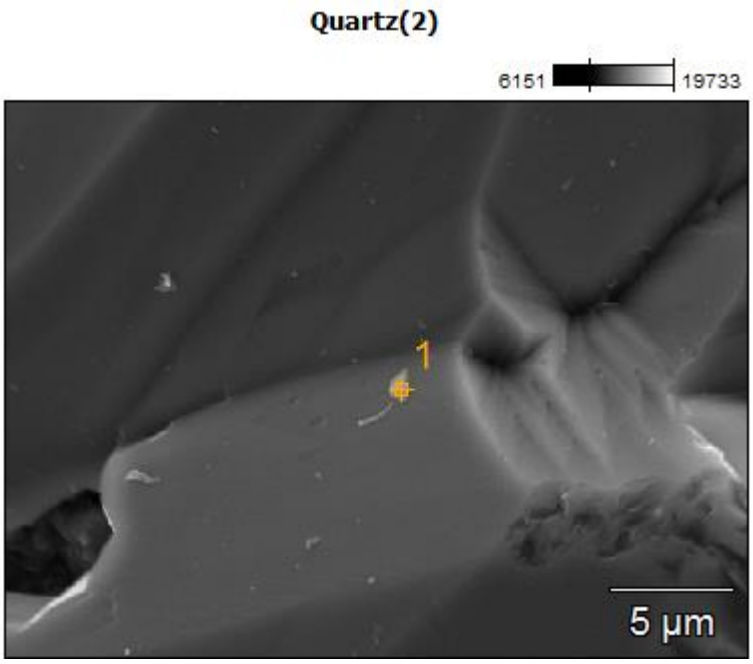

Image Name:	Quartz(2)
Image Resolution:	512 by 384
Image Pixel Size:	0.06 µm
Acc. Voltage:	15.0 kV
Magnification:	4000

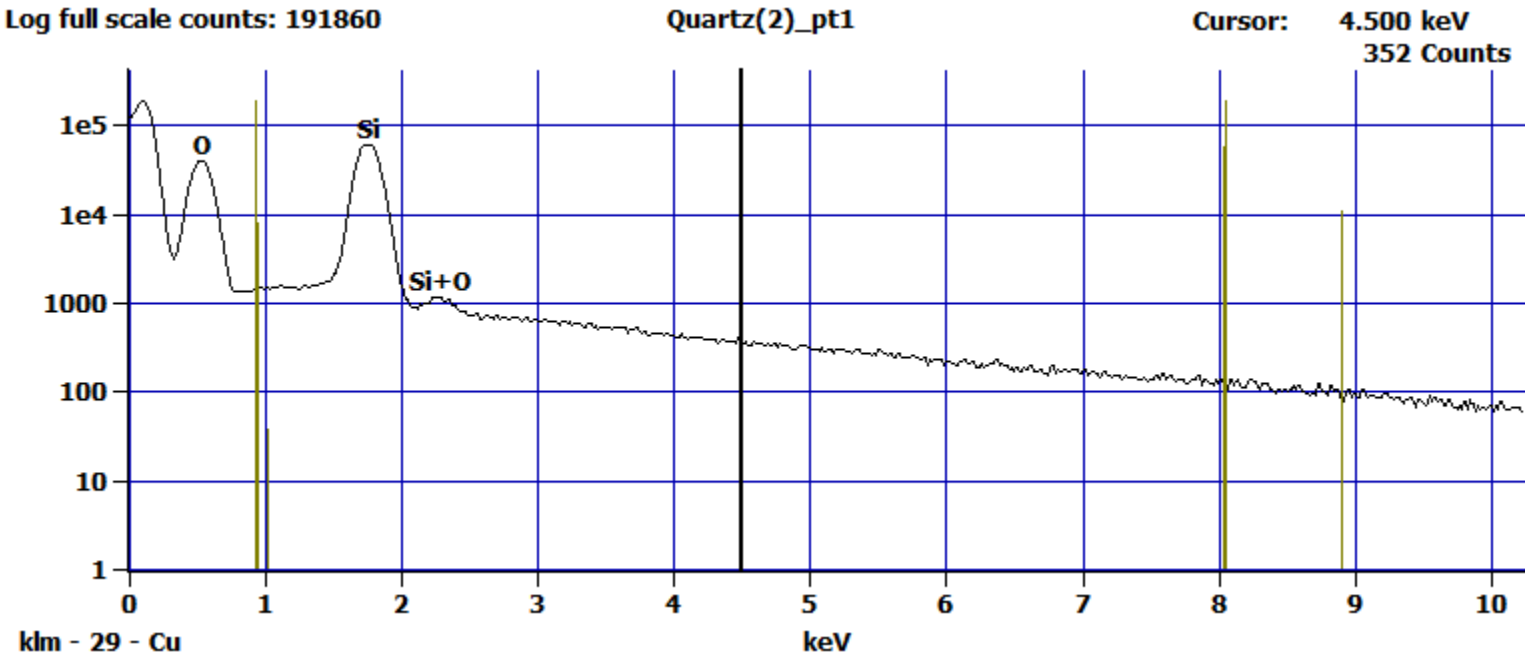

Project: Yang

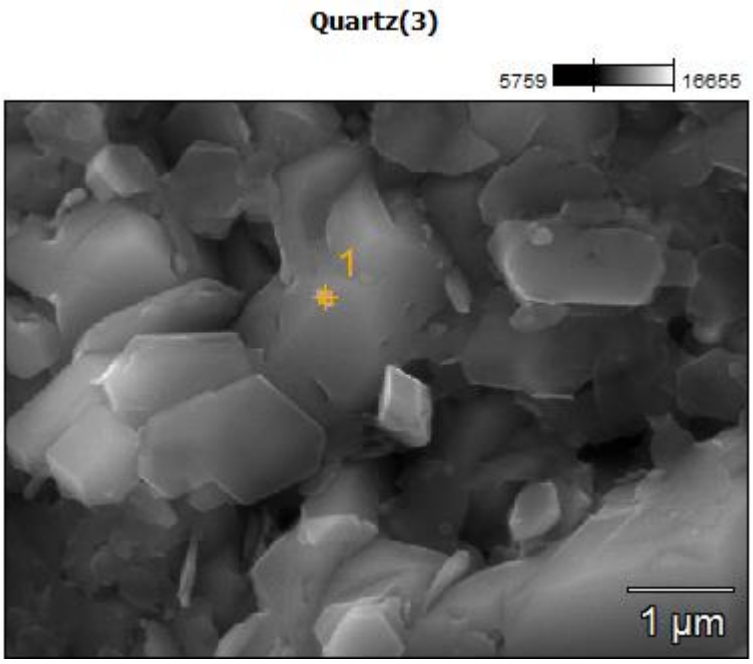

Image Name:	Quartz(3)
Image Resolution:	512 by 384
Image Pixel Size:	0.01 µm
Acc. Voltage:	15.0 kV
Magnification:	17000

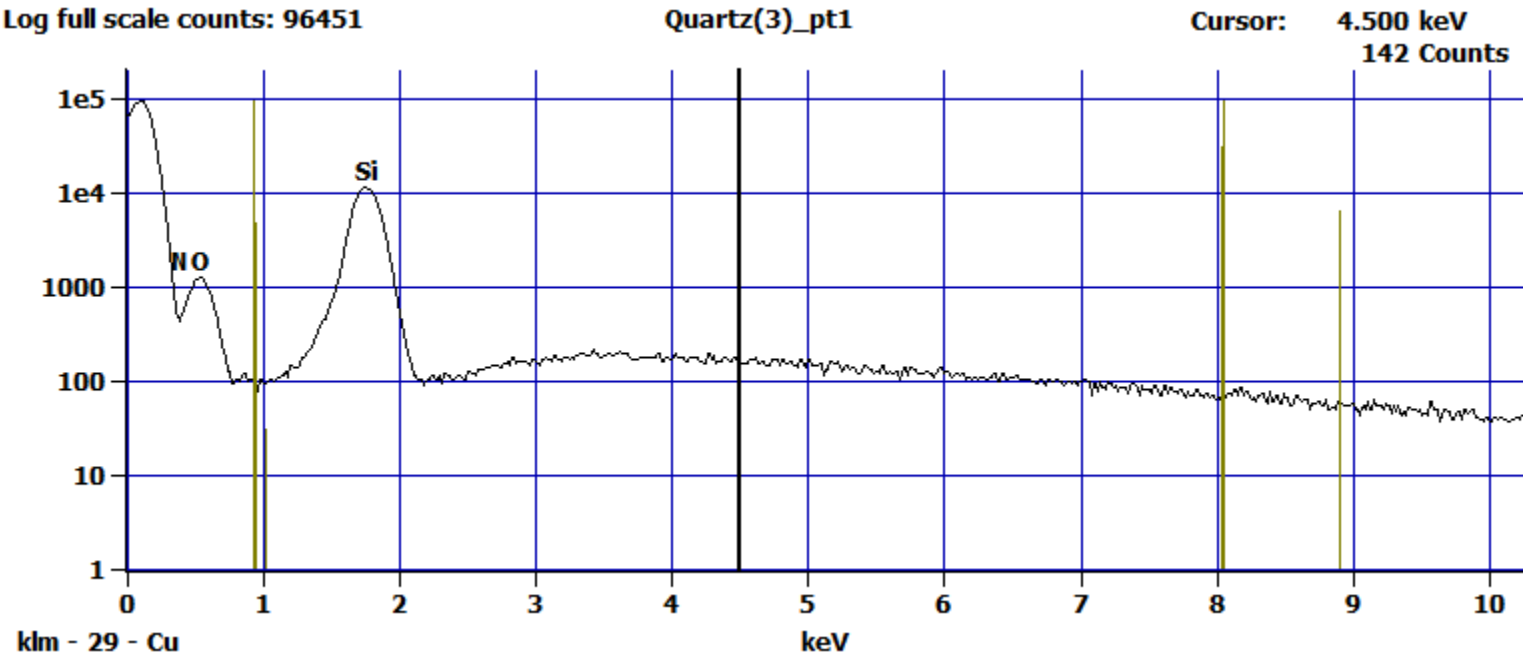

Project: Yang

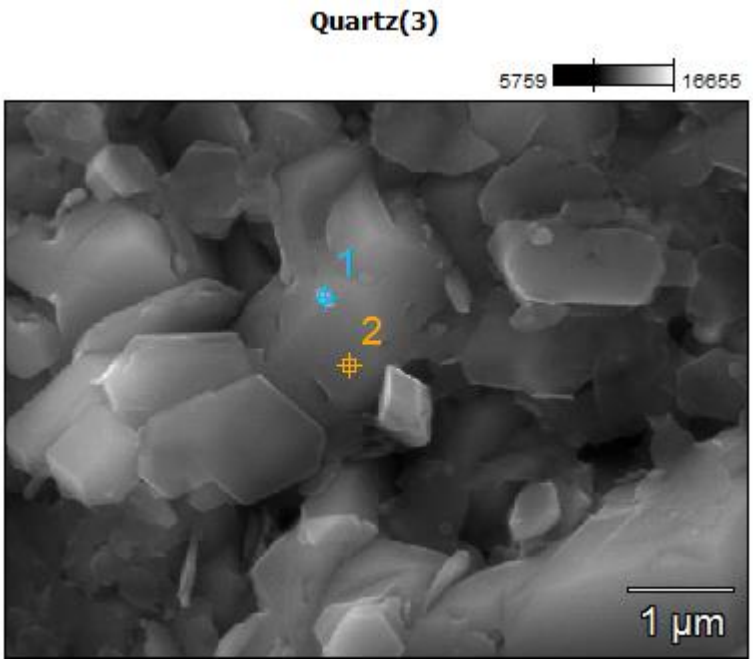

Image Name:	Quartz(3)
Image Resolution:	512 by 384
Image Pixel Size:	0.01 µm
Acc. Voltage:	15.0 kV
Magnification:	17000

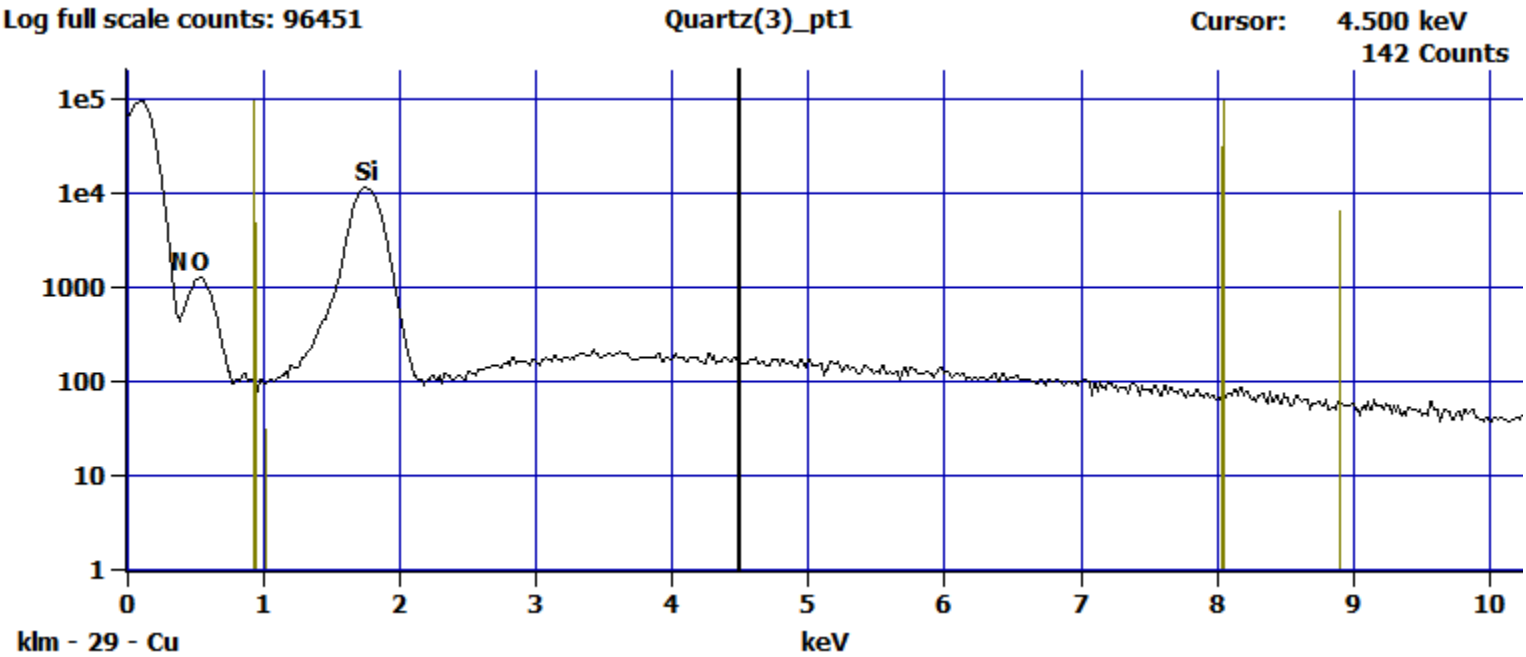

Project: Yang

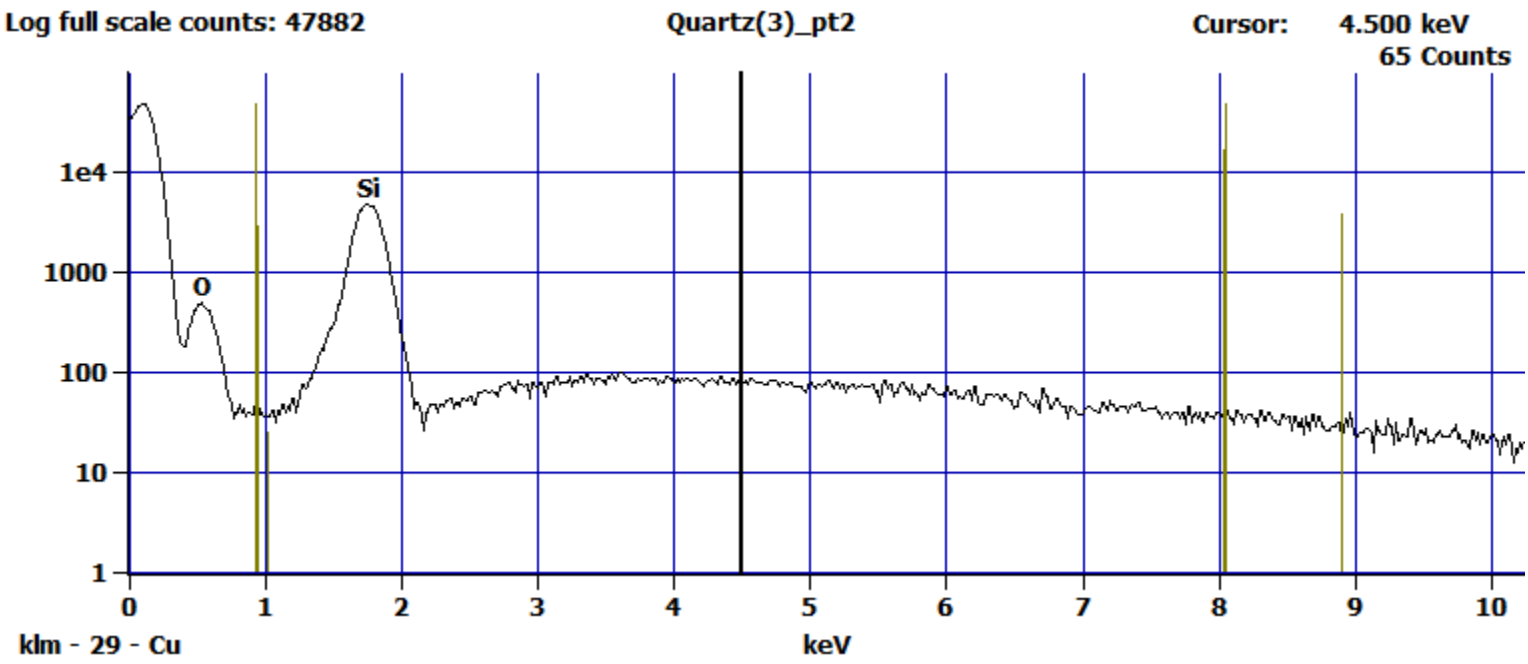

Project: Yang

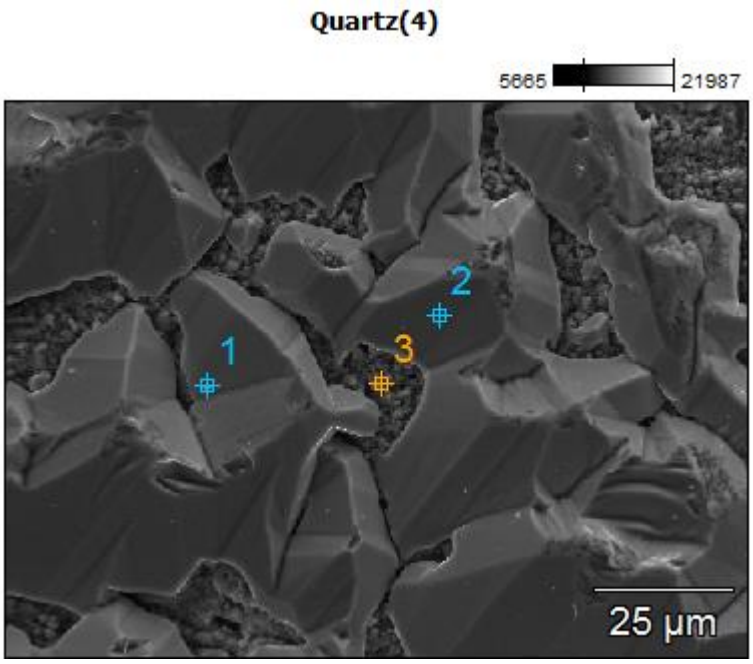

Image Name:	Quartz(4)
Image Resolution:	512 by 384
Image Pixel Size:	0.26 µm
Acc. Voltage:	15.0 kV
Magnification:	899

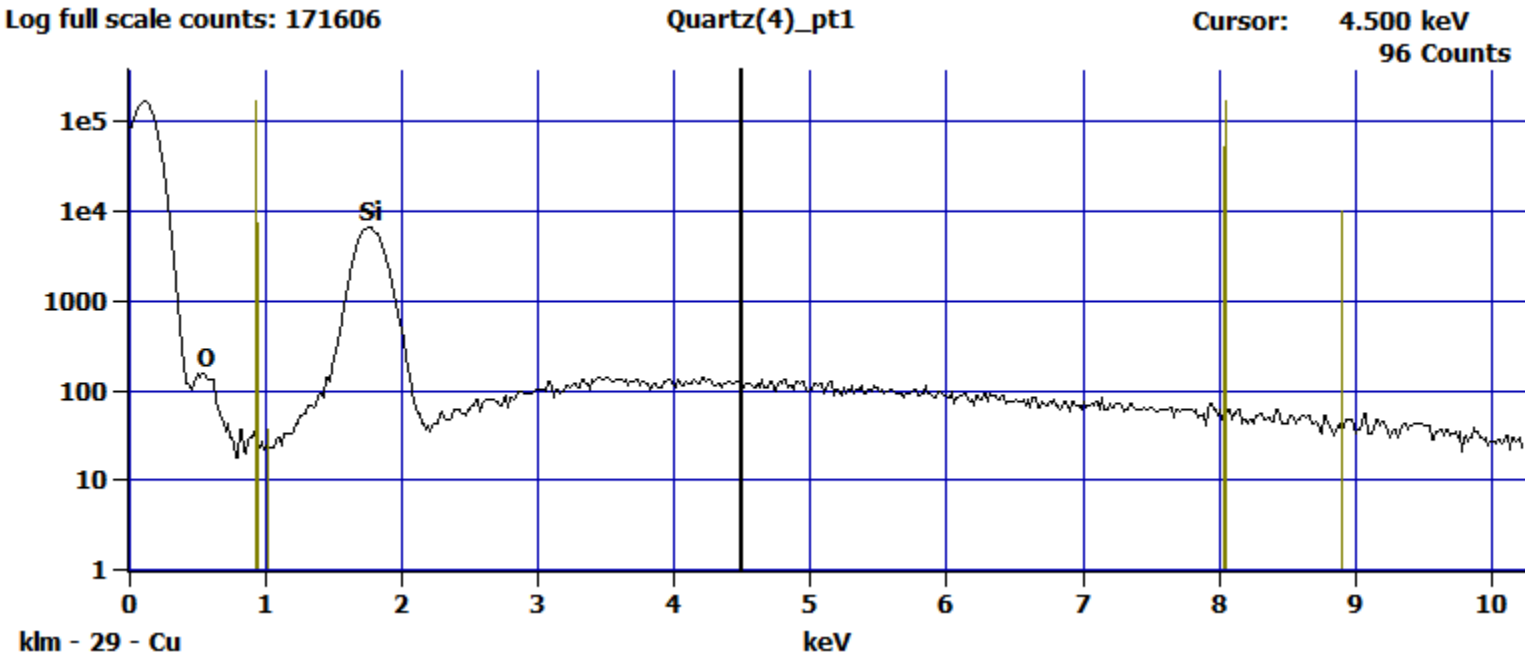

Project: Yang

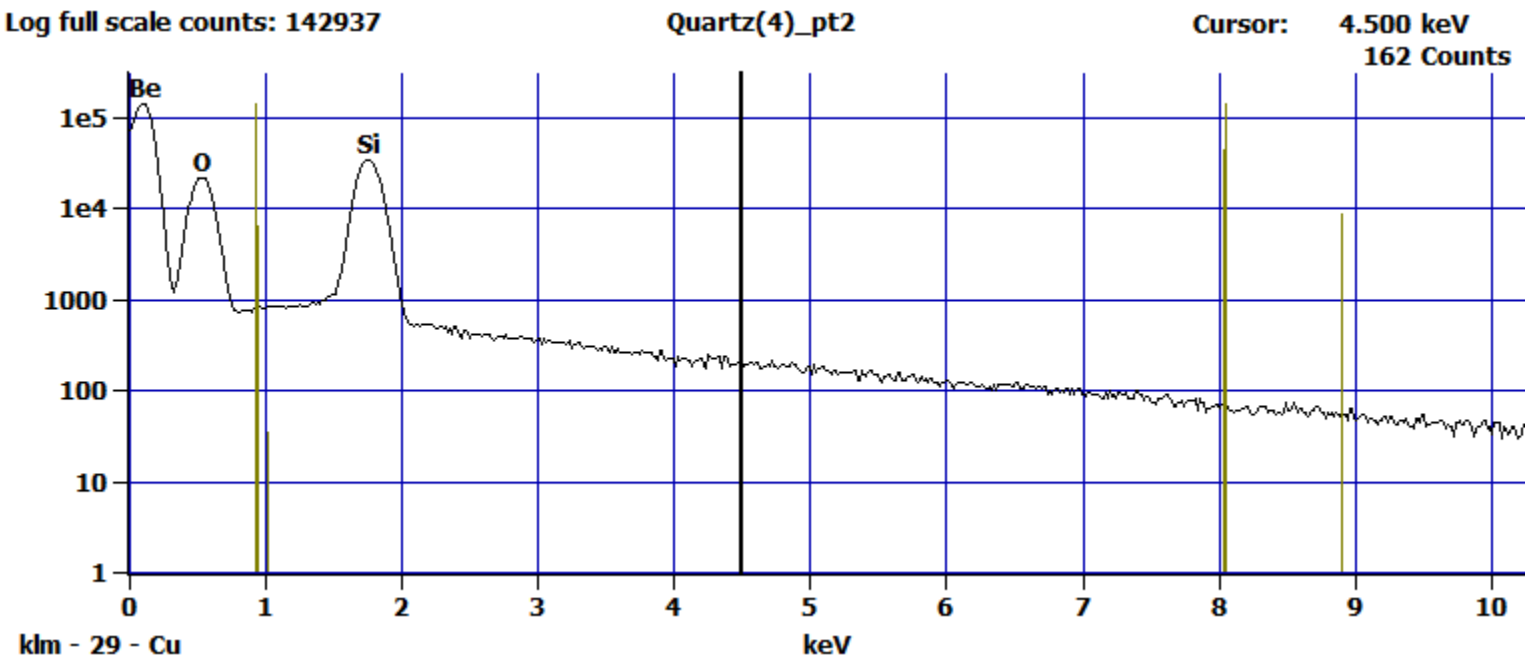

Project: Yang

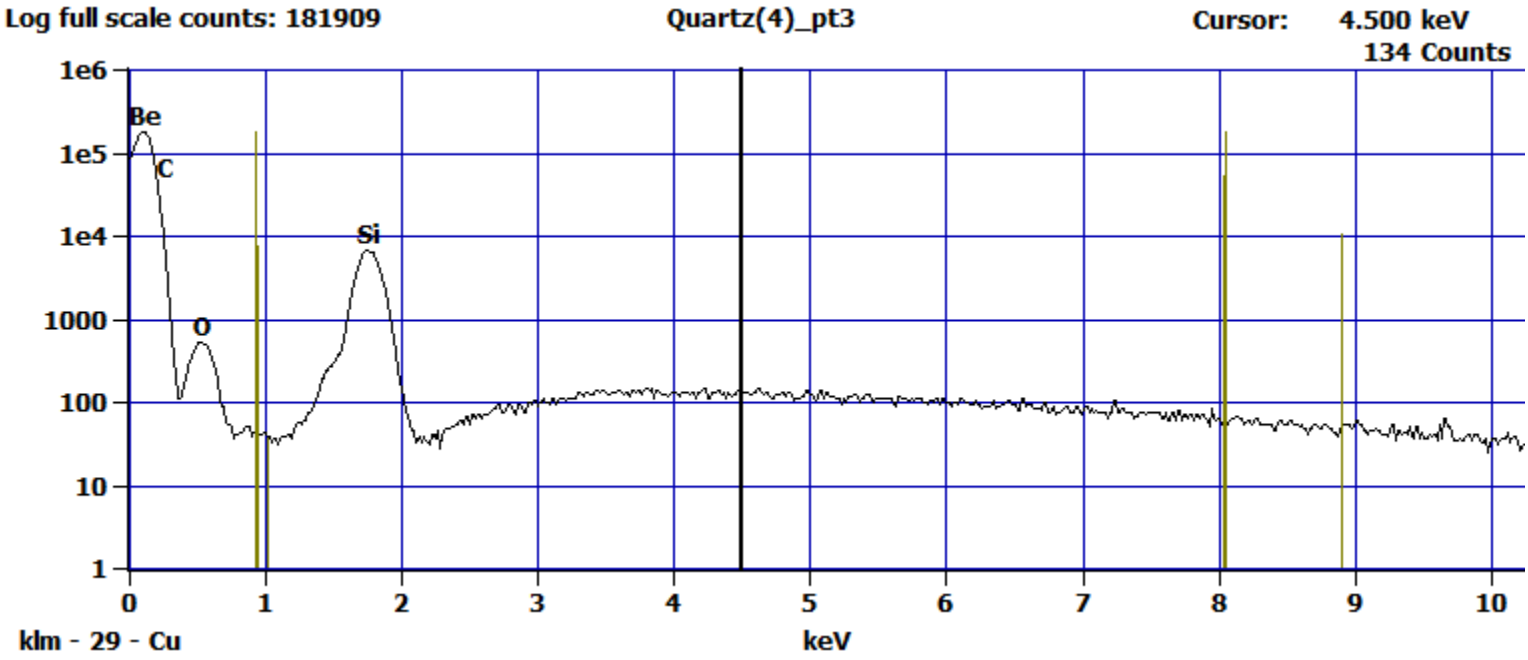

Project: Yang

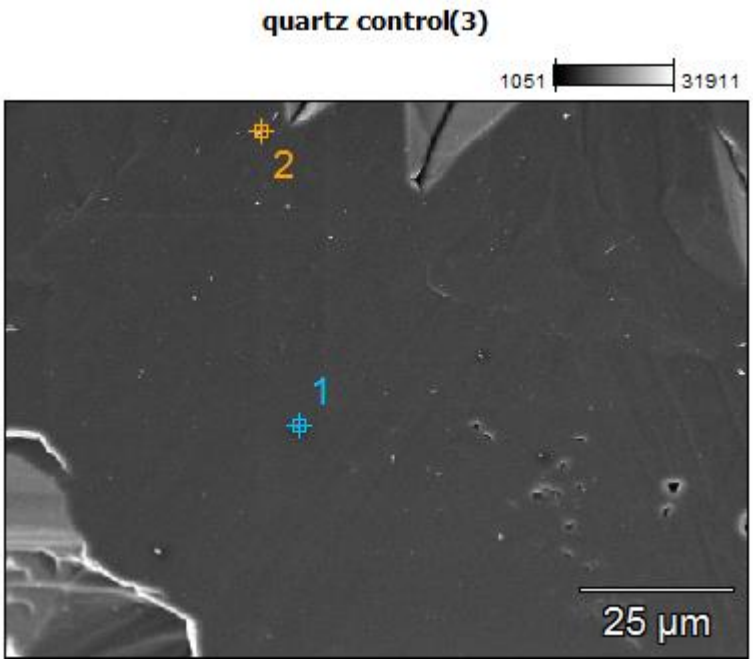

Image Name:	quartz control(3)
Image Resolution:	512 by 384
Image Pixel Size:	0.24 µm
Acc. Voltage:	15.0 kV
Magnification:	1000

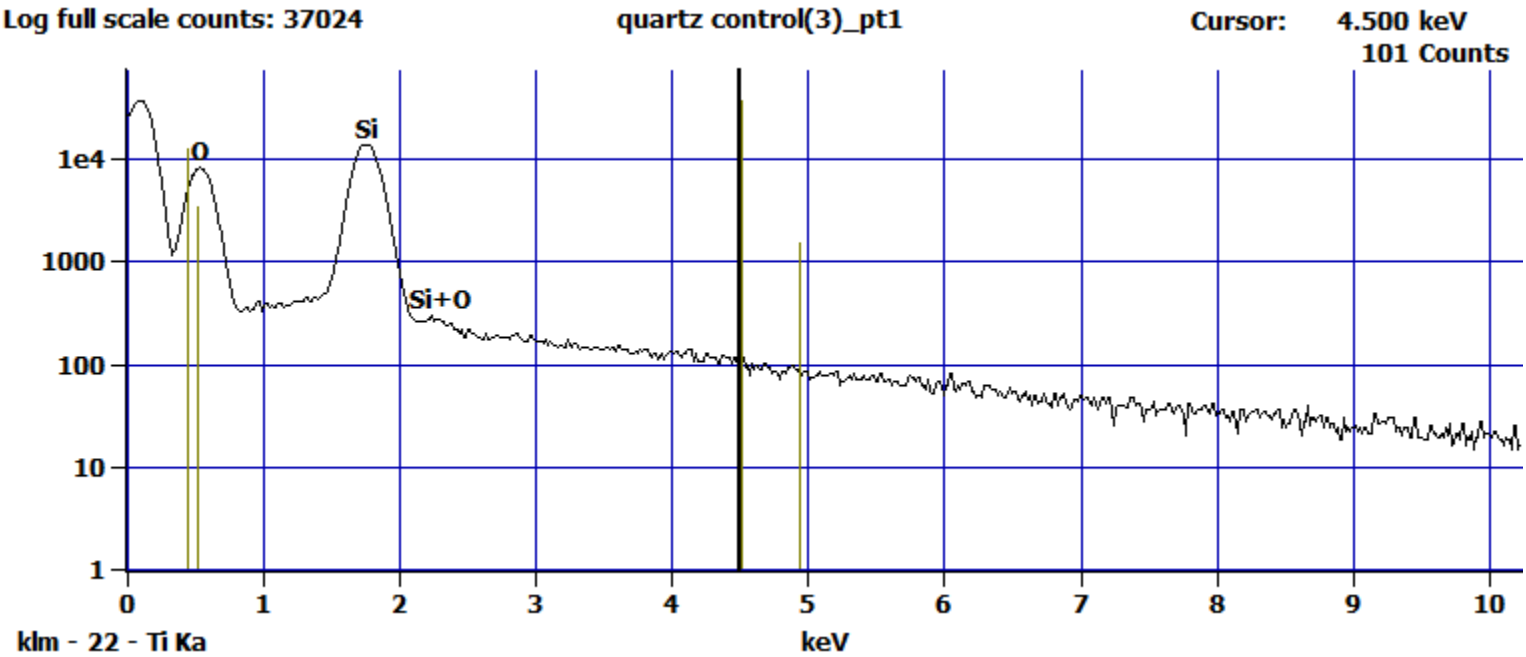

Project: Yang

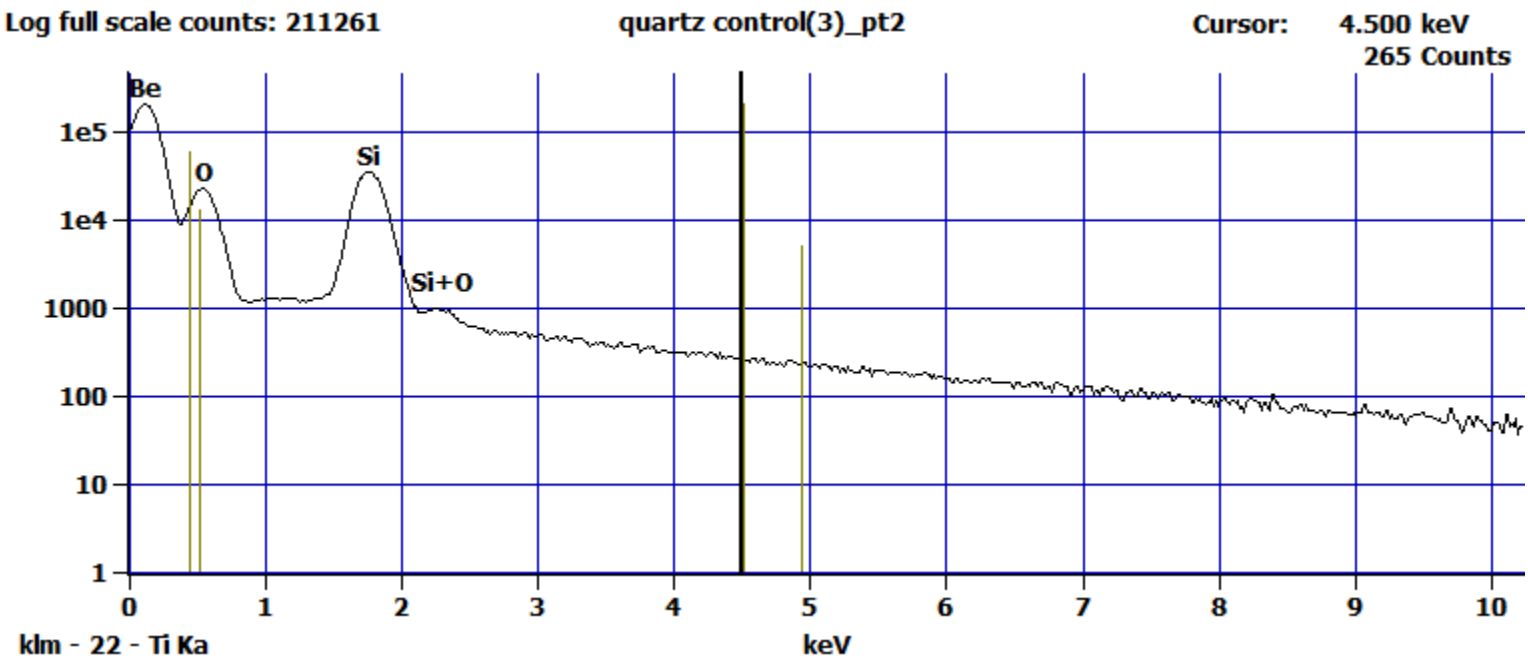

Project: Yang

EDX of Fe coated sand

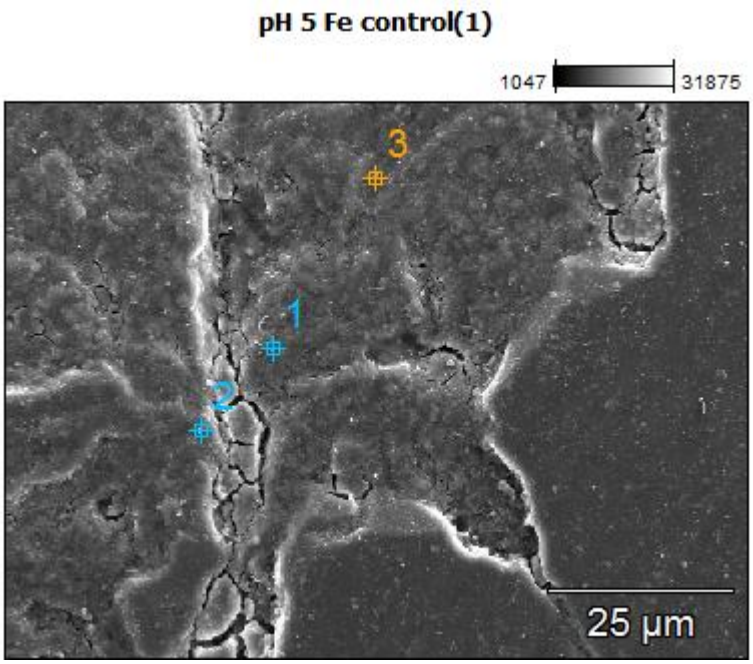

Image Name:	pH 5 Fe control(1)
Image Resolution:	512 by 384
Image Pixel Size:	0.20 µm
Acc. Voltage:	15.0 kV
Magnification:	1200

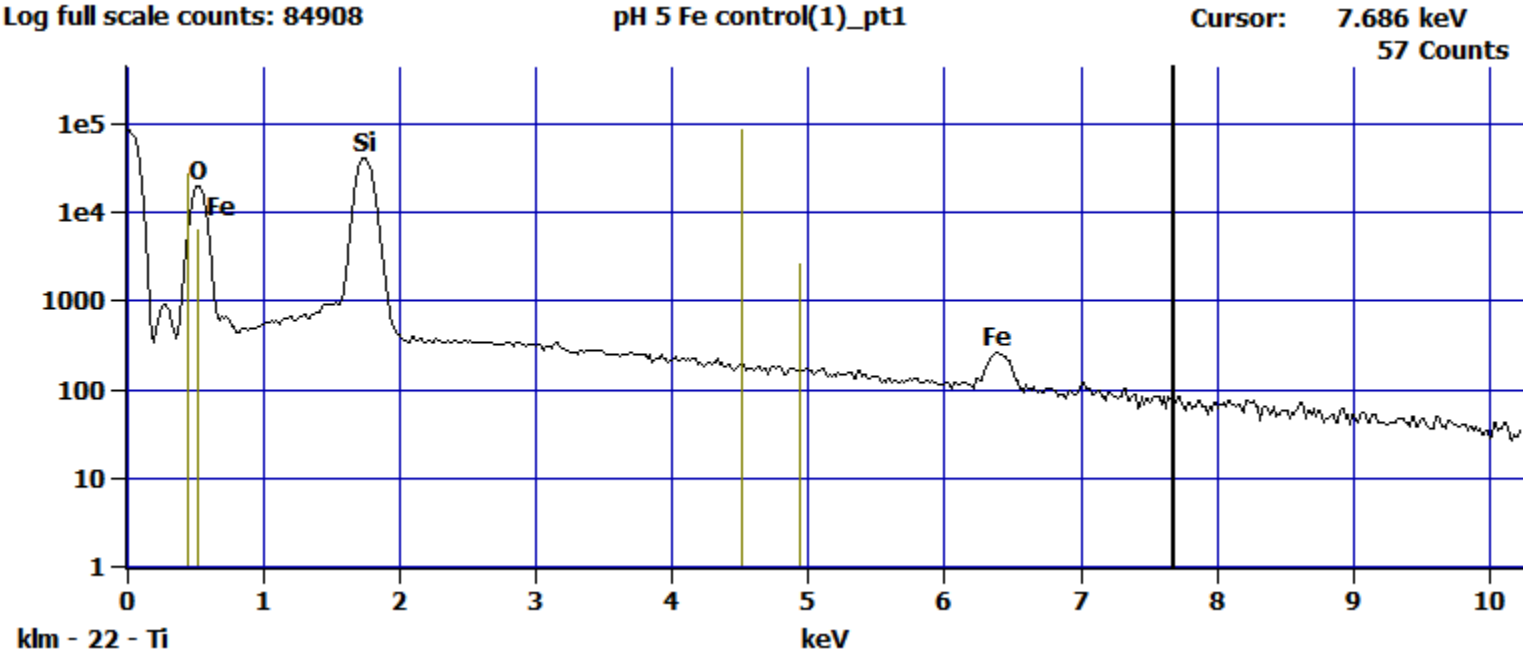

Project: Yang

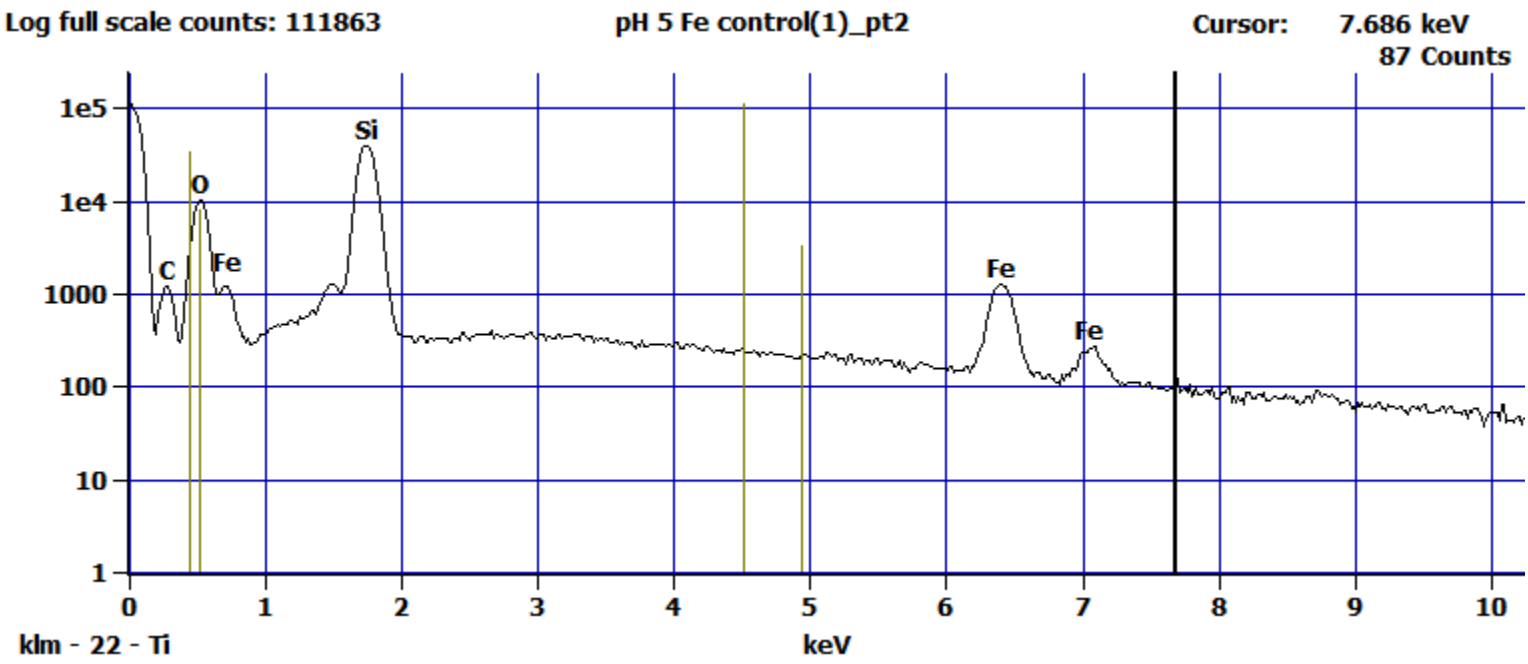

Project: Yang

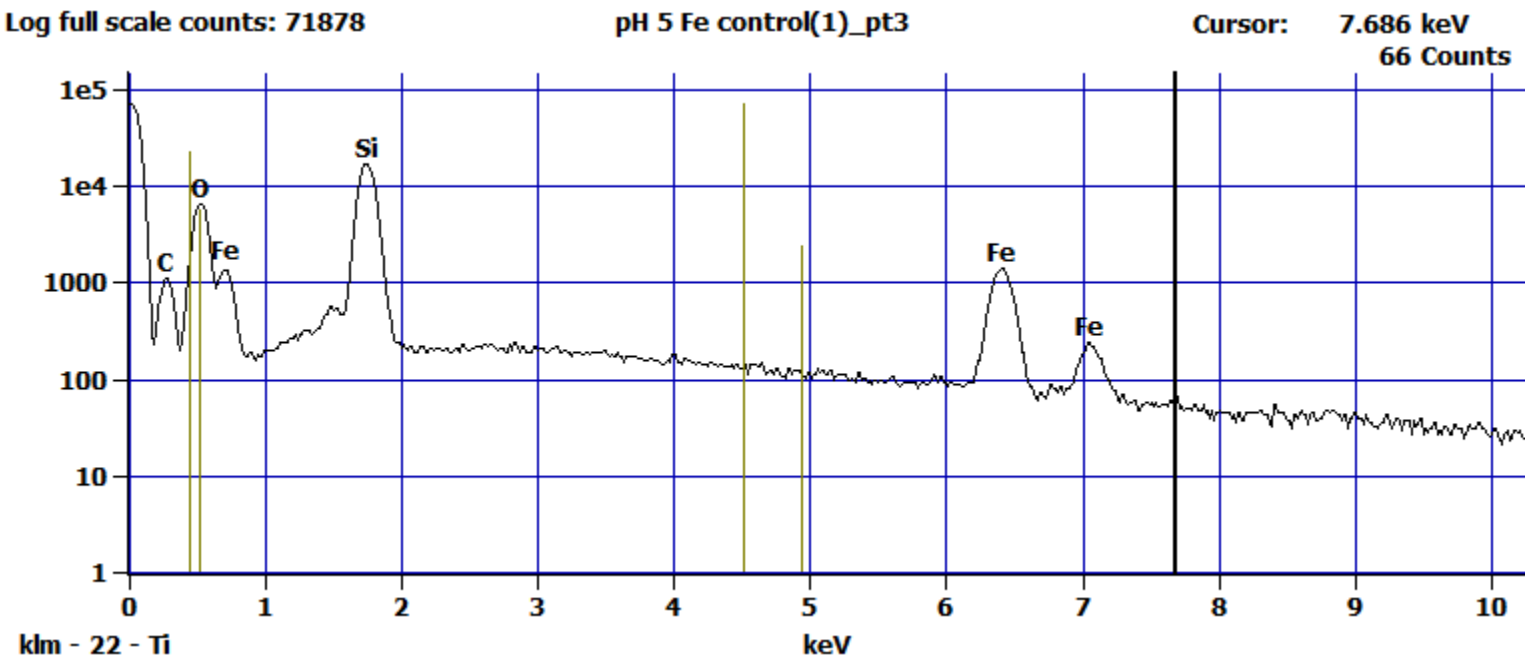

Project: Yang

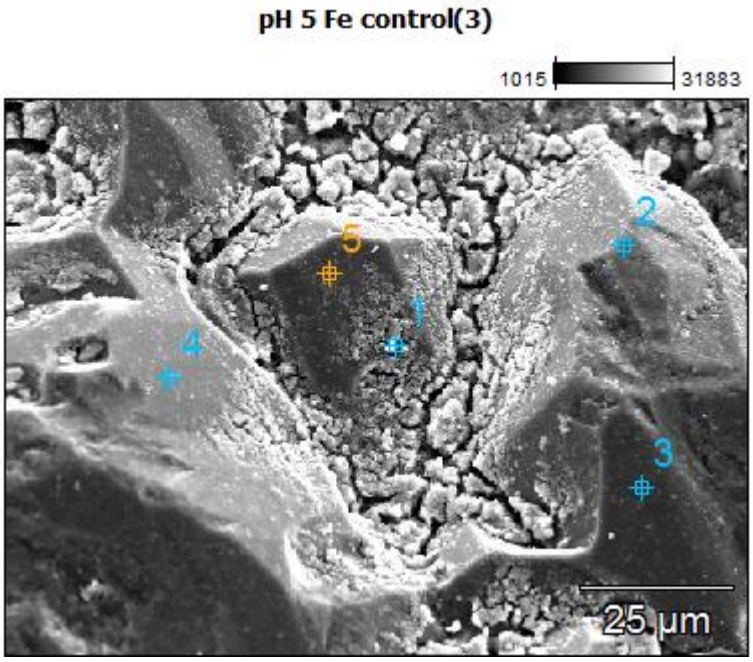

Image Name:	pH 5 Fe control(3)
Image Resolution:	512 by 384
Image Pixel Size:	0.24 µm
Acc. Voltage:	15.0 kV
Magnification:	1000

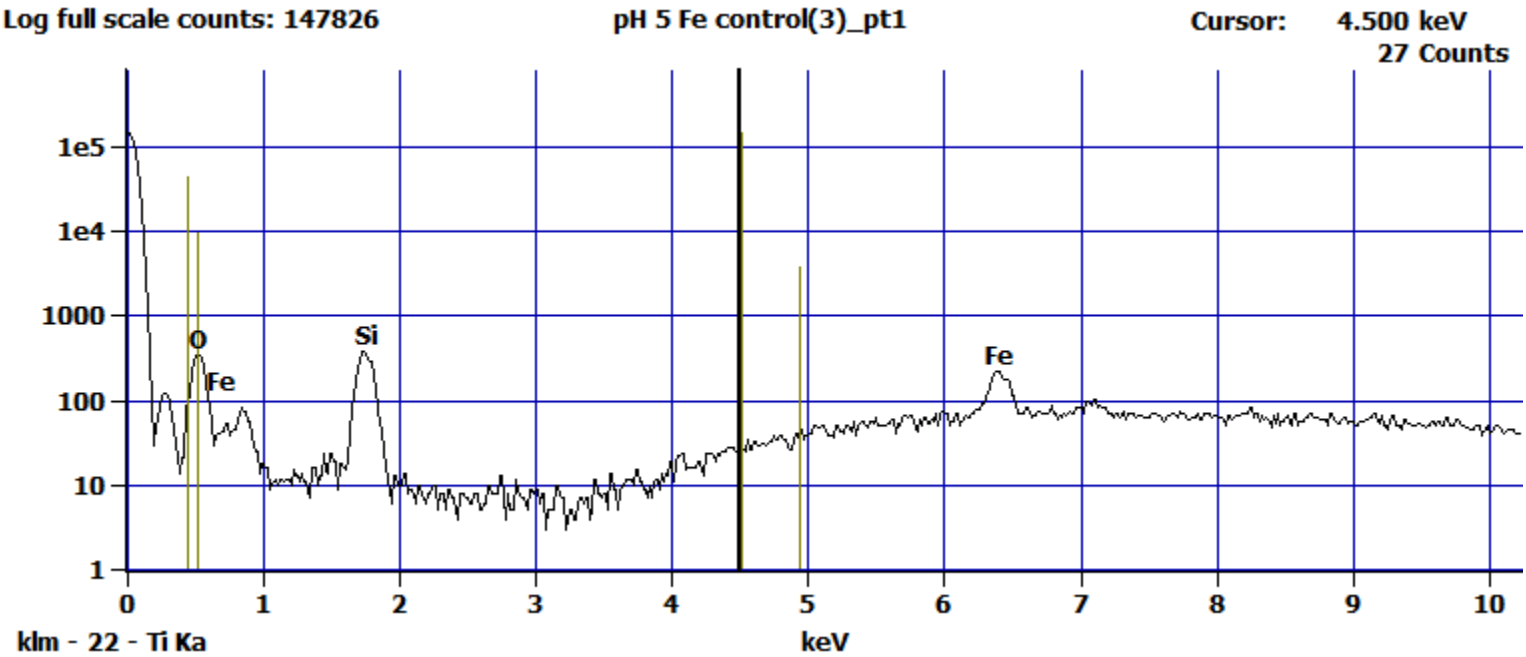

Project: Yang

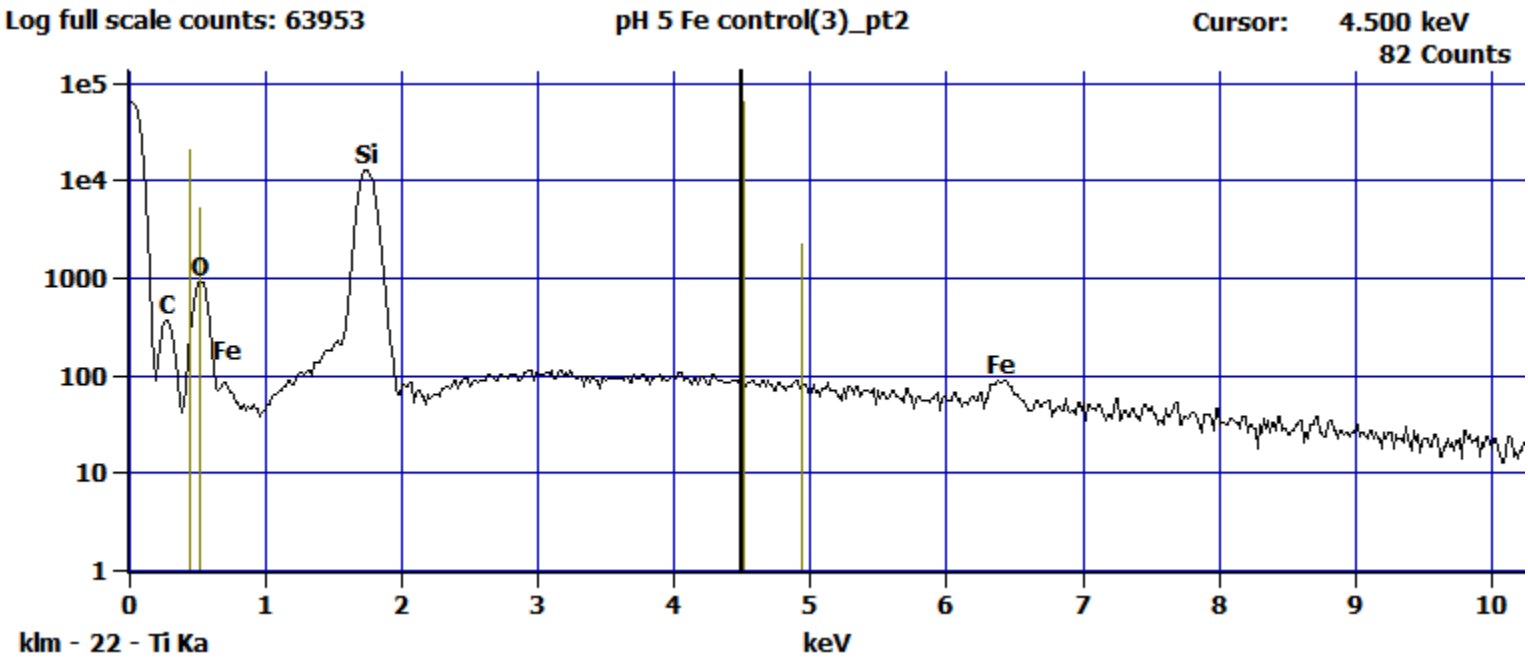

Project: Yang

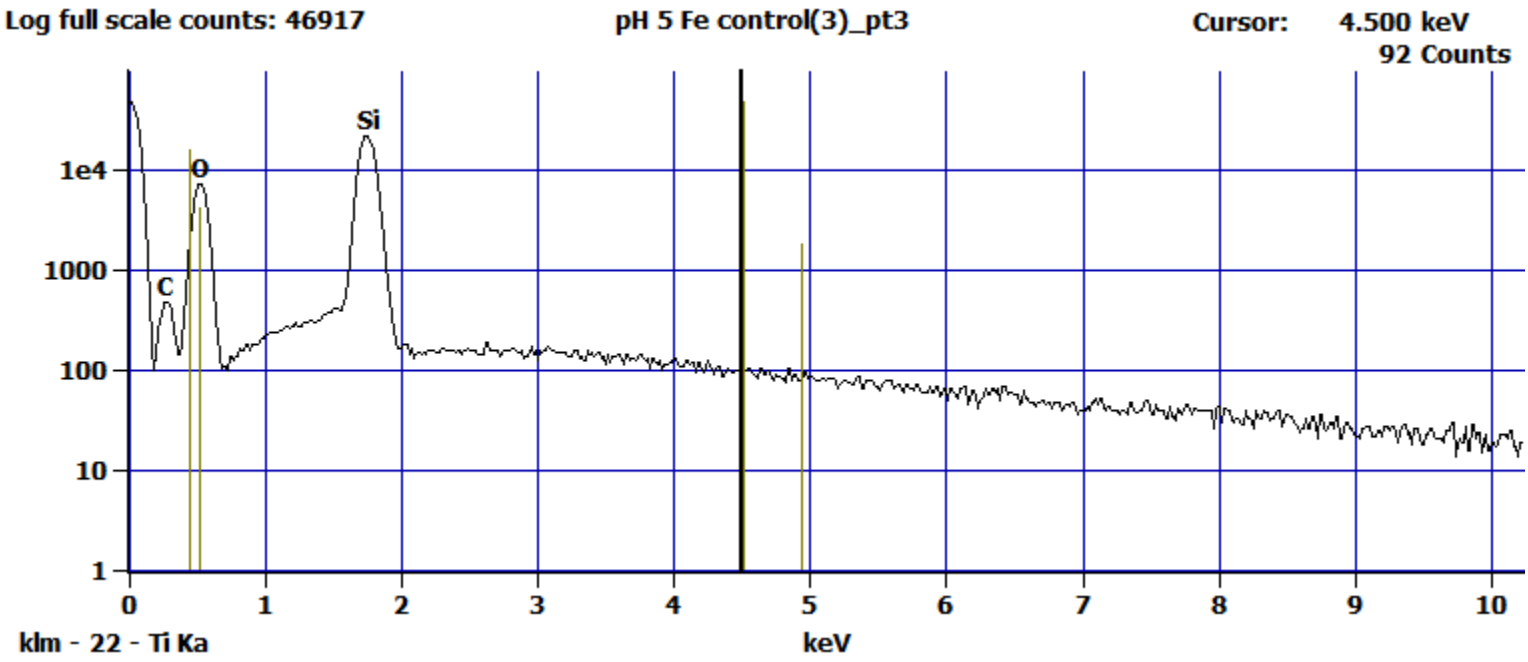

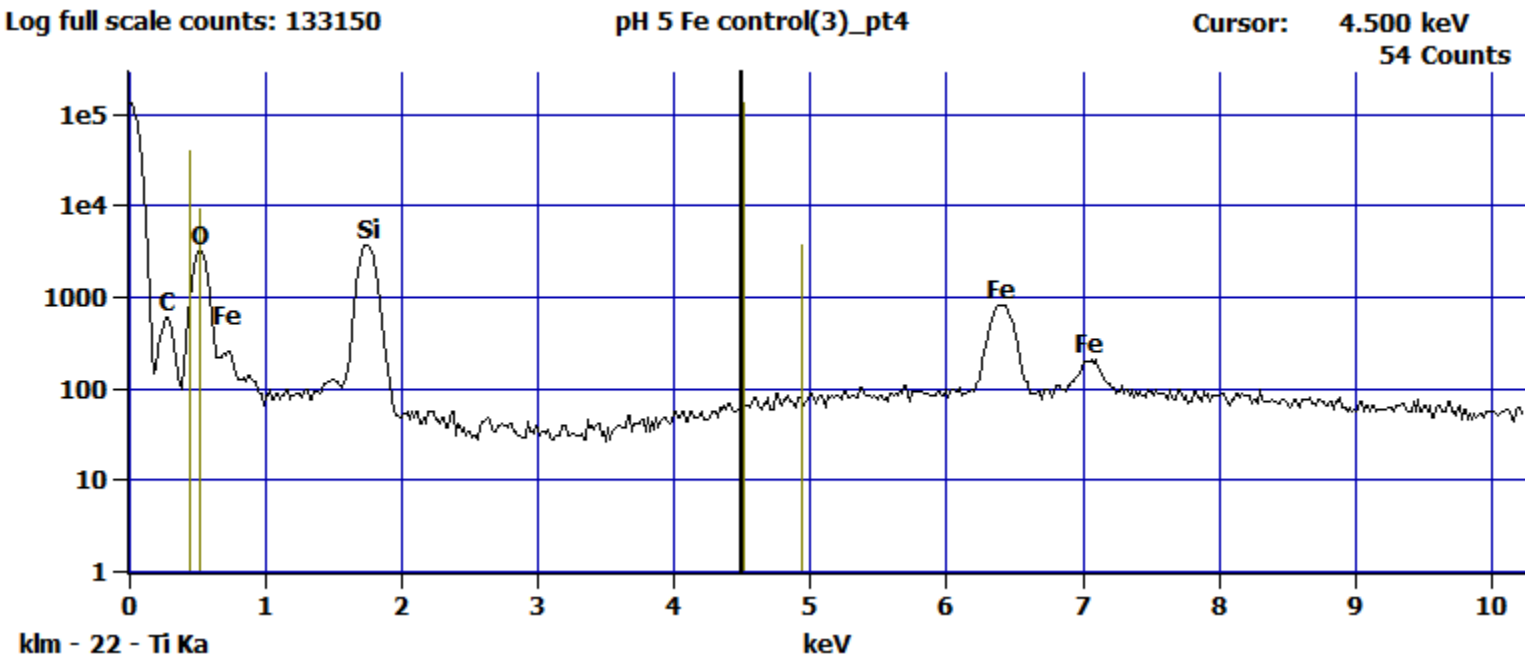

Project: Yang

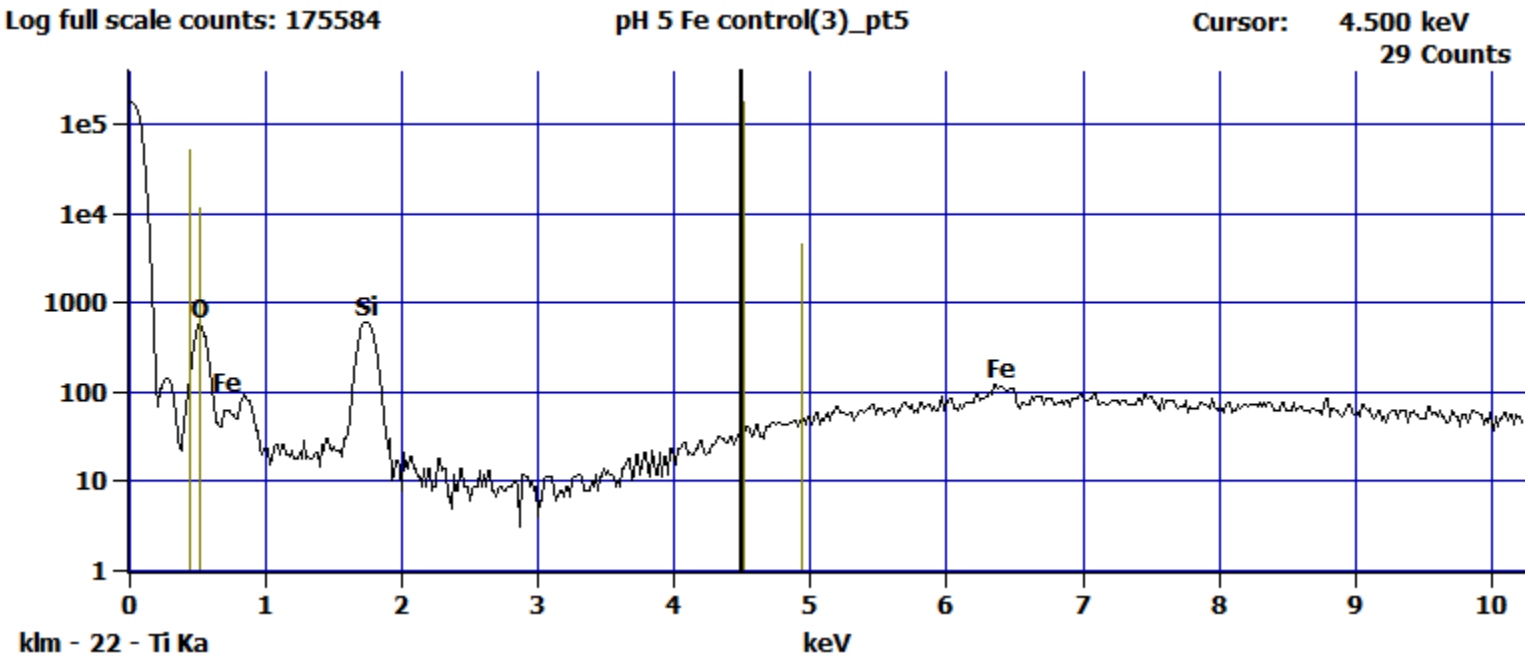

Project: Yang

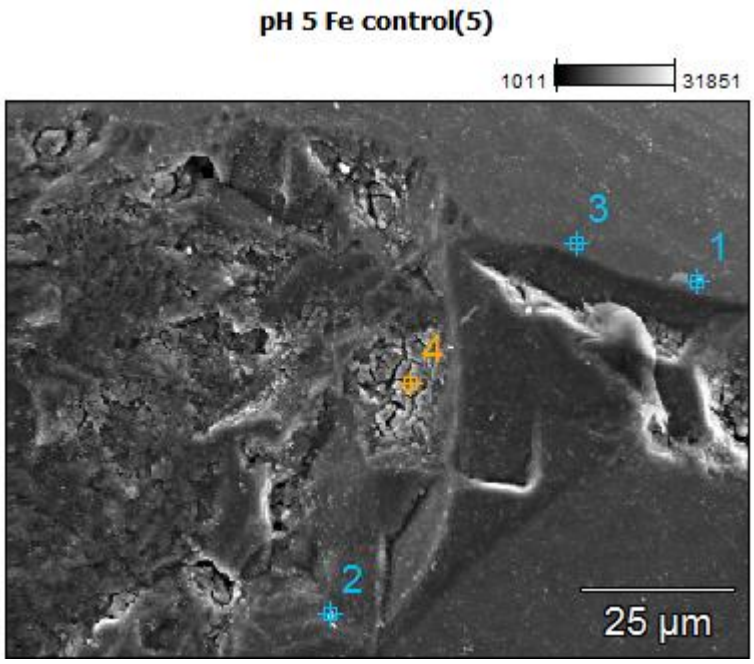

Image Name:	pH 5 Fe control(5)
Image Resolution:	512 by 384
Image Pixel Size:	0.24 µm
Acc. Voltage:	15.0 kV
Magnification:	1000

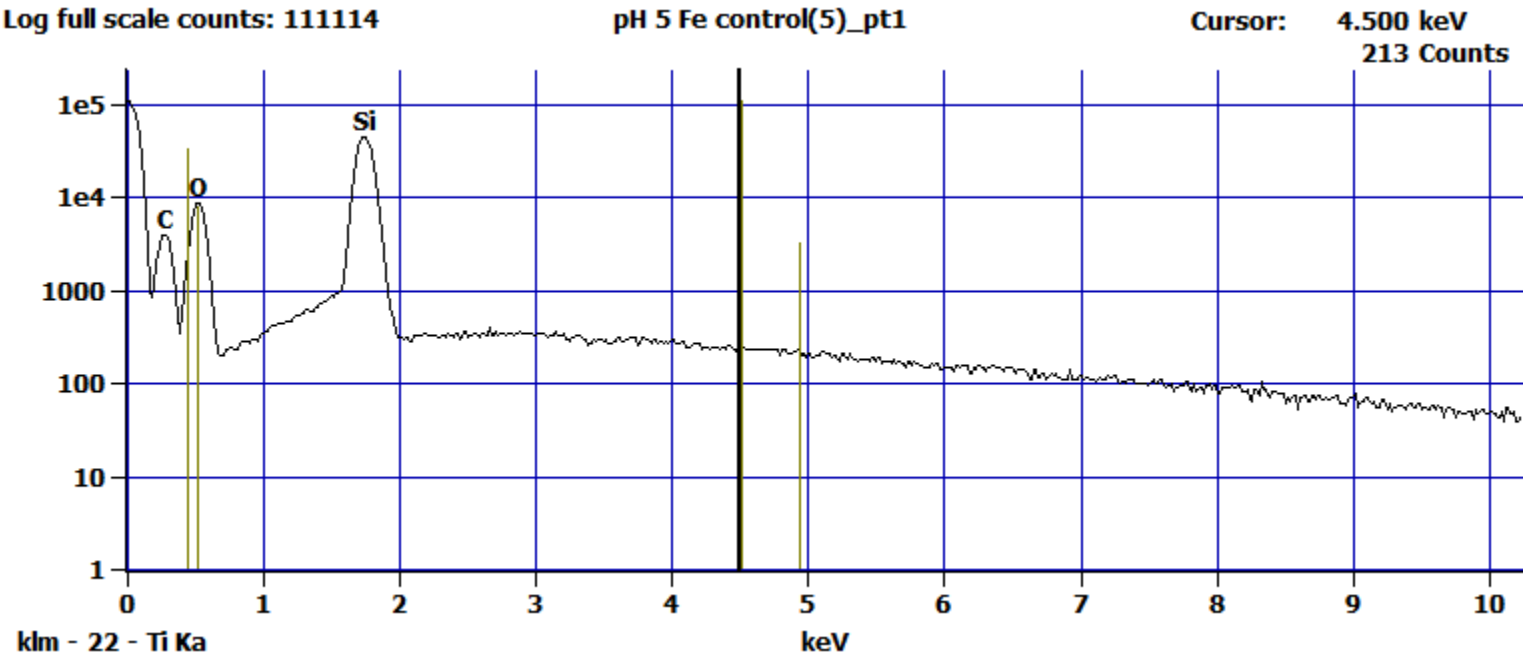

Project: Yang

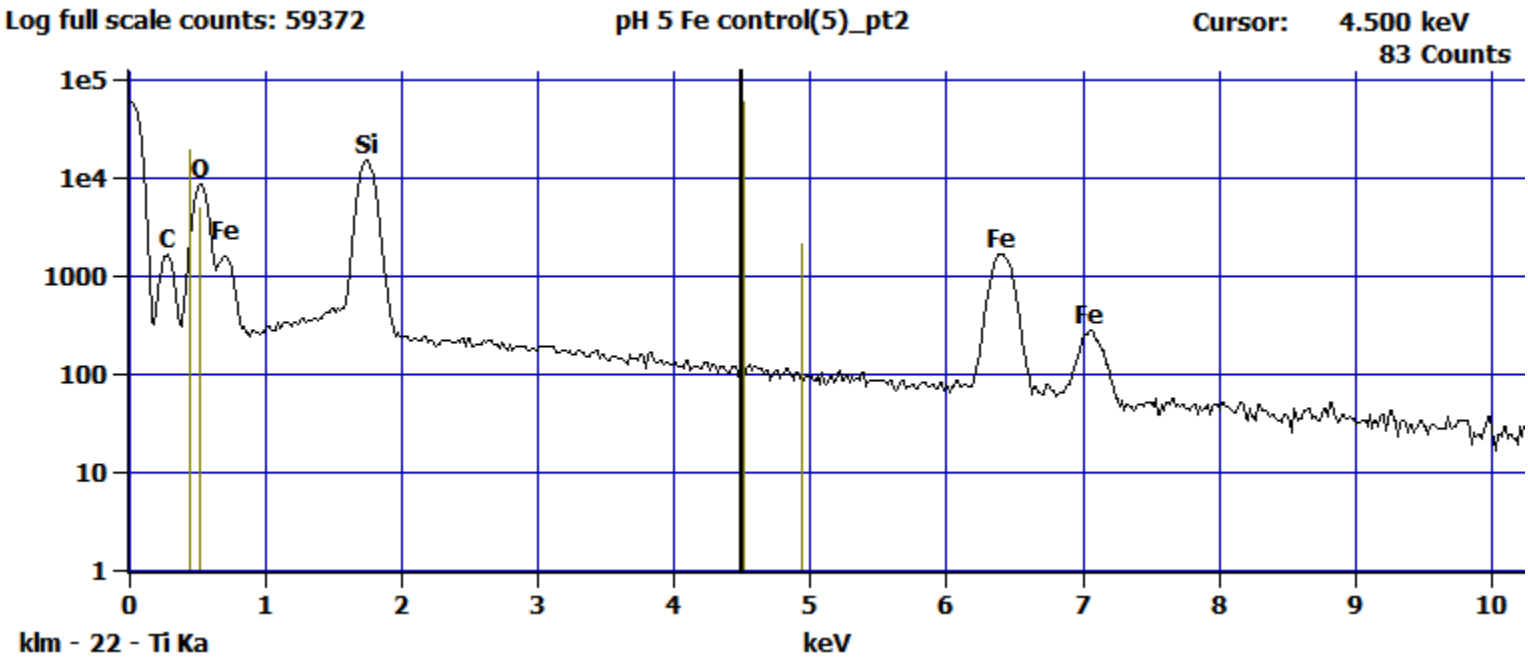

Project: Yang

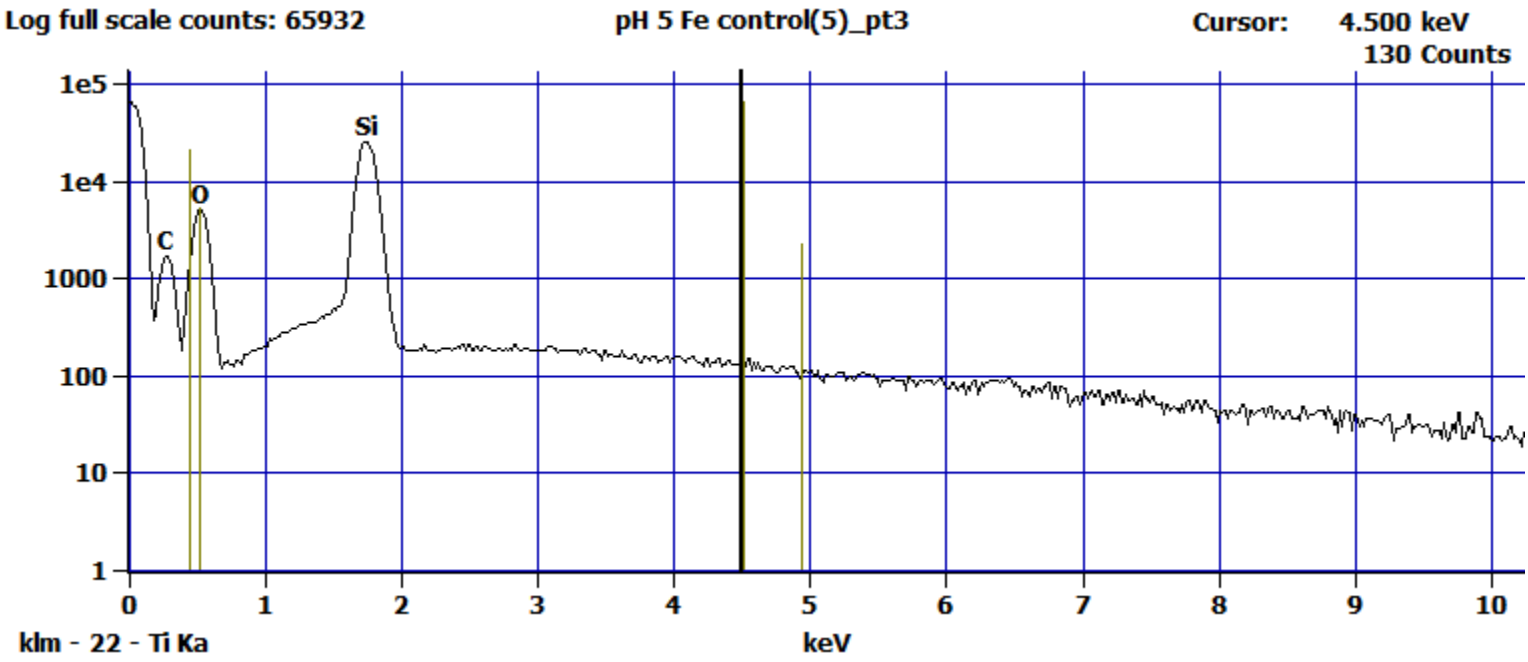

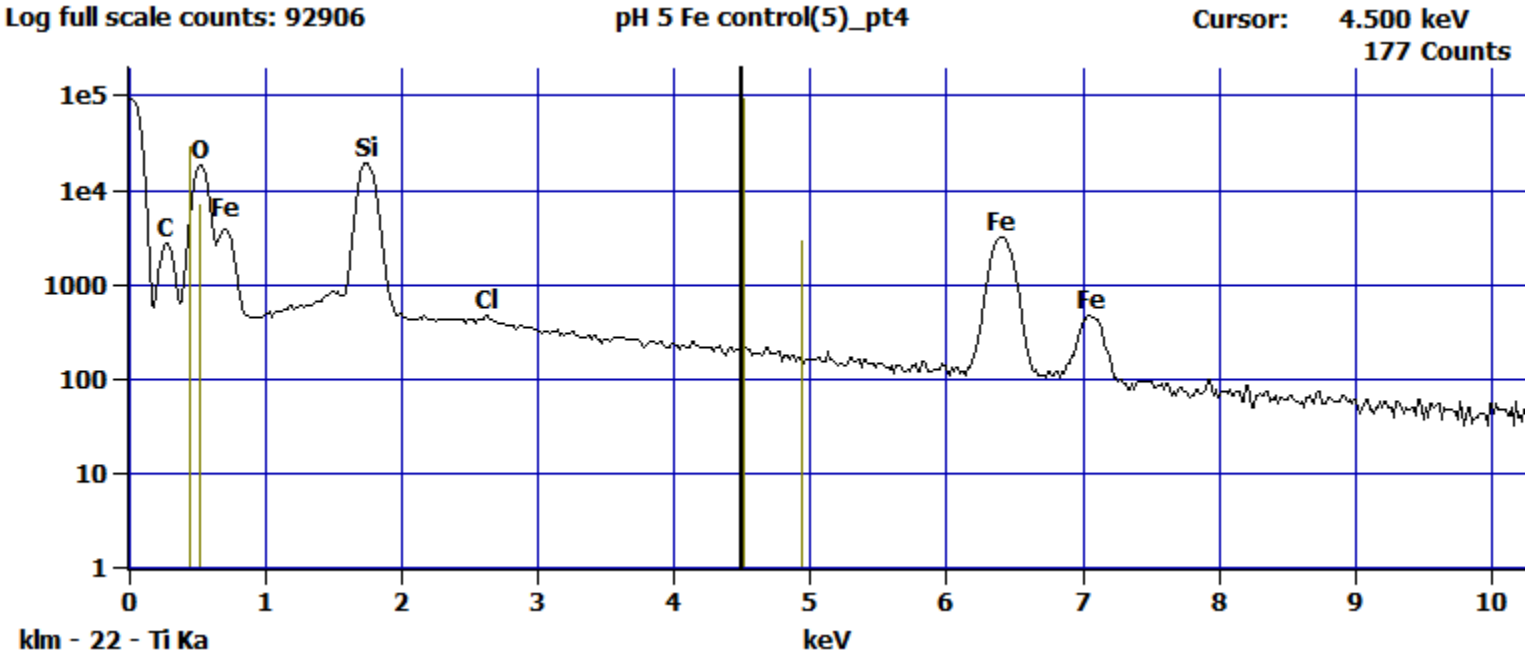

Project: Yang

EDX of quartz sand + $nTiO_2$ at pH 5

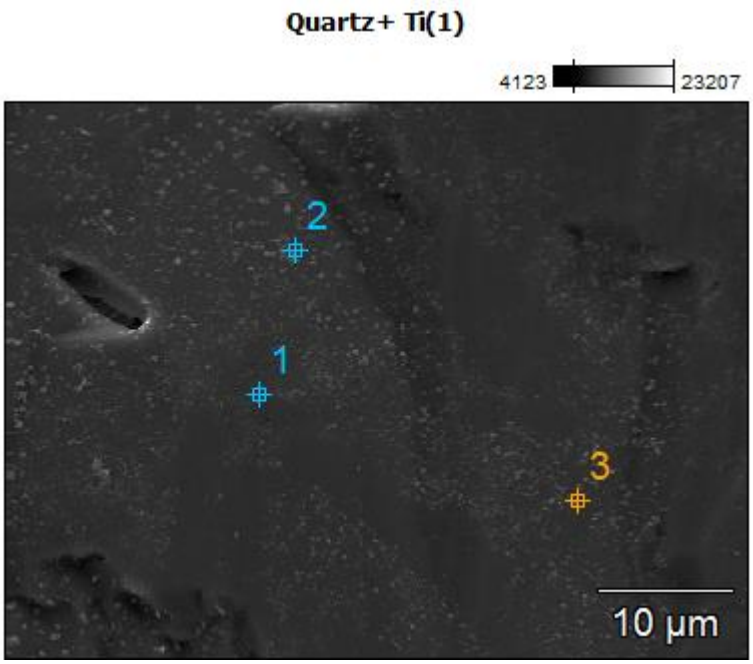

Image Name:	Quartz+ Ti(1)
Image Resolution:	512 by 384
Image Pixel Size:	0.11 µm
Acc. Voltage:	15.0 kV
Magnification:	2200

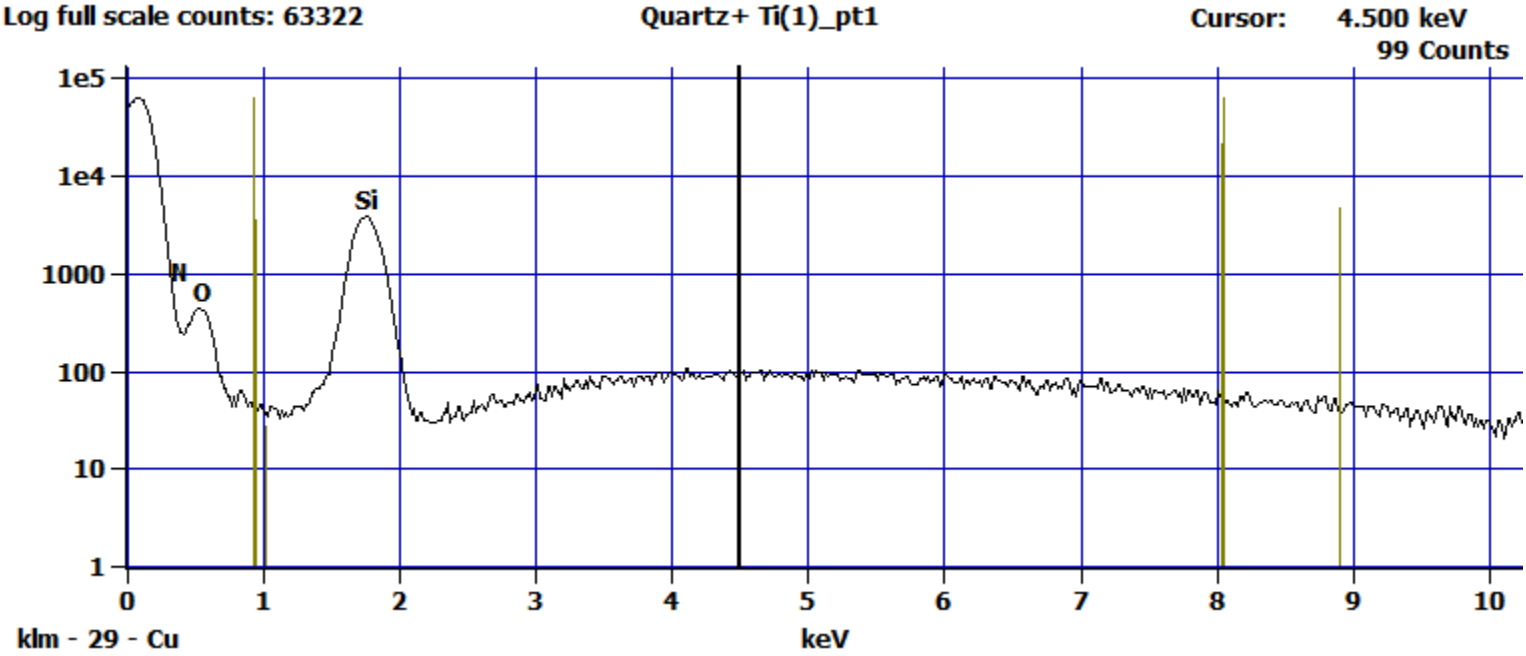

Project: Yang

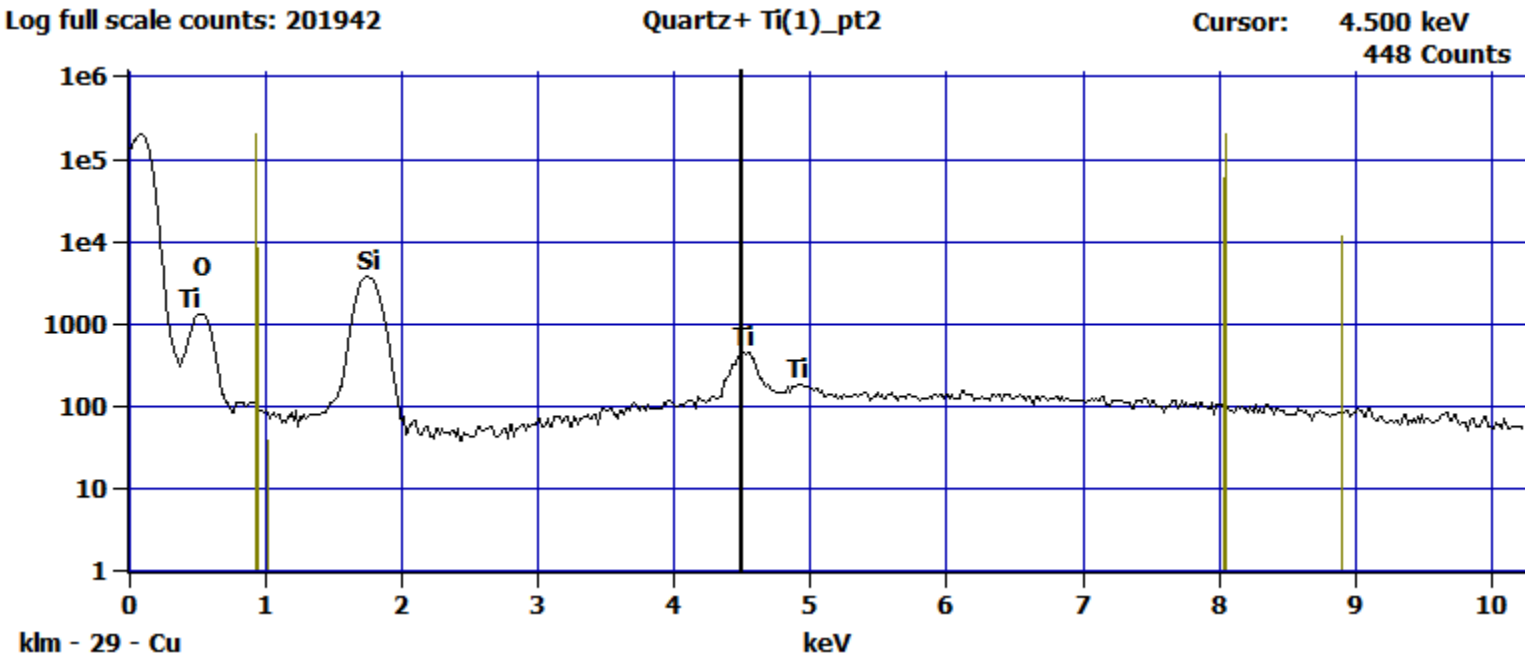

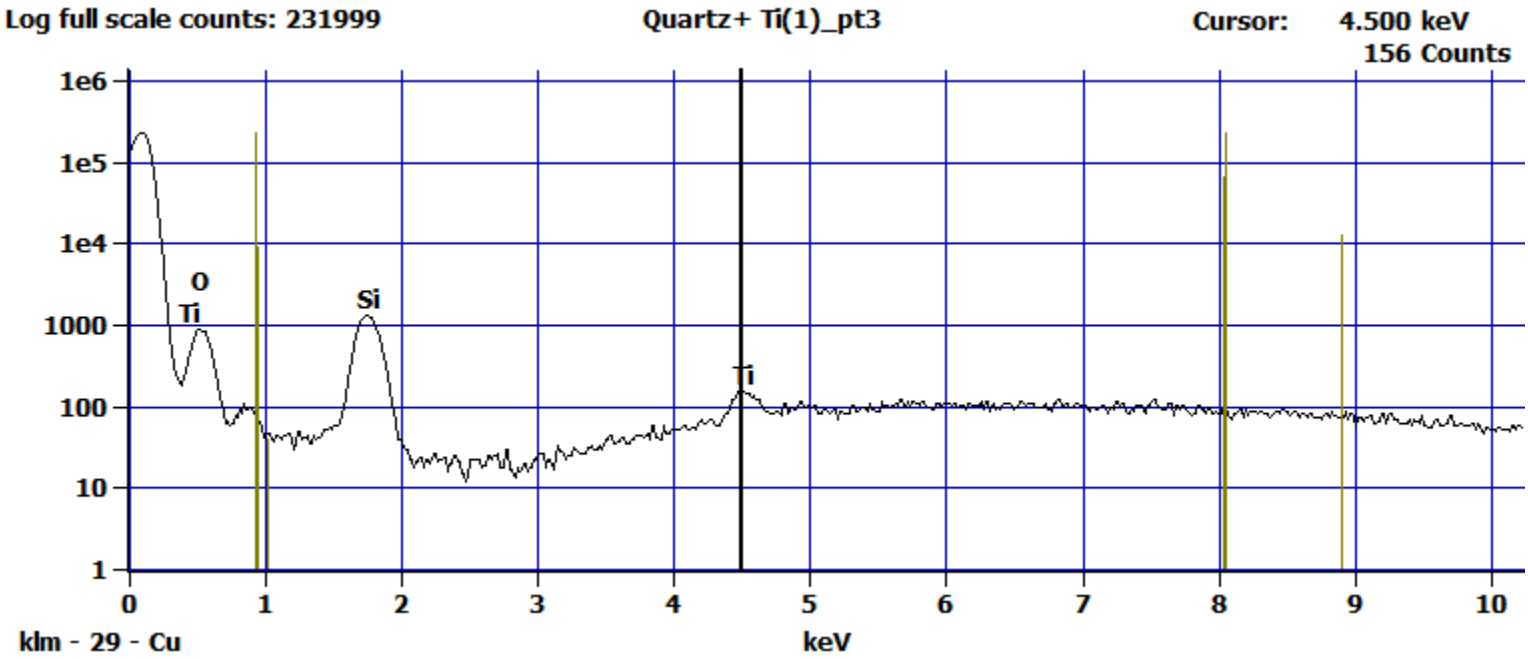

Project: Yang

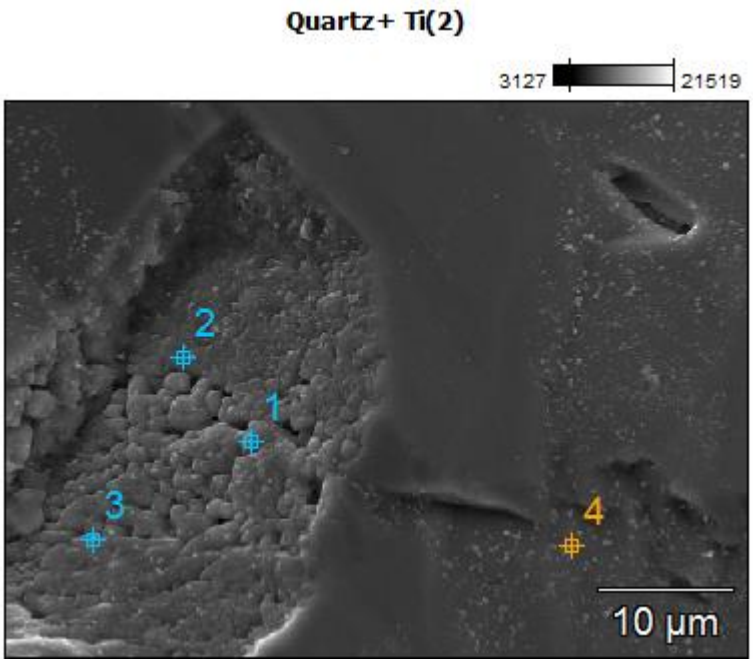

Image Name:	Quartz+ Ti(2)
Image Resolution:	512 by 384
Image Pixel Size:	0.11 µm
Acc. Voltage:	15.0 kV
Magnification:	2200

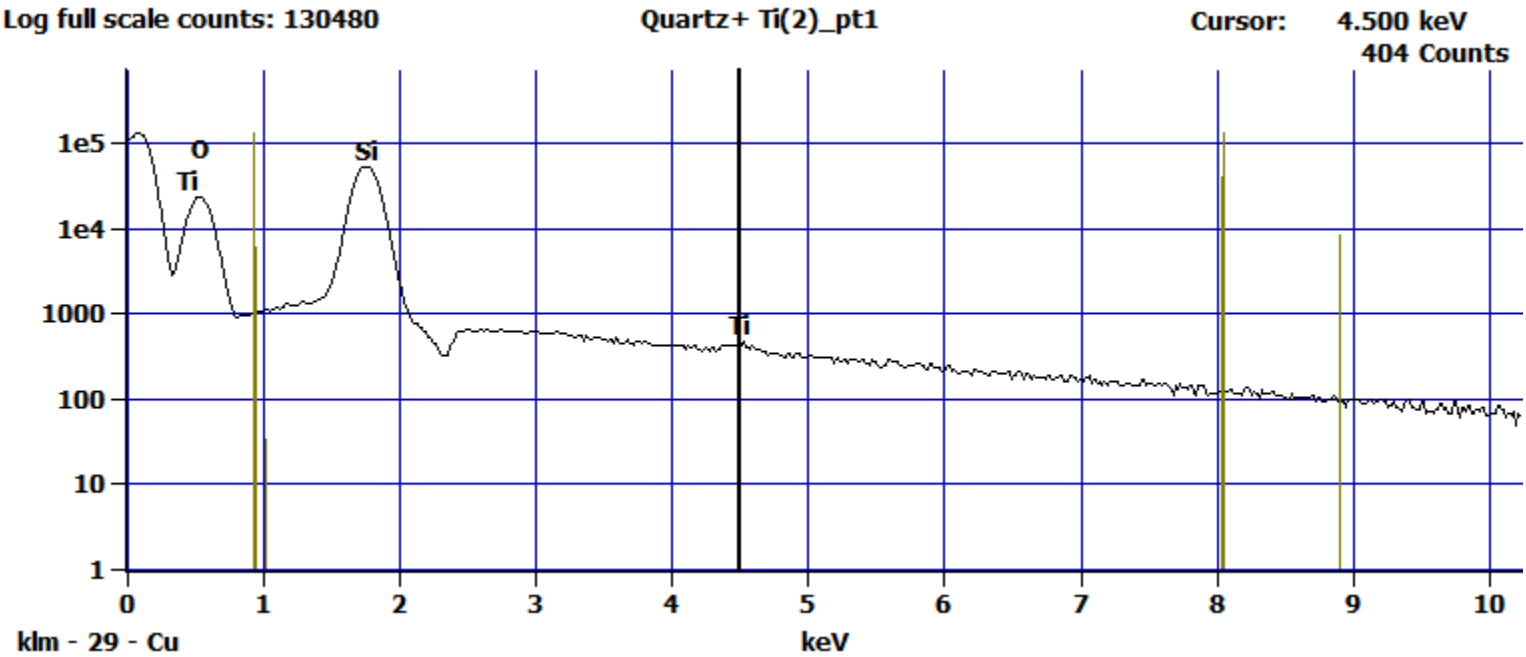

Project: Yang

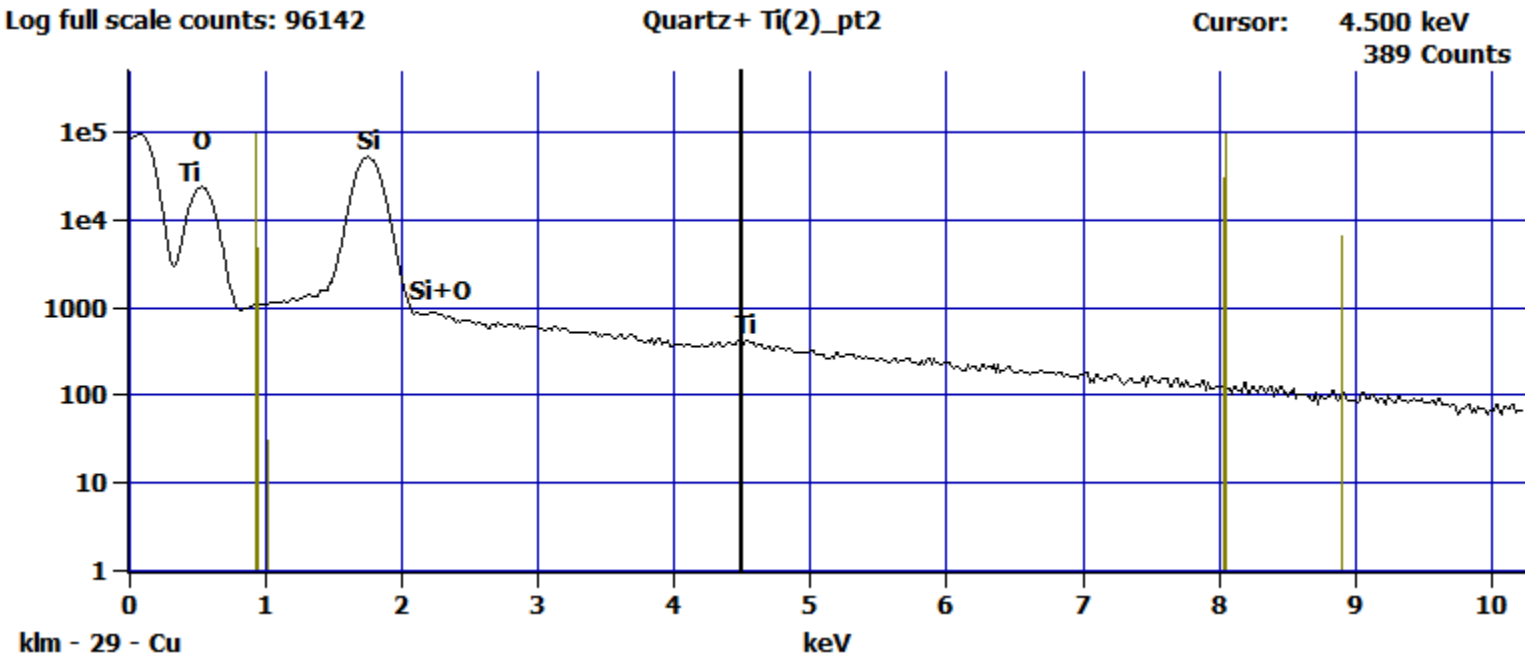

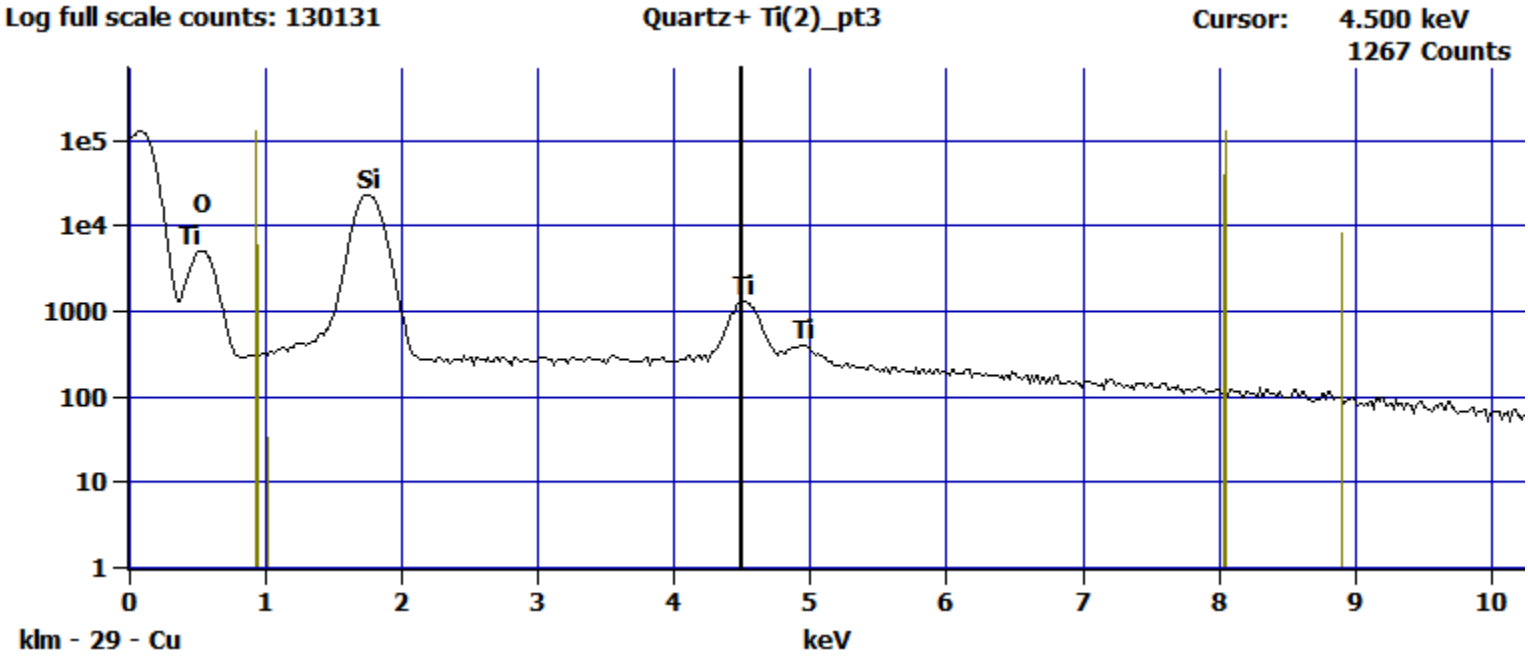

Project: Yang

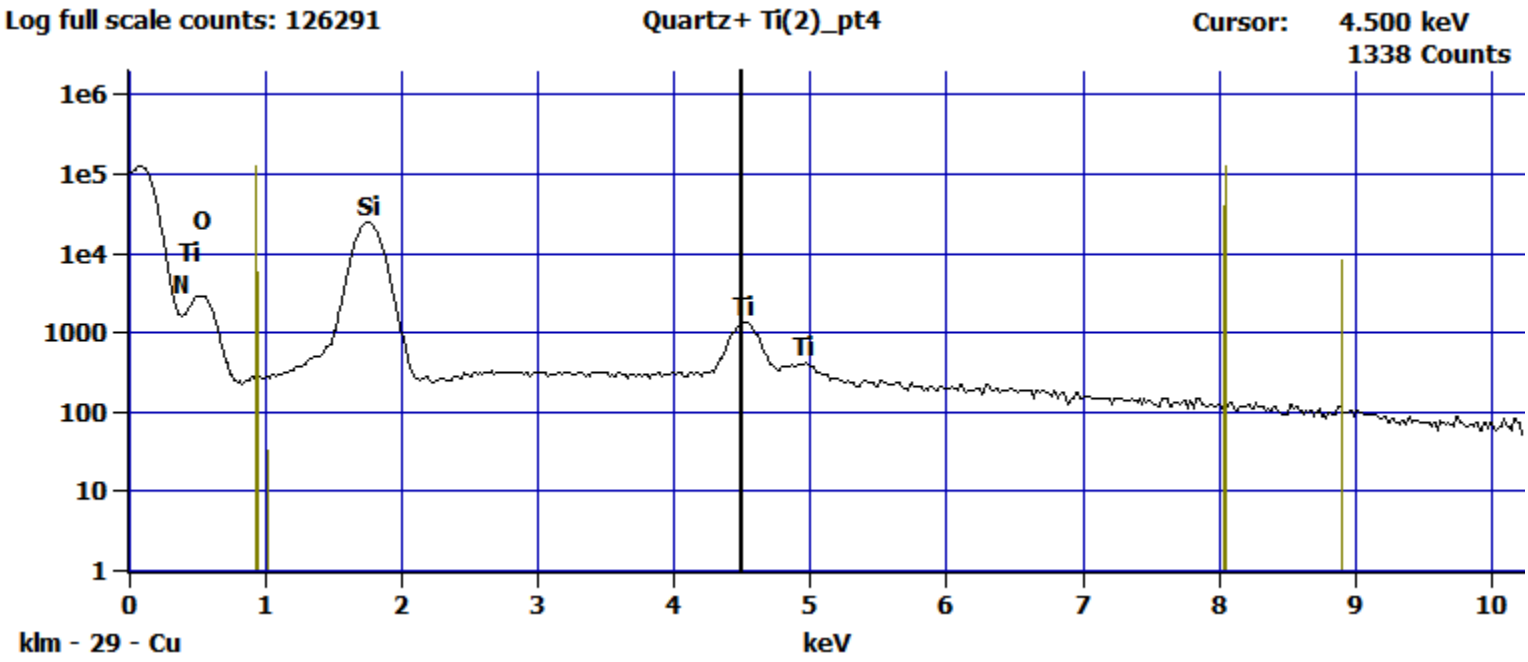

Project: Yang

EDX of Fe coated sand + $nTiO_2$ at pH 5

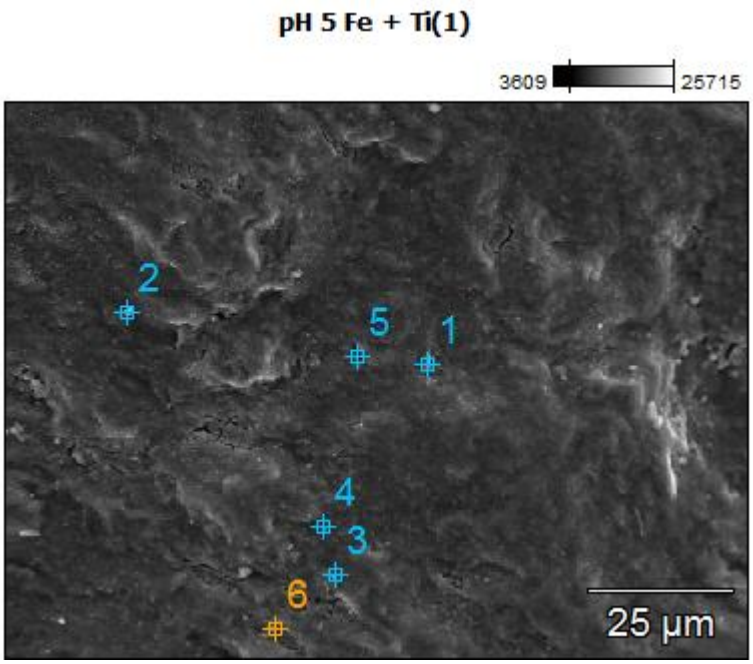

Image Name:	pH 5 Fe + Ti(1)
Image Resolution:	512 by 384
Image Pixel Size:	0.25 µm
Acc. Voltage:	15.0 kV
Magnification:	950

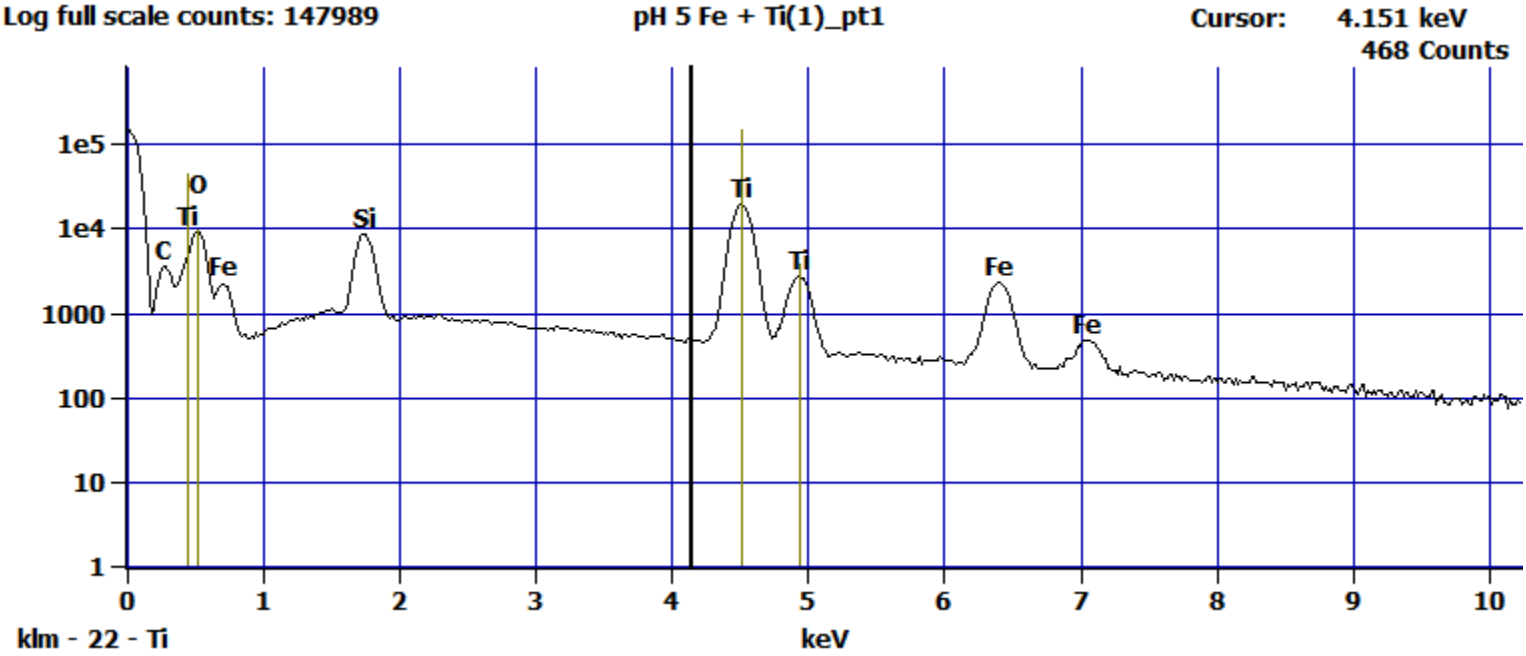

Project: Yang

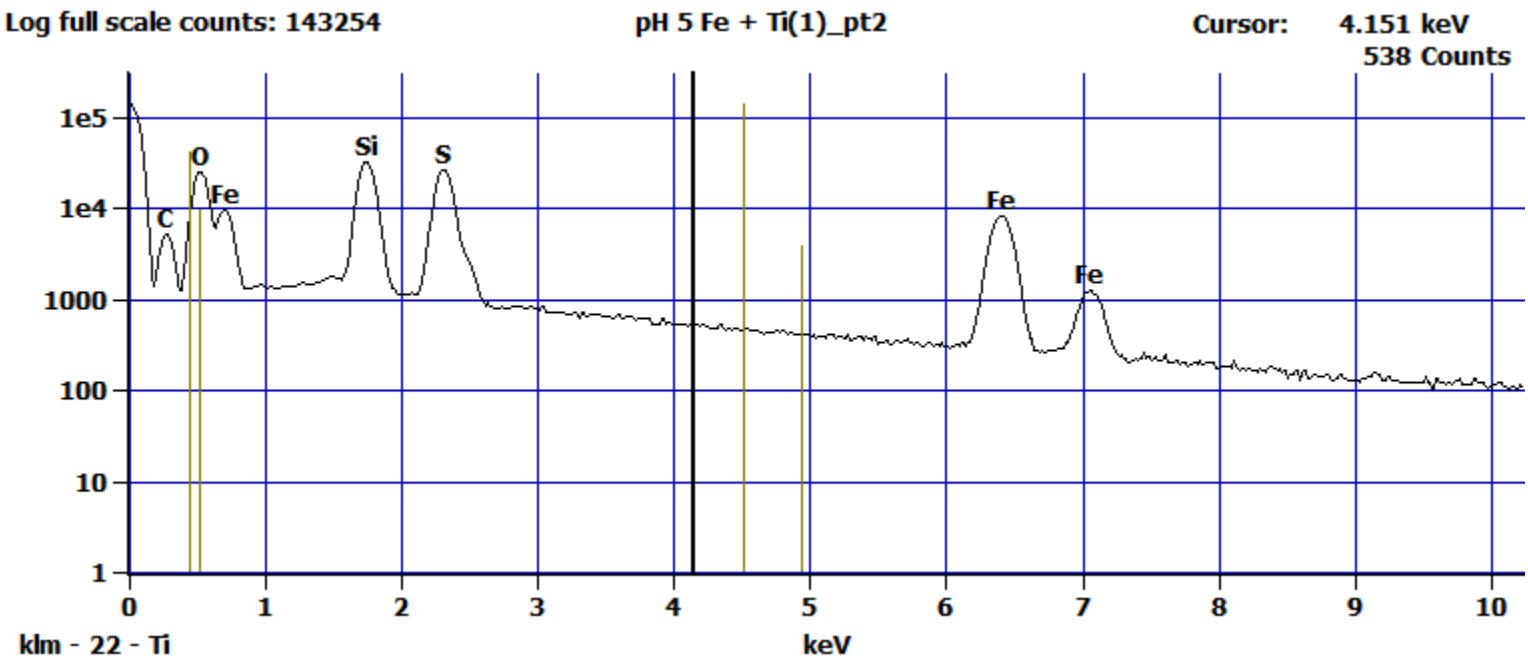

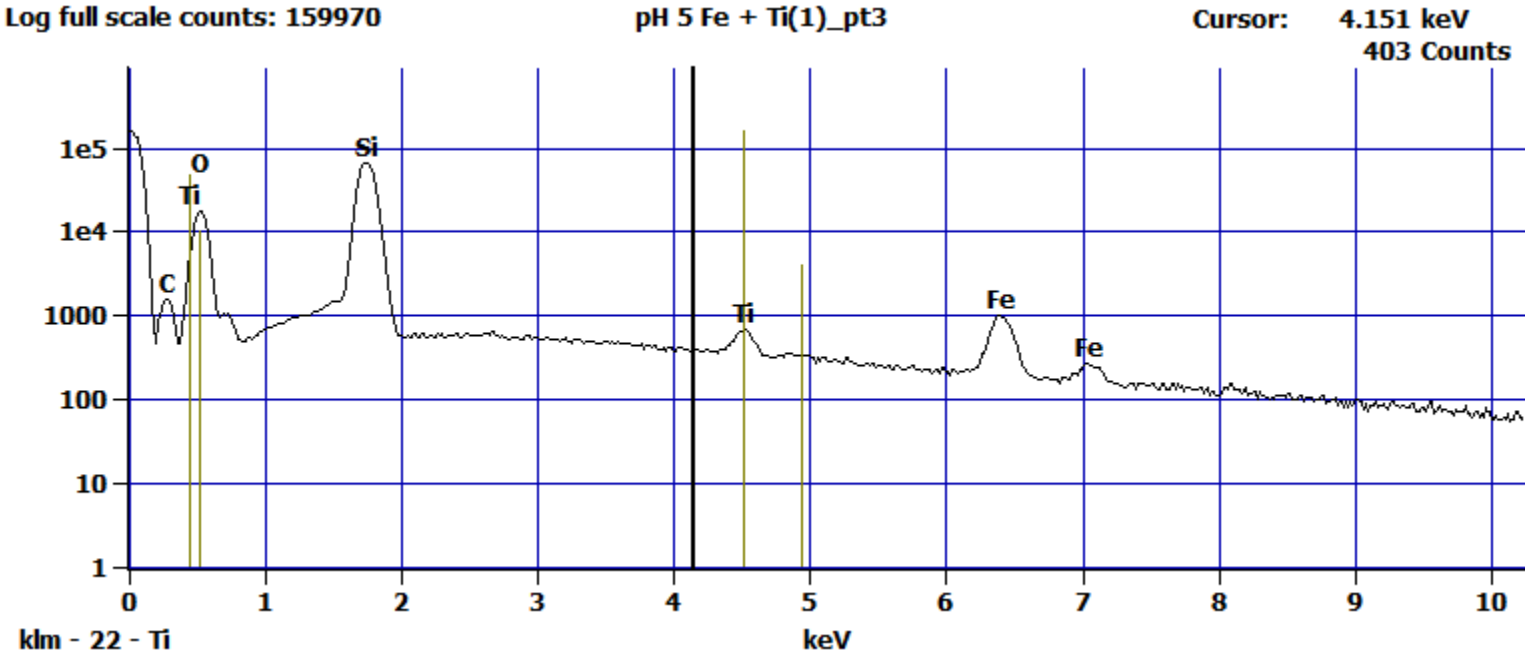

Project: Yang

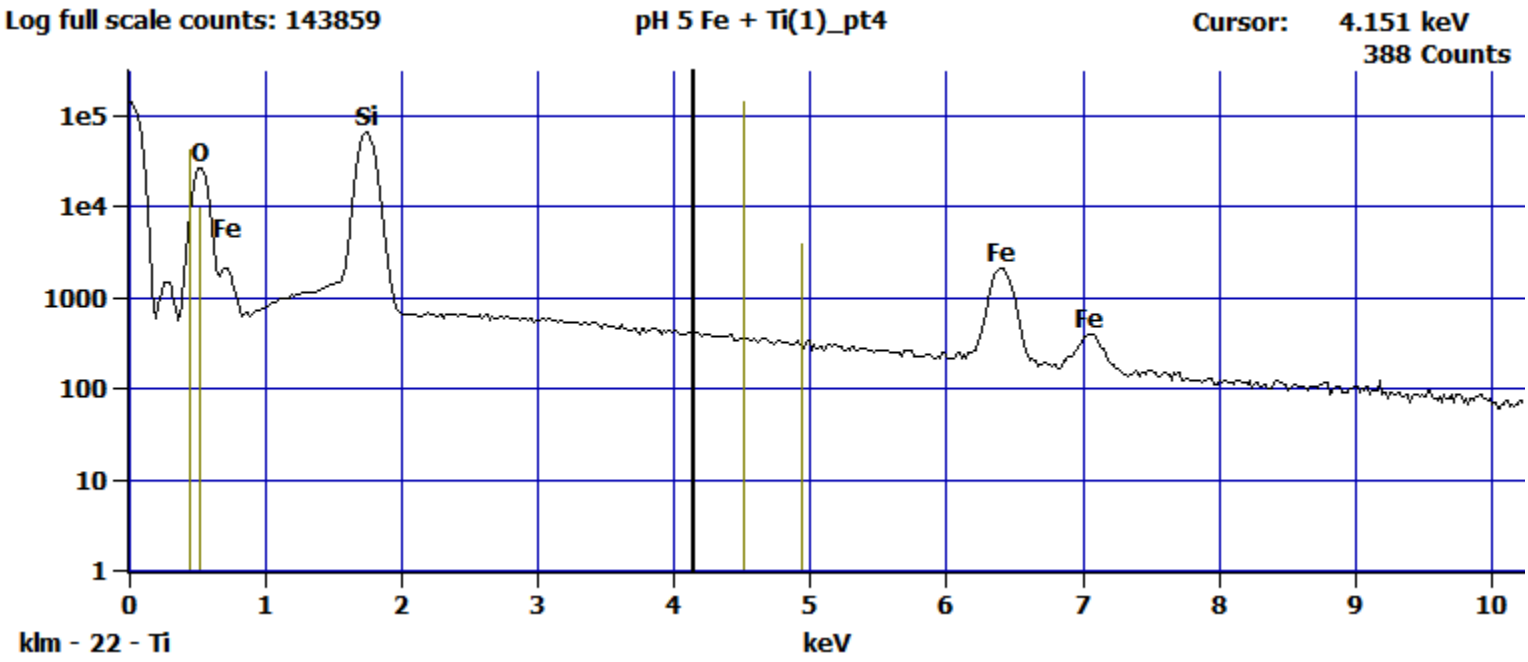

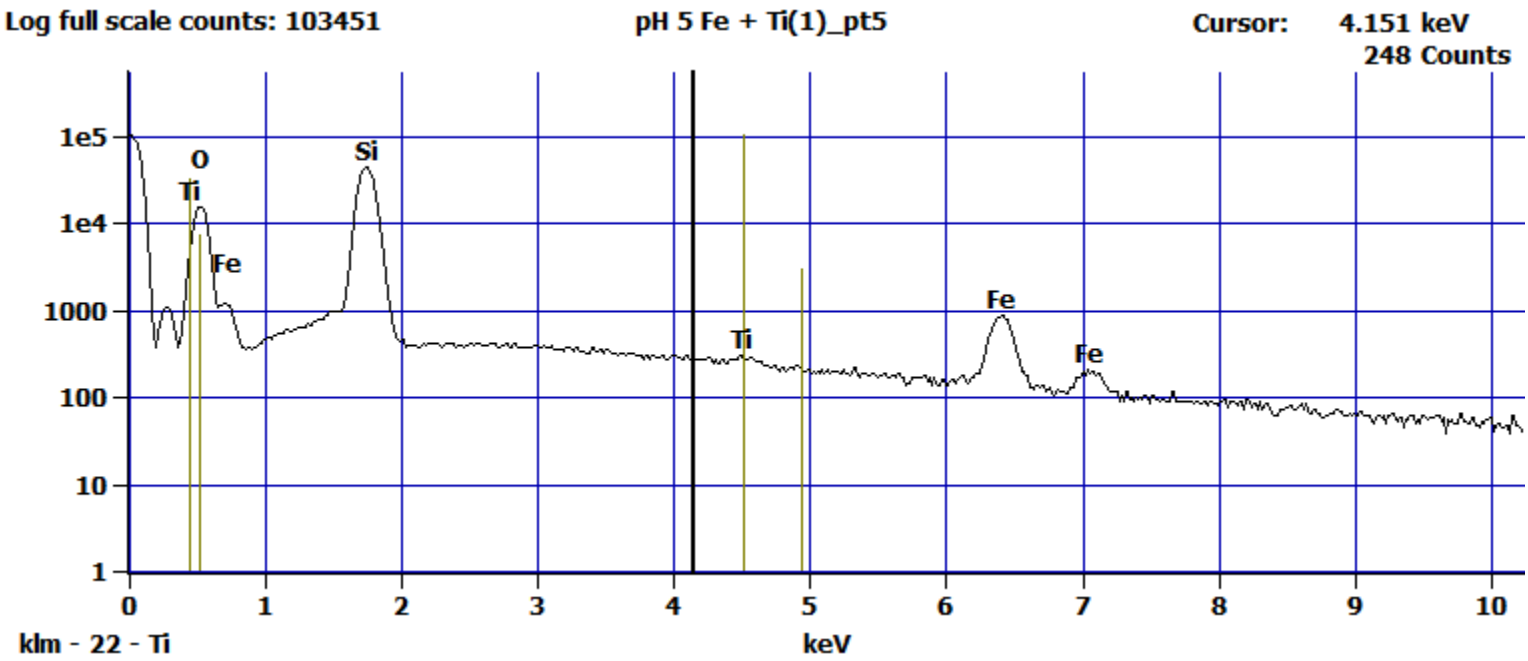

Project: Yang

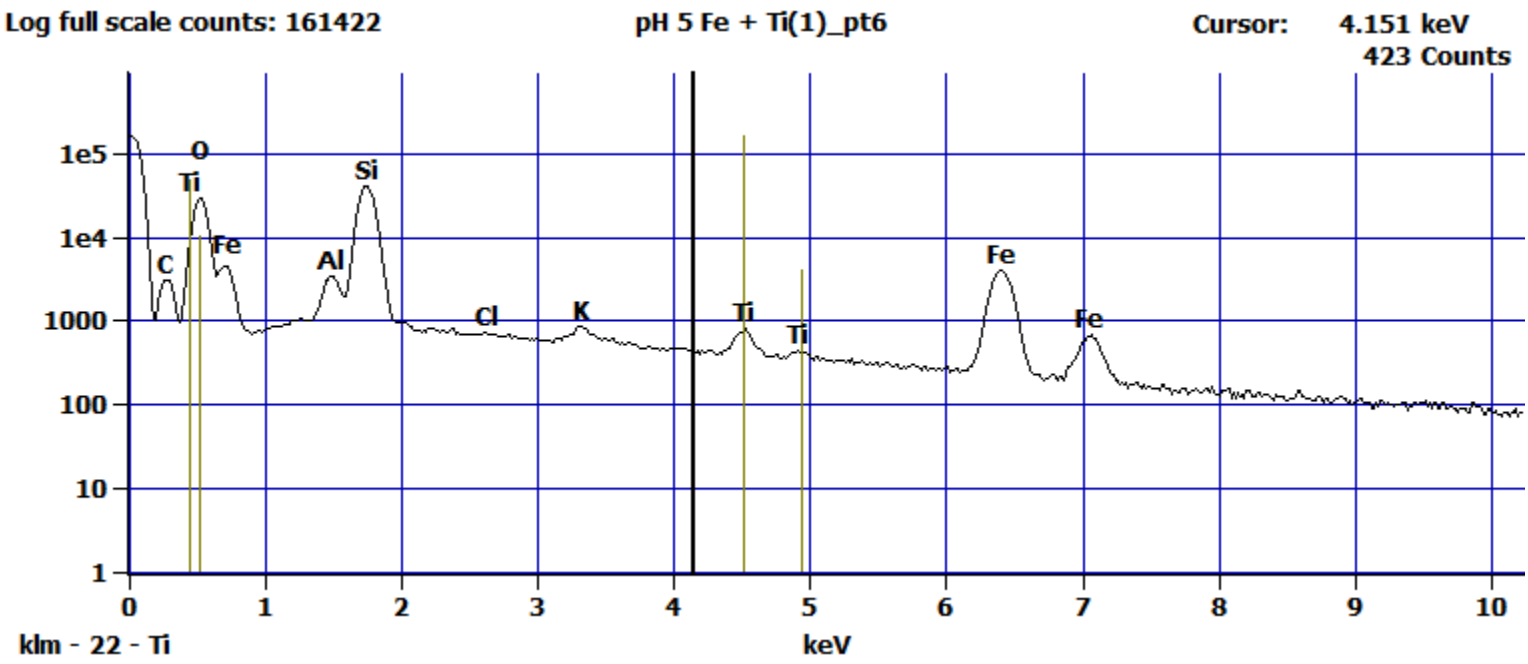

Project: Yang

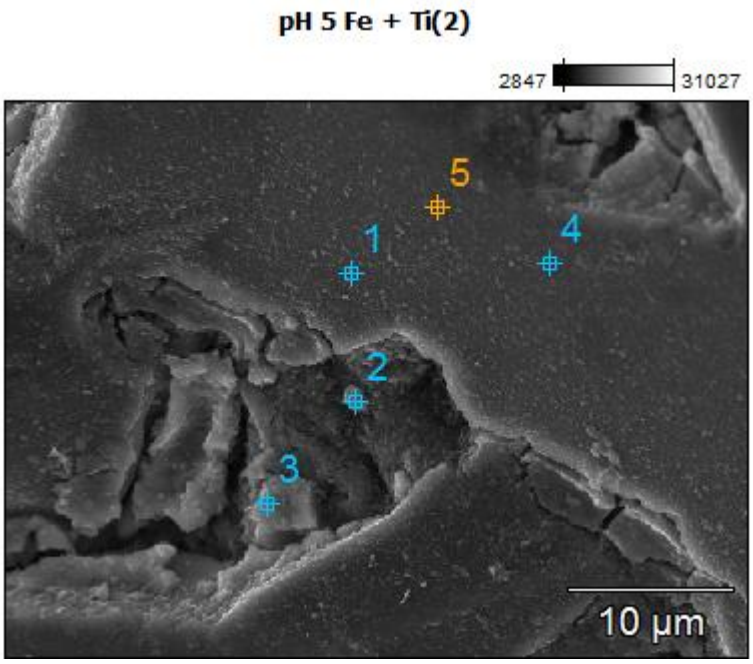

Image Name:	pH 5 Fe + Ti(2)
Image Resolution:	512 by 384
Image Pixel Size:	0.09 µm
Acc. Voltage:	15.0 kV
Magnification:	2700

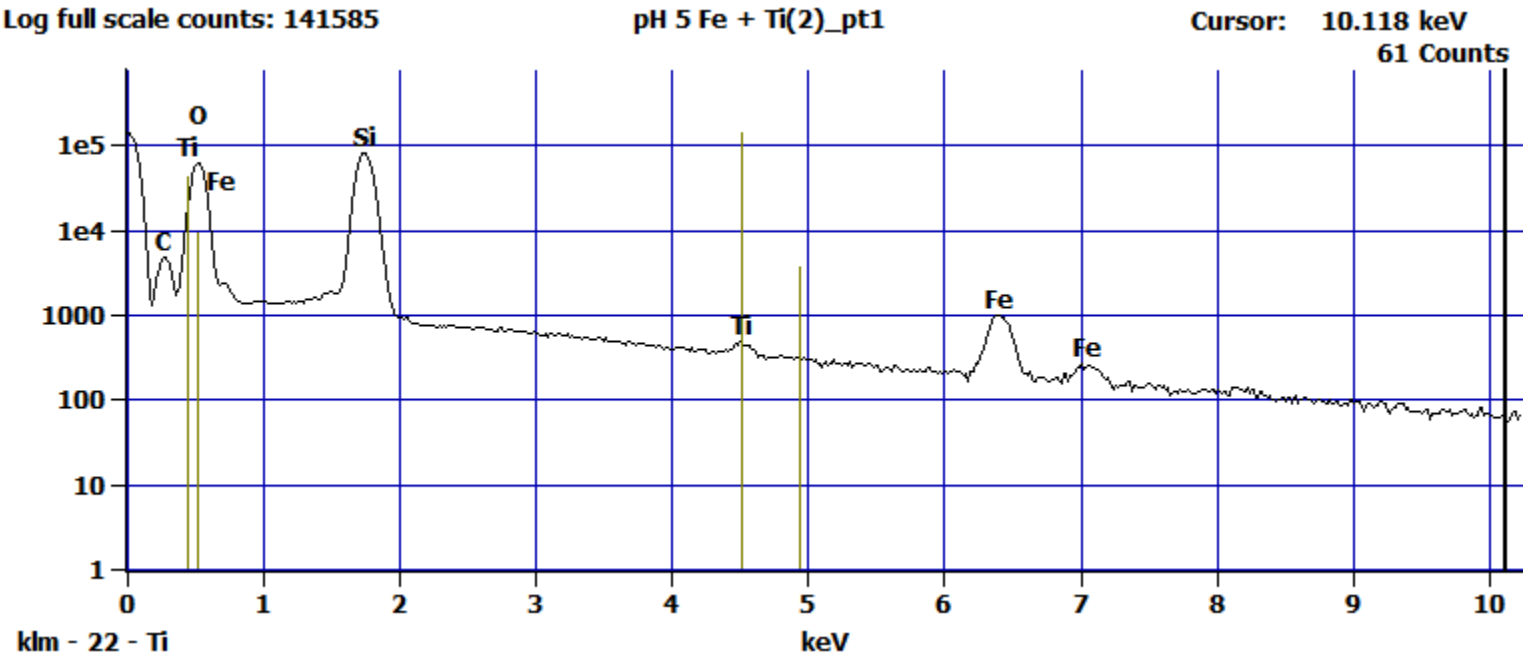

Project: Yang

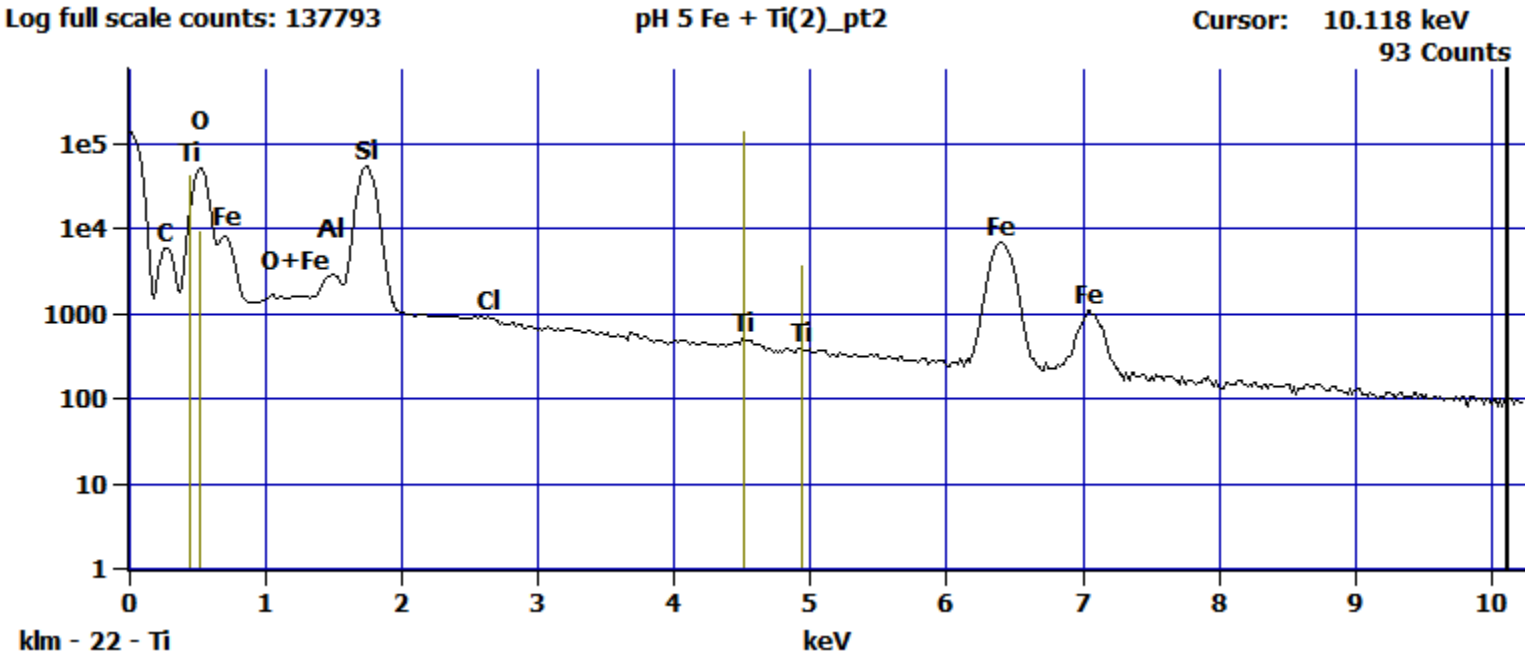

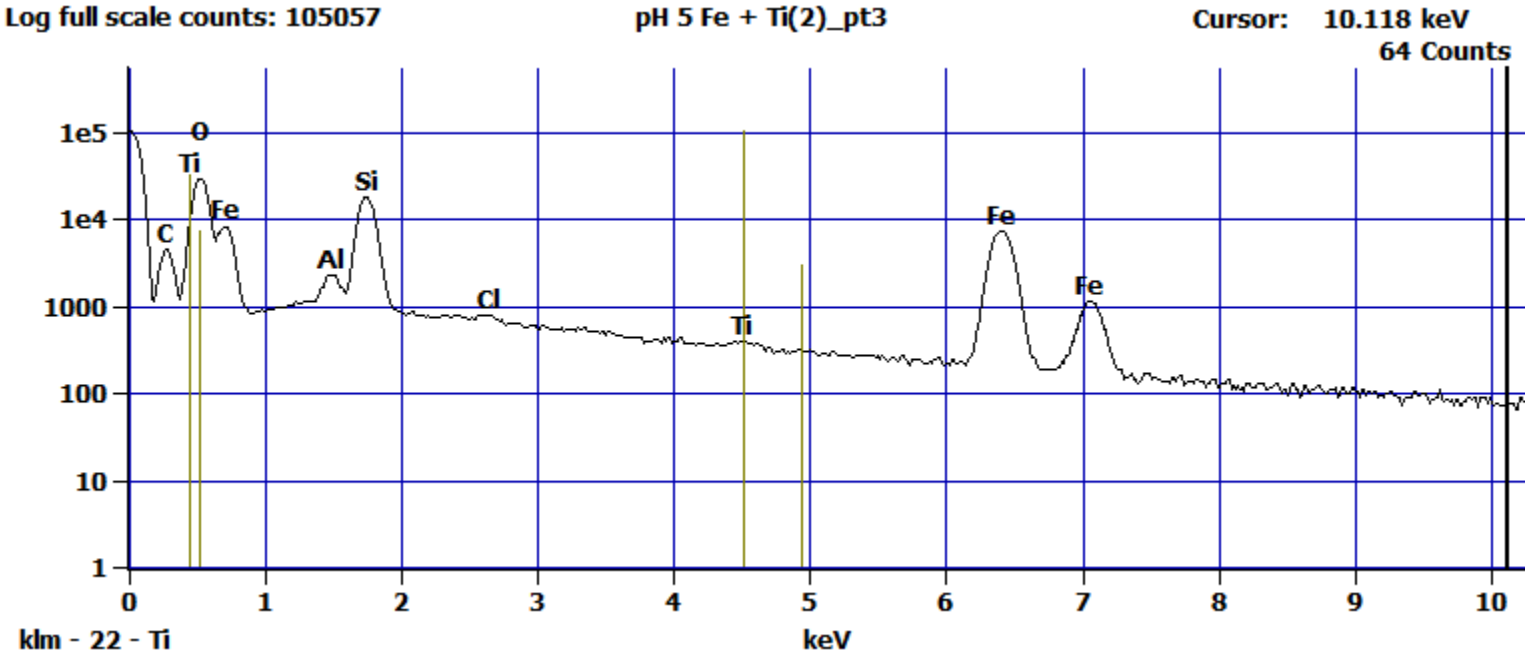

Project: Yang

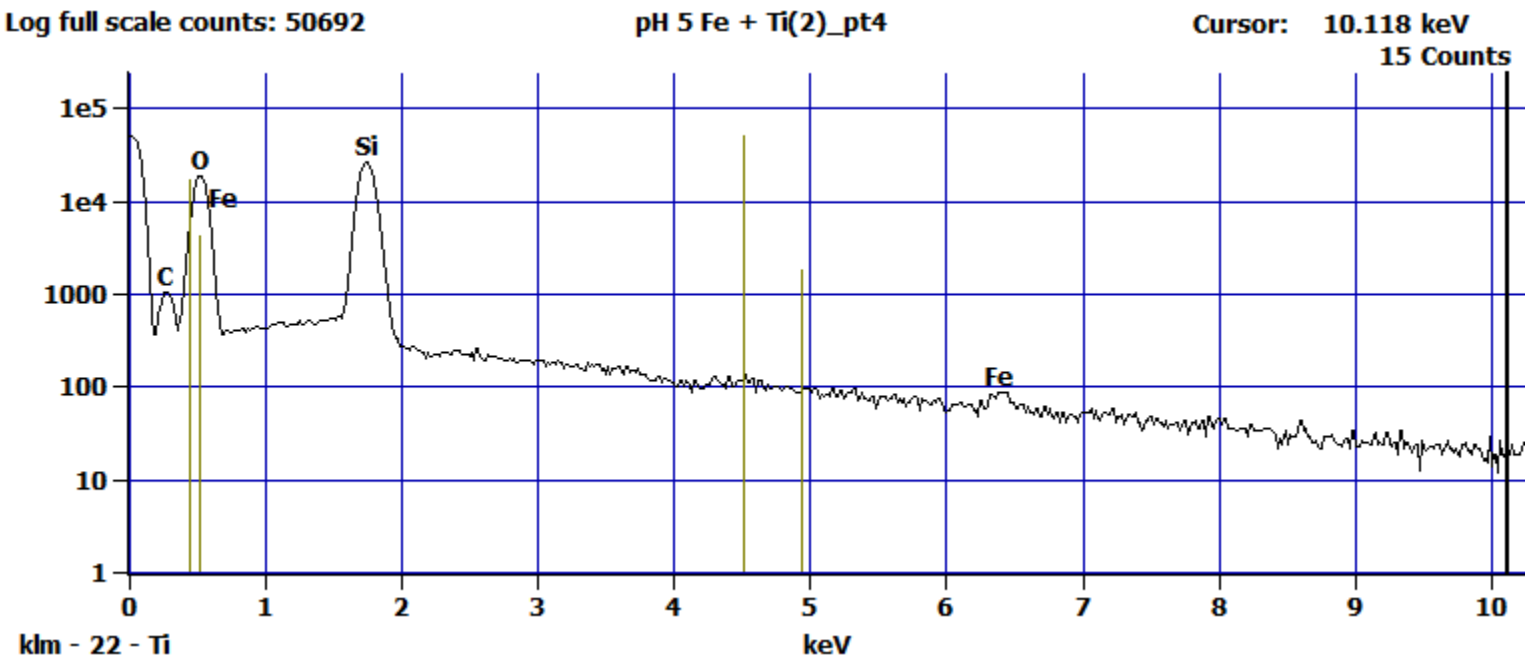

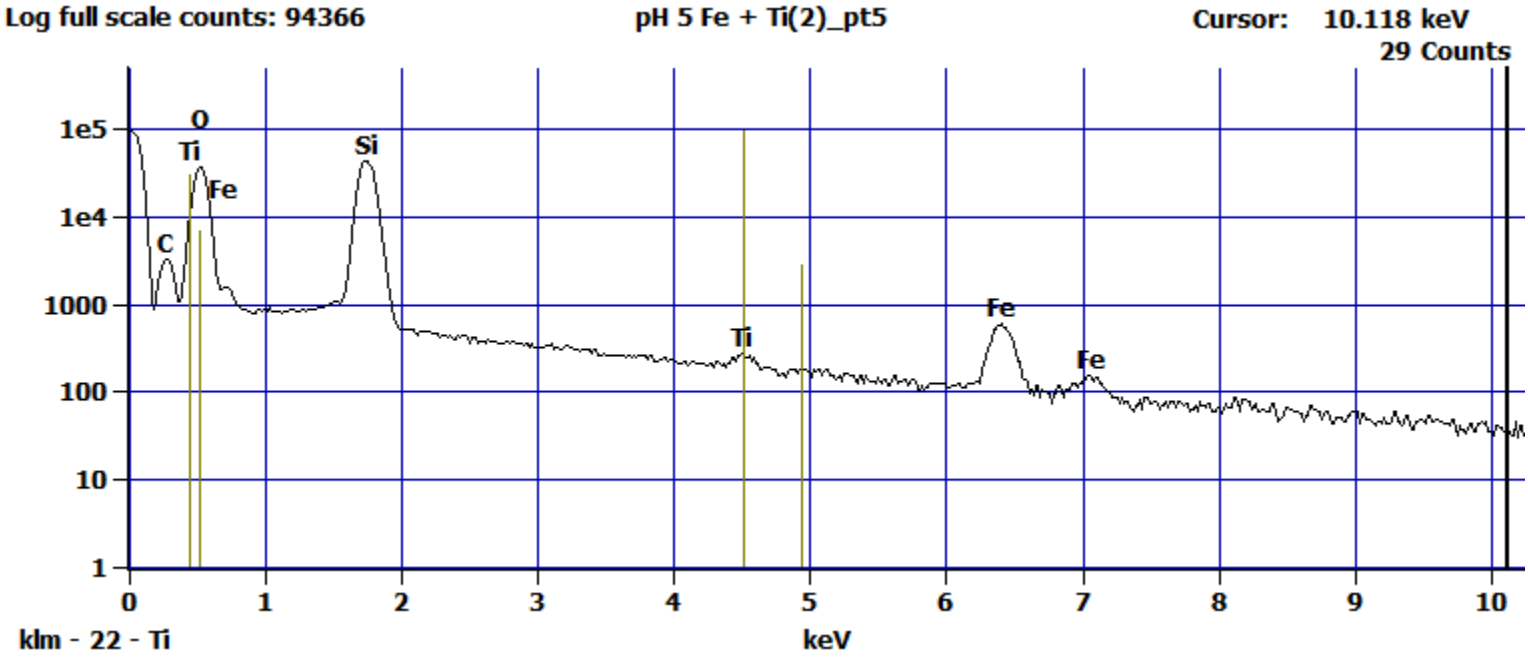

Project: Yang

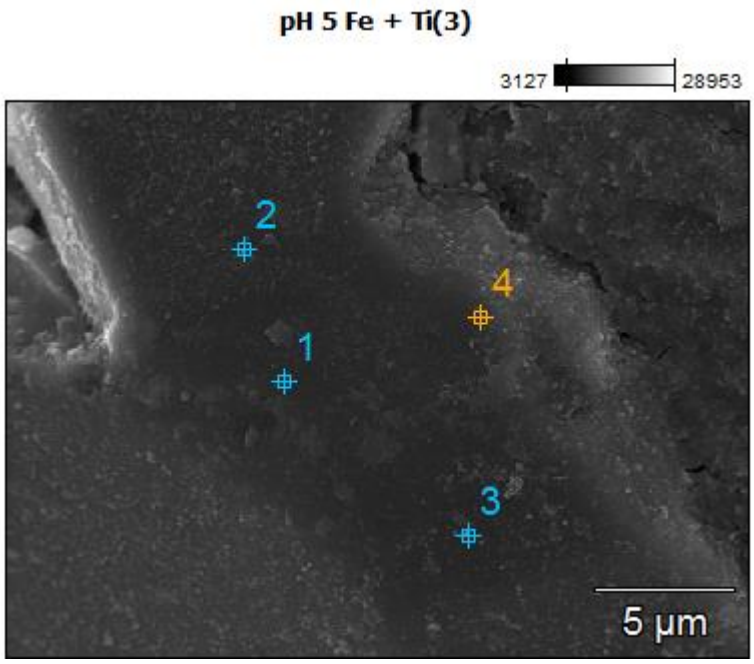

Image Name:	pH 5 Fe + Ti(3)
Image Resolution:	512 by 384
Image Pixel Size:	0.05 µm
Acc. Voltage:	15.0 kV
Magnification:	4500

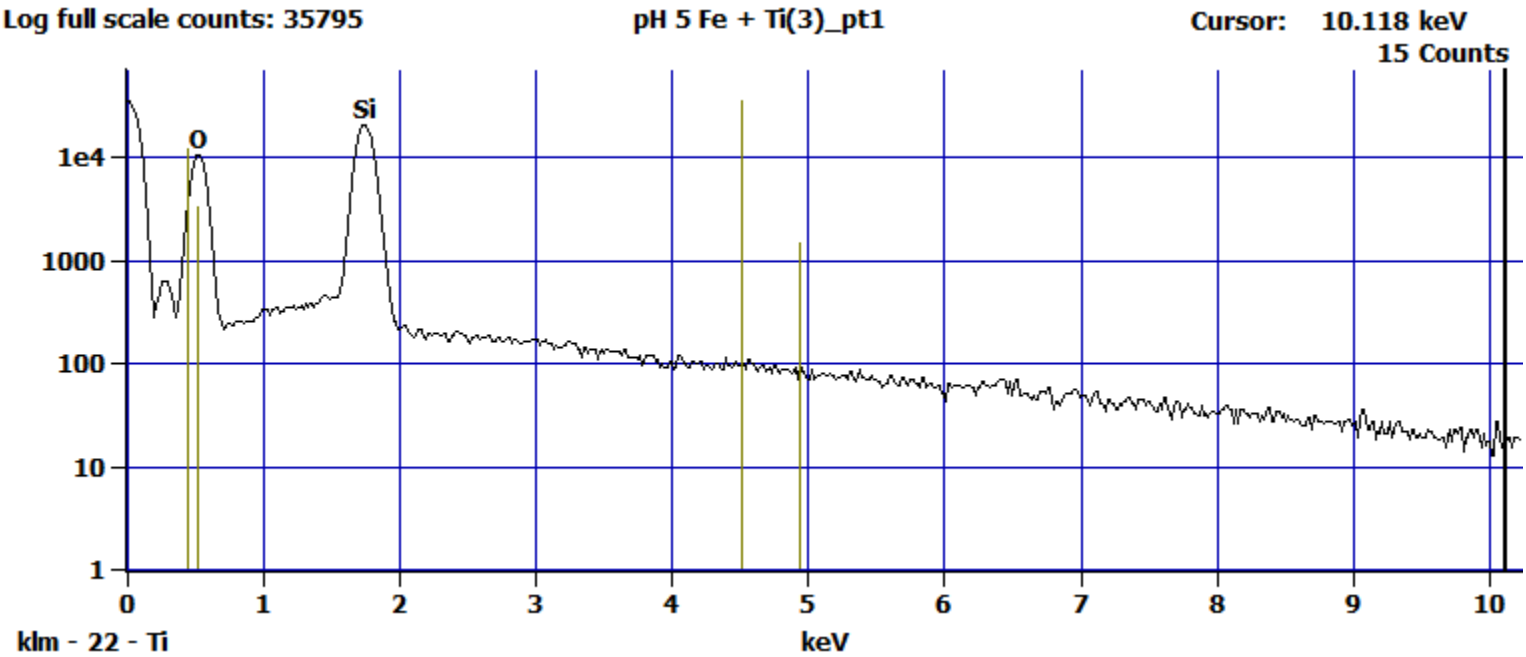

Project: Yang

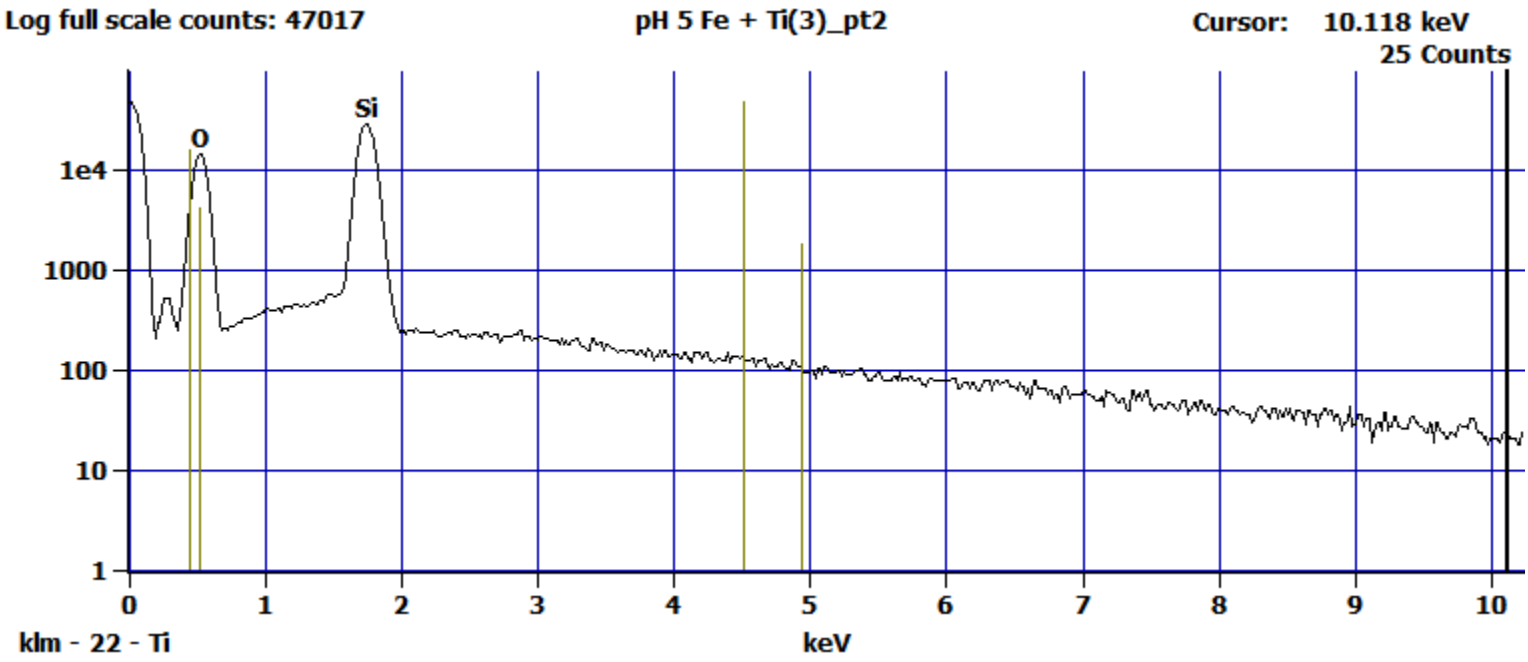

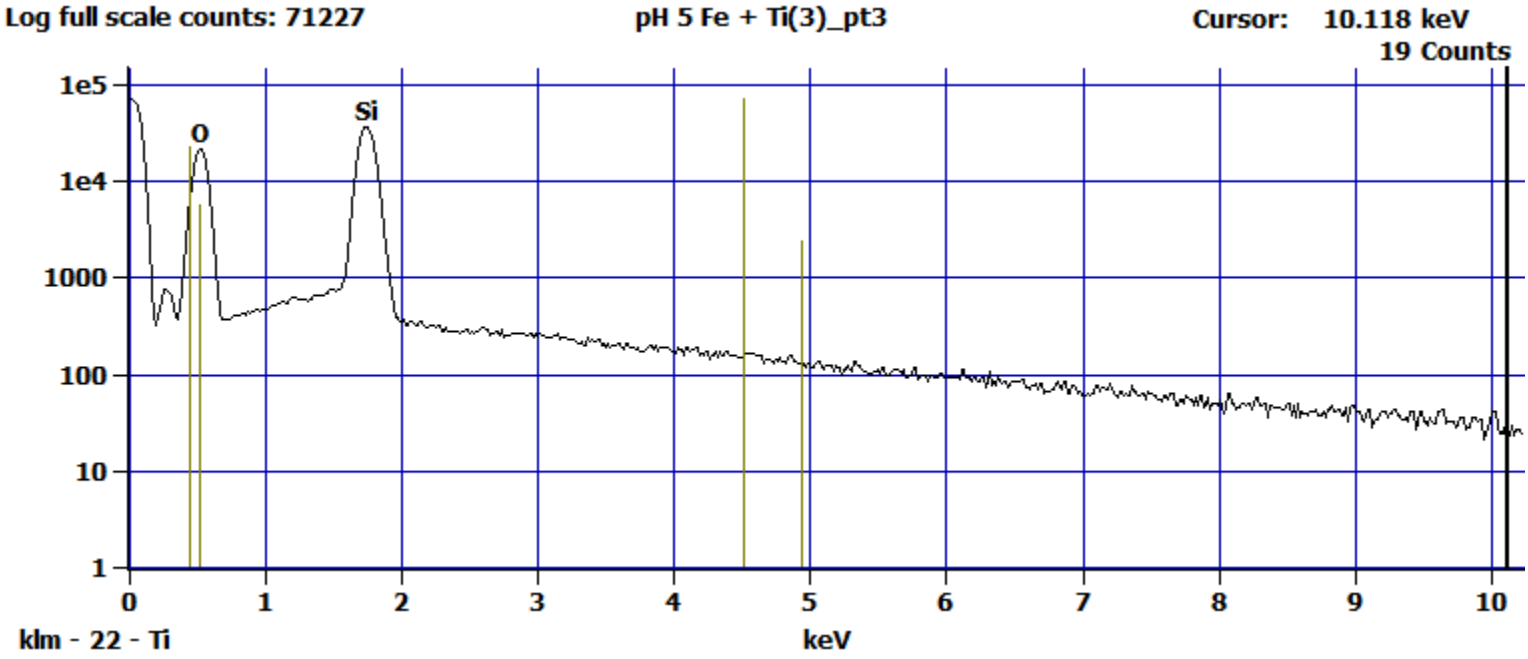

Project: Yang

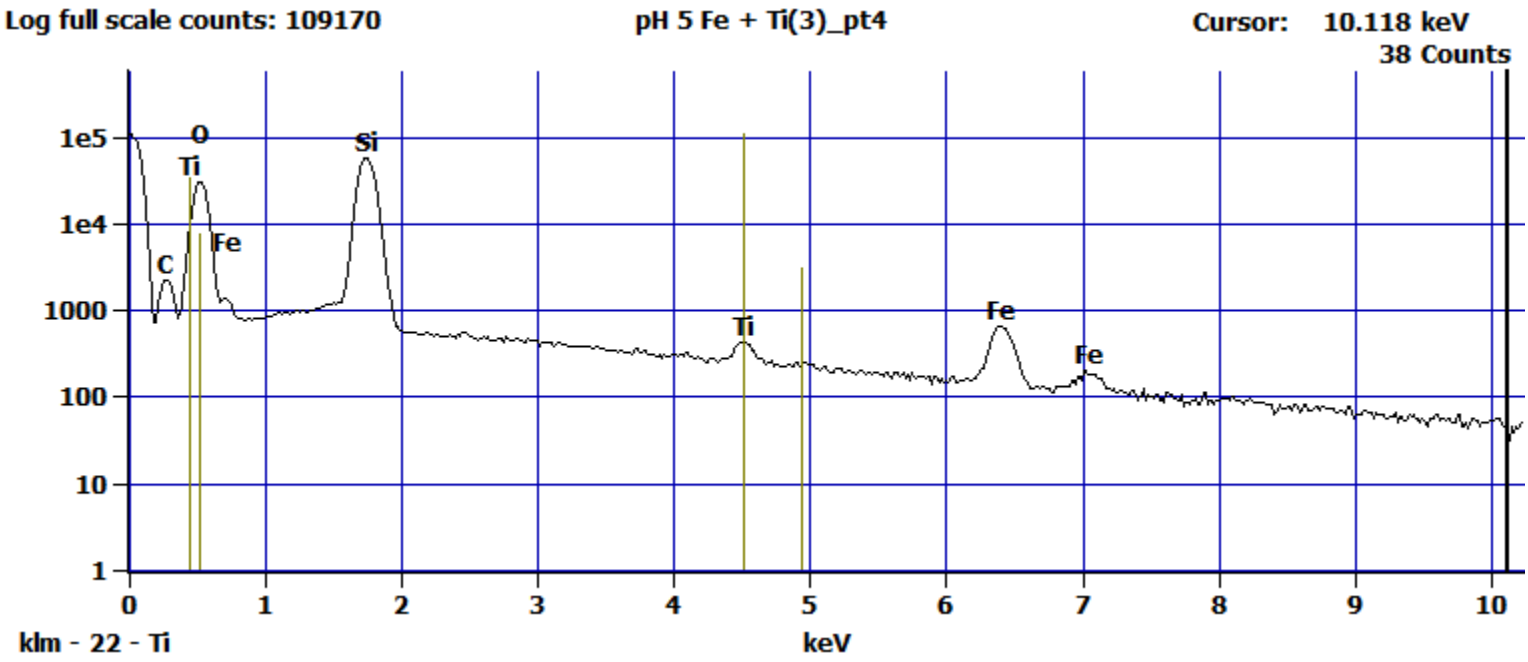

Project: Yang

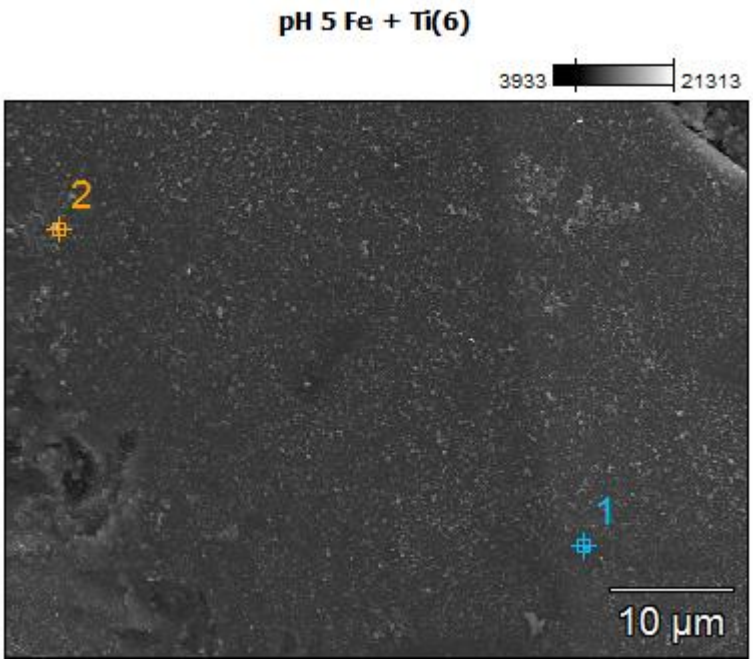

Image Name:	pH 5 Fe + Ti(6)
Image Resolution:	512 by 384
Image Pixel Size:	0.12 µm
Acc. Voltage:	15.0 kV
Magnification:	2000

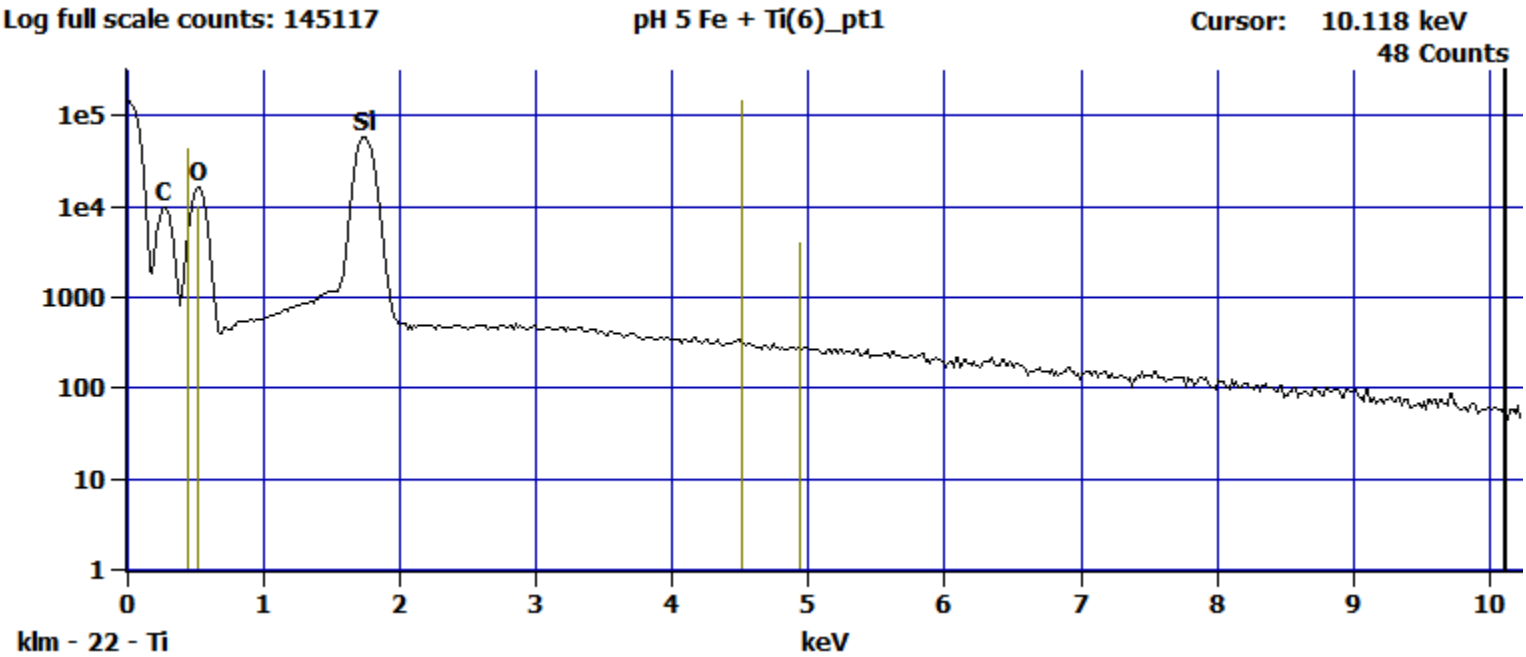

Project: Yang

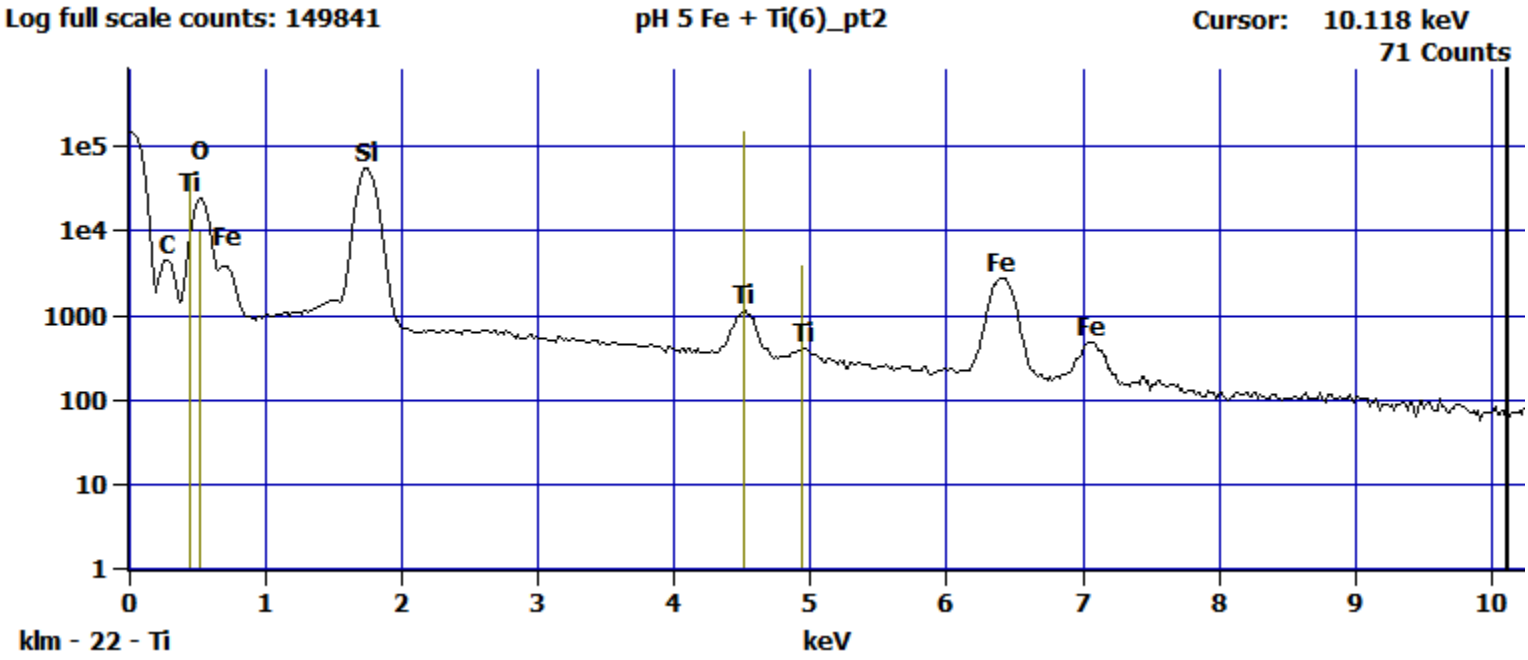

Project: Yang

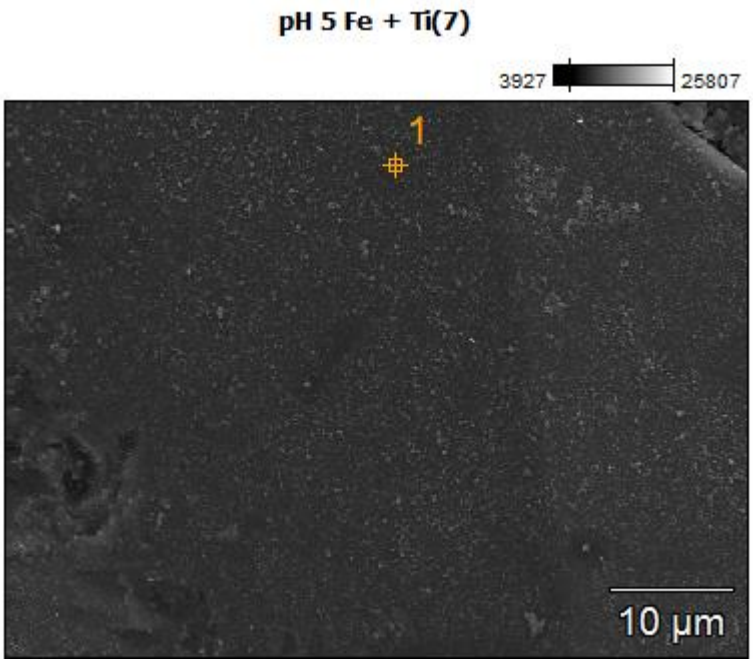

Image Name:	pH 5 Fe + Ti(7)
Image Resolution:	512 by 384
Image Pixel Size:	0.12 µm
Acc. Voltage:	15.0 kV
Magnification:	2000

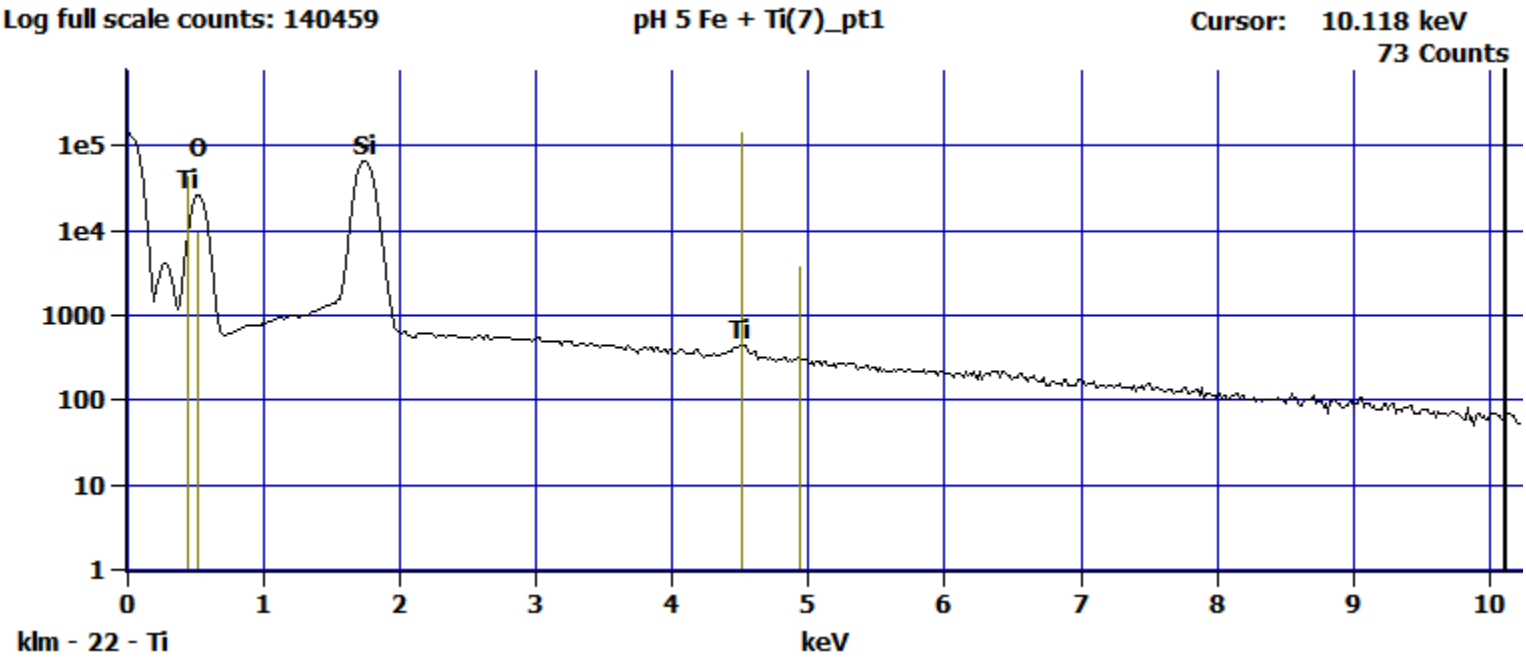

Project: Yang

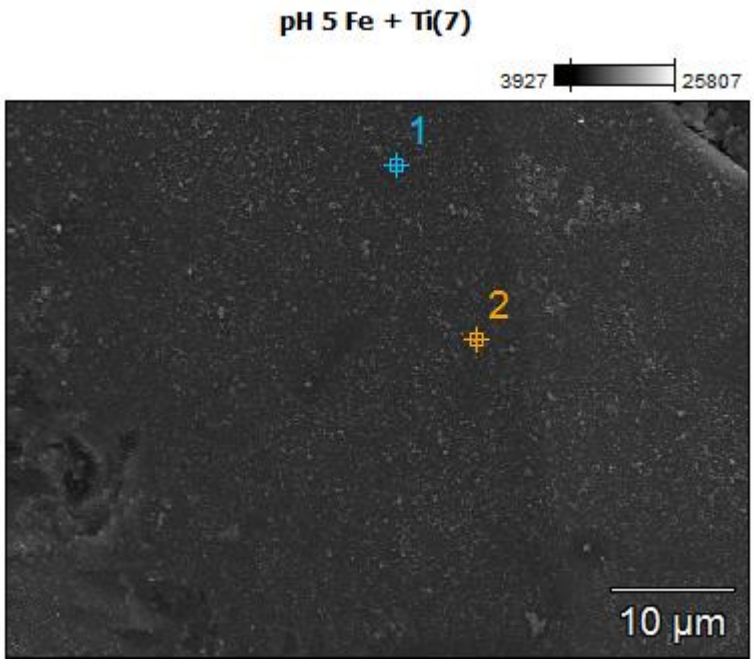

Image Name:	pH 5 Fe + Ti(7)
Image Resolution:	512 by 384
Image Pixel Size:	0.12 µm
Acc. Voltage:	15.0 kV
Magnification:	2000

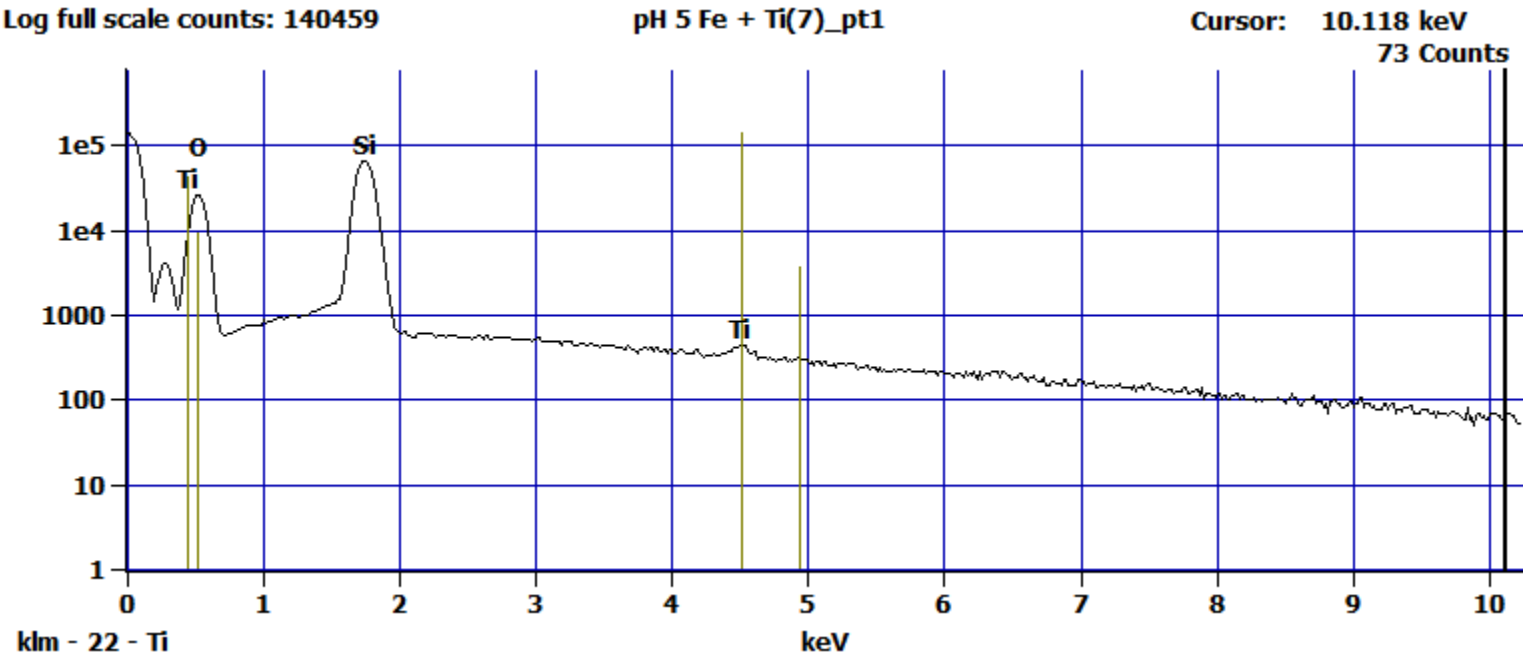

Project: Yang

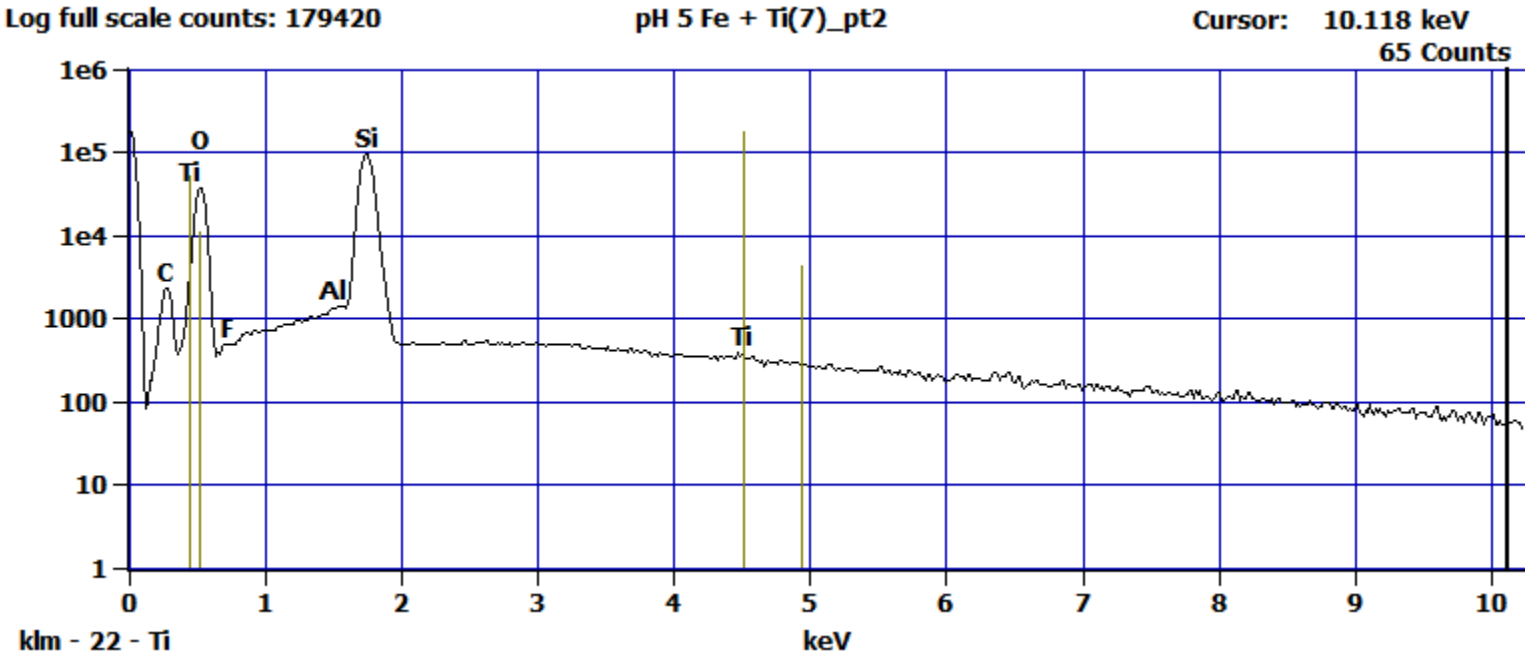

Project: Yang

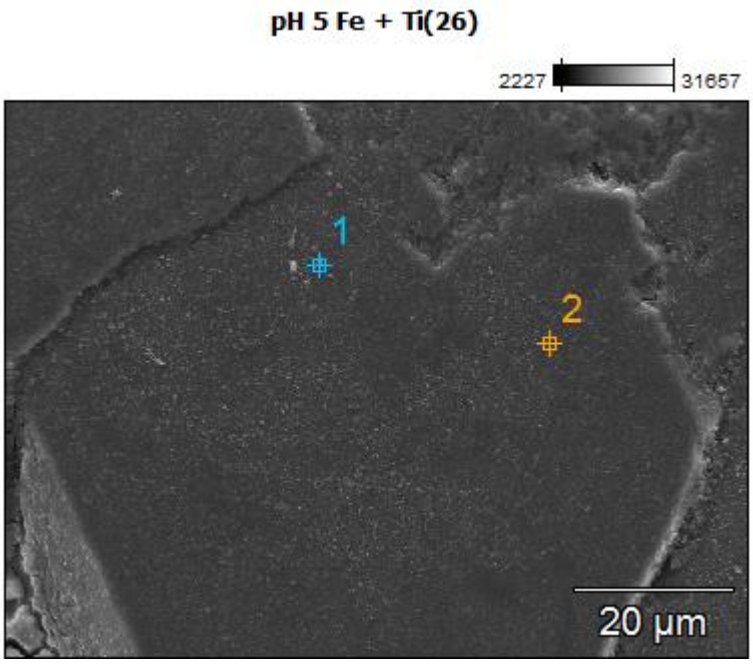

Image Name:	pH 5 Fe + Ti(26)
Image Resolution:	512 by 384
Image Pixel Size:	0.18 µm
Acc. Voltage:	15.0 kV
Magnification:	1300

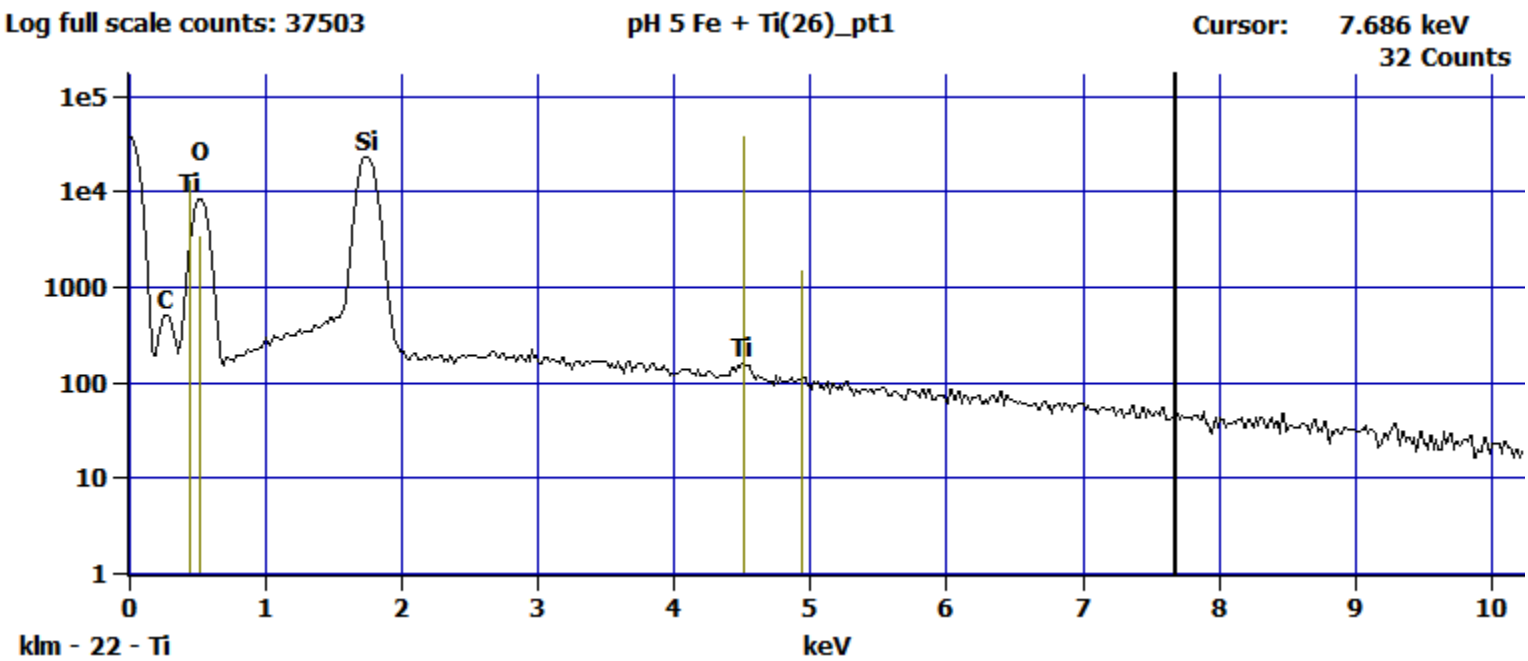

Project: Yang

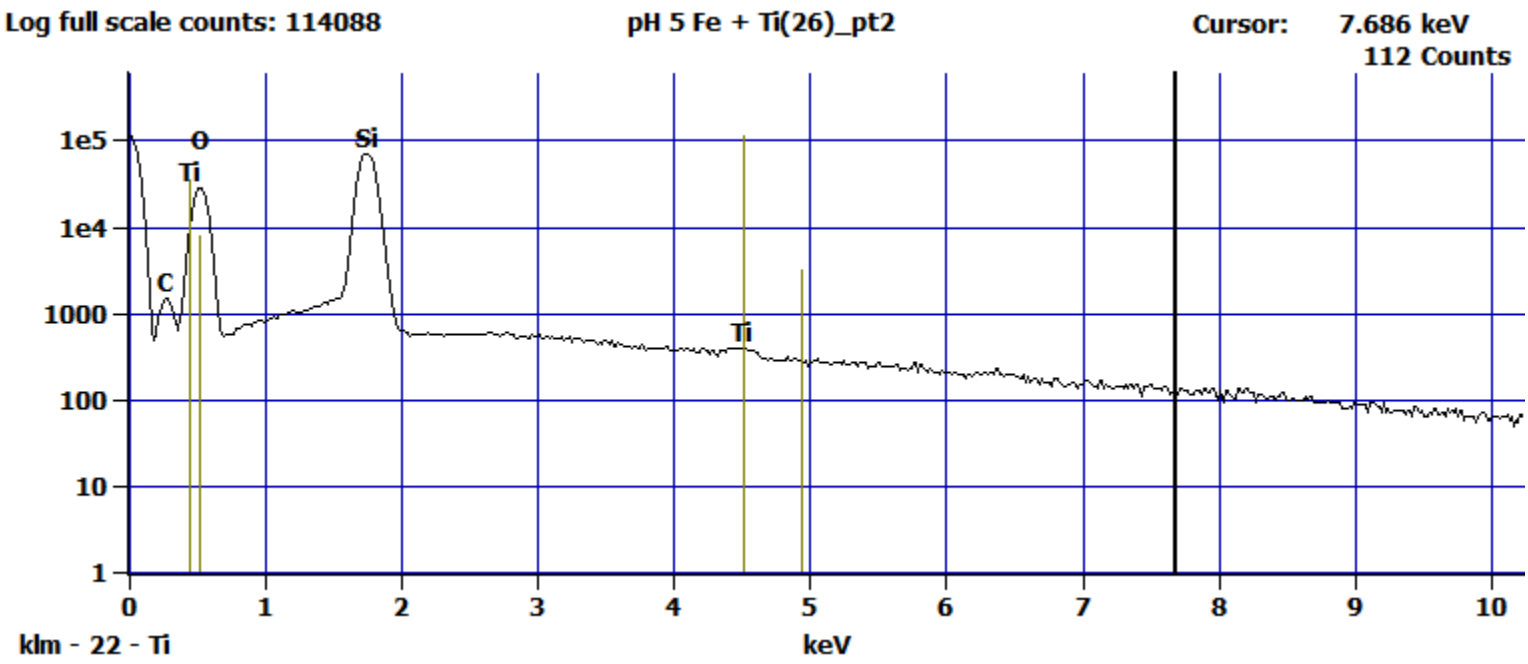

Project: Yang

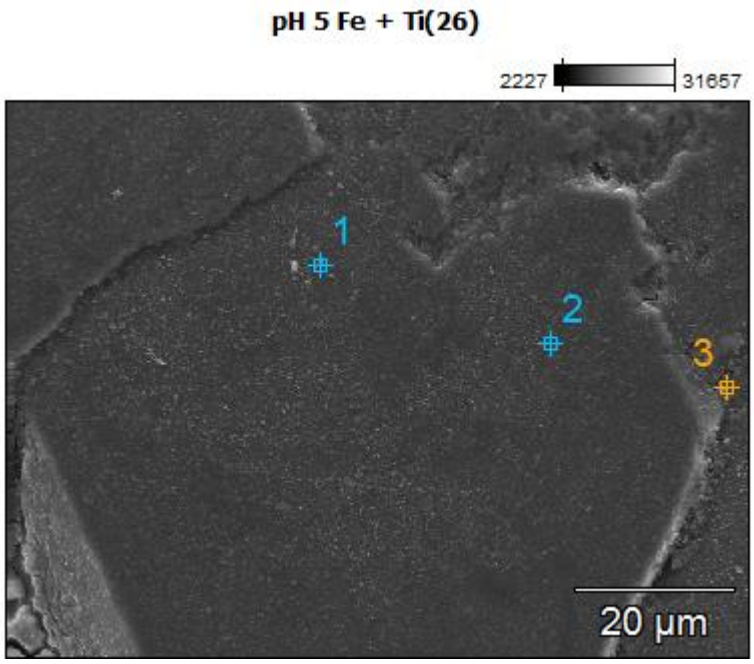

Image Name:	pH 5 Fe + Ti(26)
Image Resolution:	512 by 384
Image Pixel Size:	0.18 µm
Acc. Voltage:	15.0 kV
Magnification:	1300

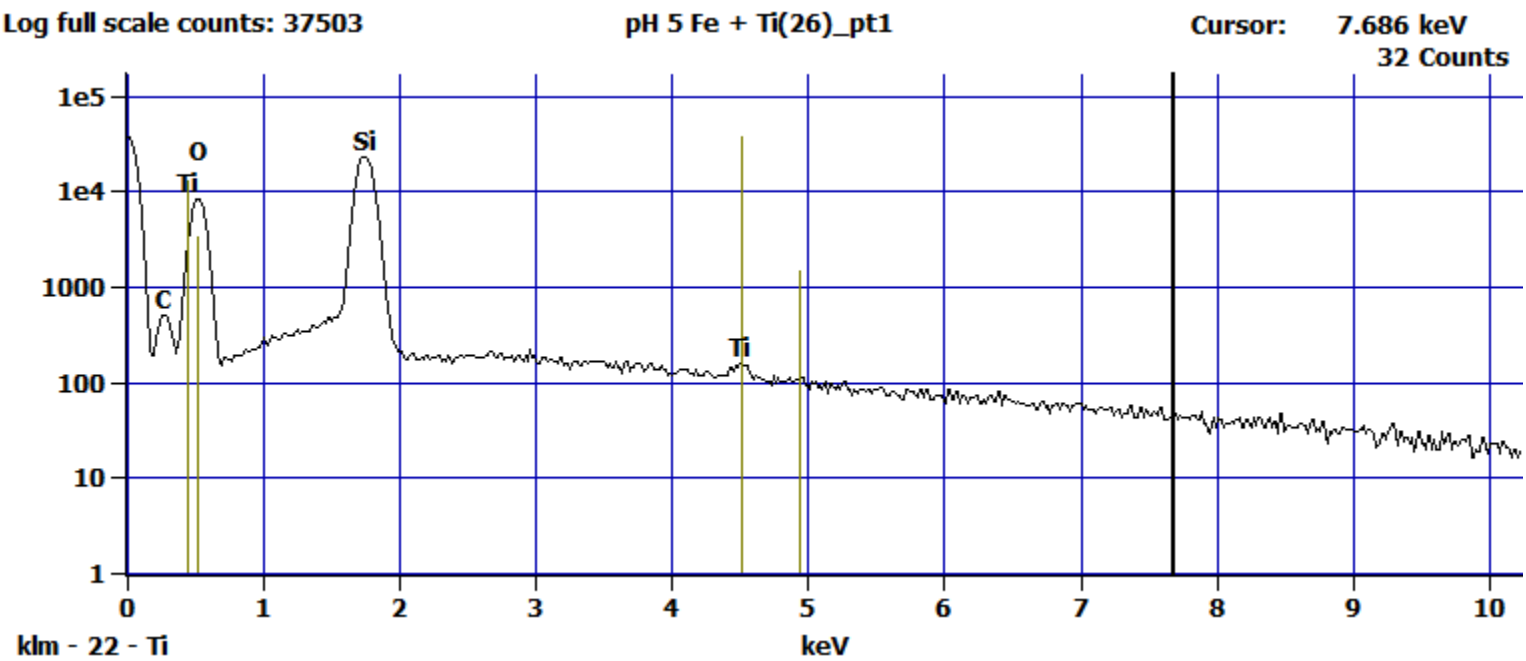

Project: Yang

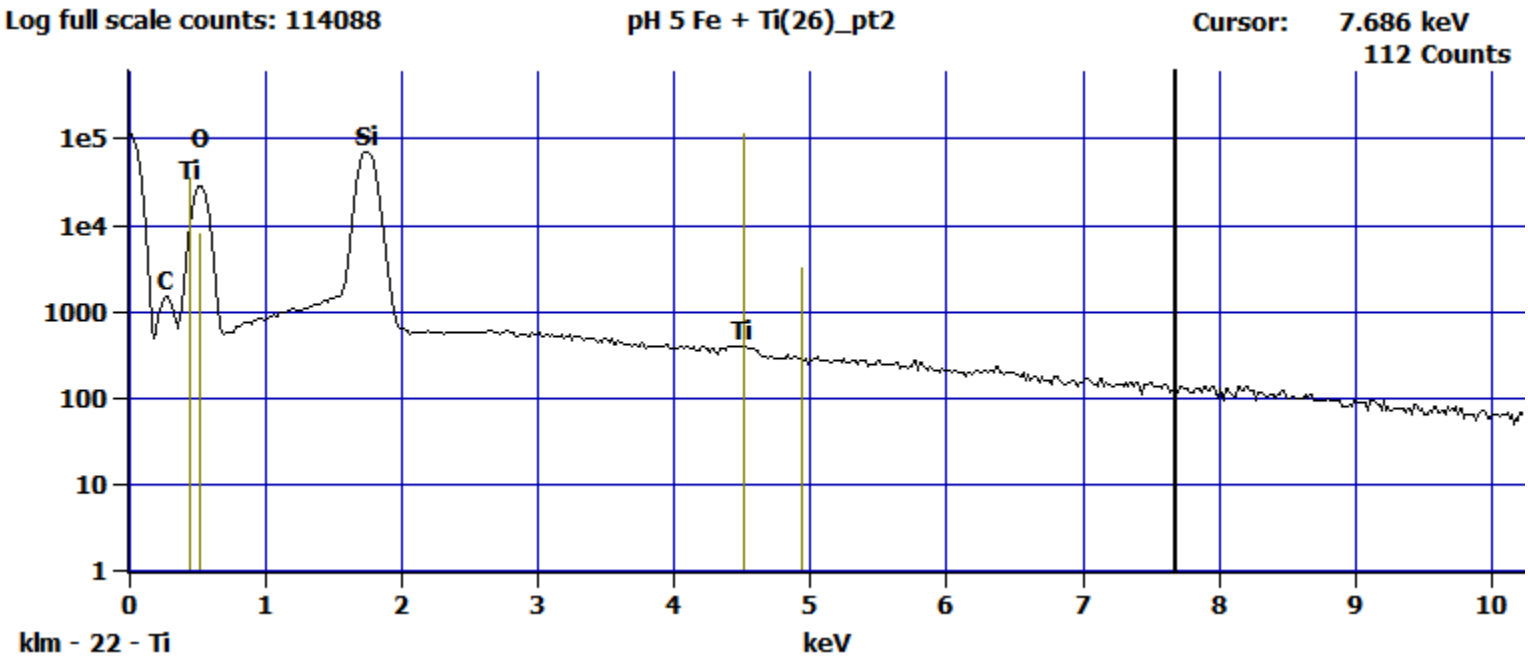

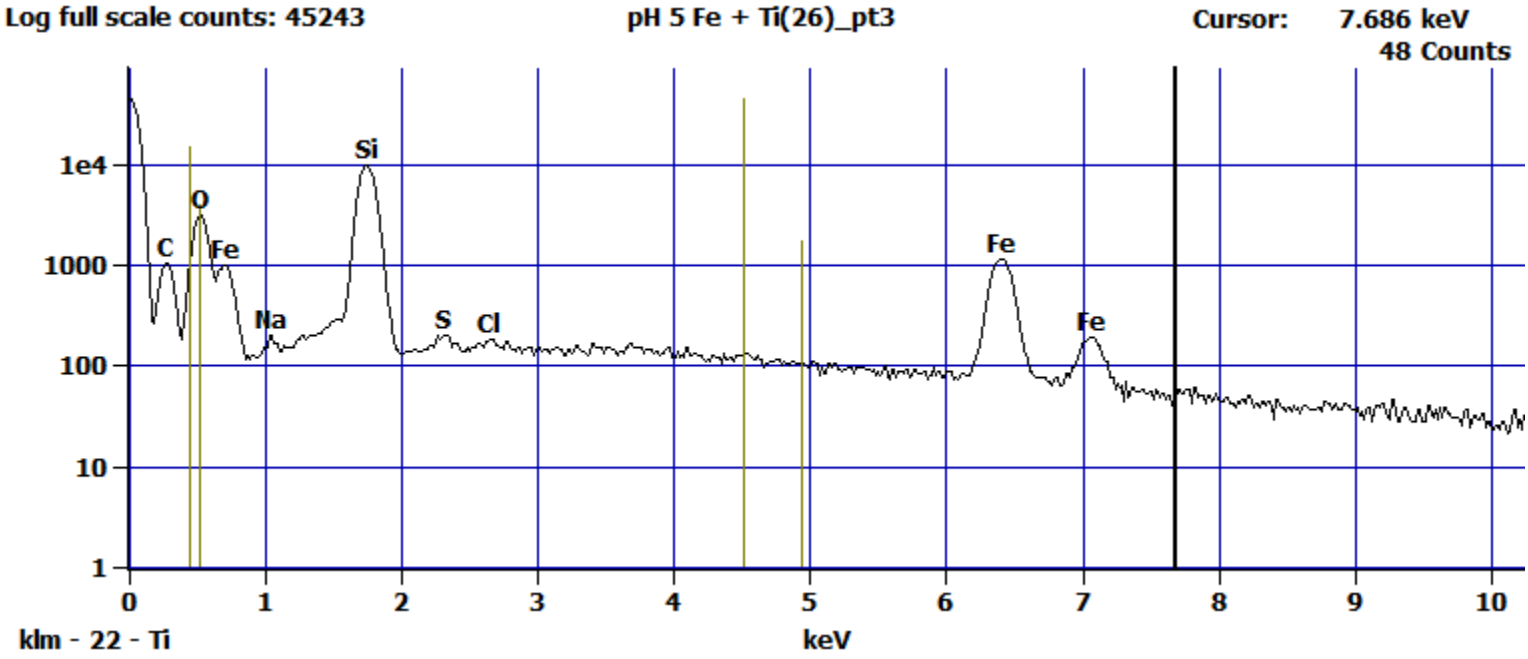

Project: Yang

EDX of quartz sand + $nTiO_2$ at pH 9

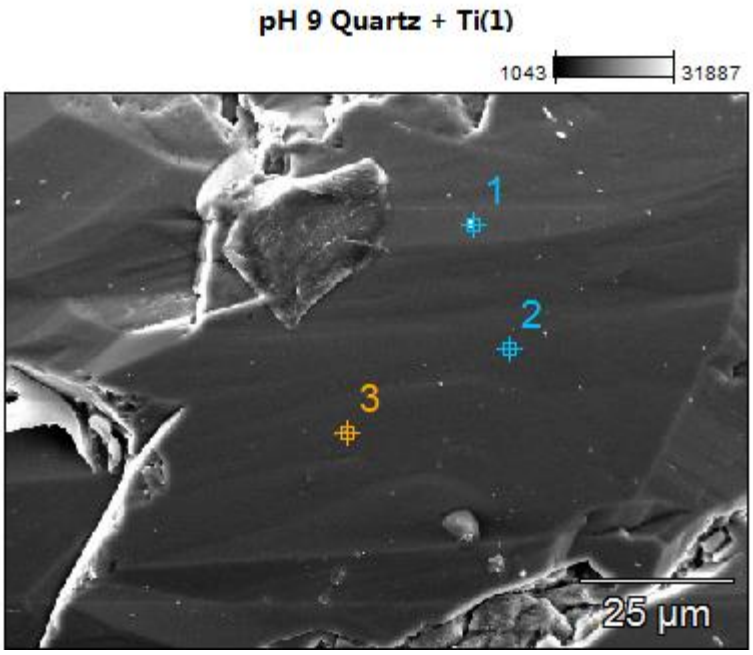

Image Name:	pH 9 Quartz + Ti
Image Resolution:	512 by 384
Image Pixel Size:	0.24 µm
Acc. Voltage:	15.0 kV
Magnification:	1000

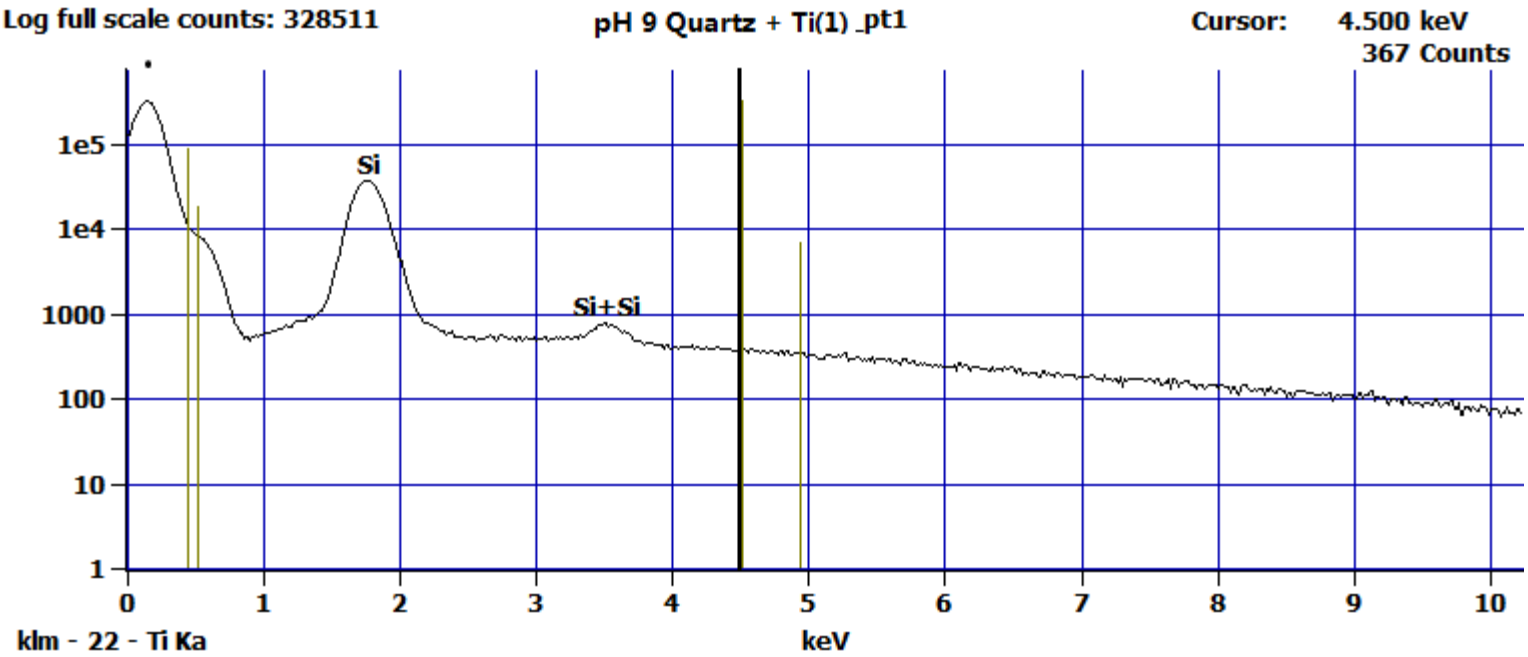

Project: Yang

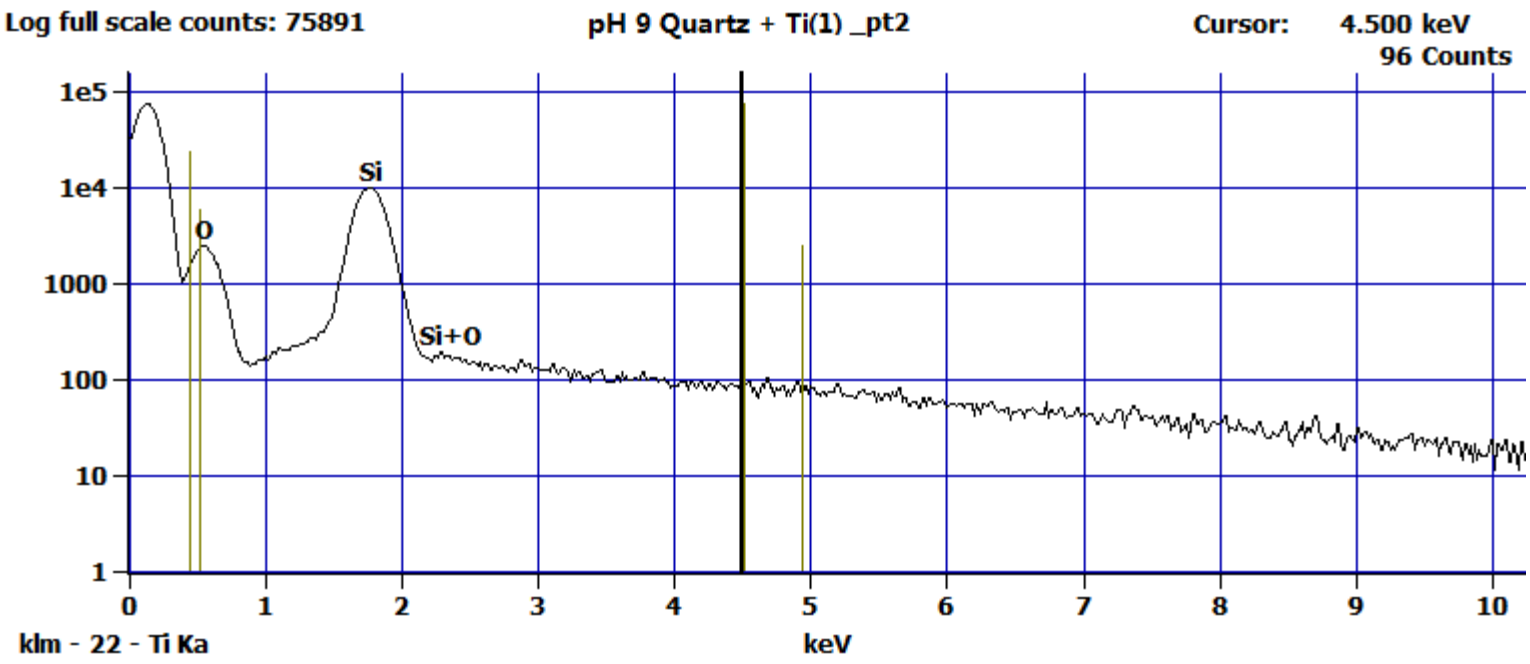

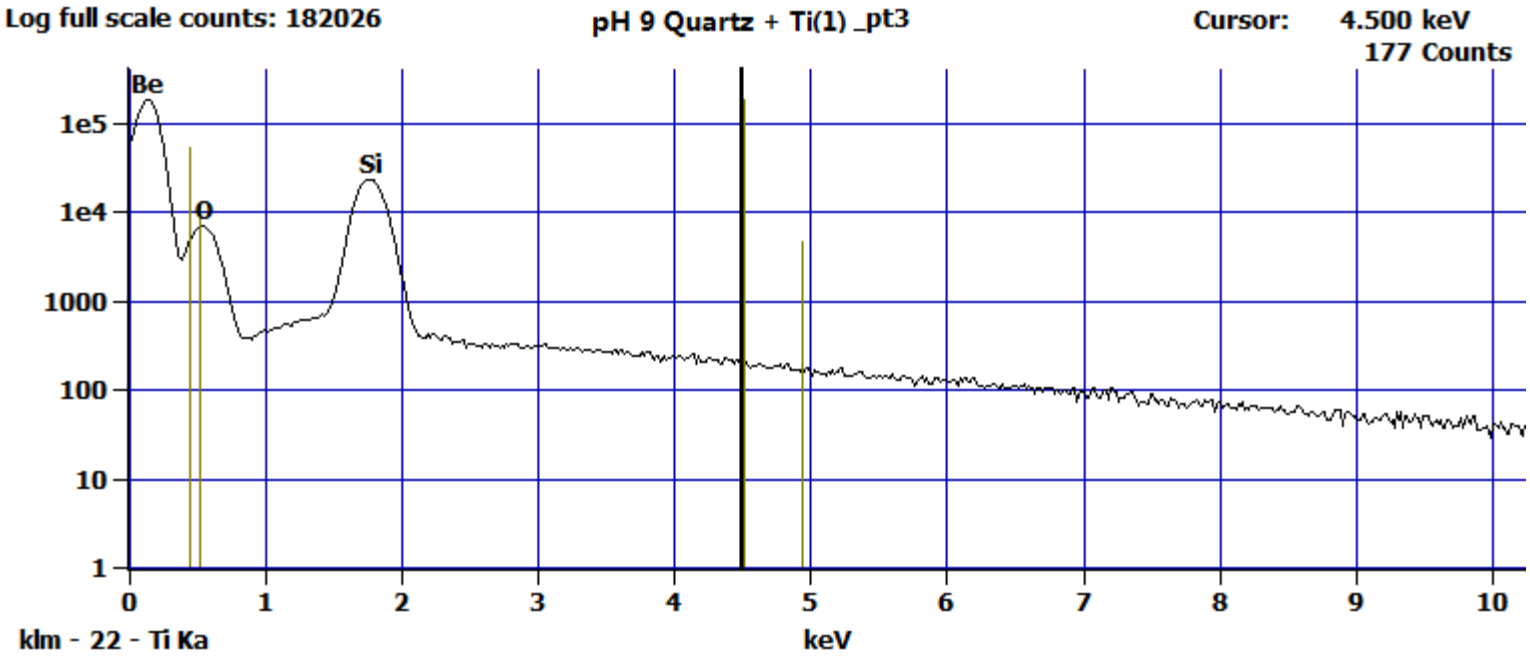

Project: Yang

EDX of Fe coated sand + $nTiO_2$ at pH 9

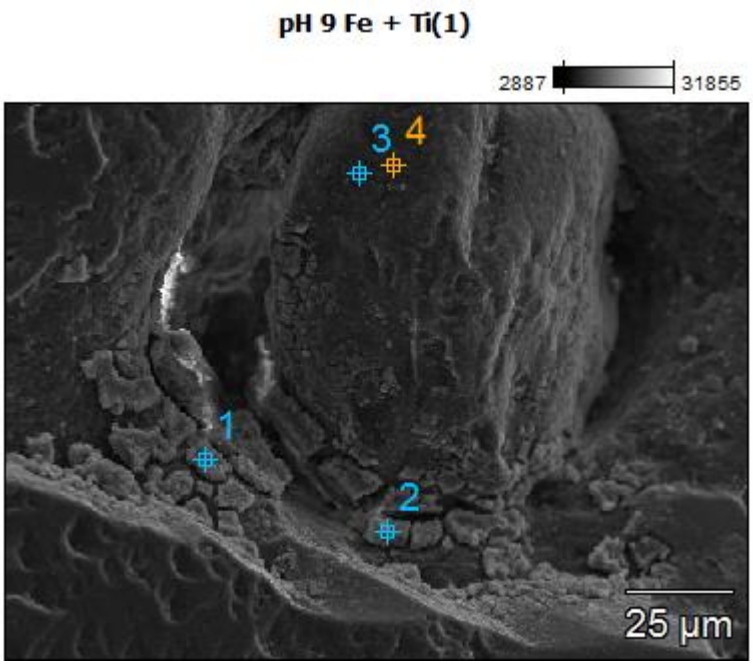

Image Name:	pH 9 Fe + Ti(1)
Image Resolution:	512 by 384
Image Pixel Size:	0.34 µm
Acc. Voltage:	15.0 kV
Magnification:	700

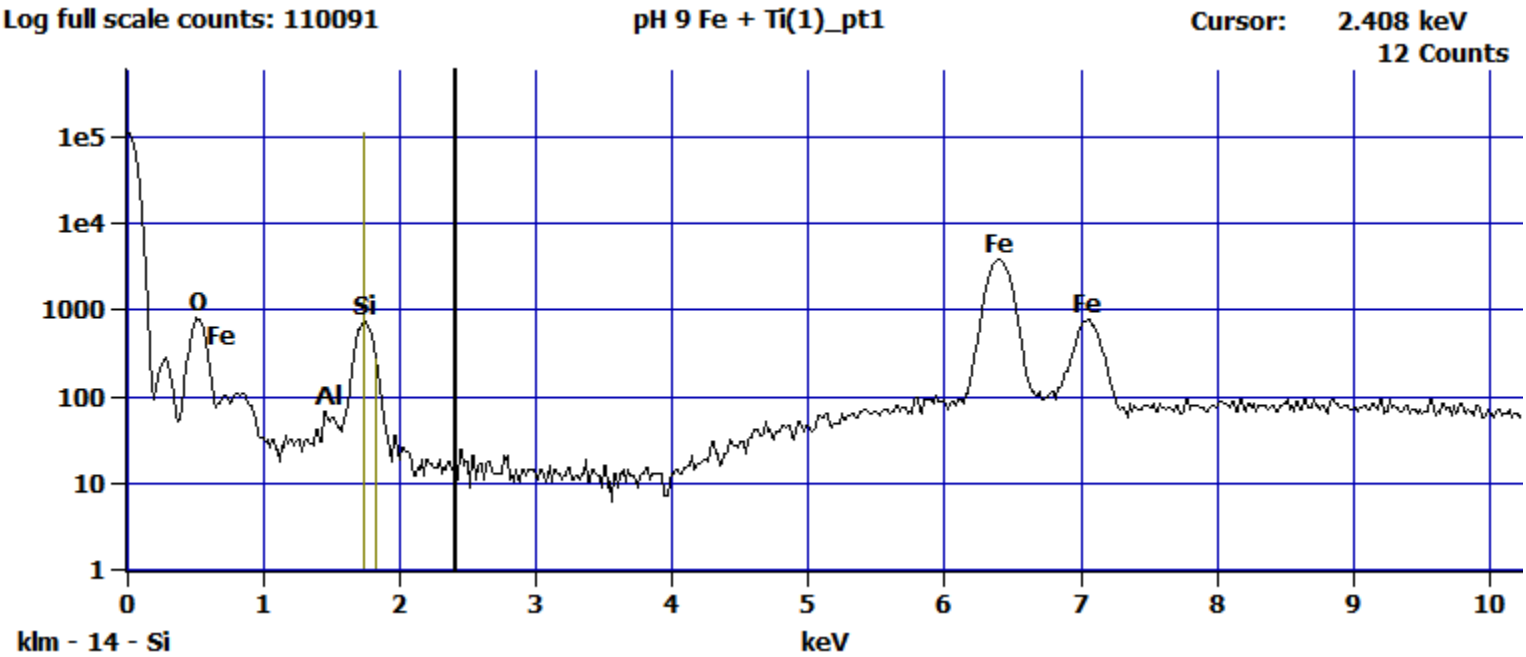

Project: Yang

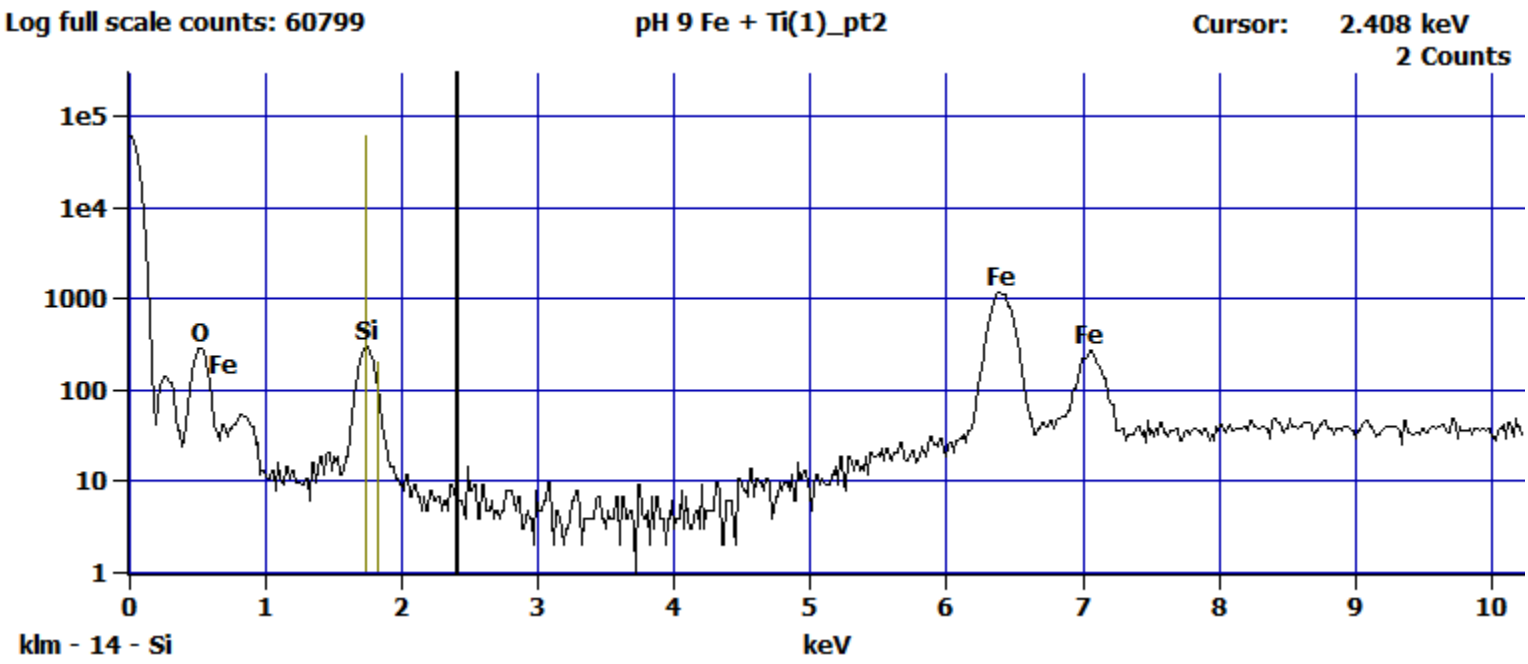

Project: Yang

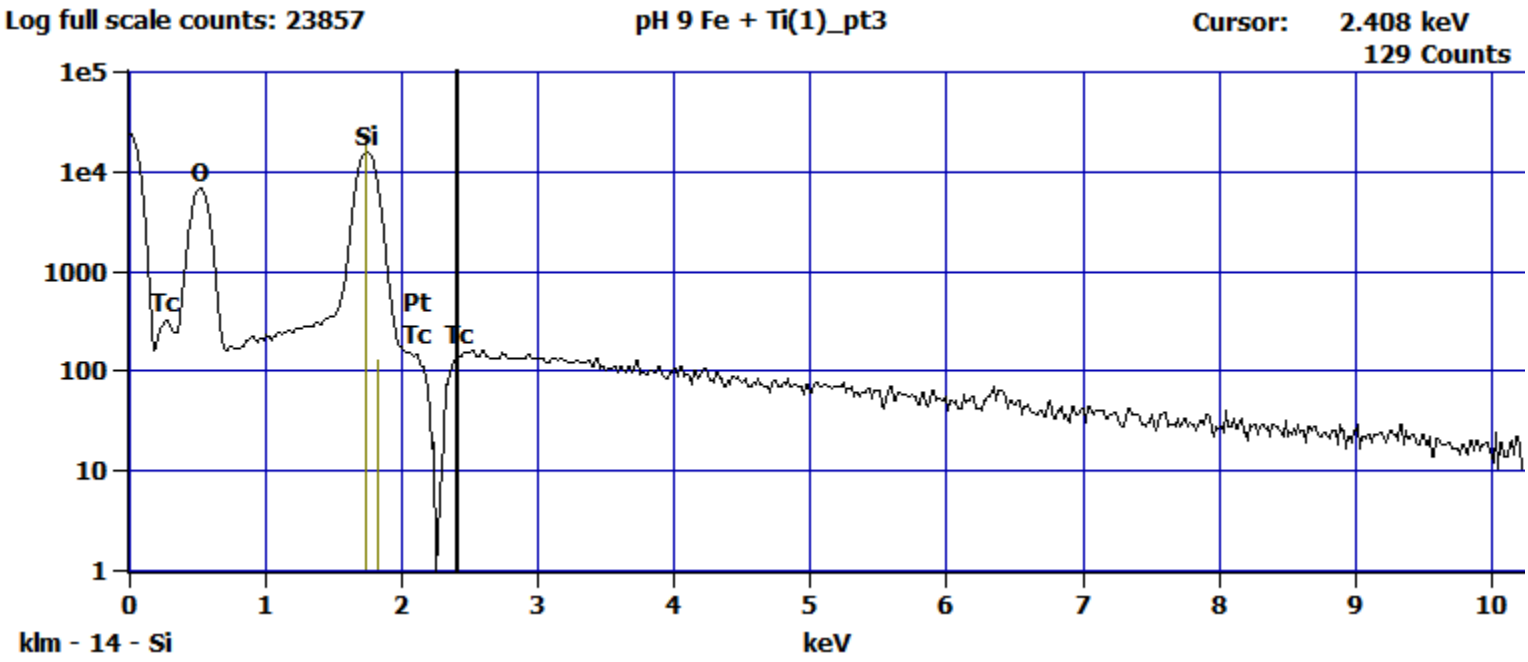

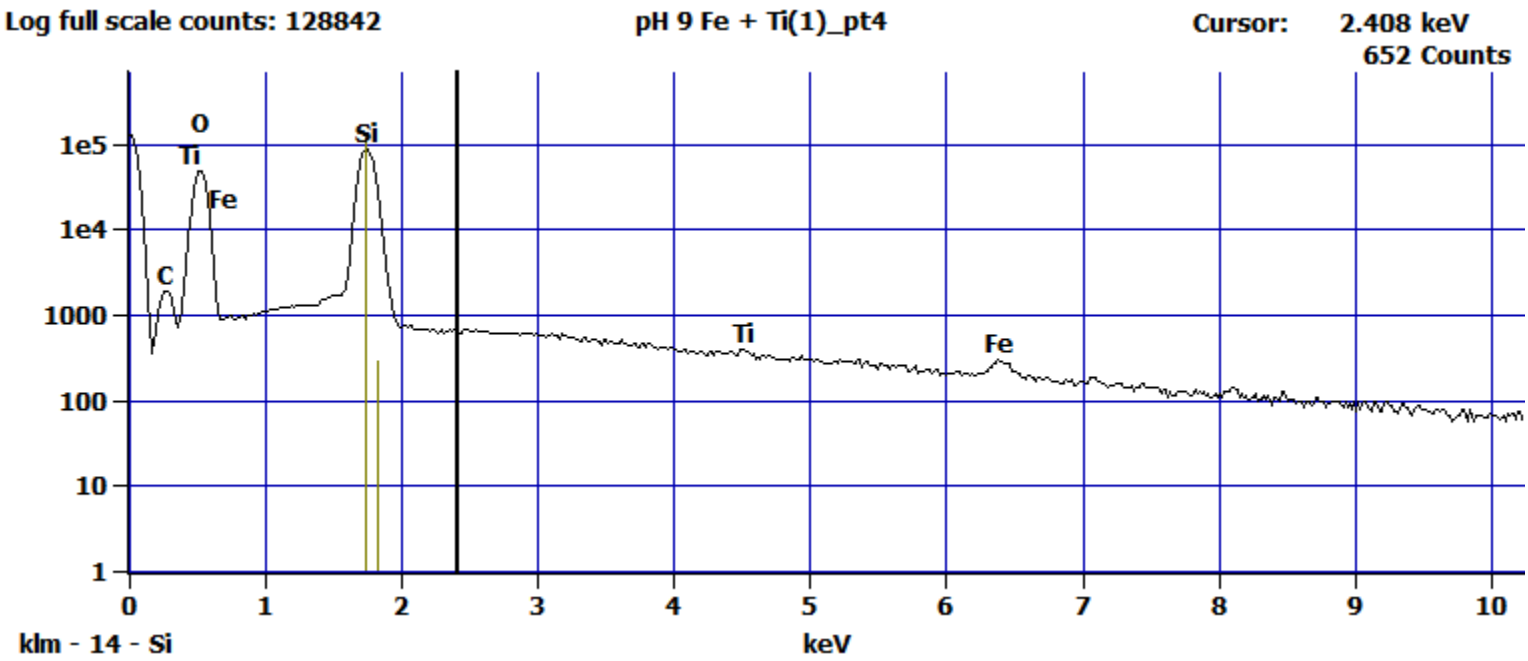

Project: Yang

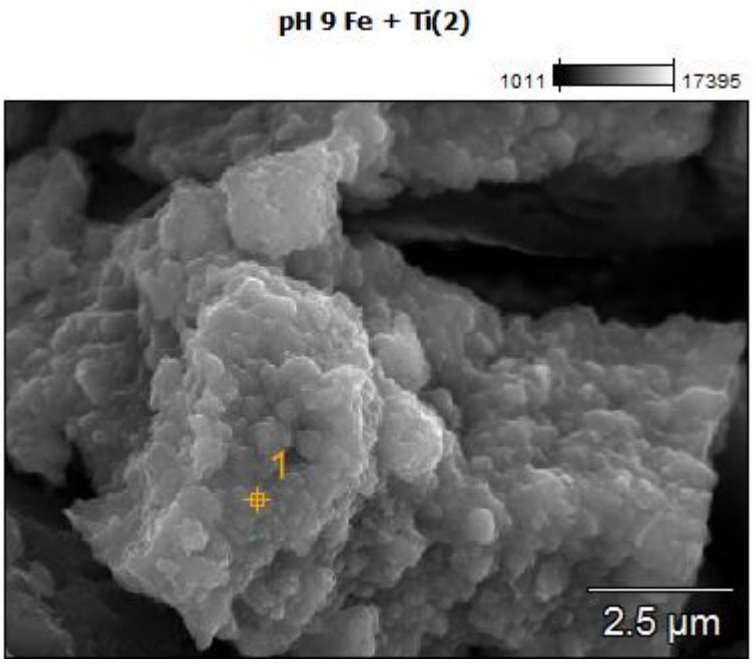

Image Name:	pH 9 Fe + Ti(2)
Image Resolution:	512 by 384
Image Pixel Size:	0.02 µm
Acc. Voltage:	15.0 kV
Magnification:	9500

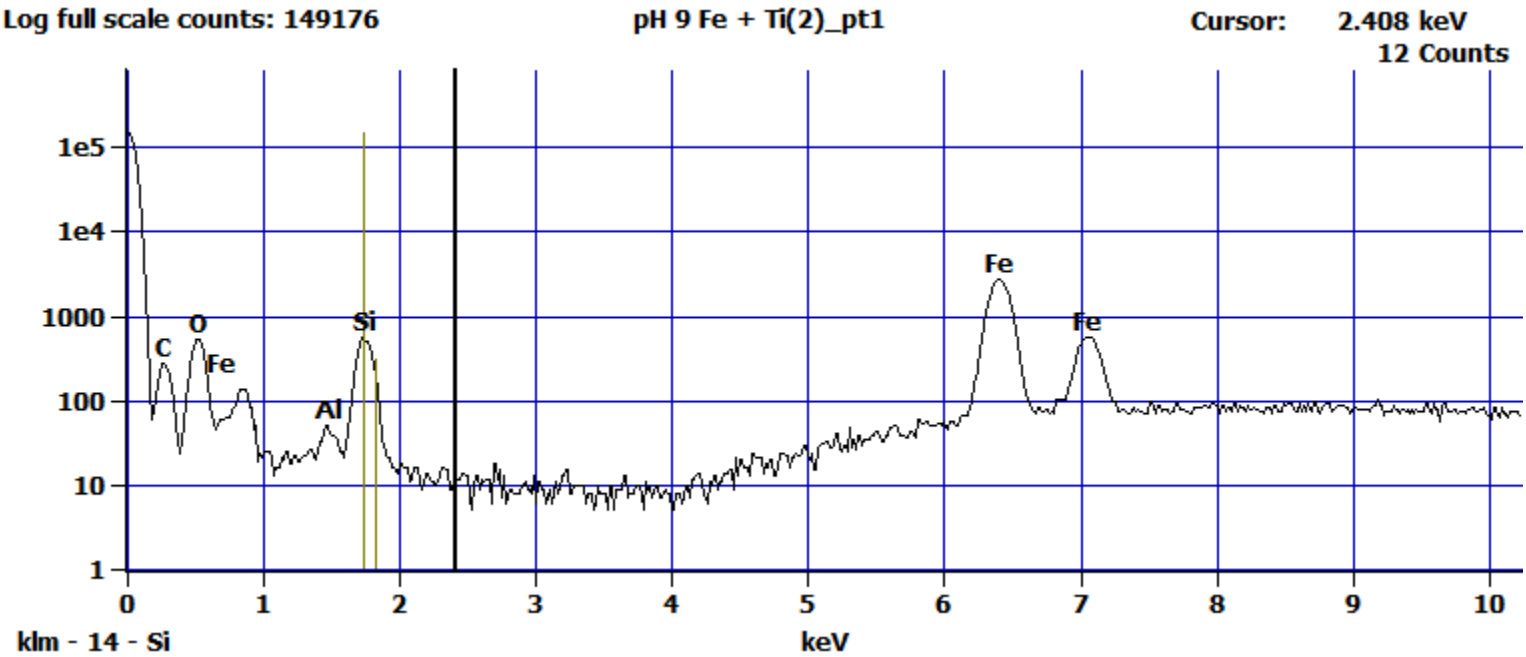

Project: Yang

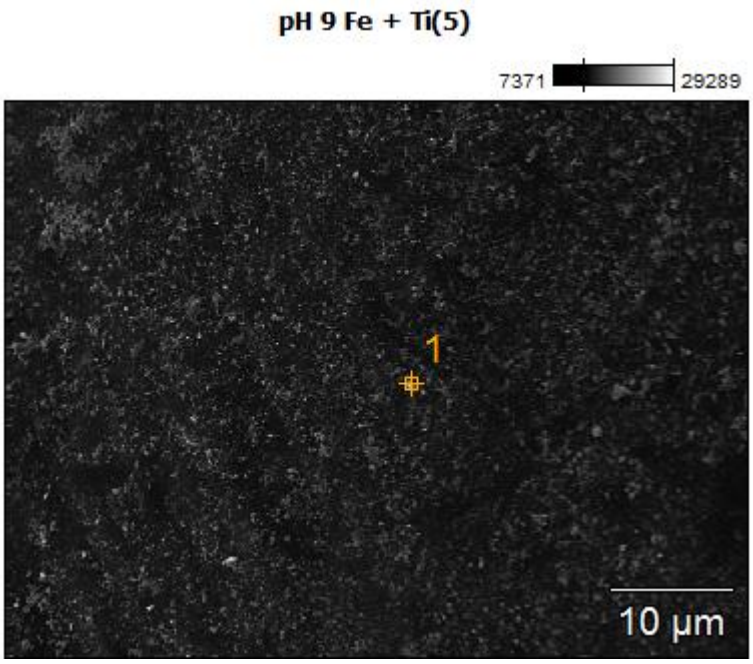

Image Name:	pH 9 Fe + Ti(5)
Image Resolution:	512 by 384
Image Pixel Size:	0.12 µm
Acc. Voltage:	15.0 kV
Magnification:	2000

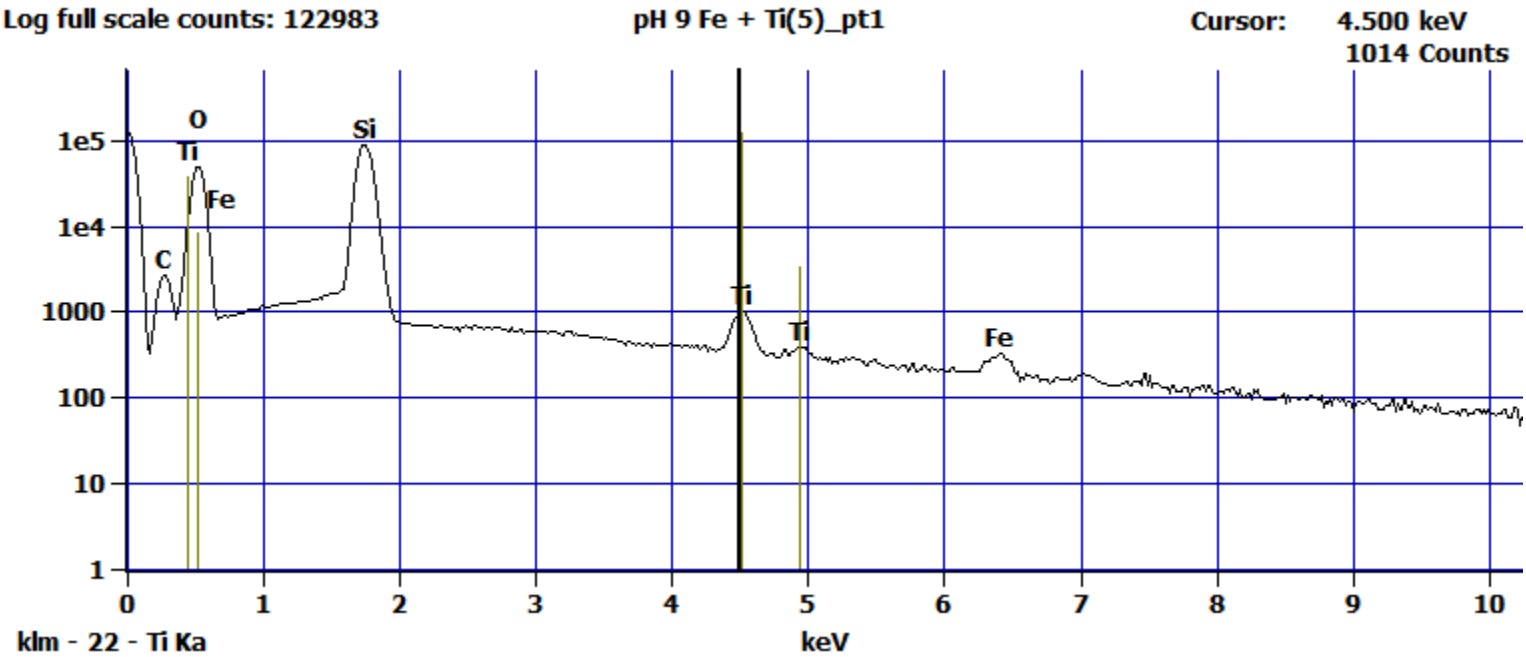

Project: Yang

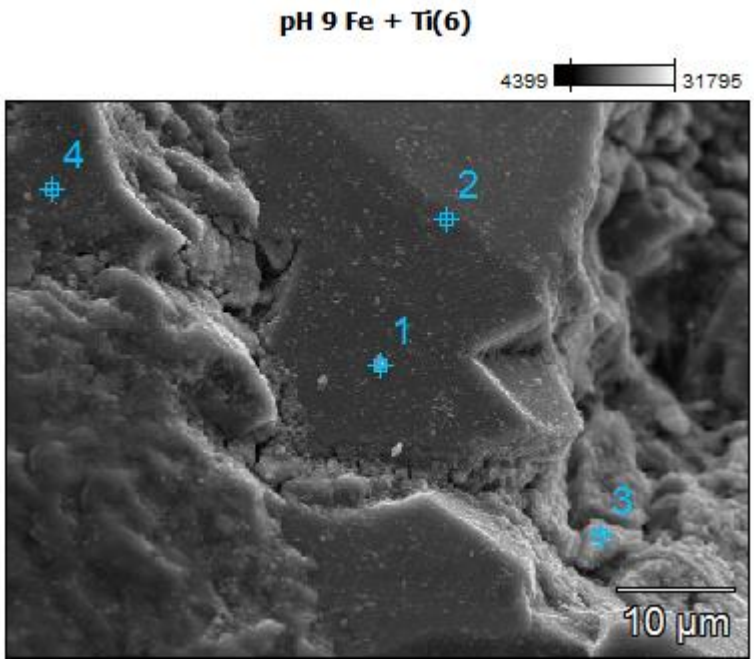

Image Name:	pH 9 Fe + Ti(6)
Image Resolution:	512 by 384
Image Pixel Size:	0.12 µm
Acc. Voltage:	15.0 kV
Magnification:	1900

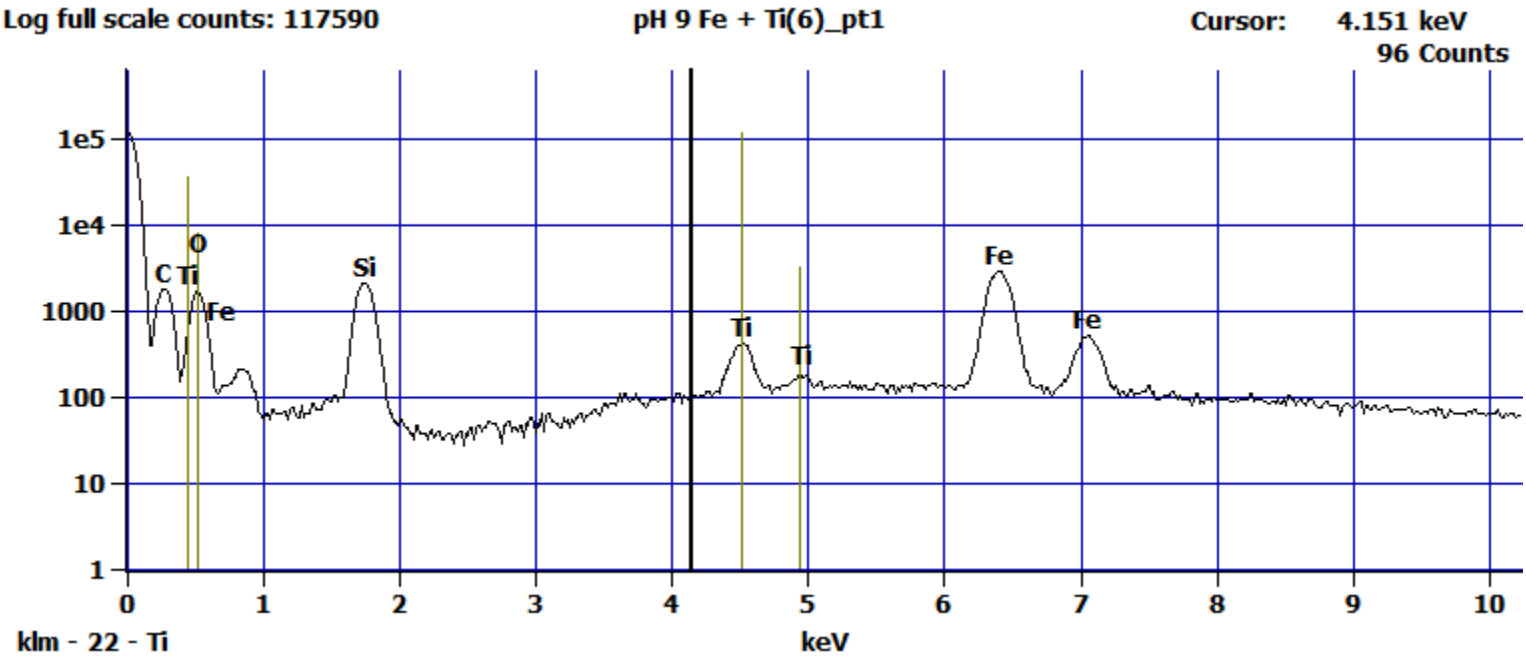

Project: Yang

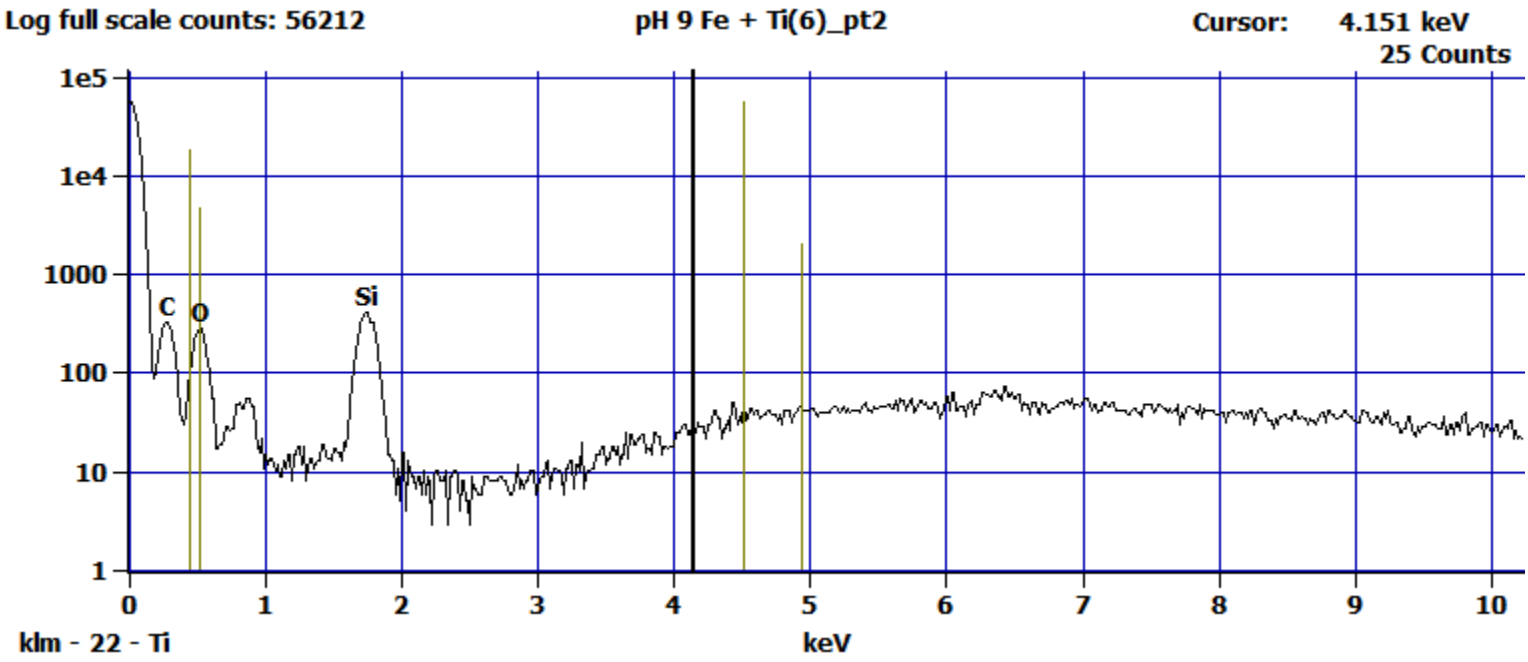

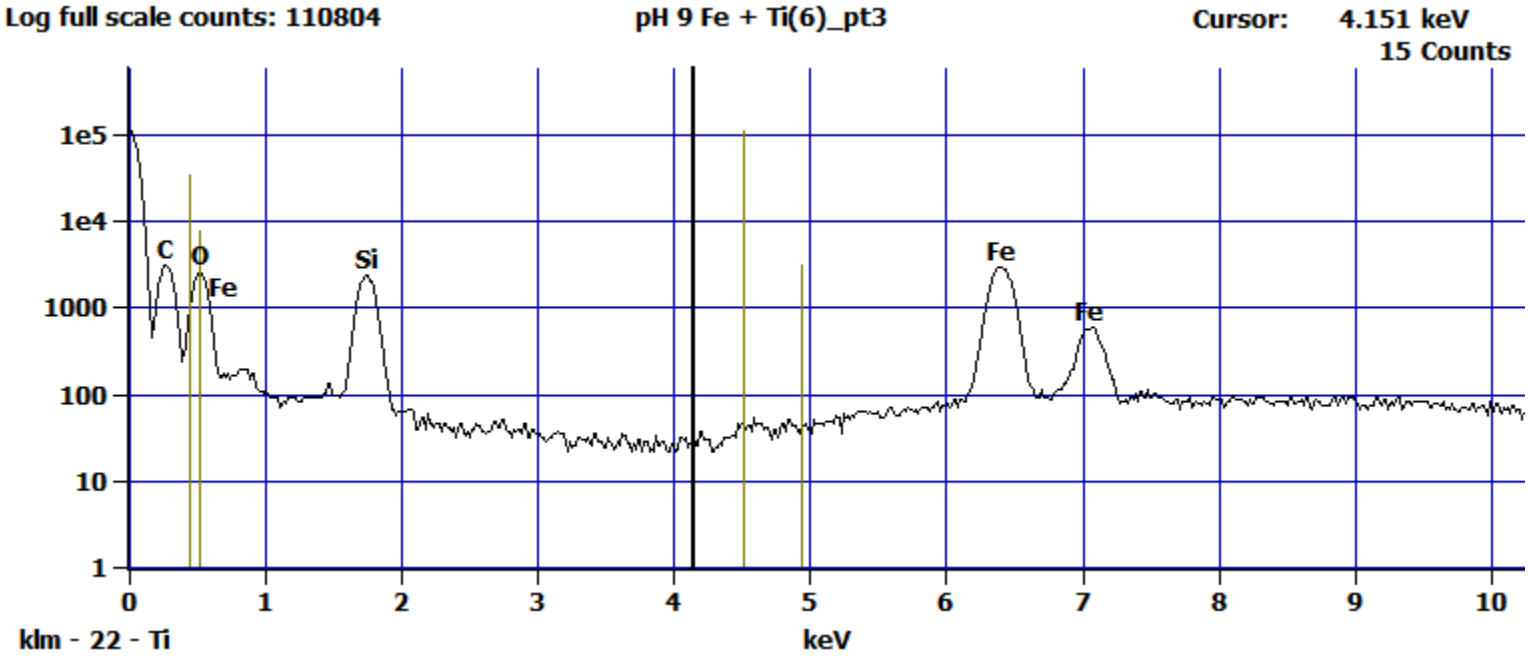

Project: Yang

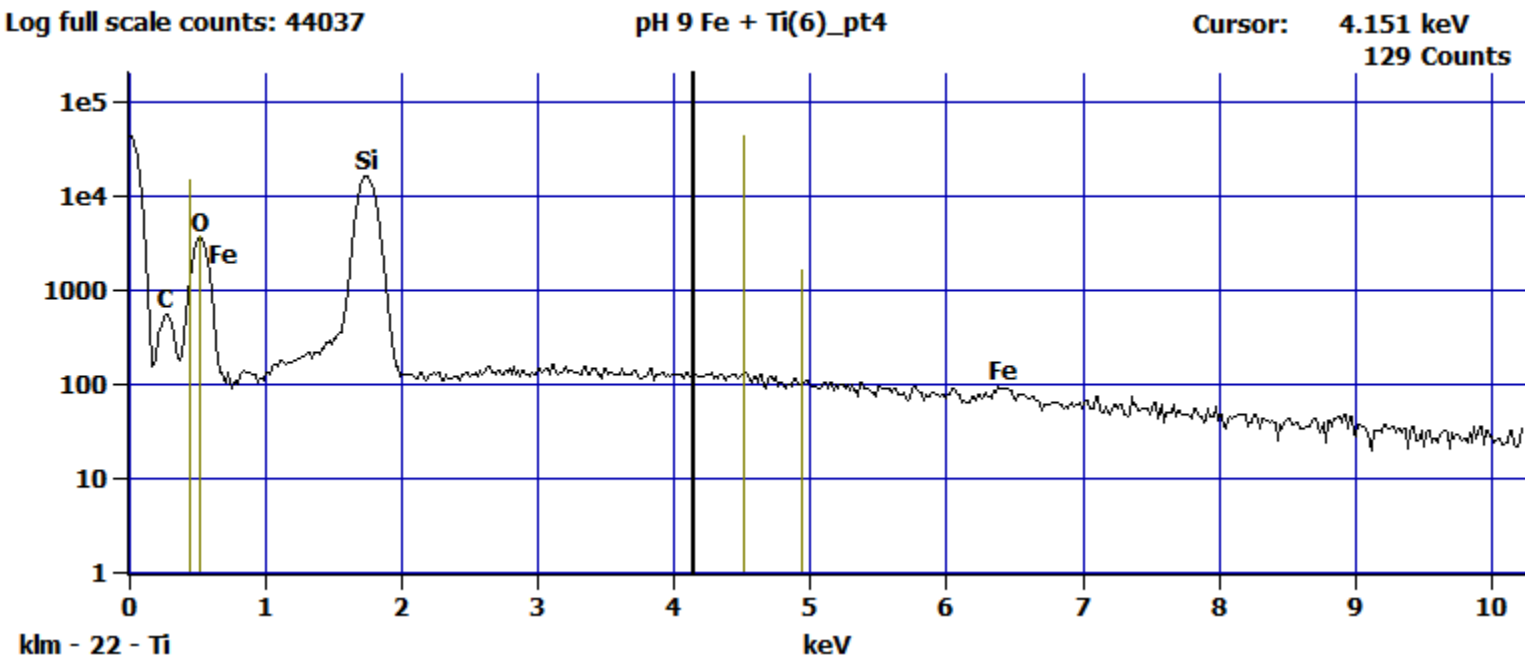

Project: Yang

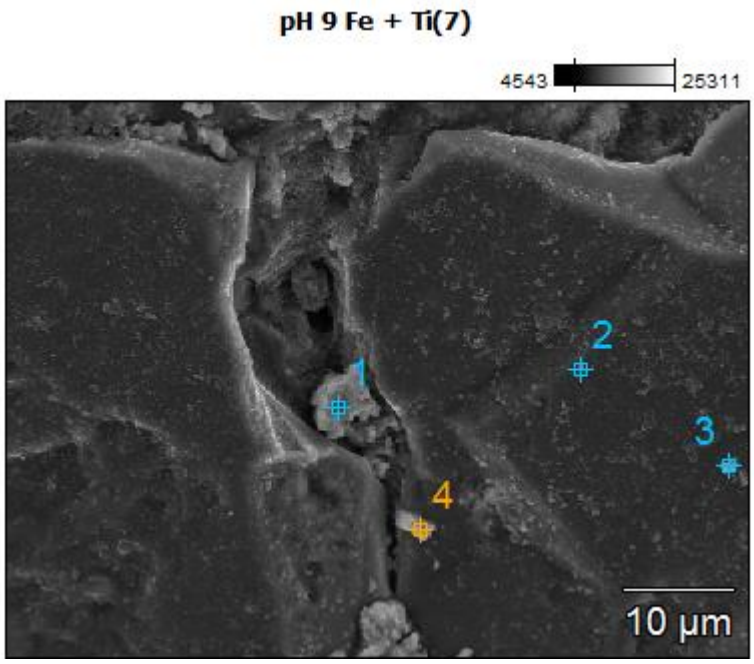

Image Name:	pH 9 Fe + Ti(7)
Image Resolution:	512 by 384
Image Pixel Size:	0.13 µm
Acc. Voltage:	15.0 kV
Magnification:	1799

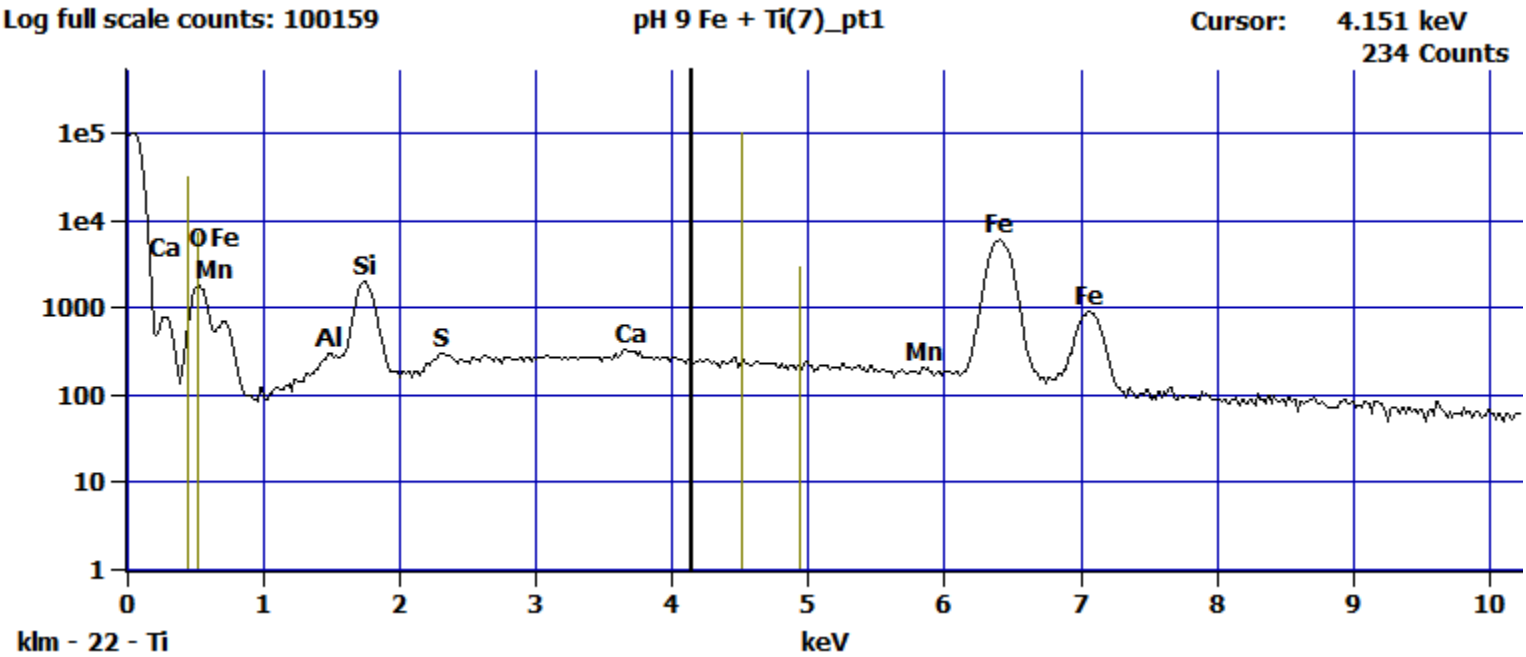

Project: Yang

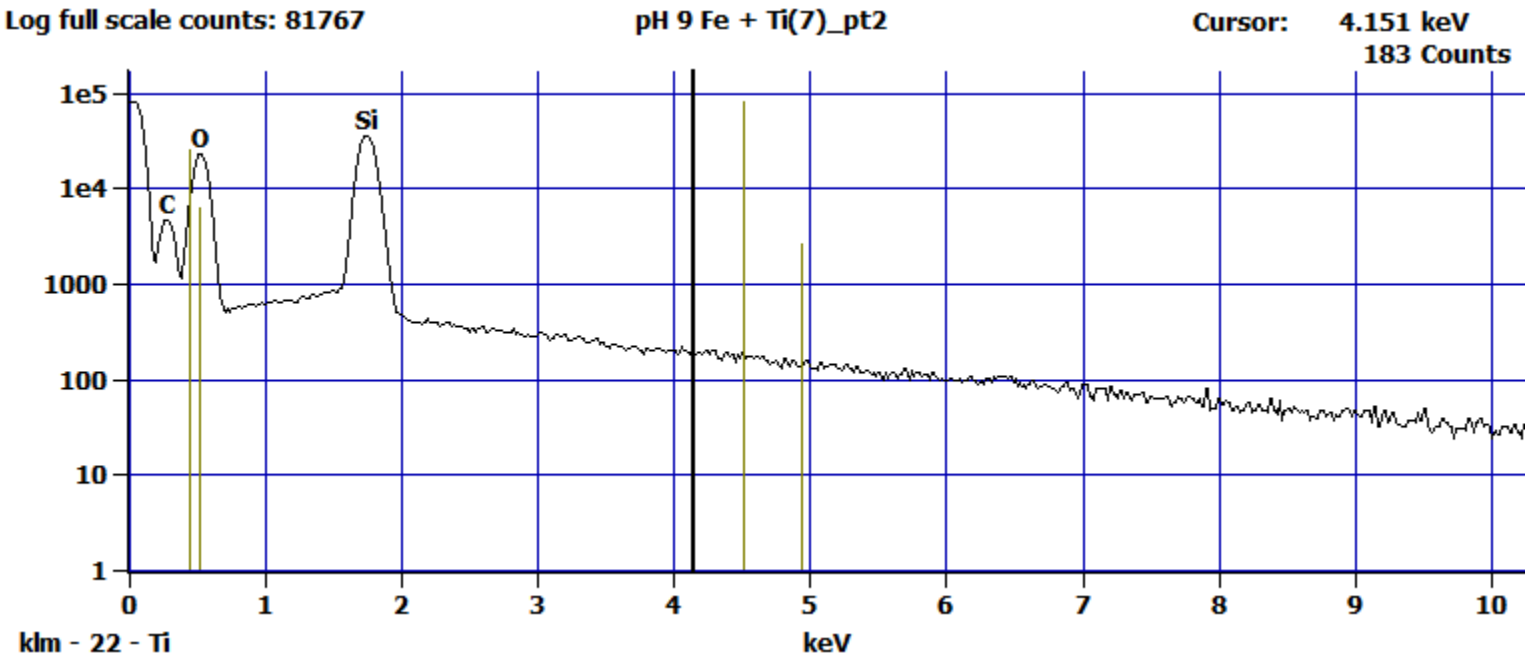

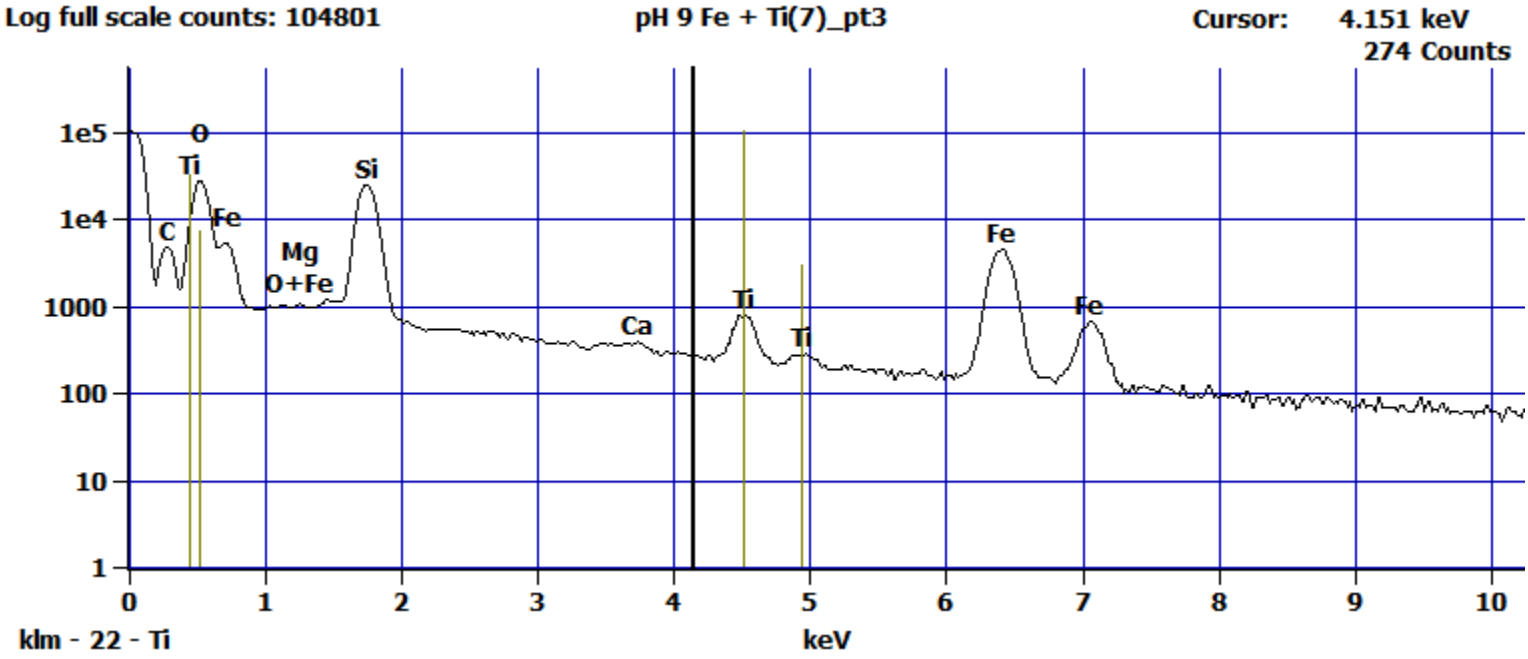

EDX mapping of Fe coated sand

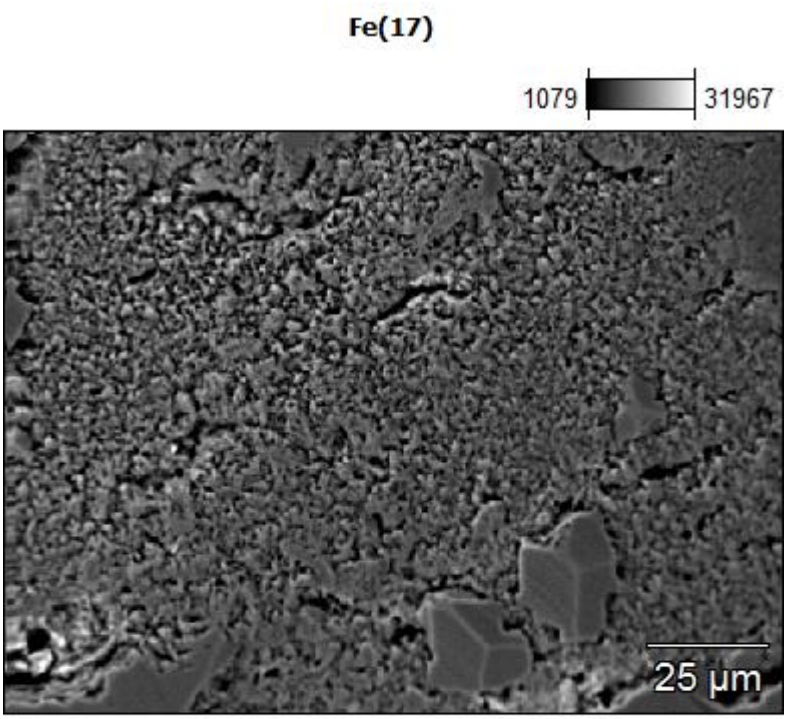

Data Type:	Counts
Image Resolution:	512 by 384
Image Pixel Size:	0.32 µm
Map Resolution:	256 by 192
Map Pixel Size:	0.63 µm
Acc. Voltage:	15.0 kV
Magnification:	750

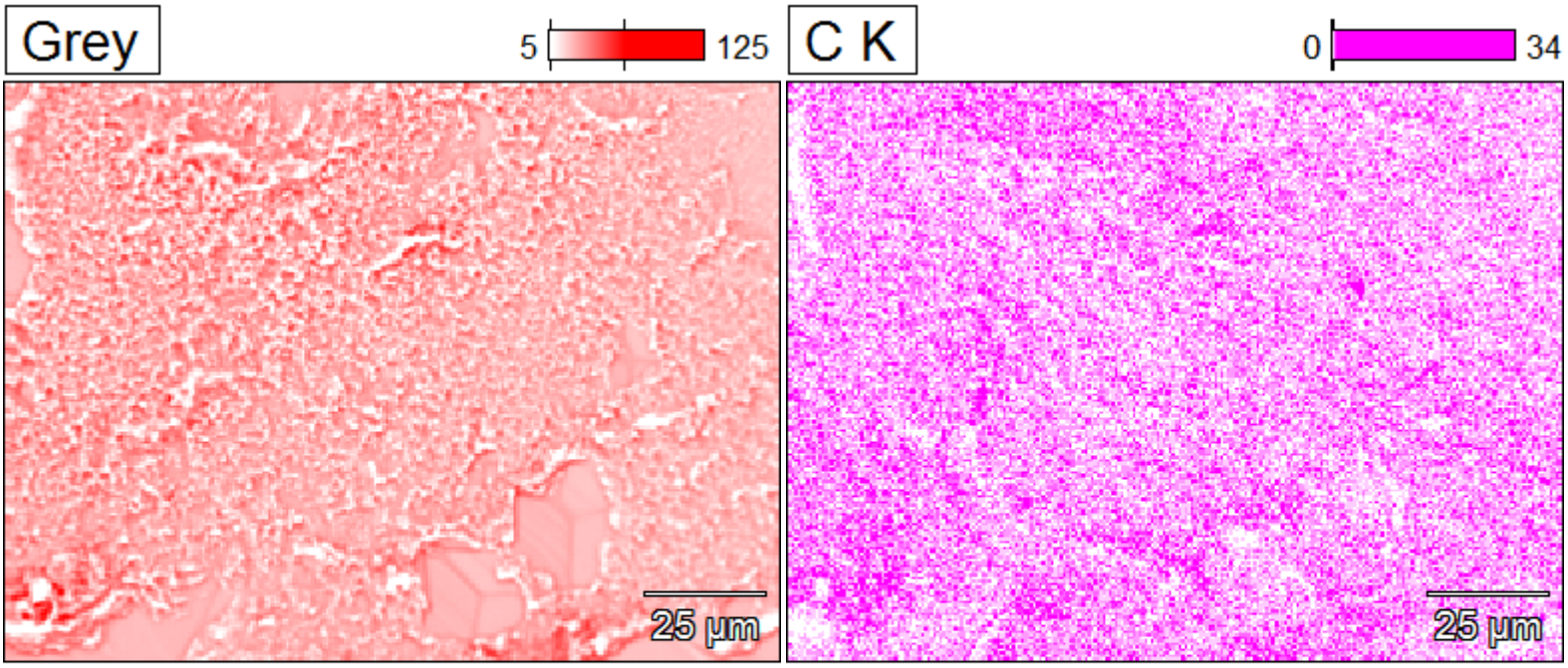
Grey
5
125
25 µm
C K
0
34
25 µm

Project: Yang

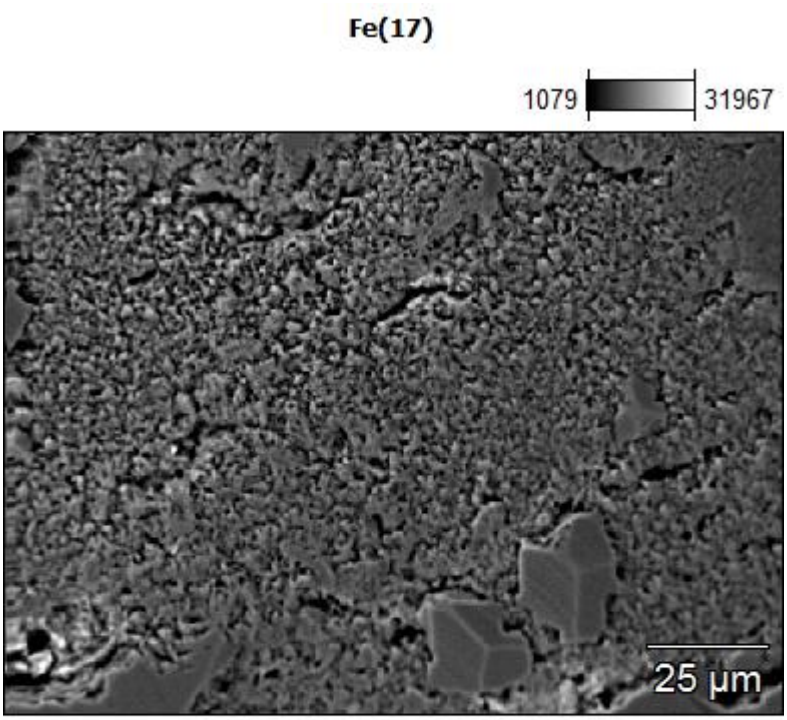

Data Type:	Counts
Image Resolution:	512 by 384
Image Pixel Size:	0.32 µm
Map Resolution:	256 by 192
Map Pixel Size:	0.63 µm
Acc. Voltage:	15.0 kV
Magnification:	750

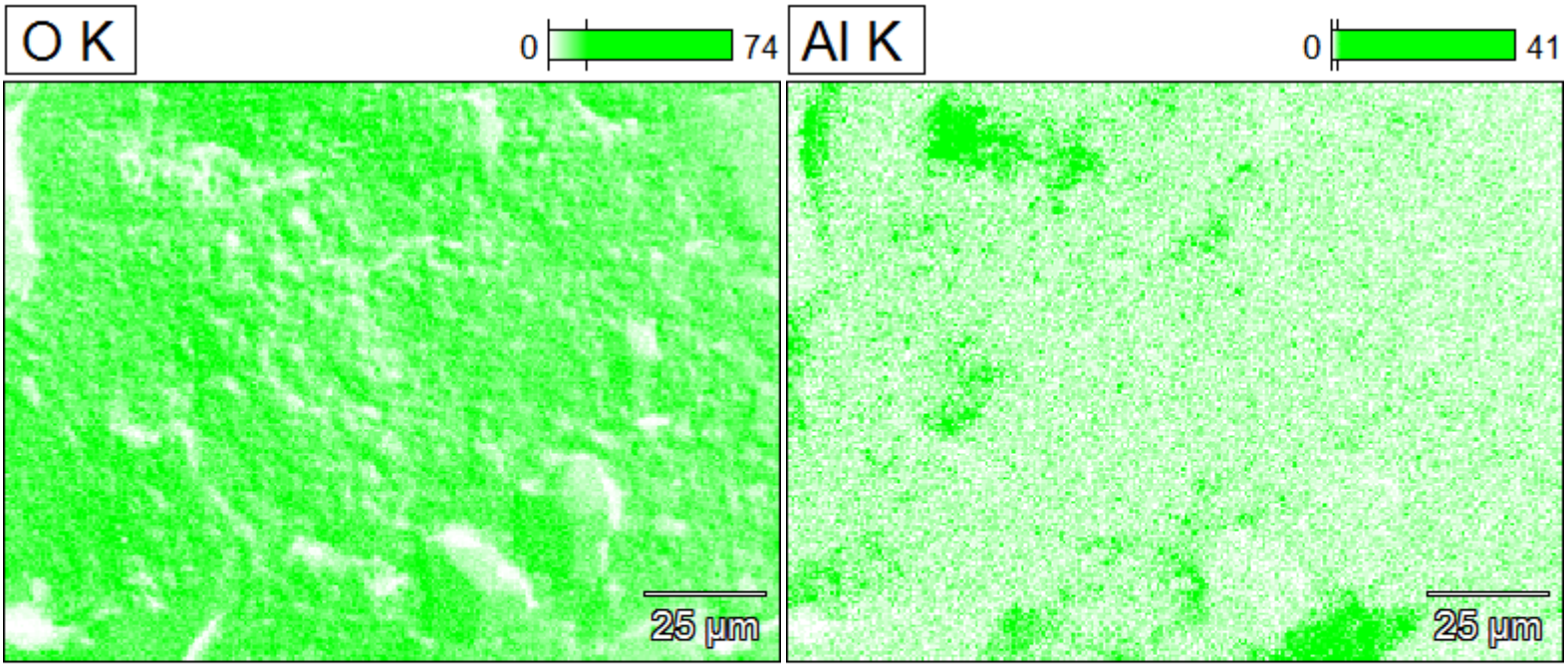
O K
0
74
25 µm
Al K
0
41
25 µm

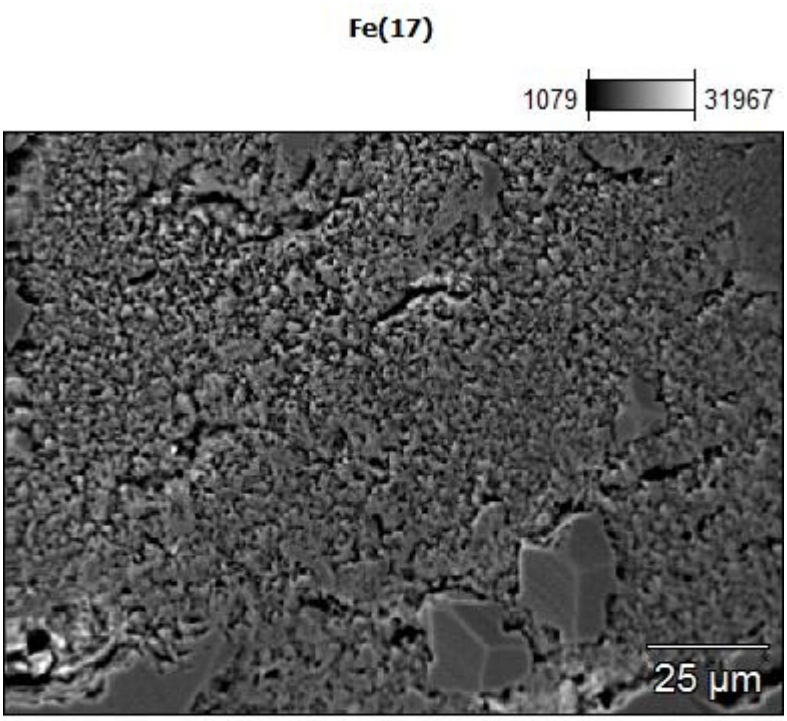

Data Type:	Counts
Image Resolution:	512 by 384
Image Pixel Size:	0.32 µm
Map Resolution:	256 by 192
Map Pixel Size:	0.63 µm
Acc. Voltage:	15.0 kV
Magnification:	750

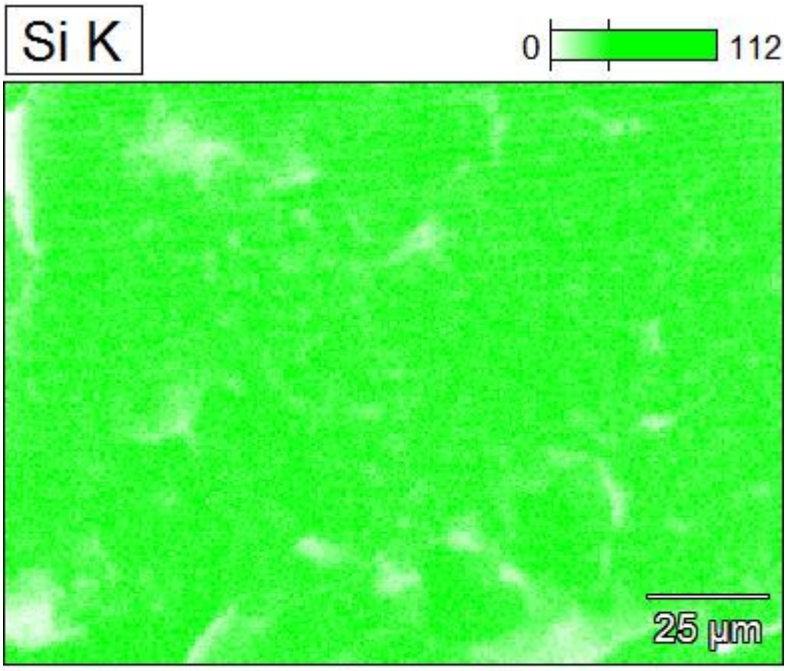
Si K
0
112
25 µm

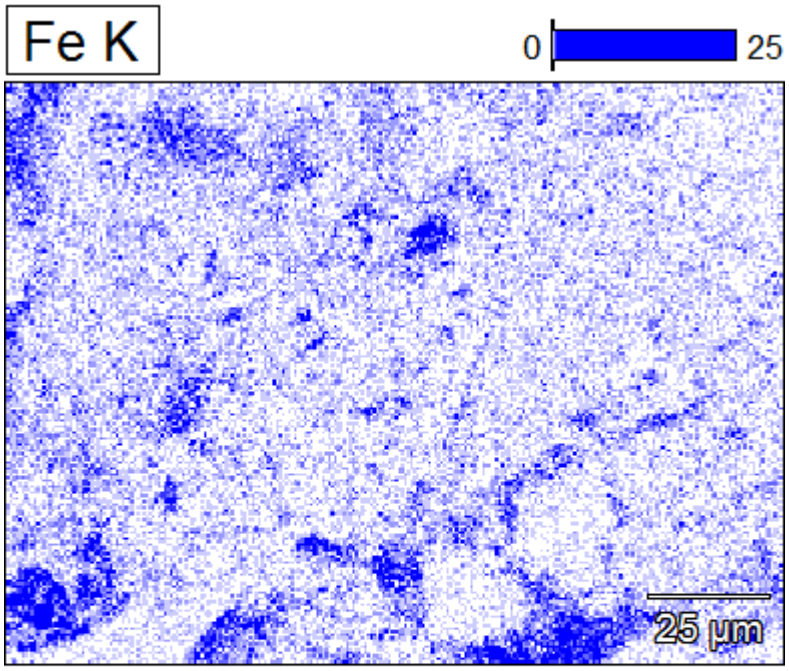
Fe K
0
25
25 µm

Project: Yang

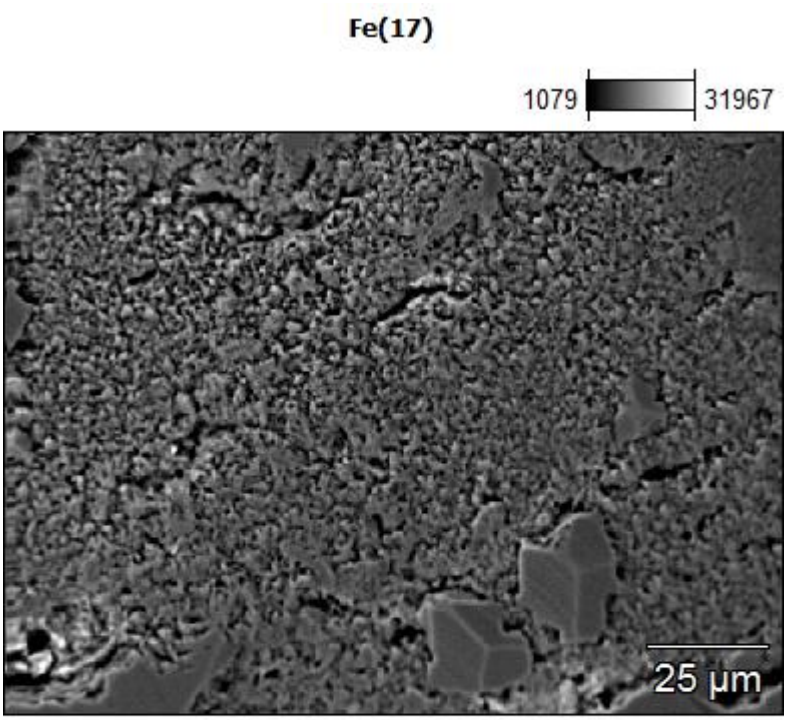

Data Type:	Counts
Image Resolution:	512 by 384
Image Pixel Size:	0.32 µm
Map Resolution:	256 by 192
Map Pixel Size:	0.63 µm
Acc. Voltage:	15.0 kV
Magnification:	750

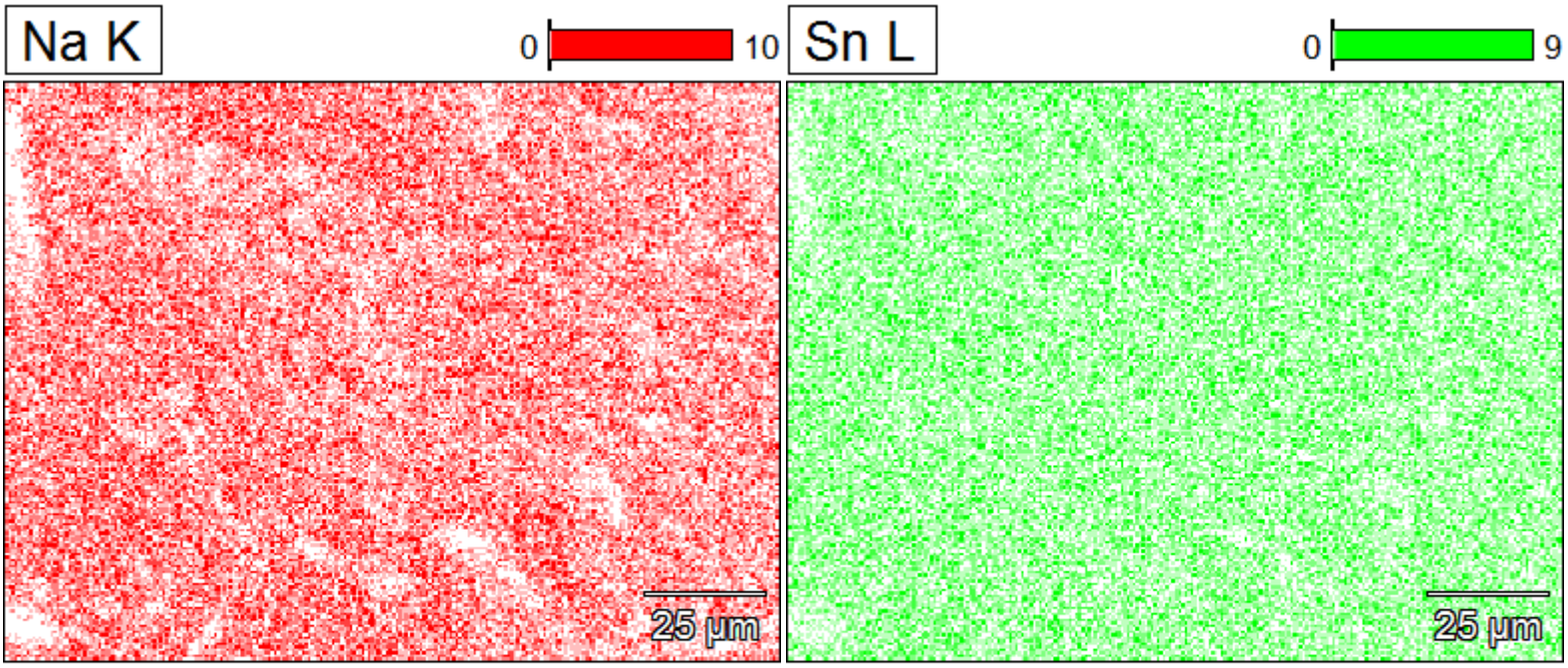
Na K
0
10
25 µm
Sn L
0
9
25 µm

Project: Yang

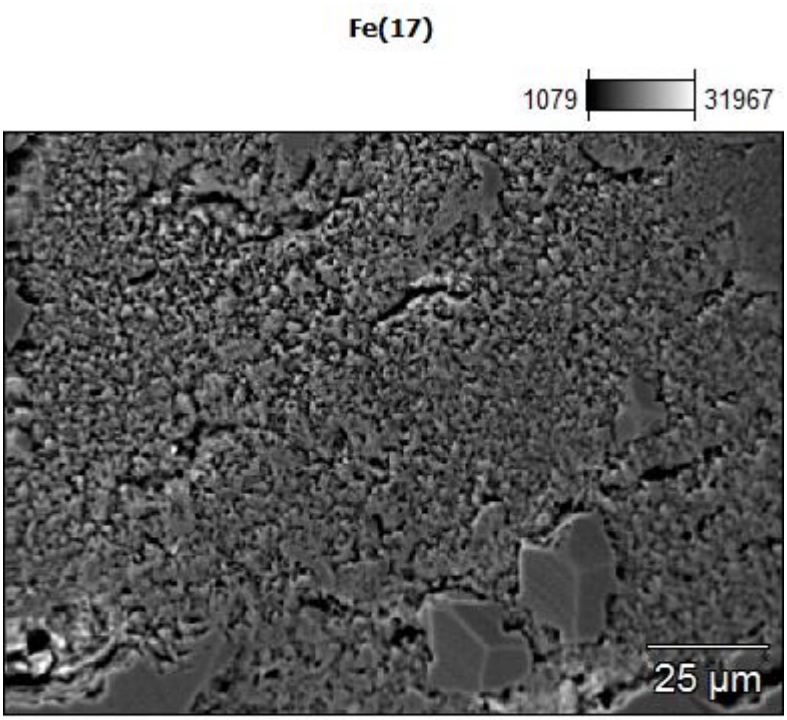

Data Type:	Counts
Image Resolution:	512 by 384
Image Pixel Size:	0.32 µm
Map Resolution:	256 by 192
Map Pixel Size:	0.63 µm
Acc. Voltage:	15.0 kV
Magnification:	750

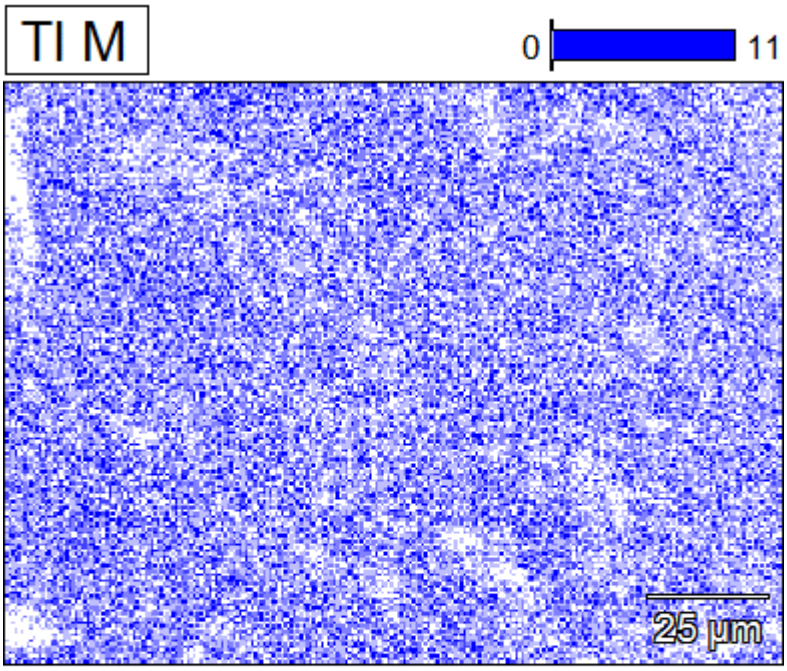
TI M
0
11
25 µm

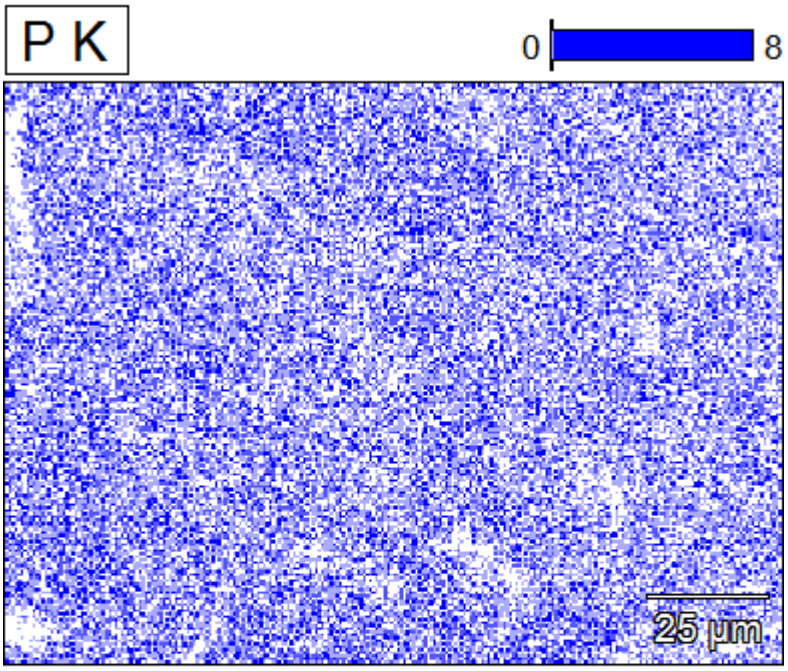
P K
0
8
25 µm

Project: Yang

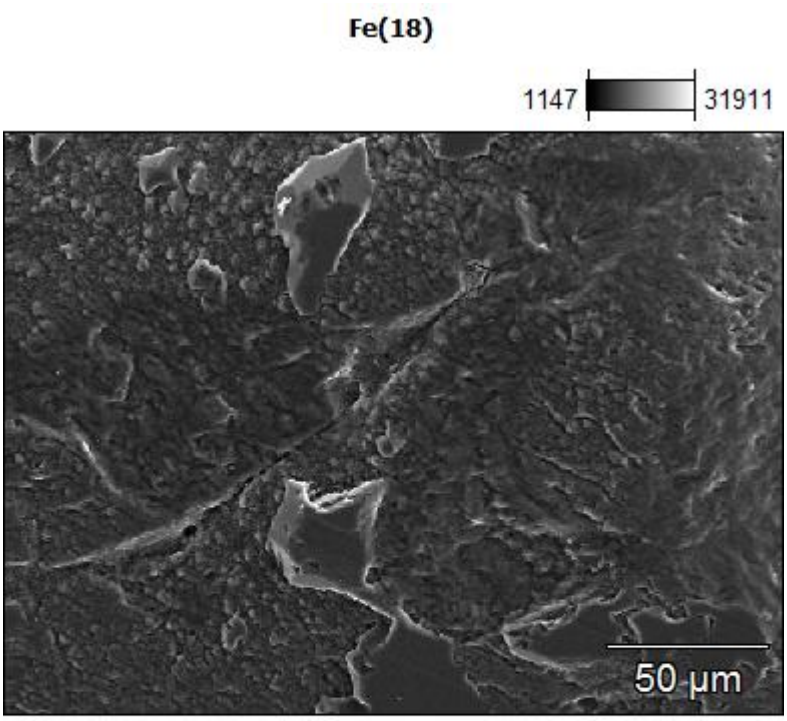

Data Type:	Counts
Image Resolution:	512 by 384
Image Pixel Size:	0.47 µm
Map Resolution:	256 by 192
Map Pixel Size:	0.95 µm
Acc. Voltage:	15.0 kV
Magnification:	500

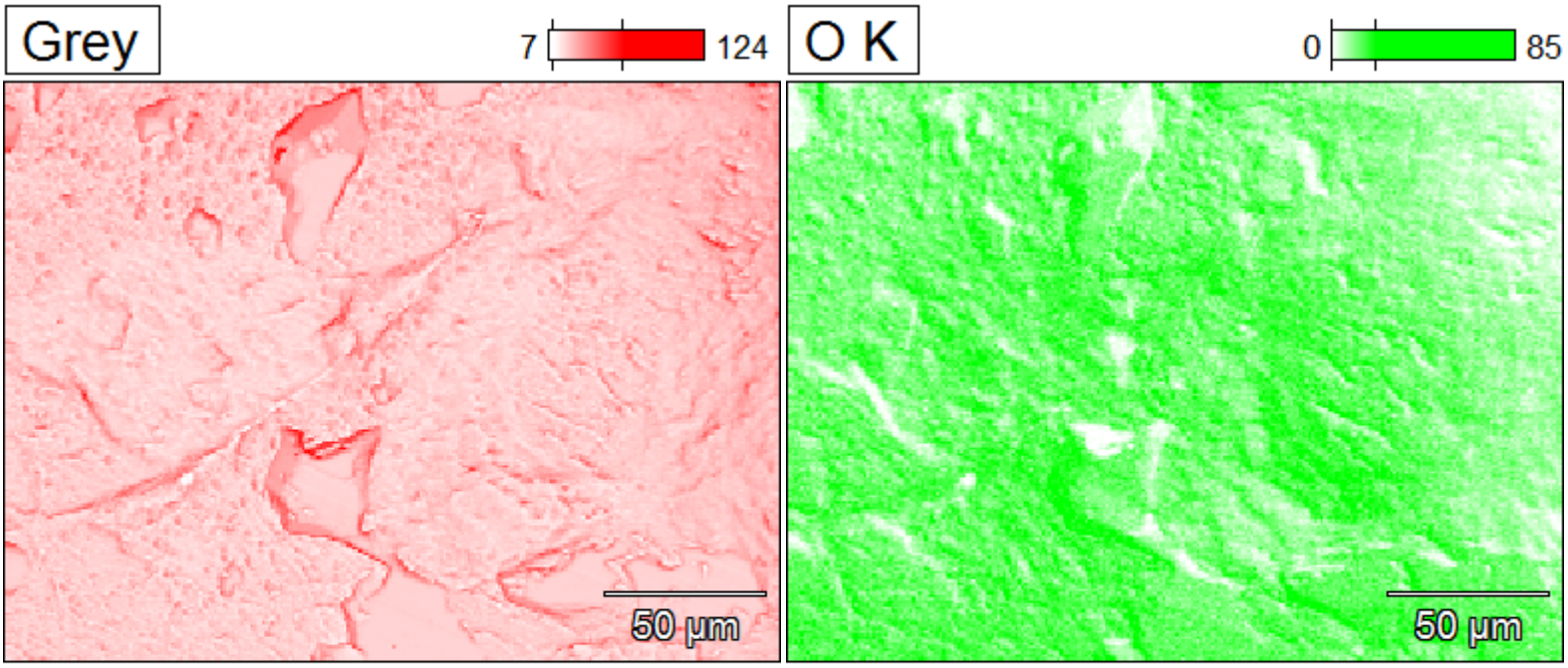
Grey
7
124
50 µm
O K
0
85
50 µm

Project: Yang

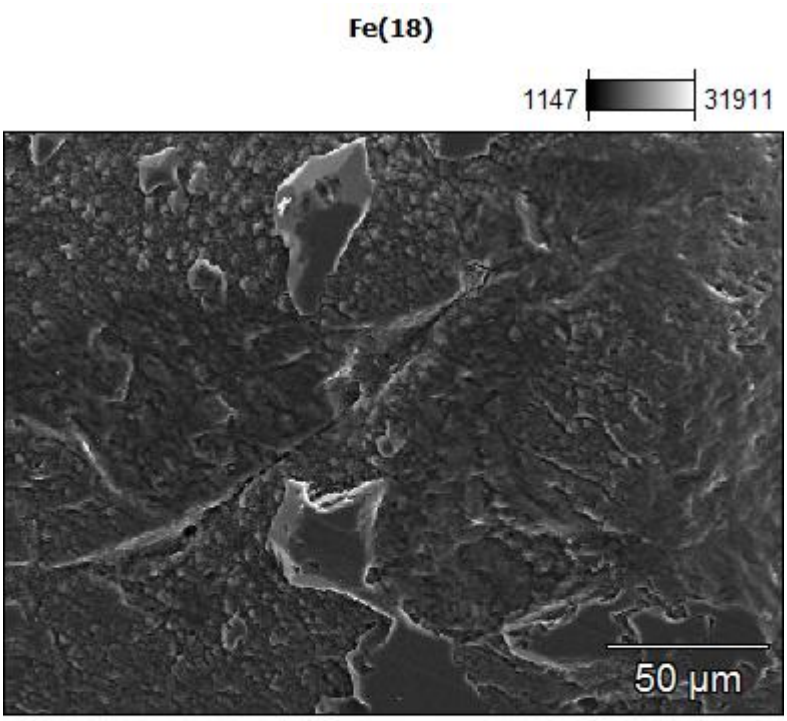

Data Type:	Counts
Image Resolution:	512 by 384
Image Pixel Size:	0.47 µm
Map Resolution:	256 by 192
Map Pixel Size:	0.95 µm
Acc. Voltage:	15.0 kV
Magnification:	500

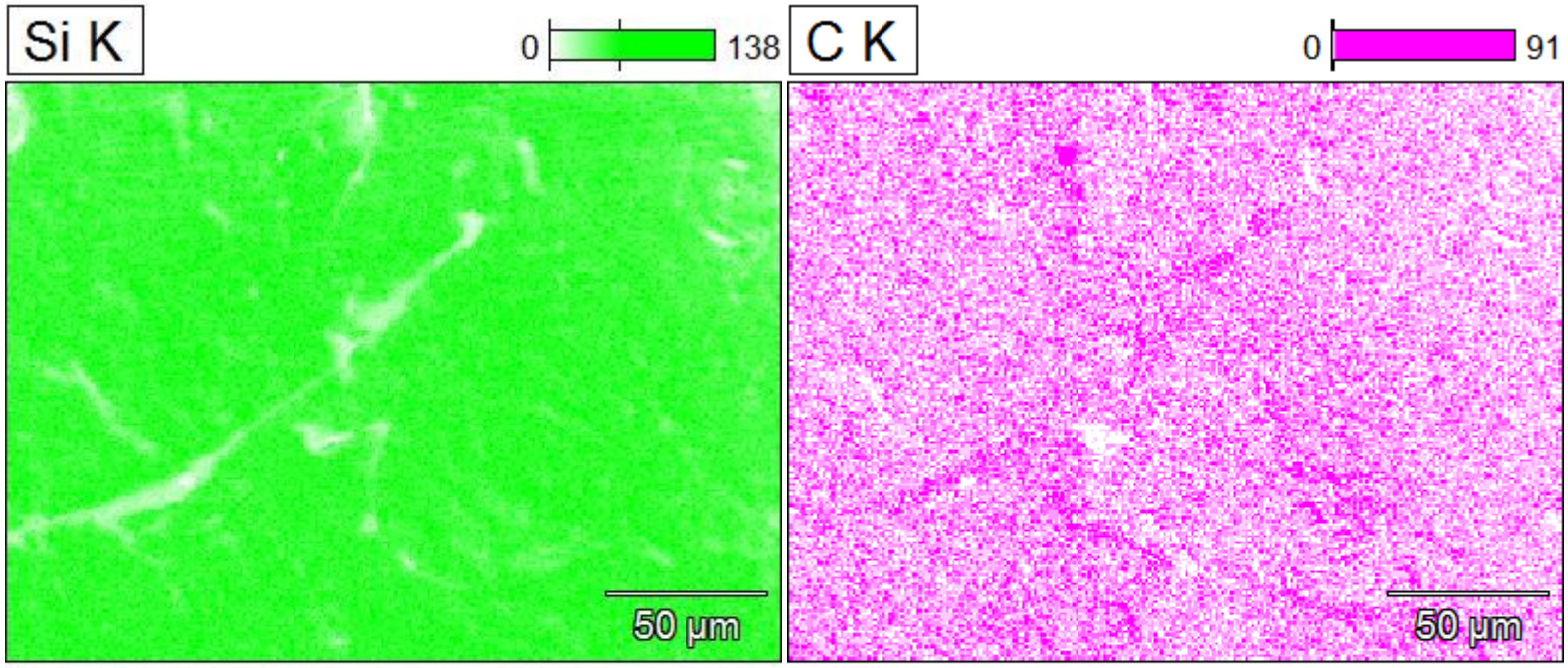
Si K
0
138
50 µm
C K
0
91
50 µm

Project: Yang

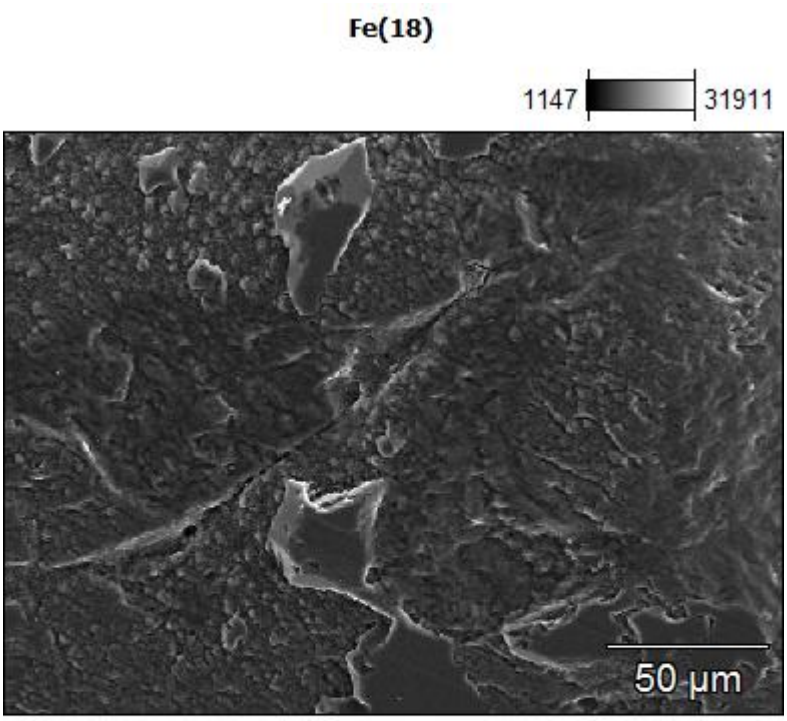

Data Type:	Counts
Image Resolution:	512 by 384
Image Pixel Size:	0.47 µm
Map Resolution:	256 by 192
Map Pixel Size:	0.95 µm
Acc. Voltage:	15.0 kV
Magnification:	500

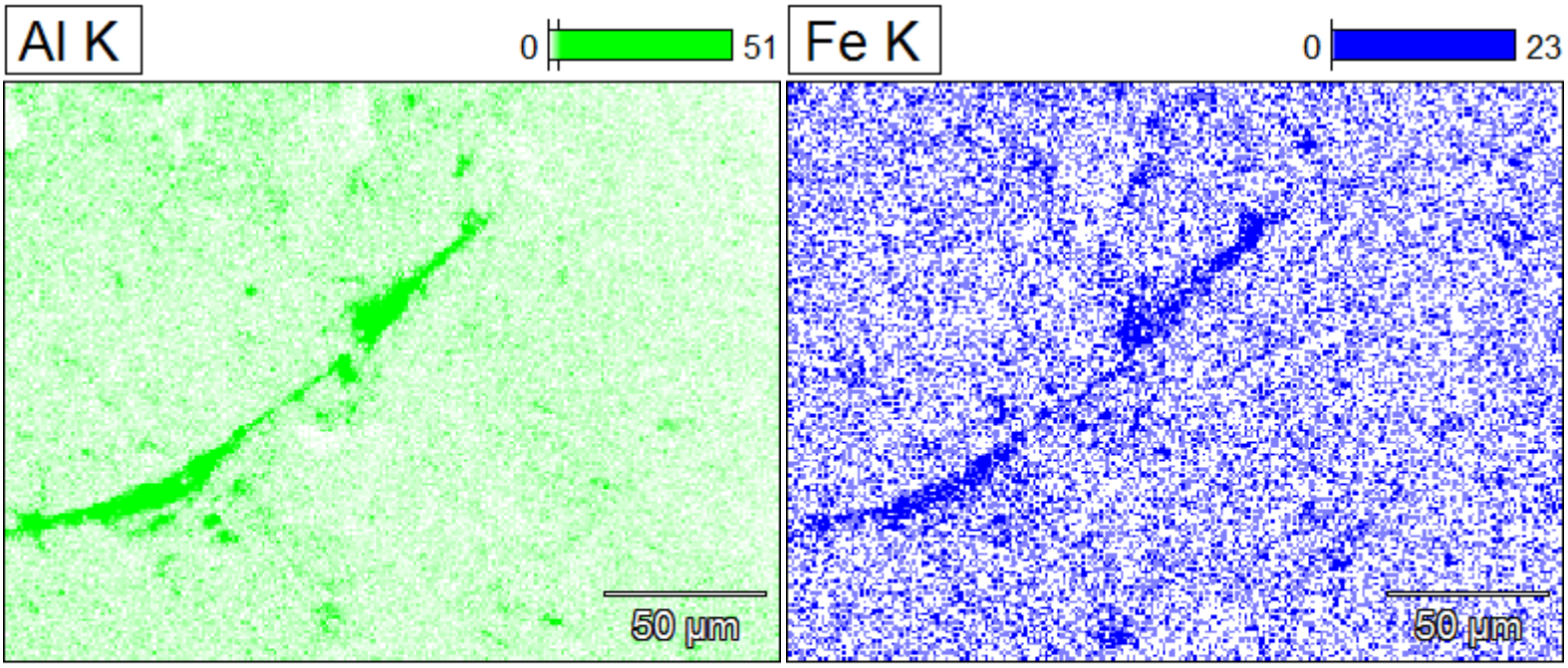
Al K
0
51
50 µm
Fe K
0
23
50 µm

Project: Yang

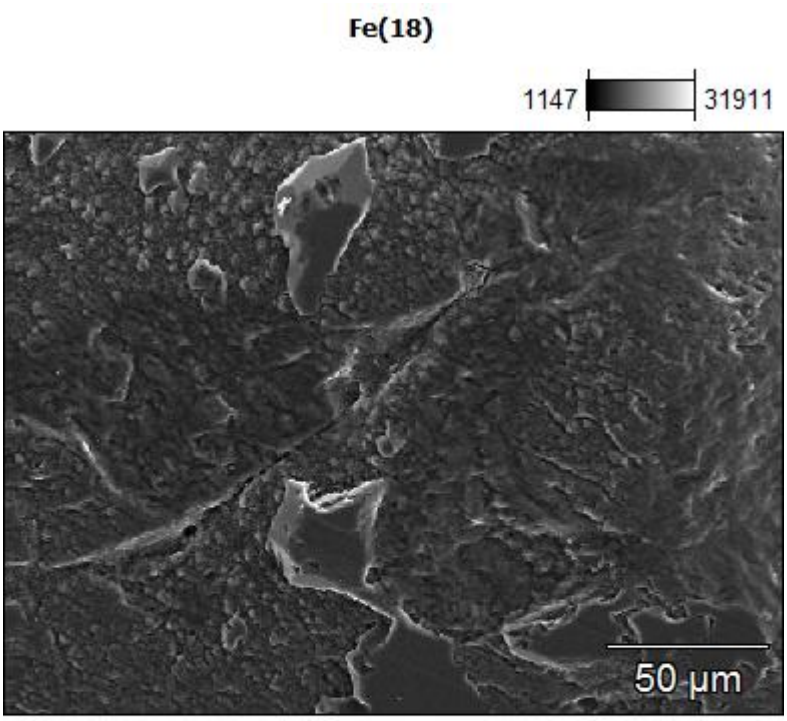

Data Type:	Counts
Image Resolution:	512 by 384
Image Pixel Size:	0.47 µm
Map Resolution:	256 by 192
Map Pixel Size:	0.95 µm
Acc. Voltage:	15.0 kV
Magnification:	500

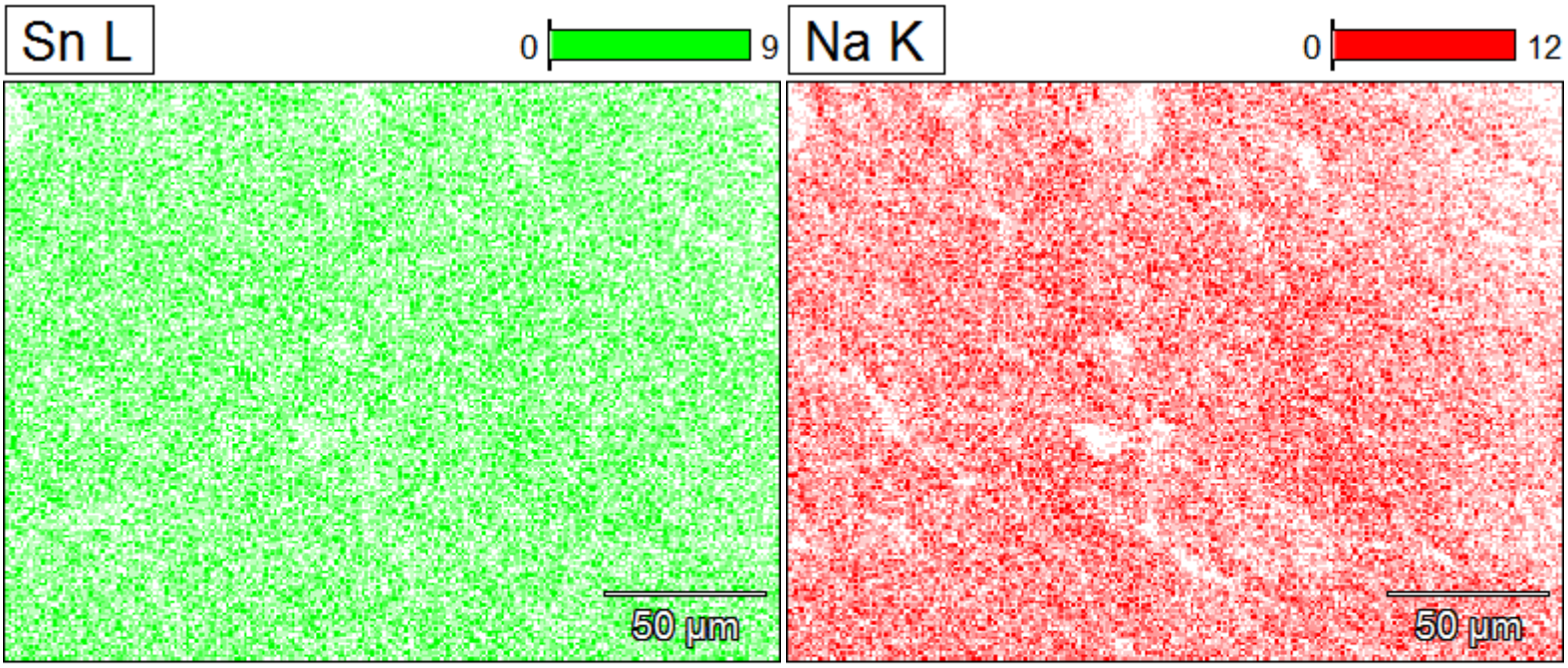
Sn L
0
9
50 µm
Na K
0
12
50 µm

Project: Yang

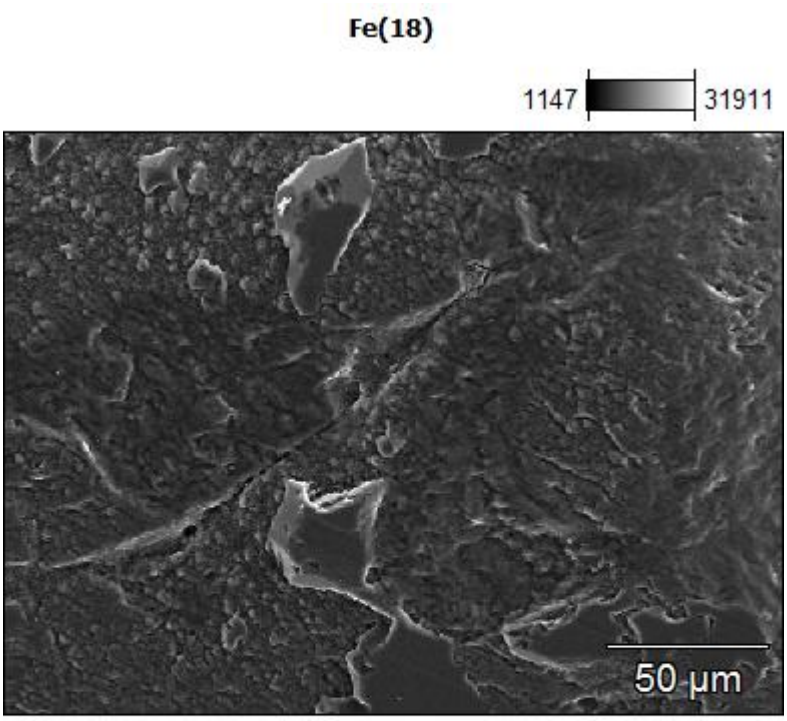

Data Type:	Counts
Image Resolution:	512 by 384
Image Pixel Size:	0.47 µm
Map Resolution:	256 by 192
Map Pixel Size:	0.95 µm
Acc. Voltage:	15.0 kV
Magnification:	500

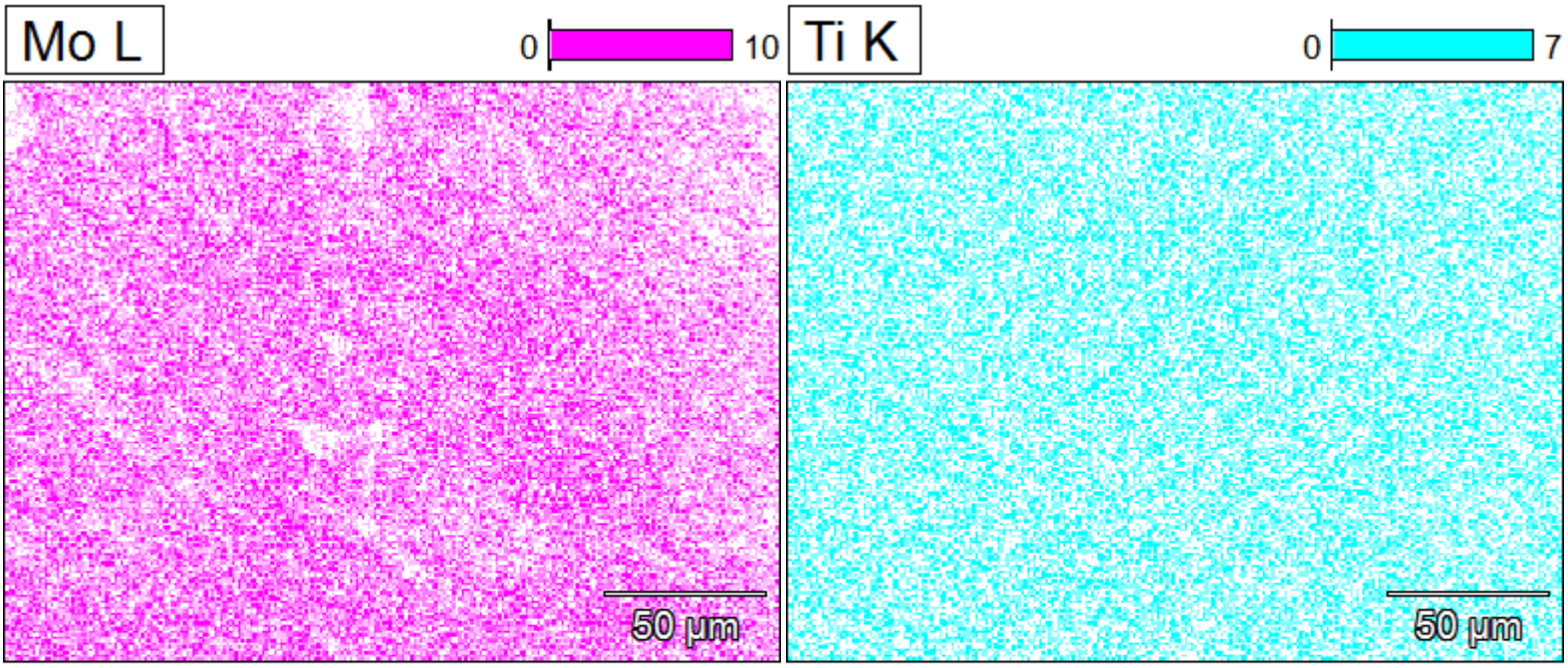
Mo L
0
10
50 µm
Ti K
0
7
50 µm

Project: Yang

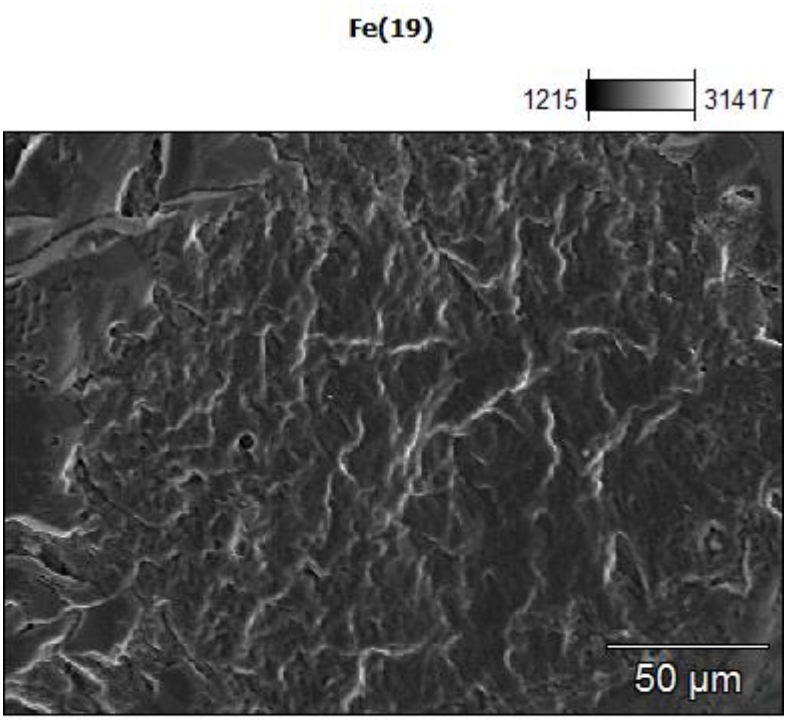

Data Type:	Counts
Image Resolution:	512 by 384
Image Pixel Size:	0.47 µm
Map Resolution:	256 by 192
Map Pixel Size:	0.95 µm
Acc. Voltage:	15.0 kV
Magnification:	500

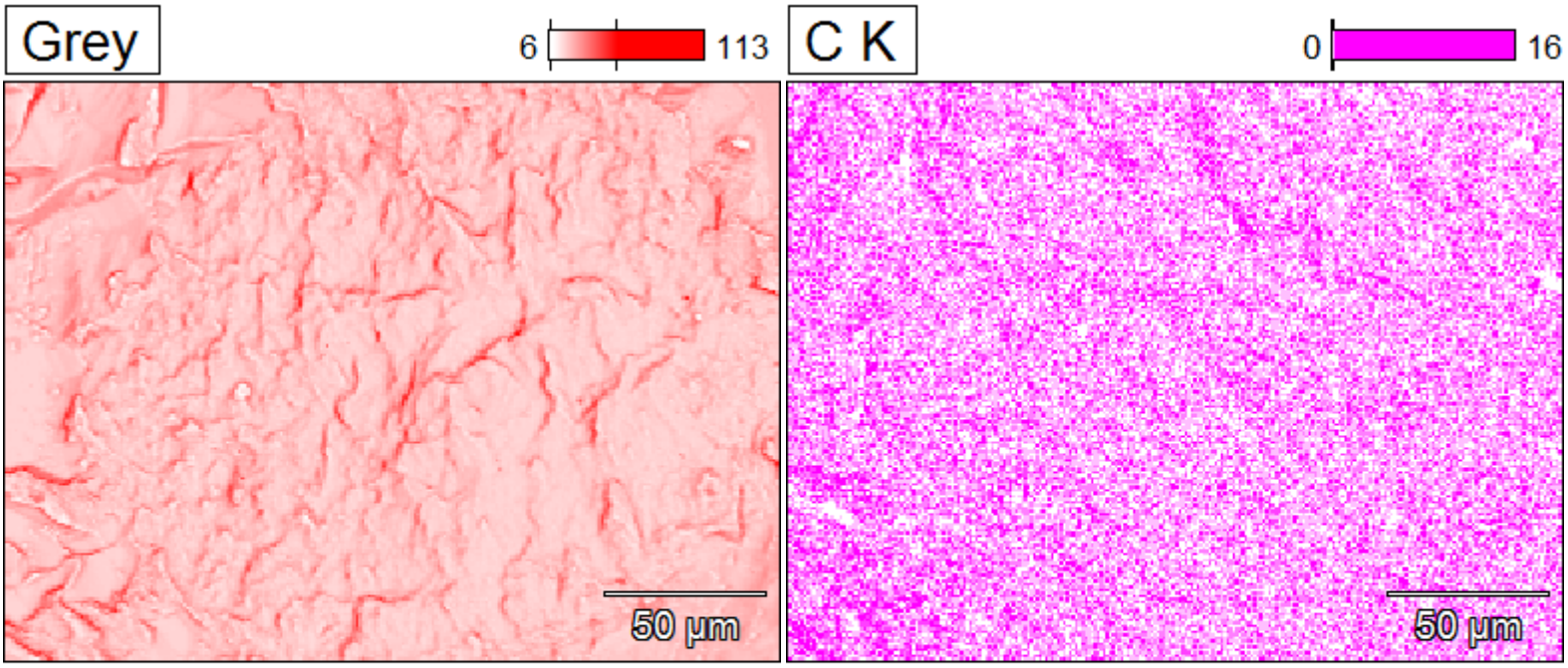
Grey
6
113
50 µm
C K
0
16
50 µm

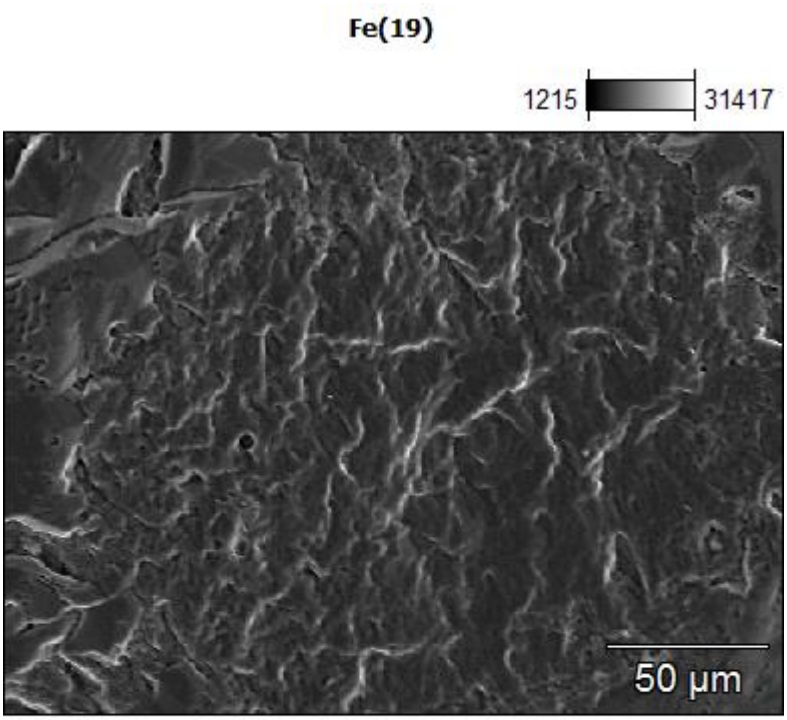

Data Type:	Counts
Image Resolution:	512 by 384
Image Pixel Size:	0.47 µm
Map Resolution:	256 by 192
Map Pixel Size:	0.95 µm
Acc. Voltage:	15.0 kV
Magnification:	500

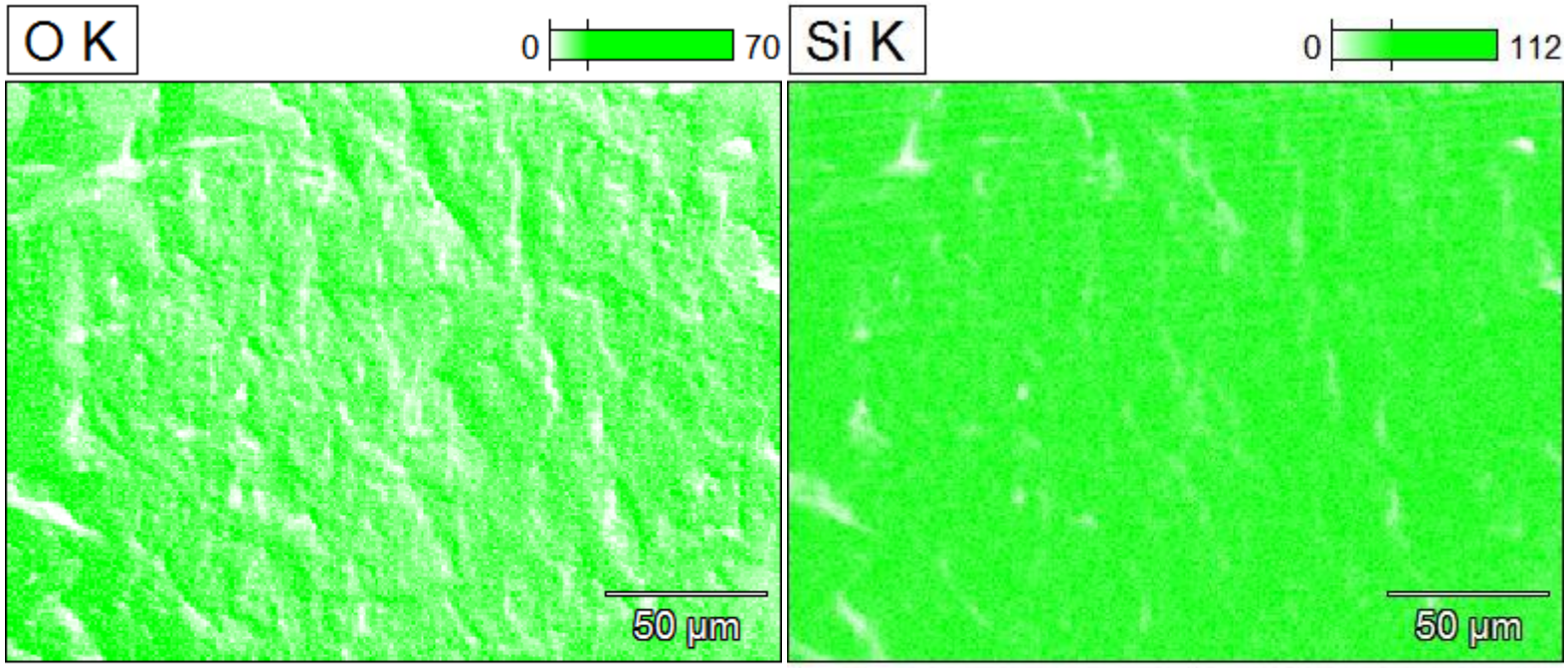
O K
0
70
50 µm
Si K
0
112
50 µm

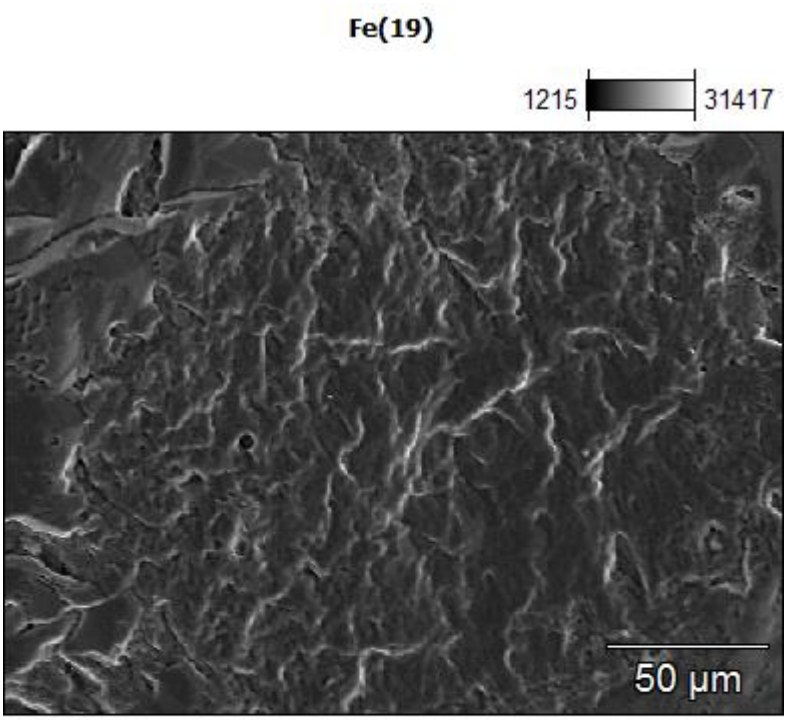

Data Type:	Counts
Image Resolution:	512 by 384
Image Pixel Size:	0.47 µm
Map Resolution:	256 by 192
Map Pixel Size:	0.95 µm
Acc. Voltage:	15.0 kV
Magnification:	500

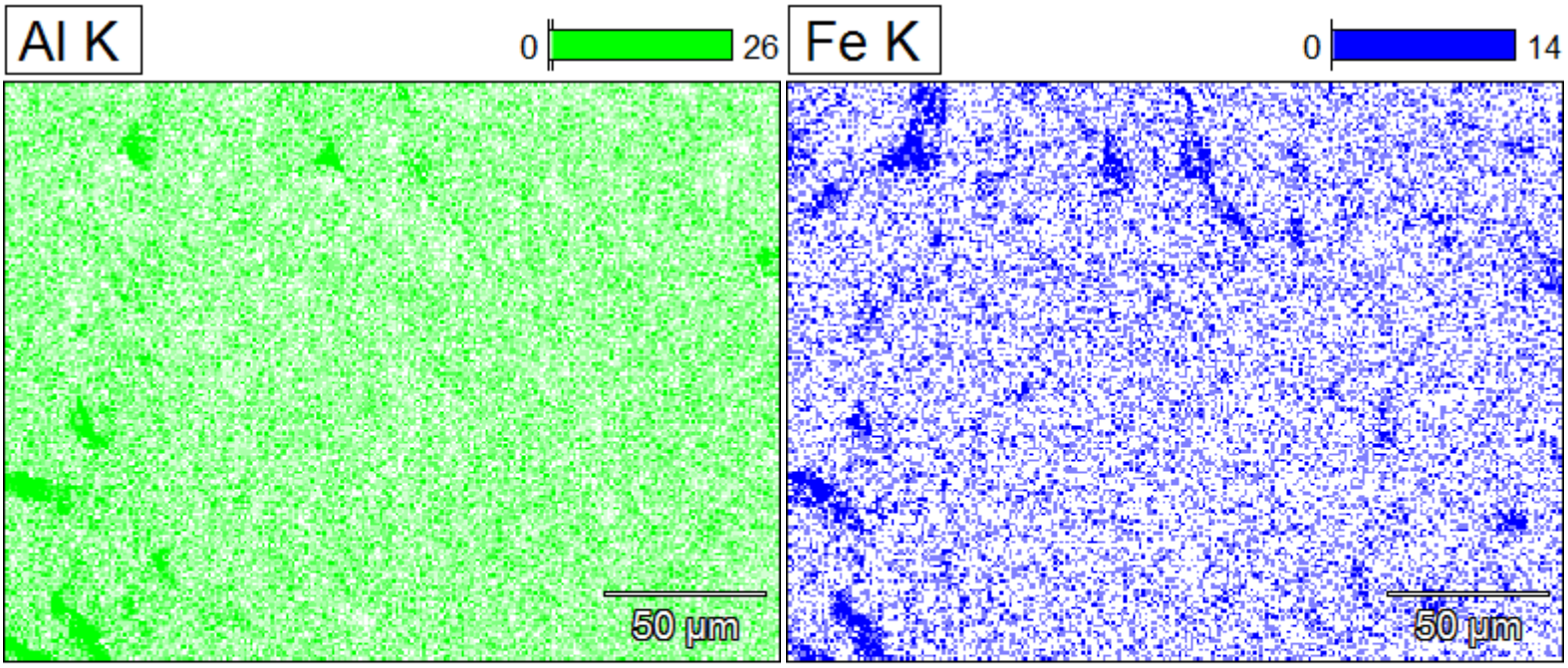
Al K
0
26
50 µm
Fe K
0
14
50 µm

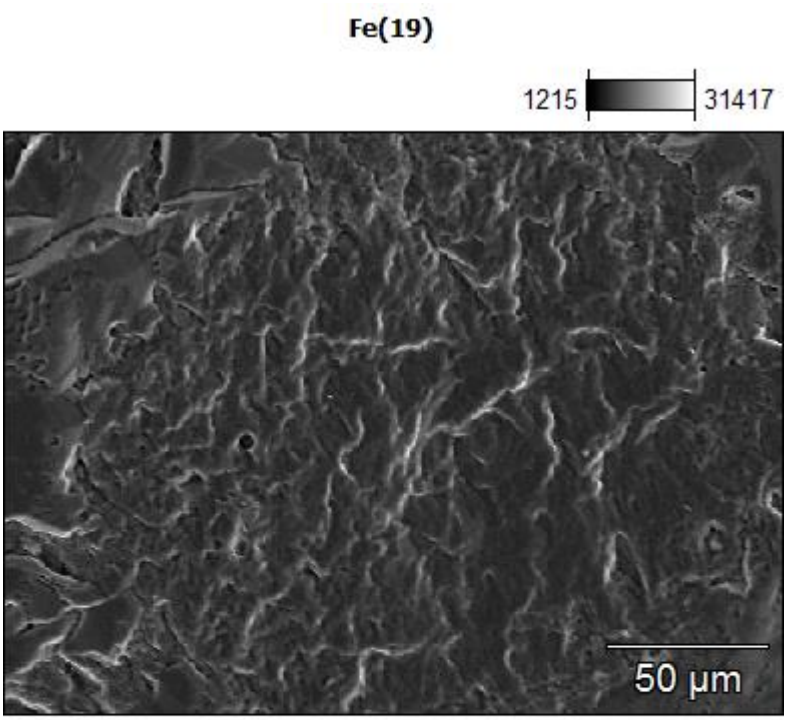

Data Type:	Counts
Image Resolution:	512 by 384
Image Pixel Size:	0.47 µm
Map Resolution:	256 by 192
Map Pixel Size:	0.95 µm
Acc. Voltage:	15.0 kV
Magnification:	500

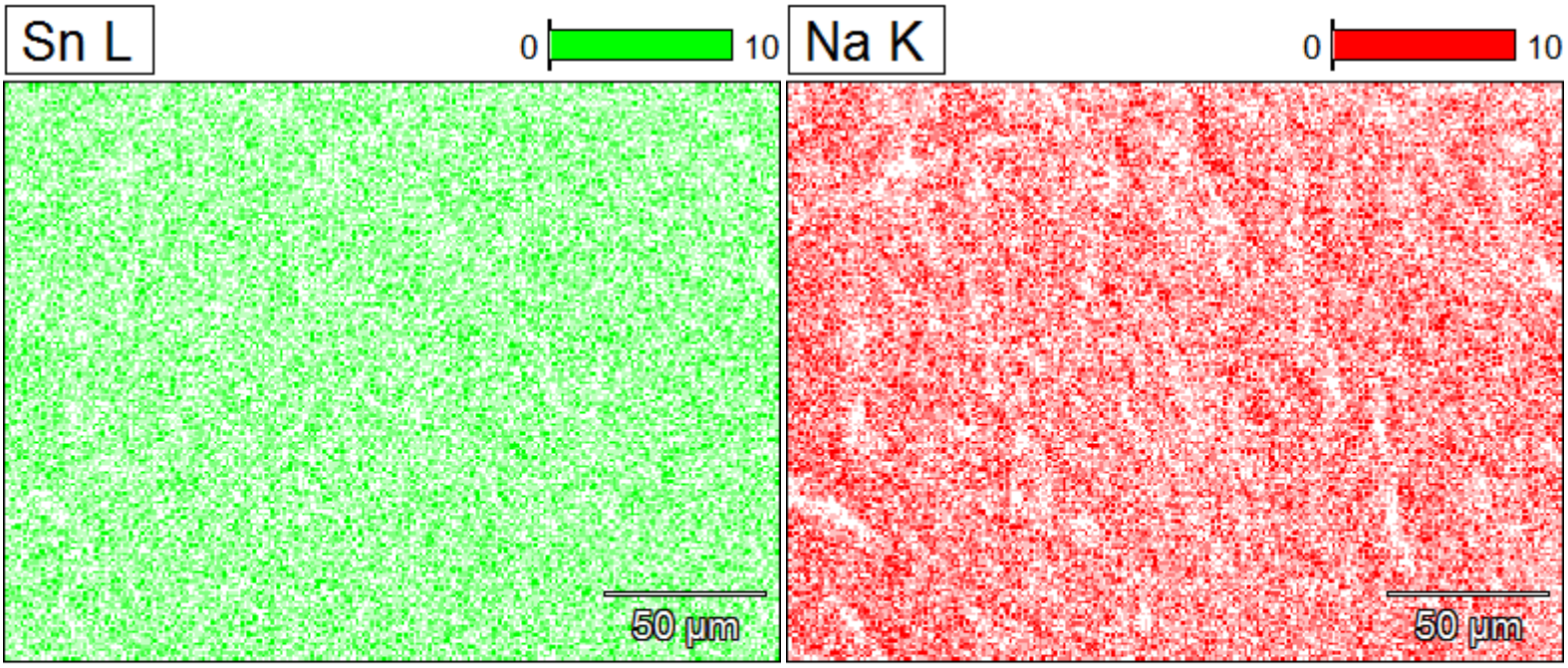
Sn L
0
10
50 µm
Na K
0
10
50 µm

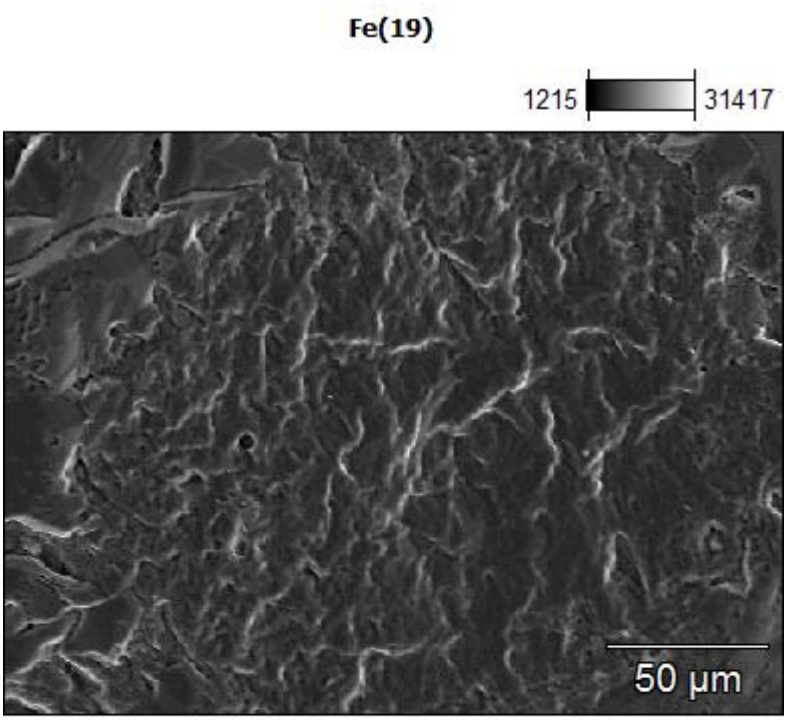

Data Type:	Counts
Image Resolution:	512 by 384
Image Pixel Size:	0.47 µm
Map Resolution:	256 by 192
Map Pixel Size:	0.95 µm
Acc. Voltage:	15.0 kV
Magnification:	500

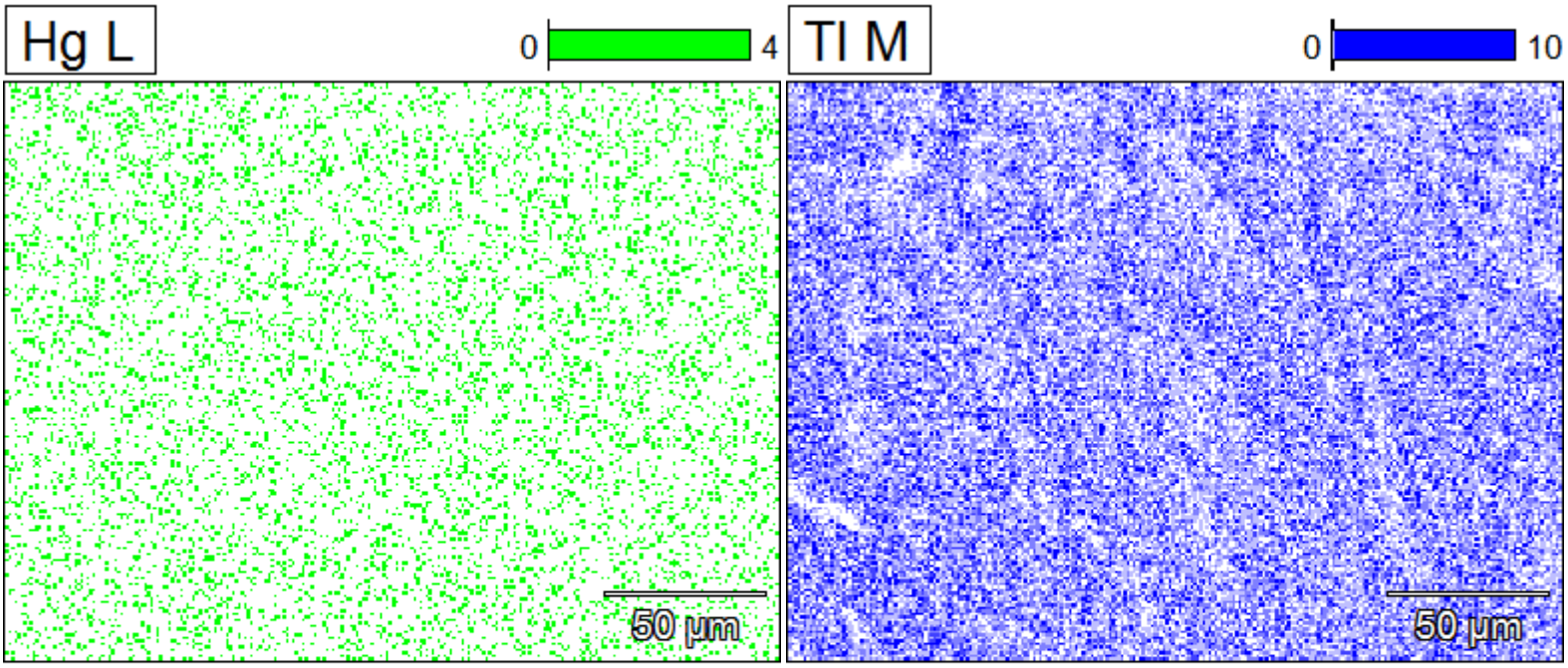
Hg L
0
4
50 µm
Tl M
0
10
50 µm

Project: Yang

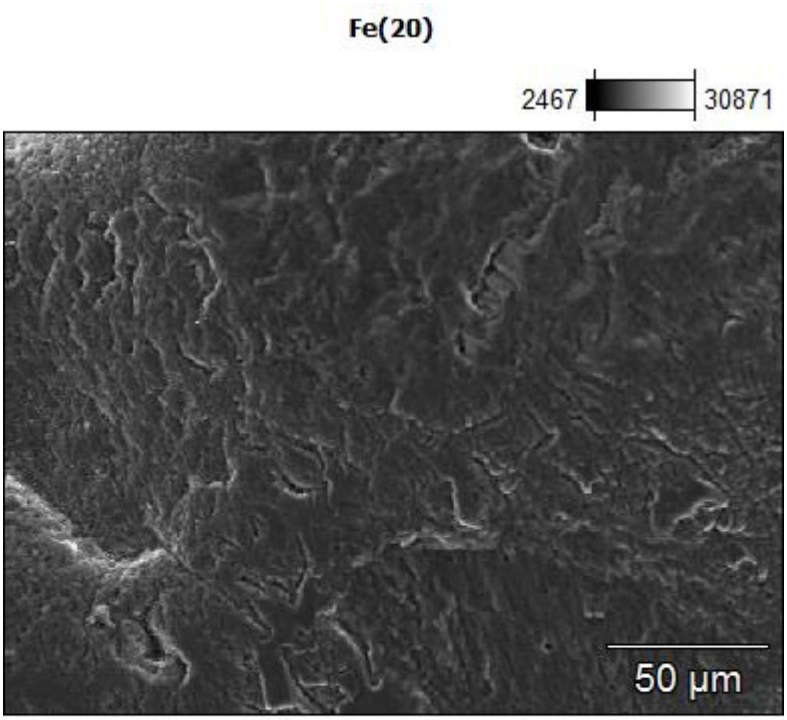

Data Type:	Counts
Image Resolution:	512 by 384
Image Pixel Size:	0.47 µm
Map Resolution:	256 by 192
Map Pixel Size:	0.95 µm
Acc. Voltage:	15.0 kV
Magnification:	500

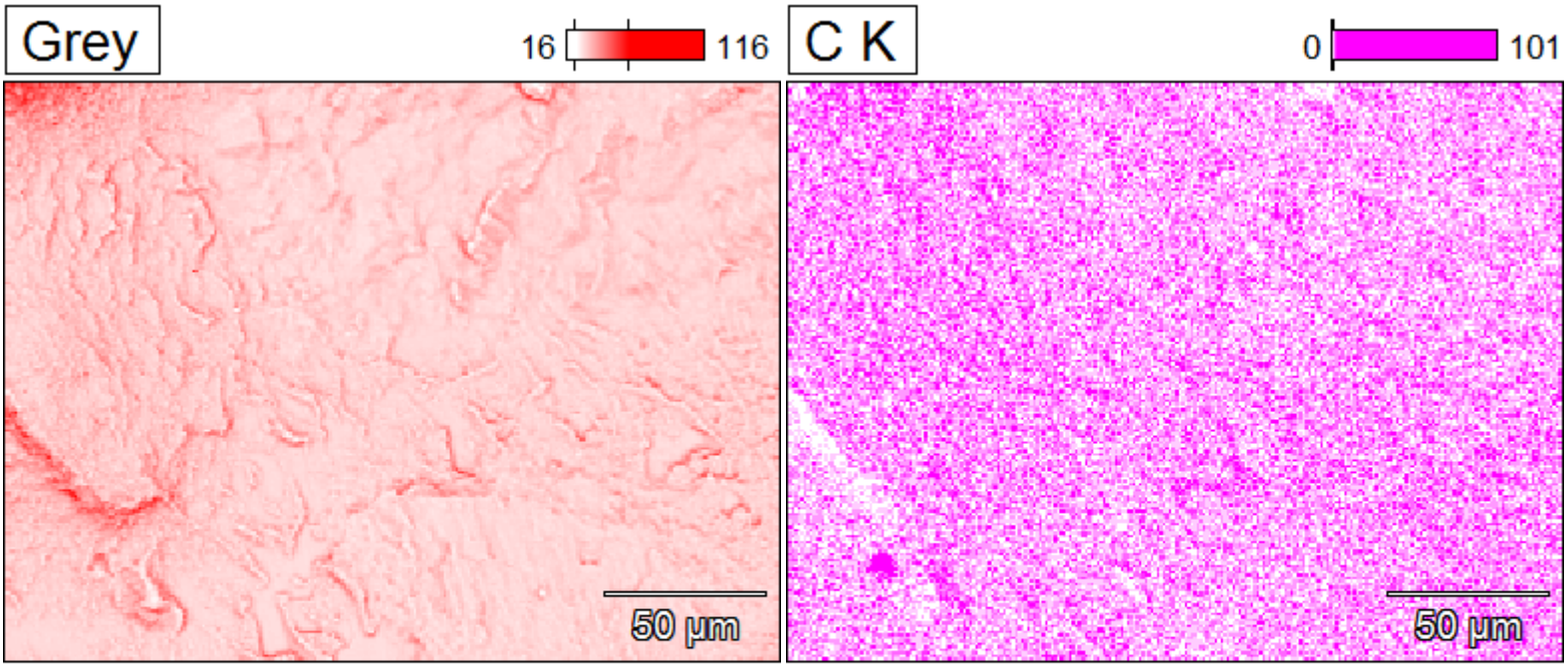
Grey
16
116
50 µm
C K
0
101
50 µm

Project: Yang

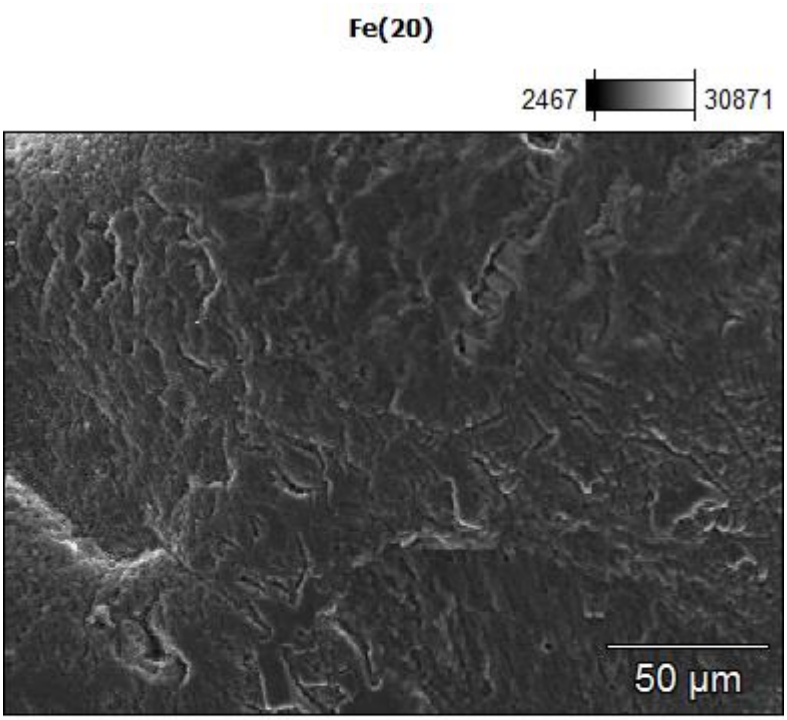

Data Type:	Counts
Image Resolution:	512 by 384
Image Pixel Size:	0.47 µm
Map Resolution:	256 by 192
Map Pixel Size:	0.95 µm
Acc. Voltage:	15.0 kV
Magnification:	500

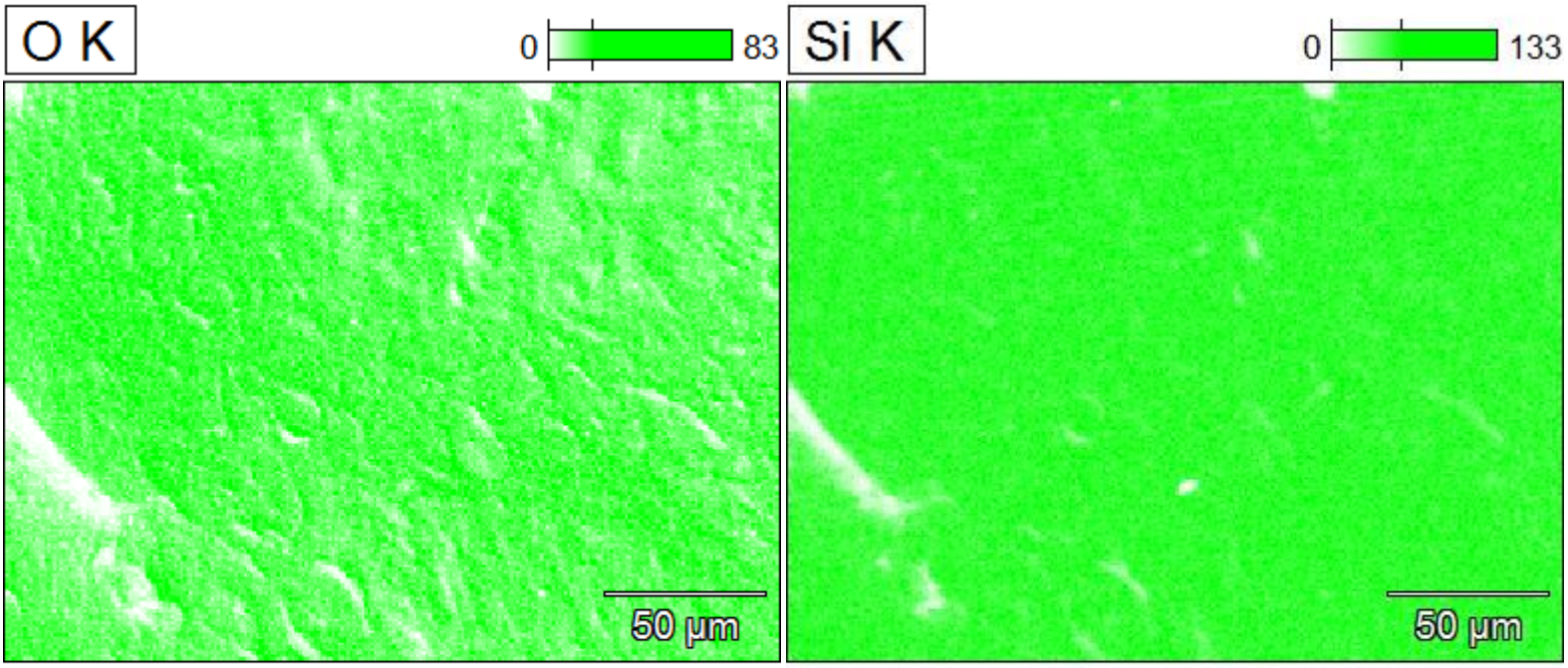
O K
0
83
50 µm
Si K
0
133
50 µm

Project: Yang

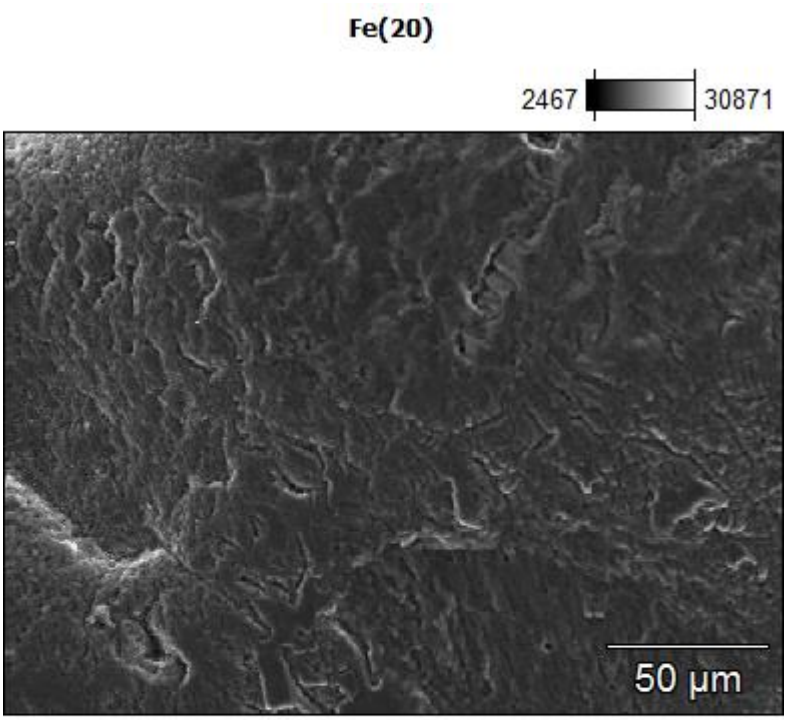

Data Type:	Counts
Image Resolution:	512 by 384
Image Pixel Size:	0.47 µm
Map Resolution:	256 by 192
Map Pixel Size:	0.95 µm
Acc. Voltage:	15.0 kV
Magnification:	500

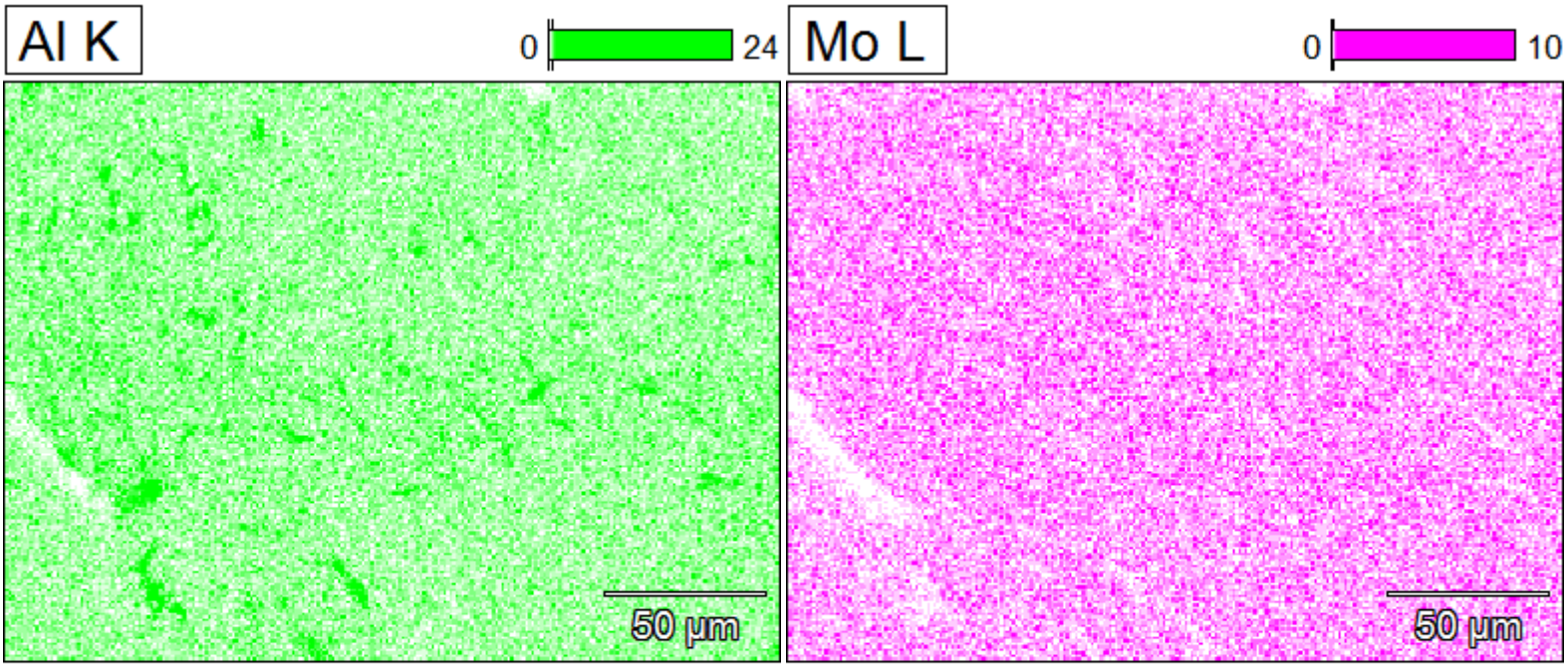
Al K
0
24
50 µm
Mo L
0
10
50 µm

Project: Yang

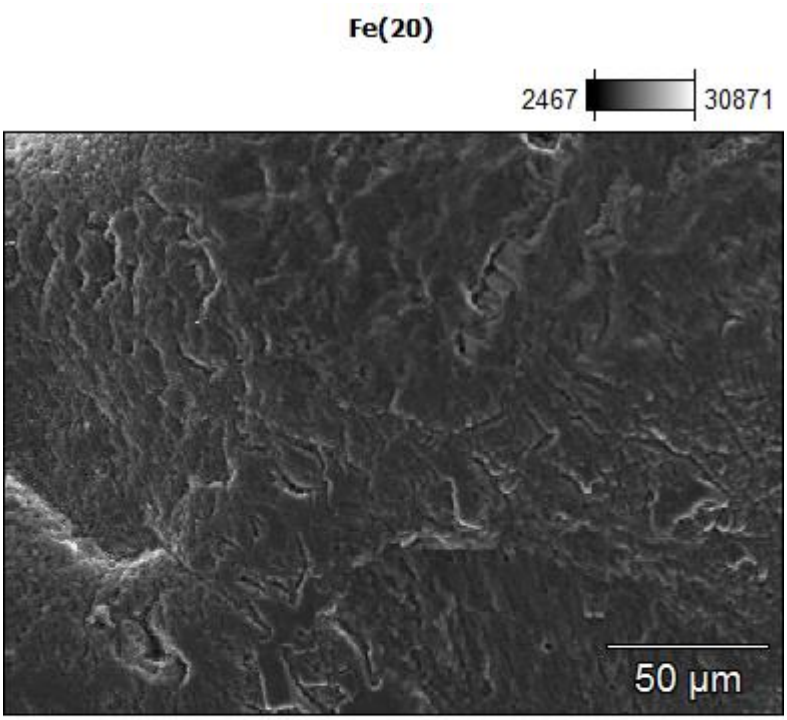

Data Type:	Counts
Image Resolution:	512 by 384
Image Pixel Size:	0.47 µm
Map Resolution:	256 by 192
Map Pixel Size:	0.95 µm
Acc. Voltage:	15.0 kV
Magnification:	500

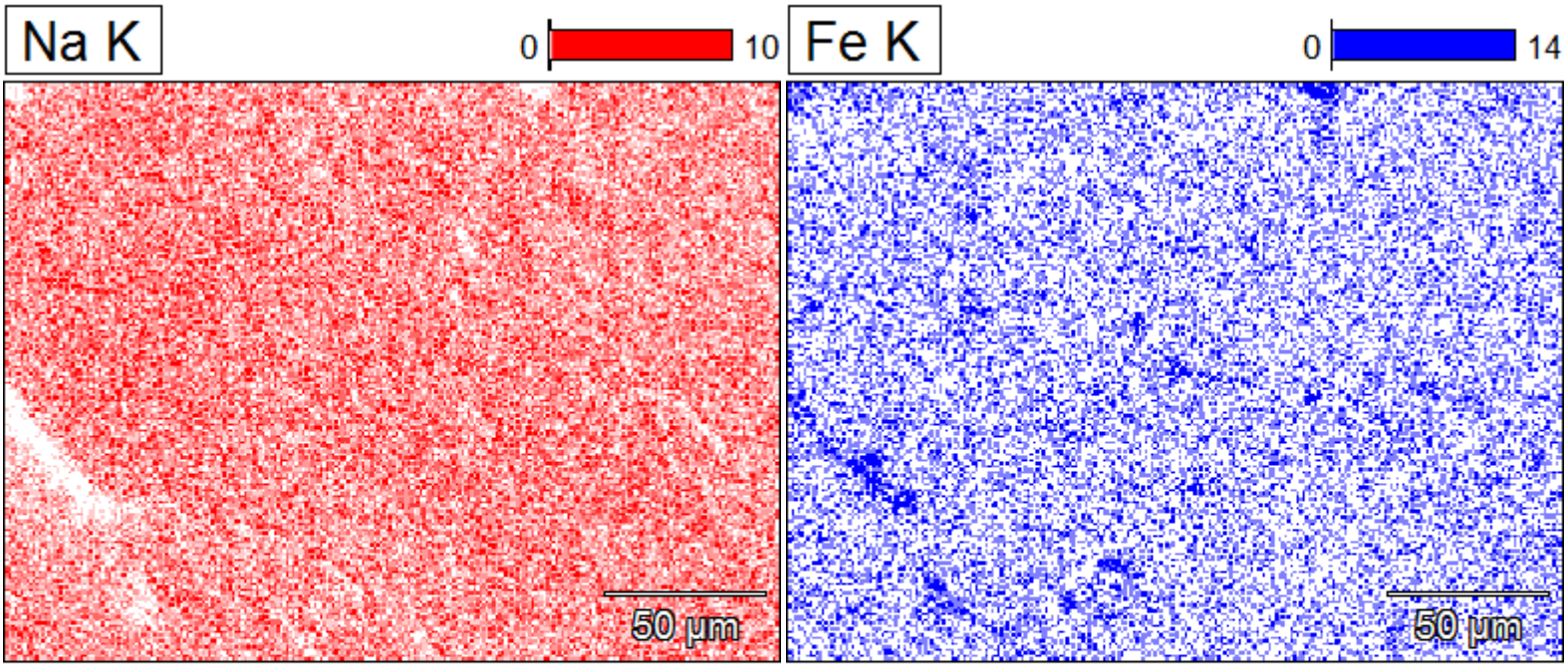
Na K
0
10
50 µm
Fe K
0
14
50 µm

Project: Yang

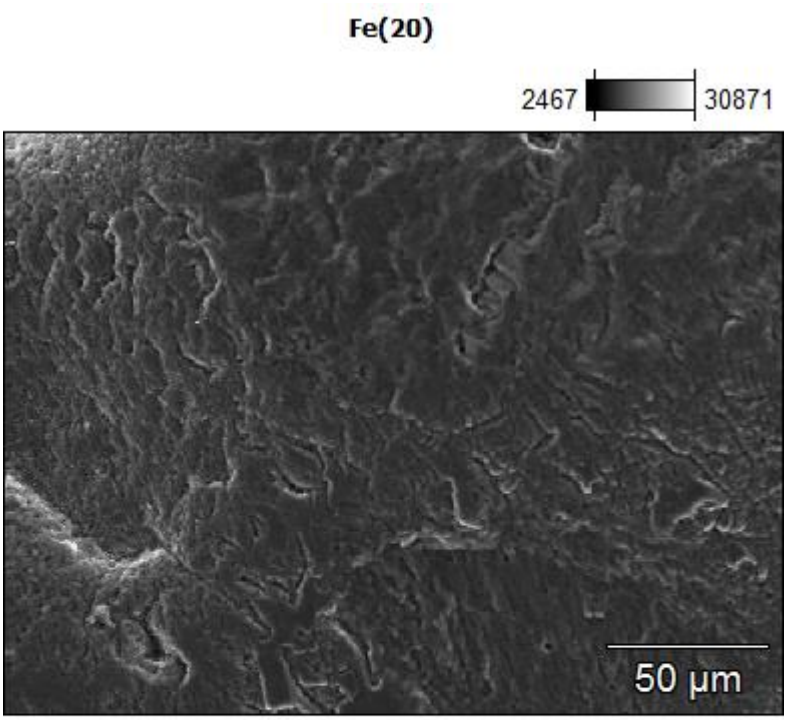

Data Type:	Counts
Image Resolution:	512 by 384
Image Pixel Size:	0.47 µm
Map Resolution:	256 by 192
Map Pixel Size:	0.95 µm
Acc. Voltage:	15.0 kV
Magnification:	500

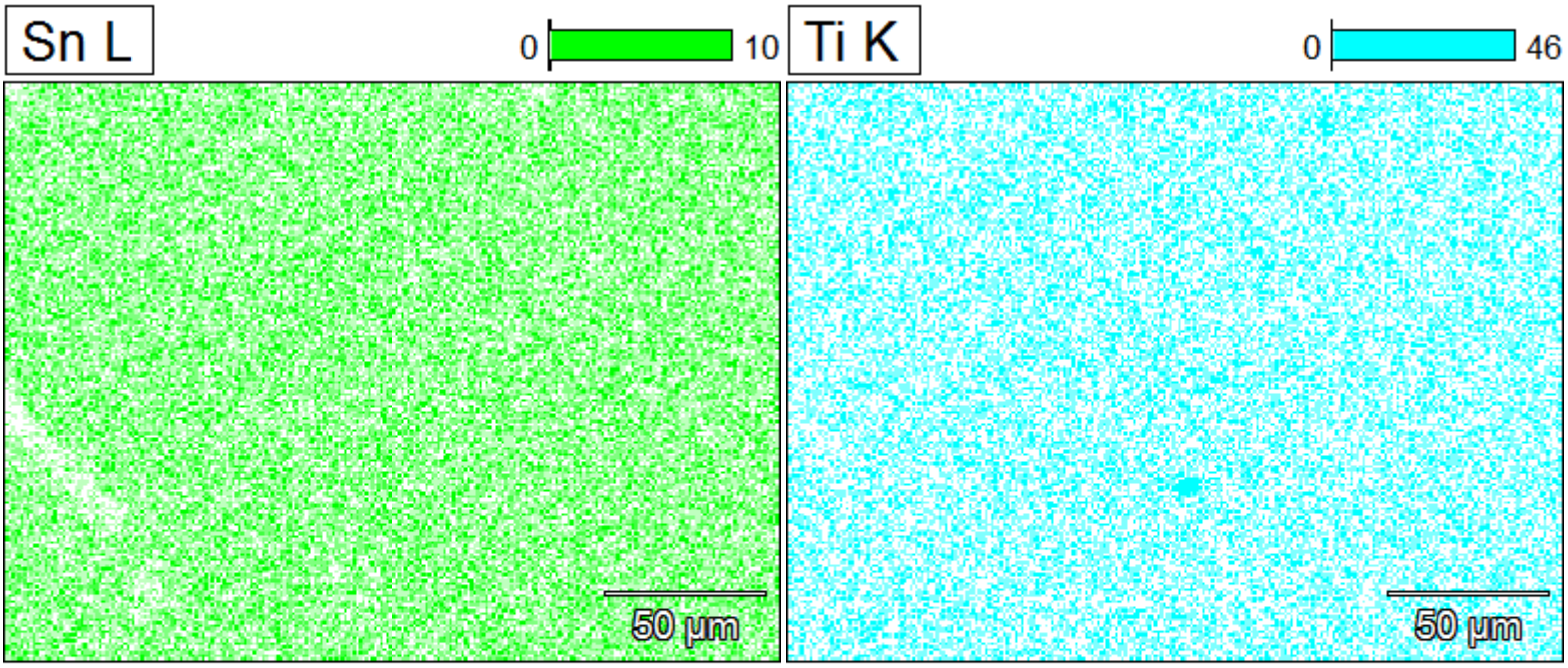
Sn L
0
10
50 µm
Ti K
0
46
50 µm

Project: Yang

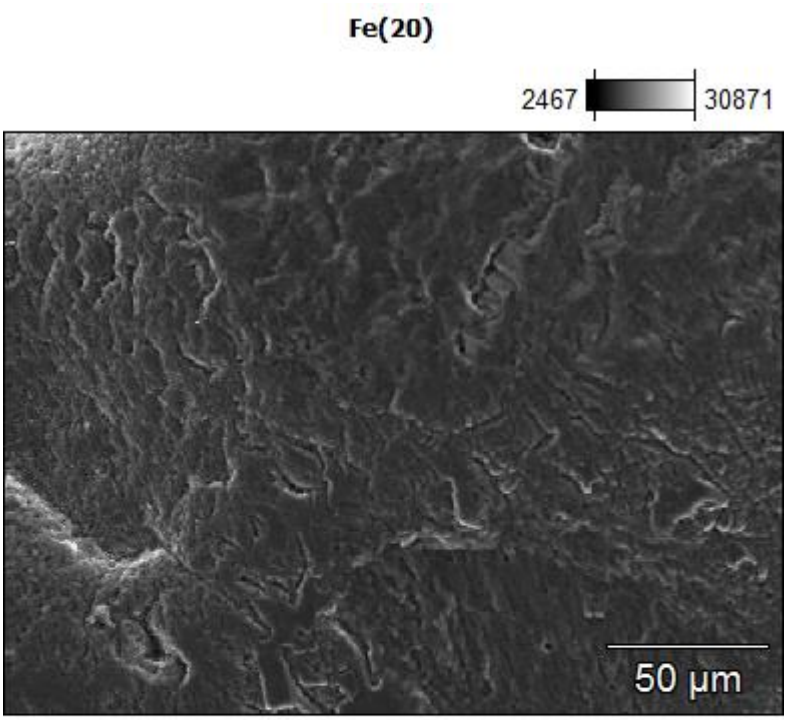

Data Type:	Counts
Image Resolution:	512 by 384
Image Pixel Size:	0.47 µm
Map Resolution:	256 by 192
Map Pixel Size:	0.95 µm
Acc. Voltage:	15.0 kV
Magnification:	500

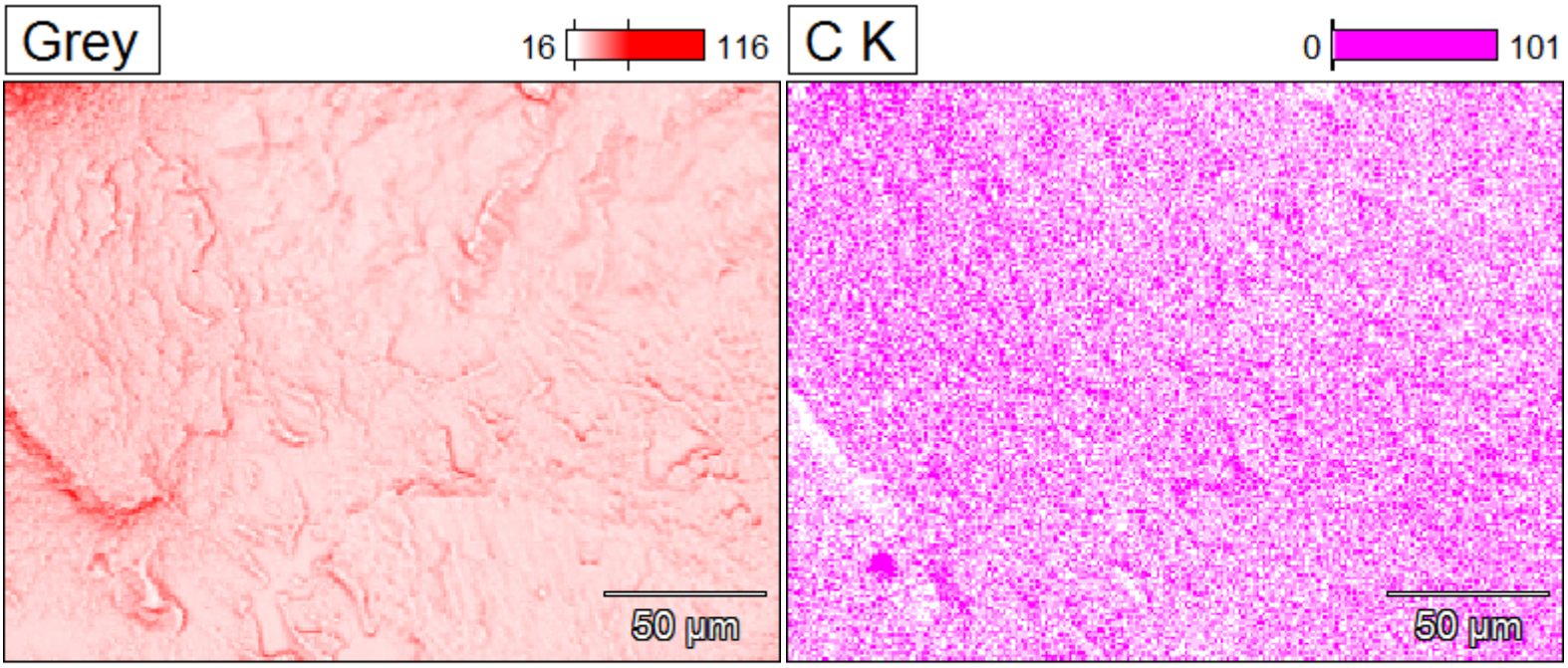
Grey
16
116
50 µm
C K
0
101
50 µm

Project: Yang

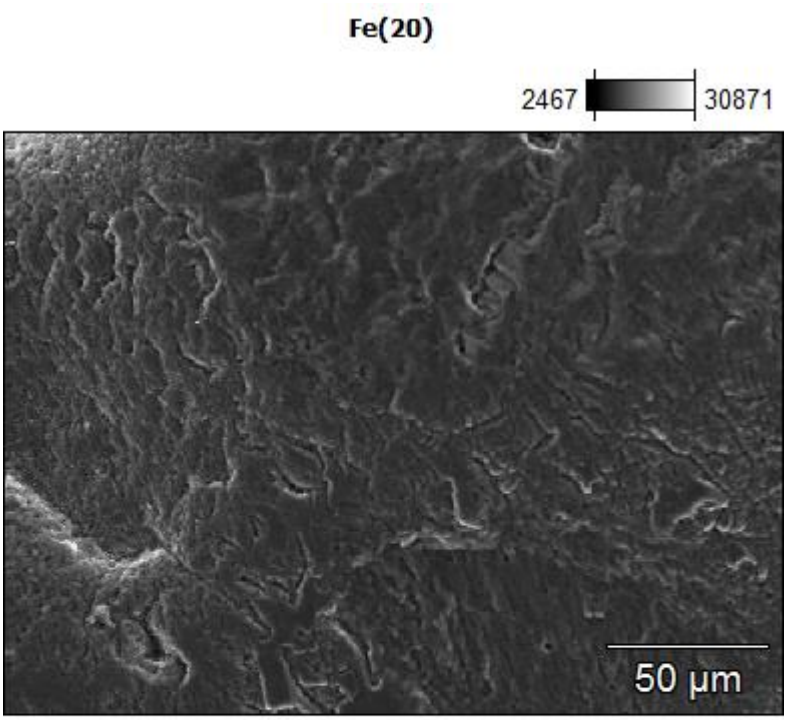

Data Type:	Counts
Image Resolution:	512 by 384
Image Pixel Size:	0.47 µm
Map Resolution:	256 by 192
Map Pixel Size:	0.95 µm
Acc. Voltage:	15.0 kV
Magnification:	500

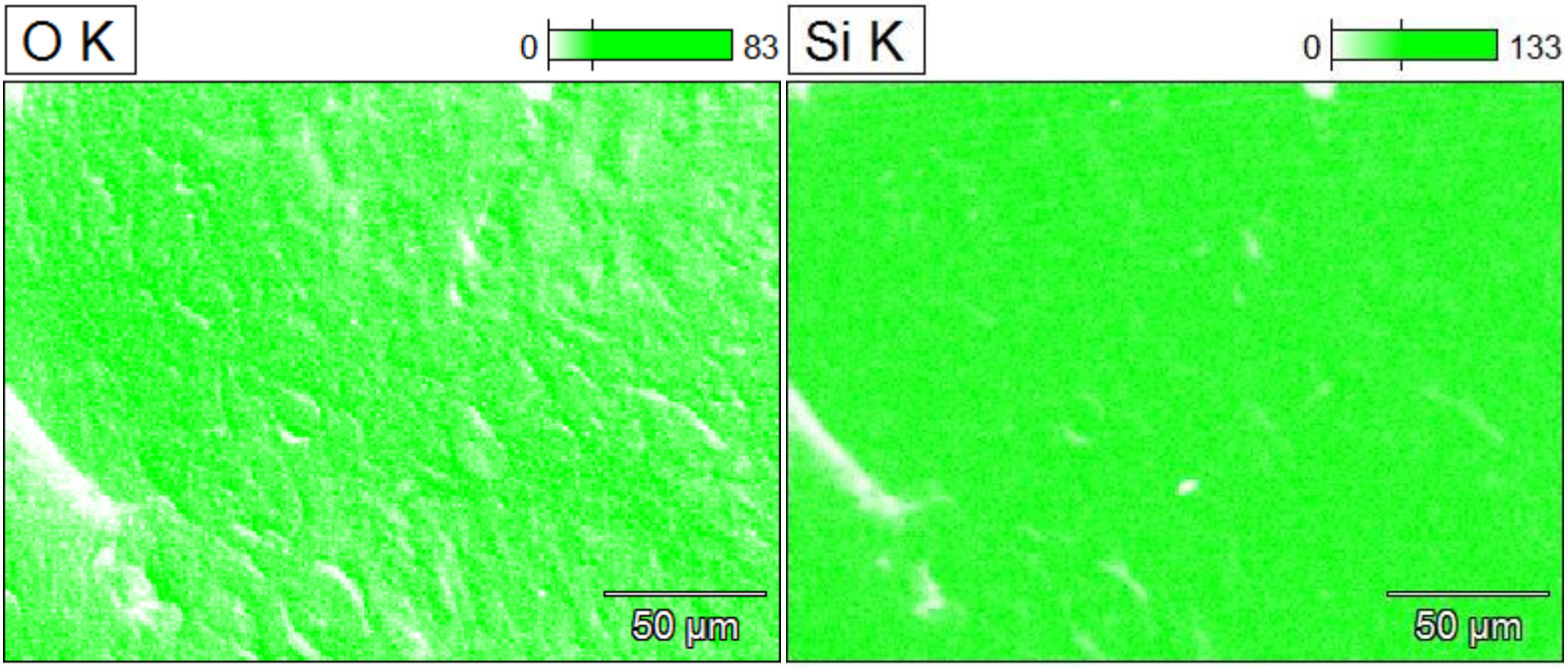
O K
0
83
50 µm
Si K
0
133
50 µm

Project: Yang

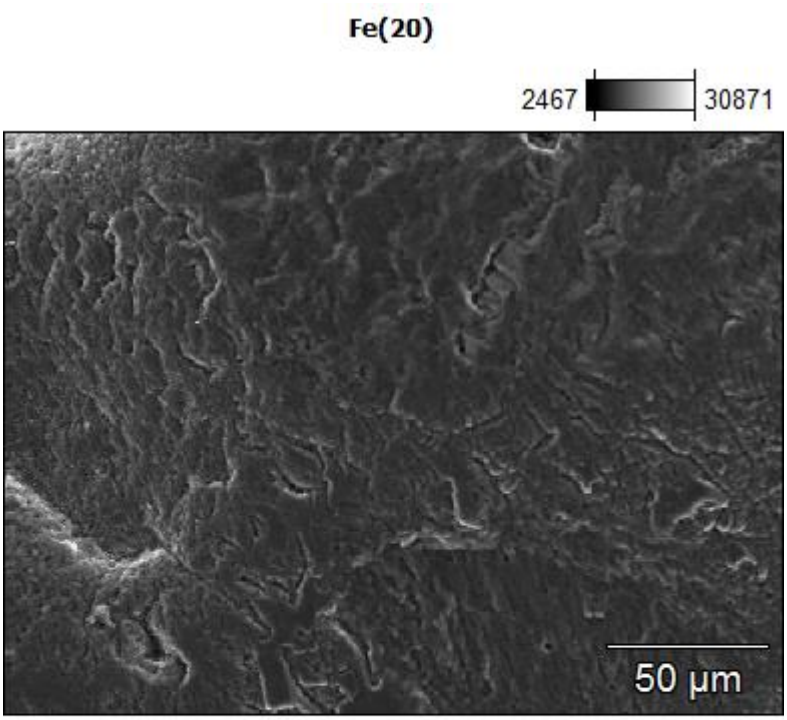

Data Type:	Counts
Image Resolution:	512 by 384
Image Pixel Size:	0.47 µm
Map Resolution:	256 by 192
Map Pixel Size:	0.95 µm
Acc. Voltage:	15.0 kV
Magnification:	500

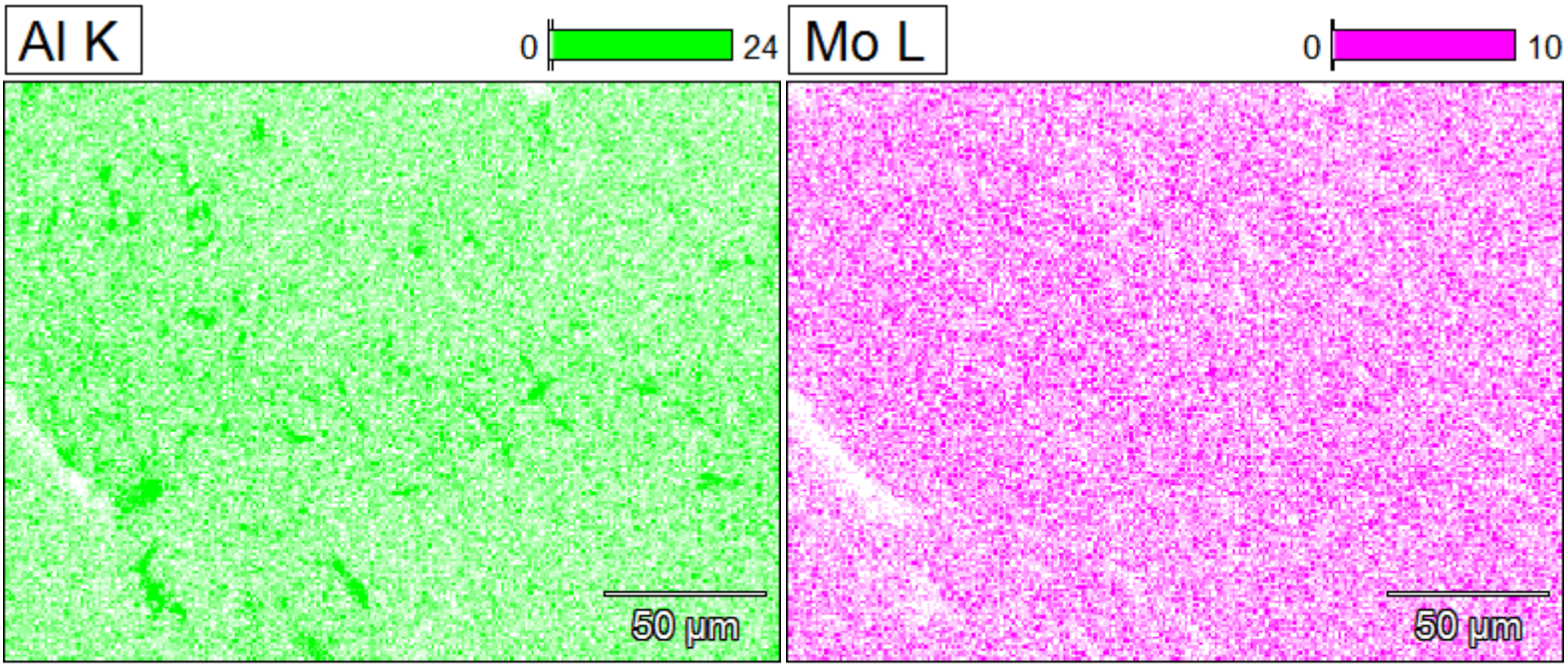
Al K
0
24
50 µm
Mo L
0
10
50 µm

Project: Yang

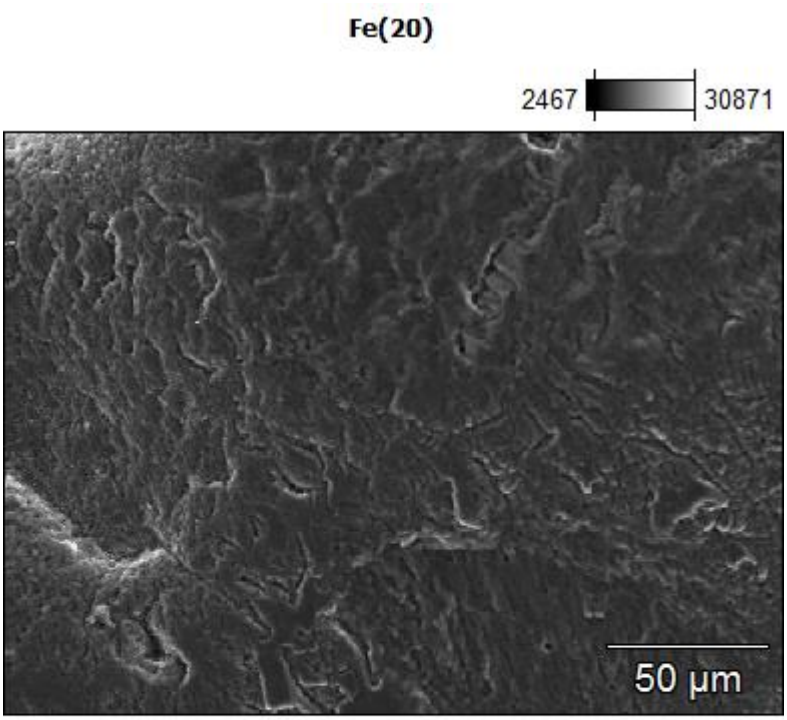

Data Type:	Counts
Image Resolution:	512 by 384
Image Pixel Size:	0.47 µm
Map Resolution:	256 by 192
Map Pixel Size:	0.95 µm
Acc. Voltage:	15.0 kV
Magnification:	500

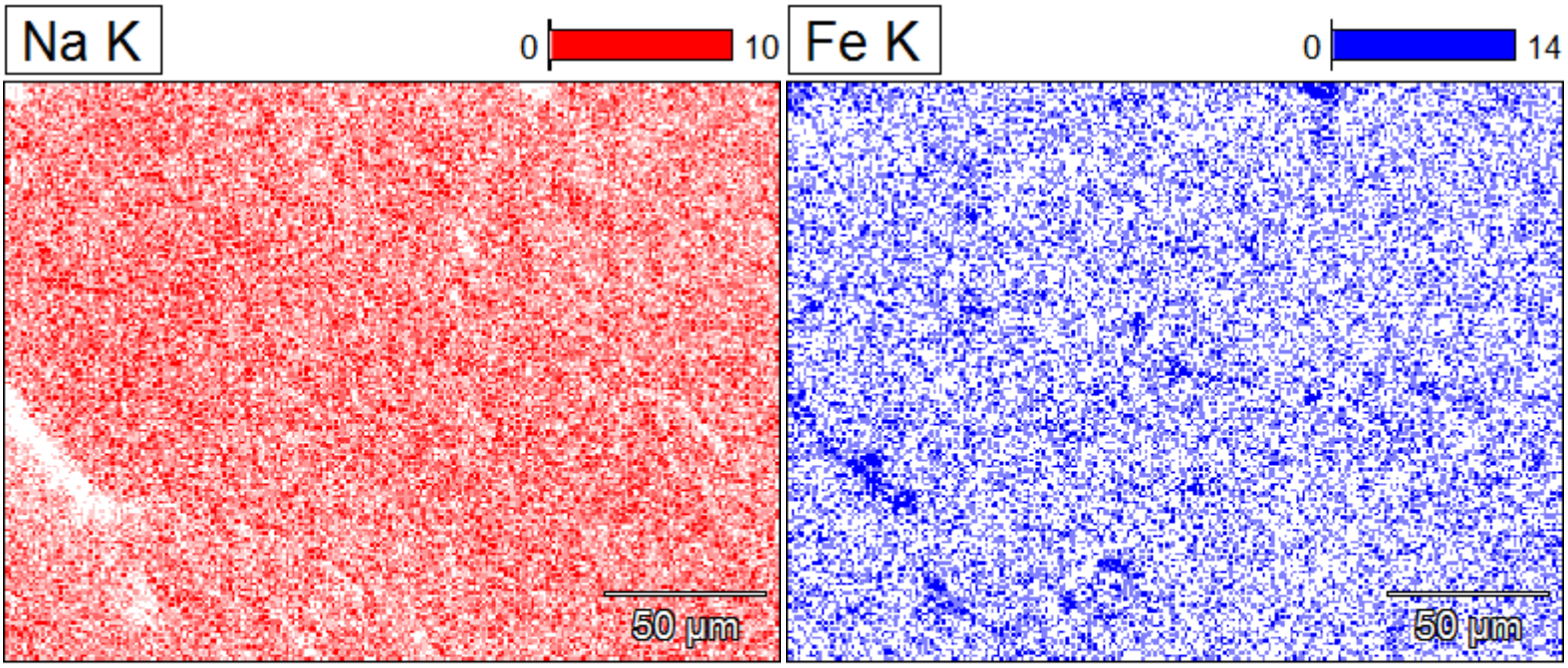
Na K
0
10
50 µm
Fe K
0
14
50 µm

Project: Yang

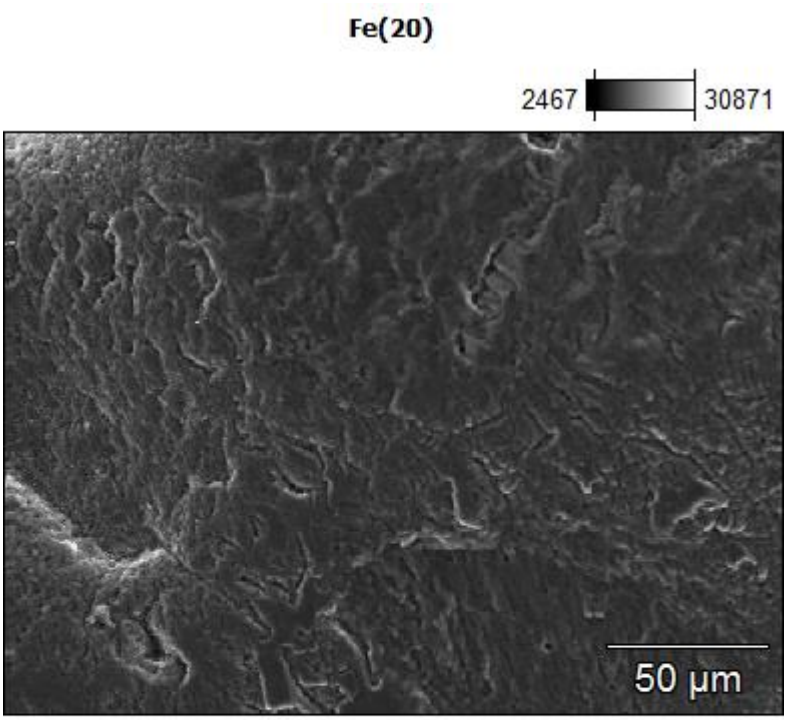

Data Type:	Counts
Image Resolution:	512 by 384
Image Pixel Size:	0.47 µm
Map Resolution:	256 by 192
Map Pixel Size:	0.95 µm
Acc. Voltage:	15.0 kV
Magnification:	500

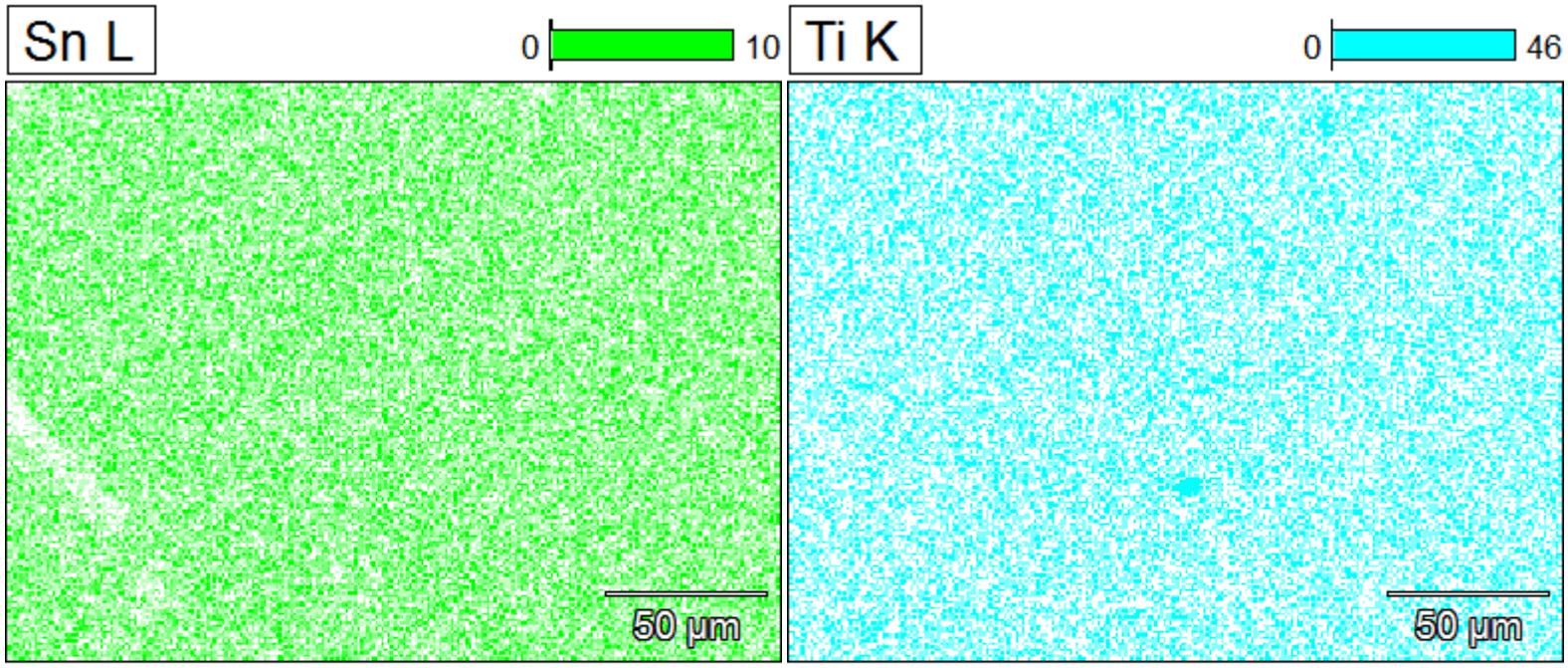
Sn L
0
10
50 µm
Ti K
0
46
50 µm

Project: Yang

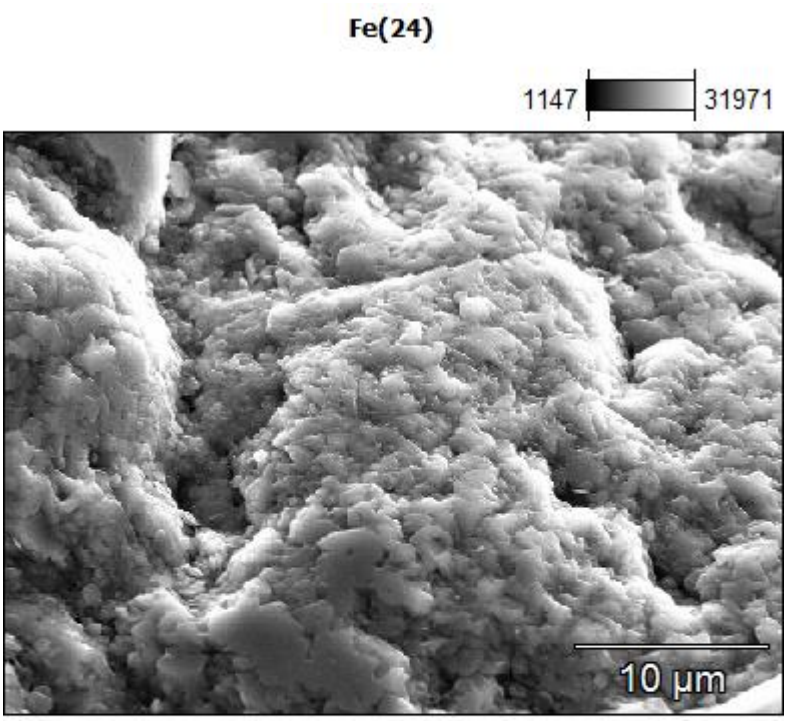

Data Type:	Counts
Image Resolution:	512 by 384
Image Pixel Size:	0.08 µm
Map Resolution:	256 by 192
Map Pixel Size:	0.16 µm
Acc. Voltage:	15.0 kV
Magnification:	3000

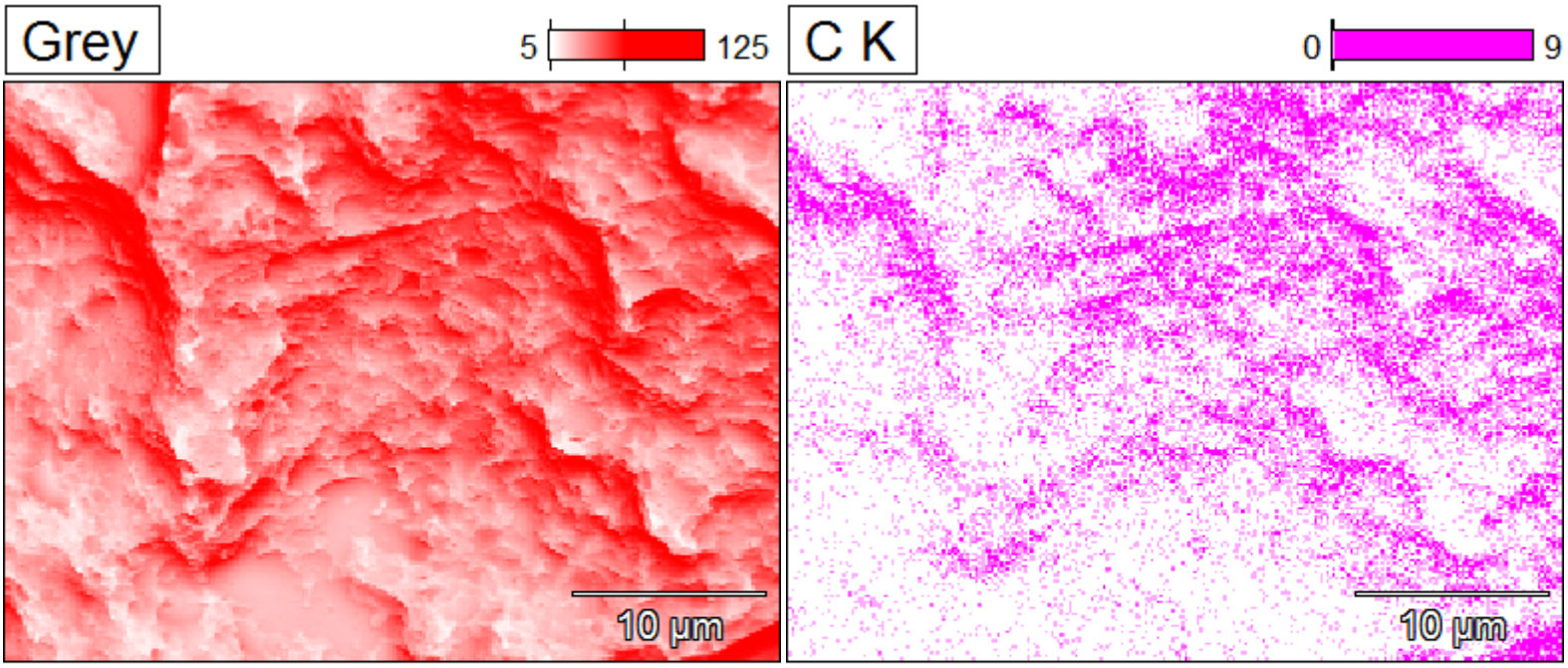
Grey
5
125
10 µm
C K
0
9
10 µm

Project: Yang

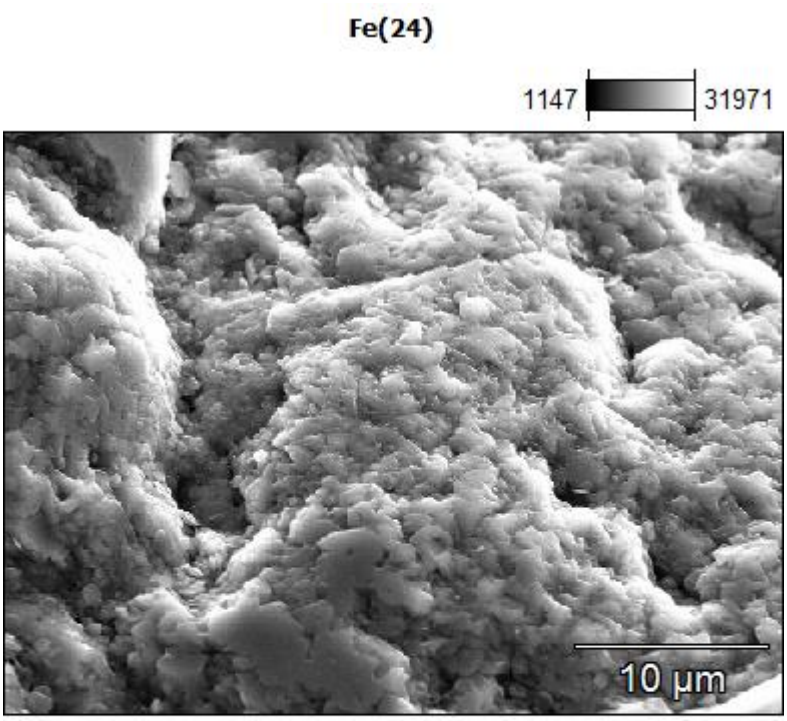

Data Type:	Counts
Image Resolution:	512 by 384
Image Pixel Size:	0.08 µm
Map Resolution:	256 by 192
Map Pixel Size:	0.16 µm
Acc. Voltage:	15.0 kV
Magnification:	3000

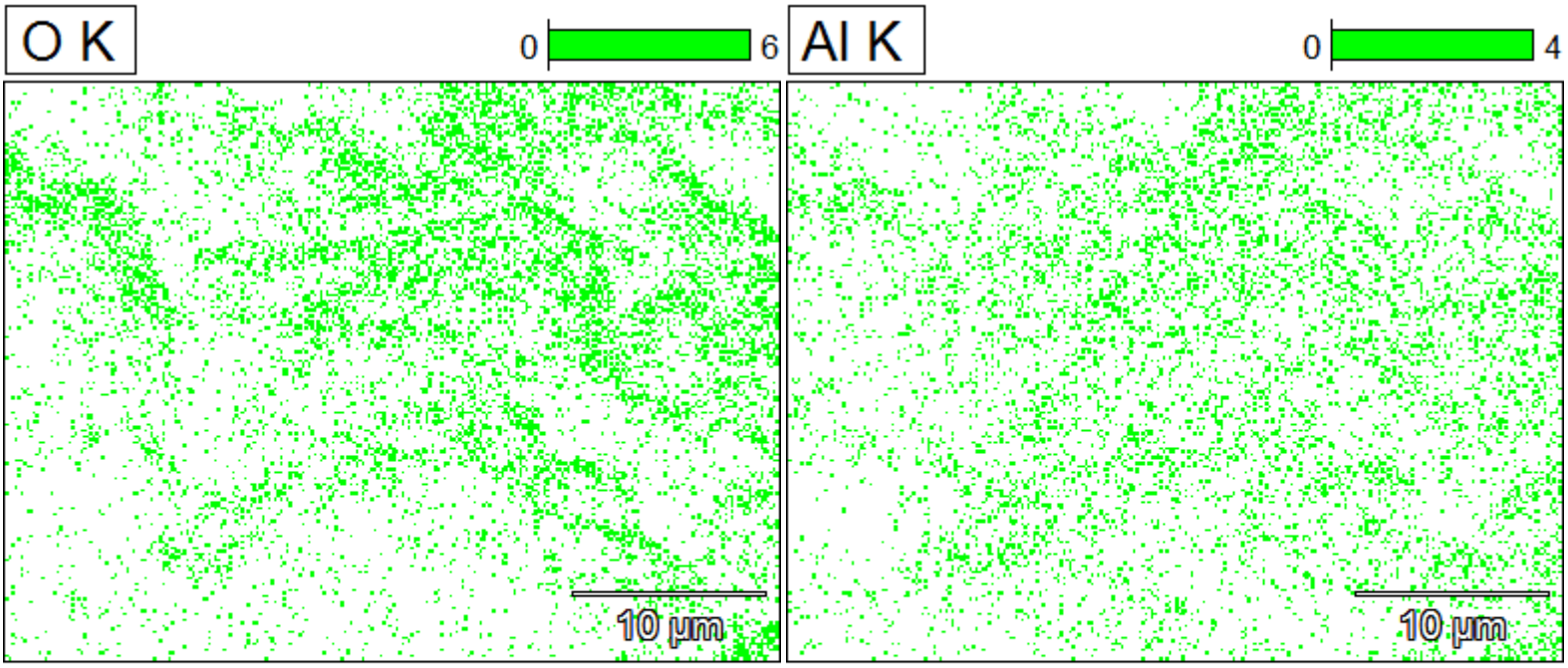
O K
0
6
10 µm
Al K
0
4
10 µm

Project: Yang

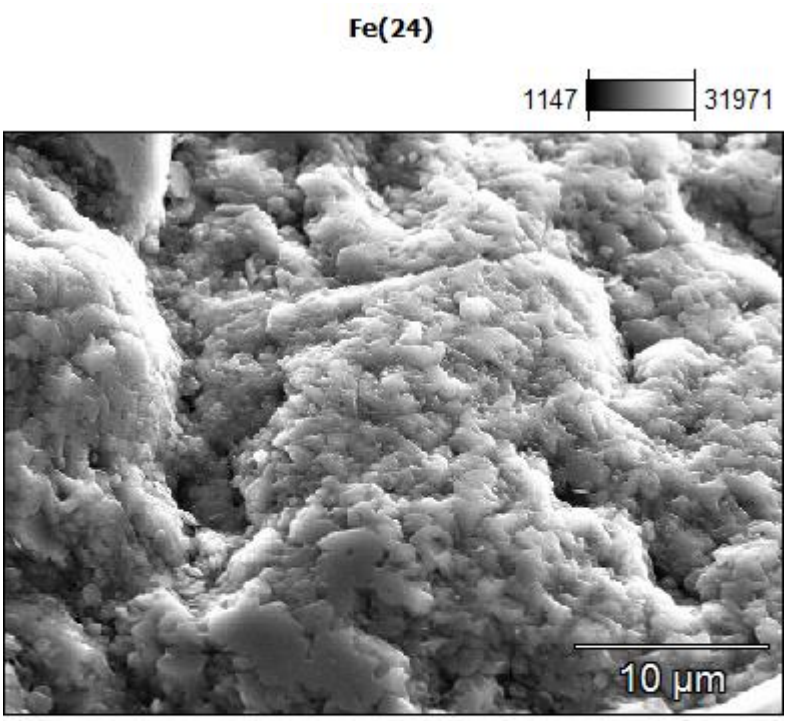

Data Type:	Counts
Image Resolution:	512 by 384
Image Pixel Size:	0.08 µm
Map Resolution:	256 by 192
Map Pixel Size:	0.16 µm
Acc. Voltage:	15.0 kV
Magnification:	3000

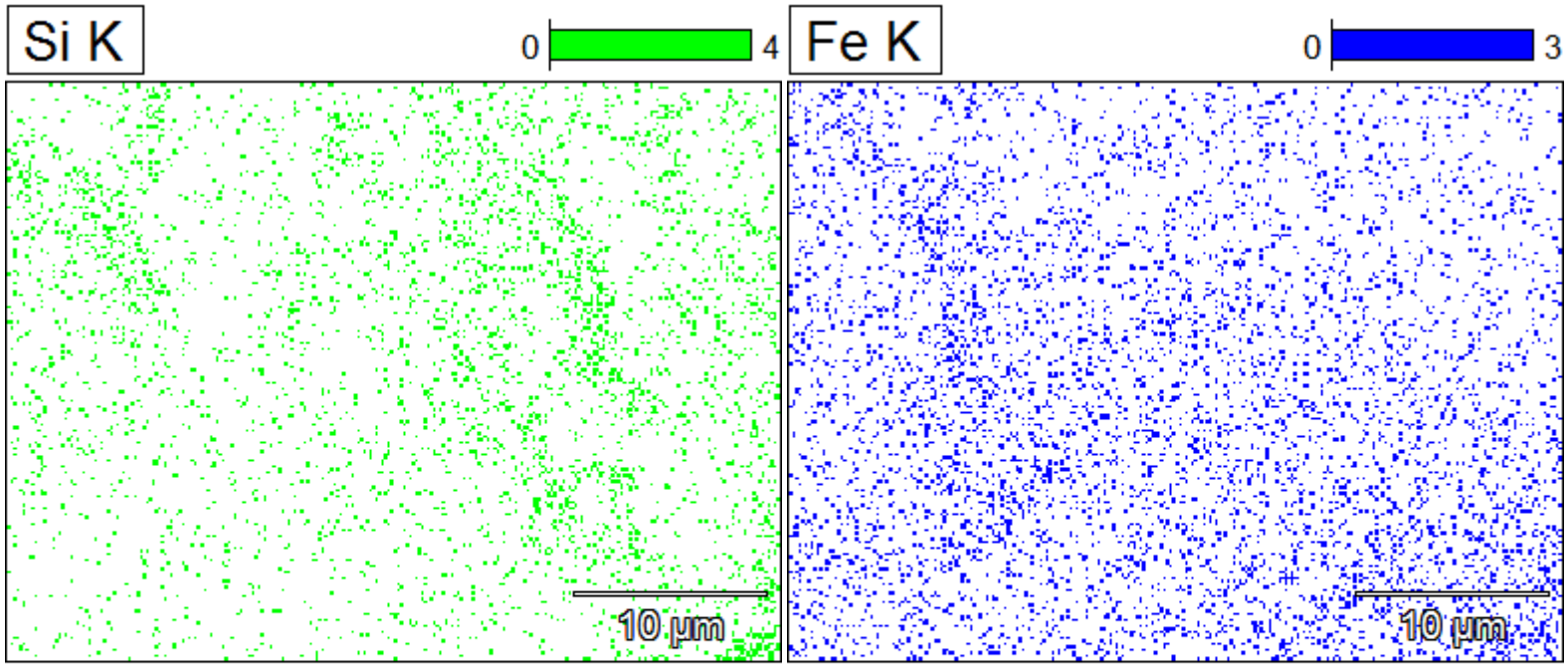
Si K
0
4
10 µm
Fe K
0
3
10 µm

Project: Yang

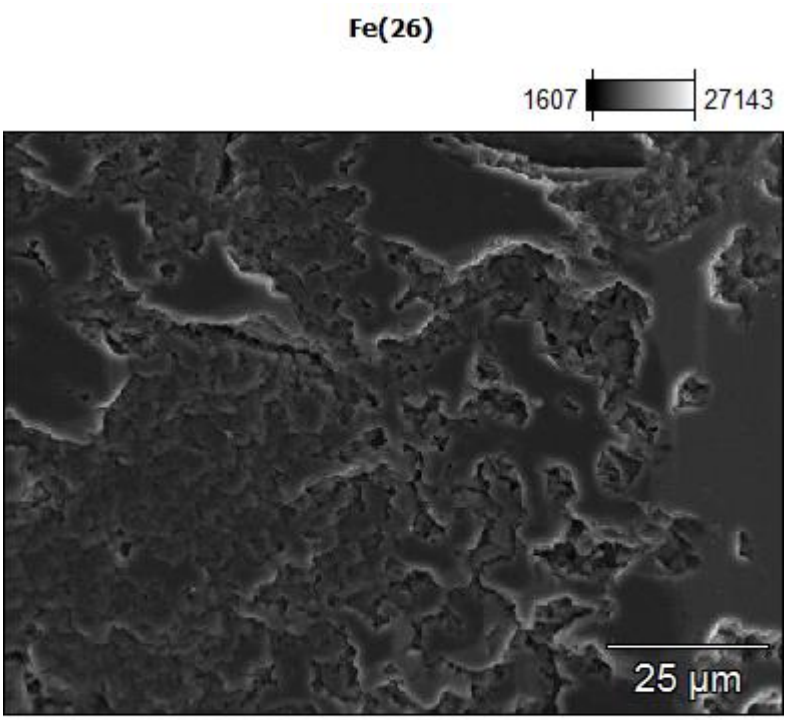

Data Type:	Counts
Image Resolution:	512 by 384
Image Pixel Size:	0.24 µm
Map Resolution:	256 by 192
Map Pixel Size:	0.47 µm
Acc. Voltage:	15.0 kV
Magnification:	1000

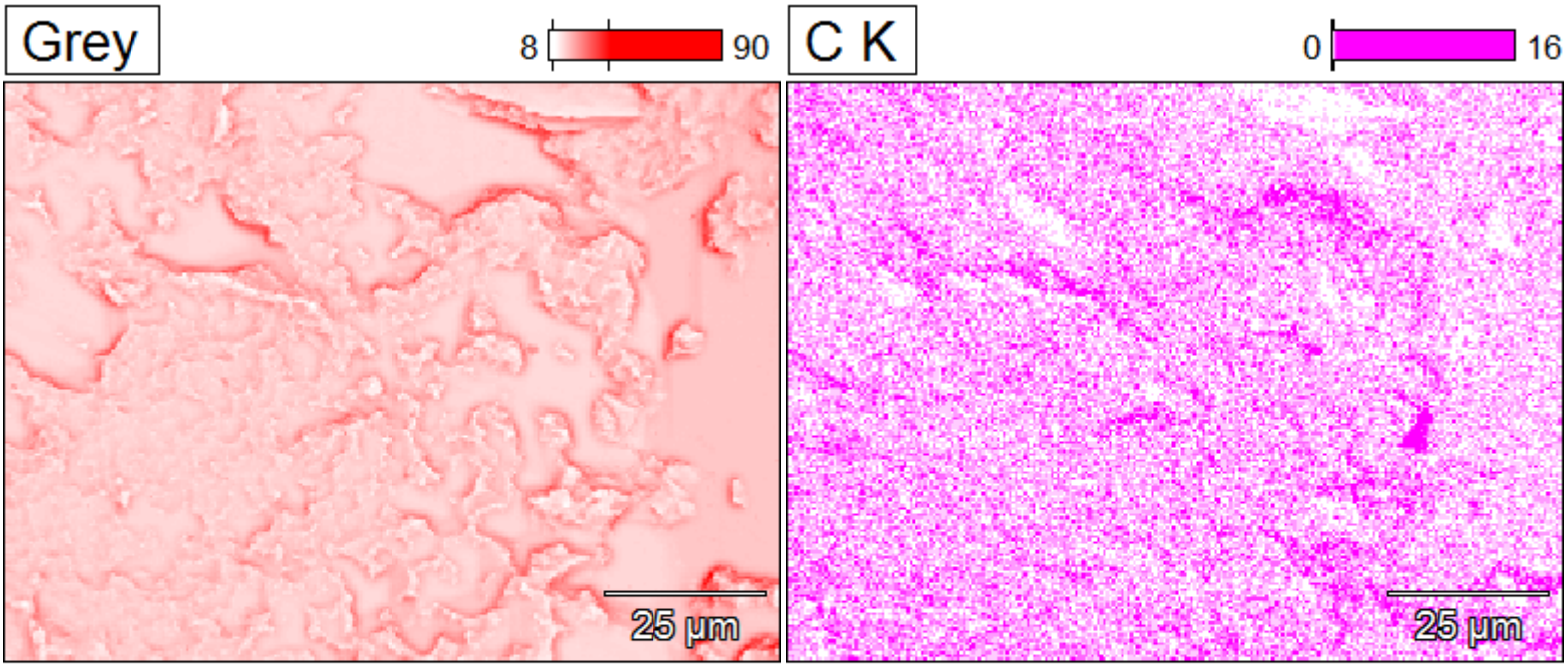
Grey
8
90
25 µm
C K
0
16
25 µm

Project: Yang

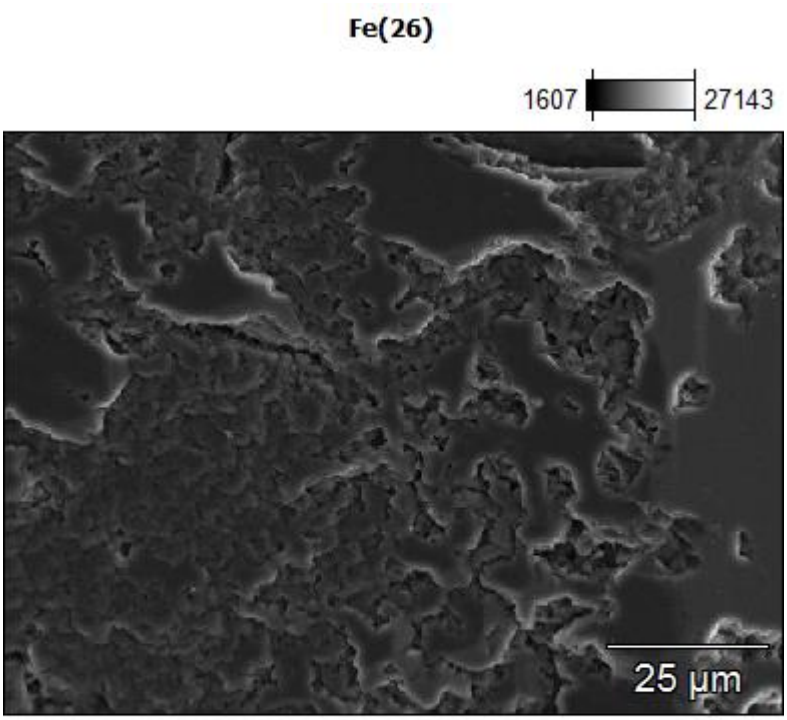

Data Type:	Counts
Image Resolution:	512 by 384
Image Pixel Size:	0.24 µm
Map Resolution:	256 by 192
Map Pixel Size:	0.47 µm
Acc. Voltage:	15.0 kV
Magnification:	1000

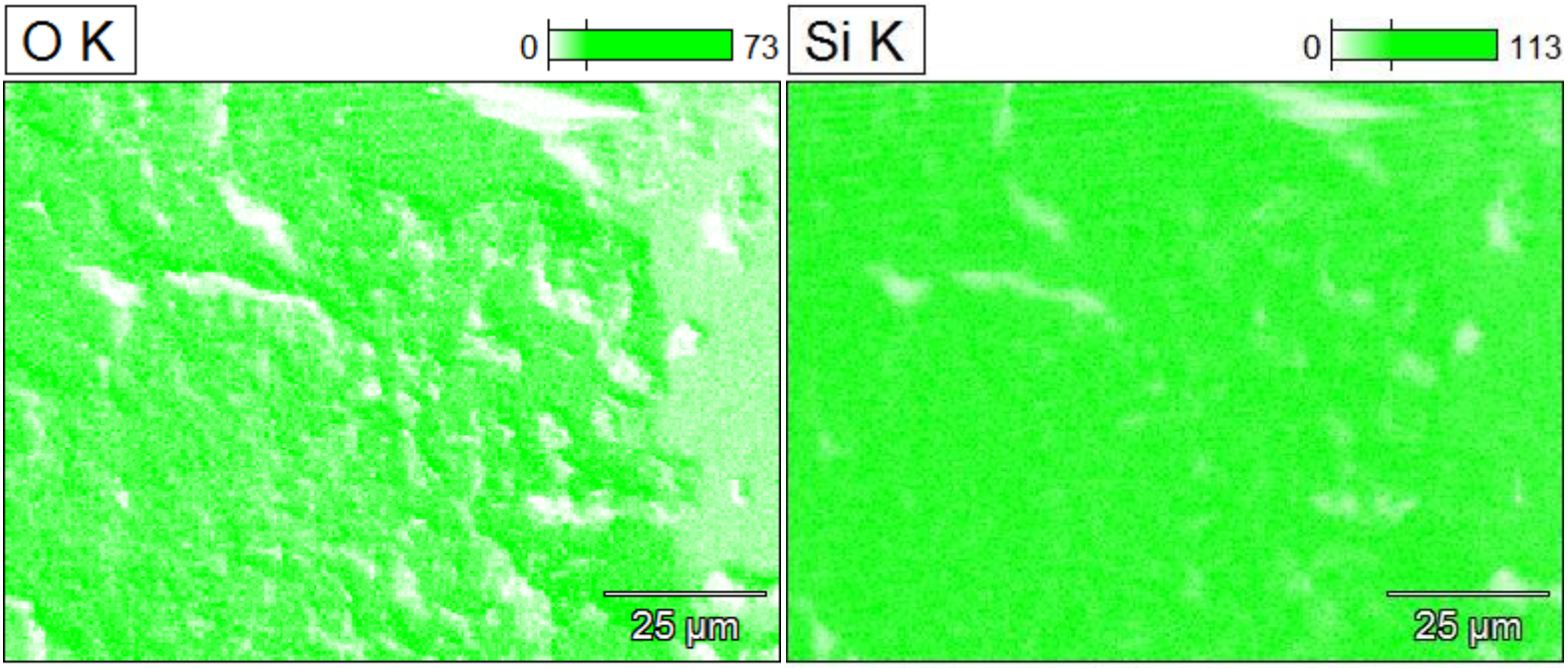
O K
0
73
25 µm
Si K
0
113
25 µm

Project: Yang

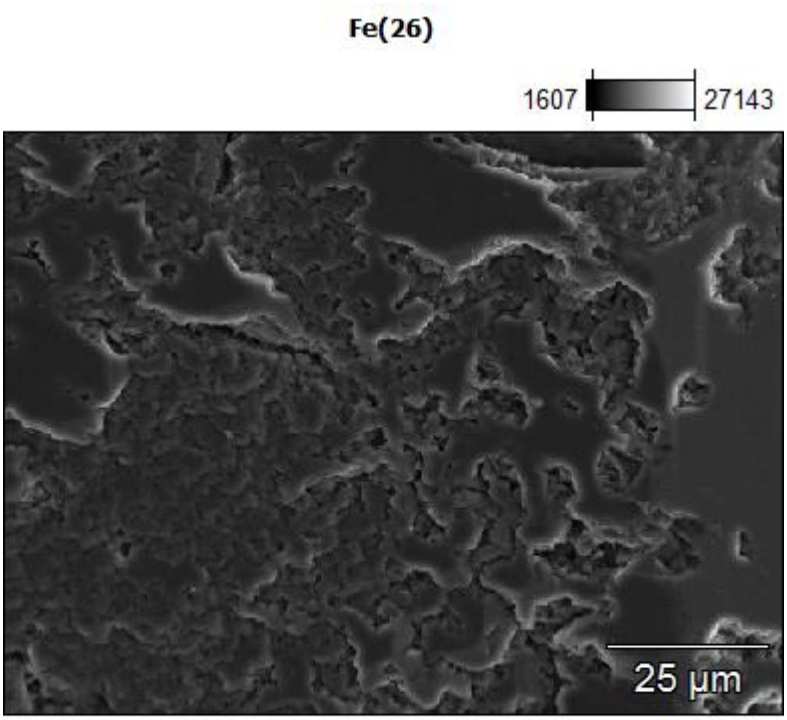

Data Type:	Counts
Image Resolution:	512 by 384
Image Pixel Size:	0.24 µm
Map Resolution:	256 by 192
Map Pixel Size:	0.47 µm
Acc. Voltage:	15.0 kV
Magnification:	1000

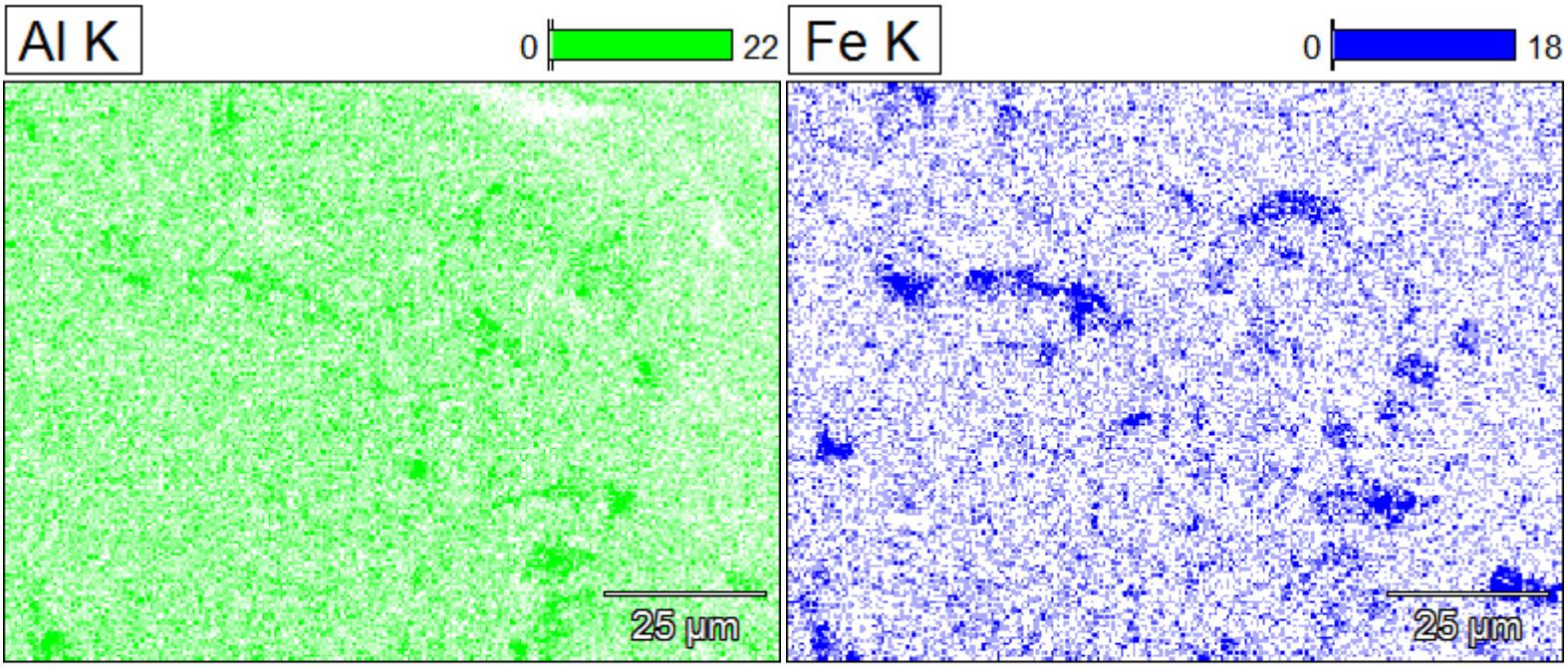
Al K
0
22
25 µm
Fe K
0
18
25 µm

Project: Yang

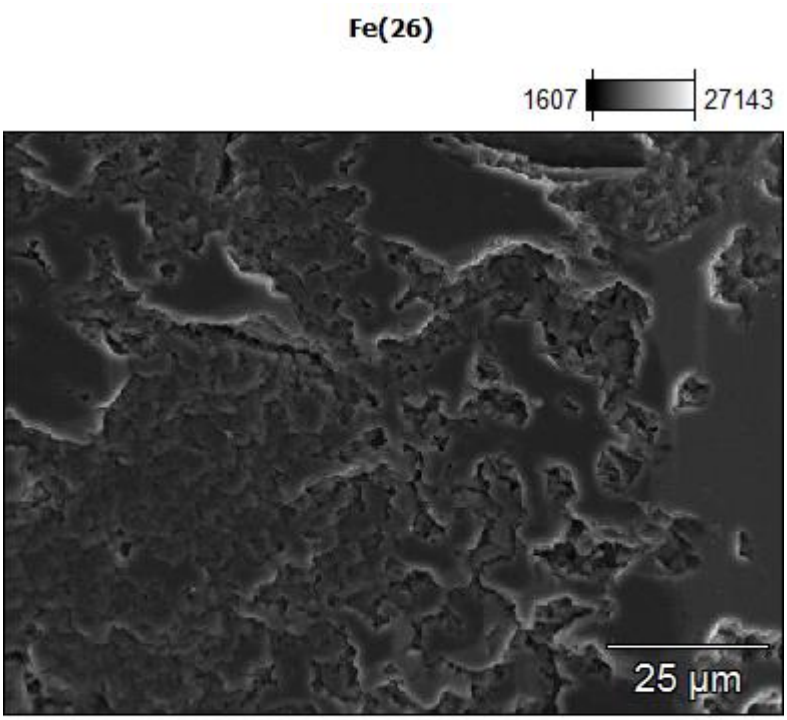

Data Type:	Counts
Image Resolution:	512 by 384
Image Pixel Size:	0.24 µm
Map Resolution:	256 by 192
Map Pixel Size:	0.47 µm
Acc. Voltage:	15.0 kV
Magnification:	1000

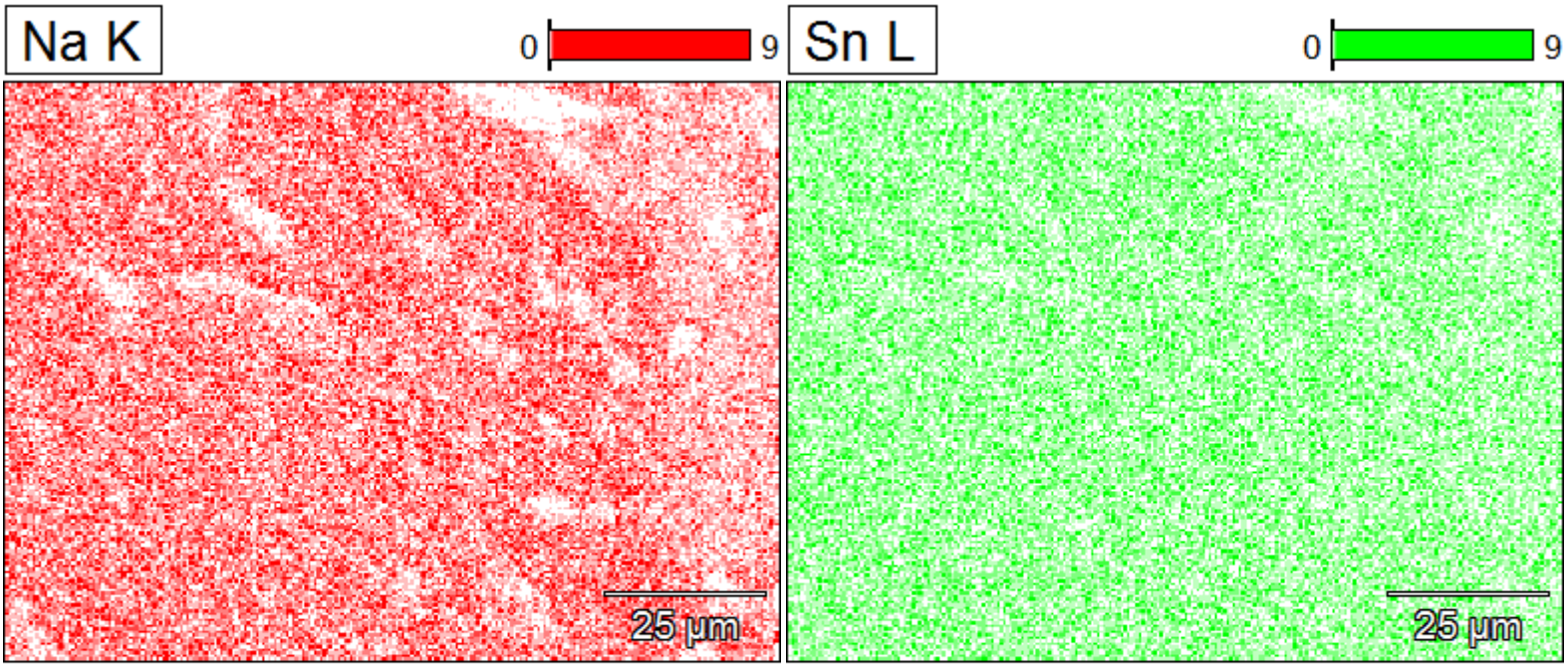
Na K
0
9
25 µm
Sn L
0
9
25 µm

Project: Yang

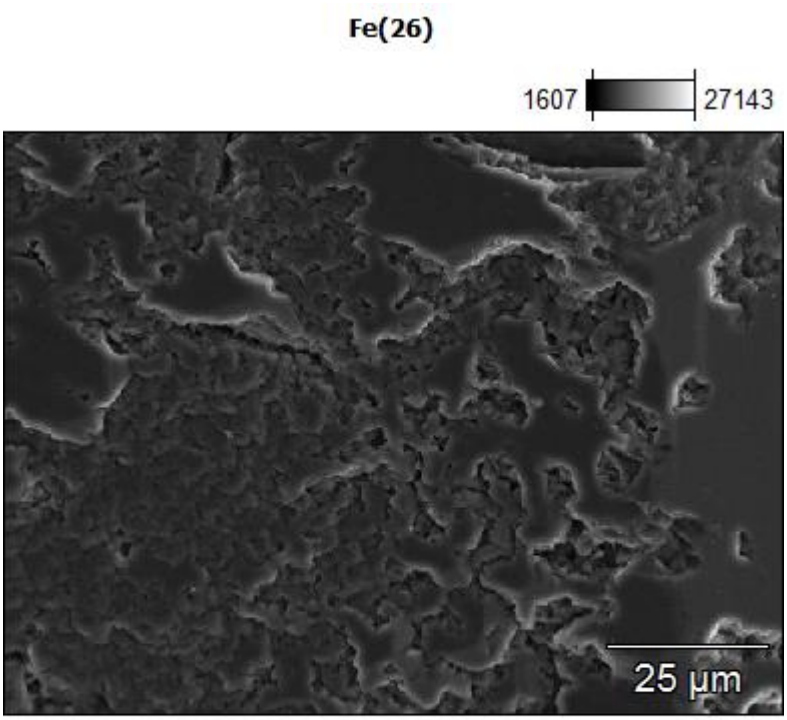

Data Type:	Counts
Image Resolution:	512 by 384
Image Pixel Size:	0.24 µm
Map Resolution:	256 by 192
Map Pixel Size:	0.47 µm
Acc. Voltage:	15.0 kV
Magnification:	1000

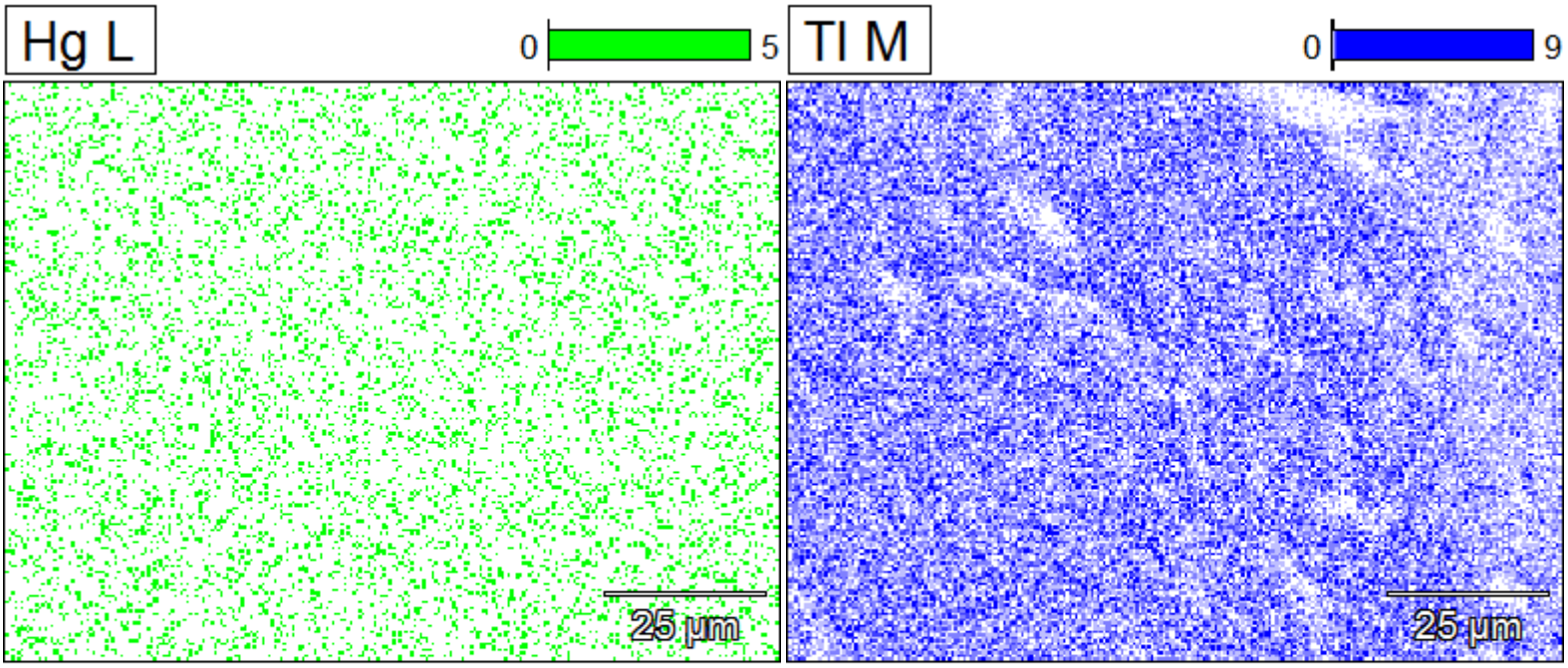
Hg L
0
5
25 µm
Tl M
0
9
25 µm

Project: Yang

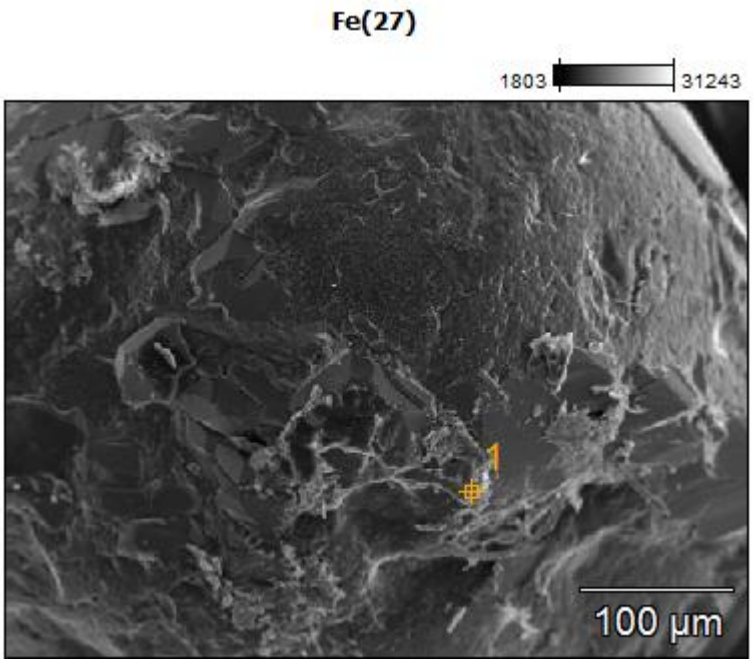

Image Name:	Fe(27)
Image Resolution:	512 by 384
Image Pixel Size:	0.95 µm
Acc. Voltage:	15.0 kV
Magnification:	250

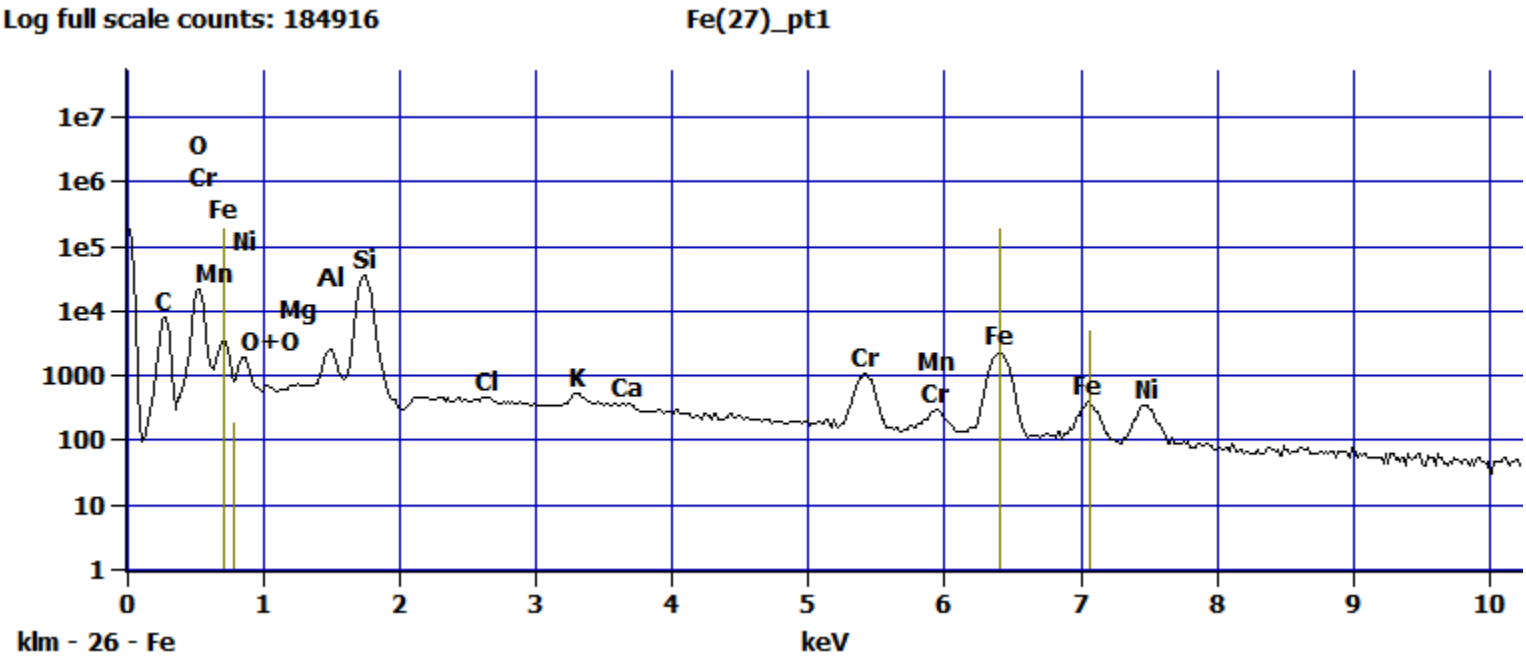

Project: Yang

Net Counts

Fe(27)_pt1-No Data.

Weight %

Fe(27)_pt1-No Data.

Atom %

Fe(27)_pt1-No Data.

Project: Yang

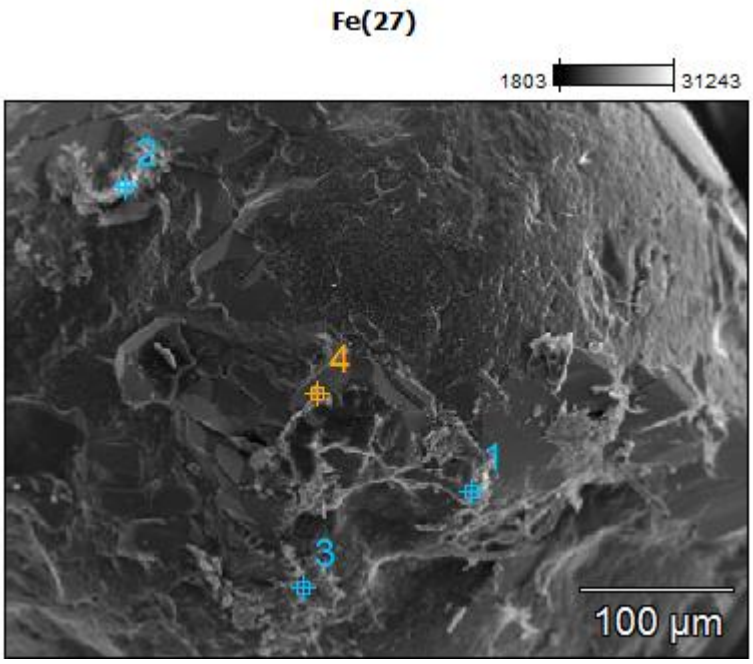

Image Name:	Fe(27)
Image Resolution:	512 by 384
Image Pixel Size:	0.95 µm
Acc. Voltage:	15.0 kV
Magnification:	250

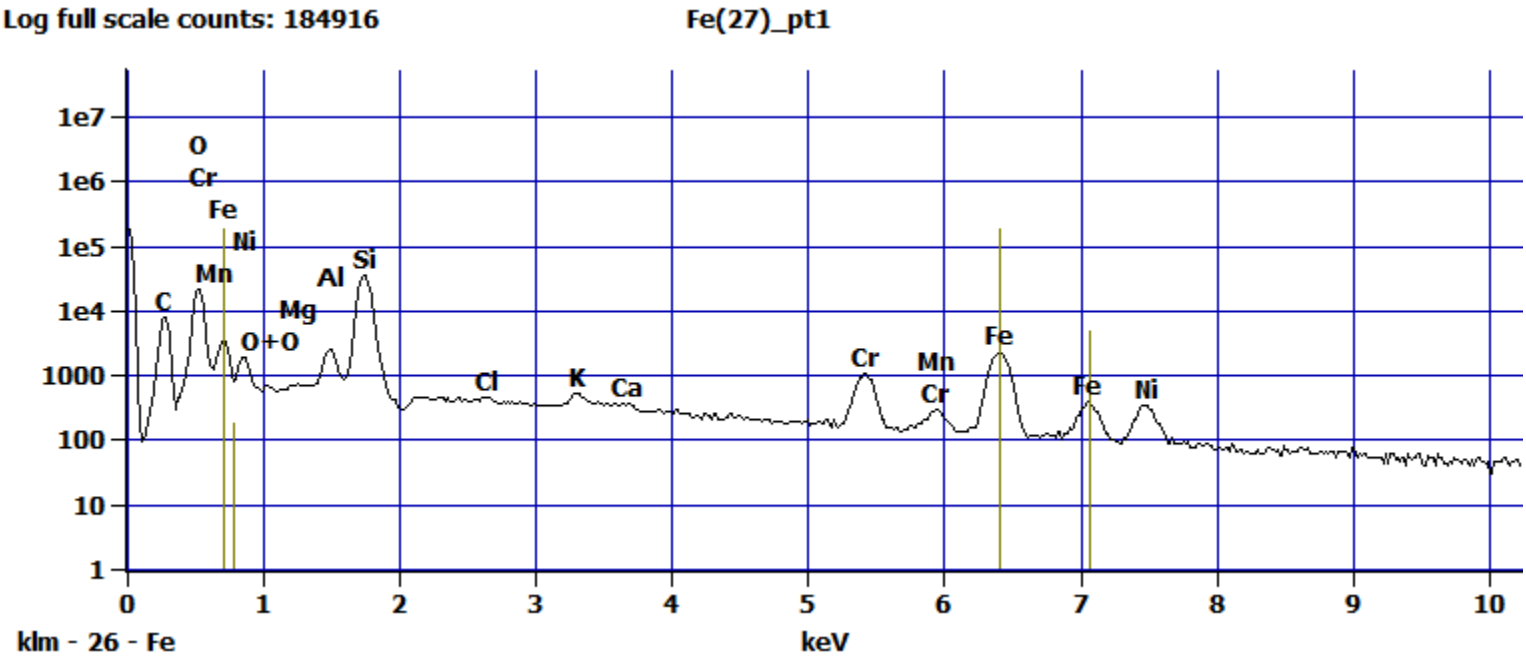

Project: Yang

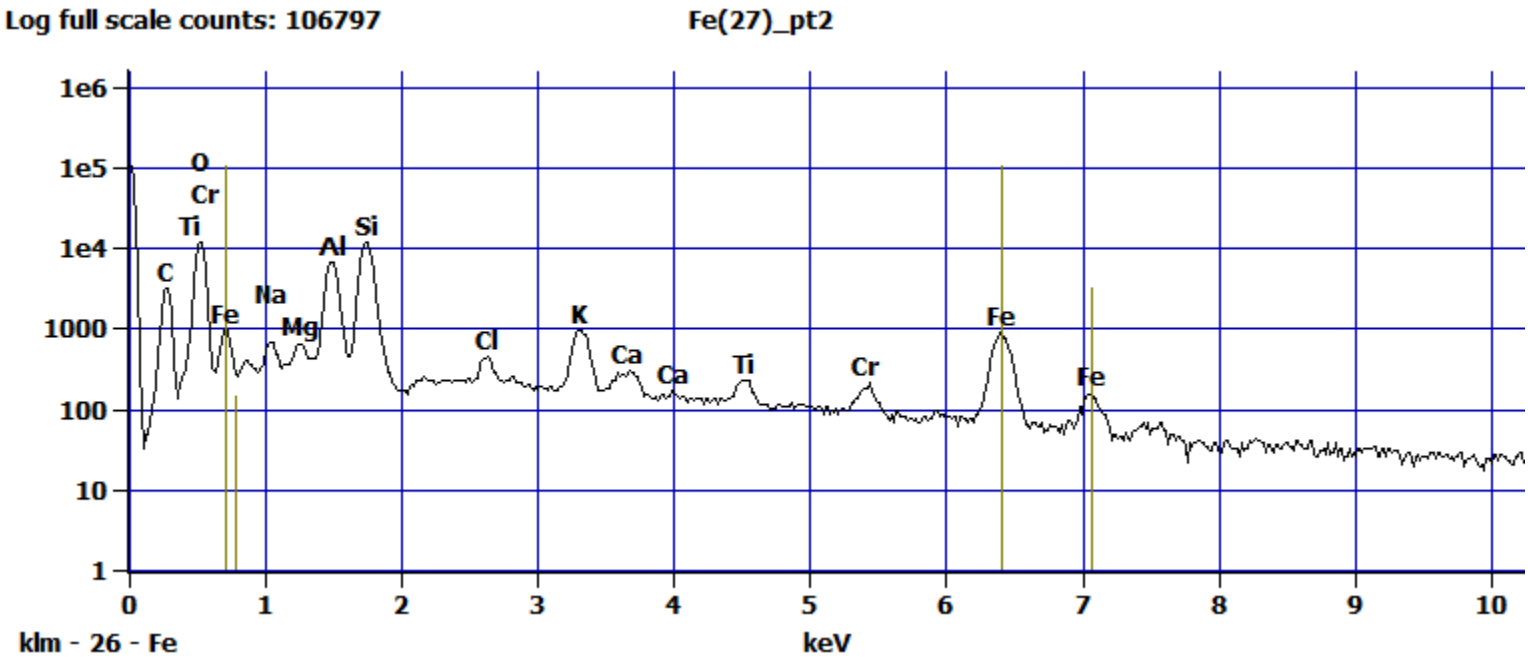

Project: Yang

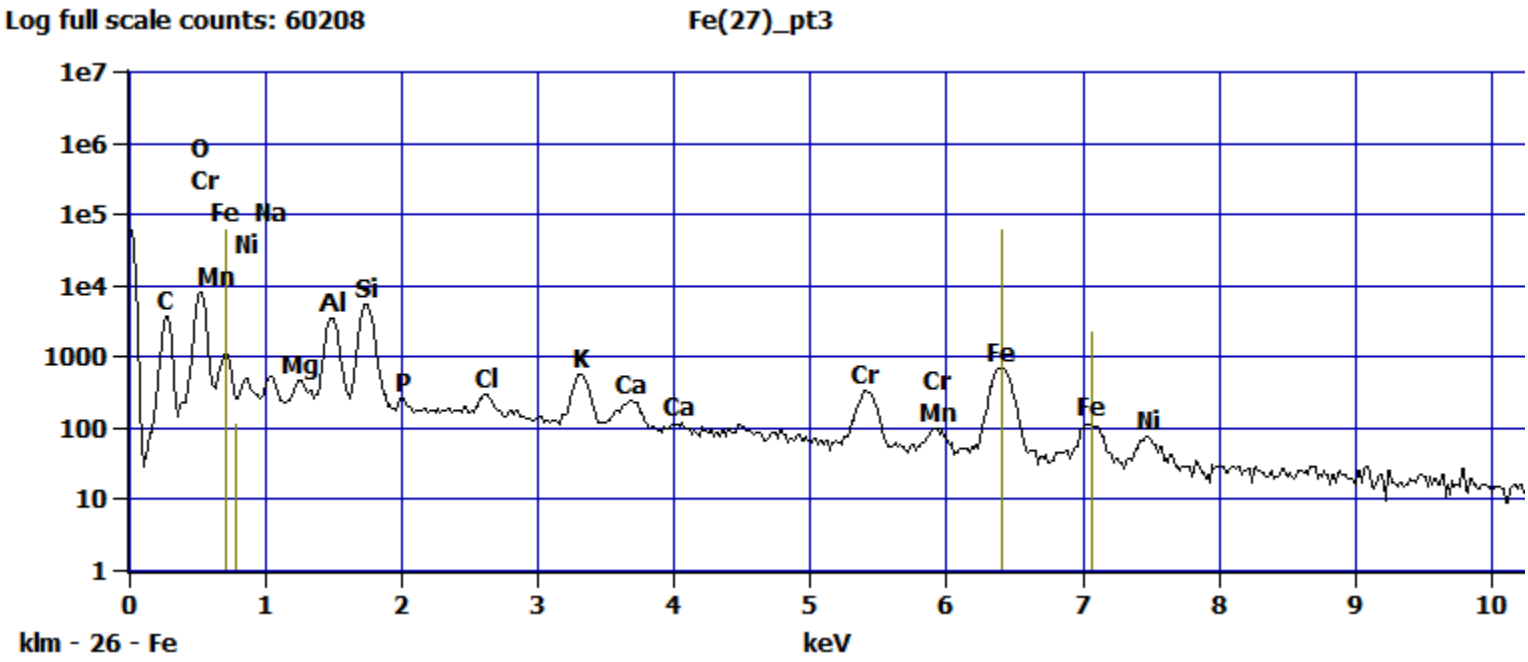

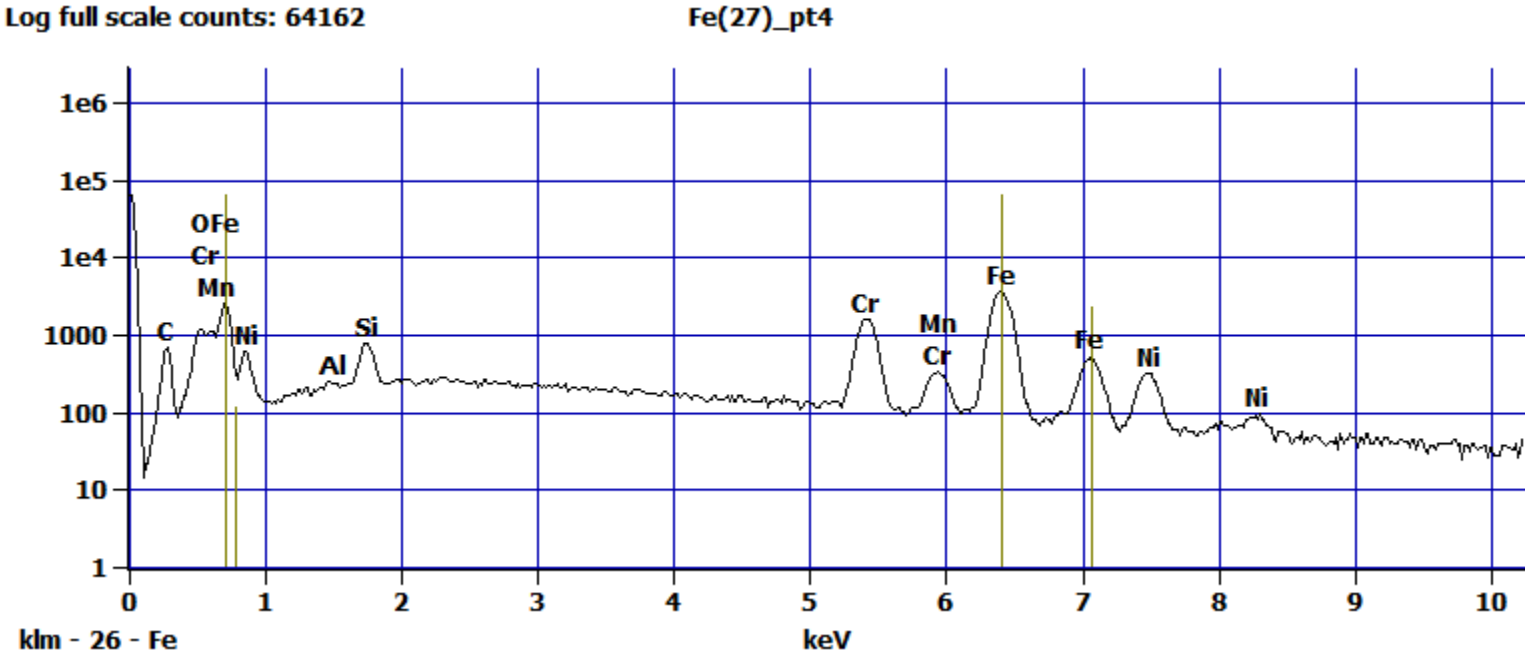

Project: Yang

Net Counts

Fe(27)_pt1-No Data.
Fe(27)_pt2-No Data.
Fe(27)_pt3-No Data.
Fe(27)_pt4-No Data.

Weight %

Fe(27)_pt1-No Data.
Fe(27)_pt2-No Data.
Fe(27)_pt3-No Data.
Fe(27)_pt4-No Data.

Atom %

Fe(27)_pt1-No Data.
Fe(27)_pt2-No Data.
Fe(27)_pt3-No Data.
Fe(27)_pt4-No Data.

Project: Yang

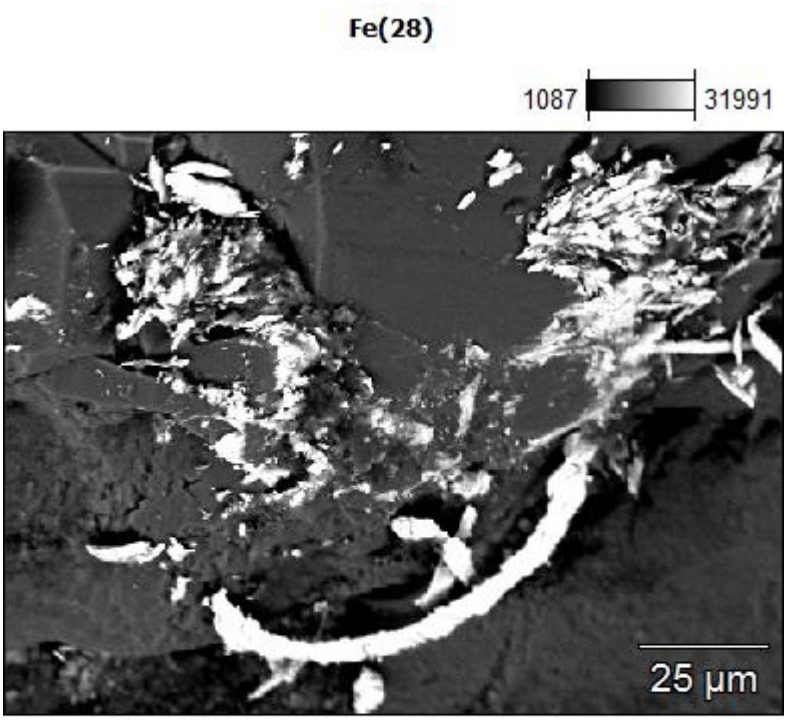

Data Type:	Counts
Image Resolution:	512 by 384
Image Pixel Size:	0.30 µm
Map Resolution:	256 by 192
Map Pixel Size:	0.59 µm
Acc. Voltage:	15.0 kV
Magnification:	800

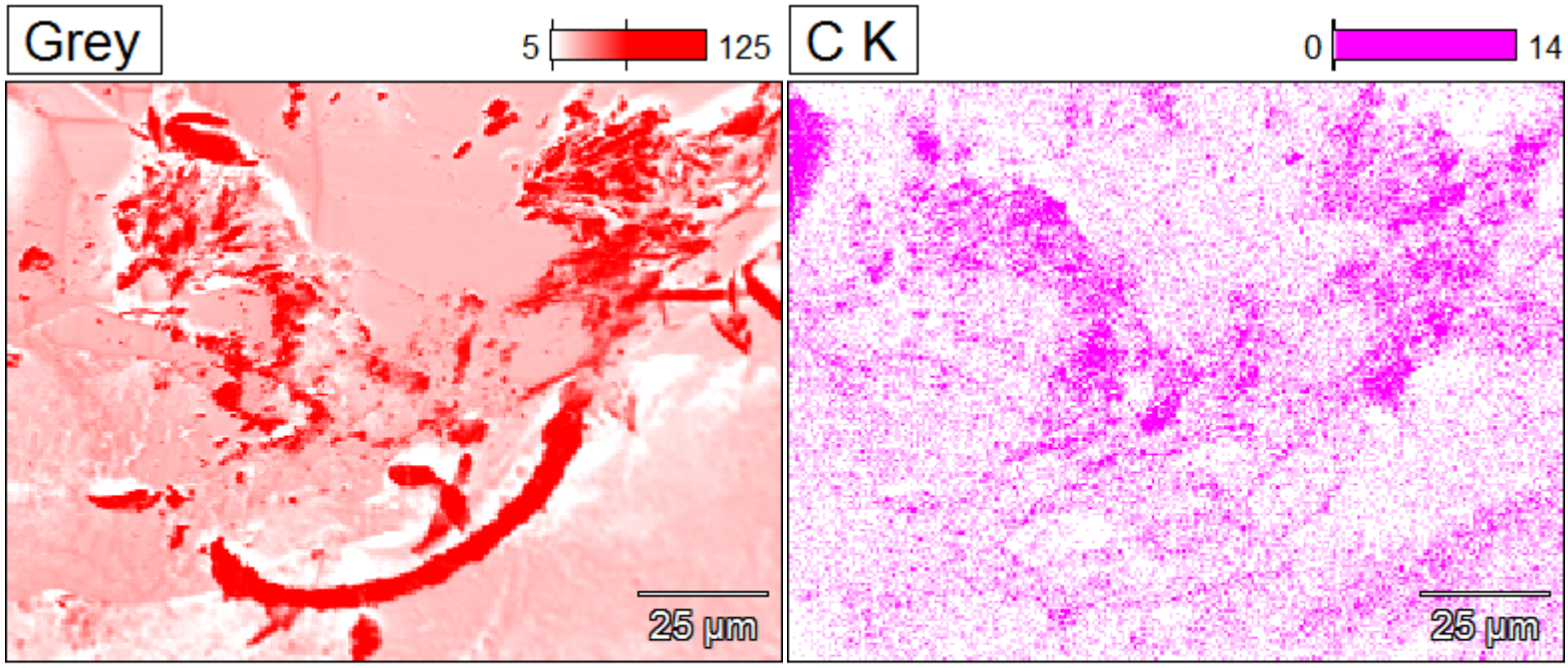
Grey
5
125
25 µm
C K
0
14
25 µm

Project: Yang

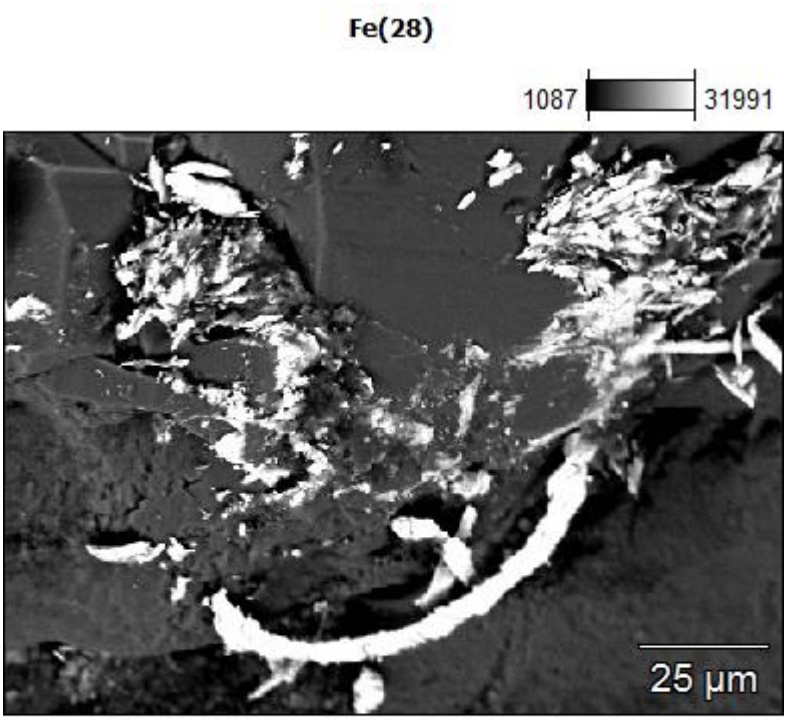

Data Type:	Counts
Image Resolution:	512 by 384
Image Pixel Size:	0.30 µm
Map Resolution:	256 by 192
Map Pixel Size:	0.59 µm
Acc. Voltage:	15.0 kV
Magnification:	800

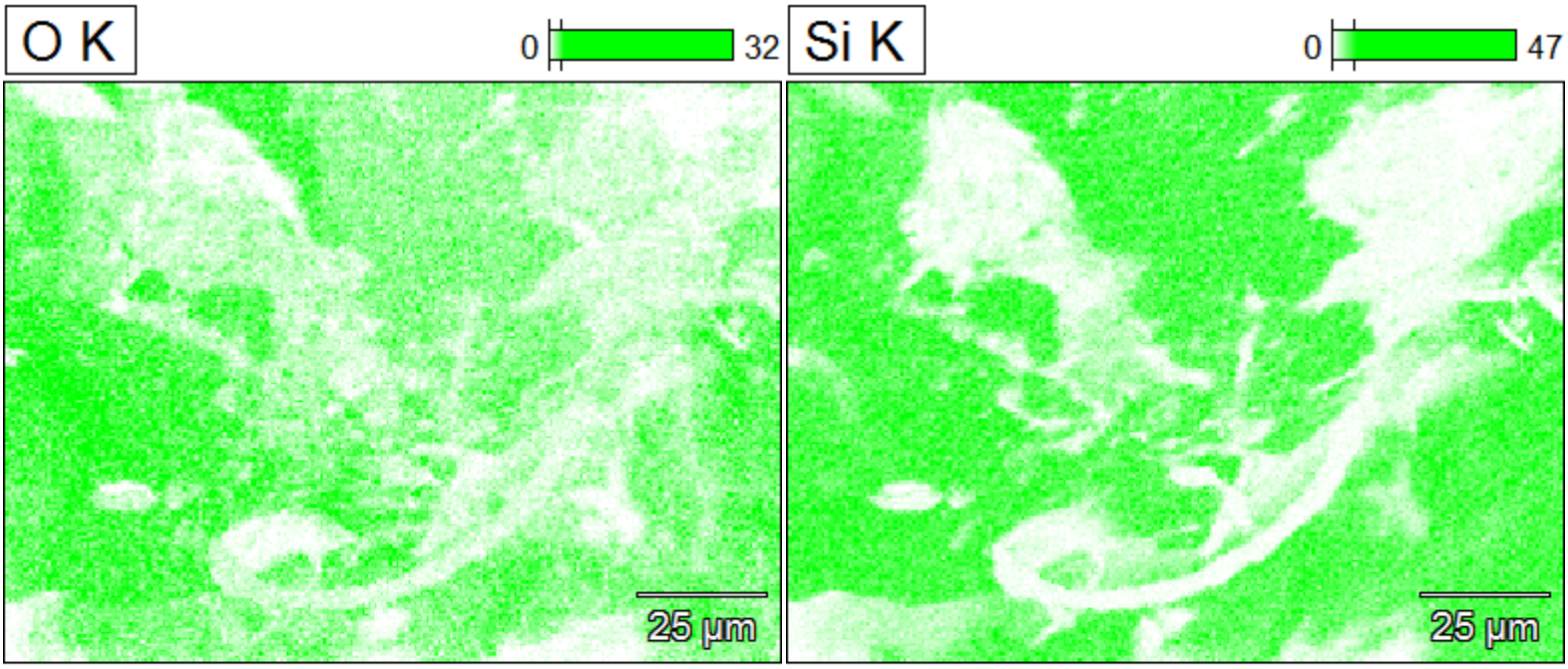
O K
0
32
25 µm
Si K
0
47
25 µm

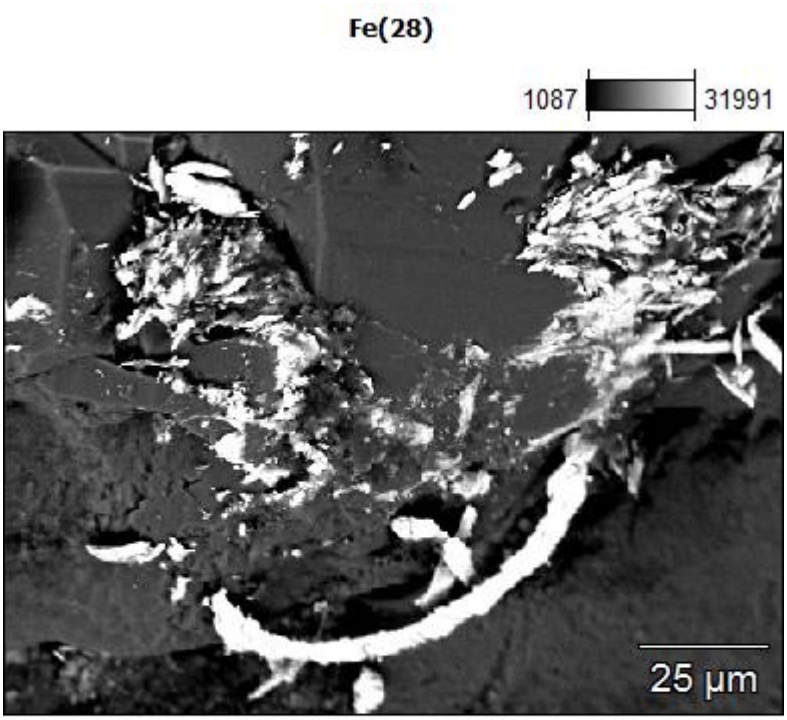

Data Type:	Counts
Image Resolution:	512 by 384
Image Pixel Size:	0.30 µm
Map Resolution:	256 by 192
Map Pixel Size:	0.59 µm
Acc. Voltage:	15.0 kV
Magnification:	800

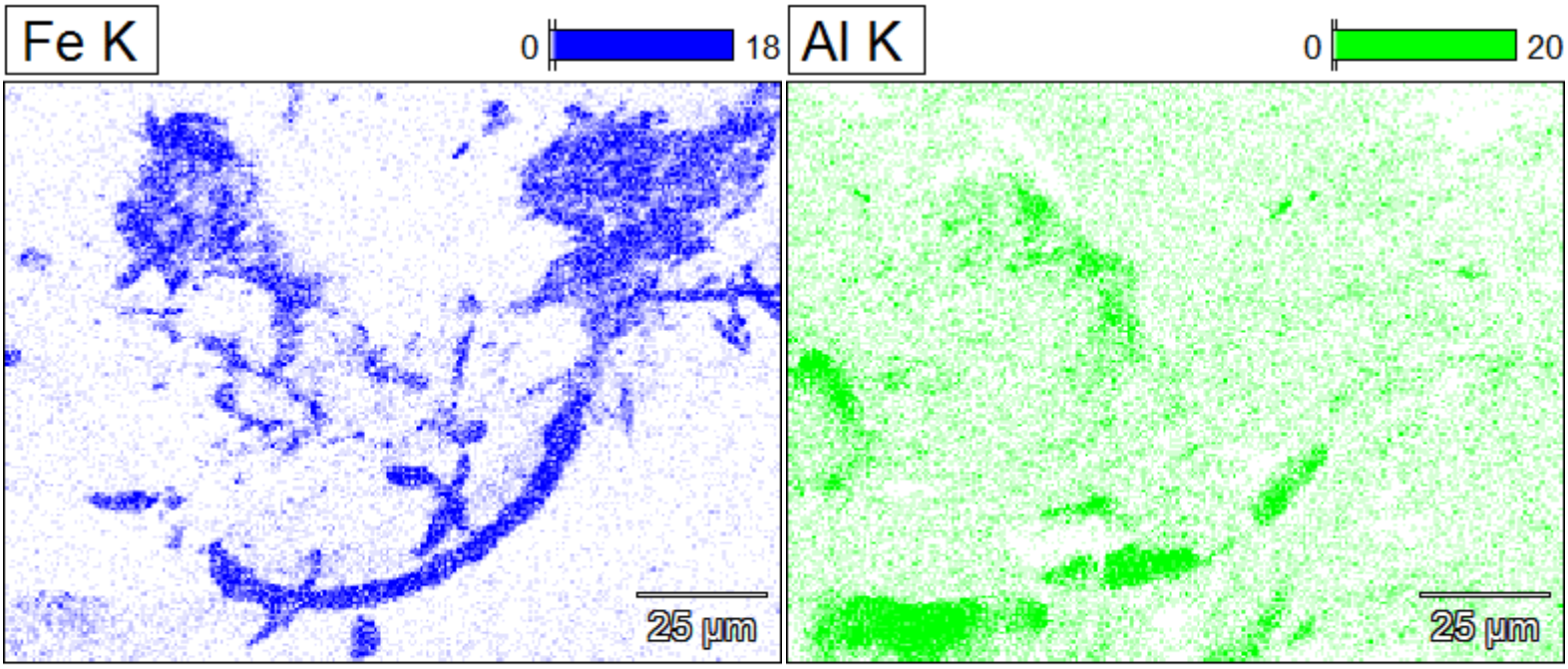
Fe K
0
18
25 µm
Al K
0
20
25 µm

Project: Yang

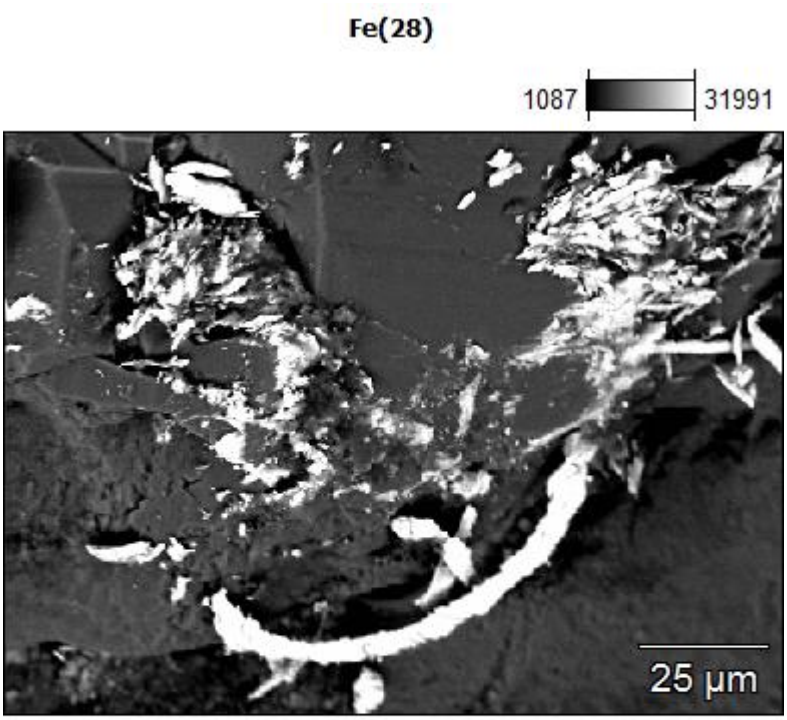

Data Type:	Counts
Image Resolution:	512 by 384
Image Pixel Size:	0.30 µm
Map Resolution:	256 by 192
Map Pixel Size:	0.59 µm
Acc. Voltage:	15.0 kV
Magnification:	800

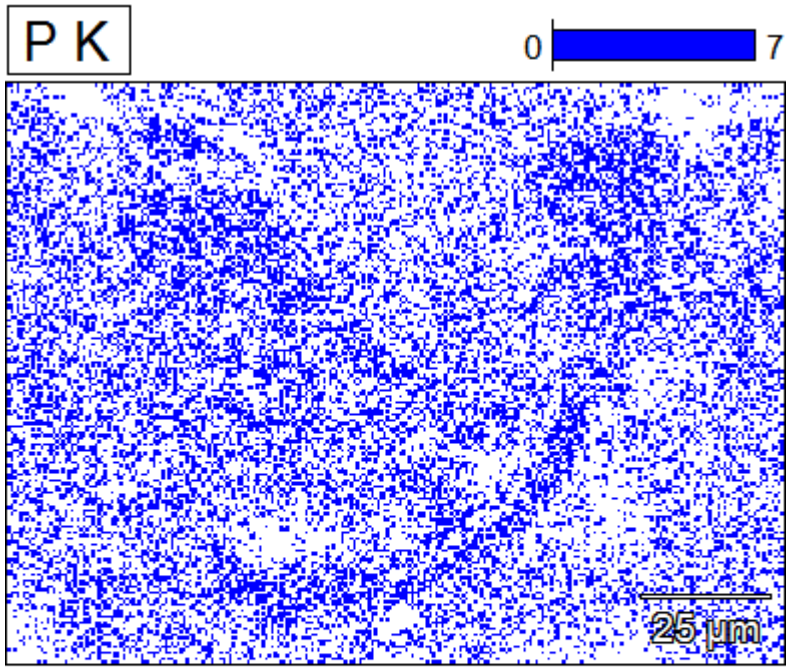
P K
0
7
25 µm

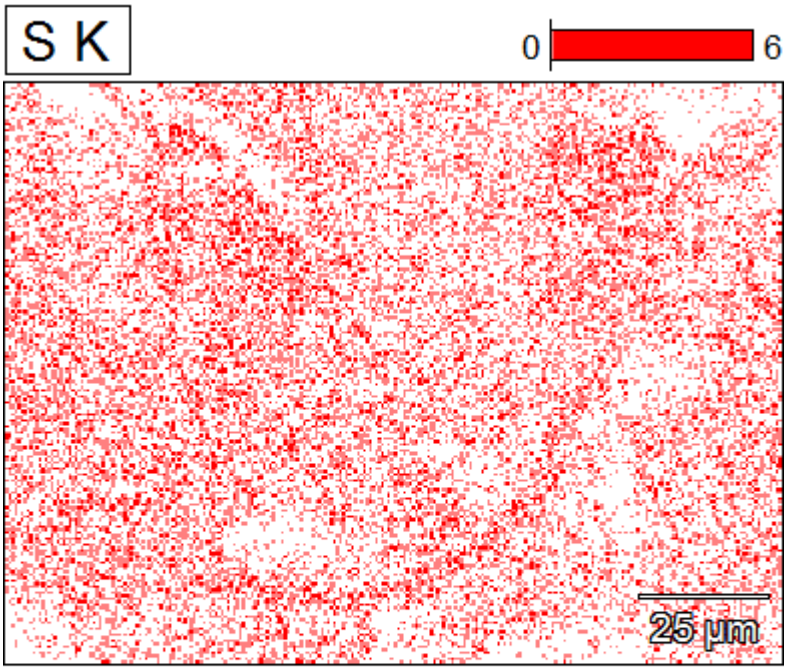
S K
0
6
25 µm

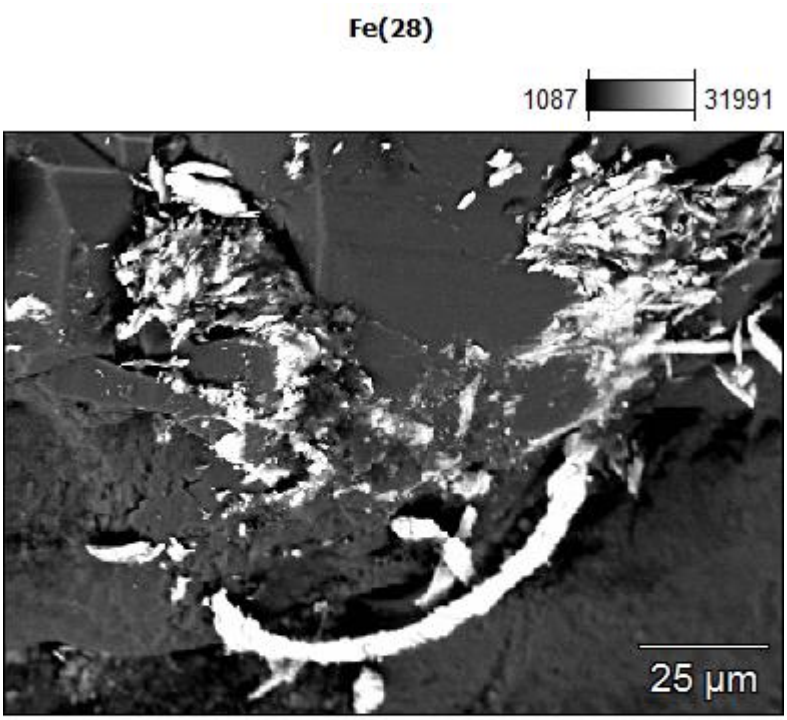

Data Type:	Counts
Image Resolution:	512 by 384
Image Pixel Size:	0.30 µm
Map Resolution:	256 by 192
Map Pixel Size:	0.59 µm
Acc. Voltage:	15.0 kV
Magnification:	800

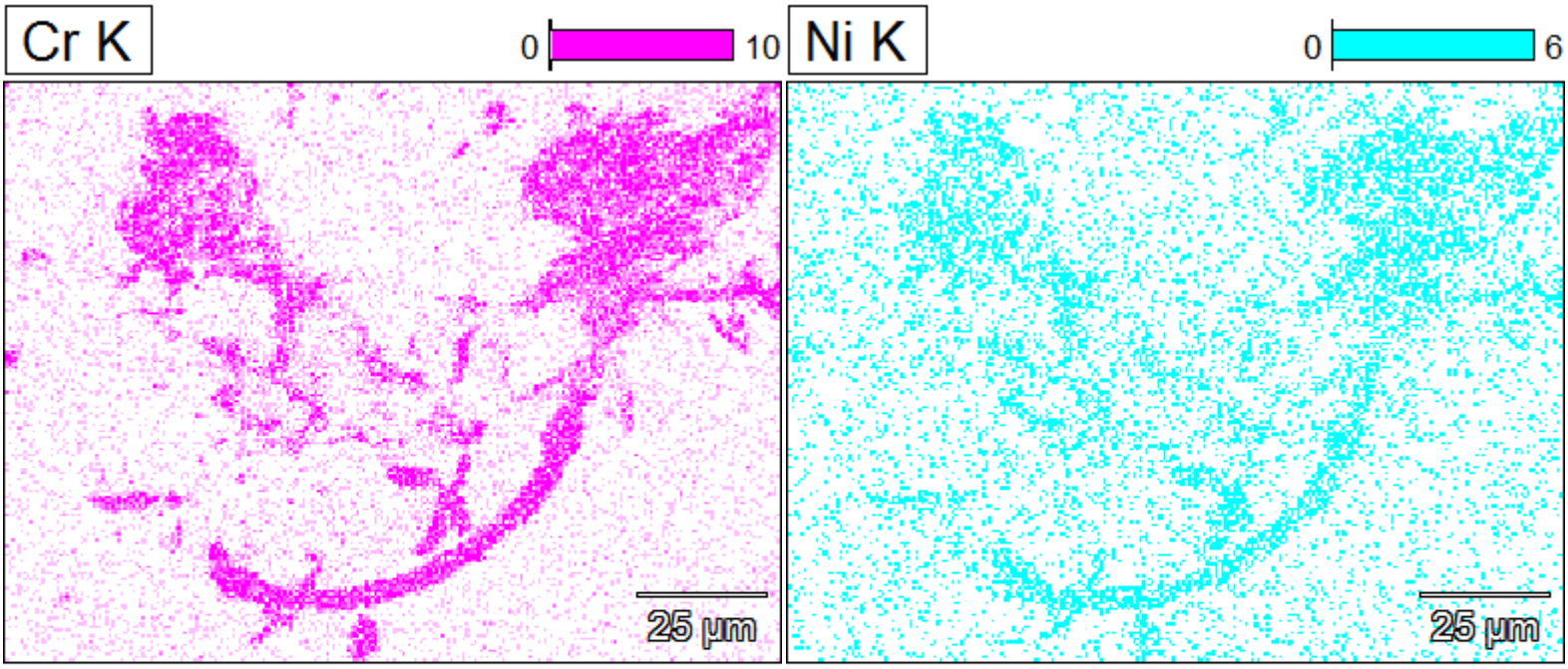
Cr K
0
10
25 µm
Ni K
0
6
25 µm

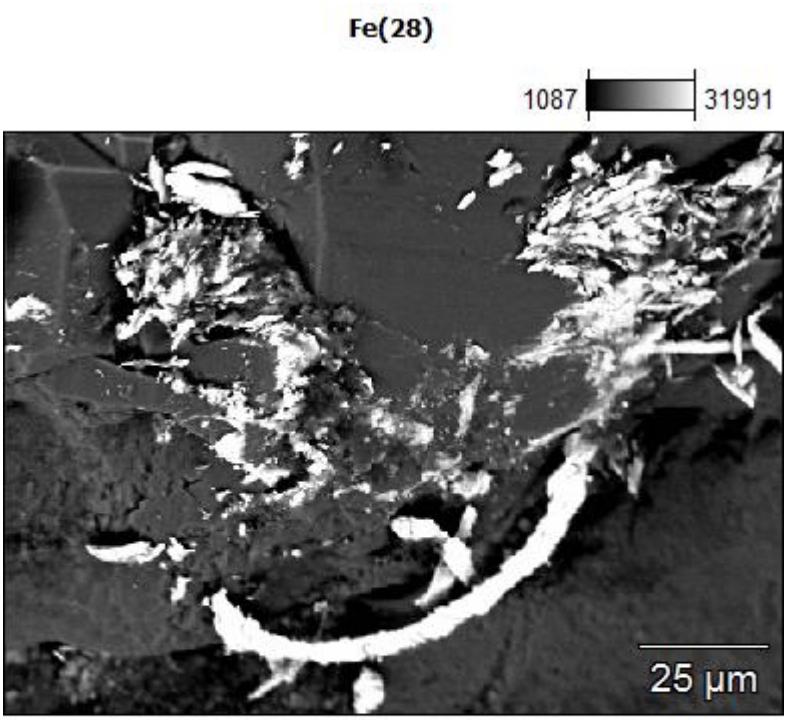

Data Type:	Counts
Image Resolution:	512 by 384
Image Pixel Size:	0.30 µm
Map Resolution:	256 by 192
Map Pixel Size:	0.59 µm
Acc. Voltage:	15.0 kV
Magnification:	800

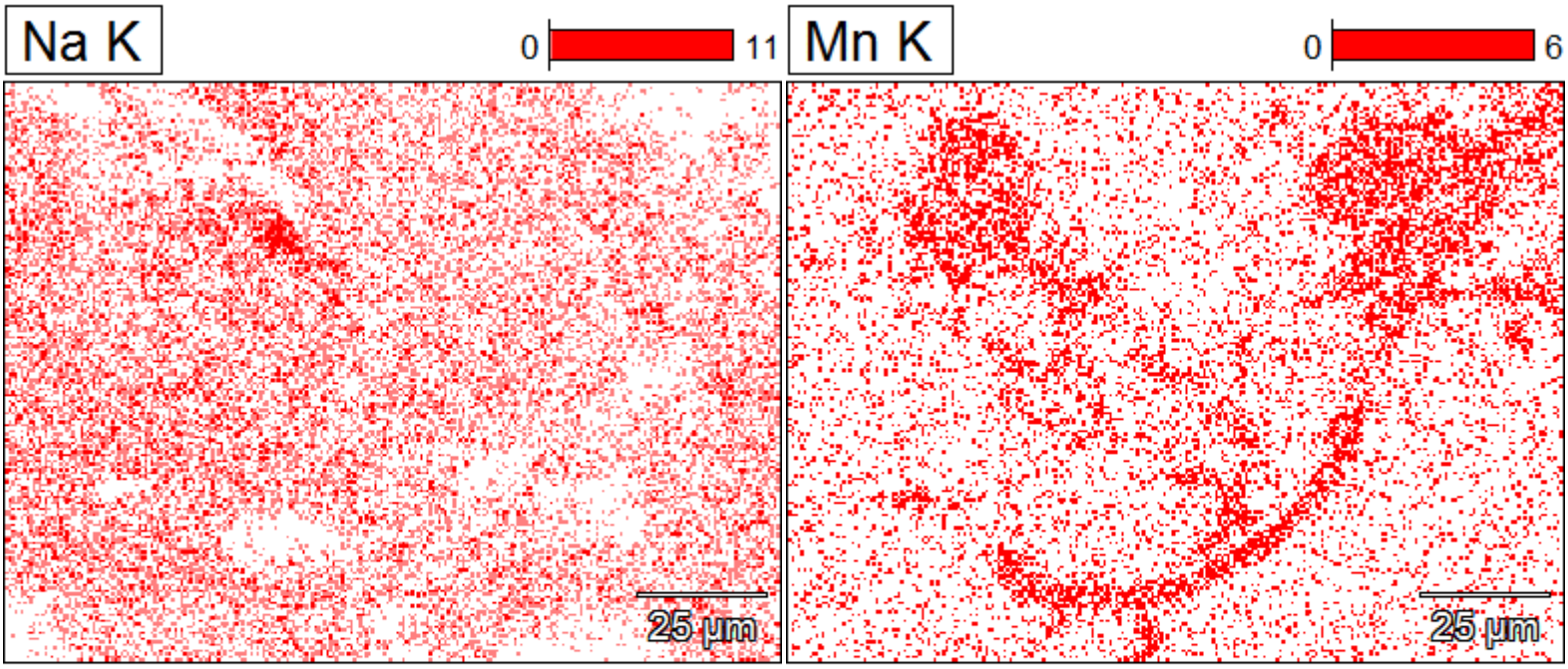
Na K
0
11
25 µm
Mn K
0
6
25 µm

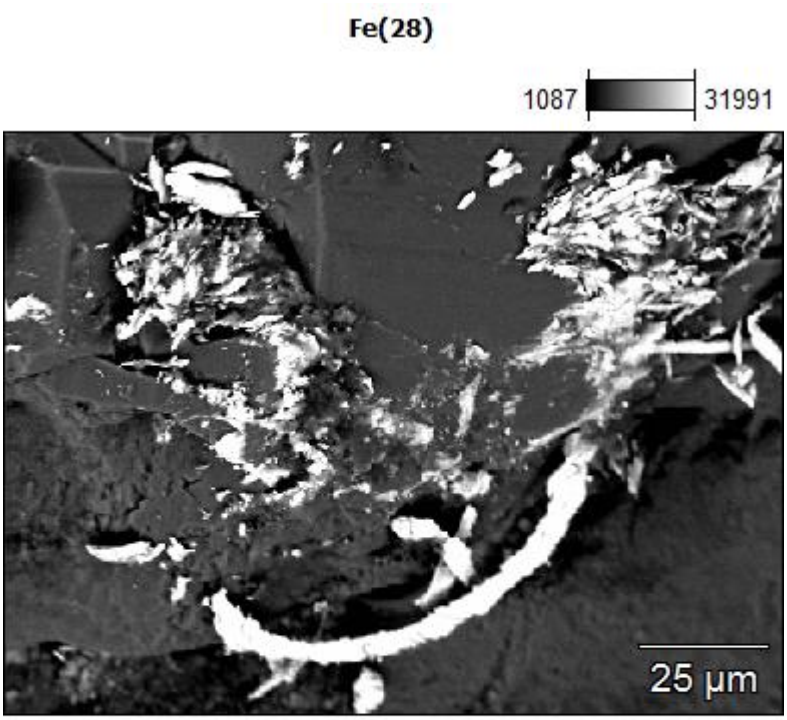

Data Type:	Counts
Image Resolution:	512 by 384
Image Pixel Size:	0.30 µm
Map Resolution:	256 by 192
Map Pixel Size:	0.59 µm
Acc. Voltage:	15.0 kV
Magnification:	800

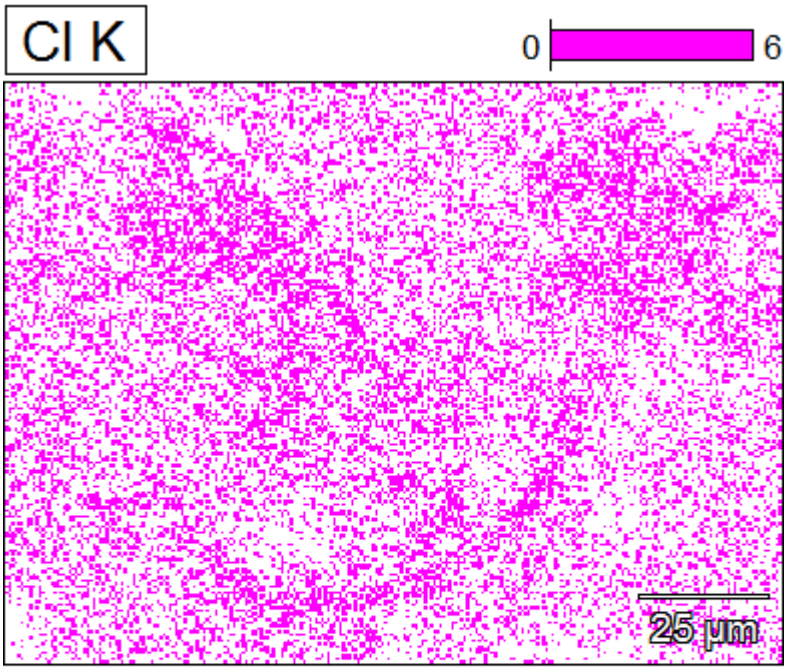
Cl K
0
6
25 µm

Project: Yang

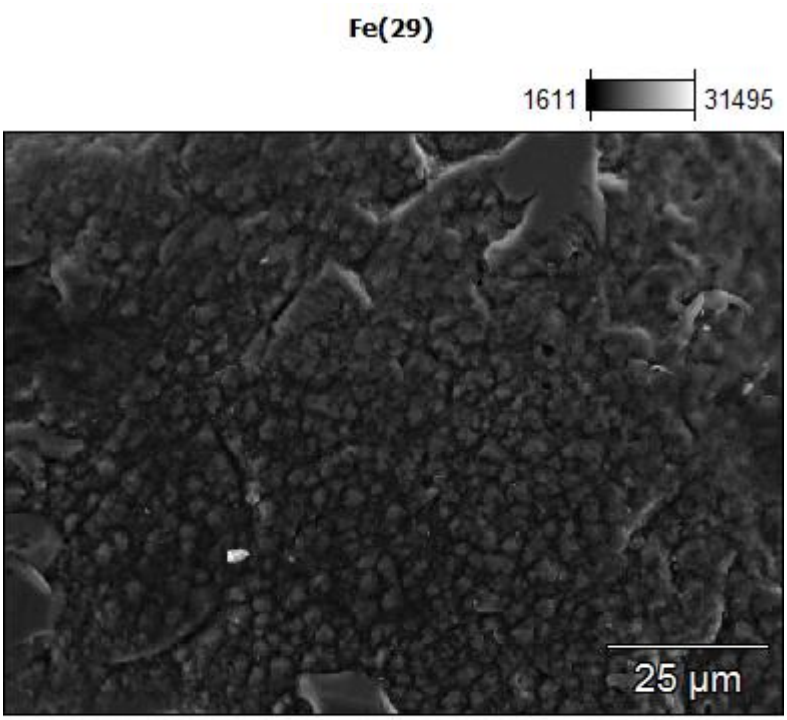

Data Type:	Counts
Image Resolution:	512 by 384
Image Pixel Size:	0.24 µm
Map Resolution:	256 by 192
Map Pixel Size:	0.47 µm
Acc. Voltage:	15.0 kV
Magnification:	1000

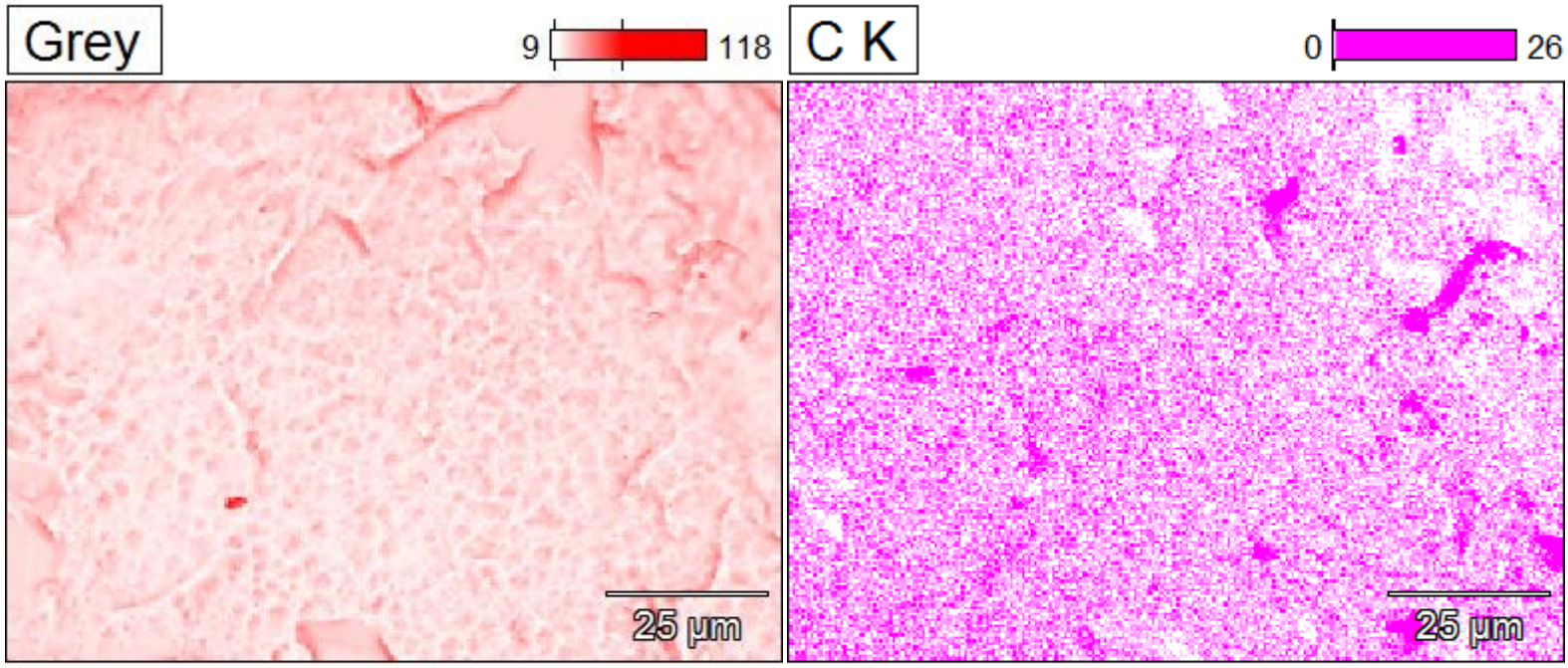
Grey
9
118
25 µm
C K
0
26
25 µm

Project: Yang

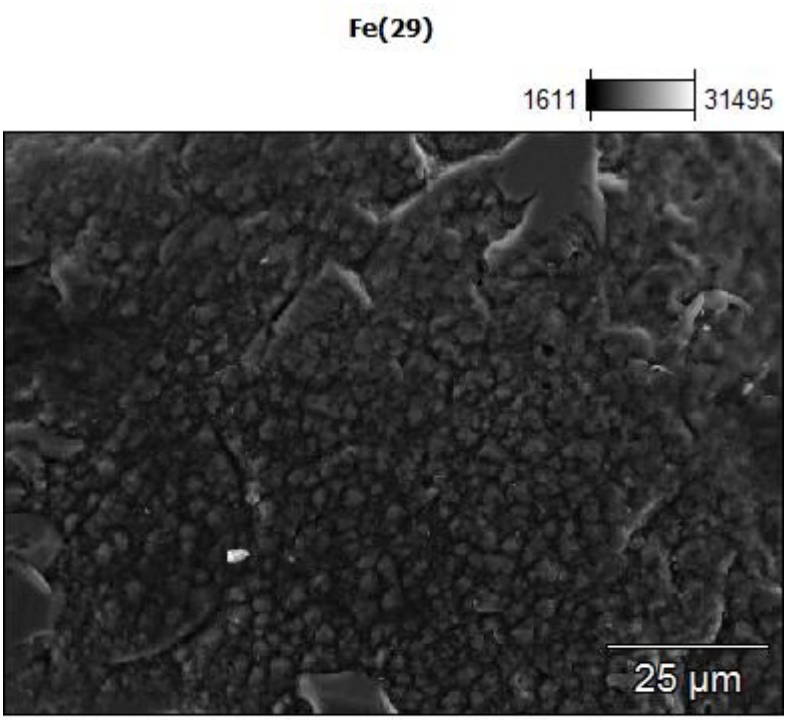

Data Type:	Counts
Image Resolution:	512 by 384
Image Pixel Size:	0.24 µm
Map Resolution:	256 by 192
Map Pixel Size:	0.47 µm
Acc. Voltage:	15.0 kV
Magnification:	1000

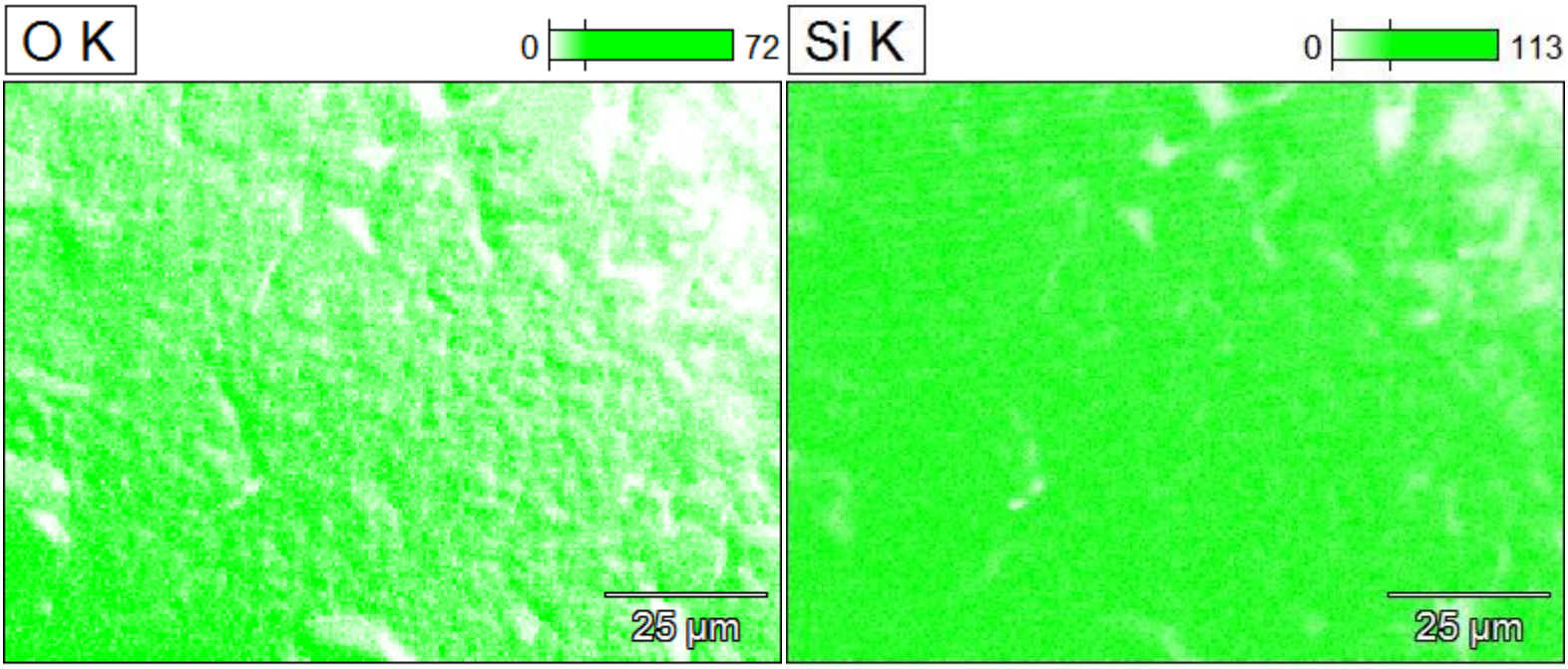
O K
0
72
25 µm
Si K
0
113
25 µm

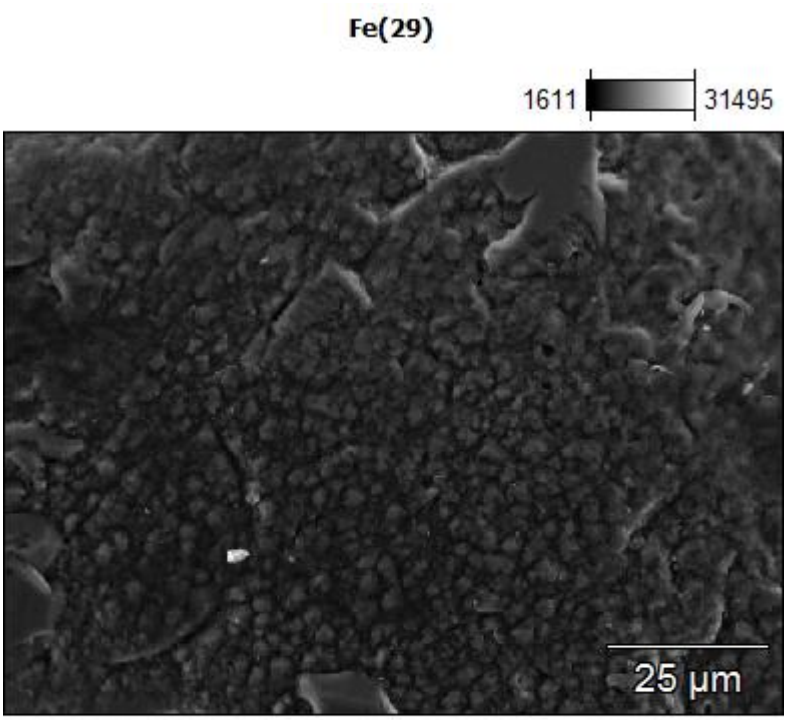

Data Type:	Counts
Image Resolution:	512 by 384
Image Pixel Size:	0.24 µm
Map Resolution:	256 by 192
Map Pixel Size:	0.47 µm
Acc. Voltage:	15.0 kV
Magnification:	1000

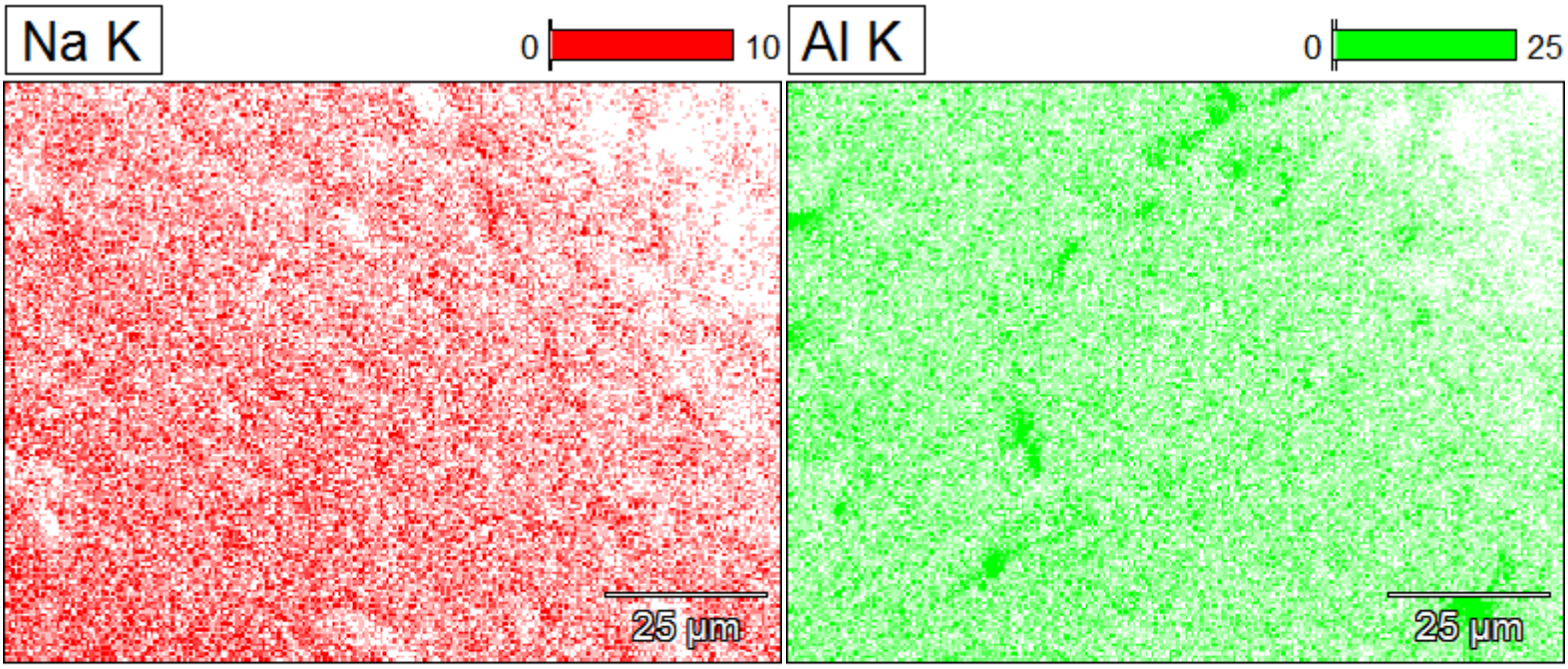
Na K
0
10
25 µm
Al K
0
25
25 µm

Project: Yang

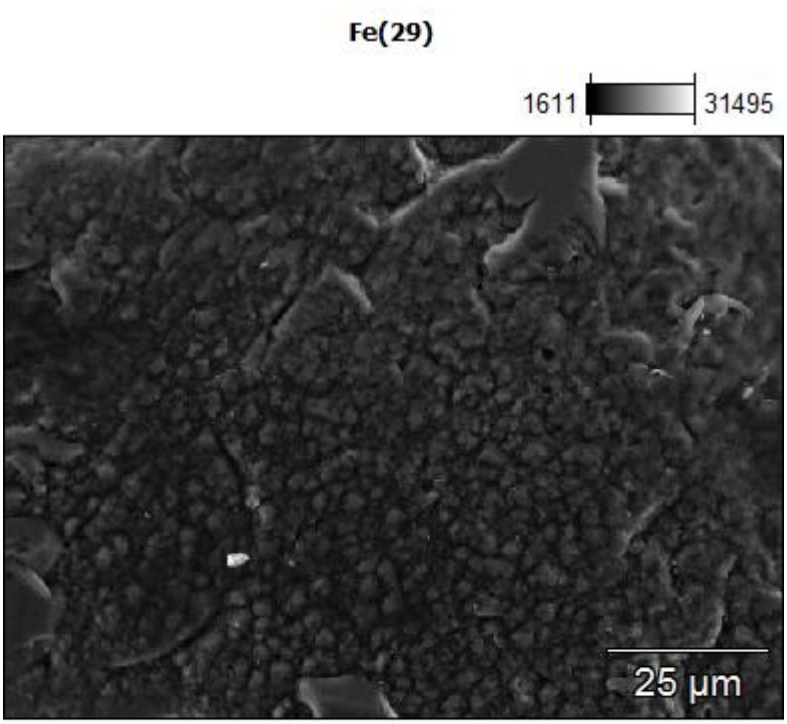

Data Type:	Counts
Image Resolution:	512 by 384
Image Pixel Size:	0.24 µm
Map Resolution:	256 by 192
Map Pixel Size:	0.47 µm
Acc. Voltage:	15.0 kV
Magnification:	1000

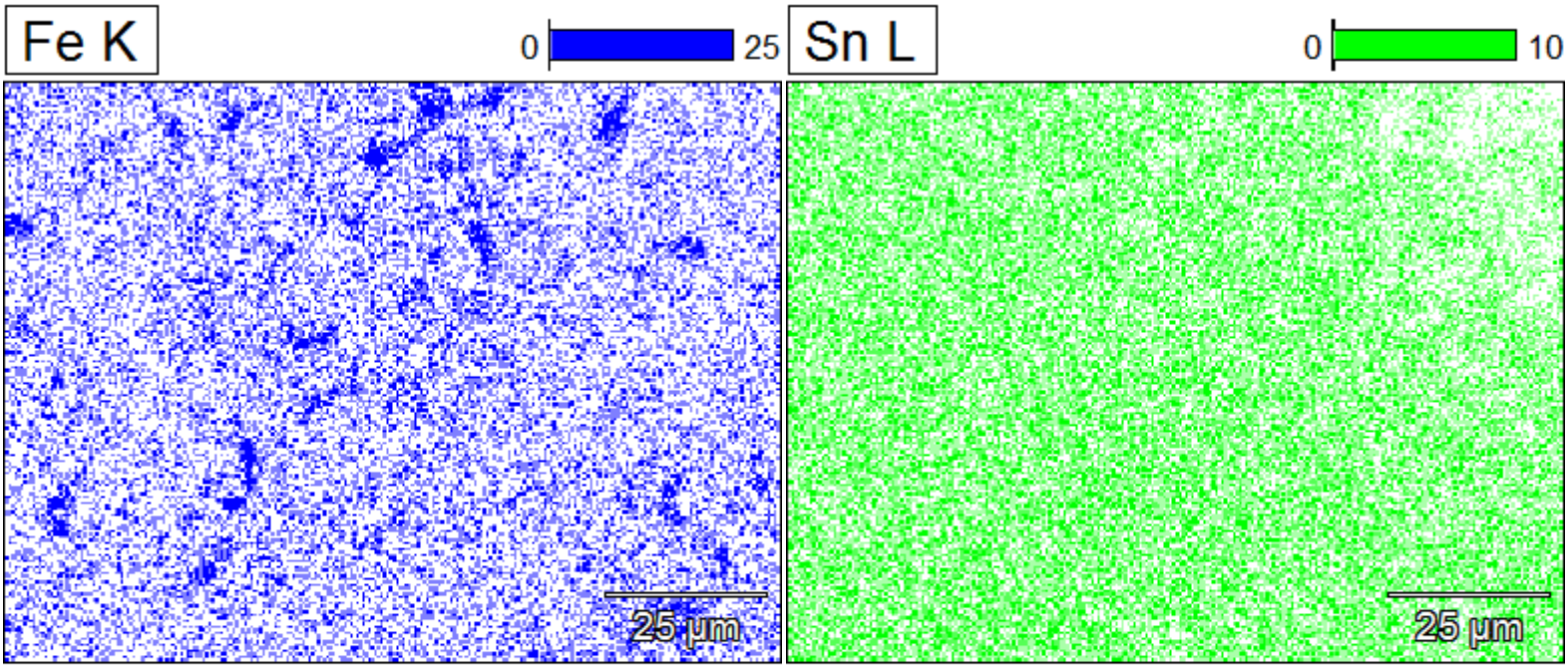
Fe K
0
25
25 µm
Sn L
0
10
25 µm

Project: Yang

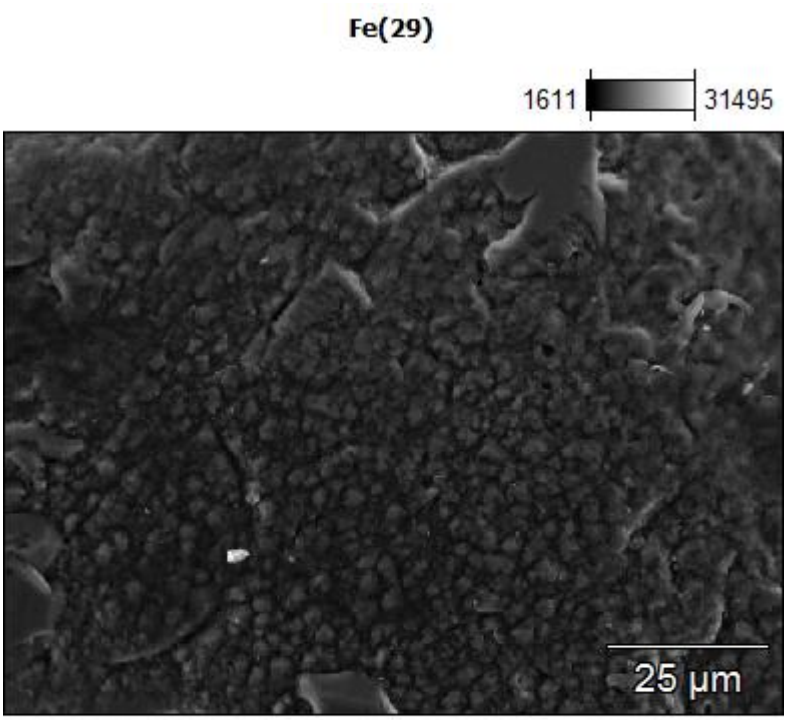

Data Type:	Counts
Image Resolution:	512 by 384
Image Pixel Size:	0.24 µm
Map Resolution:	256 by 192
Map Pixel Size:	0.47 µm
Acc. Voltage:	15.0 kV
Magnification:	1000

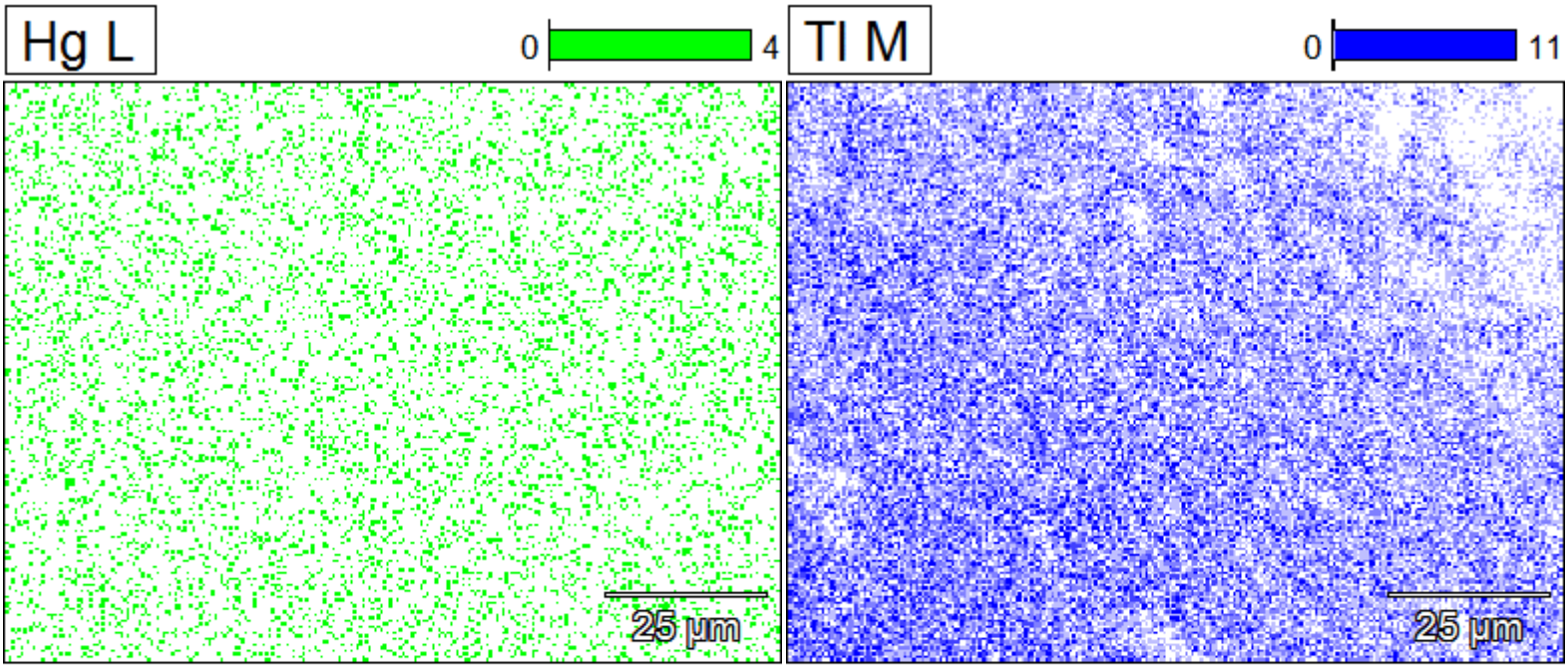
Hg L
0
4
25 µm
Tl M
0
11
25 µm

Project: Yang

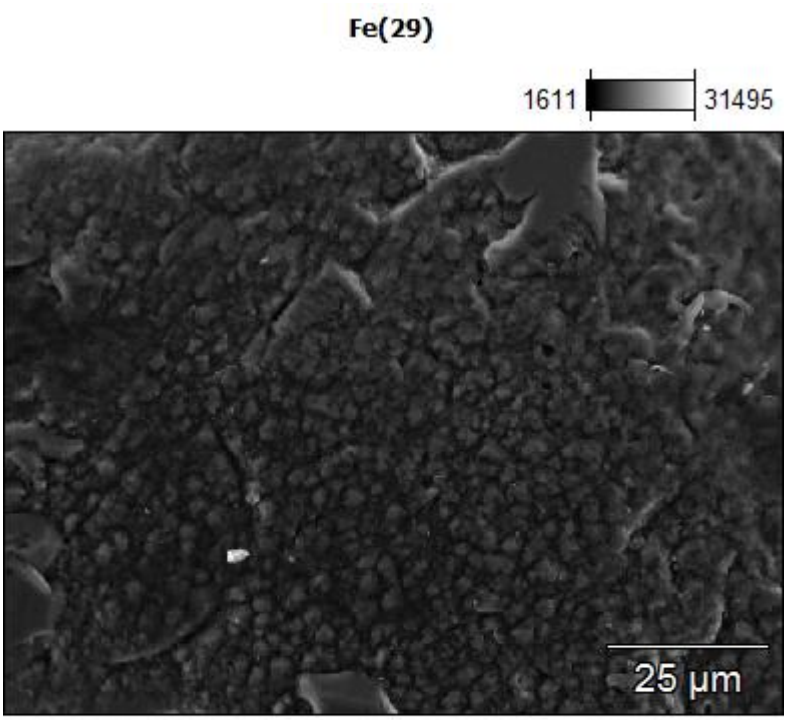

Data Type:	Counts
Image Resolution:	512 by 384
Image Pixel Size:	0.24 µm
Map Resolution:	256 by 192
Map Pixel Size:	0.47 µm
Acc. Voltage:	15.0 kV
Magnification:	1000

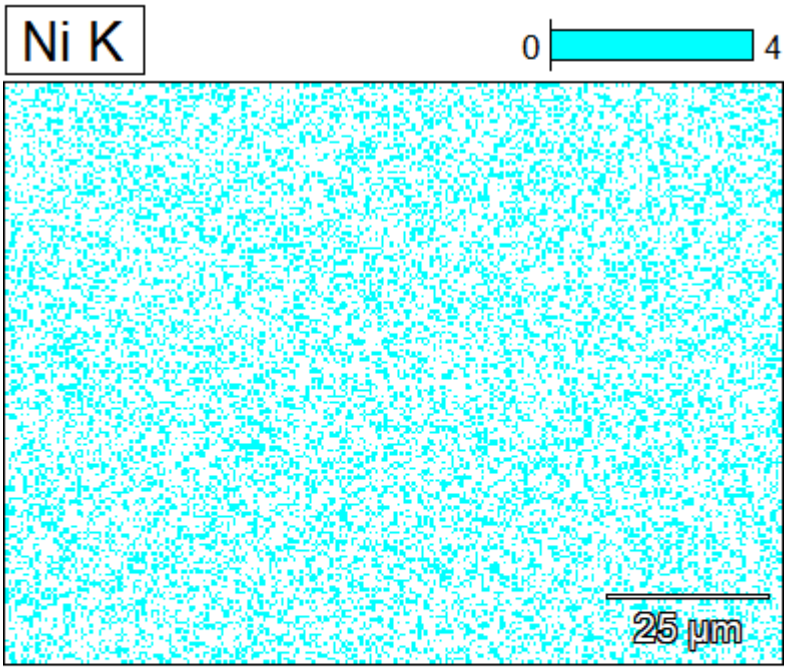
Ni K
0
4
25 µm